Synthesis and Analysis of Substituted Fluxional Carbon Cages

ROBERT ALBERT IVES

Durham University
Department of Chemistry

Synthesis and Analysis of Substituted Fluxional Carbon Cages

Robert A. Ives

A Thesis Submitted for the
Degree of Doctor of Philosophy

September 2024

Dedicated to those who have
helped me the most

My Parents

Rachel E. Ives
Roy A. Ives

My Grandparents

Olive M. Eyre
Francis D. Eyre

Table of Contents

Abstract

Fluxional carbon cages,[1] specifically those of the bullvalene and barbaralane homologues, are of fundamental interest within the organic and materials chemistry, due to their unique 'shapeshifting' properties, a term devised by Bode and co-workers.[2] These 'shapeshifting' properties, which occur due to strain-assisted Cope rearrangements within the molecular framework, allow for a dynamic series of species within their accessible population at ambient temperatures, particularly in the case of bullvalene.[3] In recent years, the efficient access to bullvalene derivatives has increased in diversity, owing to innovative synthetic methods.[4] As such, their use has been investigated in the context of more applications, namely as chemical sensors, polymers and antibiotics.[2b,5] Fluxional carbon cage derivatives with a specific structure-property relationship, particularly those with biological applicability, are infrequent in the literature. Thus, the study of shapeshifting compounds (especially in a biological context) is of fundamental interest.

This thesis examines the synthetic access to both bullvalene and barbaralane, from both a classical and modern perspective, whilst also detailing their applications to date. The 3D shape diversity of bullvalene is then explored, demonstrating how its inherent stereodynamics draw comparisons with commonly used ring systems in medicinal chemistry. Then, fluxional carbon cages are investigated in the biological milieu, exploring how these species behave in biomolecules, such as proteins. The functionalisation of the bullvalene scaffold with redox controllable moieties (i.e. viologens) is then examined, to further probe how bullvalene's shapeshifting properties may have an effect on the physical properties of appended redox active substituents.

1. (a) W. von E. Doering and W. R. Roth, *Tetrahedron,* 1963, **19**, 175; (b) J. G. Henkel and J. T. Hane, *J. Org. Chem.,* 1983, **48**, 3858; (c) P. Alhberg, D. L. Harris and S. Winstein, *J. Am. Chem. Soc.,* 1993, **115**, 7445.
2. (a) A. R. Lippert, J. Kaeobamrung and J. W. Bode, *J. Am. Chem. Soc.,* 2006, **128**, 14738–14739; (b) A. R. Lippert, V. L. Keleshian and J. W. Bode, *Org. Biomol. Chem.,* 2009, **7**, 1529–1532.
3. A. N. Bismillah, B. M. Chapin, B. A. Hussein and P. R. McGonigal, *Chem. Sci.,* 2020, **11**, 324–332.
4. O. Yahiaoui, L. F. Pašteka, B. Judeel and T. Fallon, *Angew. Chem. Int. Ed.,* 2018, **57**, 2570–2574.
5. (a) M. N. Pomfret, P. B. Sun, Z. Huang, A. C. Freund, T. Miyoshi and M. R. Golder, *Angew. Chem. Int. Ed.,* 2023, **62**, e202301695; (b) A. Ottonello, J. A. Wyllie, O. Yahiaoui, S. Sun, R. A. Koelln, J. A. Homer, R. M. Johnson, E. Murray, P. Williams, J. R. Bolla, C. V. Robinson, T. Fallon. T. P. Soares da Costa and J. E. Moses, *Proc. Natl. Acad. Sci. U. S. A.,* 2023, **120**, e2208737120.

Declaration

The scientific work described in this Thesis was carried out at the Department of Chemistry, Durham University between October 2020 – August 2022, and at the Department of Chemistry, University of York between September 2022 – August 2024. Unless otherwise stated, it is the work of the author and has not been submitted in whole or in support of an application for another degree or qualification at this or any other University or institute of learning.

Signed: 

ROBERT A IVES

Date: 6th September 2024

Conferences Attended and Presentations Given

1. RSC Macrocyclic and Supramolecular Chemistry Meeting
   Online, December 2020 | Attended

2. ChiralMat
   Online, March 2021 | Attended

3. International Symposium on SupraBiomolecular Systems
   Online, May 2021 | Attended

4. 7th Prague-Weizmann Advances in Drug Discovery Meeting
   Online, September 2021 | Attended

5. RSC Macrocyclic and Supramolecular Chemistry Meeting
   Online, December 2021 | Attended

6. Early Career Researchers Macrocyclic and Supramolecular Chemistry Meeting
   Loughborough University, UK, June 2022 | Poster Presentation
   A noncovalent model of viologen-inspired adaptive shapeshifting ligands

7. Durham University Postgraduate Chemistry Symposium
   Durham University, UK, June 2022 | Poster Presentation
   Biomacromolecular noncovalent control of shapeshifting molecules

8. 8th Prague-Weizmann Advances in Drug Discovery Meeting
   Francis Crick Institute, UK, September 2022 | Poster Presentation
   A noncovalent model of viologen-inspired adaptive shapeshifting ligands

9. RSC Chemical Biology Meets Drug Discovery
   University of Chemistry and Technology, Prague, Czech Republic, September 2022 | Attended

10. RSC Macrocyclic and Supramolecular Chemistry Meeting
    University of Nottingham, UK, December 2022 | Poster Presentation
    A noncovalent model of viologen-inspired adaptive shapeshifting ligands

11. STEM for Britain 2023
    Houses of Parliament, London, UK, March 2023 | Poster Presentation
    Shapeshifting Molecules: A key to the vault in contemporary drug discovery

12. ELRIG Therapeutic OLIGOs & European Chemical Biology Symposium
    AstraZeneca R&D, Gothenburg, Sweden, May 2023 | Invited Poster Presentation
    Exploring Novel Three-Dimensional Shape Diversity in Shapeshifting Molecules

13. York Award 25th Anniversary Event
    University of York, UK, June 2023 | Invited Oral Presentation
    Shapeshifting Molecules: A key to the vault in contemporary drug discovery

14. RSC Chemical Biology Symposium 2024
    The Royal Society of Chemistry, London, UK, May 2024 | Attended

15. Durham University Postgraduate Chemistry Symposium
    Durham University, UK, June 2024 | Oral Presentation
    Biomacromolecular noncovalent control of shapeshifting molecules

16. Society of Chemical Industry Scholars Showcase
    Society of Chemical Industry, London, UK, July 2024 | Invited Oral Presentation
    Research Leadership in Science

Awards, Grants, Scholarships and Achievements

1. Admitted as an Associate Member of the Royal Society of Chemistry
   November 2020 | Entitled to use the designatory letters AMRSC.

2. Hewley and Burton's Educational Foundation Grant
   December 2020 | Grant of £170 for use towards educational purposes.

3. St. Johns College, Durham University Student Opportunities Fund
   February 2021 | Grant of £100 to attend the International Symposium on SupraBiomolecular Systems 2021.

4. St. Johns College, Durham University Student Opportunities Fund
   February 2022 | Grant of £250 to attend the 8th Prague–Weizmann Drug Advances in Drug Discovery Meeting at the University of Chemistry and Technology, Prague, Czech Republic in September 2022.

5. RSC Advances Poster Prize
   June 2022 | Awarded 2nd place poster presentation prize at the Department of Chemistry Annual Postgraduate Research Symposium, Durham University.

6. Royal Society of Chemistry Chemical Science Photographic Award
   June 2022 | Awarded a photographic chemistry award at the Department of Chemistry Annual Postgraduate Research Symposium, Durham University.

7. Durham University Postgraduate Opportunities Fund Award
   June 2022 | Competitive grant of £100 to attend the 8th Prague–Weizmann Drug Advances in Drug Discovery Meeting at the University of Chemistry and Technology, Prague, Czech Republic in September 2022.

8. Prague–Weizmann Advances in Drug Discovery Scholarship
   June 2022 | Competitive scholarship equating to £345 to attend the 8th Prague–Weizmann Advances in Drug Discovery Meeting at the University of Chemistry and Technology, Prague, Czech Republic in September 2022.

9. Durham University Postgraduate Participation Fund
   August 2022 | Competitive grant equating to £115 to assist attendance of the 8th Prague–Weizmann Advances in Drug Discovery Meeting at the University of Chemistry and Technology, Prague, Czech Republic in September 2022.

10. 8th Prague–Weizmann Advances in Drug Discovery Poster Prize
    September 2022 | Presented with the 1st poster prize and awarded fully-funded participation in the European Chemical Biology Symposium 2023.

11. EU-Openscreen European Chemical Biology Symposium Scholarship
    September 2022 | Competitive scholarship equating to £1000 to attend and participate in the European Chemical Biology Symposium (ECBS) 2023 held at AstraZeneca R&D, Gothenburg, Sweden in May 2023.

12. St. Johns College, Durham University Student Opportunities Fund
    February 2023 | Grant of £200 to assist attendance of the European Chemical Biology Symposium (ECBS) 2023 held at AstraZeneca R&D, Gothenburg, Sweden in May 2023.

13. Associate Fellowship of the Higher Education Academy
    October 2023 | Awarded by Advance HE and Durham University for demonstrating and meeting the criteria of descriptor 1 of the UK Professionals Standards Framework for teaching and supporting learning in higher education. Entitlement to use post-nominal letters AFHEA.

14. STEM for Britain 2023 Finalist
    March 2023 | Shortlisted as 1 of 10 finalists in Great Britain and invited to present ground-breaking research in chemistry to Members of both Houses of Parliament at Westminster, London.

15. Appointed Chair of the Yorkshire and Humber Regional Interest Group, Society of Chemical Industry
    May 2023 | Providing leadership and direction to the group, which involves organising events within the region, attending chair committee meetings to discuss our regional group activities and to aid our groups vision, mission and strategic direction.

16. Co-opted on to the Careers Governance Committee, Society of Chemical Industry (reporting to the Board of Trustees)
    July 2023 | The Careers Committee helps to coordinate the wide ranging activities at SCI that support the career development of SCI members, where I am lead-organiser of the Day of Science and Careers (National STEM Centre, University of York).

17. Co-opted on to the Membership Governance Committee, Society of Chemical Industry (reporting to the Board of Trustees)
    November 2023 | The Membership Committee helps to coordinate the wide ranging activities at SCI that support the membership of SCI members.

18. Yorkshire Young Achievers Foundation Grant
    November 2023 | Competitive grant of £250 awarded to support my PhD studies. Award generally awarded for educational development purposes of young people under the age of 35 who are connected to Yorkshire.

19. Admitted as a Member of the Royal Society of Chemistry
    November 2023 | Entitled to use the designatory letters MRSC.

20. St. Johns College, Durham University Student Opportunities Fund
    February 2024 | Grant of £175 to attend of the Royal Society of Chemistry Chemical Biology Symposium 2024, held at the Royal Society of Chemistry, Burlington House, London in May 2024.

21. Royal Society of Chemistry Chemists' Community Fund
    February 2024 | Grant of £2100 awarded to support the completion of my PhD studies.

22. Elected to the Membership Governance Committee, Society of Chemical Industry (reporting to the Board of Trustees)
    July 2024 | The Membership Committee helps to coordinate the wide ranging activities at SCI that support the membership of SCI members.

Acknowledgments

I acknowledge the following for their contribution and advice over the course of this degree and thesis:

My Advisor: Prof. Paul R. McGonigal

Thank you for giving me the opportunity to work under your supervision. I am grateful for your support, advice and supervision throughout the course of challenging projects. I am incredibly appreciative of the freedom you have given me when trying to tailor our research towards my interests at the chemistry-biology interface, whilst still providing valuable input. Thank you for continuously helping me to improve and progress as a researcher and scientist.

Durham Collaborators: Prof. Ehmke Pohl, Dr. Stefanie Freitag-Pohl and the Pohl Group.

A special thank you for your continuous encouragement and generosity with your time, to teach and guide me into the world of protein crystallography and structural biology. I am extremely grateful that our research paths crossed through this inter-disciplinary endeavour.

My Former Advisors: Dr. Alyssa-Jennifer Avestro, Prof. Marek Brzozowski, Dr. Irena G. Stará and Dr. Ivo Starý.

To my former academic advisors; thank you for your ever-lasting support, words of kind reassurance and pockets of sound advice when it has been required.

York Collaborators: Dr. Conor Rankine, Luke Corbett, Dr. Chris H. Hill and Dr. Martin A. Fascione

Thank you for your efforts towards achieving success in our inter-disciplinary studies. Together, we have achieved some important results that will help to achieve success in related future studies.

The McGonigal Group and Avestro Group

I thank and acknowledge any contribution that has been made towards this thesis. Any specific contributions are stated at the start of each Chapter. Thank you for the support!

Technical Staff | Durham University and the University of York

I thank and acknowledge the contribution the technical staff have made towards the NMR, mass spectrometry and crystallography data collected for this thesis.

Family and Friends

Thank you to my parents, family and friends who have supported me from the beginning and trusted the academic journey I have chosen to follow. A special mention must go to my mother (Rachel), father (Roy) and step-dad (Gary) who have been of constant support. Thank you to all of those who have supported me through this PhD experience – we did it!

My Partner, Emily

Thank you for constantly being by my side, offering your endless support and making the PhD experience in Durham and York so much more memorable. I would definitely not have finished this journey without you! You have been there for me through the struggles and successes – and for that, I will be forever grateful.

List of Abbreviations

Å	Angstrom
A	Alanine
Ac	Acetyl
APCI	Atmospheric Pressure Chemical Ionisation
ASAP	Atmospheric Solids Analysis Probe
BB	Barbaralane
BBL	Barbaralol
BBO	Barbaralone
BDT	Bicyclo[4.2.2]deca-2,4,7,9-tetraene
BINOC	Binaphthyldioxacyclodecyne
Bpin	Boronic pinacol ester
BSA	Bovine Serum Albumin
BV	Bullvalene
BVO	Bullvalone
CHT	Cycloheptatriene
COSY	Correlated Spectroscopy
COT	Cyclooctatetraene
CV	Cyclic Voltammetry
d	doublet
δ	Chemical Shift
D	Aspartic acid
DCE	1,2-Dichloroethane
DFT	Density Functional Theory
DLS	Diamond Light Source
DMF	N,N-Dimethylformamide
DMSO	Dimethylsulfoxide
dppe	1,2-Bis(diphenylphosphino)ethane
E	Glutamic acid
eq.	Equivalents
ESI	Electrospray ionisation
Et	Ethyl
EtOAc	Ethyl acetate
EV	Exit Vector
F	Phenylalanine
FBDD	Fragment Based Drug Discovery
FPT	Freeze-Pump-Thaw

GlcNAc	*N*-acetylglucosamine
HMBC	Heteronuclear Multiple Bond Correlation
HR	High Resolution
HSA	Human Serum Albumin
HSQC	Heteronuclear Single Quantum Coherence
J	Coupling constant in Hz
kDa	kilodalton
L	Leucine
LBV	Lumibullvalene
m	multiplet
M^+	Molecular Ion
Me	Methyl
MeCN	Acetonitrile
MS	Mass Spectrometry
MurNAc	*N*-acetylmuramic acid
MV	Methyl Viologen
M_2V	Dimethyl Viologen
$MV^{+\bullet}$	Methyl Viologen radical cation
$M_2V^{+\bullet}$	Dimethyl Viologen radical cation
MV^{2+}	Methyl Viologen dication
M_2V^{2+}	Dimethyl Viologen dication
MW	Molecular Weight
MYR	Myristate
NMR	Nuclear Magnetic Resonance
PEG	Polyethylene glycol
PDB	Protein Data Bank
PDC	Pyridinium dichromate
Ph	Phenyl
PMI	Principal moments of inertia
ppm	parts per million
q	quartet
R	Arginine
rt	room temperature
S	Serine
s	singlet
SA	Serum Albumin
SBV	Semibullvalene
SCF	Self-consistent field
SEC	Size Exclusion Chromatography
SOMO	Singly Occupied Molecular Orbital

t	triplet
TBS	*tert*-Butyldimethylsilyl
TEG	Tetraethylene glycol
TFE	2,2,2-Trifluoroethanol
THF	Tetrahydrofuran
TLC	Thin-layer chromatography
Ts	*para*-Toluenesulfonyl
TsCl	Toluenesulfonylchloride
UV	Ultraviolet
UV-Vis	Ultraviolet-Visible
V	Valine
$V^{+\bullet}$	Viologen radical cation
V^{2+}	Viologen dication
VT	Variable temperature
W	Tryptophan
XRD	X-ray diffraction
Y	Tyrosine

General Experimental Methods

Materials: All starting materials and reagents were sourced from commercial suppliers (Sigma-Aldrich, Acros Organics, Fluorochem or Alfa Aesar) and were used without further purification.

Instrumentation and Analytical Techniques: Analytical thin-layer chromatography (TLC) was performed on neutral aluminium sheet silica gel plates (Fluka, 60778-25EA) and visualised under UV irradiation (254 nm). Nuclear magnetic resonance (NMR) spectra were recorded using a Bruker Advance (III)-400 (^{1}H 400.130 MHz and ^{13}C 100.613 MHz), Varian Inova-500 (^{1}H 500.130 MHz and ^{13}C 125.758 MHz), Varian VNMRS-600 (^{1}H 600.130 MHz and ^{13}C 150.903 MHz) a Varian VNMRS-700 (^{1}H 700.130 MHz and ^{13}C 176.048 MHz), or a Joel ECS-400 spectrometer (^{1}H 400 MHz and ^{13}C 101 MHz), at a constant temperature of 298 K unless otherwise stated. For variable-temperature (VT) measurements, operating temperatures were calibrated using an internal calibration solution of MeOH and glycerol. Chemical shifts (δ) are reported in parts per million (ppm) relative to the signals corresponding to residual non-deuterated solvents $CDCl_3$: δ = 7.26 or 77.16, CD_3OD: δ = 3.31 or 49.00, CD_3CD_2OD: δ = 3.56 or 56.96. Coupling constants (*J*) are reported in Hertz (Hz). ^{13}C NMR Experiments were proton-decoupled, unless otherwise stated. Assignments of ^{1}H and ^{13}C NMR signals were accomplished by two-dimensional NMR spectroscopy (COSY, NOESY, HSQC, HMBC). NMR spectra were processed using MestReNova version 14. Data are reported as follows: chemical shift; multiplicity; coupling constants; integral and assignment. Low-resolution atmospheric solids analysis probe (ASAP)-MS were performed using a Waters Xevo QTOF equipped with an ASAP. High-resolution electrospray (HR-ESI) and ASAP (HR-ASAP) mass spectra were measured using a Waters LCT Premier XE high resolution, accurate mass UPLC ES MS (also with ASAP ion source). Melting points (M.P.) were recorded using a Gallenkamp (Sanyo) apparatus and are uncorrected. Purification of all proteins was conducted using a Cytiva HiLoad™ 16/600 Superdex™ 200 prep grade (pg) set up, unless otherwise stated.

Thesis Layout

In this thesis, Chapter 1 provides an introduction to fluxional carbon cages, outlining their physical organic properties. In particular, the traditional syntheses of bullvalene and barbaralane are discussed, and their modern synthetic access is also explored. Furthermore, the control and applications of bullvalene and barbaralane are described in more detail. Next, in Chapter 2, the shape diversity of bullvalene is explored. Here, the stereodynamic properties of bullvalene are analysed using computational methods that allow for comparisons with commonly used rings systems in medicinal chemistry. In Chapter 3, shapeshifting ligands are investigated within biomolecules, in an attempt to understand their behaviour in biological environments. The synthesis and noncovalent control of adaptive shapeshifting ligands is carried out as a proof of concept investigation. Lastly, Chapter 4 describes various synthetic routes towards obtaining viologen-inspired shapeshifting ligands for use in macrocyclic noncovalent control. Insights from these studies have allowed for a greater understanding of plausible functionalisation on shapeshifting frameworks.

CHAPTER 1

FLUXIONAL CARBON CAGES: SYNTHESIS, PROPERTIES AND APPLICATIONS

Synopsis

This chapter presents the diversity within the fluxional carbon cage family, elaborating on their structural properties, thus providing an understanding as to why these structural variations allow for differences in their 'shapeshifting' properties and their ability to occupy a range of degenerate and nondegenerate isomers within a given population. This is then followed by a more thorough examination of the fluxional carbon cages, namely bullvalene and barbaralane. The seminal, more traditional syntheses of bullvalene are then reviewed, followed by the more recent advances to access bullvalene derivatives. The next section focusses similarly on the classical and modern advances to barbaralane and its substituted derivatives. Thereafter, the applications of fluxional carbon cages are discussed, offering an evaluation of the use of bullvalene as a chemical sensor and in functional materials. Lastly, the study and regulation of nondegenerate barbaralane mixtures are assessed.

1.1 Fluxional Carbon Cages

Fluxional carbon cages are a versatile class of compounds with a wide range of potential applications such as chemical sensing[1] and binding.[2] Bullvalene (**BV**),[3–6] the barbaralyl cation (**BB**$^+$),[7–10] barbaralane (**BB**),[11–13] bullvalone (**BVO**),[14] barbaralone (**BBO**)[14] and semi-bullvalene (**SBV**)[15,16] (see Figure 1.1) are key homologues of fluxional tricyclic carbon cages, colloquially termed 'shapeshifting' molecules. The aforementioned shapeshifting molecules possess the ability to undergo rapid and reversible pericyclic rearrangements giving rise to a collection of constitutional isomers. For example, **BV** and the **BB**$^+$ have approximately 1.2 million and 180 000 isomers, respectively (see Figure 1.1).[17] Resultantly, when these carbon-based skeletons are functionalised, many more distinct molecular shapes can be adopted, subject to the isomeric distribution and conformational spatiality.

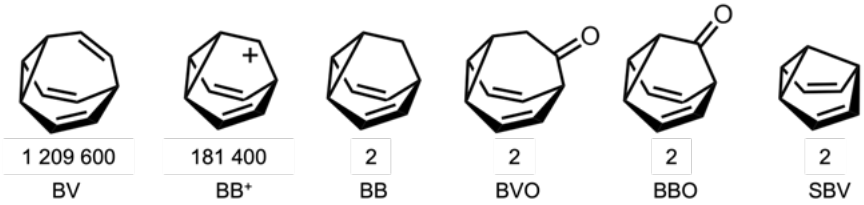

Figure 1.1. Structures of **BV**, **BB**$^+$, **BB**, **BVO**, **BBO** and **SBV**, whereby the number below represents the number of accessible degenerate isomers at ambient temperature.[17]

Fluxional carbon cages are exemplary as they demonstrate that a dynamic structural collection of compounds can co-exist from a single molecule. Over the past decade, research has revealed the potential for their chemical structures and fluxional properties to be exploited in response to an environmental change. For example, previous work has investigated the use of fluxional carbon cages as chemical sensors for biologically active compounds.[1,18] Most recently, there have been multiple applications exhibited for **BV** in the literature; these include use in polymeric materials[19] and as part of novel antibiotics.[20]

1.2 Dynamic Pericyclic Rearrangements

Dynamic pericyclic rearrangements provide the basis for constitutional dynamics that inherently occur within fluxional carbon cage frameworks. Specifically, the 'shapeshifting' properties adhered by fluxional carbon cages transpire due to strain-assisted Cope rearrangements. In 1940, Cope and co-workers reported conditions revealing initial observations of the Cope rearrangement[21] – a [3,3]-sigmatropic rearrangement. The Cope rearrangement is demonstrated on a 1,5-diene (**1.1**) whereby heating the species to 150 °C results in a single step, reversible rearrangement, proceeding through a concerted transition state (**1.2**). In this rearrangement process (Scheme 1.1), one σ-bond (C_3–C_4) and two π-bonds (C_1–C_2 and C_5–C_6) are broken and migration results in the formation of two π-bonds (C_2–C_3 and C_4–C_5) and one σ-bond (C_1–C_6) to form the rearrangement product (**1.3**).

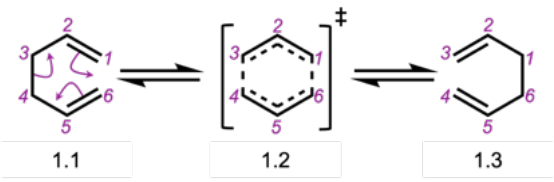

Scheme 1.1. Representative Cope rearrangement of a 1,5-diene (**1.1**) through a concerted transition state (**1.2**), resulting in the rearrangement product (**1.3**). The rearrangement proceeds at T = 150 °C.

The fluxionality resulting from the Cope rearrangement allows **BV** and $\mathbf{BB^+}$ in particular to rapidly interconvert through a mixture of constitutional isomers. **BV** isomers can interconvert *via* the result of a σ-bonded atom of the cyclopropane ring, flanked by one or more vinyl π-electron systems, which migrates to a new location resulting in the redistribution of the C–C bonds within the molecule forming two new π-bonds. The cyclopropane is appended to a methine group by three bridging vinyl moieties in **BV** which permits the interconversion between 1 209 600 degenerate valence isomers (Figure 1.2). In comparison, in **BB**, **BVO**, **BBO** and **SBV**, each species contains an olefin on only two 'arms' connected to the embedded cyclopropane ring, meaning that only one pathway is achievable. Consequently, only two isomers are feasible in these instances.

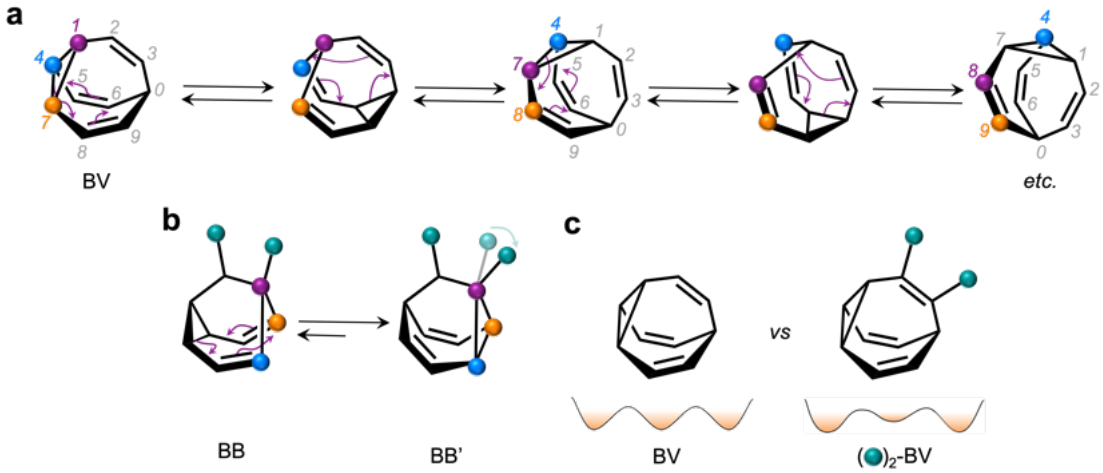

Figure 1.2. (a) Exemplary strain-assisted Cope rearrangement of **BV** with its corresponding valence isomers. Coloured circles and numbers show the positions of the cyclopropane carbon atoms, relative to the initial structure. Equilibrium arrows represent Cope rearrangements. (b) A substituted **BB** showing its Cope rearrangement, demonstrating dynamic constitutional isomerism to **BB'**. Coloured circles represent carbon atoms that remain in the same position. The green circles represent a functional group. (c) The comparison of a native degenerate **BV** with a functionalised non-degenerate **BV**. The green circles represent a functional group. The schematic illustrates the change in degeneracy upon functionalisation of native **BV** to a substituted **BV**.

As a result of the rapid interconversion *via* Cope rearrangements, nuclear magnetic resonance (NMR) spectroscopy is redundant at ambient temperatures since alkene and methine resonances appear as broad signals. At low temperatures, however, the ^{1}H NMR of **BV** gives rise to sharpened signals with distinct resolution. This realisation was demonstrated by Schröder combining the results from findings in 1963[4] and 1974[22], reporting differences *via* variable-temperature (VT) NMR spectroscopy. At 100 °C, the ^{1}H NMR spectrum showed a distinct, sharp signal at δ = 5.8 ppm for **BV**.[4] Interestingly, on cooling to –59 °C, Schröder observed four signals corresponding to four separate proton environments of **BV**, which indicated slower dynamic rearrangements in **BV** than those that occur at room temperature. Upon heating, these four distinct signals coalesced into a broad signal with subsequent sharpening again on heating to 120 °C.[22] This spectroscopic study demonstrated the initial understanding of fluxionality that occurs within the **BV** framework.

1.3 Bullvalene

BV is a unique fluxional hydrocarbon cage comprising of ten carbon atoms and ten hydrogen atoms. BV exists as a mixture of constitutional isomers owing to its structural arrangement – with the ability to fluctuate rapidly between its inherent valence isomers. The combination of this ability to undergo valence isomerisation, along with the trivial naming of its designer Doering, who was known by his mentees as 'bull', provided this distinct compound with a fitting title. Owing to its degeneracy, native BV can rearrange between thousands of constitutional isomers. The derivatisation of the native BV scaffold, whereby one or more hydrogen atoms are replaced with alternative functionality, results in a non-degenerate BV system.

The earliest explorations of BV chemistry provided the understanding as to how BV could be synthesised through the ultraviolet (UV) irradiation of cyclic hydrocarbon intermediates.[23,24] With foundational routes to native BV in the comprehensive domain, subsequent efforts focused on producing bromo BV[25] as an important intermediate for further functionalisation. More recently, incorporation of synthetic advances in organic chemistry has allowed access to functionalised BVOs,[26] which have proven to be significant intermediates in more succinct and efficient routes to functionalised BVs. Since 2018, more applicable BV research has re-emerged and has become increasingly popular – seemingly as a result of the latest and more efficient route to BV *via* bicyclodecatetraenes (BDT) intermediates, which has made functionalised BVs more accessible than ever before.[27,28]

1.3.1 Traditional Syntheses of Bullvalene

In 1963, Doering and Roth reported the first prediction of the structure and the properties of BV as part of a wider investigation into the thermal rearrangements.[3] Shortly thereafter, whilst investigating the dimerisation of cyclooctatetraene (COT), Schröder inadvertently synthesised BV by sequential photolysis of a COT dimer (Scheme 1.2).[4] Although this reaction is still one of the shortest synthetic routes to BV,[4] there is an obvious downside, which is that the reaction is low yielding. The synthetic

route involves the dimerisation of **COT** at 100 °C which forms compound **1.4** with subsequent photochemical transformation to form **BV** in 75% yield, with benzene as a by-product.

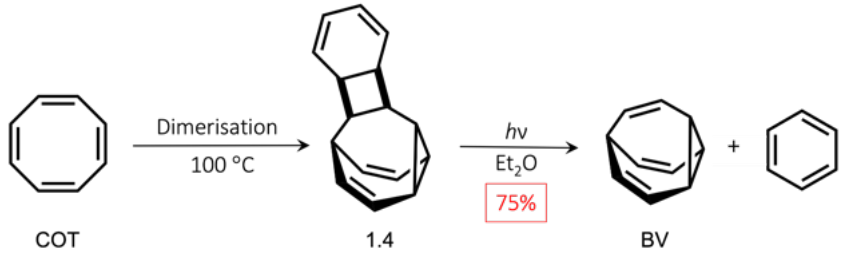

Scheme 1.2. The first synthesis of **BV** demonstrated by Schröder.[4]

Encouraged by the previously reported synthesis, Doering and Scott independently made further advances to access **BV** using the photolysis of other unsaturated alicyclic systems (Scheme 1.3).[23,24] In 1966, Doering and co-workers prepared **BV** by irradiating 4a,8a-dihydronaphthalene (**1.5**) in *n*-pentane at 0 °C, following the partial thermal decomposition of hydrocarbon **1.6**. Whilst this route is synthetically short and desirable at first sight, the formation of by-products such as naphthalene combined with the challenging separation to isolate **BV** make this route impractical overall.[6] The following year, the Scott research group developed a similar yet different route to **BV** involving the irradiation of bicyclo[4.2.2]deca-2,4,7,9-tetraene (**1.7**) – **BV** was formed in 64% yield. The route to form **BV**, where the thermal decomposition of the precursor tosylhydrazone sodium salt (**1.8**) takes place, is low yielding due to the mixture of unwanted $C_{10}H_{10}$ isomers this decomposition can result in.

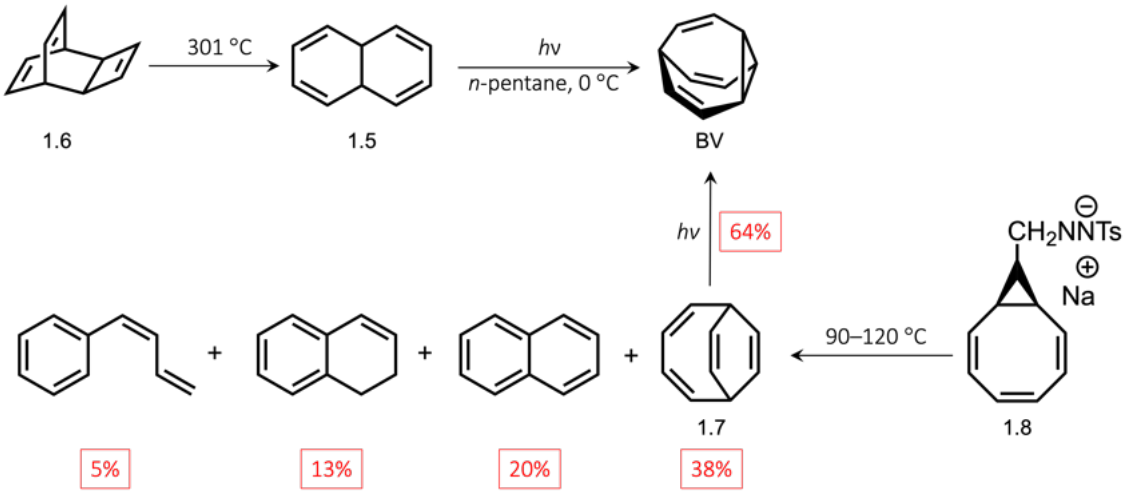

Scheme 1.3. Synthetic routes to **BV** reported by Doering and Scott.[23,24]

Longer, more diverse routes to **BV** were then reported by Doering[14] and Serrotosa.[29] They employed sequential transformations from an initial **BBO** feedstock. Doering and co-workers treated **BBO** with diazomethane resulting in a one-carbon homologation. This yielded **BVO** (**1.9**) in 24%, along with its isomeric aldehyde (**1.10**) in 34% (Scheme 1.4).[14] Subsequent reduction of **BVO** (**1.9**) with sodium borohydride forms alcohol **1.11** which is then acetylated with acetic anhydride in pyridine at 130 °C to form compound **1.12**. This route to **BV** concluded with pyrolysis of compound **1.12** at 345 °C to afford the desired **BV**. Subsequently, the Serrotosa group followed a comparable route to treating **BBO** in a similar manner to yield **BVO** (**1.9**) and aldehyde (**1.10**).[29] **BVO** (**1.9**) was then treated with *p*-toluenesulphonyl hydrazine in acetic acid to yield a tosylhydrazone intermediate formed in 70% yield (Scheme 1.4). The anionic fragmentation of compound **1.13** through treatment with methyllithium in benzene at 0 °C produced compound **1.7**, which is followed by photochemical conversion to form the desired **BV** in 82% yield.

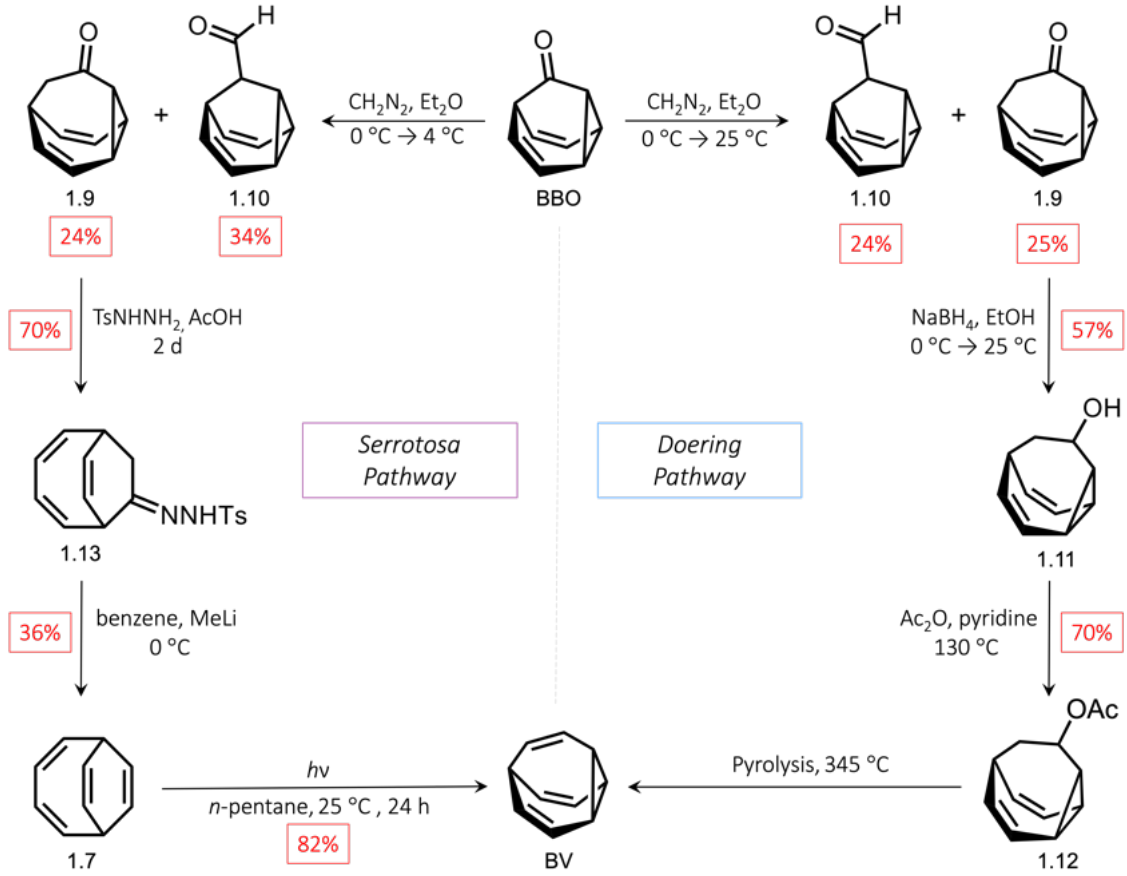

Scheme 1.4. Synthetic pathways to **BV** reported by Doering[14] and Serratosa.[29]

Pioneering work into preparation of both mono- and poly-substituted **BV** derivatives was initiated and conducted by Schröder, Oth and co-workers – in the most part, exercising bromo **BV** (**1.15**)[25] and dibromo **BV** (**1.18**)[30,31] as intermediates (Scheme 1.5). The sequential dibromination of **BV** with bromine, followed by dehydrobromination of the intermediate with potassium *tert*-butoxide forming bromo **BV** (**1.15**). Moreover, dibromo **BV** (**1.18**) can be accessed from bromo **BV** (**1.15**) by repeating the forementioned steps. These intermediates can be used to access a range of **BV** derivatives.[30,32,33] For example, bromo **BV** (**1.15**) can be treated with magnesium to make a **BV** Grignard reagent (**1.16**).[34] Equally, dibromo **BV** (**1.18**) can be treated with respective lithium organocuprate reagents to access organo-disubstituted **BV** (**1.19** and **1.20**), forming mixtures of their nondegenerate valence isomers.[35]

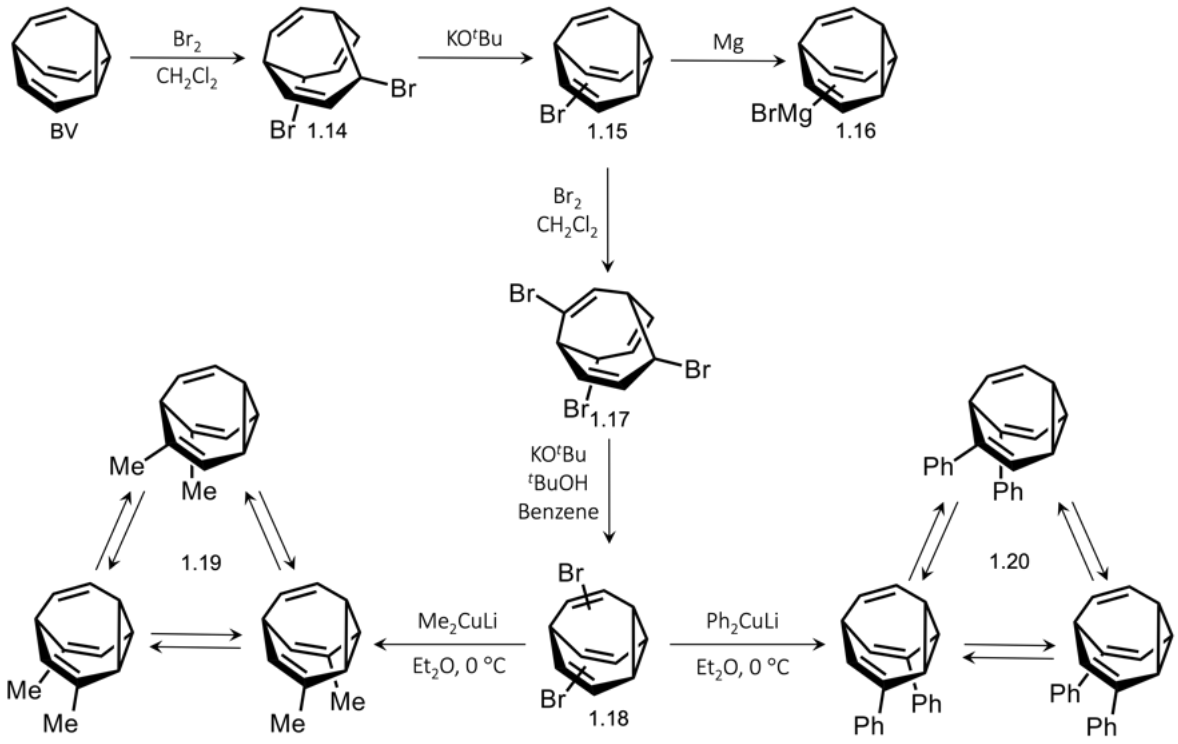

Scheme 1.5. Synthesis of bromo **BV** (**1.15**) and dibromo **BV** (**1.18**), where **1.18** is reacted with lithium organocuprate reagents to access dimethyl **BV** (**1.19**) and diphenyl **BV** (**1.20**) respectively.[36] Only the three most energetically prevalent **BV** isomers for each species of **1.19** and **1.20** are shown.

1.3.2 Modern Synthetic Access to Bullvalenes

In 2006, the Bode research group published an innovative synthetic pathway to tetra-substituted **BV**[26] (**1.21**) (Scheme 1.6) which has consequently allowed for exploration into more complex substituted **BVs** such as oligo-substituted **BVs**. These systems have been investigated for their rearrangements, equilibria and supramolecular interactions with guest molecules.[1,37]

The synthesis to the tetra-substituted **BV** (**1.21**) starts with the Mukaiyama–Michael addition[38] of cycloheptadienone (**1.22**) to form enone (**1.23**) in a yield of 93%. This enone is subjected to sequential radical bromination, followed by oxidation with *N*-methylmorpholine-*N*-oxide (NMO) to provide compound **1.24** in 49% yield. The subsequent *tert*-butyl deprotection of the alcohol of **1.24** in trifluoroacetic acid gives compound **1.25**. This exposed functionality allowed for the formation of the stabilised ylide (**1.26**) *via* treatment with *iso*-butyl chloroformate followed by a sulfur ylide. This stabilised ylide (**1.26**) is subjected to intramolecular cylcopropanation catalysed by scandium triflate, which acts as a Lewis acid to form triketone (**1.27**) in a respectable 69% yield. Next, two of the three carbonyl groups of triketone (**1.27**) were treated with allylmagnesium bromide to form a 3:2 mixture of *meso*-**1.28** and *D,L*-**1.29.** Treatment of both **1.28** and **1.29** with thionyl chloride and pyridine in dichloromethane resulted in BV (**1.21**).

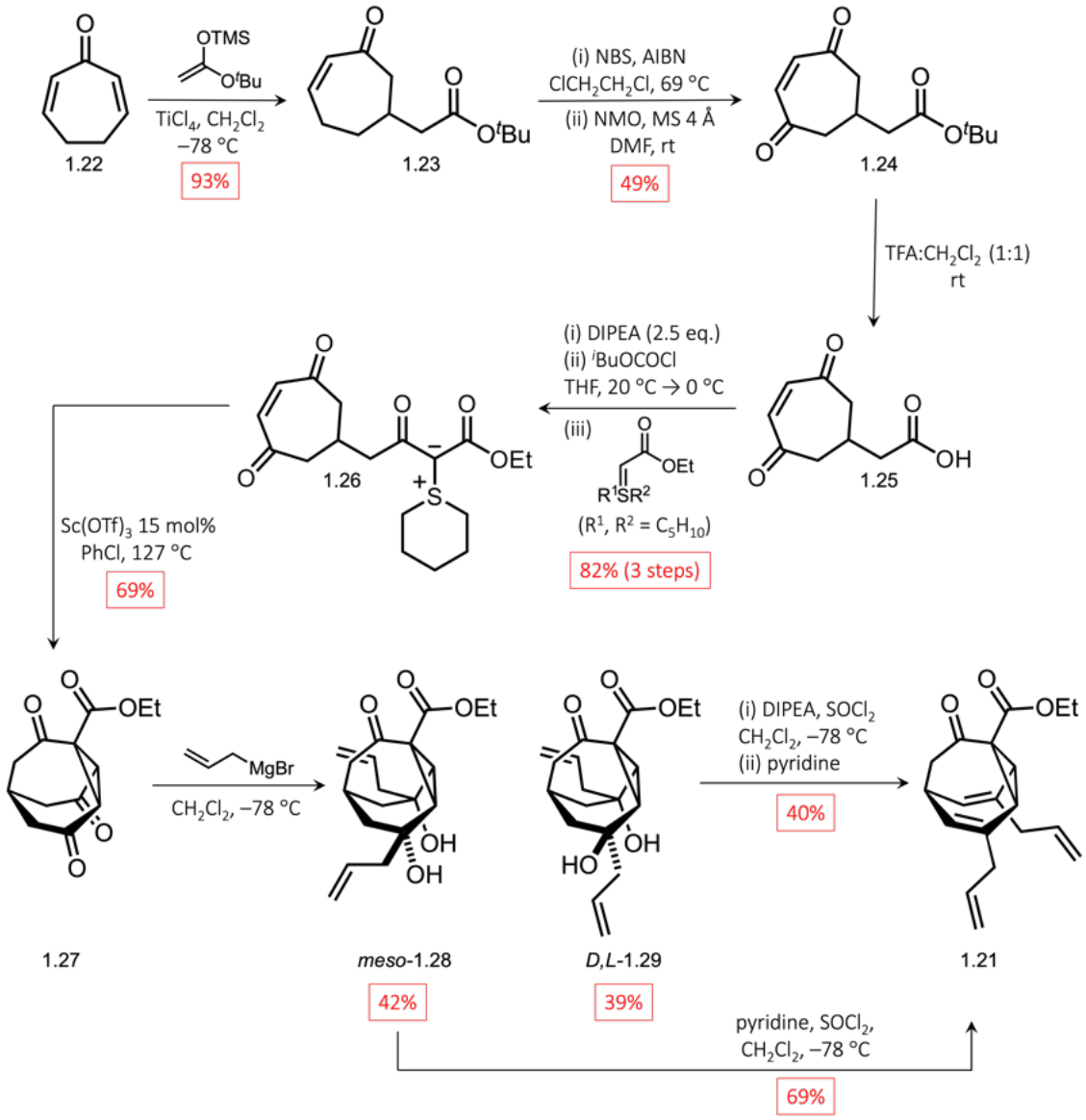

Scheme 1.6. Bode's multi-step synthesis to tetra-substituted BVs (1.21).[26]

Moreover, transition metal-mediated cycloadditions have proven to be a powerful tool in the construction of ring-bearing cyclic compounds within synthetic organometallic chemistry.[39,40] This methodology has provided more direct access to a range of five and six membered carbocycles and heterocycles *via* deviations of formal [4+2] and [3+2] cycloadditions.[41,42] Even so, the formation of seven, eight or ten membered rings are still infrequent by these methods.[40] In line with our focus on BV research, we will move our attention to metal-mediated catalysis which has played a pivotal role in the development of efficient routes to fluxional carbon cages, in particular BV.[28]

In 2005, Buono and co-workers reported seminal results on the first cobalt(I) catalysed formal [6+2] cycloaddition of cycloheptatriene (**CHT**) with alkynes to construct 7-alkyl-bicyclo[4.2.1]nona-2,4,6-trienes (**1.30**) (Scheme 7).[43] Previous to this work, a range of cobalt(II) catalysed conditions were screened for their formal [6+2] cycloaddition suitability. The use of diiodo(bis(diphenylphosphino)ethane)cobalt(II) (CoI_2(dppe)) as a catalyst, zinc iodide as a Lewis acid and zinc dust as a reducing agent (1:2:3 mol percent ratio) in either 1,2-dichloroethane or trifluoroethanol surpassed other alternatives. The combination to form this catalytic mixture permitted the addition of a wide range of terminal alkynes when forming compound **1.30**. Interestingly, the success of this reaction was influenced by the nature of the alkyne substituent, for example distantly substituted functional groups produced excellent yields, whilst electron poor alkynes accessed only poor yields. These poor yields are likely due to the favoured coordination of the cobalt with electron poor alkynes resulting in cyclotrimerisation.

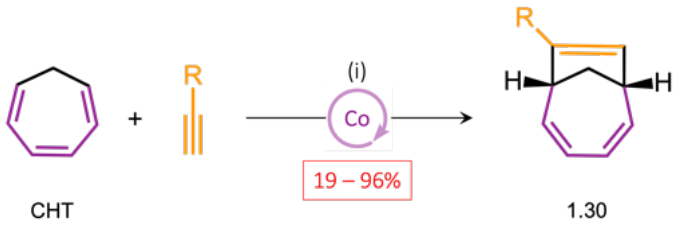

Scheme 1.7. Synthetic route to compound (**1.30**) *via* a cobalt catalysed formal [6+2] cycloaddition of cycloheptatriene (**CHT**). Reaction conditions: (i) CoI_2(dppe) (10 mol%) / ZnI_2 (20 mol%) / Zn dust (30 mol%) / DCE / 20 h / 40 °C.

Mechanistically, the reaction is thought to proceed *via* the zinc iodide mediated-reduction of CoL_2I_2 by zinc dust forming the cationic $[CoL_2]^+$ complex, which subsequently coordinates to both the alkyne and **CHT** (Scheme 1.8).[43] This step is then followed by oxidative cyclometallation producing a cobalta-cyclopentene intermediate (**1.31**). Intermediate (**1.31**) then undergoes a 1,5-migration of the C(sp^3)-cobalt bond through two successive σ,π-allyl complexes (**1.32** and **1.33**) and leads to a bicyclo colbalta-cycle (**1.34**). Species **1.34** then undergoes reductive elimination to generate the cycloadduct product (**1.30**) and regenerate the $[CoL_2]^+$.

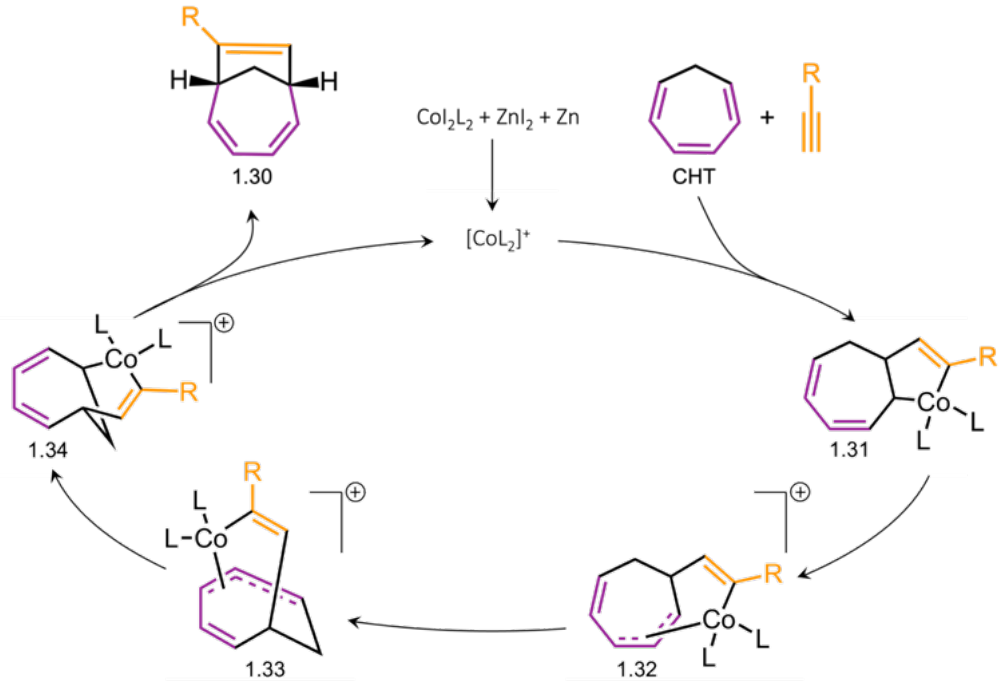

Scheme 1.8. Proposed catalytic cycle for the cobalt catalysed formal [6+2] cycloaddition of cycloheptatriene (**CHT**) to form species **1.30**. L = dppe.

Furthermore, in 2006, Buono and co-workers carried out additional studies applying the previously developed cobalt catalysis methodology[44] with alkynes in order to access monosubstituted bicyclo[4.2.2]-deca-2,4,7,9-tetraenes (**BDT**) (Scheme 1.9).[44] The reaction was carried out under the corresponding cobalt-catalysed conditions focusing on CHTs[43] yielding the desired **BDT** products with varying functionality in moderate to good yields ranging from of 56% to 94% yield. A variated approach employing a tetramethylammonium borohydride and zinc iodide mixture was attempted – it was not as successful only yielding 66% of **1.35**.

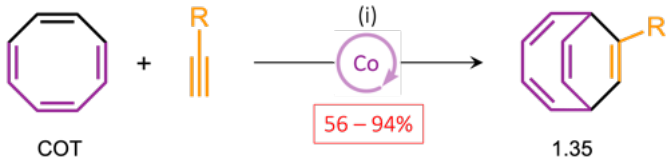

Scheme 1.9. Synthetic route to BDT (**1.35**) *via* a cobalt catalysed formal [6+2] cycloaddition of **COT** with an alkyne. Reaction conditions: (i) CoI_2(dppe) (5mol%) / ZnI_2 (10 mol%) / Zn dust (15 mol%) / DCE / 40 °C / 20 h.

This formal [6+2] cycloaddition methodology was found to be an equally good approach when treated with symmetrical alkynes (e.g. 2-butyne-1,4-diol, for example) to form **BDTs 1.36**, **1.37** and **1.38**. (Scheme 1.10). It was also noted that the choice of

solvent proved to be an important consideration for reactions involving alkynols, most likely due to solubility issues. For this reason, trifluoroethanol was chosen but the reaction was incompatible for unknown reasons with diphenylethyne, even at higher reaction temperatures.

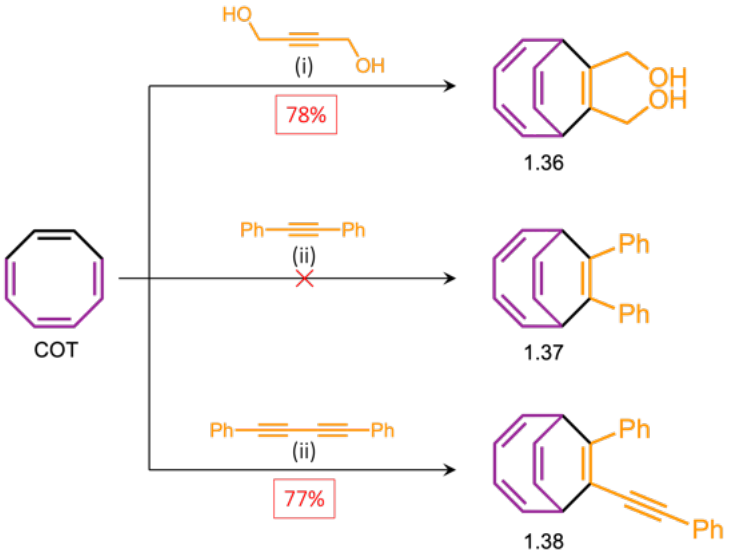

Scheme 1.10. Synthetic route to disubstituted **BDTs** (**1.36–1.38**) *via* a cobalt catalysed formal [6+2] cycloaddition of **COT** with the corresponding alkyne. Conditions (i) CoI_2(dppe) / Zn / ZnI_2 in a 5:15:10 mol% ratio / TFE / 55 °C / 48 h; (ii) CoI_2(dppe) / Zn / ZnI_2 in a 5:15:10 mol% ratio / DCE / 40 °C / 20 h.[44]

Comparable to the mechanism of CHT with terminal alkynes, the cobalt(I)-catalysed reaction between **COT** and an alkyne is considered to progress through two alternate pathways (Scheme 1.11).[44] In the first pathway, **COT** is first subjected to oxidative cyclometallation forming the species **1.39**, with subsequent coordination of the alkyne resulting in the generation of the cobaltacycle (**1.40**). The following alkyne is inserted into the Co–C bond giving rise to cobaltacycle (**1.41**) which undergoes reductive elimination of cobalt yielding the cycloadduct product (**1.35**) whilst also regenerating $[CoL_2]^+$ in the catalytic cycle. Alternatively, the oxidative cyclometallation of the alkyne-bound complex **1.42** leads to species **1.43**, which can then undergo a 1,3-migration of the Co–C(sp^3) bond through a σ,π-allyl complex, producing a cobaltabicycle adduct (**1.44**). Similarly, reductive elimination of cobalt in the **1.41** species ultimately yields the **BDT** product (**1.35**).

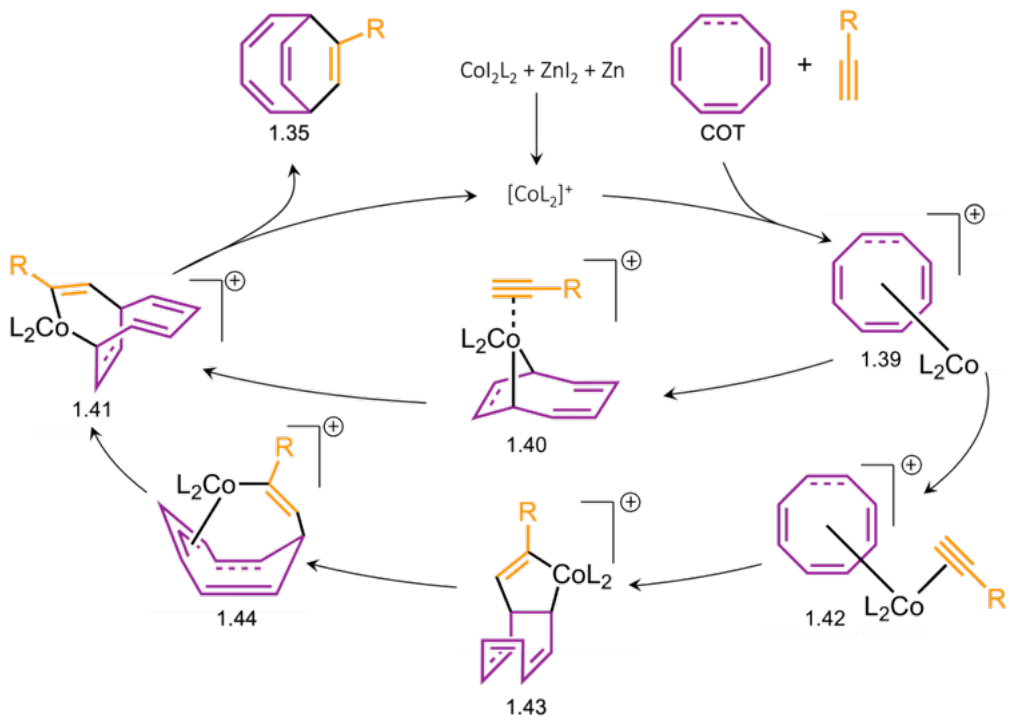

Scheme 1.11. Proposed catalytic cycle for the cobalt catalysed formal [6+2} cycloaddition of **COT** with alkynes to form **BDT** (**1.35**), as reported by Buono and co-workers.[44] L = dppe.

Significantly, **BDTs** produced by the aforementioned method have recently been exploited for **BV** synthesis. This will be highlighted and discussed in results reported by Fallon and co-workers[4] in due course.

After a decade, in 2016, Echavarren and co-workers reported a new approach to, which at the time, was the shortest synthesis of **BV**, phenyl **BV** and disubstituted **BVs**.[45] Echavarren's synthetic methodology relied heavily on the gold(I)-catalysed oxidative cyclisation of 7-ethynylcyclohepta-1,3,5-trienes (**1.45**), achieving this transformation in excellent yields (83–97%) to access **BBOs** (**1.46**) (Scheme 12). The subsequent one carbon homologation *via* the addition of diazo(trimethylsilyl)methane accessed the respective **BVOs** (**1.47**) in modest yields (22–37%). Formation of analogous **BVs** ensued firstly by the transformation to an enol triflate (**1.48**), followed by a Stille coupling to yield the **BV** derivatives (**1.49**). This five-step synthetic route provides access to compound **1.49** in yields ranging from 7–10%.[45]

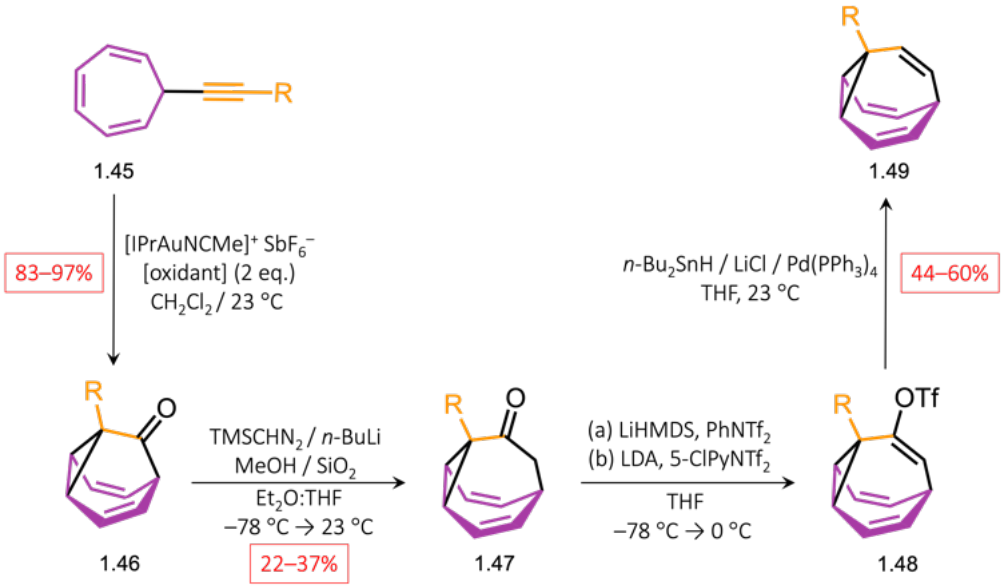

Scheme 1.12. Gold(I)-catalysed oxidative cyclisation of 7-ethynylcyclohepta-1,3,5-trienes (R = H and Ph) (**1.45**) to access the respective **BBOs** (**1.46**), followed by homologation and synthetic steps to BV derivatives (**1.49**).[45] Reaction conditions: (a) for R = H; (b) for R = Ph. The oxidants used in this study include diphenylsulfoxide, *N*-oxides of pyridine, 3,5-dichloropyridine or 8-methylquinoline.

In more recent years, previously reported[44] metal-mediated cycloadditions have been employed in combination with photochemical techniques to develop more efficient syntheses to **BV**, mono- and di-substituted **BV** derivatives. The di-π-methane rearrangement, first discovered in 1967 by Zimmerman *et al.*, arrived at the realisation that the photolysis of reactants containing two vinyl moieties directly bonded to an sp^3-hybridised carbon led to the formation of a vinylcyclopropane species.[46] Rationally, it was deemed that the main structural requirement for a di-π-methane rearrangement is that the species contains two π-systems separated by a saturated carbon atom, exemplified in a 1,4-diene (**1.50**) or an allyl-substituted aromatic ring system. In the simple example (Scheme 1.13) of a 1,4-diene, the di-π-methane rearrangement proceeds *via* biradical **1.51** and biradical **1.52** accounting for a 1,2 shift of one olefin group, which results in carbon-carbon bond formation between the lateral carbons of the stationary moiety within the molecule, forming the cyclopropane containing compound **1.53**.[47]

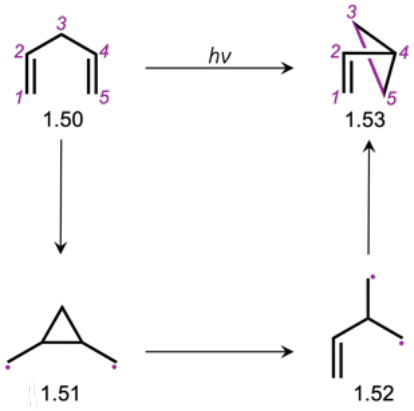

Scheme 1.13. Mechanism and transformation accounting for a di-π-methane rearrangement in a 1,4-diene (**1.50**) forming an ene-substituted cyclopropane (**1.53**).

Experimentally, the discovery of the di-π-methane rearrangement was serendipitous following the treatment of a newly synthesised bicyclic hydrocarbon, named barrelene (**1.54**).[48] The photolysis of compound **1.54** in the presence of acetone and a photosensitiser revealed a C_8H_8 isomer, subsequently named **SBV** (**1.58**) (Scheme 1.14).[15] Notably, **1.54** exhibits the prerequisite for a di-π-methane rearrangement of two π-bonds attached to an sp^3-hybridised carbon.

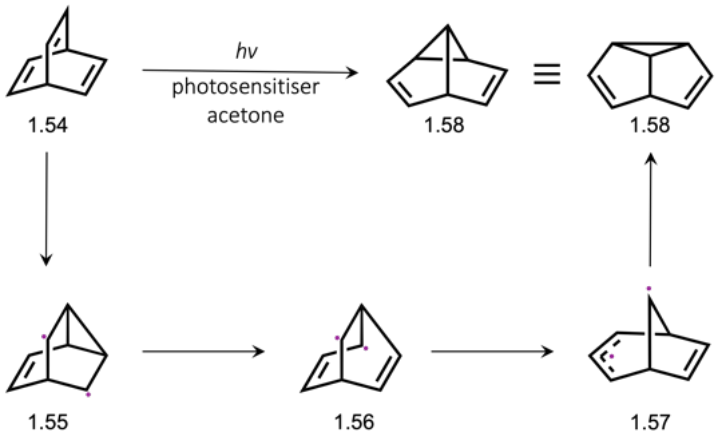

Scheme 1.14. Photochemical conversion of barrelene (**1.54**) to **SBV** (**1.58**) *via* three biradical species (**1.55–1.57**) following a di-π-methane rearrangement.[46]

Moreover, the photochemical di-π-methane rearrangement of a **BDT**-species has been recognised as an exceptionally rare transformation. In 1970, building on their previous work in 1967,[24] Jones and Scott reported the photoisomerisation of a unsubstituted **BDT** which affords **BV** in low yields.[49] Opportunely however, it was found that the **BDT** photoisomerises back to **BV**, when irradiated with a medium-pressure mercury lamp

filtered by Pyrex. The use of the di-π-methane rearrangement to bicyclic compounds was influential in the development of routes to more elaborate **BVs**.

Shortly after, in 1969, Paquette and co-workers utilised this photoisomerisation as part of their synthetic methodology to access an azaBV system.[50] The unfiltered irradiation of 7-azabicyclo[4.2.2]deca-2,4,9-trien-8-one (**1.59**) in methanol at 25 °C formed the isomeric lactam (**1.60**) in 54% yield (Scheme 1.15).[50] The reaction was monitored by ultraviolet-visible (UV-vis) spectroscopy until deemed complete due to the disappearance of the characteristic absorption bands in the amide starting material. Upon treatment of compound **1.60** with trimethyloxonium fluoroborate (Meerwein's salt), methoxyaza **BV** (**1.61**) was formed which was established by ^{1}H NMR spectroscopy in excellent yield of 92%. With this information in hand, a more efficient synthesis was developed employing the photochemical rearrangement of imino ether (**1.62**) by the means of acetone sensitisation filtered by Pyrex to yield methoxyaza **BV** (**1.61**) in an improved 71% yield over two steps.

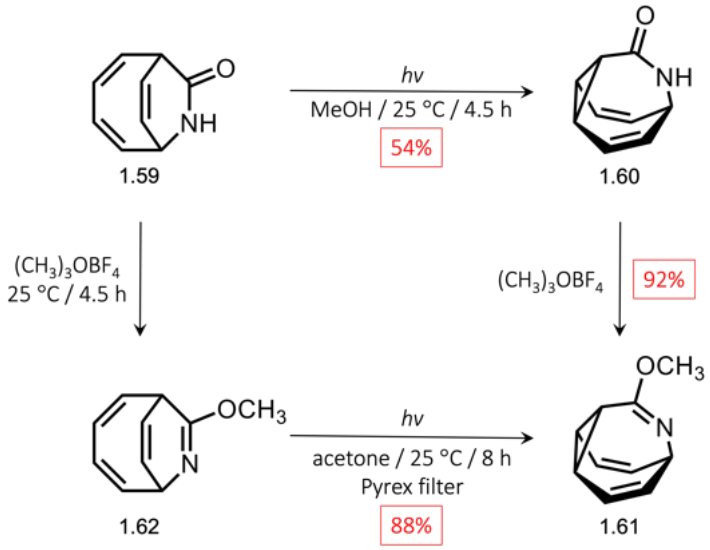

Scheme 1.15. Synthetic route to methoxyaza **BV** (**1.61**) *via* a di-π-methane rearrangement as reported by Paquette and co-workers.

In light of the aforementioned methods, in 2018, Fallon and co-workers reported the construction of a range of mono-substituted and di-substituted **BDT** precursors (**1.63** and **1.64**) in 63% to quantitative yields, which were then exposed to ultraviolet (UV)

irradiation in acetone to afford the related functionalized mono- and di-substituted **BVs** (**1.6** and **1.66**) in 40–81% yield (Scheme 1.16).[28]

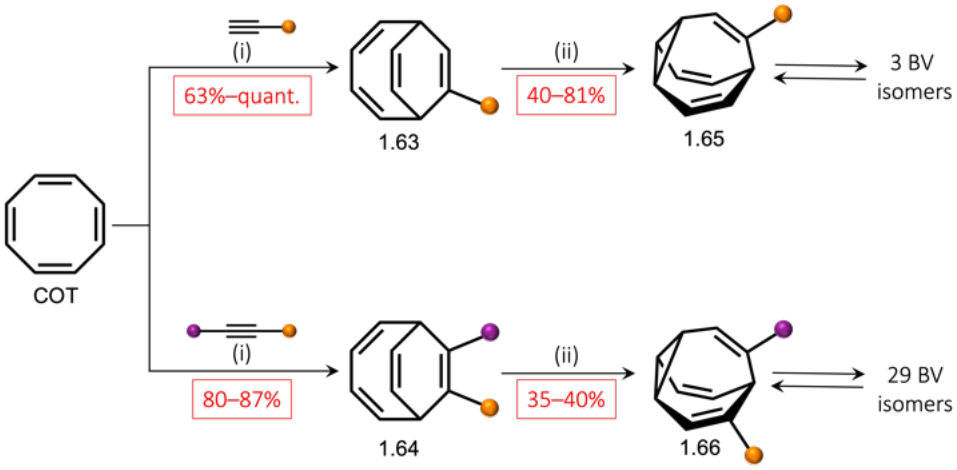

Scheme 1.16. Synthetic route to mono-substituted **BV** (**1.65**) and di-substituted **BV** (**1.66**) *via* a metal catalysed formal [6+2] cycloaddition of **BDTs** (**1.63** and **1.64**) followed by photoisomerisation as reported by Fallon and co-workers.[28] The orange and magenta circles represent a functional group, whereby appended substituents include H, Me, *n*-hexane, CH_2OH and Bn, for example. Reaction conditions: (i) $CoBr_2$(dppe) / Zn / ZnI_2 in a 10:30:20 mol% ratio / DCE or TFE / 25–55 °C / 16–24 h; (ii) 365 nm / acetone / 25 °C / 16–24 h.

Whilst this procedure clearly exhibits progression from previous routes to **BVs**, it still has its obstacles, notably presenting incompatibility with electron-withdrawing groups and aryl-substituted functionality. Moreover, it was found in the attempt to access phenyl-substituted **BV** *via* UV irradiation of phenyl **BDT** (**1.67**), **LBV** (**1.68**) was isolated instead (Scheme 1.17). Interestingly, the desired **BVs** was not present in the reaction mixture likely due to an alternative rearrangement being followed from the **BDT** intermediate.

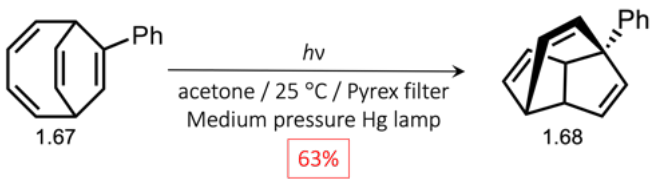

Scheme 1.17. Synthesis of phenyl **LBV** (**1.68**) *via* the phenyl-substituted BDT (**1.67**).

Building on this seemingly efficient synthesis, Fallon and co-workers reported a family of mono-, di- and tri-substituted boronate ester BDTs (**1.69**–**1.72**), which were isomerised to **BVs** (**1.73**–**1.76**).[27] Subsequent Suzuki cross-coupling reactions allowed access to a series of aryl-substituted **BVs** (**1.77**–**1.80**).[27] Fallon incorporated pinacol

boronate ester (Bpin), in addition to a *N*-methyliminodiacetic acid (MIDA) boronate ester (B_{MIDA}) group in order to employ heterogenous substituted **BVs** (**1.80**). The suitability for boronate esters to provide reactivity in Suzuki cross-coupling reactions paved the way for exploration of shapeshifting chemical behaviour in more diverse **BV** systems. The previously mentioned synthetic methodology, developed by Fallon and co-workers, was similarly employed with alkynyl boronate esters. The formal [6+2] cobalt catalysed cycloadditions of **COT** with Bpin-acetylenes forms mono- and di-substituted Bpin **BDT** (**1.73** and **1.74**). For tri-substituted Bpin species, **COT Bpin** was first prepared in two steps prior to the cycloaddition reaction. For the BPin-B_{MIDA} compounds, compound **1.70** was subjected to MIDA in dimethyl sulfoxide at 120 °C to yield the heterogenous **BDT** (**1.72**). The BDT precursors (**1.69**–**1.72**) were then subjected to irradiation at 365 nm, resulting in the di-π-methane rearrangement accessing the corresponding boronate ester substituted **BVs** (**1.73**–**1.76**) (Scheme 1.18).[27] These boronate ester functionalised **BVs** have allowed access to aryl **BVs** (**1.77**–**1.80**) in a succinct and efficient manner, through treatment with tetrakis(triphenylphosphine) palladium catalysed conditions with a range of bromoarenes. (Scheme 1.18).

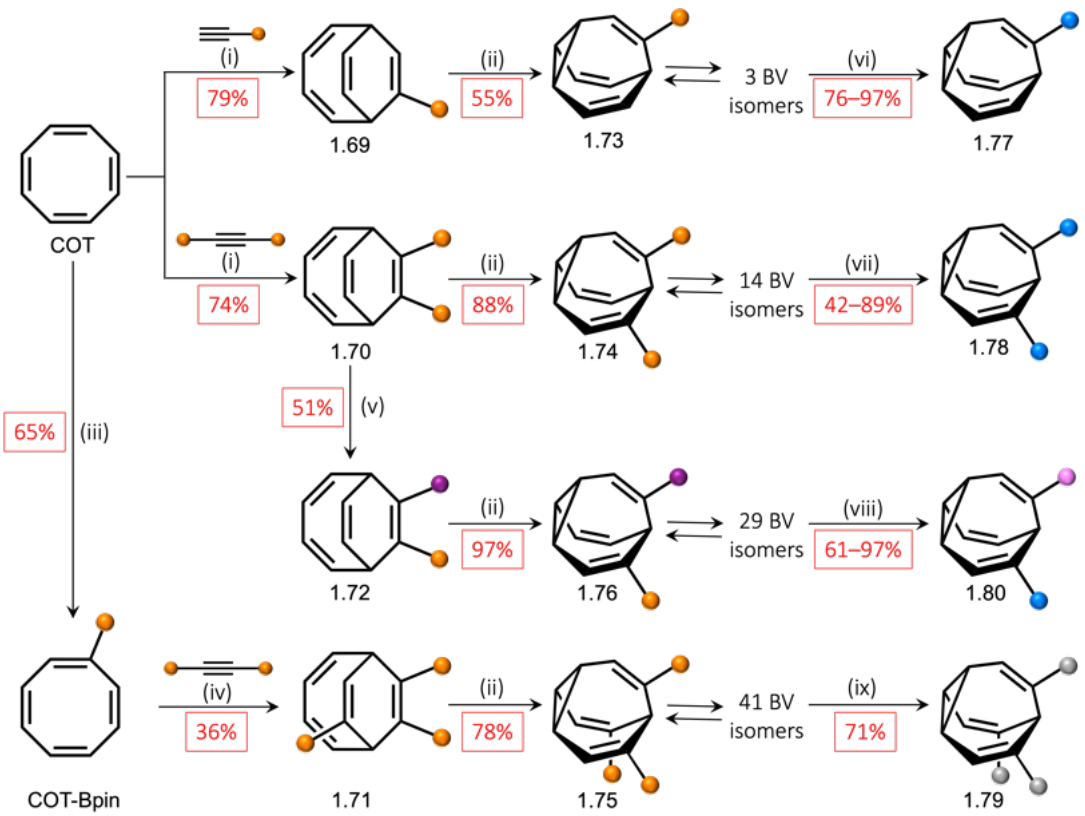

Scheme 1.18. Synthesis of aryl-substituted **BVs** (**1.77**–**1.80**) *via* boronate ester-substituted **BDTs** (**1.73**–**1.76**). Conditions (i) alkyne (1.0 equiv.) / $CoBr_2$(dppe) (10 mol%) / ZnI_2 (20 mol%) / Zn (30 mol%) / DCE / rt; (ii) *9H*-thioxanthen-9-one (1 mol%) / THF / 365 nm LED lamp / rt; (c) (iii) (1) Br_2 (1.0 equiv.) / KO^tBu (1.0 equiv.) / THF / –78 °C; then (2) n-BuLi (1.0 equiv.) / MeOBPin (1.0 equiv.) / THF / –78 °C → rt; (iv) alkyne (1.0 equiv.) / $CoBr_2$(dppe) (50 mol%) / ZnI_2 (100 mol%) / Zn (150 mol%) / DCE / rt; (v) MIDA (12.0 equiv.) / dimethyl sulfoxide / 120 °C / 8 h; (vi) Ar–Br (1.0 equiv.) / $Pd(PPh_3)_4$ (5 mol%) / $NaOH_{(aq)}$ / THF / 60 °C; (vii) Ar–Br (2.2 equiv.) / $Pd(PPh_3)_4$ (5 mol%) / $NaOH_{(aq)}$ / THF / 60 °C; (viii) (1) *p*-bromobenzotrifluoride (1.1 equiv.) / $Pd(PPh_3)_4$ (5 mol%) / Ag_2CO_3 (1.5 equiv.) / THF / 60 °C; then (2) Ar–Br (1.1 equiv.) / $Pd(PPh_3)_4$ (5 mol%) / $NaOH_{(aq)}$ / THF / 60 °C; (ix) Ph–Br (3.3 equiv.) / $Pd(PPh_3)_4$ (10 mol%) / $NaOH_{(aq)}$ / THF / 80 °C. The circles represent a functional groups, whereby; orange = Bpin, magenta = B_{MIDA}, blue = aryl, pink = benzotrifluoride, grey = phenyl.

1.4 Barbaralane

The compound **BB** is a fluxional C_9H_{10} tricyclic hydrocarbon cage that has found premise for foundational study of shapeshifting equilibria in small dynamic systems.[3] Although there are structural similarities between **BB** and **BV** (whereby the ethylene unit in **BB** is replaced by a methylene unit in **BV**), the number of valence isomers that each compound can access is vastly different due to the subtle structural differences.

Despite its fluxional character, **BB** can access only two valence isomers facilitated by strain-assisted Cope rearrangements, a far smaller number relative to **BV**. Synthetically, seminal reports detailing the first **BB** was shown by von Doering in conjunction with investigations into thermal rearrangements and the initial synthesis of **BV**.[51] Given the intriguing chemical properties of **BB**, more recently, modern synthetic advances have focussed on preparing **BB** in more efficient and reliable methodologies,[45,52] which has allowed more thorough investigations into **BB** valence isomerism to be investigated.

1.4.1 Classical Syntheses of Barbaralanes

Historically, the first synthetic route to a BB derivative (**BBO**) occurred in 1963,[51] prior to studies carried out by von Doering and co-workers in 1967,[53] focussing on investigations towards the synthesis of **BV**. This synthetic methodology encompasses the intramolecular carbene insertion to the CHT double bond to form **BBO**. In this synthetic pathway, benzene is first treated with ethyl diazoacetate and irradiated over 7 days to afford the CHT (**1.81**). The subsequent hydrolysis of ester (**1.81**) to the carboxylic acid (**1.82**) is then treated with thionyl chloride to form the acyl choride (**1.83**). The following treatment with diazomethane allows for the formation of diazomethyl ketone (**1.84**), which is then subjected to copper(II) sulfate in a hexanes/benzene mixture under reflux to afford **BBO** *via* intramolecular cylcopropanation of the ketocarbene.

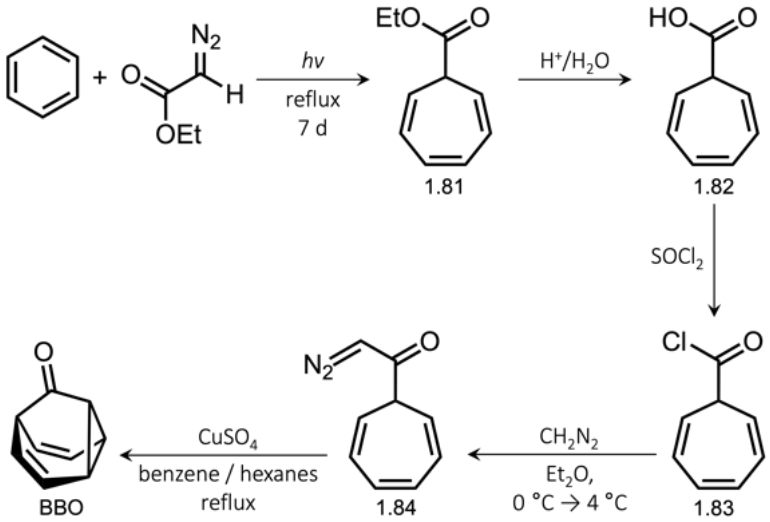

Scheme 1.19. Synthesis of barbaralone (**BBO**) by Doering and Roth.

Furthermore, in 1983,[54] Henkel and co-workers reported the five-step synthesis of **BB** from 2-adamantone (**1.85**) in an overall yield of 59%. This method avoids Doering and Roth's previously described low yielding cyclisation steps, shown throughout the carbene insertion method. Thus, Henkel's procedure is first initiated through the treatment of 2-adamantone (**1.85**) with sodium azide and methanesulfonic acid, affording the carboxylic acid intermediate (**1.86**) in a respectable 80% yield. Through the treatment of carboxylic acid (**1.86**) with lithium diisopropylamide, followed by oxygenation and acidic workup, oxidative decarboxylation was achieved to give the corresponding cyclic ketone (**1.87**) in 70% yield. Next, allylic bromination was accomplished through subjecting compound **1.87** to *N*-bromosuccinimide (NBS) to give the analogous bromo ketone (**1.88**), which was then subjected to a base-catalysed ring closing transformation yielding **BBO** in 95% yield. Finally, **BBO** was then treated with 1) *p*-toluenesulfony hydrazide; and 2) *n*-BuLi in THF to convert **BBO** into **BB** through a Shapiro type elimination reaction, where **BB** was produced in a 59% yield.

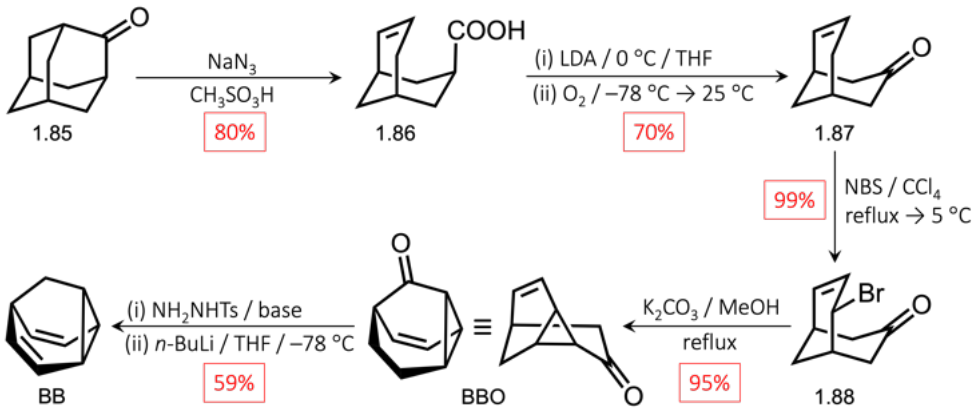

Scheme 1.20. Synthetic route to **BB** from 2-adamantone (**1.85**) as demonstrated by Henkel and co-workers.

In 1995, Quast and co-workers devised a synthetic route towards 3,7-substituted **BBs**, presenting the ability to introduce varied functionality on the **BB** scaffold, starting from 3,7-bicyclo[3.3.1]nonanedione (**1.89**) (Scheme 1.21).[55] First, compound **1.89** was reduced with phenyllithium, producing phenyl-1-oxaadamantol (**1.90**) as the reduction product. The resulting phenyl-1-oxaadamantol (**1.90**) was then treated with a boron trifluoride/diethyl ether mixture, with the addition of acetic anhydride to yield compound **1.91**. The resulting compound was subjected to cerium(III) chloride, with

the subsequent addition of phenyllithium, to afford the alcohol (**1.92**) in 99% yield. Treatment of tertiary alcohol (**1.92**) with a sulfuric acid:acetic acid solution resulted in dehydration of the alcohol to quantitatively form the diphenyldiene product (**1.93**). Next, the diphenyldiene was exposed to NBS allowing for allylic bromination, thus forming the dibrominated diphenyldiene (**1.94**). Reductive cyclisation of the bicyclic precursor (**1.94**) yielded the 3,7-phenyl **BB** (**1.95**) in 82% yield.

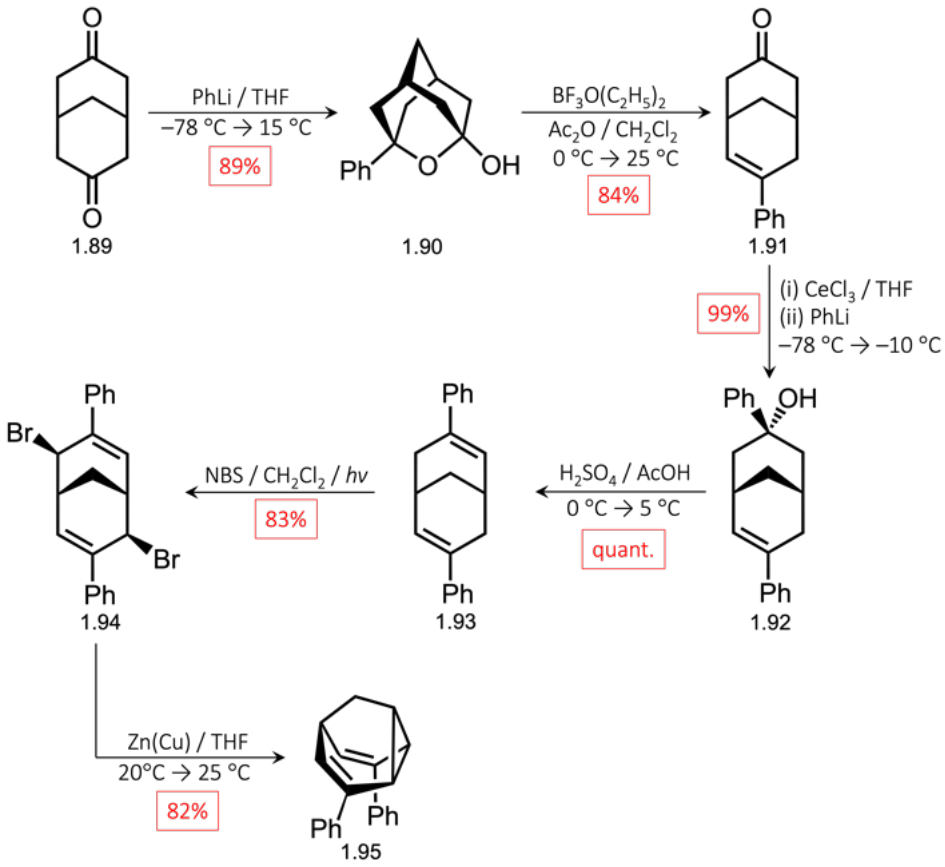

Scheme 1.21. Synthetic route to 3,7-phenyl **BB** (**1.95**) from 3,7-bicyclo[3.3.1]nonanedione (**1.89**) by Quast and co-workers.

1.4.2 Modern Synthetic Access to Barbaralanes

Most recently, synthetic advances to **BB** have been reported by Echavarren and co-workers,[52] who have utilised gold-catalysed cycloisomerisation of alkynyl CHTs. Gold complexes present the ability to promote a variety of cyclisations, whilst allowing for exceptional control over competitive reaction pathways, through the stabilisation of carbenic intermediates. First, in Echavarren's route, alkynyl CHTs (**1.45**) are prepared through the nucleophilic treatment of tropylium tetrafluoroborate with an acetylide.

The ensuing activated (η^2-alkynyl)gold(I) complex (**1.96**), which is formed through the treatment of the alkynyl CHT (**1.45**) with a gold catalyst, endures cycloisomerisation to form a gold stabilised fluxional barbaralyl cation. The resultant barbaralyl cation can then be trapped through solvolysis, employing a nucleophilic solvent such as methanol, producing BB methyl ethers (**1.97**) as a major product, along with a minor amount of indenyl by-product. Additionally, the use of different gold salts was also investigated, whereby gold catalyst 2 was found to provide excellent regioselectivity towards indene **1.98**, whereas the more electrophilic phosphite-gold(I) complex (Au catalyst 3) exclusively favoured the indene regioisomer (**1.99**). Overall, this synthetic methodology provides evidence for the accessibility towards functionalised barbaralanes, whereby the specified functionality can be varied through modification to the alkynyl CHT or the alteration of an intercepting nucleophile.

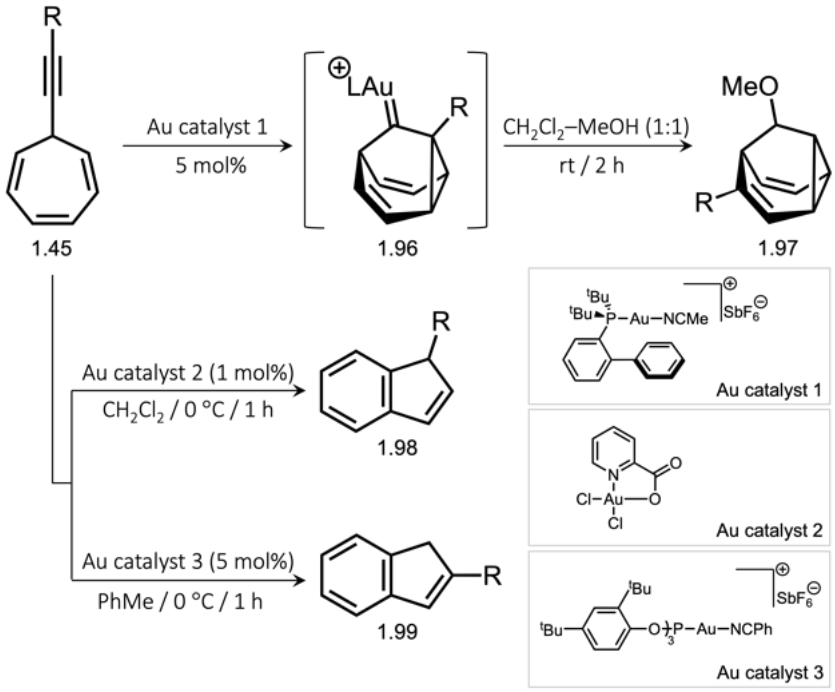

Scheme 1.22. Synthetic route to synthesise substituted **BB** methyl ether (**1.97**) from alkynyl CHT (**1.45**). Treatment with different gold-catalysts leads to regioisomeric indenes (**1.98** and **1.99**). Reagents: Au catalyst 1 = [JohnPhosAu(MeCN)][SbF_6]; Au catalyst 2 = dichloro(2-picolinato)Au(III); Au catalyst 3 = [2,4-^{t}BuPhO)$_3$PAu(NCPh)][SbF_6]. JohnPhos = (2-biphenyl)di-*tert*-butylphosphine; ^{t}Bu = *tert*-butyl; R = variable group.

Building upon the aforementioned methodology, in 2016,[45] Echavarren and co-workers reported the synthesis of **BBO** and 1-substituted **BBOs** (**1.46**) produced

through the addition an oxidant to the gold-catalysed 1,6-enyne cyclisations of CHT (**1.45**). Optimisation of reaction conditions involved the addition of an oxidant, such as diphenyl sulfoxide, as well as the employment of the gold(I) catalyst (acetonitrile)[(2-biphenyl)di-*tert*-butylphosphine]gold(I) hexafluoroantimonate (gold catalyst 4). It was proposed that the use of the gold catalyst 4 activates the alkyne before coordinating, followed by oxidation from the oxidant to from an *α*-oxo gold(I) carbene, which then undergoes intramolecular cylcopropanation to form **BBO**. This method was shown to be successful and endure a range of alkynyl CHTs (**1.45**), affording substituted **BBOs** (**1.46**) (bearing electron-donating and electron-withdrawing groups, with *ortho*-, *meta*- and *para*- regiochemistry) in 45–97% yield.

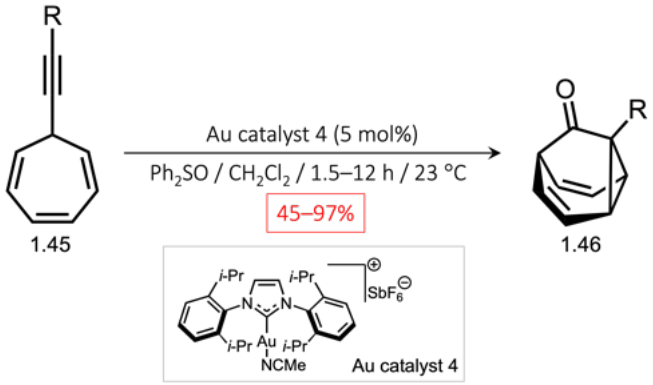

Scheme 1.23. Synthetic route to substituted **BBOs** (**1.46**) from substituted alkynyl CHTs (**1.45**) as reported by Echavarren *et al*. *i*-Pr = 1,3-bis(2,6-diisopropylphenyl)imidazole-2-ylidene. R = variable group.

1.5 Applications of Fluxional Carbon Cages

1.5.1 Regulation of Nondegenerate Barbaralane Mixtures

In 2018, McGonigal and co-workers reported the shape-selective crystallisation of substituted **BB** compounds[56] showing that the preferential crystallisation of compounds **1.100** and **1.101** are controlled by molecular size and shape irrespective of equilibrium distribution in the solution-state and noncovalent interactions (Figure 1.3). Despite the dynamic fluxional nature of **BBs** which equilibrate between two sets of non-equivalent valence isomers[57], solution-phase NMR spectroscopic analysis and X-ray crystal structures demonstrated two minor solution-phase valence isomers which adopt molecular structures that are energetically preferential for crystal packing. It was

found that the size and shape of the molecule outweighs the inherent energetic preference displayed by the shapeshifting equilibrium. Differing functionality, size and dihedral angle between the **BB** substituents revealed preference for different crystal packing modes in the subjected derivatives.

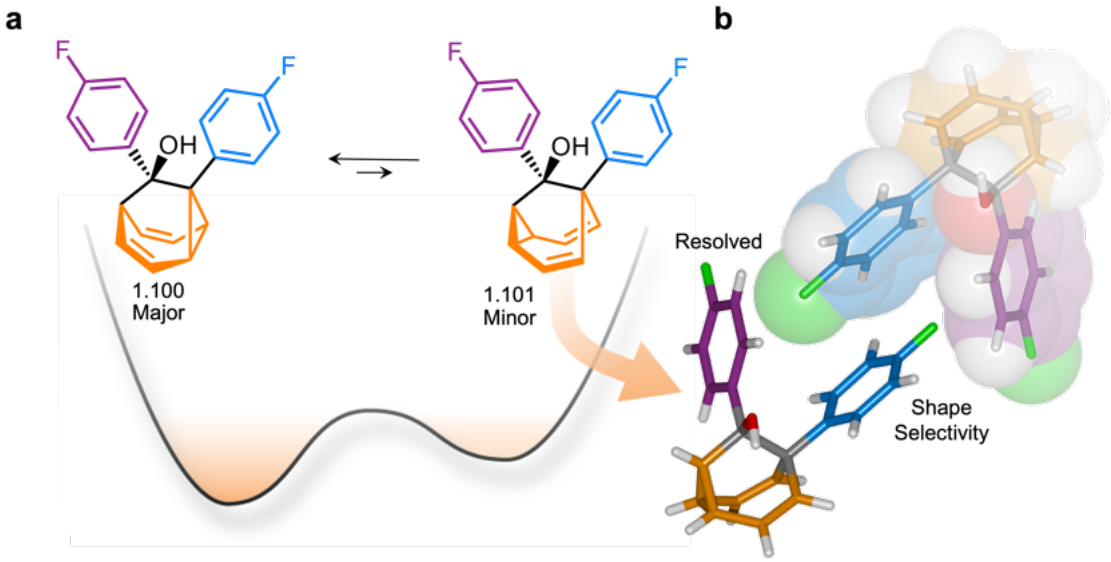

Figure 1.3. (a) Schematic potential energy diagram illustrating the equilibrium between **BBs** **1.100** and **1.101**; (b) Crystal structure of **1.100** showing arrangement of head-to-head allowing aromatic group interdigitation.

1.5.2 Control of Dynamic Barbaralane sp^3-C Stereochemistry

Furthermore, in 2023, the McGonigal group documented a series of chiral fluxional **BBs** that exhibited responsive sp^3-carbon centred stereochemistry, allowing for the adaptation and transmission of stereochemical information.[58] This investigation presented the synthesis of **BBs** functionalised with a fixed stereocentre in a chiral auxiliary, namely the Mosher's ester moiety (**1.102**). The study showed that by incorporating the (*S*)- or (*R*)-Mosher's ester, the overall configuration of the **BB** was biased towards (*S,S*)-**1.102** or (*R,R*)-**1.102**.

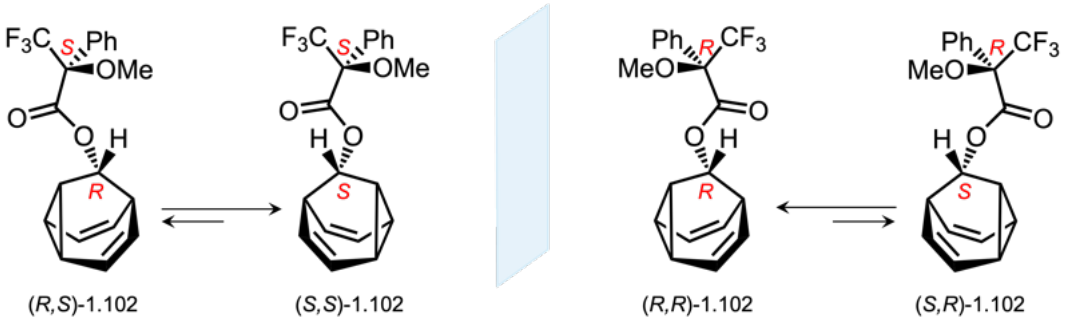

Figure 1.4. Adaptation of the fluxional **BB** core in **1.102**, through the incorporation of the chiral auxiliary, Mosher's ester.

Additionally, the report showed that a **BB**-phosphoramidite ligand (**1.103**), coordinates *via* the **BB** alkene and the phosphorus centre, to form a **BB** complex (**1.104**) with $PdCl_2$ (where the Pd is a stereogenic element) (see Figures 1.5a and 1.5b). In this coordination complex (**1.104**), two stereoisomers are possible, which is dependent on the stereochemistry of the **BB** phosphoramidite ligand (*S,S* or *R,S*). The **BB** moiety was shown to transmit stereochemical information from the fixed stereocentre of the ligand, resulting in a bias towards the configuration at the Pd metal centre in $PdCl_2$.

The two complexes of **1.104** ((*A,S,S*) and (*C,R,S*)) were shown to be in slow exchange at 240 K by ^{1}H NMR spectroscopy (Figure 1.5b). It was evidenced that the coordination to the Pd(II) centre resulted in a slower rate of Cope rearrangements, relative to other ligands. Moreover, the mechanism for interconversion between (*A,S,S*)-**1.104** and (*C,R,S*)-**1.104** was deciphered by DFT modelling and experimental NMR spectroscopy. These investigations showed that, in the transition state structure, the Pd(II) centre remains coordinated to the **BB** moiety. Therefore, this result suggested that throughout the Cope rearrangements to access each stereochemical species, the Pd(II) ion shifts along one side of the **BB** scaffold which is indicative of a mechanism at a pentavalent metal centre that is reliant on the dynamic properties of **BB**.

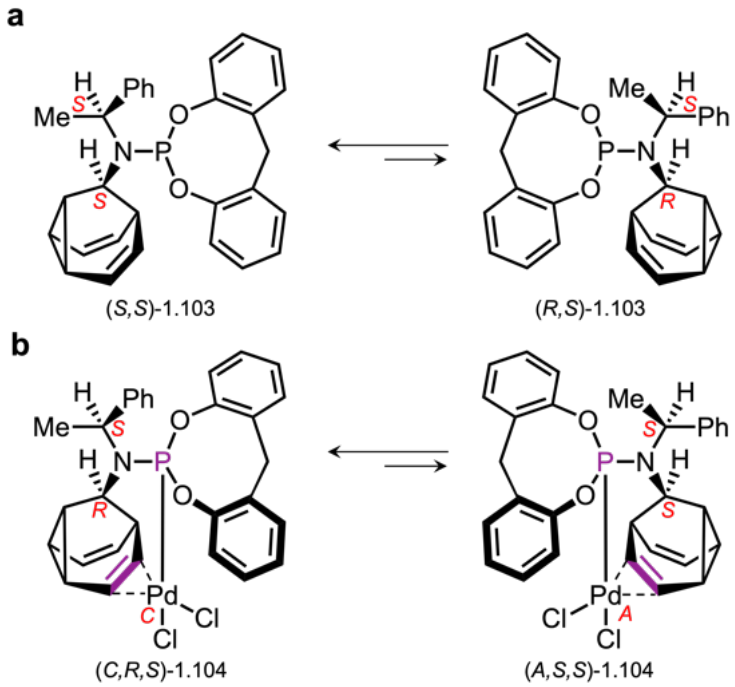

Figure 1.5. (a) The incorporation of a chiral moiety results in the bias of the BB ligand to the (*S,S*) and (*R,S*) configuration of 1.103; (b) Transfer of dynamic sp^3 stereochemistry *via* the BB moiety in the Pd(II) complex, 1.104.

1.5.3 Functional Bullvalenes as Chemical Sensors

In 1979, Schröder and co-workers reported the first use of BV derivatives as adapted shapeshifting molecules – reporting crown ether-functionalised BVs (1.105) with varying sizes of crown ether rings (Scheme 1.24).[2] The crown ether was installed to explore the potential selective binding of metal ions, specifically ammonium and alkali metal cations. The intramolecular relationship between the BVs shapeshifting properties and the crown ether ring size was probed. Whilst weak binding was recorded between the BV crown ether and cations of different size, Schröder was unable to elucidate which BV isomers were present and which species were binding to metal cations preferentially. This was the earliest study to provide evidence for the potential of shapeshifting molecules to be applied as chemical sensors.

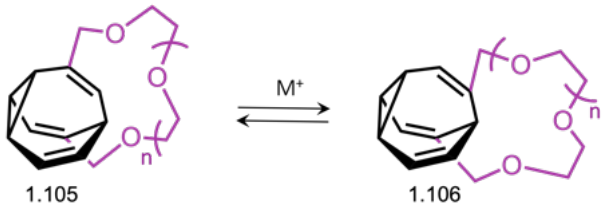

Scheme 1.24. Binding of metal cation (M^+) with crown ether functionalised BV (1.105).[2]

Initial studies by Bode and co-workers reported the capacity of oligo-functionalised **BVs** to shift the equilibrium distribution in response to the interaction between fixed groups and a fullerene analyte dopant (Scheme 1.25).[59] The aim of this investigation was to demonstrate the ability for dynamic host discovery. Bisporphyrin moieties were integrated into the **BV** design to promote π-π interactions with a C_{60} guest molecule, thus establishing intermolecular binding affinity. The isomer distribution of the oligo-substituted **BV** (**1.107**) was found to shift towards isomers that bind with the C_{60} additive on addition (**1.108**), demonstrating the adaptation of **BV** shape to bind guest molecules.

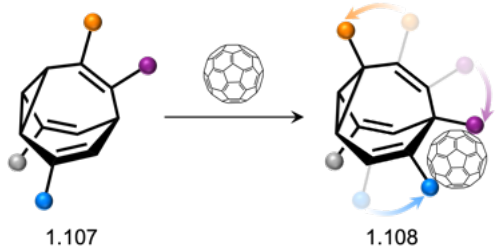

Scheme 1.25. Shifted equilibrium of oligo-substituted **BV** (**1.107**) based on the addition of a fullerene analyte. Coloured circles represent oligo functionality; coloured arrows represent change in substituent position through an adjusted equilibrium. N.B: C_{60} not to scale.

In line with the aforementioned research aims, in 2012, Bode and co-workers prepared a ^{13}C-labelled bisporphyrin **BV** (**1.109**) to investigate its capability to chemically sense fullerene derivatives.[37] The comparison of ^{13}C NMR spectra of the bisporphyrin **BV** (**1.109**) both in the presence and absence of a fullerene analyte C_{70} provided evidence through a distinct alteration in the corresponding peaks. Simplification of the ^{13}C NMR spectrum, by plotting the chemical shift of each peak against its corresponding intensity showed this change more clearly. Similarly, further investigations into the ability for **BV** (**1.109**) to chemically sense was carried out with other fullerene analytes including C_{60}. Equally, ^{13}C NMR spectral analysis subsequently strengthened the notion that the **BV** core could clearly distinguish analytes with structural similarity (Figure 1.6).

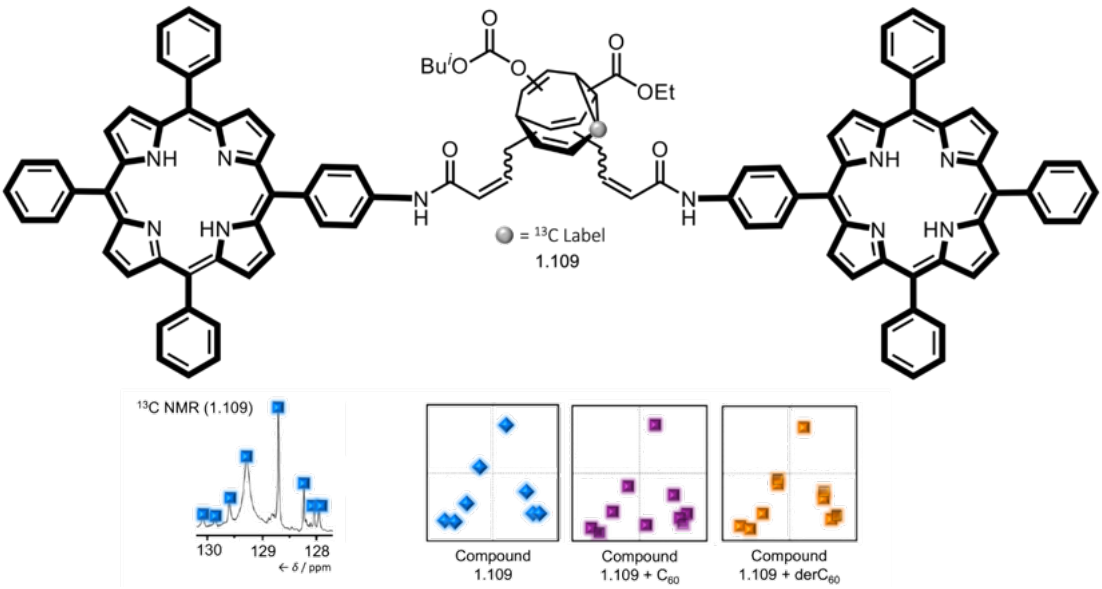

Figure 1.6. ^{13}C-labelled bisporphyrin BV (1.109) complemented with the graphical representation of its ^{13}C NMR spectrum and corresponding peak pattern showing the equilibrium position of the addition of C_{60} and derC_{60} fullerene analytes.

Furthermore, in 2013 Bode and co-workers built upon the previously discussed idea reporting the first example of analyte binding through covalent bonding.[37] A bis-boronic acid functionalised BV (1.110) was prepared and subsequently demonstrated the ability to act as a chemical sensor for the detection of polyols, namely those with closely related structures like flavanols and carbohydrates *via* dynamic covalent condensation reactions. These structures resulted in distinguishable ^{13}C NMR signals that were astutely converted into more comprehensible barcodes for easier interpretation (Figure 1.7). For example, the comparison of bis-boronic acid BV 1.110's ^{13}C NMR spectrum against a mixture of BV (1.110) with chlorogenic acid (1.111) demonstrated a shift in the equilibrium position when the analyte was present. This result showed BVs (1.111) nature to successfully distinguish different polyols with similar structures.

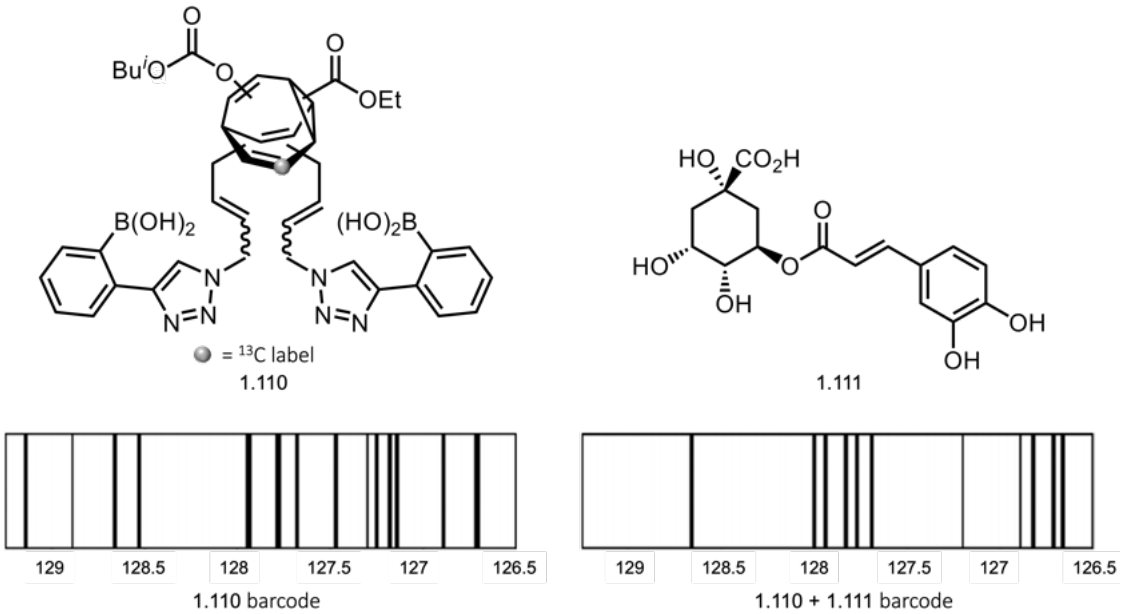

Figure 1.7. ^{13}C-labelled bis-boronic acid BV (1.110) and chlorogenic acid (1.111) with comparison of corresponding barcodes for 1.110 and a mixture of 1.110 and 1.111.

A key aim in developing applicable fluxional carbon cages is to control the reversibility of their inherent fluxional equilibrium. With this realisation, Bode and co-workers prepared a unique BV possessing a photolabile carbonate substituent *via* the trapping of compound 1.21 with a lithium enolate. This transformation produced a *o*-nitroveratryloxycarbonate (NVOC) bisallyl BV (1.112) (Scheme 1.26) which was observed by HPLC.[60] BV (1.112) was then irradiated at 365 nm for 20 hours resulting in the disappearance of peaks corresponding to the starting materials and NVOC bisallyl BV (1.113) whilst peaks analogous with the adapted BV remained. This observation demonstrated that the fluxional nature of the carbon cage can be stopped through the addition of a photocleavable group, freezing the Cope rearrangements within.

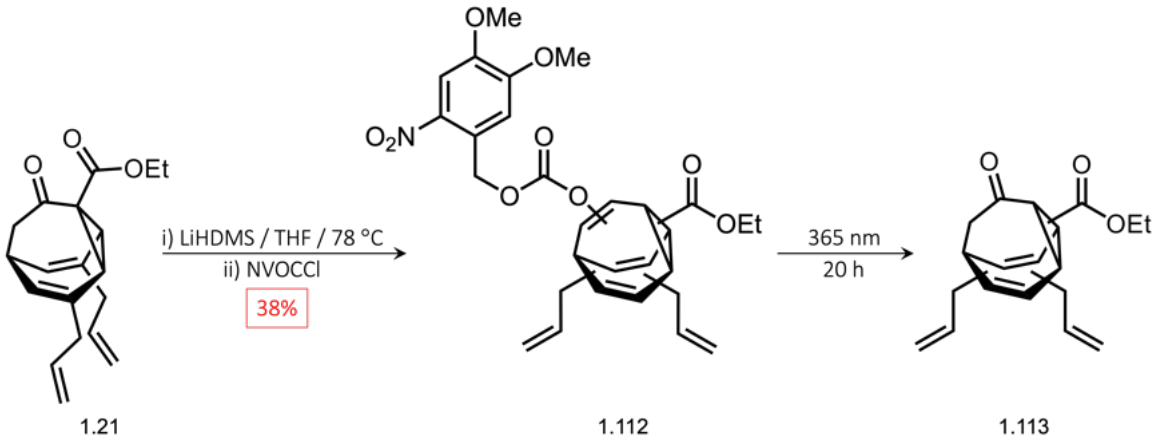

Scheme 1.26. Synthesis and subsequent photolysis of NVOC bisallyl **BV** (**1.112**).

In 2021, Fallon and co-workers reported computational results for the complexation of **BV** within *β*- and *γ*-cyclodextrin (CD) respectively, employing potential energy profiling to determine host-guest binding interactions.[61] The study subjected **BV** and the four hydroxymethylene **BV** isomers in different orientations for binding to CDs. The computational methodology permitted three orientations for the **BV**: (1) where the cyclopropane ring was positioned upwards; (2) downwards and (3) horizontally rotating through a perigon whilst the molecule was simultaneously passed through the CD cavity. These simulations allowed the calculation of binding energies through the consideration of van der Waals and Coulombic interaction potential energies. The gathering of these values also allowed the assessment of binding *via* a heat map of binding energies (Figure 1.8). Computational results disclosed the likelihood for unsubstituted **BV** to fit inside the cavity of *γ*-CD but not *β*-CD. In contrast, hydroxymethylene **BV** isomers to bind preferentially in *β*-CD whilst *γ*-CD did not display any preference.

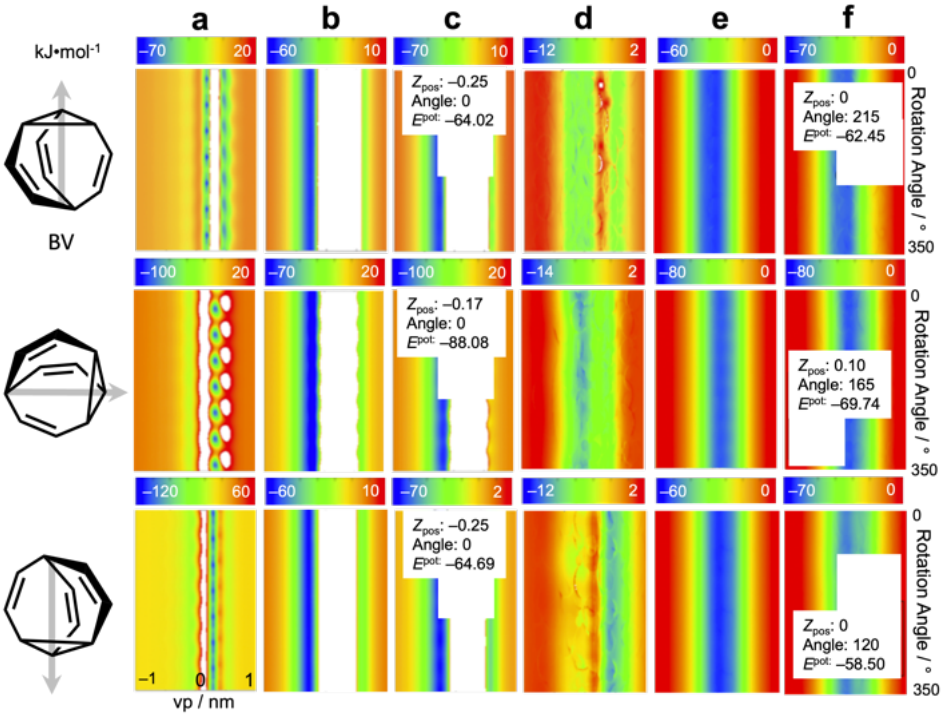

Figure 1.8. Heatmaps for the complexation of unsubstituted **BV** with (**a**–**c**) *β*-CD and (**d**–**f**) *γ*-CD, where each row exhibits different types of non-bonded potential energies: (**a**) and (**d**) van der Waals, (**b**) and (**e**) Coulombic interactions, (**c**) and (**f**) total. vp = vertical position

Further building upon the seminal efficient synthetic methodology to **BVs**, in 2021, the Fallon group reported the use of bis-pyridyl **BVs**, which have been shown to self-assemble in the presence of Pt^{2+} or Pd^{2+}, to form the first metallo-supramolecular cage bearing shapeshifting **BV** ligands.[62] Bis-3-pyridyl **BV** (**1.114**) was synthesised to study the coordination behaviour of M_2L_4 cages, which have well-defined structural features. Synthetically, bis-3-pyridyl **BV** (**1.114**) was synthesised by employing Suzuki coupling conditions to bis-(Bpin) **BV** (**1.74**) and 3-bromopyridine proceeding in 92% yield (Scheme 1.27).

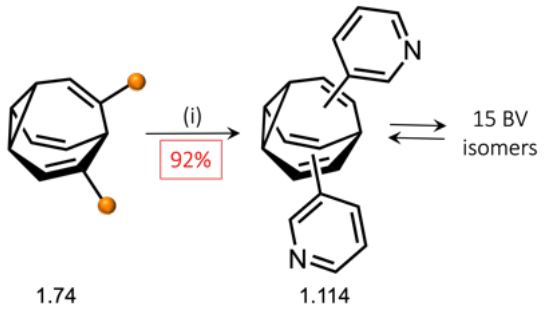

Scheme 1.27. Synthetic route to bis-3-pyridyl **BV** (**1.114**) from bis-Bpin **BV** (**1.74**). Reaction conditions: (i) 3-bromopyridine / $Pd(PPh_3)_4$ / NaOH (5 mol%) / $THF:H_2O$ / 65 °C. The orange circles represent Bpin.

Subsequent VT ^1H NMR spectroscopy exhibited the dynamic equilibrium of three constitutional **BV** isomers (**1.114**$_a$, **1.114**$_b$, **1.114**$_c$) in 48:38:13 ratio, which are in fast exchange at room temperature between a total of 15 isomers.

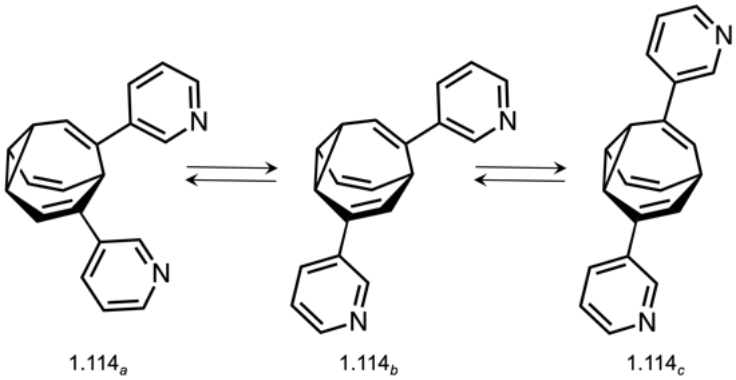

Scheme 1.28. Interconversion of the three constitutional isomers of **1.114**$_a$, **1.114**$_b$ and **1.114**$_c$. Only the three most energetically prevalent isomers of **1.114** are shown for clarity.

The treatment of **1.114** with 0.5 equivalents of $[Pd(CH_3CN)_4](BF_4)_2$ resulted in a complex mixture of a M_2L_4 cage isomers, with encapsulation of BF_4^- (as shown by ^{19}F NMR spectroscopy). However, subsequent anionic exchange with Cl^- or I^- showed the induced shift to one resultant dominant cage species (as shown by solution-state ^1H NMR), whereby **1.114**$_b$ was shown to be the dominant **BV** isomer. With this said, solution-state ^1H NMR continued to exhibit characteristic broad **BV** signals, indicating the presence of fluxional character within the cage complex.

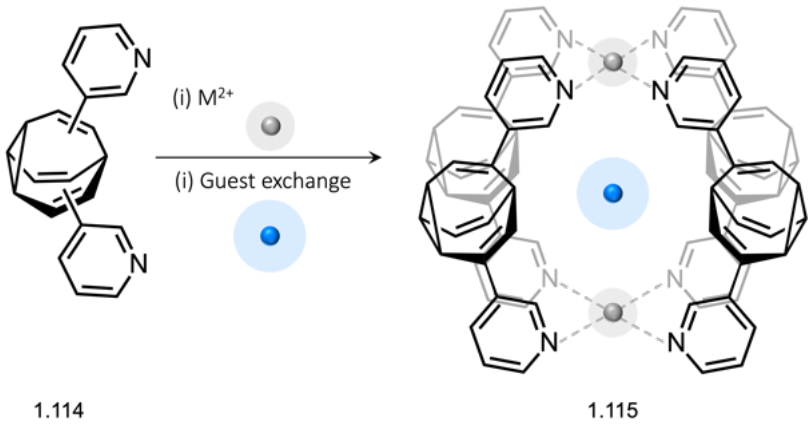

Scheme 1.29. Metal mediated self-assembly of cage **1.115** from **BV 1.114**. Guest exchange from BF_4^- to Cl^- or I^- induces convergence to the **1.114**$_b$ **BV** isomer forming cage **1.115**. M^{2+} = Pt^{2+} or Pd^{2+}.

Furthermore, in 2022, Ihmels and co-workers described the synthesis and photophysical characterisation of novel aryl-substituted **BVs**, demonstrating that the fluxional **BV** core supports excimer formation of aroyl substituents.[63] Resultantly, the excimer formation of the di-aroyl **BV** was shown to be influenced by the association with analytes, allowing for fluorimetric detection of metal cations. First, BDT (**1.36**) was subjected to a photochemical di-π-methane rearrangement to yield bis(hydroxymethyl) **BV** (**1.116**) in 46% yield. Bis(hydroxymethyl) **LBV** (**1.117**), a by-product obtained from the rearrangement reaction of BDT (**1.36**), was also isolated as an inseparable mixture of 3 isomers in 39% yield (Scheme 1.30). Since **LBV** is a static molecule, this forms an ideal comparison analogue to the fluxional **BV** species. The aryl-functionalised **BV** (**1.118**) and **LBV** (**1.119**) was obtained through the treatment of compounds **1.116** and **1.117** with 2-napthoyl chloride in the presence of *N*-methylmorpholine in 64% and 67% yield, respectively (Scheme 1.30). Photophysical studies for **BV** (**1.118**) indicated distinct excimer fluorescence, whereby arene units were located in close vicinity of one another. This observation was corroborated by VT-NMR spectroscopy, which showed the presence of two major **BV** isomers allowing for intramolecular excimer formation. Building upon this observation, the addition of metal cations to **BV** (**1.118**) resulted in significant changes in excimer emission, indicating the applicability of **BV** (**1.118**) to be utilised as a tool for fluorimetric detection of analytes in host-guest chemistry.

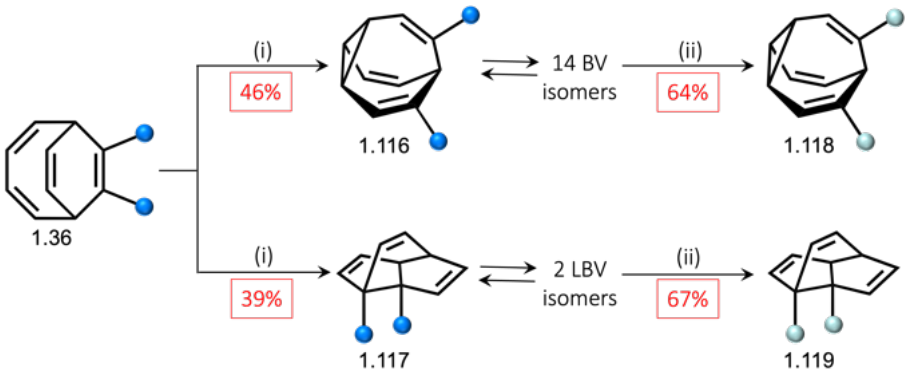

Scheme 1.30. Synthetic route to bis(2-naphthoyloxymethyl) **BV** (**1.118**) and bis(2-naphthoyloxymethyl) **LBV** (**1.119**) from bis(hydroxymethyl) **BV** (**1.116**) and bis(hydroxymethyl) **LBV** (**1.117**). Reaction conditions: (i) 3-bromopyridine / $Pd(PPh_3)_4$ / NaOH (5 mol%) / THF:H_2O / 65 °C; (ii) 2-naphthoyl chloride / *N*-methylmorpholine / CH_2Cl_2 / 0 °C → rt / 1 d. The blue circles represent CH_2OH; the teal circles represent 2-napthoyloxymethyl.

Ihmels and co-workers built upon the aforementioned results in 2023,[64] reporting the reversible restrain and release of a bis(harmane)-functionalised **BV** (**1.120**) as a chelating ligand for metal ions. The **BV**-harmane conjugate (**1.120**) was synthesised *via* Suzuki–Miyaura coupling from bis(Bpin) **BV** (**1.74**) in 82% yield (Scheme 1.31a). Spectrometric titrations were conducted which showed the BV-harmane conjugate (**1.120**) complexed with a range of transition metal ions. In addition, NMR analysis established that **BV**-harmane (**1.120**) formed a tweezer-type complex with Ag^+ ions to form a **BV**–Ag^+ complex (**1.121**), hampering the valence isomerisation of **BV** due to the increased barrier (11 kJ•mol^{-1}) of the Cope rearrangement (Scheme 1.31b). As a result of this increased barrier to rearrangement, one predominant **BV** isomer was formed at 5 °C. The addition of hexacyclene (**HC**), a macrocycle known for its high affinity towards Ag^+, resulted in decomplexation of the **BV**–Ag^+ complex and formation of a HC–Ag^+ (**1.122**) complex (Scheme 1.31b), demonstrating the reversible restrain and release within **BV** complexation systems.

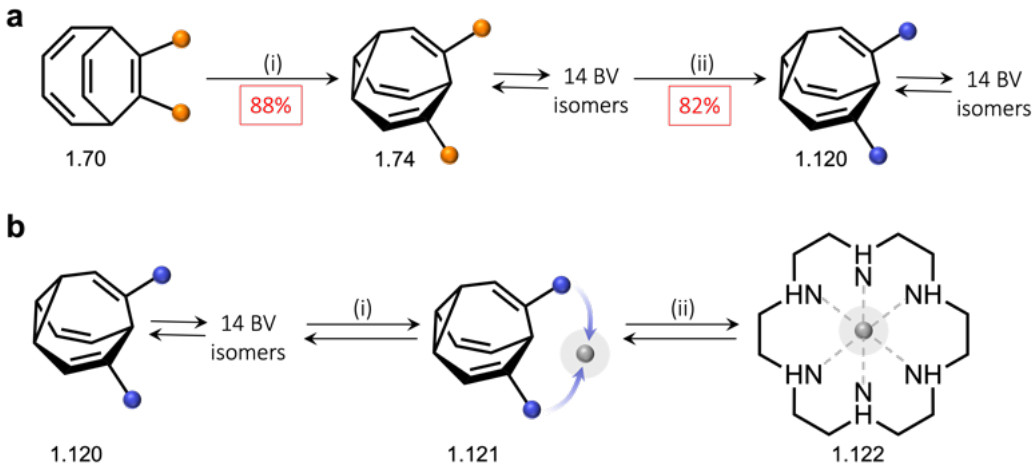

Scheme 1.31. (**a**) Synthetic route to bis(Bpin) **BV** (**1.74**) and bis(harmane) **BV** (**1.120**) from bis(Bpin) **BDT** (**1.70**). Reaction conditions: (i) *9H*-thioxanthen-9-one (1 mol%) / THF / 365 nm LED lamp / rt; (ii) 1-methyl-9-(4-bromobenzyl)-pyrido[3,4-b]indole (2.2 equiv.) / $Pd(PPh_3)_4$ / NaOH (10 mol%) / THF / 60 °C / 16 h. The coloured circles represent a functional group: orange = Bpin, indigo = 1-methyl-9-benzyl-pyrido[3,4-b]indole, grey = Ag^+ (**b**) Complexation of the Ag^+ cation with the bis(harmane) **BV** (**1.120**), forming the **BV**–Ag^+ complex (**1.121**). The addition of hexacyclene (**HC**) results in decomplexation of the **BV**–Ag^+ complex (**1.121**) and formation of the HC–Ag^+ complex (**1.122**). Reaction conditions: (i) Ag^+ (1.0 equiv.) / ΔT; (ii) **HC** (1.0 equiv.).

1.5.4 Exotic Bullvalenes for Medicine, Materials and Electronics

In 2023, Moses and co-workers[20] reported the merger of **BV** with the glycopeptide antibiotic, vancomycin (which has previously been known as the 'antibiotic of last resort'). However, clinical resistance to vancomycin has been shown to have developed in *Enterococci* (1987)[65] and in *Staphylococcus aureus* (2002)[66] due to the emergence of antibiotic resistance through single point mutation D-Ala-D-Ala to D-Ala-D-Lac. As a result of this mutation, which plays a pivotal role in bacterial cell wall production, there is a reduction in vancomycin binding and resultantly a 1000-fold decrease in antimicrobial activity of vancomycin. With this in mind, it has been shown that the covalent tethering of glycopeptides (including vancomycin) to form polyvalent structures show improved antibiotic activity against vancomycin-resistant bacteria. The reasons for this improved activity are not fully understood, although for 'head-to-tail' and 'back-to-back' dimers, the hydrogen bonds at the dimer interface originate from the same amide moieties that are involved in binding to the D-Ala-D-Ala binding site. It is thought that this co-operative interaction means that the vancomycin dimer has an increased affinity for D-Ala-D-Ala, in comparison with the monomer species.

With this said, current chemical systems to overcome antibiotic resistance have been shown to suffer from long equilibration times, requiring additional reagents to regulate reversibility and to restrict the equilibrium once adaptation has taken place.[67]

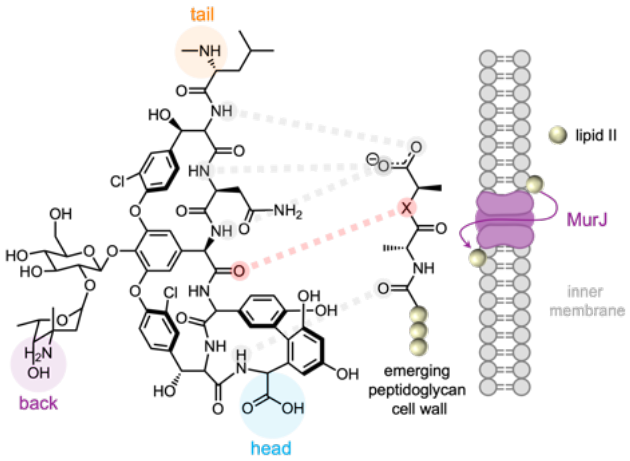

Figure 1.9. Structure of vancomycin and the binding mechanism of vancomycin to the bacterial peptidoglycan cell wall analogue. The red dotted line indicates the key binding site to the bacterial cell wall, whereby when (**a**) X = NH (D-Ala-D-Ala) is susceptible to vancomycin in susceptible bacteria and (**b**) X = O (D-Ala-D-Lac) is resistant to vancomycin in resistant strains. The grey dotted lines indicate vancomycin binding interactions to the bacterial cell wall in both susceptible and resistant strains, regardless of mutations.

To this end, Moses and co-workers explored the possibility for 'shapeshifting' antibiotics to offer a different avenue to overcome vancomycin-resistant bacteria.[20] The **BV** vancomycin dimer was synthesised in a modular manner connecting the 1) **BV** core; 2) flexible linker; and 3) vancomycin warhead. First, bis(hydroxymethyl) **BDT** (**1.36**) was treated with sodium hydride, then propargyl bromide to afford the bis(propargyl ether) **BDT** (**1.123**) in 87% conversion (Scheme 1.32). The subsequent photochemical di-π-methane rearrangement of compound **1.123** allowed access to the bis(propargyl ether) **BV** (**1.119**) in 50% yield. With bis(propargyl ether) **BV** (**1.124**) in hand, this was subjected to CuAAC conditions with azides (**1.125a–k**) to yield the aldehyde-containing **BVs** (**1.126a–k**) with varying linker lengths. The ensuing reductive amination of aldehydes (**1.127a–k**) with the vancosamine unit of vancomycin and sodium cyanoborohydride showed conversion to **BV** vancomycin dimers (**1.127a–k**) in relatively low yields of 8–30%.

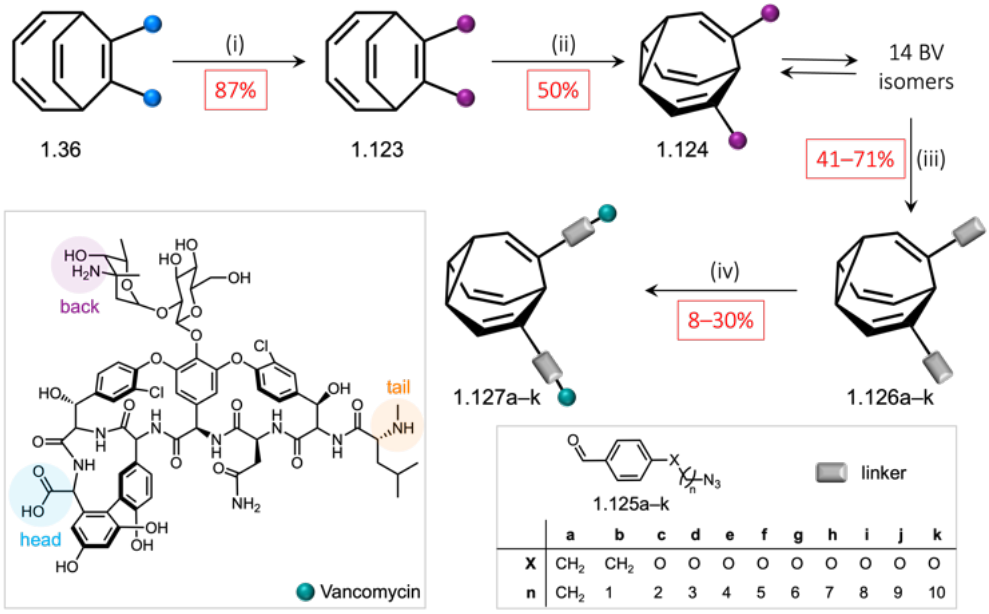

Scheme 1.32. Synthetic route to bis(vanc) **BVs** (**1.127a–k**) from bis(hydroxymethyl) **BDT** (**1.36**). Reaction conditions: (i) propargyl bromide (7.0 equiv.) / NaH (6.0 equiv.) / THF / 0 °C → rt / 16 h; (ii) *hv* high-pressure mercury lamp / Pyrex glassware / acetone / 0 °C / 2 d; (iii) aromatic azide (2.2 equiv.) / $CuSO_4$•$5H_2O$ (0.5 equiv.) / sodium ascorbate (0.25 equiv.) / ^tBuOH:H_2O, 3:1 ratio (0.01 M) / 85 °C / 16 h; (iv) 1) vancomycin (2.2 equiv.) / MeOH:DMF, 1:1 (0.01 M) / iPr_2NEt (8.0 equiv.) / 70 °C / 2 h; then 2) $NaCNBH_3$ (10.0 equiv.) / 70 °C / 16 h. The coloured circles represent a functional group: blue = CH_2OH, magenta = 3-ethoxyprop-1-yne, teal = vancomycin appended chain. The grey rectangle represents a the ethoxymethyl-triazol-1-yl-methyl benzaldehyde linker (a–k).

To assess the antibacterial activity, bis(vanc) **BVs** (**1.127a–k**) were tested against drug-sensitive and drug-resistant strains of *Enterococci* and *Staphylococcus aureus*. All bis(vanc) **BVs** (**1.127a–k**) were shown to display some degree of antibacterial activity, whereby there was enhanced activity towards vancomycin resistant strains. Resistance studies were also conducted to probe if the incorporation of a **BV** core could minimise the development of vancomycin resistance. The results were compared against rigid aryl vancomycin-dimers (**1.128a–c**) with different regiochemistry of the aryl group (in ortho, meta and para positions). This study showed that the rigid aryl vancomycin dimers developed a 4–16 fold increase in the minimum inhibitory concentration (MIC) of an antibiotic (where bacterial growth was completely inhibited), indicating the emergence of early-stage vancomycin resistance. On the contrary, **BV** analogue **1.127d** did not show any significant change in resistance to the bacterial strain, suggesting that

the incorporation of a fluxional linker may provide advantages to overcome antibiotic resistance, relative to their rigid counterparts.

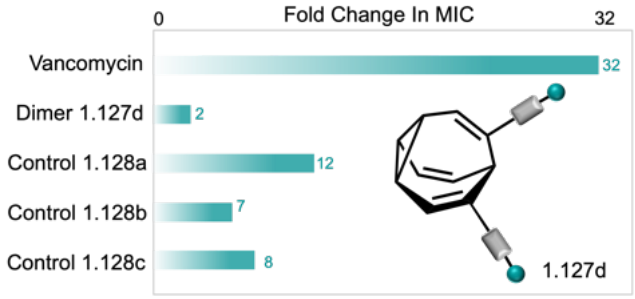

Figure 1.10. Propensity of *Enterococcus faecium* to develop resistance against Vancomycin, compound **1.127d** and control compounds (**1.128a–c**). *Enteroccoccus facium* was exposed to increasing concentrations of vancomycin, the **BV**-vanc dimer (**1.127d**) and aryl-vanc dimers (**1.128a–c**), up to 4× MIC. The data plotted shows the fold change in MIC value.

Furthermore, in 2023, Golder *et al.* reported the incorporation of **BV** into a π-rich polymer to demonstrate methods to modulate structural rigidity.[19] This study highlights how the variation in the amount of **BV** incorporation allows for the tuning of thermal properties and solution-state conformation, which are brought about by kinked architectures inherently caused by stochastic **BV** isomers within the polymer backbone. Golder *et al*. explored this concept by linking **BV** co-monomers with relatively rigid *p*-phenylenes to produce poly(**BV**-co-phenylene)s, represented by $\mathbf{PB_xP_y}$ (x = **BV**% and y = phenylene%). Synthetically, bis(Bpin) **BV** (**1.74**) was produced through the sequential cobalt-catalysed cycloaddition of 1,2-bis(Bpin) ethyne with **COT** to produce bis(Bpin) **BDT** (**1.70**), followed by the ensuing di-π-methane rearrangement to yield bis(Bpin) **BV** (**1.74**) in a respectable 60% yield. The bis(Bpin) **BV** (**1.74**) was then polymerised with 2,5-di-hexyl-1,4-bromobenzene (**1.129**) under Suzuki–Miyaura polycondensation conditions to access alternating co-polymers $\mathbf{PB_{50}P_{50}}$, with average molar masses of 1.5–21kDa. Additionally, in order to compare the structural role of **BV** with a π-rich polymer framework, analogous rigid poly(*p*-phenylene)s were also synthesised through the additional incorporation of bis(Bpin)-1,4-benzene (**1.130**), as well as some samples doped with **BV**, to form random co-polymers $\mathbf{PB_xP_y}$.

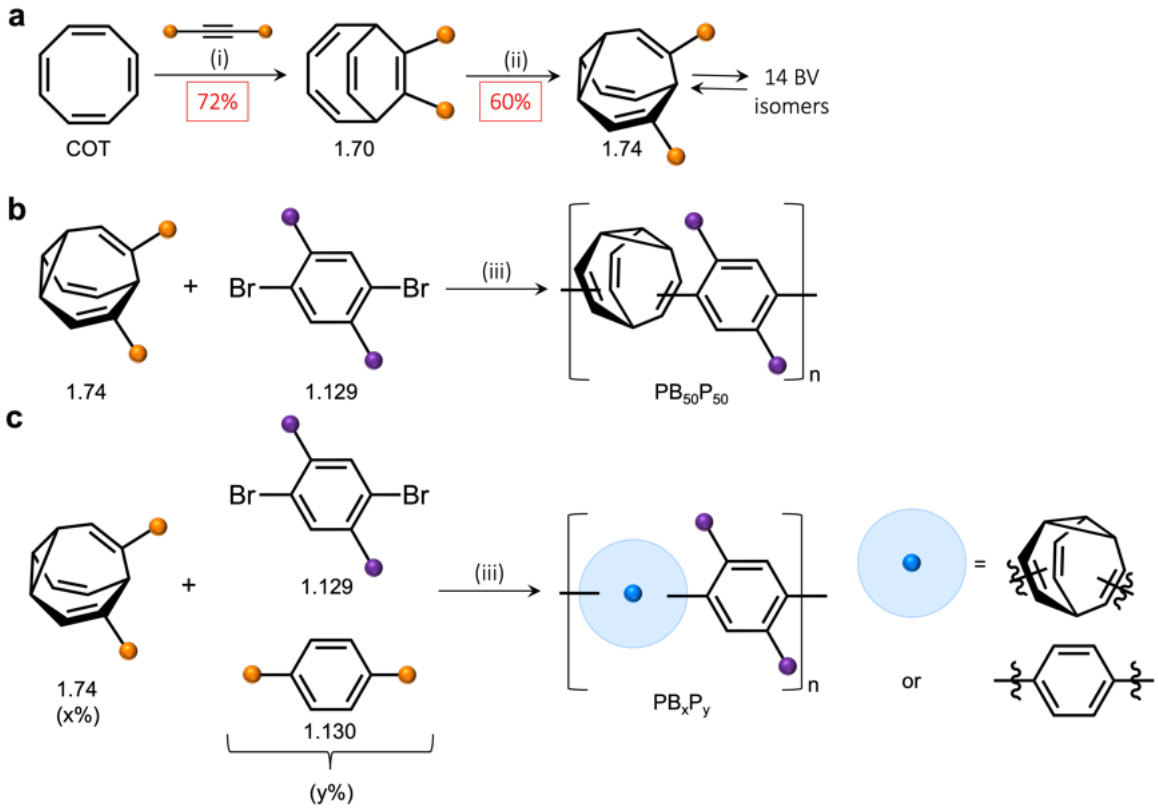

Scheme 1.33. Synthetic route to polymers **PB$_{50}$P$_{50}$** and **PB$_x$P$_y$** from bis(Bpin) **BDT** (**1.70**). Reaction conditions: (**a**) (i) bis(Bpin) acetylene (1.00 equiv.) / $CoBr_2$(dppe) (10 mol%) / ZnI_2 (20 mol%) / Zn (30 mol%) / DCE / rt / 6 h / N_2 atmosphere; (ii) thioxanthene-9-one (25 mol%) / 365 nm / acetone / rt / 18 h; (**b** and **c**) (iii) Pd XPhos G3 (20 mol%) / K_3PO_4 (2 M) / toluene / 60 °C / 48 h; The coloured circles represent a functional group: orange = Bpin, purple = hexyl, blue = **BV** or Ph moiety within the polymer backbone; x = **BV** loading (034%).

Interestingly, the polymers produced (**PB$_{50}$P$_{50}$** and **PB$_x$P$_y$**) exhibit good thermal stability ($T_{10\%}$ = 243 °C), showing tuneable thermal properties relative to **PB$_0$P$_{100}$** (where M_n = 5.0 kDa). In addition, the polymers with composition **PB$_{50}$P$_{50}$** have low glass transition temperatures (21–44 °C), caused by randomly kinked **BV** within the polymer framework, which are otherwise difficult to introduce, whilst also being unachievable with adamantane or norbornadiene moieties. Furthermore, varying the **BV** composition (x = 0–34%) with randomly doping poly(*p*-phenylene)s allows for thermal- and solution-state properties to be modulated. Hence, the incorporation of **BV** has been shown as a new method to control polymer chain rigidity as a result of stochastic kinks within the polymer backbone. It is anticipated that **BV** containing polymers may serve as effective internal plasticisers to modulate polymer properties within other π-rich polymers, as well as being implemented into responsive soft materials.

Most recently, Darwish and co-workers reported the use of **BV** isomerism as a technique for controlling piezoresistance with a single molecule.[68] More generally, the term piezoresistivity relates to the change in electrical resistivity of a semiconductor or a metal when mechanical strain is applied. This study exploits the combination of constitutional and conformational isomerism to create fast-switching transistor-like circuits that uses single molecule **BV** isomerism on the millisecond timescale, owing to **BVs** ability to significantly change shape through sigmatropic rearrangements. In single molecule conductance studies, molecules are held between two gold contacts whereby the molecule can conduct electricity. Sulfur is typically used to allow the molecule in question to be attached to the gold surface. In this study, bis(4-thioanisole) **BV** (**1.131**) was prepared from bis(Bpin) **BV** (**1.74**) through subjection to Suzuki cross-coupling with 4-bromothioanisole in 85% yield. The isomer distribution was explored experimentally and computationally, whereby the lowest energy isomers have aryl rings conjugated to alkenes within the **BV** scaffold. The introduction of SCH_3 allows for a molecule-electrode contact point. Then, to investigate if bis(4-thioanisole) **BV** (**1.131**) could control conductance, scanning tunnelling microscopy break junction (STMBJ) techniques were used to follow a single molecule reaction in real time. In STMBJ, a gold STM tip is used to defect a gold surface and then retracted, which then allows for single molecules to bridge the broken contacts. Therefore, this bridging of molecules allows for conductance to be measured as the electrode-electrode separation is varied. Single bis(4-thioanisole) **BV** (**1.131**) molecules are observed to undergo constitutional and configurational isomerisation through STMBJ experiments, as well as computational simulations, controlled through the distance adjustments of the gold contacts. This also demonstrates that piezoresistance can be stabilised on a scale of 3–9 Å, due to **BV** isomerisation-driven piezoresistivity.

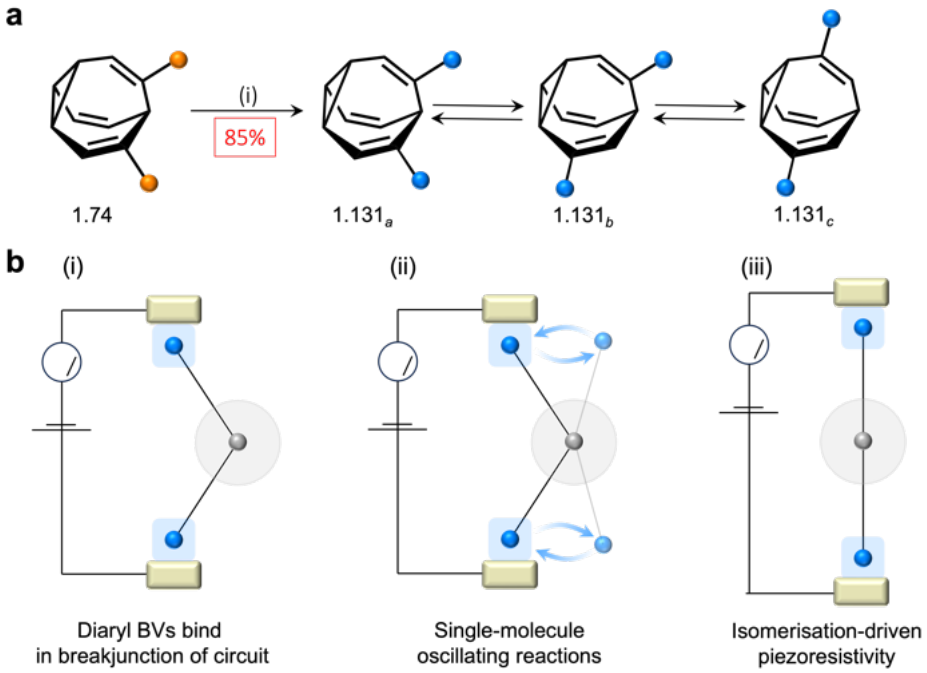

Scheme 1.34. (**a**) Synthetic route to bis(4-thioanisole) **BV** (**1.131**) from bis(Bpin) **BV** (**1.74**). Reaction conditions: (i) 4-bromothioanisole (2.2 equiv.) / $Pd_2(dba)_3$ (20 mol%) / $[HP(^tBu)_3]BF_4$ (80 mol%) / NaOH / THF:H_2O / 65 °C; isomers **1.131**$_{a–c}$ are present in 53:33:14% in solution, respectively. The coloured circles represent a functional group: orange = Bpin, blue = 4-thioanisole; (**b**) (i) bis(4-thioanisole) **BV** (**1.131**) bind within the circuit in a bent isomer at short gold tip-tip distances in STMBJ experiments; (ii) At specific gold tip extensions, **BV** (**1.131**) isomers present different conductances and appear in equilibrium, allowing for oscillating single-molecule reactions (represented by blue arrows), that occur on the ms timescale to be followed; (iii) **BV** (**1.131**) isomerism is induced by tip retraction allows for control of conductance, demonstrating molecular isomerisation-driven piezoresistance. For (i), (ii) and (iii), the coloured circles represent molecular functionality: grey = **BV**, blue = 4-thioanisole; the gold tip present in the STMBJ experiments is represented by a gold rectangle within the circuit.

1.6 Overview

Fluxional carbon cages have been shown to be a distinctive class of molecule, exhibiting a varied array of 'shapeshifting' properties, owing to rearrangement processes which arise from their structural arrangement. Compared with the large majority of static chemical compounds, this atypical occurrence has allowed for a more thorough understanding of valence isomerisation, given the chemical toolbox to study a fluxional library of compounds that inconspicuously exist as a single, inseparable entity.

As previously described in the introduction, historically, the synthetic access to fluxional carbon cages proved challenging, relying upon inefficient and lengthy synthetic pathways. More recently, however, the development of more efficient synthetic methodology has allowed for an increased access to fluxional carbon cages (particularly in the case of **BV**). Additionally, investigations into the behaviour of substituted nondegenerate **BBs** have been undertaken, demonstrating that their equilibria and stereochemistry can be controlled in the solution and solid state. This new-found understanding into the equilibria and rearrangement processes of **BB** could allow for its use in more complex systems, whereby these physical properties are applied for functional modality.

As such, these synthetic advancements have made it possible for **BV** to be incorporated into an array of potential applications, for use in medicines, materials and electronics, whilst the equilibria and rearrangement processes in **BV** have been more thoroughly investigated and validated alongside computational predictions.

1.7 References

1 J. F. Teichert, D. Mazunin and J. W. Bode, *J. Am. Chem. Soc.*, 2013, **135**, 11314–11321.

2 G. Schröder and W. Witt, *Angew, Chem. Int. Ed. Engl.*, 1979, **18**, 311–312.

3 W. v. E. Doering and W. R. Roth, *Tetrahedron*, 1963, **19**, 715–737.

4 G. Schröder, *Angew. Chem. Int. Ed. Engl.*, 1963, **2**, 481–482.

5 R. Merényi, J. F. M. Oth and G. Schröder, *Chem. Ber.*, 1964, **97**, 3150–3161.

6 S. Ferrer and A. M. Echavarren, *Synthesis*, 2019, **51**, 1037–1048.

7 P. Ahlberg, D. L. Harris and S. Winstein, *J. Am. Chem. Soc.*, 2002, **92**, 4454–4456.

8 D. Cremer, P. Svensson, E. Kraka and P. Ahlberg, *J. Am. Chem. Soc.*, 2002, **115**, 7445–7456.

9 P. Ahlberg, J. B. Grutzner, D. L. Harris and S. Winstein, *J. Am. Chem. Soc.*, 2002, **92**, 3478–3480.

10 J. B. Grutzner and S. Winstein, *J. Am. Chem. Soc.*, 2002, **92**, 3186–3187.

11 L. G. Greifenstein, J. B. Lambert, M. J. Broadhurst and L. A. Paquette, *J. Org. Chem.*, 1973, **38**, 1210–1215.

12 G. G. Christoph, S. Hardwick, U. Jacobsson, Y. B. Koh, R. Moerck and L. A. Paquette, *Tetrahedron Lett.*, 1977, **18**, 1249–1252.

13 C. Engdahl and P. Ahlberg, *J. Am. Chem. Soc.*, 1979, **101**, 3940–3946.

14 W. v. E. Doering, B. M. Ferrier, E. T. Fossel, J. H. Hartenstein, M. Jones, G. Klumpp, R. M. Rubin and M. Saunders, *Tetrahedron*, 1967, **23**, 3943–3963.

15 H. E. Zimmerman and G. L. Grunewald, *J. Am. Chem. Soc.*, 1966, 88, 183–184.

16 S. Zhang, W.-X. Zhang and Z. Xi, *Acc. Chem. Res.*, 2015, **48**, 1823–1831.

17 A. N. Bismillah, B. M. Chapin, B. A. Hussein and P. R. McGonigal, *Chem. Sci.*, 2020, **11**, 324–332.

18 K. K. Larson, M. He, J. F. Teichert, A. Naganawa and J. W. Bode, *Chem. Sci.*, 2012, **3**, 1825–1828.

19 M. N. Pomfret, P. B. Sun, Z. Huang, A. C. Freund, T. Miyoshi and M. R. Golder, *Angew. Chem. Int. Ed.*, 2023, **62**, e202301695.

20 A. Ottonello, J. A. Wyllie, O. Yahiaoui, S. Sun, R. A. Koelln, J. A. Homer, R. M. Johnson, E. Murray, P. Williams, J. R. Bolla, C. V. Robinson, T. Fallon, T. P. Soares da Costa and J. E. Moses, *Proc. Natl. Acad. Sci. U. S. A.*, 2023, **120**, e2208737120.

21 A. C. Cope and E. M. Hardy, *J. Am. Chem. Soc.*, 1940, **62**, 441–444.

22 J. F. M. Oth, K. Müllen, J. -M Gilles and G. Schröder, *Helv. Chim. Acta.*, 1974, **57**, 1415–1433.

23 W. von E. Doering and J. W. Rosenthal, *J. Am. Chem. Soc.*, 1966, **88**, 2078–2079.

24 M. Jones and L. T. Scott, *J. Am. Chem. Soc.*, 1967, **89**, 150–151.

25 J. F. M. Oth, R. Merényi, J. Nielsen and G. Schröder, *Chem. Ber.*, 1965, **98**, 3358.

26 A. R. Lippert, J. Kaeobamrung and J. W. Bode, *J. Am. Chem. Soc.*, 2006, **128**, 14738–14739.

27 H. D. Patel, T. H. Tran, C. J. Sumby, L. F. Pašteka and T. Fallon, *J. Am. Chem. Soc.*, 2020, **142**, 3680–3685.

28 O. Yahiaoui, L. F. Pašteka, B. Judeel and T. Fallon, *Angew. Chem. Int. Ed.*, 2018, **57**, 2570–2574.

29 J. Font, F. López and F. Serratosa, *Tetrahedron Lett*, 1972, **13**, 2589–2590.

30 G. Schröder and J. F. M. Oth, *Angew. Chem. Int. Ed. Engl.*, 1967, **6**, 414–423.

31 J. F. M. Oth, R. Merényi and G. Engel Und, *Tetrahedron Lett.*, 1966, **7**, 3377–3382.

32 C. Hoogzand, J. Nielsen and J. F. M. Oth, *Tetrahedron Lett.*, 1970, **11**, 2287–2292.

33 W. K. Sarma and W. and G. Schröder, *Chem. Ber.*, 1986, **119**, 2339.

34 J. F. M. Oth, E. Machens, H. Röttele and G. Schröder, *Liebigs Ann.* 1971, **745**, 112.

35 K. Rebsamen, H. Röttele and G. Schröder, *Chem. Ber.*, 1993, **126**, 1429–1433.

36 A. N. Bismillah PhD Thesis, Durham University, 2019.

37 K. K. Larson, M. He, J. F. Teichert, A. Naganawa and J. W. Bode, *Chem. Sci.*, 2012, **3**, 1825–1828.

38 T. Mukaiyama, *Angew. Chem. Int. Ed. Engl.*, 1977, **16**, 817–826.

39 N. E. Schore, *Chem. Rev.*, 1988, **88**, 1081–1119.

40 A. Anand, P. Singh, V. Kumar and G. Bhargava, *RSC. Adv.*, 2019, **9**, 25554–25568.

41 B. M. Trost, *Acc. Chem. Res.*, 2002, **35**, 695–705.

42 M. Dai, D. Sarlah, M. Yu, S. J. Danishefsky, G. O. Jones and K. N. Houk, *J. Am. Chem. Soc.*, 2007, **129**, 645–657.

43 M. Achard, A. Tenaglia and G. Buono, *Org. Lett.*, 2005, **7**, 2353–2356.

44 M. Achard, M. Mosrin, A. Tenaglia and G. Buono, *J. Org. Chem.*, 2006, **71**, 2907–2910.

45 S. Ferrer and A. M. Echavarren, *Angew. Chem. Int. Ed.*, 2016, **55**, 11178–11182.

46 H. E. Zimmerman, R. W. Binkley, R. S. Givens and M. A. Sherwin, *J. Am. Chem. Soc.*, 1967, **89**, 3932–3933.

47 H. E. Zimmerman and D. Armesto, *Chem. Rev.*, 1996, **96**, 3065–3112.

48 H. E. Zimmerman and R. M. Paufler, *J. Am. Chem. Soc.*, 1960, **82**, 1514–1515.

49 M. Jones, S. D. Reich and L. T. Scott, *J. Am. Chem. Soc.*, 1970, **92**, 3118–3126.

50 L. A. Paquette, J. R. Malpass, G. R. Krow and T. J. Barton, *J. Am. Chem. Soc.*, 1969, **91**, 5296–5306.

51 W. von E. Doering and W. R. Roth, *Angew. Chem. Int. Ed. Engl.*, 1963, **2**, 115–122.

52 P. R. McGonigal, C. De León, Y. Wang, A. Homs, C. R. Solorio-Alvarado and A. M. Echavarren, *Angew. Chem. Int. Ed.*, 2012, **51**, 13093–13096.

53 W. v. E. Doering, B. M. Ferrier, E. T. Fossel, J. H. Hartenstein, M. Jones, G. Klumpp, R. M. Rubin and M. Saunders, *Tetrahedron*, 1967, **23**, 3943–3963.

54 J. G. Henkel and J. T. Hane, *J. Org. Chem.*, 2002, **48**, 3858–3859.

55 H. Quast, M. Witzel, E.-M. Peters, K. Peters, H. G. Von Schnering, H. Quast, M. Witzel, E.-M. Petersb, K. Petersb and H. Georg Von Schneringb, *Liebigs Ann.*, 1995, **5**, 725–738.

56 A. N. Bismillah, J. Sturala, B. M. Chapin, D. S. Yufit, P. Hodgkinson and P. R. McGonigal, *Chem. Sci.*, 2018, **9**, 8631–8636.

57 C. W. Jefford, J. C. Rossier and J. A. Zuber, *Angew. Chem. Int. Ed. Engl.*, 1982, **21**, 549–549.

58 A. N. Bismillah, T. G. Johnson, B. A. Hussein, A. T. Turley, P. K. Saha, H. C. Wong, J. A. Aguilar, D. S. Yufit and P. R. McGonigal, *Nat. Chem.*, 2023, **15**, 615–624.

59 A. R. Lippert, V. L. Keleshian and J. W. Bode, *Org. Biomol. Chem.,* 2009, **7**, 1529–1532.

60 J. F. Teichert, D. Mazunin and J. W. Bode, *J. Am. Chem. Soc.*, 2013, **135**, 11314–11321.
61 Z. Shadfar, O. Yahiaoui, T. A. Collier, T. Fallon and J. R. Allison, *J. Chem. Phys.*, 2021, **154**, 154105.
62 A. P. Birvé, H. D. Patel, J. R. Price, W. M. Bloch and T. Fallon, *Angew. Chem. Int. Ed*., 2022, **61**, e202115468.
63 C. Dohmen, H. Ihmels and T. Paululat, *Eur. J. Org. Chem.*, 2022, e202201172.
64 C. Dohmen, T. Paululat and H. Ihmels, *Chem. Eur. J.,* 2024, **30**, e202304311.
65 R. Leclercq, E. Derlot, J. Duval and P. Courvalin, *N. Engl. J. Med.*, 1988, **319**, 157–161.
66 L. M. Weigel, D. B. Clewell, S. R. Gill, N. C. Clark, L. K. McDougal, S. E. Flannagan, J. F. Kolonay, J. Shetty, G. E. Killgore and F. C. Tenover, *Science*, 2003, **302**, 1569–1571.
67 L. L. Silver, *Clin. Microbiol. Rev.* 2011, **24**, 71–109.
68 J. R. Reimers, T. Li, A. P. Birvé, L. Yang, A. C. Aragonès, T. Fallon, D. S. Kosov and N. Darwish, *Nat. Commun.,* 2023, **14**, 1–13.

Chapter 2

A Guide To Bullvalene Stereodynamics And 3-Dimensional Shape Diversity

Published as *"A Guide to Bullvalene Stereodynamics"*

R. A. Ives,‡ W. Maturi,‡ M. T. Gill, C. Rankine and P. R. McGonigal,

Chem. Sci. 2024, Advance Article.

‡ These authors contributed equally.

Synopsis

Here, we analyse the stereodynamic properties of bullvalenes using principal moments of inertia and exit vector plots to draw comparisons with commonly used ring systems in medicinal chemistry. To aid these analyses, we first classify (i) the four elementary rearrangement steps available to substituted bullvalenes, which (ii) can be described by applying positional descriptors (α, β, γ, and δ) to the substituents. We also (iii) derive an intuitive equation to calculate the number of isomers for a given bullvalene system. Using DFT-modelled structures for di-, tri-, and tetrasubstituted bullvalenes, generated using a newly developed computational tool (*bullviso*), we show that their 3-D shapes and the exit vectors available from the bullvalene scaffold make them comparable to other bioisosteres currently used to replace planar aromatic ring systems in drug discovery. Unlike conventional ring systems, the shapeshifting valence isomerism of bullvalenes gives rise to numerous shapes and substituent relationships attainable as a concentration-independent dynamic covalent library from a single compound. We visualise this property by applying population weightings to the principal moments of inertia and exit vector analyses to reflect the relative thermodynamic stabilities of the available isomers.

Acknowledgments

The following people are gratefully acknowledged for their contribution to this chapter: W. Maturi for contributions to this work and editing the text; Dr. M. Gill for contributions to editing the text; Dr. C. Rankine for developing the *bullviso* tool for isomer generation and performing the DFT computational work; Dr. J. Firth and Prof. Peter O'Brien for useful discussions.

2.1 Introduction

2.1.1 The Nomenclature of Bullvalene

In 1963, von Eggers Doering hypothesized the existence of **BV** which, through sequential strain-assisted Cope rearrangements, may adopt any one of 1 209 600 degenerate isomers.[1] **BV** comprises three 1,5-hexadiene motifs, each positioned on one of **BVs** three faces, whereby one of the two olefins in this motif is always 'shared' on the edge of two adjacent faces. Representing the structural variability that **BV** can access makes identifying all of its isomers a tedious and time consuming task. In light of this complexity and in order to comprehend **BVs** fluxionality more easily, in 2013 Bode and co-workers pioneered a 10-digit nomenclatural barcode to readily identify each **BV** isomer.[2] Each number in the code represents an individual carbon atom within the **BV** structure. Additionally, these numbers are grouped into three triads, representing the three arms attached to the cyclopropane moiety. The final single digit represents the apical bridgehead carbon (Figure 2.1).[2]

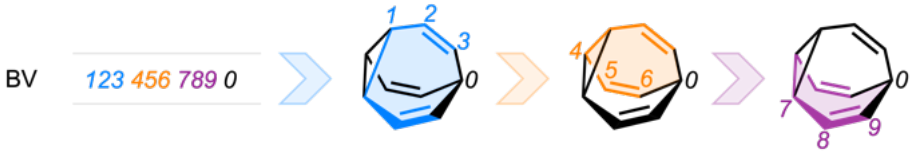

Figure 2.1. Depiction of the 10-digit nomenclatural barcode proposed by Bode and co-workers for carbon atoms positions in the **BV** framework. The blue, orange and magenta shading highlights the three faces of **BV**, whilst numbers emphasise the respective carbon atoms that reside on the edge of the highlighted face.

As a consequence of **BVs** C_{3v} symmetry, three codes are feasible for each isomer respectively. Conventionally, the smallest number is selected to represent a particular isomer where all three bridges are chemically equivalent, meaning that, in accordance with the barcode, the positions (1, 4, 7), (2, 5, 8) and (3, 6, 9) are indistinguishable from one another. This is more clearly depicted through the rotational relationship of substituents on **BV** with the barcode system, where by convention, the lowest barcode value is the correct barcode used to represent the disubstituted **BV** isomer (**2.1**), as shown in Figure 2.2.[2] Importantly, the barcode system requires the assignment of

priorities to groups attached to **BV** core in accordance to the Cahn-Ingold-Prelog rules,[3] allowing for substituted **BVs** to be assigned isomerically.

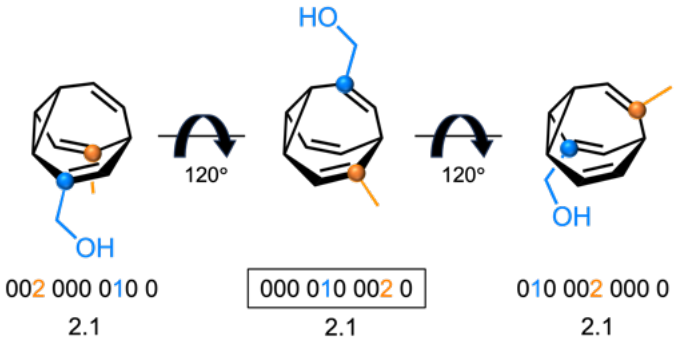

Figure 2.2. An example of a disubstituted **BV** (**2.1**) and its isomer barcode system, whereby three codes are possible. The rotational relationship of substituents on **BV**, owing to its C_{3v} symmetry, is shown *via* 120° rotations with the respective barcode system. Conventionally, the lowest barcode value is the correct barcode (as highlighted in the rectangle). The blue and orange circles represent carbon atoms, allowing for these atoms to be tracked upon rotation of the **BV**.

Furthermore, given that **BV** has the ability to access three sets of enantiomeric pairs (owing to its inherent symmetry), is was highlighted by Bode and co-workers that it is important to be able to distinguish between enantiomers by the barcode system.[2] Resultantly, pairs of **BV** enantiomers can be easily recognised *via* the barcode system, where the two triads corresponding to the two substituted arms of the **BV** are exchanged with one another, to create a new code (Figure 2.3). Notably, as a consequence of **BVs** C_{3v} symmetry, a **BV** can only be chiral if all three 'arms' are non-identical, resulting in the breakdown of symmetry about the horizontal mirror plane through the centre of the **BV** core.

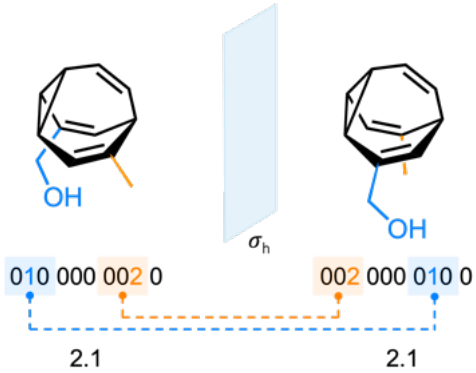

Figure 2.3. An example of an enantiomeric pair of **BV** (**2.1**) and their respective isomer barcodes. The horizontal mirror plane, σ_h, is shown with the two disubstituted **BV** enantiomers. The blue and orange shading shows the exchange of triads within each code.

Building upon Bode's isomer barcode system, Fallon and co-workers advanced systems further, allowing for transition states to be generated computationally *via* algorithmic predictions.[4] In doing so, this computational methodology allowed for the comparison between experimental VT NMR analysis and computational simulations of **BV** isomer population ratios, for both mono- and disubstituted **BVs**. Evidently, there is clear agreement between predicted and experimental observations, demonstrating that these computational analyses are valuable to understand **BV** isomer distributions (Figure 2.4).[4]

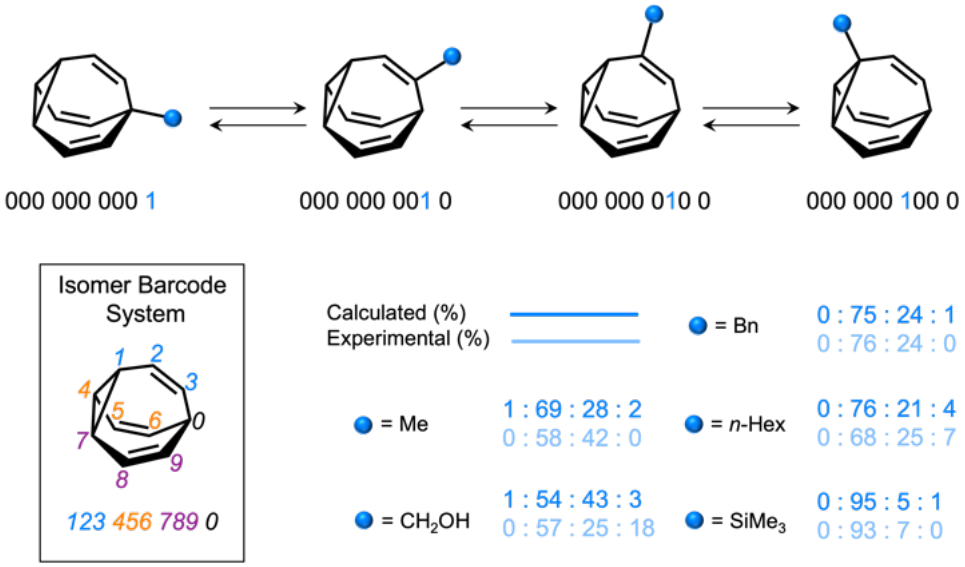

Figure 2.4. Depiction of the isomer barcode system for monosubstituted **BVs**. The analysis shows both computational predictions and experimental observations for isomer population ratios.[4] The blue circle represents an appended substituent, as described.

The **BV** rearrangement processes have also been frequently represented mathematically by network graphs, allowing for the visual representation of the relationship between interconverting **BV** isomers. The earliest example of a network graph applied to **BV** interconversion originates from Brant and co-workers in 1994.[5] Apart from documenting the number of: 1) **BV** isomers; 2) enantiomers pairs; and 3) rearrangement processes, the published network graphs illustrate the interconversion of homo-substituted **BVs** (up to homo-pentasubstituted **BVs**).[5]

Table 2.1. Number of BV isomers, enantiomers pairs and rearrangement processes for homo-substituted BVs. n_i represents the number of substituents appended to BV.[5]

n_i	BV Isomers	Enantiomeric Pairs	Rearrangement Processes
1	4	0	10
2	15	3	45
3	42	13	120
4	72	25	210
5	84	30	252

In these BV networks, and with understanding of graph theory, *nodes* represent objects (BV isomers) and are connected between one another by *edges*, which represent the relationship (Cope rearrangement) between those objects. In addition to this convention, Brant plotted the network graph with bidirectional line topology, where achiral isomers are located along a central mirror plane, whilst enantiomeric isomers deviate from the bisecting mirror plane in opposite directions horizontally.[5] The network graph for a homo-trisubstituted BV is shown in Figure 2.5.

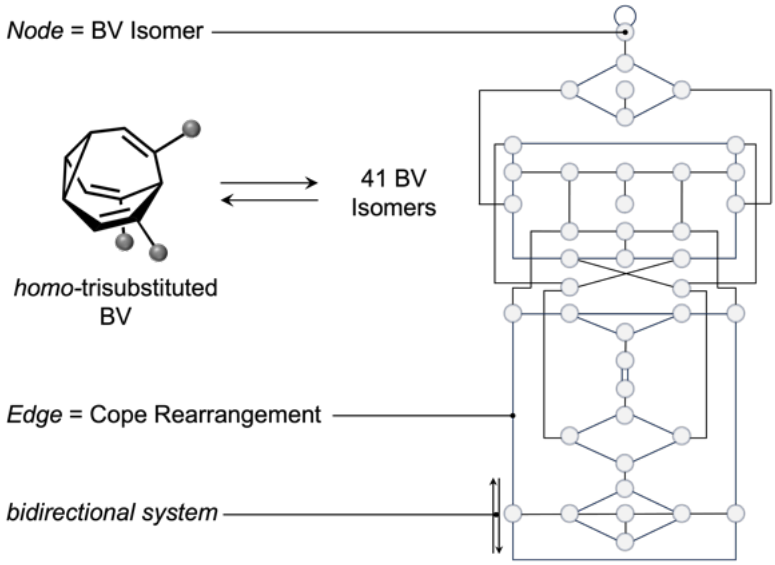

Figure 2.5. Adaptation of Brant's network graph for a homo-trisubstituted BV, illustrating the 42 possible BV isomers and 120 rearrangement processes.[5] The grey circles represent an appended substituent.

These interconversion network graphs have been further developed to include additional information regarding BV interconversion. For example, in 2018[4] and 2019[6], Fallon and co-workers reported network graphs for disubstituted BVs, incorporating

coloured *nodes* and *edges* to represent the isomer relative energies and the transition state structure energies, respectively (Figure 2.6).

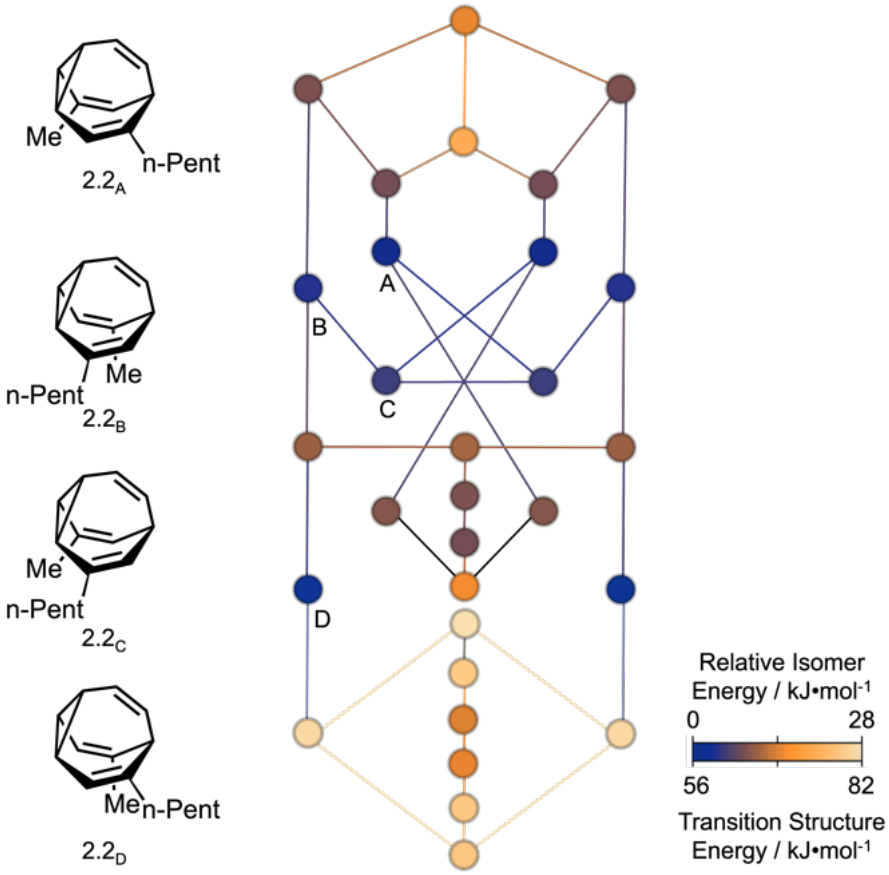

Figure 2.6. Adaptation of Fallon and co-workers network graph for a disubstituted methyl(*n*-pentyl) BV (2.2), illustrating the rearrangements between all possible isomers for a hetero-disubstituted BV. The incorporation of colour to nodes represents isomer relative energies (kJ•mol^{-1}) and to edges represents transition state structure energies (kJ•mol^{-1}).[4]

2.1.2 The 3-Dimensional Shape and Coverage Analysis of Compounds in Chemical Space

The ability to quantitatively assess the 3-dimensionality of molecules has become ever-more important in the iterative design process of medicinally active compounds. As such, a range of computational methods have been designed and implemented into the pharmaceutical design process in order to gain a better understanding of coverage in 3-D chemical space. With this said, there is no universal convention on which methods are preferred, given that they all have advantages and downfalls. Six of the most common methods for assessing 3-D molecular shape are discussed.

Fraction of sp^3 centres

In 2009, Lovering and co-workers proposed a method for investigating the fraction of sp^3 carbons (Fsp^3) present within a given compound.[7] Fsp^3 is calculated by the mathematical relationship described in *equation 1.*

$$Fsp^3 = \frac{\text{number of } sp^3 \text{ hybridised carbon atoms}}{\text{total number of carbon atoms}} \quad (1)$$

Lovering demonstrated the aforementioned methodology on compounds that were in the drug development stage as well as marketed drugs, showing that compounds that were promising candidates from market had a higher degree of Fsp^3 character (Figure 2.7).

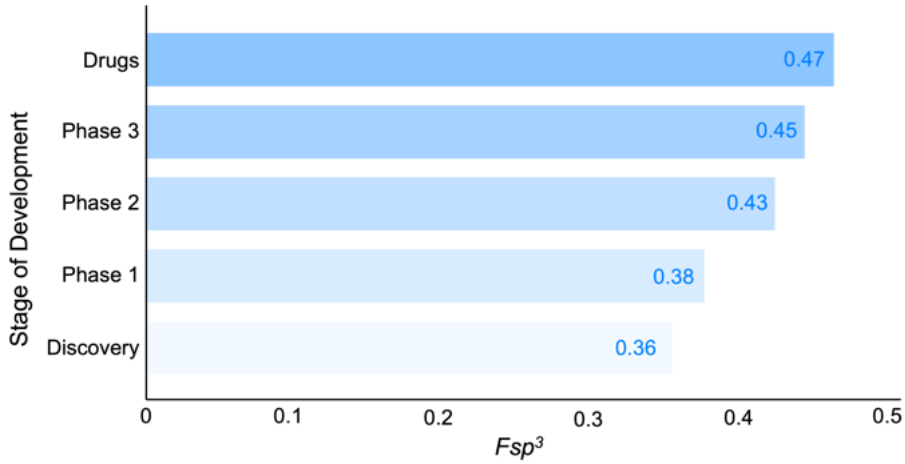

Figure 2.7. Plot of the mean Fsp^3 for compounds in different stages of drug development. Figure adapted from Lovering and co-workers, Escape from Flatland.[7]

Although calculating the number of Fsp^3 is efficient and, as such, advantageous, Fsp^3 studies have some downsides. In 2012, Blagg and co-workers made the point that Fsp^3 does not distinguish between sp^3 carbon atoms that are located in chemical space out of the main plane of the compound, and in turn, of the appended vector moieties.[8] As such, these sp^3 carbon atoms would (in theory) offer more 3-dimensional character to the molecule. This also means that two compounds with equal number of Fsp^3 may adopt dissimilar 3-D shape. For example, Blagg and co-workers reported the comparison of the compounds **2.3** and **2.4** (Figure 2.8). For both compounds, $Fsp^3 = 0$, implying that both **2.3** and **2.4** are planar; however, qualitatively it is evident that this

is the case for compound **2.3**, as predicted by its Fsp^3 value. In contrast, compound **2.4** has a V-shaped geometry displaying 3-D character.[8a]

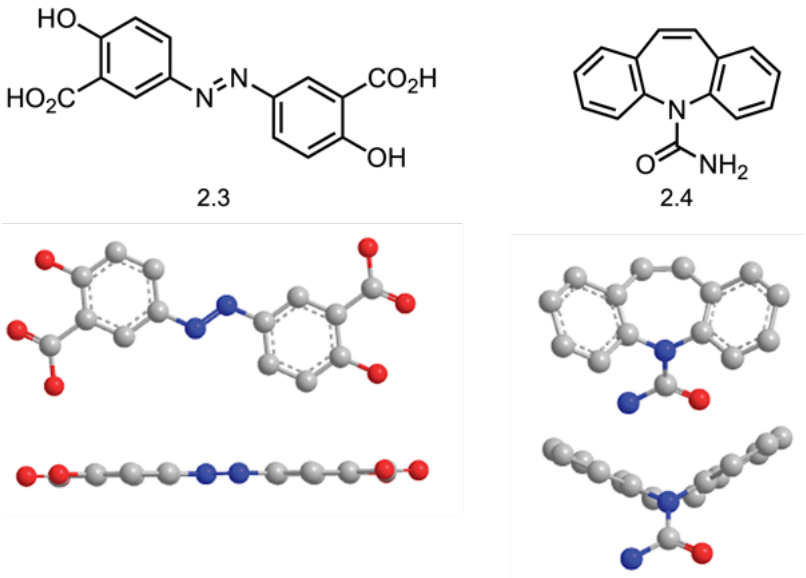

Figure 2.8. Chemical structures and calculated conformations for **2.3** and **2.4**, where Fsp^3 = 0. Molecules were generated and studied in their CORINA-derived conformation, a literature standard method.[8b]

Rapid Overlay of Chemical Structures

In 1996, Grant and co-workers reported this method by which the atom-centred Gaussian description of molecular shape is used to calculate the maximal intersection of volume between respective molecules.[9] This then allows for a comparison of molecular shape based on volume overlay. The Rapid Overlay of Chemical Structures (ROCS) model builds upon the hard-model sphere, whereby a molecule is treated as a set of intersecting spheres. The exposed surface of these spheres then defines the boundary of a molecular volume, but, treating molecules as spheres does not take into account the electron charge distributions and quantum nature of subjected molecules. As such, Grant *et al.* implemented a generalised coalescence theorem, allowing for the generation of nuclear coordinates, molecular volume and areas.[9] This improvement means that atom type is considered and, as such, also takes into account electron charge distribution.

Molecular Globularity

The notion of molecular globularity was first conceived by Timmermans in 1954.[10] Molecular globularity was used further by Meyer in 1986 – applying the concept of computational analysis to quantify 3-D molecular shape.[11] For this method, first the molecule's geometry is optimised using molecular mechanics. The molecule is then treated as a solid in space, where the van der Waals radius sphere is traced around the atomic nuclei giving the 3-D shape of the molecule.[11] Resultantly, this gives the van der Waals volume (V_w) and surface area (S_w), which can subsequently be used to calculate the globularity (G_w). Thus, for a compound with a given volume, V_w, the radius and surface area can be calculated using *equations* 2 and 3.

$$r_{c,w} = \left(\frac{3V_w}{4\pi}\right)^{\frac{1}{3}} \qquad (2)$$

$$S_{c,w} = 4\pi r_{c,w}^{\,2} \sim 4.836 V_w^{\frac{2}{3}} \qquad (3)$$

With the calculated surface area ($S_{c,w}$) and van der Waals surface area (S_w) in hand, the globularity (G_w) can then be calculated by measuring the ratio of the aforementioned surface area values in *equation* 4. Note, for a perfect sphere, $S_{c,w} / S_w = 1$.

$$G_w = \frac{S_{c,w}}{S_w} \qquad (4)$$

Plane of Best Fit

In 2012, Firth, Brown and Blagg proposed a new method to characterise the 3-dimensionality of molecules – a method termed the plane of best fit (PBF) model.[8a] Unambiguously, the method determines how far subjected molecules deviate from a 2-D plane, based on the average distance of heavy atoms in the compound from the plane. The lowest energy conformation of a given compound is calculated computationally, which allows the plane to be fitted (Figure 2.9).

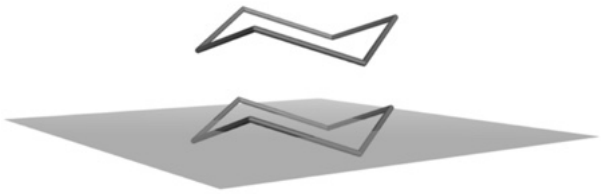

Figure 2.9. Lowest energy conformation of cyclohexane with the plane of best fit, showing deviation of atoms from the plane. Adapted from Blagg and co-workers.[8a]

Each molecule is prepared by removing salts and then coordinates are generated for the molecule. The coordinates are then used to calculate the PBF, which is solved using a least-squares method, resulting in the plane given by *equation* 5.

$$Ax + By + Cz + D = 0 \qquad (5)$$

The equation of best fit can then be used to determine the distance, Δ, of each heavy atoms from the plane (*equation* 6). The output of this method gives a PBF score, which theoretically ranges $0 \rightarrow \infty$, however in reality, the PBF score is < 2 for small drug-like molecules.[8]

$$\Delta = \frac{|Ax_i + By_i + Cz_i + D|}{\sqrt{A^2 + B^2 + C^2}} \qquad (6)$$

Following the development of the PBF method, Blagg and co-workers compared PBF values for a set of compounds against other methods to probe 3-dimensionality. Interestingly, PBF showed a good correlation with molecular globularity, but there is no apparent correlation between PBF and Fsp^3. This further corroborates that Fsp^3 is not an entirely suitable method for examining 3-D molecular shape.

Principal Moments of Inertia

Principal moments of inertia (PMI) plots are another way of visually representing the shape-based distribution of a set of molecules. As developed by Saur and Schwarz in 2003, PMI plots project the 3-dimensionality of a compound based on normalised principal moments of inertia, which can be derived from computational molecular mechanics.[12] The moments of inertia of a molecule along the *x*, *y* and *z* axis in 3-D space are calculated computationally using molecular mechanics. These values are then sorted into ascending order of magnitude to give I_1, I_2, and I_3, where I represents the

principal moment of inertia. In order to account for the difference in size of molecules, the three principal moments of inertia are then normalised (*equations* 7 and 8) to give *NPR1* and *NPR2*.

$$NPR1 = \frac{I_1}{I_3} \qquad (7) \qquad NPR2 = \frac{I_2}{I_3} \qquad (8)$$

The aforementioned NPR values can then be plotted onto a triangular plot, which gives a representation of the compounds 3-dimensionality. The vertices on the plot are defined by values associated with rod [0,1], disk-like [0.5, 0.5] and spherical [1,1] geometries, analogous to alkyne, benzene and adamantane structures, respectively (Figure 2.10).

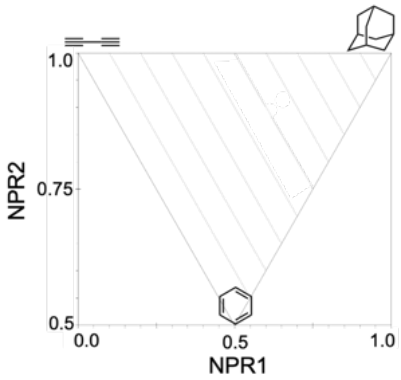

Figure 2.10. Generic PMI plot, where each vertex exhibits shape extremes, analogous to alkyne, benzene and adamantane structures.

Exit Vector Analysis

Exit vector (EV) analysis allows to determine the 3-D geometric relationship between two substituents on bifunctional scaffolds. EV analysis was initially introduced in the 1990's for CAVEAT[13] software but has more recently been utilised by Grygorenko and co-workers for the geometric analysis of common functionalised ring systems.[14–17] The relative orientation of two exit vectors (v_1 and v_2), appended to a central scaffold, can be described by four geometric parameters: the distance between the appended carbons (r); the dihedral angle of the vectors (θ) and the plane angles of each vector (φ_1 and φ_2) (Figure 2.11).[15,16] EVs are commonly considered when understanding the geometry of ring systems in bioisostere studies,[18–21] since the geometry of ring system fragments can be deemed critical to achieve the desired directionality for interactions with residues present in biological targets.

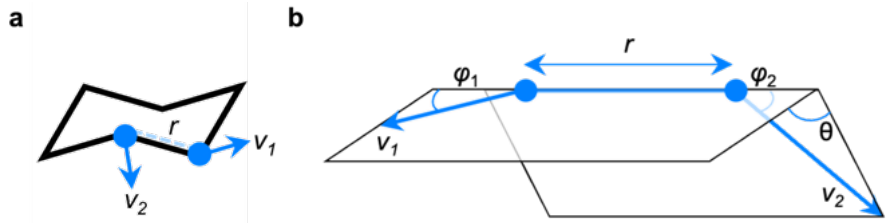

Figure 2.11. (**a**) Definition of vectors v_1 and v_2 (depicted on a 1,2-disubstituted cyclohexane scaffold as an example); (**b**) Definition of geometric parameters r, φ_1, φ_2, and θ.[15]

In recent years, Grygorenko *et al.* have been at the forefront of EV analysis, studying a range of ring systems commonly used in organic chemistry. In 2016, Grygorenko and co-workers performed EV analysis on cycloalkanes, specifically 3- to 7-membered carbocycles, which showed categorical clustering in four distinct regions (*α*, *β*, *γ* and *δ*).[15] Each defined region was shown to present the following systems: *α: cis*- and *trans*-1,2 rings; *β: cis*-1,3 and *cis*-1,4 6-membered rings; *γ: trans*-1,4 6-membered rings; and *δ: trans*-1,3 5-membered and *trans*-1,4 6-membered rings (Figure 2.12). In this initial study, Grygorenko and co-workers found that only two *trans*-1,4 7-memberered rings lie outside the range of these defined regions.[15]

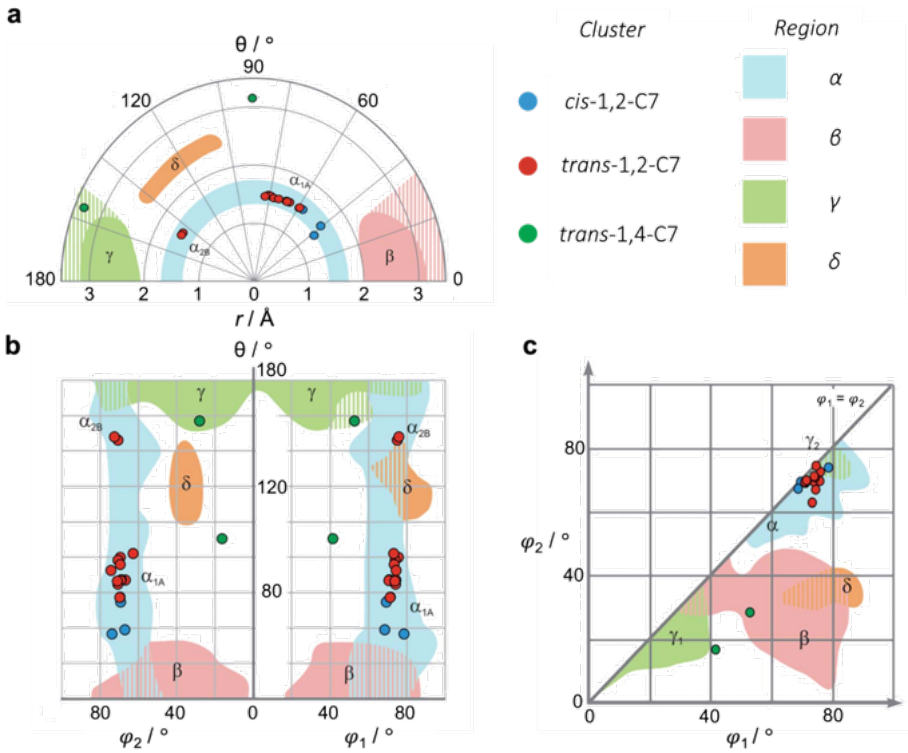

Figure 2.12. Grygorenko's EV plots for disubstituted cycloheptanes, where; (**a**) *r*–θ EV plot; (**b**) θ–φ_1/φ_2 EV plots; and (**c**) φ_1–φ_2 EV plot.[15]

Grygorenko and co-workers added to their existing EV studies in 2018, focussing instead on heterocyclic scaffolds.[16] This further analysis showed significant differences in the respective dihedral angles of heterocyclic scaffolds, compared with the previously discussed carbocycles. The designation of a new region, denoted *ε*, is of particular note – encompassing a region located at *r* ~ 2.5 Å occupied by 1,3-disubstituted heterocycles that was previously vacant (Figure 2.13a). These species also gave rise to a well-defined region in the plane angle plots (Figure 2.13b and 2.13c).

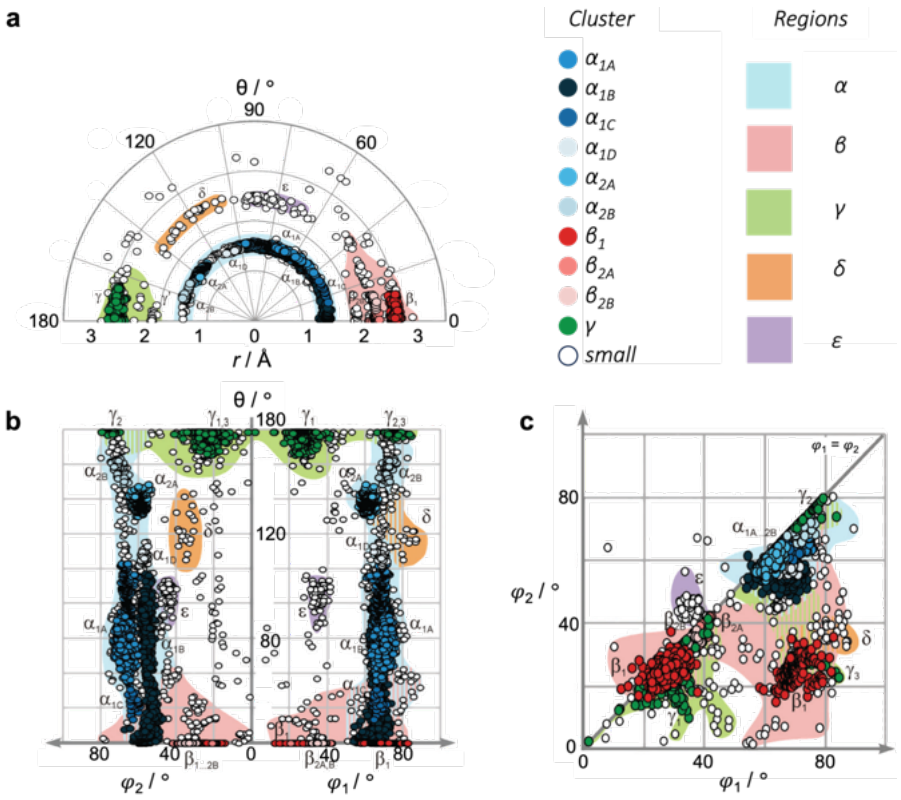

Figure 2.13. Grygorenko's EV plots for heterocyclic compounds, where; (**a**) r–θ EV plot; (**b**) θ–φ_1/φ_2 EV plots; and (**c**) φ_1–φ_2 EV plot.[16]

Many research groups have utilised the concept of EV analysis to complement the synthesis of compound libraries, combining computational modelling with x-ray crystal measurements to investigate bioisostere comparisons. For example, in 2022 Brown and co-workers accompanied the synthesis of *cis*- and *trans*-2,6-disubstituted [2]-ladderanes with EV analysis,[22] showing the similarities in geometry to *m*-substituted aromatic rings and rigidified cyclohexanes. Additionally, Mykhailiuk and co-workers used the EV model to show the isosteric similarities between 1,2-disubstituted

piperidines and 1-azaspiro[3.3]heptanes, leading to the bioisosteric replacement of 1-azaspiro[3.3]heptane creating a new analogue of the anaesthetic drug, bupivacaine.[23]

In summary, the methods described provide a wide-ranging set of approaches to analyse the 3-D shape and space coverage of compounds. Evidently, the methods discussed provide a number of benefits and drawbacks; however in the most part, they are quantitative methods which deliver a certain level of credibility. Furthermore, the methods described allow for a quick assessment of shape diversity within a compound library, without the need analyse compounds by other methods (such as x-ray crystallography). To further improve the analysis of compound 3-D shape and space coverage, the use of multiple methods in combination with one another should be considered, giving a more thorough representation of a compound. Moreover, the introduction of additional parameters may prove useful in some methods, particularly from a visual aspect on representative graphs. Given that all of the discussed methods have computational origins, there is inevitably a margin of error that could only be reduced by experimental supplementation or additional computationally demanding calculations. These extra steps inevitably reduce the high-throughput nature of all of these methods, ultimately making this a more time-consuming approach in the long term.

2.2 Results and Discussion

Historically, research into **BV** chemistry has proved challenging due to its inefficient synthesis and functional group compatibility.[24–29] Recent methodologies, however, have provided shorter and more effective synthetic strategies to access substituted **BVs**[30–33] which can rearrange between a range of nondegenerate constitutional isomers with different shapes. The unique 'shapeshifting' properties of **BV** and its inherent fluxional behaviour give rise to interesting physical properties, presenting new opportunities for organic and materials chemistry.[34] To date, there have been multiple inclusions of **BV** as structural units in functional molecules, such as in the use of chemical sensors,[35] polymeric materials,[36] and as part of antibiotics.[37] There has not

yet been a clear and definitive guide to understanding the fundamentals of **BV**'s rearrangement processes and its shape in 3-D chemical space.[38]

Despite the robust foundation of research that has been built within the field of medicinal chemistry,[7,39–50] 3-D scaffolds remain underused, limiting the coverage of chemical space in established molecular frameworks.[51–55] The molecular framework of pharmaceuticals is considered particularly important for its influence on the overall shape of a molecule, whilst reports have shown increased 3-dimensionality of a compound can lead to enhanced biological activity. In an attempt to access a greater degree of chemical space for exploration in medicinal chemistry and to escape the 'flatland', a larger number of 3-D fragments are desired, particularly exotic hydrocarbon frameworks that can be easily employed and elaborated upon as fragments in fragment-based drug discovery (FBDD).[56–60] The effective design process of **BV**-containing pharmaceuticals requires a fundamental understanding of **BV** stereodynamics, which in turn dictates the overall 3-D shapes, exit vectors of warhead substituents and the probability that certain isomers exist within a given **BV** population.

The **BV** ring system has the seemingly contradictory characteristics of, on one hand, being highly dynamic through its reversible Cope rearrangements, while on the other hand, being a rigid 3-D structure. Its tricyclic hydrocarbon skeleton is a shape-persistent structure with substituents projecting outwards at well-defined angles. Therefore, designing effective materials based on **BV** derivatives requires understanding of their stereodynamics, i.e., their overall 3-D shapes, the relative orientations that are accessible to appended substituents, and the relative energies of the isomers at equilibrium. Herein, the individual rearrangement processes of substituted **BVs** and how this allows **BVs** to access many nondegenerate geometries is described. To fulfil this aim, a new computational tool (*bullviso*) has been developed, which allows for the automatic generation of the: 1) entire **BV** isomer population for any given substituted **BV**; 2) **BV** isomer relative energies; and 3) **BV** isomer exit vector angles. To demonstrate its utility, *bullviso* is used to examine di-, tri- and tetramethyl substituted **BVs**. Subsequently, the information enables the examination of **BV**

stereodynamics, by further computational analysis through energy-weighted PMI and EV analyses. This 3-D shape and coverage analysis reveals that: 1) substituted **BVs** exhibit a high level of sphericity compared to common ring systems found in pharmaceuticals; and 2) substituted **BV** mixtures can access different areas of chemical space and possess a range of exit vector angles, extending beyond those typically found in *cis*-disubstituted cycloalkanes, while maintaining a higher degree of sphericity than most common ring systems found in biologically active molecules. Overall, these analyses demonstrate the scope and limitations of the structural diversity in substituted **BV** libraries and how this may potentially be utilised in future pharmaceutical applications.

2.2.1 The Structure of Bullvalene

BV has the molecular formula $C_{10}H_{10}$ and its structure consists of a cyclopropyl ring (Figure 2.14a: positions 1, 4 and 7) which is connected to a methine group (Figure 2.14: position 0) by three alkene bridges. Given the large number of possible **BV** isomers, a method for naming them is essential for any discussion involving their interconversion. As previously discussed in the introduction, Bode and co-workers developed an elegant barcode labelling system[61] that can be parsed by computer algorithms to construct a full network map for interconversion of all the non-degenerate isomers of a substituted **BV** – a task that is otherwise impractical to do by hand. Each digit of the barcode represents one of the carbon atoms in the **BV** structure (Figure 2.14a) and each type of substituent is given a numeral, enabling each isomer to be described with a unique numeric code (see examples in Figure 2.18). Importantly, this system enables isomer information to be coded unambiguously. Whilst this naming system, however, is ideally suited to comprehensively describing the positions of all substituents in any given isomer, its high level of detail is not always needed.

Therefore, in order to describe and discuss the elementary types of **BV** rearrangements and make reference to the individual positions in the **BV** structure, a positional naming system has been devised using Greek alphabetical locants as positional nomenclatural labels. The threefold rotational symmetry of the **BV** core reduces the number of

chemically inequivalent positions to four, where the naming system denotes: 1) *α*: the apical bridgehead position; 2) *β* and *γ*: the two energetically favoured olefin sites for any non-hydrogen substituents; and 3) *δ:* the cyclopropyl position. Prime and double prime labels are used to distinguish the same locants on different 'arms' of the **BV** (Figure 2.14b). As such, this naming system allows individual positions of **BV** to be quickly referenced, without using the barcode system in its entirety.

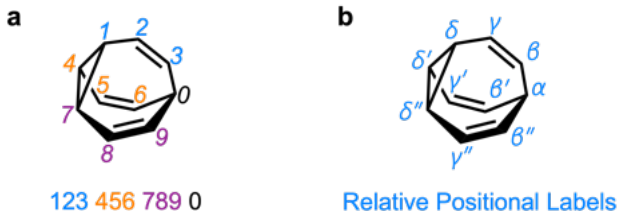

Figure 2.14. (**a**) Isomer barcode labelling system for a **BV** scaffold[61]; and (**b**) Proposed relative positional labelling system for a **BV** scaffold.

2.2.2 Elementary Types of Positional Exchange

Each Cope rearrangement occurs on one of the three 1,5-hexadiene "faces" (Figure 2.15) involving two 'arms' of the **BV**. The positions of the **BV** that comprise the 1,5-hexadiene motif undergoing a given Cope rearrangement can be referred to as participating sites (P), whilst the other four positions are non-participating sites (NP). Whether a substituent is located on a P or a NP site determines its resulting position following isomerisation (Figure 2.16a). The *α* position is never part of the 1,5-hexadiene motif, thus it is always considered to be a NP site. In contrast, for each of the other sites *(β, γ* and *δ*), there exists two potential positional outcomes following a single rearrangement step.

Figure 2.15. The three faces of **BV** that can each participate in a potential Cope rearrangement. Each face is highlighted in blue, orange and magenta incorporating its two olefins, respectively.

Applying the *α*–*δ* and P/NP labels, it becomes clear that there are just four elementary types of positional exchange that occur during any Cope rearrangement step, which are illustrated in Figure 2.16a using a mono-substituted **BV** as a model. Firstly, the sole possible outcome for the *α* position is migration to a newly formed *δ* position on the

NP arm. A substituent at a *β* position will migrate to a *γ* position when on a NP arm, whereas P rearrangement exchanges the *β* position with a *δ* site. Finally, a *γ* substituent remains at a *γ* position on a P arm following the Cope rearrangement on account of symmetry in the transition state (Figure 2.16b). As the Cope rearrangement is reversible, the reciprocal of each of these exchange processes must also occur. Overall, therefore, the elementary types of positional exchange that govern the outcome of any BV rearrangement are (i) $\alpha_{NP} \rightleftharpoons \delta_{NP}$, (ii) $\beta_{NP} \rightleftharpoons \gamma_{NP}$, (iii) $\beta_{P} \rightleftharpoons \delta_{P}$, and (iv) $\gamma_{P} \rightleftharpoons \gamma_{P}$. These elementary types of positional exchange apply equally to every BV substituent in every isomer, regardless of the total number of substituents or their relative positions. For example, the functional groups of a hetero-disubstituted BV migrate relative to one another during sequential Cope rearrangement steps, allowing them to switch from being on separate arms to occupying the same arm and back again (Figure 2.16c).

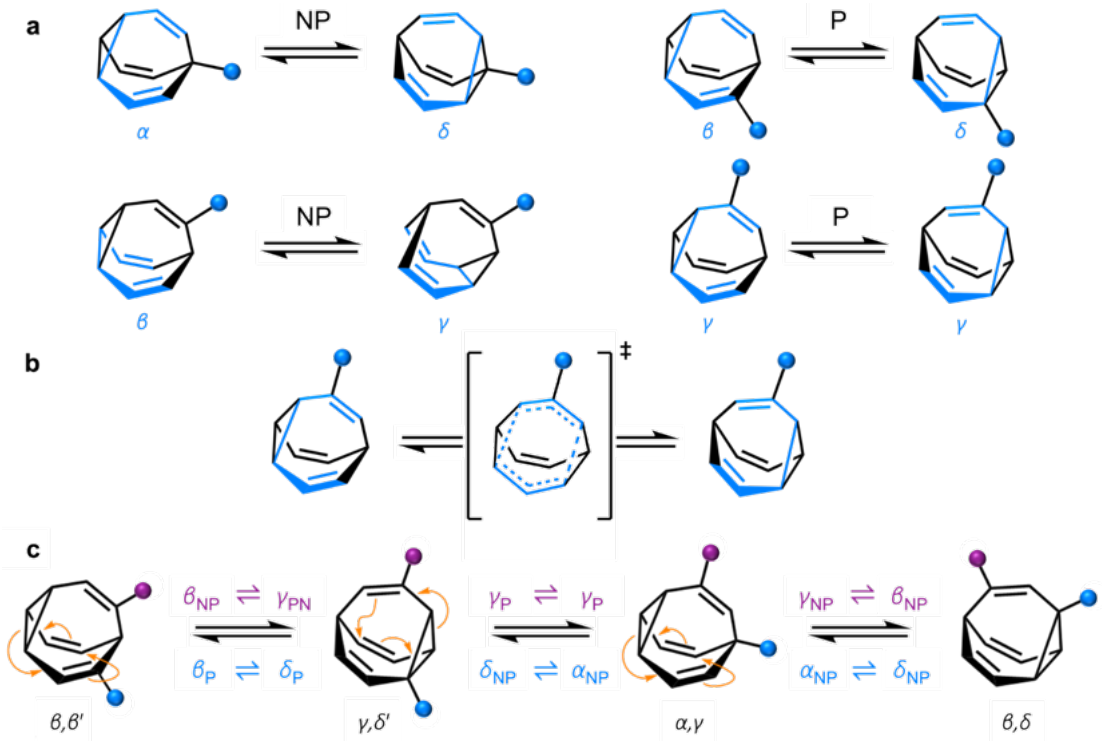

Figure 2.16. (a) The possible exchange processes following one Cope rearrangement step, enumerated for each BV position. Full isomerisation requires sequential steps that include (P = participating) and exclude (NP = non-participating) the substituent in the rearranging 1,5-hexadiene motif (shown in blue). (b) Illustration of the higher symmetry in the transition state for $\gamma_{P} \rightleftharpoons \gamma_{P}$ Cope rearrangement relative to the ground state. (c) The partial isomer network of a hetero-disubstituted BV showing the positional exchange arising from three sequential Cope rearrangement steps. The blue and magenta circles represent a functional group.

2.2.3 Calculating the Number of Unique Bullvalene Permutations

Deriving the total number of unique nondegenerate **BV** isomers for a given substitution pattern is one of the most important considerations for the construction of **BV** interconversion networks. Bode previously reported a MATLAB code to calculate the number of unique **BV** isomers.[2] Taking account of the symmetry present in **BV**s, however, it is possible to perform a simple 'back-of-the-envelope' calculation to determine the number of isomers for a given **BV** system using equation 9:

$$N_{iso} = \frac{1}{3}\left(\frac{10!}{\prod_{a=1}^{A} N_a!} + 2S\right) \qquad (9)$$

Equation 9. *Equation* for calculating the number of nondegenerate isomers within a given **BV** system.

Where:

- N_{iso}: the number of unique nondegenerate isomers of **BV** (enantiomers are considered to be distinct from one another).
- N_a*:* the number of occurrences of a given type of substituent.
- $\prod_{a=1}^{A} N_a!$: the product of multiplying together the factorial of this term for each unique type of substituent (including hydrogen substituents).
- S: is a correction value that accounts for the C_{3v} symmetry of **BV** and has a value of 0, 1, 3 or 6.

In the same manner as the isomer barcode system, Equation 9 treats each substituent as a number within a group of ten numbers. Combinatorics is used to derive the total number of ways in which these substituents can be ordered. Taking hetero-trisubstituted **BV** (**2.5**) as an example (Figure 2.17a), there are seven hydrogen substituents and three distinct non-hydrogen substituents. Therefore, the product operation in the denominator of the equation is 7! × 1! × 1! × 1!. In compound **2.6** (Figure 2.17b) there are six hydrogens, a substituent type that occurs three times, and another substituent type that occurs just once, so the product operation is 6! × 3! × 1!. The 1/3 multiplier adjusts for the fact that the parent **BV** has C_3 symmetry, offsetting triple counting in the $10!/\prod_{a=1}^{A} N_a!$ term that arises for structures related by rotation. A further correction factor, $2S$, readjusts for the **BV** isomers that have three identically

substituted arms and so are represented just once each in the $10!/\Pi_{a=1}^{A} N_a!$ term. The term, *S*, is the number of ways that the substituents can be arranged around the **BV** core to retain its C_3 symmetry, or in other words, where all three arms of the **BV** possess identical substitution patterns. For example, the substituents on **2.5** cannot be arranged to give C_3 symmetry, hence *S* = 0. However, three of the substituents of **2.6** are the same and thus there are three different ways in which they can be arranged such that the **BV** possesses C_3 symmetry (Figure 2.17b). The C_3-symmetric isomers can only be obtained when the unique substituent is at the *α* position and the three identical substituents occupy the same position on each of the three **BV** arms, i.e., either all *β*, all *γ*, or all *δ*. Therefore, *S* = 3 for **2.6**. Applying this approach, N_{iso} = 240 for **2.5** and 282 for **2.6**. There are 42 possible variations of substituted **BVs** having different numbers and identities of substituents. A reference table is provided in the Supporting Information (Table S2.1) where this method and Equation 9 have been applied to generate a complete list of N_{iso} and *S* for each possible substituted **BV**, as well as the numbers of achiral and chiral isomers.

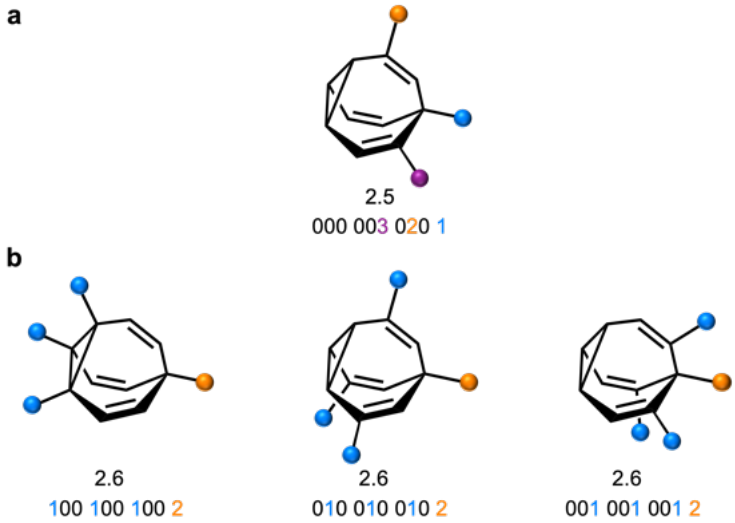

Figure 2.17. (**a**) Structural formula of an isomer of **BV 2.5**; and (**b**) the three isomers of **BV 2.6** with C_3 symmetry and the respective isomer codes using Bode's isomer barcode system. The coloured circles represent substituents, whereby the colour indicates identical and different substituents.

2.2.4 The Generation of Bullvalene Isomers (*bullviso*)

A Python3 code, *bullviso*,[62] has been developed, which interfaces with RDKit[63,64] to generate the Cartesian coordinates of substituted **BVs**. It is publicly available under the

GNU Public License (GPLv3) on GitLab. The *bullviso* code generates exhaustively all possible isomer barcodes for a substituted **BV** and filters out the non-unique isomer barcodes according to the protocol outlined by Bode.[2] It also outputs the connectivity between isomers, which can be used to generate interconversion network diagrams.[5] Cartesian coordinates sampling the constitutional isomers of the substituted **BV** are generated by grafting given substituents (supplied as SMILES strings) onto a **BV** to produce a unique structure corresponding to each isomer barcode. The *bullviso* code generates up to *N* configurational and conformational isomers according to the experimental-torsion distance geometry with 'basic knowledge' embedding approach (ETKDGv3)[65,66] implemented in RDKit. These configurational and conformational isomers are then (pre-)optimized using the Universal Force Field [67] and the *M* lowest-energy isomers are outputted. Cartesian coordinates can be written in *xyz* file format or, alternatively, as pre-prepared inputs for computational chemistry packages, e.g., Gaussian[68] or Orca,[69–71] to enable subsequent optimization and analysis at higher levels of theory. Figure 2.18 depicts the methyl-substituted **BVs** (**2.7**–**2.9**) generated by *bullviso* in this study.

2.7 2.8 2.9

Figure 2.18. Compounds Me_2BV (**2.7**), Me_3BV (**2.8**) and Me_4BV (**2.9**). The coloured circles represent a methyl group.

2.2.5 3-Dimensional Shape Analysis of Bullvalene

Over the past decade, there has been an increased interest in FBDD as an alternative method for generating leads for small-molecule therapeutics.[56–61] In the most part, the FBDD method has primarily caught the attention of chemists due to the increasing difficulty faced by researchers to identify interactable biological targets, at many stages of drug discovery timeline.[58] FBDD is a complementary approach to high-throughput screening, where, instead of screening a large library of compounds, a smaller library of compounds with a lower molecular weight (< 300 Da) is used instead to identify a

fragment that provides an interaction with the target of interest. Once a suitable fragment has been identified, the fragment is elaborated upon to increase its binding efficiency and incorporated into a larger molecule. This method relies upon access to a library of diverse fragments that cover as much chemical space as possible, such that the best possible starting point can be identified. There are concerns, however, that a large majority of organic fragments are planar, aromatic and are rich in sp^2-carbon centres, and therefore offer limited shape diversity for use in FBDD libraries.[72] Consequently, there is a desire for a greater number of diverse 3-D fragments to be included within these libraries, in order to access more chemical space and escape planarity.[7] One way that this objective could be achieved is by exploring and employing more exotic hydrocarbon frameworks as fragments, particularly as the shape of the molecular core is considered the key factor in shape diversity,[72,73] as opposed to substituent placement or binding potential. It has also been suggested that increasing the 3-dimensionality of drug leads and the fraction of sp^3-carbon centres can result in enhanced binding activity.[72,73] Herein, the 3-D shape diversity of **BV** and how its fluxional behaviour could allow **BV** to be used in the quest to explore new areas of chemical space is discussed.

2.2.5.1 Principal Moments of Inertia Analysis

The PMI analysis, as developed by Saur and Schwartz,[74] has been used as a straightforward and quantitative method to assess shape diversity of potential pharmaceutical molecules.[56,72,75] Typical PMI plots are constructed for: (i) the lowest energy conformer of any given compound to compare the inherent shapes of an array of molecules;[76,77] or (ii) a range of conformers to gain insight into conformational diversity of a limited number of molecules.[78] First, di-, tri-, and tetrasubstituted **BVs** (Figure 2.18) were selected as targets to examine shape diversity present in dynamic **BV** networks arising from rapid constitutional isomerism. In order to focus the analysis on the dynamic shape that is inherent to the functionalised **BV** scaffold itself, rather than any potential conformational processes in the attached substituents, methyl-substituted derivatives were chosen to investigate, i.e., dimethyl- (**2.7**), trimethyl- (**2.8**), and tetramethyl-BV (**2.9**).

All possible isomers of the methyl-substituted **BVs** were generated using *bullviso*, then their geometries were optimised by performing density functional theory (DFT) calculations. The PBE0[79,80] functional with Grimme's D3 dispersion correction[81] and the def2-SV(P)[82] basis set were deemed suitable for modelling the energetics of **BV** systems. Using this level of theory, we constructed isomer interconversion networks and predicted relative isomer populations for **2.7** (Figure S2.1), **2.8** (Figure S2.2) and **2.9** (Figure S2.3), which have 15, 42, and 72 unique isomers, respectively. For each of these isomers, the three principal moments of inertia (I_1, I_2, and I_3 in ascending order) were calculated using a KNIME[83] Vernalis[84] chemoinformatic protocol, allowing for normalised PMI ratios (NPRs) for all isomers to be calculated (*equations* 7 and 8).

$$7)\ NPR1 = \frac{I_1}{I_3} \qquad 8)\ NPR2 = \frac{I_2}{I_3}$$

Equations: (**7**) for calculating NPR1; and (**8**) for calculating NPR2, where I_1, I_2 and I_3 represent the three principal moments of inertia in ascending order.

The resulting PMI plots (Figure 2.19a–c) follow the standard layout, where the vertices are defined by values associated with rod-like [0,1], disc-like [0.5, 0.5] and spherical [1,1] geometries, analogous to butadiyne, benzene and adamantane, respectively (Figure 1.21a). Parallel lines on the PMI plot correspond to ΣNPR values (where ΣNPR = NPR1 + NPR2, where $1.00 \leq \Sigma NPR \leq 2.00$). The points that lie furthest from the rod-disc axis (ΣNPR = 1.00) are associated with greater sphericity.

The PMI plot of the Me_2BV (**2.7**) (Figure 2.19a) shows structural diversity in the population of constitutional isomers, which are located in the range $1.44 \leq \Sigma NPR \leq 1.57$. For ease of reference, isomers in Figure 2.19a are labelled using the *α*–*δ* locants, however, the full isomer barcodes are also given in the Supporting Information (Tables S2.2–S2.4). The darker coloured points indicate the overlap of enantiomers on the diagram as they give identical PMI coordinates e.g., for (±)-*β*,*γ*'-**2.7**. As the unique isomers of a substituted **BV** are non-degenerate, they are present in varying concentrations at equilibrium. To visualise how this property influences which molecular shapes are most prevalent, population-weighted PMI plots with the data points scaled by the Boltzmann distribution at 298 K are introduced. A population-

weighted PMI plot (Figure 2.19d) shows that the shapeshifting network of **2.7** consists predominantly (~93%) of the four lowest-energy isomers, which include two achiral isomers, *β,β′*-**2.7** and *γ,γ′*-**2.7**, and the enantiomeric pair of (±)-*β,γ′*-**2.7**. The *β,δ*-**2.7**, (±)-*β,δ′*-**2.7**, and (±)-*γ,δ′*-**2.7** isomers are also present in ~0.5–2% each (Table S2.2), leaving ~0.3% of the remaining six isomers combined.

The introduction of more substituents to the **BV** scaffold (i.e., in **2.8** and **2.9**) increases structural variety and overall sphericity (Figures 2.19e and 2.19f). Several structures extend beyond ΣNPR > 1.6, reaching maxima of 1.89 and 1.90 for **2.8** and **2.9**, respectively. In both cases, the PMI distributions are markedly broader than that of **2.7**, spanning 1.3 ≤ ΣNPR ≤ 1.9, which reflects the change in shape that can occur when several substituents are located close to one another around the **BV** scaffold (giving rod-like shape) or are spread around the **BV** evenly to maintain sphericity. Like **2.7**, a subset of the **2.8** and **2.9** constitutional isomers are most prevalent in the network at equilibrium. The 14 most stable isomers of **2.8** are within ~15 kJ·mol^{-1} of one another, so they are each present in amounts ranging from 0.1% to 60% (Table S2.3). Similarly, there are 12 isomers of **2.9** present in proportions of 0.1% to 52%. The energetically preferred isomers are those with most of their substituents at *β* and *γ* positions, and in which substituents do not neighbour one another directly. Therefore, the population-weighted PMI plots (Figures 2.19e and 2.19f) show that the most spherical isomers are present in higher populations. To contextualise the PMI data of the functionalised **BVs**, it is useful to compare the **2.7** isomers (Figure 2.19g) to a small representative library of rings prominent in pharmaceuticals (Table S2.8).[85,86] PMI analysis of the dimethyl derivatives of these pharmaceutical building blocks (Figure 2.19h) shows the relative lack of 3D diversity in most currently used ring systems.[85,86] The majority of compounds are close to the rod-disc axis (ΣNPR ≤ 1.3) with the notable exception of a few structures such as substituted adamantanes and cubanes **2.10**–**2.12** (Figure 2.19i), which are increasingly popular as more spherical replacements for flat ring systems.[18–20,87–90] The PMI ratios of the **2.7** isomers (1.44 ≤ ∑NPR ≤ 1.57) and **2.10**–**2.12** (1.40 ≤ ∑NPR ≤ 1.53) are nearly identical, suggesting that **BVs** could be similarly useful as 3-D

scaffolds in medicinal chemistry. **BVs** have the additional, unique property of spontaneously sampling different structures through their Cope rearrangements and are now readily accessible by short synthetic routes.[6,30,31,35,91]

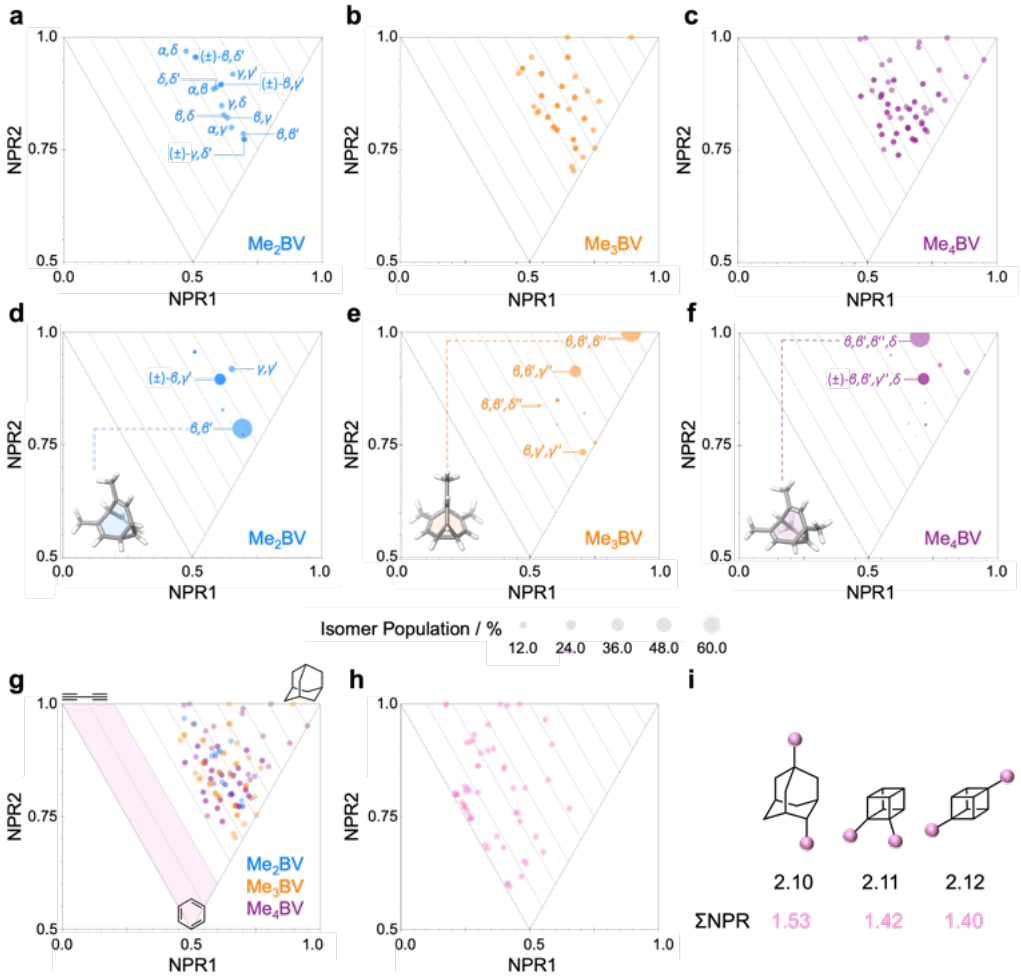

Figure 2.19. (**a–c**) PMI plots for the shapeshifting networks of (**a**) Me_2BV (**2.7**), (**b**) Me_3BV (**2.8**), and (**c**) Me_4BV (**2.9**). Substituent positional labels are given for Me_2BV (**2.7**). For clarity, these labels are not shown on the plots for Me_3BV (**2.8**) and Me_4BV (**2.9**). See Tables S6 and S7 for labelled data. (**d–e**) Population-weighted PMI plots for the shapeshifting networks of (**d**) Me_2BV (**2.7**), (**e**) Me_3BV (**2.8**), and (**f**) Me_4BV (**2.9**), where the data points are scaled by calculated Boltzmann distributions at 298 K (PBE0-D3/ def2-SV(P)). The modelled structure of the lowest-energy isomer for each **BV** is shown; (**g**) An overlay of the PMI plots of Me_2BV (**2.7**) (blue), Me_3BV (**2.8**) (orange), and Me_4BV (**2.9**) (purple) showing that no **BV** isomers have ΣNPR values close to the rod–disc axis. (**h**) PMI plot for common ring systems. See Table S8 for compound identities. (**i**) Structural formulas and ΣNPR values for 1,4-dimethyladamantane (**2.10**), 1,2-dimethylcubane (**2.11**), and 1,4-dimethylcubane (**2.12**). The pink circles represent a methyl group.

2.2.5.2 Exit Vector Analysis of Methyl Bullvalenes

EV plots are used to analyse the relationship between two substituents attached to a central scaffold.[15,16] They are useful in FBDD and bioisostere studies to show the geometries that are available when elaborating a structure outward starting from different ring systems. The relative orientations (Figure 2.20a) of bonds emanating from the scaffold are defined as the exit vectors, v_1 and v_2. They are described (Figure 2.20b) by four geometric parameters; the distance between the functionalised carbon atoms of the scaffold (r), the dihedral angle of the vectors (θ), and the plane angles of each vector (φ_1 and φ_2).[15,16] Like PMI plots, the EV plot for a single molecule possesses only one data point if a compound is conformationally rigid, whereas multiple points are plotted to show the effects of conformational flexibility or to compare multiple molecules with different covalent structures on a single diagram.

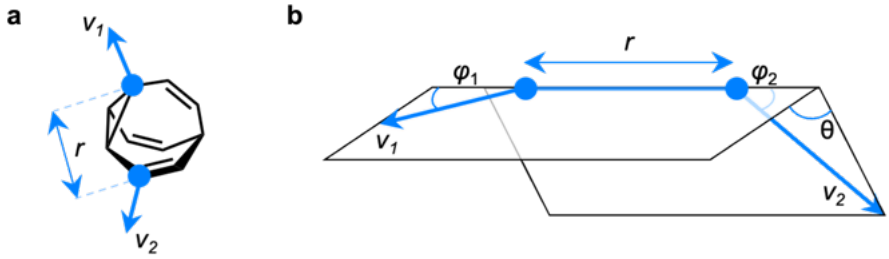

Figure 2.20. (**a**) The vectors v_1 and v_2 for two substituent attachment points on a **BV** (shown for (*αS)-γ,δ′*-**2.7**) which are defined by (**b**) the geometric parameters r, φ_1, φ_2, and θ.

We constructed EV plots (Figure 2.21) for the C–Me bonds of the methyl-substituted **BVs** to quantify the stereodynamics of the **BV** scaffold, i.e., the relative orientations and spacings of its substituents. Typically, EV plots span θ values of 0° to 180°, where all dihedral angles are defined as being positive. For **BV** isomer networks, however, it is also beneficial to extend the EV plots to include negative values of θ, allowing pairs of enantiomers that are present in the dynamic equilibrium to be shown on the same diagram (e.g., (±)-*β,γ′*-**2.7** (Figure 2.21a), as well as revealing enantiotopic relationships between substituents at equivalent positions on different arms (e.g., the *β′* and *β″* positions of *β,β′,β″,δ*-**2.9**, Figure 2.23c(ii)). As the cage-like structure of **BV** imposes dihedral angles between −60° and 60°, plotting θ from −90° to +90° (Figures 2.21a–c) gives an informative representation of the data. An EV plot of the **2.7** isomers reveals

C–Me dihedral angles clustered in two regions of either θ ~ 0° or θ ~ ±30°. The points in the former region span distances of r ~ 1.3–3.1 Å (Figure 2.21a). The majority of coplanar EVs (θ ~ 0°) arise from isomers that are either functionalized (i) at two different positions on the same arm of the **BV** or (ii) at the same type of position on **BV** on different arms, e.g., *β,β′*-**2.7**, accounting for nine of the 15 possible substitution patterns. The four points at θ ~ ±30° correspond to two of the three enantiomer pairs of the isomers with differently substituted arms ((±)-*β,γ′*-**2.7** and (±)-*β,δ′*-**2.7**). The final enantiomer pair, (±)-*γ,δ′*-**2.7**, has coplanar EVs of θ = ±0.5°. Boltzmann population-weighted EV analysis of **2.7** (Figure 2.21d) reveals that the most populated isomers *β,β′*-**2.7** (r = 2.5 Å, θ = 0°, p = 53%) and (±)-*β,γ′*-**2.7** (r = 3.1 Å, θ = 30°, p = 17% for each enantiomer) exhibit substantial changes in the dihedral angles between the C–Me EVs. Standard EV plots of **2.7**, **2.8**, and **2.9** spanning θ values of 0° to 180° (Figures 2.21g–j) are also shown to aid comparison to the four regions, *a*–*d*, determined by Grygorenko *et al.* that are characteristic of EVs found in common disubstituted cycloalkanes.[15,16] The majority of data points for the **BV** isomers fall within the *a* or *b* region. EVs in region *a* are characteristic of *cis*-1,2-disubstituted cyclopropyl compounds while region *b* is associated with *cis*-1,3-disubstituted and *cis*-1,4-disubstituted aliphatic rings.[15,16] The presence of EVs in these regions for **BV** is expected, therefore, as the structure of **BV** contains these motifs.

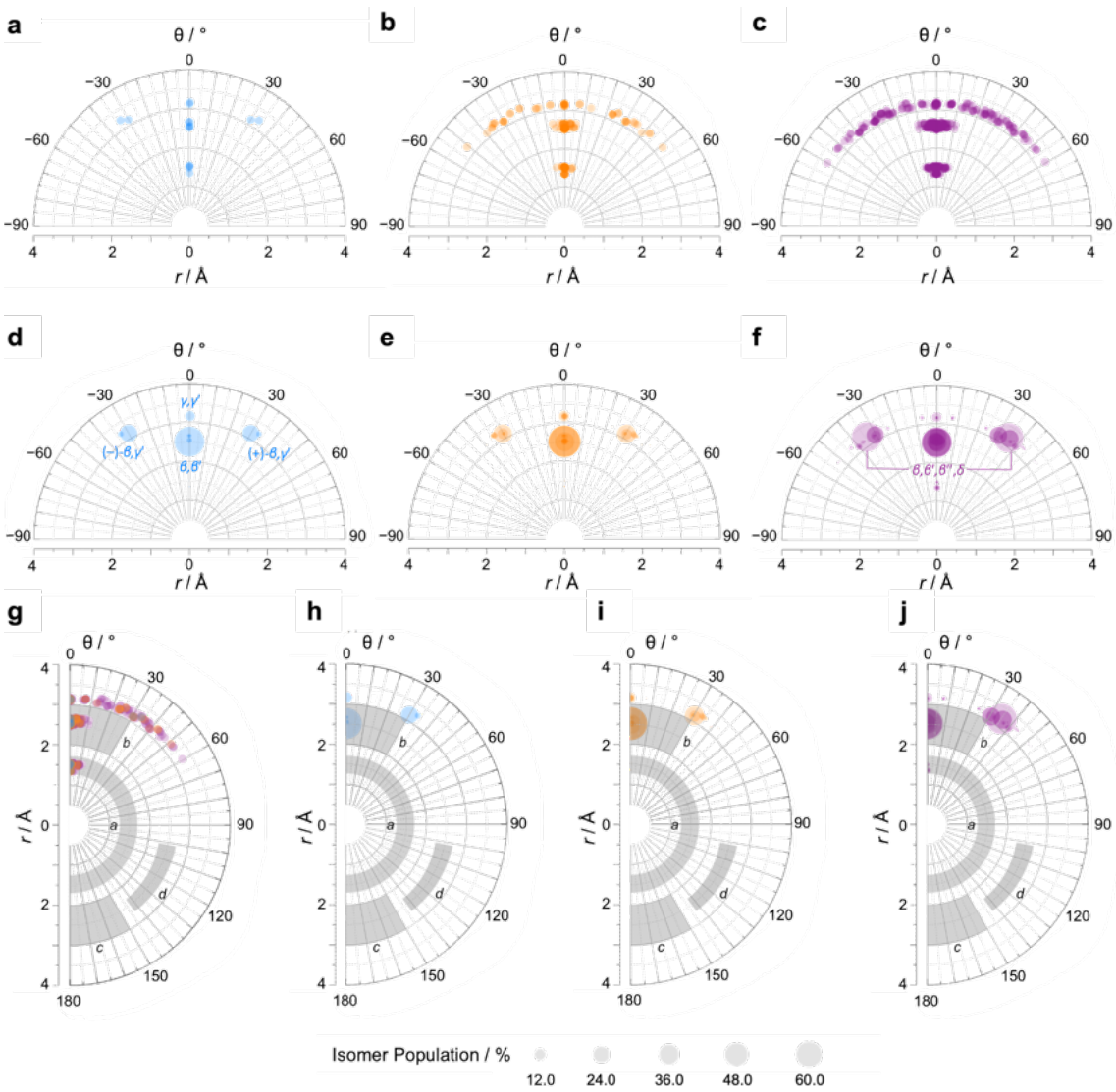

Figure 2.21. (a–c) Distance–dihedral angle EV plots and (d–i) Boltzmann population-weighted distance–dihedral angle EV plots (298 K, PBE0-D3/def2-SV(P)) for the isomers of (a,d,h) Me_2BV (**2.7**), (b,e,i) Me_3BV (**2.8**), and (c,f,j) Me_4BV (**2.9**). (g) Overlaid distance versus dihedral angle EV plot of all three methyl-substituted **BVs**. (h–j) Plots include characteristic areas of EV plots in grey that correspond to those found in disubstituted cycloalkanes[15,16], *a* = *cis*-1,2-disubstituted cyclopropanes, *b* = *cis*-1,3-disubstituted aliphatic rings and *cis*-1,4-disubstituted cyclohexanes, *c* = *trans*-1,4-disubstituted cyclohexanes, *d* = *trans*-1,3-disubstituted cyclopentanes and cyclohexanes.

The diversity of EVs arising from the shapeshifting isomerisation becomes even more apparent when considering the plane angles subtended by the C–Me EVs, φ_1 and φ_2 (Figure 2.20), of the **2.7** isomers. There is a spread of possible plane angles spanning from 15° to 60° found in the most energetically accessible isomers (Figure 2.22), extending to 67° for higher-energy isomers. Therefore, sequential Cope

rearrangements between isomers significantly alter the relative orientations of substituents in space, granting **BV** its unique stereodynamic properties.

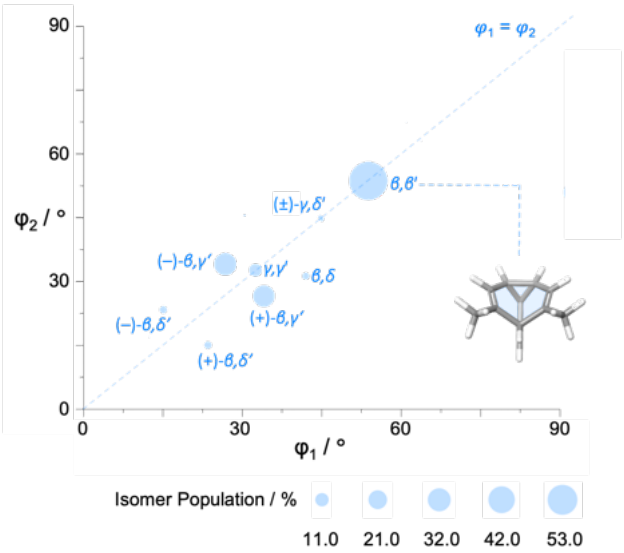

Figure 2.22. The plane angles subtended by C–Me EVs in the nine lowest energy isomers of Me_2BV (**2.7**). Data points are scaled according to the Boltzmann population at 298 K (PBE0-D3/def2-SV(P)).

As the cage-like geometry of the **BV** scaffold is well defined and insensitive to the addition of more substituents, **2.8** and **2.9** would be expected to exhibit similar EVs between pairs of their C–Me bonds as those found for **2.7**. This generalisation applies when considering the plane angles and distances between substituents. It is also the case for the dihedral angles, but only when considering the most energetically favourable isomers (Figures 2.21e and 2.21f). A wider spread of dihedral angles (Figures 2.21b and 2.21c) that extends beyond region *b* to angles between −60° and +60° is apparent when the complete isomer networks of **2.8** and **2.9** are taken into account (Figure 2.21g), including isomers that lie at higher energy. Significant deviations from the 0° and ±30° dihedral angles arise to minimise unfavourable steric interactions when substituents are close to one another in space. For the di-, tri-, and tetrasubstituted **BVs** investigated, the isomers that bear methyl groups at neighbouring positions are relatively high in energy, so are not very prevalent. The most significant (albeit still low) populations of such isomers are present for **2.9** because of the increased likelihood of substituents being close to one another in the

tetrasubstituted system, such as the ~0.1% of *β,β′,γ,δ′*-**2.9**, which has θ = 51° between its *β* and *δ′* methyl groups. More highly substituted **BV**s, or those bearing bulkier substituents, will likely have larger isomer populations with varied dihedral angles.

Of course, shape differentiation between the orientations of functional groups attached to **BV** diminishes if conformationally flexible linking groups are used, so elaborating **BV**s with short rigid groups[31,36,92]or fused rings[93] may be advantageous. Each of the molecular shapes described by the PMI (Figures 2.19a–2.19c) and EV plots (Figures 2.21a–2.21c) correspond to accessible states for the methyl-substituted **BV**s, demonstrating that a single **BV** derivative can cover a significant region of chemical space on its own. Heterosubstituted systems with varied functional groups possess still greater structural diversity. Although realising the full extent of this shape diversity in some **BV**s may require higher-energy isomers to be invoked, it is important to note that, in the contexts of drug discovery and materials chemistry, noncovalent bonding interactions with biomolecular targets, confinement effects, or forces imposed by the surrounding medium may compensate for the moderately low energy differences between isomers to amplify certain **BV** structures within the shapeshifting network.[35,94–97] Therefore, isomers that have otherwise low populations should not be dismissed, as they may become more significant components of the network in the right environment.

2.3 Conclusions

In summary, the appealing complexity of dynamic **BV** networks is built upon four types of positional exchange between different sites around the **BV** scaffold. Isomers in these networks tend to position functional groups with dihedral angles of either 0° or 30° and at a range of plane angles between 15° and 60°, originating from vertices of the **BV** that are spaced apart by 1.3–3.1 Å. The **BV** scaffold itself has quasi-spherical overall structure. Functionalised derivatives generally retain this characteristic, particularly because the most energetically favoured isomers that emerge are typically those that space substituents out from one another around the scaffold. PMI analysis shows that

they have a similar degree of sphericity as adamantane and cubane building blocks, while they orient functional groups at vectors that are characteristic of *cis*-disubstituted cycloalkanes. Greater shape diversity emerges with the inclusion of more substituents, not just because it gives rise to greater numbers of unique isomers, but also because interactions between neighbouring groups reduces the predisposition toward them being coplanar with one another, giving more varied EVs. Currently, the most accessible syntheses of **BVs** produce structures with two or three functional groups attached, implying it remains advantageous to develop new synthetic approaches that give efficient access to higher-order multifunctional **BVs**. The analysis described here, which is accelerated using *bullviso*, can be exploited to pre-screen computationally the diversity and accessibility of molecular shapes in complex **BV** libraries.

2.4 Experimental

Computational Methods

Computational DFT modelling and the development of the *bullviso* coding protocol was carried out in collaboration with Dr Conor Rankine at the Department of Chemistry, University of York. The KNIME shape analysis workflow was designed and developed by Robert Ives in collaboration with Dr James Firth at the Department of Chemistry, University of York. Data analysis, processing and evaluation was carried out by Robert Ives.

Isomer Generation

All initial sets of Cartesian coordinates sampling the constitutional isomers of **2.7**, **2.8**, and **2.9** were generated *via* the in-house-developed *bullviso*[62] code. *bullviso* is publicly available under the GNU Public License (GPLv3) on GitLab. All constitutional isomers were subsequently pre-optimised at the GFN2-xTB[81,98] (extended tight binding; xTB) level of theory using *xtb* (v6.4.1).[99] An SCF convergence criterion of 1.0×10^{-6} a.u. was used with convergence criteria of 5.0×10^{-6} and 1.0×10^{-3} a.u. for the energy change and

gradient, respectively, in all geometry optimisations. All constitutional isomers verified at the GFN2-xTB level of theory were progressed to DFT geometry optimisation.

DFT Geometry Optimisation

All DFT geometry optimizations and energy evaluations of the constitutional isomers of **2.7**, **2.8**, and **2.9** were carried out at the PBE0-D3 level of theory (*i.e.* with the PBE0[79,80] density functional of Adamo and Barone coupled with the D3[81] dispersion correction of Grimme *et al.*) using ORCA (v5.0.2).[69–71] All calculations were carried out under the resolution-of-identity (RI) approximation for the Coulomb integrals (RIJONX). A tightened SCF convergence criterion of 1.0×10^{-9} a.u. was used in all calculations; convergence criteria of 2.0×10^{-7} and 3.0×10^{-5} a.u. were used for the energy change and gradient, respectively, in all geometry optimisations. The def2-SV(P)[82] basis set of Weigend and Ahlrichs was coupled with the def2/J[100] auxiliary basis set; the two were used together throughout. The proper convergence of all geometry optimisations to real minima was verified *via* vibrational frequency inspection. As exact mirror-image geometries were not generated by the optimisation, the energies, PMIs, and EVs are not identical. Derived exit vector angles were then plotted on 2D exit vector plots in OriginPro.

Numbers of Unique BV Permutations

Varying the number of different substituents, there are 42 possible BV systems, which are listed in Table S2.1 below. The total number of unique isomers, N_{iso}, is calculated according to Equation 9. We further divide N_{iso} into the number of achiral and chiral isomers. To do so, we counted the number of isomers where at least two of the arms are identically substituted. The presence of these two identical arms gives a symmetrical (achiral) structure with a mirror plane bisecting the molecule parallel to the third arm. Each of the possible systems with at least two identical arms are determined, and combinatorics performed with the remaining four substituents to determine all the ways in which they may be organized. For example, in the case of 0000000112, there are four systems with two identical arms, ("000 000", "001 001", "010 010", and "100 100"). In the first system, the remaining substituents are 0112, so

there are (4!/∏ N_A! =4!/2!) 12 different isomers possible that have two 000 arms. For the three remaining cases, the four substituents left over are 0002 so there are (4!/∏ N_A! =4!/3!) four different isomers possible for each of the 001, 010, and 100 cases. Summing these together makes 24 achiral isomers of the 120 total possible unique isomers of 0000000112.

Table S2.1. All possible BV systems, including the numbers of unique substituents R^x, the total number of isomers N_{iso}, the symmetry term *S*, and the number of achiral and chiral isomers.

Occurrences of Each Substituent										Substituent System	*S*	N_{iso}	Achiral	Chiral
R^0	R^1	R^2	R^3	R^4	R^5	R^6	R^7	R^8	R^9					
10	0	0	0	0	0	0	0	0	0	0000000000	1	1	1	0
9	1	0	0	0	0	0	0	0	0	0000000001	1	4	4	0
8	1	1	0	0	0	0	0	0	0	0000000012	0	30	12	18
8	2	0	0	0	0	0	0	0	0	0000000011	0	15	9	6
7	1	1	1	0	0	0	0	0	0	0000000123	0	240	24	216
7	2	1	0	0	0	0	0	0	0	0000000112	0	120	24	96
7	3	0	0	0	0	0	0	0	0	0000000111	3	42	16	26
6	1	1	1	1	0	0	0	0	0	0000001234	0	1680	24	1656
6	2	1	1	0	0	0	0	0	0	0000001123	0	840	48	792
6	2	2	0	0	0	0	0	0	0	0000001122	0	420	48	372
6	3	1	0	0	0	0	0	0	0	0000001112	3	282	40	242
6	4	0	0	0	0	0	0	0	0	0000001111	3	72	22	50
5	1	1	1	1	1	0	0	0	0	0000012345	0	10080	0	10080
5	2	1	1	1	0	0	0	0	0	0000011234	0	5040	72	4968
5	2	2	1	0	0	0	0	0	0	0000011223	0	2520	96	2424
5	3	1	1	0	0	0	0	0	0	0000011123	0	1680	72	1608
5	3	2	0	0	0	0	0	0	0	0000011122	0	840	96	744
5	4	1	0	0	0	0	0	0	0	0000011112	0	420	48	372
5	5	0	0	0	0	0	0	0	0	0000011111	0	84	24	60
4	1	1	1	1	1	1	0	0	0	0000123456	0	50400	0	50400
4	2	1	1	1	1	0	0	0	0	0000112345	0	25200	72	25128
4	2	2	1	1	0	0	0	0	0	0000112234	0	12600	144	12456
4	2	2	2	0	0	0	0	0	0	0000112233	0	6300	168	6132
4	3	1	1	1	0	0	0	0	0	0000111234	0	8400	72	8328
4	3	2	1	0	0	0	0	0	0	0000111223	0	4200	120	4080
4	3	3	0	0	0	0	0	0	0	0000111222	6	1404	96	1308
4	4	1	1	0	0	0	0	0	0	0000111123	0	2100	72	2028
4	4	2	0	0	0	0	0	0	0	0000111122	0	1050	48	1002
3	1	1	1	1	1	1	1	0	0	0001234567	0	201600	0	201600
3	2	1	1	1	1	1	0	0	0	0001123456	0	100800	0	100800
3	2	2	1	1	1	0	0	0	0	0001122345	0	50400	144	50256
3	2	2	2	1	0	0	0	0	0	0001122334	0	25200	240	24960
3	3	1	1	1	1	0	0	0	0	0001112345	0	33600	0	33600
3	3	2	1	1	0	0	0	0	0	0001112234	0	16800	144	16656
3	3	2	2	0	0	0	0	0	0	0001112233	0	8400	168	8232
3	3	3	1	0	0	0	0	0	0	0001112223	6	5604	144	5460
2	1	1	1	1	1	1	1	1	0	0012345678	0	604800	0	604800
2	2	1	1	1	1	1	1	0	0	0011234567	0	302400	0	302400
2	2	2	1	1	1	1	0	0	0	0011223456	0	151200	144	151056
2	2	2	2	1	1	0	0	0	0	0011223345	0	75600	288	75312
2	2	2	2	2	0	0	0	0	0	0011223344	0	37800	360	37140
1	1	1	1	1	1	1	1	1	1	0123456789	0	1209600	0	1209600

Stereochemical Assignment and Priority Rules

M and *P* stereochemical descriptors have been used previously by Fallon[32] to distinguish BV enantiomers from one another. The assignment requires a viewing direction to be assigned to the BV C_{3v} axis, which has been as running in the direction from the cyclopropyl to the *α* position. We prefer to use the point chirality of the *α* position to assign an *R* or *S* stereochemical descriptor as this can be done using the established Cahn-Ingold-Prelog (CIP) priority rules without needing to define a direction for an additional axis. The *α* position of BV is the highest priority sp^3-hybridised carbon and only unique position on the BV structure. It is also useful to assign priority to the arms of the BV to determine which should be labelled without a prime symbol, with a single prime symbol (′), or with a double prime symbol (′′). Priority can also be assigned to the three arms using the CIP priority rules. Substituents on the highest priority bridge are given with no prime symbol, substituents on the second priority bridge are given with a single prime symbol and substituents the lowest priority bridge are given with a double prime symbol. The positional labels for each of the isomers for Me_2BV, Me_3BV and Me_4BV are presented in Tables S2.2, S2.3, and S2.4 respectively, including stereochemical descriptors for the chiral isomers.

Isomer Populations

Table S2.2. Energy (*E*), Relative energies (E_{rel}) and the Boltzmann distribution population percentage (*P* / %) for Me_2BV (2.7).

Isomer	Positional Label	E / Hartree	E_{rel} / kJ·mol^{-1}	*P* / %
000 000 001 1	α,β	-464.735969	20.59	0.013
000 000 010 1	α,γ	-464.738464	14.04	0.183
000 000 011 0	β,γ	-464.737758	15.89	0.087
000 000 100 1	α,δ	-464.736512	19.16	0.023
000 000 101 0	β,δ	-464.740612	8.40	1.777
000 000 110 0	γ,δ	-464.736491	19.22	0.023
000 001 001 0	β,β′	-464.743810	0.00	52.646
000 001 010 0	(α*R*)-β,γ′	-464.742721	2.86	16.607
000 001 100 0	(α*R*)-β,δ′	-464.740664	8.26	1.880
000 010 001 0	(α*S*)-β,γ′	-464.742780	2.70	17.714
000 010 010 0	γ,γ′	-464.741728	5.47	5.794
000 010 100 0	(α*R*)-γ,δ′	-464.739697	10.80	0.675
000 100 001 0	(α*S*)-β,δ′	-464.740682	8.21	1.918
000 100 010 0	(α*S*)-γ,δ′	-464.739675	10.86	0.659
000 100 100 0	δ,δ′	-464.733729	26.47	0.001

Table S2.3. Energy (*E*), Relative energies (E_{rel}) and the Boltzmann distribution population percentage (*P* / %) for **Me_3BV (2.8)**.

Isomer	Positional Label	*E* / Hartree	E_{rel} / kJ·mol^{-1}	*P* / %
000 000 011 1	α,β,γ	-503.968652	43.80	0.000
000 000 101 1	α,β,δ	-503.974248	29.11	0.000
000 000 110 1	α,γ,δ	-503.973677	30.61	0.000
000 000 111 0	β,γ,δ	-503.970754	38.29	0.000
000 001 001 1	α,β,β′	-503.972914	32.61	0.000
000 001 010 1	(α*R*)-α,β,γ′	-503.976285	23.76	0.004
000 001 011 0	(α*S*)-β,β′,γ	-503.979301	15.85	0.101
000 001 100 1	(α*R*)-α,β,δ′	-503.974363	28.81	0.001
000 001 101 0	(α*S*)-β,β′,δ	-503.982174	8.3	2.118
000 001 110 0	(α*R*)-β,γ′,δ′	-503.978096	19.01	0.028
000 010 001 1	(α*S*)-α,β,γ′	-503.976318	23.68	0.004
000 010 010 1	α,γ,γ′	-503.978773	17.23	0.058
000 010 011 0	(α*S*)-β,γ,γ′	-503.978373	18.28	0.038
000 010 100 1	(α*R*)-α,γ,δ′	-503.976846	22.29	0.007
000 010 101 0	(α*S*)-β,γ′,δ	-503.981157	10.97	0.721
000 010 110 0	(α*S*)-γ,γ′,δ	-503.976996	21.9	0.009
000 011 001 0	(α*R*)-β,β′,γ	-503.979298	15.85	0.101
000 011 010 0	(α*R*)-β,γ,γ′	-503.978334	18.38	0.036
000 011 100 0	(α*R*)-β,γ,δ′	-503.976206	23.97	0.004
000 100 001 1	(α*S*)-α,β,δ′	-503.974408	28.69	0.001
000 100 010 1	(α*S*)-α,γ,δ′	-503.976816	22.37	0.007
000 100 011 0	(α*S*)-β,γ,δ′	-503.976229	23.91	0.004
000 100 100 1	α,δ,δ′	-503.971059	37.48	0.000
000 100 101 0	(α*S*)-β,δ,δ′	-503.975111	26.85	0.001
000 100 110 0	(α*S*)-γ,δ,δ′	-503.969699	41.05	0.000
000 101 001 0	(α*R*)-β,β′,δ	-503.98216	8.34	2.084
000 101 010 0	(α*R*)-β,γ′,δ	-503.981121	11.07	0.693
000 101 100 0	(α*R*)-β,δ,δ′	-503.975151	26.74	0.001
000 110 001 0	(α*S*)-β,γ′,δ′	-503.978071	19.07	0.027
000 110 010 0	(α*R*)-γ,γ′,δ	-503.976989	21.91	0.009
000 110 100 0	(α*R*)-γ,δ,δ′	-503.969765	40.88	0.000
001 001 001 0	β,β′,β″	-503.985336	0	60.266
001 001 010 0	β,β′,γ″	-503.984343	2.61	21.028
001 001 100 0	β,β′,δ″	-503.982227	8.16	2.241
001 010 010 0	β,γ′,γ″	-503.98326	5.45	6.687
001 010 100 0	(α*R*)-β,γ′,δ″	-503.981171	10.93	0.733
001 100 010 0	(α*S*)-β,γ′,δ″	-503.981155	10.98	0.718
001 100 100 0	β,δ′,δ″	-503.975147	26.75	0.001
010 010 010 0	γ,γ′,γ″	-503.982133	8.41	2.026
010 010 100 0	γ,γ′,δ″	-503.980126	13.68	0.242
010 100 100 0	γ,δ′,δ″	-503.974214	29.2	0.000
100 100 100 0	δ,δ′,δ″	-503.965015	53.35	0.000

Table S2.4. Energy (*E*), Relative energies (E_{rel}) and the Boltzmann distribution population percentage (*P* / %) for **Me_4BV (2.9)**.

Isomer	Positional Label	*E* / Hartree	E_{rel} / kJ·mol^{-1}	*P* / %
000 000 111 1	α,β,γ,δ	-543.201058	59.60	0.000
000 001 011 1	(α*S*)-α,β,β′,γ	-543.205509	47.92	0.000

000 001 101 1	(α*S*)-α,β,β′,δ	-543.211306	32.70	0.000
000 001 110 1	(α*R*)-α,β,γ′,δ′	-543.211751	31.53	0.000
000 001 111 0	(α*S*)-β,β′,γ,δ	-543.212477	29.63	0.000
000 010 011 1	(α*S*)-α,β,γ,γ	-543.209119	38.44	0.000
000 010 101 1	(α*S*)-α,β,γ′,δ	-543.214680	23.84	0.003
000 010 110 1	(α*S*)-α,γ,γ′,δ	-543.214078	25.42	0.002
000 010 111 0	(α*S*)-β,γ,γ′,δ	-543.211407	32.43	0.000
000 011 001 1	(α*R*)-α,β,β′,γ	-543.205524	47.88	0.000
000 011 010 1	(α*R*)-α,β,γ,γ′	-543.209146	38.37	0.000
000 011 011 0	β,β′,γ,γ′	-543.215144	22.62	0.006
000 011 100 1	(α*R*)-α,β,γ,δ′	-543.207151	43.61	0.000
000 011 101 0	(α*R*)-β,β′,γ,δ′	-543.217729	15.84	0.086
000 011 110 0	(α*R*)-β,γ,γ′,δ′	-543.213770	26.23	0.001
000 100 011 1	(α*S*)-α,β,γ,δ′	-543.207204	43.47	0.000
000 100 101 1	(α*S*)-α,β,δ,δ′	-543.209013	38.72	0.000
000 100 110 1	(α*S*)-α,γ,δ,δ′	-543.206971	44.08	0.000
000 100 111 0	(α*S*)-β,γ,δ,δ′	-543.203636	52.84	0.000
000 101 001 1	(α*R*)-α,β,β′,δ	-543.211278	32.77	0.000
000 101 010 1	(α*R*)-α,β,γ′,δ	-543.214731	23.71	0.004
000 101 011 0	(α*S*)-β,β′,γ,δ′	-543.217733	15.83	0.087
000 101 100 1	(α*R*)-α,β,δ,δ′	-543.209013	38.72	0.000
000 101 101 0	β,β′,δ,δ′	-543.216658	18.65	0.028
000 101 110 0	(α*R*)-β,γ′,δ,δ′	-543.211289	32.74	0.000
000 110 001 1	(α*S*)-α,β,γ′,δ′	-543.211756	31.52	0.000
000 110 010 1	(α*R*)-α,γ,γ′,δ	-543.214090	25.39	0.002
000 110 011 0	(α*S*)-β,γ,γ′,δ′	-543.213744	26.30	0.001
000 110 100 1	(α*R*)-α,γ,δ,δ′	-543.206983	44.05	0.000
000 110 101 0	(α*S*)-β,γ′,δ,δ′	-543.211245	32.86	0.000
000 110 110 0	γ,γ′,δ,δ	-543.205433	48.12	0.000
000 111 001 0	(α*R*)-β,β′,γ,δ	-543.212485	29.60	0.000
000 111 010 0	(α*R*)-β,γ,γ′,δ	-543.211438	32.35	0.000
000 111 100 0	α*R*)-β,γ,δ,δ′	-543.203646	52.81	0.000
001 001 001 1	α,β,β′,β″	-543.207757	42.02	0.000
001 001 010 1	α,β,β′,γ″	-543.213382	27.25	0.001
001 001 011 0	β,β′,β″,γ	-543.220959	7.36	2.645
001 001 100 1	α,β,β′,δ″	-543.211517	32.15	0.000
001 001 101 0	β,β′,β″,δ	-543.223761	0.00	51.514
001 001 110 0	β,β′,γ″,δ″	-543.219802	10.39	0.779
001 010 010 1	α,β,γ′,γ″	-543.216707	18.52	0.029
001 010 011 0	(α*R*)-β,β′,γ,γ″	-543.220027	9.80	0.988
001 010 100 1	(α*R*)-α,β,γ′,δ″	-543.214856	23.38	0.004
001 010 101 0	(α*R*)-β,β′,γ″,δ	-543.222765	2.61	17.974
001 010 110 0	(α*S*)-β,γ′,γ″,δ′	-543.218583	13.59	0.214
001 011 010 0	(α*S*)-β,β′,γ,γ″	-543.219986	9.91	0.946
001 011 100 0	(α*S*)-β,β′,γ,δ″	-543.217838	15.55	0.097
001 100 010 1	(α*S*)-α,β,γ′,δ″	-543.214790	23.55	0.004
001 100 011 0	(α*R*)-β,β′,γ,δ″	-543.217797	15.66	0.093
001 100 100 1	α,β,δ′,δ″	-543.208991	38.78	0.000
001 100 101 0	(α*R*)-β,β′,δ,δ″	-543.216676	18.60	0.028
001 100 110 0	(α*S*)-β,γ′,δ′,δ″	-543.211294	32.73	0.000
001 101 010 0	(α*S*)-β,β′,γ″,δ	-543.222754	2.64	17.758
001 101 100 0	(α*S*)-β,β′,δ″,δ	-543.216628	18.73	0.027

001 110 010 0	(α*R*)-β,γ′,γ″,δ′	-543.218600	13.55	0.218
001 110 100 0	(α*R*)-β,γ′,δ′,δ″	-543.211265	32.81	0.000
010 010 010 1	α,γ,γ′,γ″	-543.219091	12.26	0.366
010 010 011 0	β,γ,γ′,γ″	-543.218926	12.69	0.308
010 010 100 1	α,γ,γ′,δ″	-543.217194	17.24	0.049
010 010 101 0	β,γ′,γ″,δ	-543.221662	5.51	5.579
010 010 110 0	γ,γ′,γ″,δ	-543.217491	16.46	0.067
010 011 100 0	(α*S*)-β,γ,γ′,δ″	-543.21686	18.12	0.034
010 100 011 0	(α*R*)-β,γ,γ′,δ″	-543.216835	18.18	0.034
010 100 100 1	α,γ,δ′,δ″	-543.211495	32.20	0.000
010 100 101 0	(α*R*)-β,γ′,δ,δ″	-543.215660	21.27	0.010
010 100 110 0	(α*R*)-γ,γ′,δ,δ″	-543.210233	35.52	0.000
010 101 100 0	(α*S*)-β,γ′,δ,δ″	-543.215670	21.24	0.010
010 110 100 0	(α*S*)-γ,γ′,δ,δ″	-543.210282	35.39	0.000
011 100 100 0	β,γ,δ′,δ″	-543.210698	34.30	0.000
100 100 100 1	α,δ,δ′,δ″	-543.202482	55.87	0.000
100 100 101 0	β,δ,δ′,δ″	-543.206421	45.52	0.000
100 100 110 0	γ,δ,δ′,δ″	-543.199442	63.85	0.000

Interconversion Networks

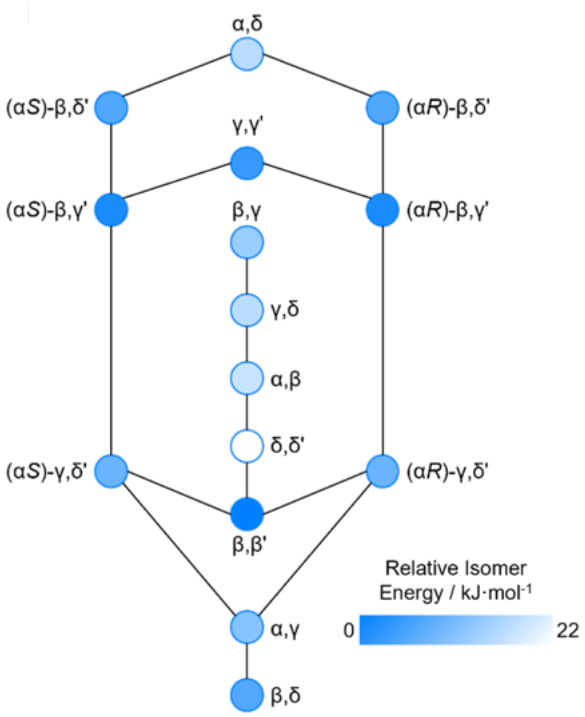

Figure S2.1. The energy-weighted isomer interconversion network calculated for Me_2BV (PBE0-D3/def2-SV(P)). Interconversion network prepared using a templated overlay of Brant and co-worker's disubstituted **BV** interconversion network diagram, in combination with calculated energy values from *bullviso*.[5,62]

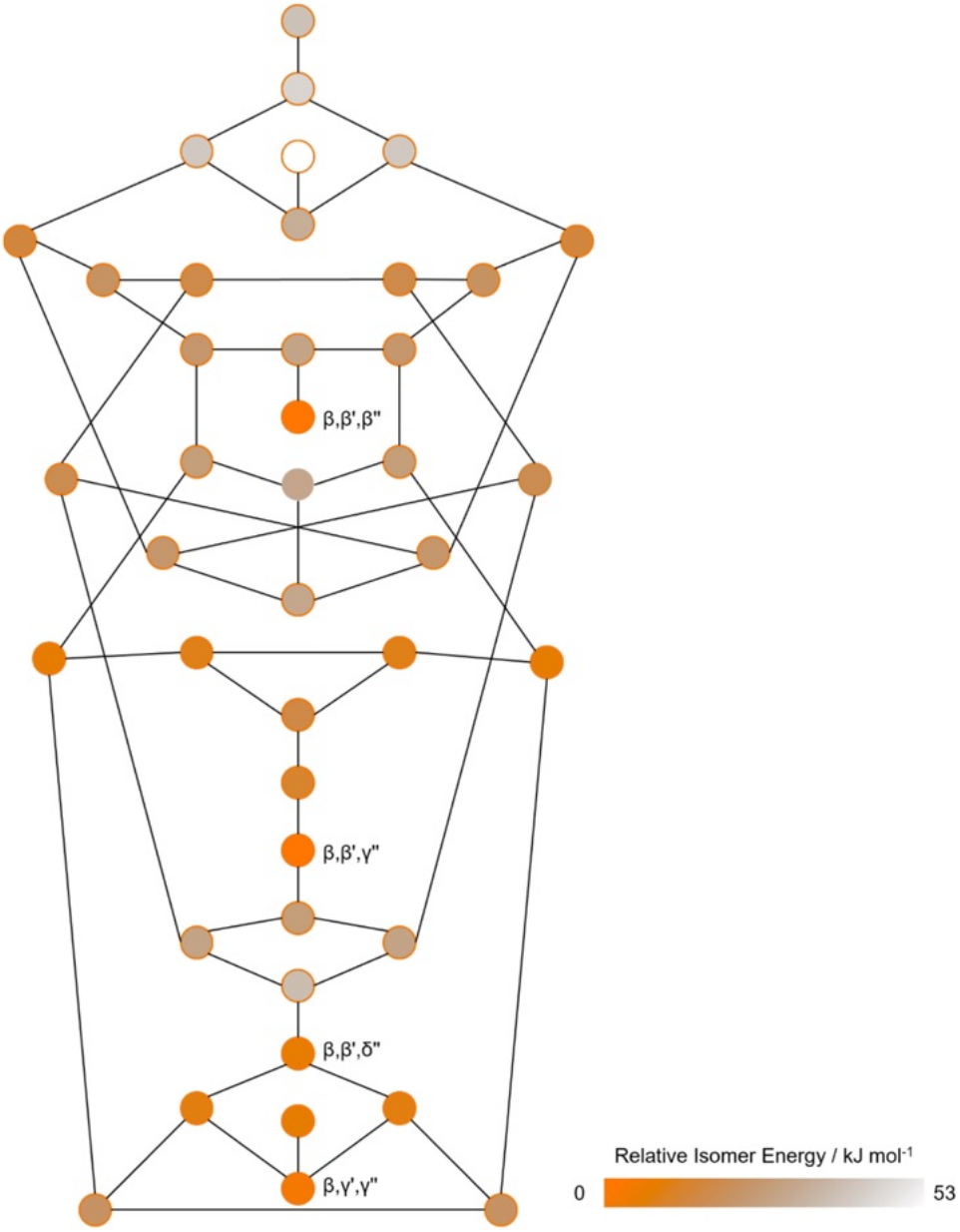

Figure S2.2. The energy-weighted isomer interconversion network calculated for **Me$_3$BV** (PBE0-D3/def2-SV(P)). Interconversion network prepared using a templated overlay of Brant and co-worker's trisubstituted **BV** interconversion network diagram, in combination with calculated energy values from *bullviso*.[5,62]

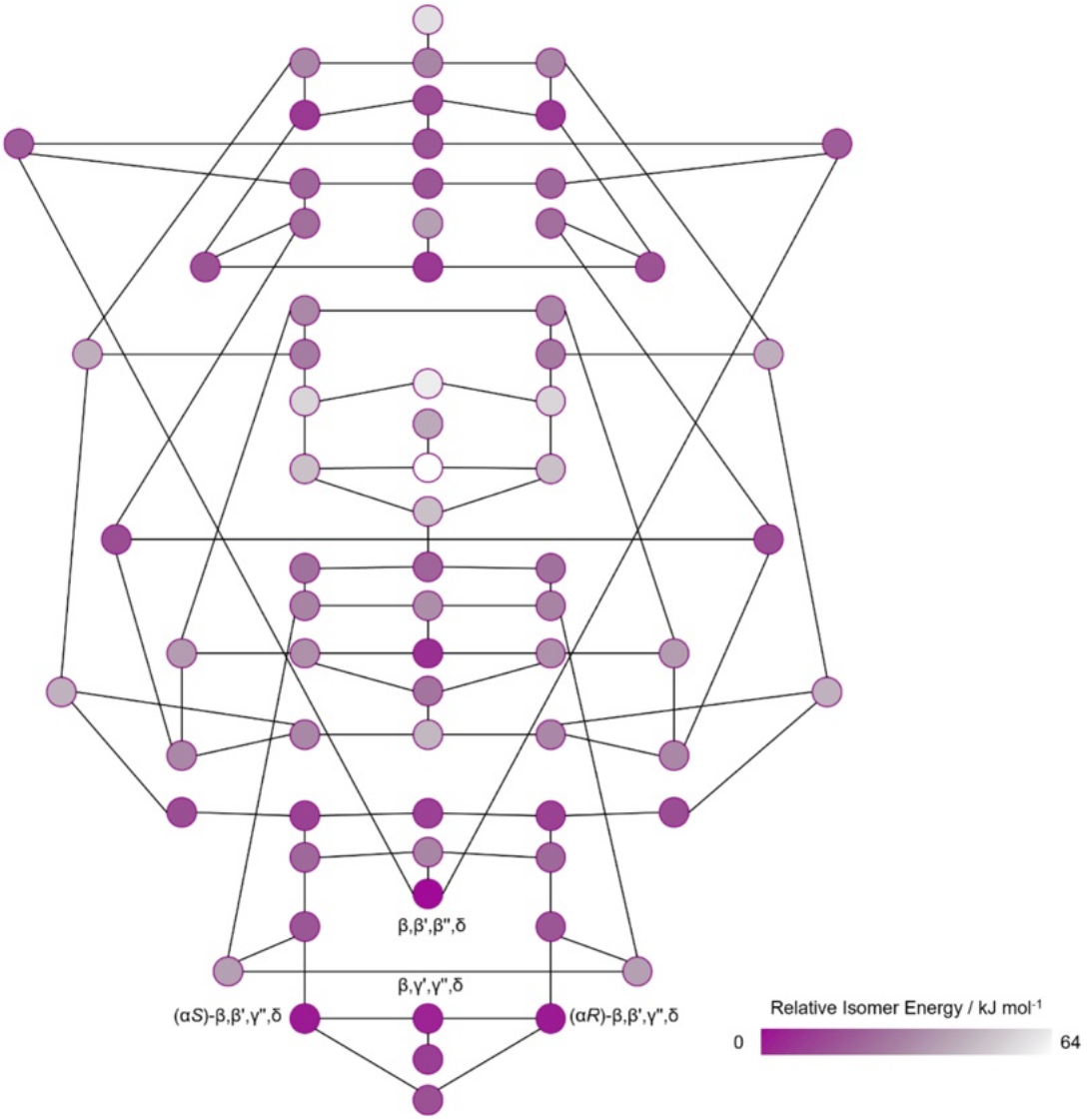

Figure S2.3. The energy-weighted isomer interconversion network calculated for **Me$_4$BV** (PBE0-D3/def2-SV(P)). Interconversion network prepared using a templated overlay of Brant and co-worker's tetrasubstituted **BV** interconversion network diagram, in combination with calculated energy values from *bullviso*.[5,62]

Principal Moments of Inertia Generation

3-D structures of compounds were generated using Vernalis KNIME nodes v1.34.1[84] and RDKit v4.5.0 in KNIME v4.4.1, based upon the Vernalis example workflow (https://hub.knime.com/vernalis/spaces/Public/latest/PMI%20Plotting%20Example~zuyv2AxB_dFVs0Ym, accessed November 2022). DFT optimised (PBE0 functional, def2-SV(P) basis set) were imported into the KNIME[83] workflow *via* an SDF reader. A

maximum of 30 conformers were generated for each molecule, using experimental torsions and 'basic knowledge' – i.e. flat rings etc. The geometry of each was optimised using MMFF94 force field with 1000 iterations. Prior to calculation, explicit hydrogens were added. Post calculation, explicit hydrogens were kept and the lowest energy conformer of each molecule was selected. Normalised principal moments of inertia (PMI) values (NPR1 and NPR2) were then derived and plotted on a 2D PMI plot in Microsoft Excel 2023.

Table S2.5. PMI generation of normalised principal moments of inertia (NPR1 and NPR2) for Me_2BV (2.7).

Isomer	NPR1	NPR2
000 000 001 1 (*N*)	0.579451568	0.884053394
000 000 010 1 (*J*)	0.648490572	0.798908463
000 000 011 0 (*K*)	0.633008369	0.820297516
000 000 100 1 (*L*)	0.473739491	0.968402290
000 000 101 0 (*G*)	0.619009668	0.826640516
000 000 110 0 (*M*)	0.611689113	0.847342749
000 001 001 0 (*A*)	0.694590202	0.785185086
000 001 010 0 (*C*)	0.609014942	0.894473552
000 001 100 0 (*F*)	0.510598953	0.955380037
000 010 001 0 (*B*)	0.609010310	0.894471363
000 010 010 0 (*D*)	0.654156352	0.917353765
000 010 100 0 (*H*)	0.698308763	0.772691736
000 100 001 0 (*E*)	0.510591262	0.955397691
000 100 010 0 (*I*)	0.698304702	0.772702604
000 100 100 0 (*O*)	0.590581046	0.888824493

Table S2.6. PMI generation of normalised principal moments of inertia (NPR1 and NPR2) for Me_3BV (2.8).

Isomer	NPR1	NPR2
000 000 011 1	0.662971310	0.712488254
000 000 101 1	0.516496035	0.846370614
000 000 110 1	0.528833382	0.832863467
000 000 111 0	0.670738372	0.703398101
000 001 001 1	0.652346910	0.839580720
000 001 010 1	0.625540139	0.890769526
000 001 011 0	0.669654028	0.773255566
000 001 100 1	0.473135465	0.930891427
000 001 101 0	0.607636684	0.848361464
000 001 110 0	0.546430483	0.919287752
000 010 001 1	0.625540963	0.890759877
000 010 010 1	0.746792262	0.793448936
000 010 011 0	0.647718778	0.955680574
000 010 100 1	0.593820861	0.800836680
000 010 101 0	0.711872896	0.819256412

000 010 110 0	0.674476176	0.866517628
000 011 001 0	0.669658721	0.773251710
000 011 010 0	0.647723374	0.955691226
000 011 100 0	0.570785225	0.822385486
000 100 001 1	0.473128508	0.930888432
000 100 010 1	0.593814445	0.800843681
000 100 011 0	0.570770626	0.822386315
000 100 100 1	0.457564827	0.919742134
000 100 101 0	0.546856878	0.869661457
000 100 110 0	0.677790124	0.753007295
000 101 001 0	0.607639268	0.848363075
000 101 010 0	0.711872514	0.819246991
000 101 100 0	0.546848992	0.869664043
000 110 001 0	0.546438566	0.919289540
000 110 010 0	0.674467592	0.866524433
000 110 100 0	0.677798780	0.753011319
001 001 001 0	0.892975057	0.999995568
001 001 010 0	0.676531071	0.912325595
001 001 100 0	0.536304976	0.836139627
001 010 010 0	0.706239380	0.733588598
001 010 100 0	0.605649669	0.794098332
001 100 010 0	0.605648288	0.794101934
001 100 100 0	0.507145821	0.956196177
010 010 010 0	0.753482798	0.753485031
010 010 100 0	0.768961471	0.857654514
010 100 100 0	0.723964861	0.880883726
100 100 100 0	0.646586940	0.999996888

Table S2.7. PMI generation of normalised principal moments of inertia (NPR1 and NPR2) for Me_4BV (2.9).

Isomer	NPR1	NPR2
000 000 111 1	0.563051215	0.751696738
000 001 011 1	0.674686669	0.775069595
000 001 101 1	0.555183858	0.873884216
000 001 110 1	0.524845860	0.906436938
000 001 111 0	0.612853060	0.786923960
000 010 011 1	0.687754380	0.824019790
000 010 101 1	0.630662518	0.821485164
000 010 110 1	0.656495218	0.800477250
000 010 111 0	0.710933870	0.808541740
000 011 001 1	0.674685300	0.775066330
000 011 010 1	0.687750916	0.824010651
000 011 011 0	0.650410620	0.846078320
000 011 100 1	0.555926360	0.784486640
000 011 101 0	0.684549860	0.772347480
000 011 110 0	0.601847940	0.905901900
000 100 011 1	0.555921690	0.784492220
000 100 101 1	0.474779760	0.869858100
000 100 110 1	0.546817392	0.804077475
000 100 111 0	0.600965544	0.768555240
000 101 001 1	0.555190288	0.873874502
000 101 010 1	0.684566608	0.772346810

000 101 011 0	0.684562483	0.772343273
000 101 100 1	0.474779337	0.869866035
000 101 101 0	0.587400463	0.823499121
000 101 110 0	0.618288850	0.841957250
000 110 001 1	0.524854429	0.906432500
000 110 010 1	0.656492730	0.800476170
000 110 011 0	0.601839460	0.905906190
000 110 100 1	0.546813110	0.804079130
000 110 101 0	0.618282800	0.841953650
000 110 110 0	0.731480740	0.790645070
000 111 001 0	0.612864740	0.786922310
000 111 010 0	0.710928400	0.808529240
000 111 100 0	0.600962510	0.768545750
001 001 001 1	0.809209990	0.999993550
001 001 010 1	0.697889580	0.979044680
001 001 011 0	0.777979461	0.928502653
001 001 100 1	0.517980060	0.882348820
001 001 101 0	0.700049140	0.989860770
001 001 110 0	0.587054020	0.950107760
001 010 010 1	0.727553751	0.831528016
001 010 011 0	0.723262451	0.795699963
001 010 100 1	0.579461478	0.852400313
001 010 101 0	0.714882263	0.897453794
001 010 110 0	0.657390165	0.798637152
001 011 010 0	0.723267062	0.795699518
001 011 100 0	0.620258594	0.739152709
001 100 010 1	0.579467520	0.852404580
001 100 011 0	0.620257270	0.739153250
001 100 100 1	0.471633060	0.997681370
001 100 101 0	0.551907470	0.868170480
001 100 110 0	0.575908430	0.834141260
001 101 010 0	0.714899330	0.897457410
001 101 100 0	0.551914366	0.868172360
001 110 010 0	0.657386370	0.798639360
001 110 100 0	0.575907431	0.834135051
010 010 010 1	0.950846377	0.950854008
010 010 011 0	0.720698637	0.844085604
010 010 100 1	0.745382690	0.839053390
010 010 101 0	0.881862400	0.912984280
010 010 110 0	0.799755990	0.861150800
010 011 100 0	0.663252290	0.841042480
010 100 011 0	0.663252420	0.841039070
010 100 100 1	0.594341440	0.883316360
010 100 101 0	0.682183630	0.857493310
010 100 110 0	0.775420660	0.874045650
010 101 100 0	0.682188570	0.857492320
010 110 100 0	0.775414600	0.874038310
011 100 100 0	0.579943440	0.901650508
100 100 100 1	0.492922242	0.999997408
100 100 101 0	0.555813522	0.939994105
100 100 110 0	0.710702857	0.812443988

Table S2.8. PMI generation of normalised principal moments of inertia (NPR1 and NPR2) for 3-D and common ring systems.

Compound	NPR1	NPR2
1,4-dimethyladamantane	0.560813614	0.965283098
1,2-dimethylcubane	0.654554766	0.768061524
1,4-dimethylcubane	0.386724171	0.999990450
p-xylene	0.216879256	0.797921538
o-xylene	0.416028907	0.600580363
m-xylene	0.336329337	0.679090911
1,4-dimethylpiperazine	0.248330953	0.816390622
(1*S*,2*S*)-1,2-dimethylcyclobutane	0.479827723	0.650785997
(1*R*,3*R*)-1,3-dimethylcyclobutane	0.279549544	0.919459774
(1*R*,2*S*)-1,2-dimethylcyclobutane	0.553180758	0.671158082
(1*S*,3*S*)-1,3-dimethylcyclobutane	0.255843764	0.914094127
(1*R*,4*R*,6*R*)-2,6-dimethylbicyclo[2.2.1]hept-2-ene	0.482384578	0.813203336
1,3-dimethylazetidine	0.268972148	0.915622214
1,2-dimethylazetidine	0.487557647	0.646360335
2,5-dimethylpyridine	0.216330750	0.798840434
2,3-dimethylpyridine	0.422075200	0.594999842
2,4-dimethylpyridine	0.328569016	0.687151837
3,4-dimethylpyridine	0.414936199	0.601949465
1,4-dimethylpiperidine	0.259618894	0.813581832
2,6-dimethyl-2-azaspiro[3.3]heptane	0.174720498	0.998096293
2,5-dimethyloctahydrocyclopenta[*c*]pyrrole	0.285180132	0.931848441
3,6-dimethyl-3-azabicyclo[3.1.0]hexane	0.412421426	0.995728438
1,5-dimethylazocane	0.437109773	0.813556375
2,6-dimethyl-2,6-diazaspiro[3.3]heptane	0.177391885	0.999617791
1,6-dimethyl-1,6-diazaspiro[3.3]heptane	0.309926511	0.891222204
(*R*)-1,7-dimethyl-1,7-diazaspiro[4.4]nonane	0.359787851	0.901014064
2,5-dimethyl-2,5-diazaspiro[3.4]octane	0.338226173	0.895946912
(1*S*,4*S*)-2,5-dimethyl-2,5-diazabicyclo[2.2.1]heptane	0.587353006	0.910167407
(1*S*,3*S*)-1,3-dimethylcyclohexane	0.453685408	0.758132605
(1*R*,2*R*)-1,2-dimethylcyclopropane	0.299772204	0.862461341
(1*s*,4*s*)-1,4-dimethylcyclohexane	0.400440242	0.856168260

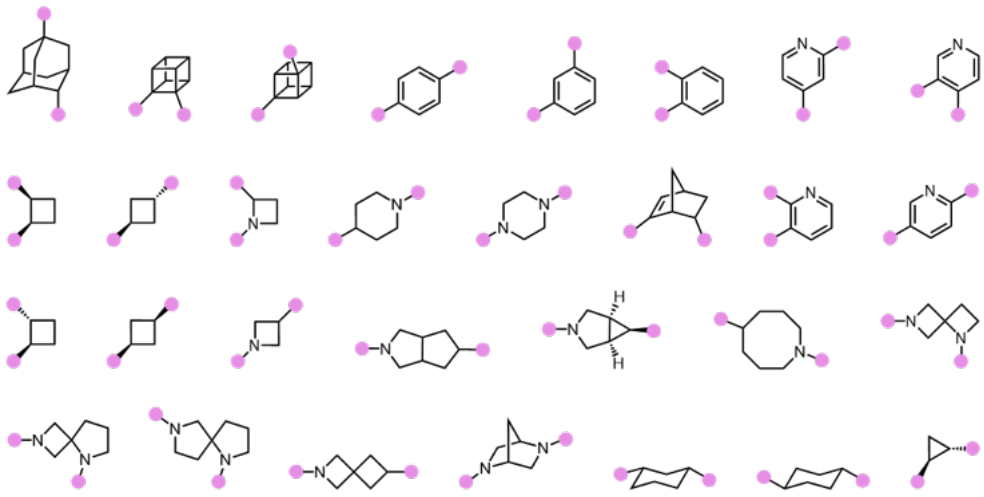

Figure S2.4. The commonly used ring systems in medicinal chemistry (listed in Table S2.8) that are compared to methylated BVs in Figure 2.19.

Exit Vector Analysis

Table S2.9. Isomer codes, Energy (E) and Relative energies (E_{rel}), Dipole moment (μ) and Geometric parameters *r*, φ_1, φ_2, and θ for **Me_2BV (2.7)**. v_1 and v_2 correspond to positions to which the vectors are appended.

Isomer	E / Hartree	E_{rel} / kJ·mol^{-1}	v_1	v_2	*r* / Å	φ_1 /°	φ_2 / °	θ / °	μ / D
000 000 001 1	-464.735969	20.59	β	α	1.537	61.0	67.4	-0.2	0.311
000 000 010 1	-464.738464	14.04	γ	α	2.554	30.4	45.6	0.2	0.755
000 000 011 0	-464.737758	15.89	γ	β	1.353	56.0	55.1	-0.1	0.477
000 000 100 1	-464.736512	19.16	δ	α	3.122	12.4	16.9	-0.1	0.609
000 000 101 0	-464.740612	8.40	δ	β	2.544	42.0	31.3	-0.2	0.302
000 000 110 0	-464.736491	19.22	δ	γ	1.494	63.8	63.0	-0.3	0.727
000 001 001 0	-464.743810	0.00	β′	β	2.509	53.8	53.7	-0.2	0.126
000 001 010 0	-464.742721	2.86	β	γ′	3.14	34.1	26.6	30.0	0.399
000 001 100 0	-464.740664	8.26	β	δ′	3.237	15.1	23.4	33.4	0.258
000 010 001 0	-464.742780	2.70	γ′	β	3.139	26.8	34.1	-30.0	0.399
000 010 010 0	-464.741728	5.47	γ′	γ	3.166	32.5	32.7	0.2	0.774
000 010 100 0	-464.739697	10.80	γ	δ′	2.662	45.0	44.7	-0.5	0.654
000 100 001 0	-464.740682	8.21	δ′	β	3.236	23.5	15.1	-33.3	0.257
000 100 010 0	-464.739675	10.86	δ′	γ	2.662	44.7	45.1	0.2	0.656
000 100 100 0	-464.733729	26.47	δ′	δ	1.542	61.3	61.4	0.0	0.566

Table S2.10. Isomer codes, Energy (E) and Relative energies (E_{rel}), Dipole moment (μ) and Geometric parameters *r*, φ_1, φ_2, and θ for **Me_3BV (2.8)**. v_1 and v_2 correspond to positions to which the vectors are appended.

Isomer	E / Hartree	E_{rel} / kJ·mol^{-1}	v_1	v_2	*r* / Å	φ_1 / °	φ_2 / °	θ / °	μ / D
000 000 011 1	-503.968652	43.80	γ	β	1.357	59.0	59.3	-0.4	0.544
000 000 011 1	-503.968652	43.80	γ	α	2.544	28.3	40.4	0.4	0.544
000 000 011 1	-503.968652	43.80	β	α	1.542	63.3	67.1	0.7	0.544
000 000 101 1	-503.974248	29.11	δ	β	2.561	42.6	34.6	-0.2	0.365
000 000 101 1	-503.974248	29.11	δ	α	3.114	13.2	12.2	0.1	0.365
000 000 101 1	-503.974248	29.11	β	α	1.535	61.1	67.2	0.2	0.365
000 000 110 1	-503.973677	30.61	δ	γ	1.492	63.6	63.1	0.1	0.833
000 000 110 1	-503.973677	30.61	δ	α	3.12	8.8	17.8	0.1	0.833
000 000 110 1	-503.973677	30.61	γ	α	2.569	33.7	46.2	-0.2	0.833
000 000 111 0	-503.970754	38.29	δ	γ	1.505	63.8	65.9	0.2	0.549
000 000 111 0	-503.970754	38.29	δ	β	2.534	37.6	25.7	0.0	0.549
000 000 111 0	-503.970754	38.29	γ	β	1.356	58.7	54.9	-0.1	0.549
000 001 001 1	-503.972914	32.61	β′	β	2.492	52.6	52.4	-0.2	0.209
000 001 001 1	-503.972914	32.61	β′	α	1.539	61.1	68.6	-7.8	0.209
000 001 001 1	-503.972914	32.61	β	α	1.539	61.1	68.6	7.6	0.209
000 001 010 1	-503.976285	23.76	β	γ′	3.143	32.1	27.4	23.2	0.457
000 001 010 1	-503.976285	23.76	β	α	1.536	60.9	67.4	0.9	0.457
000 001 010 1	-503.976285	23.76	γ′	α	2.563	30.8	47.7	5.9	0.457
000 001 011 0	-503.979301	15.85	β′	γ	3.132	35.3	25.4	39.4	0.318
000 001 011 0	-503.979301	15.85	β′	β	2.524	54.2	56.9	-2.6	0.318
000 001 011 0	-503.979301	15.85	γ	β	1.353	56.0	55.2	-0.3	0.318
000 001 100 1	-503.974363	28.81	β	δ′	3.258	16.7	23.6	-21.0	0.316
000 001 100 1	-503.974363	28.81	β	α	1.536	61.0	67.3	-0.6	0.316

000 001 100 1	-503.974363	28.81	δ′	α	3.134	12.2	19.4	-13.9	0.316
000 001 101 0	-503.982174	8.30	β′	δ	3.221	15.5	23.6	-34.0	0.179
000 001 101 0	-503.982174	8.30	β′	β	2.504	53.4	53.8	-0.2	0.179
000 001 101 0	-503.982174	8.30	δ	β	2.54	41.8	31.1	0.4	0.179
000 001 110 0	-503.978096	19.01	β	δ′	3.248	15.1	24.2	42.6	0.471
000 001 110 0	-503.978096	19.01	β	γ′	3.15	34.1	28.4	23.0	0.471
000 001 110 0	-503.978096	19.01	δ′	γ′	1.493	63.7	63.0	0.2	0.471
000 010 001 1	-503.976318	23.68	γ′	β	3.144	27.3	32.3	23.0	0.457
000 010 001 1	-503.976318	23.68	γ′	α	2.563	30.8	47.6	5.6	0.457
000 010 001 1	-503.976318	23.68	β	α	1.536	60.9	67.5	0.6	0.457
000 010 010 1	-503.978773	17.23	γ′	γ	3.151	32.7	32.8	0.0	0.892
000 010 010 1	-503.978773	17.23	γ′	α	2.55	30.1	45.6	0.8	0.892
000 010 010 1	-503.978773	17.23	γ	α	2.55	30.1	45.6	-0.6	0.892
000 010 011 0	-503.978373	18.28	γ′	γ	3.18	32.4	34.7	7.1	0.560
000 010 011 0	-503.978373	18.28	γ′	β	3.161	26.2	36.1	-36.2	0.560
000 010 011 0	-503.978373	18.28	γ	β	1.352	55.9	55.1	0.1	0.560
000 010 100 1	-503.976846	22.29	γ	δ′	2.658	44.8	44.6	-0.8	0.762
000 010 100 1	-503.976846	22.29	γ	α	2.55	30.3	45.4	0.8	0.762
000 010 100 1	-503.976846	22.29	δ′	α	3.11	12.1	16.8	-0.5	0.762
000 010 101 0	-503.981157	10.97	γ′	δ	2.655	44.6	44.7	-0.9	0.408
000 010 101 0	-503.981157	10.97	γ′	β	3.124	26.6	34.2	-29.8	0.408
000 010 101 0	-503.981157	10.97	δ	β	2.54	41.9	31.0	0.4	0.408
000 010 110 0	-503.976996	21.90	γ′	δ	2.673	45.3	46.5	3.2	0.828
000 010 110 0	-503.976996	21.90	γ′	γ	3.158	33.5	31.5	-6.8	0.828
000 010 110 0	-503.976996	21.90	δ	γ	1.494	63.8	62.9	0.4	0.828
000 011 001 0	-503.979298	15.85	γ	β	1.352	56.0	55.1	0.2	0.310
000 011 001 0	-503.979298	15.85	γ	β′	3.134	25.2	35.0	-39.6	0.310
000 011 001 0	-503.979298	15.85	β	β′	2.527	56.8	53.9	2.4	0.310
000 011 010 0	-503.978334	18.38	γ	β	1.352	55.9	55.1	0.3	0.560
000 011 010 0	-503.978334	18.38	γ	γ′	3.18	34.7	32.3	7.0	0.560
000 011 010 0	-503.978334	18.38	β	γ′	3.161	36.0	26.2	-36.4	0.560
000 011 100 0	-503.976206	23.97	γ	β	1.352	56.1	55.0	0.3	0.456
000 011 100 0	-503.976206	23.97	γ	δ′	2.679	48.6	45.3	2.7	0.456
000 011 100 0	-503.976206	23.97	β	δ′	3.241	13.7	24.3	-50.8	0.456
000 100 001 1	-503.974408	28.69	δ′	β	3.258	23.6	16.6	-20.7	0.315
000 100 001 1	-503.974408	28.69	δ′	α	3.134	12.2	19.5	-13.5	0.315
000 100 001 1	-503.974408	28.69	β	α	1.536	61.0	67.3	-0.9	0.315
000 100 010 1	-503.976816	22.37	δ′	γ	2.657	44.7	44.9	-0.8	0.763
000 100 010 1	-503.976816	22.37	δ′	α	3.11	12.1	16.8	0.2	0.763
000 100 010 1	-503.976816	22.37	γ	α	2.55	30.2	45.4	0.5	0.763
000 100 011 0	-503.976229	23.91	δ′	γ	2.68	45.3	48.6	-2.7	0.457
000 100 011 0	-503.976229	23.91	δ′	β	3.241	24.3	14.0	51.1	0.457
000 100 011 0	-503.976229	23.91	γ	β	1.352	56.1	55.0	0.0	0.457
000 100 100 1	-503.971059	37.48	δ′	δ	1.54	61.4	61.4	-0.1	0.670
000 100 100 1	-503.971059	37.48	δ′	α	3.132	15.3	16.7	12.5	0.670
000 100 100 1	-503.971059	37.48	δ	α	3.133	15.4	16.7	-12.3	0.670
000 100 101 0	-503.975111	26.85	δ′	δ	1.54	61.2	61.5	-0.1	0.324
000 100 101 0	-503.975111	26.85	δ′	β	3.228	20.1	16.1	-25.8	0.324
000 100 101 0	-503.975111	26.85	δ	β	2.554	44.6	31.5	-5.3	0.324
000 100 110 0	-503.969699	41.05	δ′	δ	1.548	61.1	63.4	-2.7	0.750
000 100 110 0	-503.969699	41.05	δ′	γ	2.645	40.2	42.5	3.6	0.750
000 100 110 0	-503.969699	41.05	δ	γ	1.498	65.7	62.8	6.7	0.750

000 101 001 0	-503.982160	8.34	δ	B	2.54	41.8	31.2	-0.2	0.183
000 101 001 0	-503.982160	8.34	δ	β′	3.22	23.7	15.7	34.1	0.183
000 101 001 0	-503.982160	8.34	β	β′	2.504	53.7	53.6	0.0	0.183
000 101 010 0	-503.981121	11.07	δ	B	2.539	41.9	31.0	-0.4	0.407
000 101 010 0	-503.981121	11.07	δ	γ′	2.655	44.8	44.6	1.1	0.407
000 101 010 0	-503.981121	11.07	β	γ′	3.124	34.3	26.5	29.8	0.407
000 101 100 0	-503.975151	26.74	δ	β	2.554	44.6	31.6	5.0	0.323
000 101 100 0	-503.975151	26.74	δ	δ′	1.539	61.5	61.2	-0.1	0.323
000 101 100 0	-503.975151	26.74	β	δ′	3.229	15.9	20.2	25.3	0.323
000 110 001 0	-503.978071	19.07	δ′	γ′	1.493	63.7	63.0	0.3	0.470
000 110 001 0	-503.978071	19.07	δ′	β	3.249	24.2	15.0	42.2	0.470
000 110 001 0	-503.978071	19.07	γ′	β	3.151	28.3	34.0	22.9	0.470
000 110 010 0	-503.976989	21.91	δ	γ	1.493	63.8	62.9	0.3	0.830
000 110 010 0	-503.976989	21.91	δ	γ′	2.673	46.5	45.4	3.5	0.830
000 110 010 0	-503.976989	21.91	γ	γ′	3.156	31.6	33.7	-6.8	0.830
000 110 100 0	-503.969765	40.88	δ	γ	1.498	65.7	62.9	6.6	0.750
000 110 100 0	-503.969765	40.88	δ	δ′	1.548	63.4	61.1	-2.6	0.750
000 110 100 0	-503.969765	40.88	γ	δ′	2.645	42.5	40.1	3.6	0.750
001 001 001 0	-503.985336	0.00	β″	β′	2.513	53.6	53.5	-0.2	0.248
001 001 001 0	-503.985336	0.00	β″	β	2.515	53.3	53.3	0.0	0.248
001 001 001 0	-503.985336	0.00	β′	β	2.513	53.5	53.6	0.1	0.248
001 001 010 0	-503.984343	2.61	β	β′	2.504	54.2	54.1	0.1	0.144
001 001 010 0	-503.984343	2.61	β	γ″	3.143	33.8	26.5	30.4	0.144
001 001 010 0	-503.984343	2.61	β′	γ″	3.142	33.9	26.6	-30.3	0.144
001 001 100 0	-503.982227	8.16	β	β′	2.51	53.8	54.0	0.4	0.051
001 001 100 0	-503.982227	8.16	β	δ′	3.236	14.7	23.2	-34.2	0.051
001 001 100 0	-503.982227	8.16	β′	δ′	3.237	14.3	23.3	33.3	0.051
001 010 010 0	-503.983260	5.45	β	γ′	3.137	34.5	27.1	30.6	0.505
001 010 010 0	-503.983260	5.45	β	γ″	3.136	34.7	27.0	-30.3	0.505
001 010 010 0	-503.983260	5.45	γ′	γ″	3.166	32.6	32.7	-0.2	0.505
001 010 100 0	-503.981171	10.93	β	γ′	3.143	34.1	26.4	29.9	0.380
001 010 100 0	-503.981171	10.93	β	δ″	3.233	15.3	23.5	-35.1	0.380
001 010 100 0	-503.981171	10.93	γ′	δ″	2.663	44.9	44.7	0.0	0.380
001 100 010 0	-503.981155	10.98	β	δ″	3.233	15.3	23.5	35.4	0.380
001 100 010 0	-503.981155	10.98	β	γ′	3.143	34.1	26.3	-30.0	0.380
001 100 010 0	-503.981155	10.98	δ″	γ′	2.663	44.8	45.0	-0.2	0.380
001 100 100 0	-503.975147	26.75	β	δ′	3.248	15.3	26.2	25.3	0.296
001 100 100 0	-503.975147	26.75	β	δ″	3.247	15.3	26.2	-25.5	0.296
001 100 100 0	-503.975147	26.75	δ′	δ″	1.544	61.4	61.4	0.1	0.296
010 010 010 0	-503.982133	8.41	γ″	γ′	3.166	33.1	33.0	0.1	0.876
010 010 010 0	-503.982133	8.41	γ″	γ	3.165	33.2	33.0	0.0	0.876
010 010 010 0	-503.982133	8.41	γ′	γ	3.163	33.3	33.3	0.0	0.876
010 010 100 0	-503.980126	13.68	γ	γ′	3.172	32.2	32.4	-0.1	0.761
010 010 100 0	-503.980126	13.68	γ	δ″	2.663	45.2	44.9	-0.4	0.761
010 010 100 0	-503.980126	13.68	γ′	δ″	2.663	45.1	44.9	0.1	0.761
010 100 100 0	-503.974214	29.20	γ	δ′	2.668	45.4	45.8	6.2	0.696
010 100 100 0	-503.974214	29.20	γ	δ″	2.669	45.2	45.7	-6.6	0.696
010 100 100 0	-503.974214	29.20	δ′	δ″	1.545	61.4	61.4	0.1	0.696
100 100 100 0	-503.965015	53.35	δ″	δ′	1.541	61.0	61.0	0.1	0.609
100 100 100 0	-503.965015	53.35	δ″	δ	1.541	61.0	61.0	0.0	0.609
100 100 100 0	-503.965015	53.35	δ′	δ	1.541	61.1	61.0	0.1	0.609

Table S2.11. Isomer codes, Energy (E) and Relative energies (E_{rel}), Dipole moment (μ) and Geometric parameters *r*, φ_1, φ_2, and θ for **Me_4BV (2.9).** v_1 and v_2 correspond to positions to which the vectors are appended.

Isomer	E / Hartree	E_{rel} / kJ·mol^{-1}	v_1	v_2	*r* / Å	φ_1 / °	φ_2 / °	θ / °	μ / D
000 000 111 1	-543.201058	59.60	δ	γ	1.505	63.3	67.6	-0.5	0.6261
000 000 111 1	-543.201058	59.60	δ	β	2.558	37.8	29.0	-0.2	0.6261
000 000 111 1	-543.201058	59.60	δ	α	3.097	8.0	11.0	-0.5	0.6261
000 000 111 1	-543.201058	59.60	γ	β	1.363	58.6	57.4	0.3	0.6261
000 000 111 1	-543.201058	59.60	γ	α	2.559	28.2	39.9	0.7	0.6261
000 000 111 1	-543.201058	59.60	β	α	1.546	65.8	66.4	0.1	0.6261
000 001 011 1	-543.205509	47.92	β′	γ	3.118	35.5	27.6	-27.2	0.4404
000 001 011 1	-543.205509	47.92	β′	β	2.500	52.7	56.4	0.3	0.4404
000 001 011 1	-543.205509	47.92	β′	α	1.538	60.8	69.2	8.6	0.4404
000 001 011 1	-543.205509	47.92	γ	β	1.357	58.5	59.5	3.4	0.4404
000 001 011 1	-543.205509	47.92	γ	α	2.552	28.1	42.2	-10.2	0.4404
000 001 011 1	-543.205509	47.92	β	α	1.544	63.6	68.4	-10.7	0.4404
000 001 101 1	-543.211306	32.70	β′	δ	3.231	19.4	24.2	22.7	0.2501
000 001 101 1	-543.211306	32.70	β′	β	2.489	52.2	52.3	0.0	0.2501
000 001 101 1	-543.211306	32.70	β′	α	1.538	61.0	68.6	-7.3	0.2501
000 001 101 1	-543.211306	32.70	δ	β	2.559	42.3	35.2	-2.5	0.2501
000 001 101 1	-543.211306	32.70	δ	α	3.127	13.1	14.8	21.5	0.2501
000 001 101 1	-543.211306	32.70	β	α	1.537	61.2	68.5	7.3	0.2501
000 001 110 1	-543.211751	31.53	β	δ′	3.272	16.1	24.2	-28.7	0.5216
000 001 110 1	-543.211751	31.53	β	γ′	3.158	31.5	28.7	-16.5	0.5216
000 001 110 1	-543.211751	31.53	β	α	1.534	60.7	67.4	-2.1	0.5216
000 001 110 1	-543.211751	31.53	δ′	γ′	1.490	63.4	63.1	-0.5	0.5216
000 001 110 1	-543.211751	31.53	δ′	α	3.132	8.7	20.3	-13.6	0.5216
000 001 110 1	-543.211751	31.53	γ′	α	2.578	34.0	48.3	-5.0	0.5216
000 001 111 0	-543.212477	29.63	β′	δ	3.225	15.3	24.8	-47.3	0.3858
000 001 111 0	-543.212477	29.63	β′	γ	3.150	35.3	26.3	-30.9	0.3858
000 001 111 0	-543.212477	29.63	β′	β	2.515	53.8	58.5	3.0	0.3858
000 001 111 0	-543.212477	29.63	δ	γ	1.503	63.7	65.9	-0.6	0.3858
000 001 111 0	-543.212477	29.63	δ	β	2.531	37.5	25.7	1.6	0.3858
000 001 111 0	-543.212477	29.63	γ	β	1.356	58.6	55.0	1.2	0.3858
000 010 011 1	-543.209119	38.44	γ′	γ	3.156	32.9	33.1	5.5	0.6033
000 010 011 1	-543.209119	38.44	γ′	β	3.161	27.1	32.1	-29.4	0.6033
000 010 011 1	-543.209119	38.44	γ′	α	2.559	30.4	48.5	-6.4	0.6033
000 010 011 1	-543.209119	38.44	γ	β	1.357	58.8	59.3	0.7	0.6033
000 010 011 1	-543.209119	38.44	γ	α	2.540	28.0	40.4	-2.5	0.6033
000 010 011 1	-543.209119	38.44	β	α	1.541	63.1	67.3	-2.3	0.6033
000 010 101 1	-543.214680	23.84	γ′	δ	2.642	44.5	44.5	-0.9	0.4750
000 010 101 1	-543.214680	23.84	γ′	β	3.126	27.4	32.7	-22.7	0.4750
000 010 101 1	-543.214680	23.84	γ′	α	2.560	30.7	47.4	-5.5	0.4750
000 010 101 1	-543.214680	23.84	δ	β	2.557	42.5	34.4	0.0	0.4750
000 010 101 1	-543.214680	23.84	δ	α	3.103	13.0	12.2	-0.8	0.4750
000 010 101 1	-543.214680	23.84	β	α	1.535	61.0	67.3	-0.2	0.4750
000 010 110 1	-543.214078	25.42	γ′	δ	2.668	45.3	46.4	-3.4	0.9506
000 010 110 1	-543.214078	25.42	γ′	γ	3.145	33.5	31.5	6.7	0.9506
000 010 110 1	-543.214078	25.42	γ′	α	2.542	29.8	45.3	-1.2	0.9506
000 010 110 1	-543.214078	25.42	δ	γ	1.492	63.7	63.0	-0.4	0.9506
000 010 110 1	-543.214078	25.42	δ	α	3.109	8.6	17.7	-0.1	0.9506
000 010 110 1	-543.214078	25.42	γ	α	2.566	33.4	46.2	0.9	0.9506

000 010 111 0	-543.211407	32.43	γ′	δ	2.667	44.5	47.5	-3.2	0.6007
000 010 111 0	-543.211407	32.43	γ′	γ	3.185	32.6	32.1	-0.5	0.6007
000 010 111 0	-543.211407	32.43	γ′	β	3.139	25.8	36.8	39.0	0.6007
000 010 111 0	-543.211407	32.43	δ	γ	1.504	63.9	65.8	-1.3	0.6007
000 010 111 0	-543.211407	32.43	δ	β	2.530	37.6	25.5	-1.4	0.6007
000 010 111 0	-543.211407	32.43	γ	β	1.356	58.5	54.9	0.4	0.6007
000 011 001 1	-543.205524	47.88	γ	β	1.357	58.5	59.5	-3.7	0.4384
000 011 001 1	-543.205524	47.88	γ	β′	3.118	27.6	35.3	27.4	0.4384
000 011 001 1	-543.205524	47.88	γ	α	2.551	28.0	42.3	10.3	0.4384
000 011 001 1	-543.205524	47.88	β	β′	2.498	56.7	52.6	0.2	0.4384
000 011 001 1	-543.205524	47.88	β	α	1.544	63.6	68.4	11.2	0.4384
000 011 001 1	-543.205524	47.88	β′	α	1.537	60.8	69.1	-8.4	0.4384
000 011 010 1	-543.209146	38.37	γ	β	1.357	58.9	59.3	0.0	0.6116
000 011 010 1	-543.209146	38.37	γ	γ′	3.156	33.5	33.0	-5.0	0.6116
000 011 010 1	-543.209146	38.37	γ	α	2.540	28.1	40.5	1.3	0.6116
000 011 010 1	-543.209146	38.37	β	γ′	3.156	33.3	27.3	28.4	0.6116
000 011 010 1	-543.209146	38.37	β	α	1.541	63.1	67.3	0.8	0.6116
000 011 010 1	-543.209146	38.37	γ′	α	2.558	30.4	48.4	6.7	0.6116
000 011 011 0	-543.215144	22.62	γ′	β′	1.351	55.7	55.1	-0.5	0.4003
000 011 011 0	-543.215144	22.62	γ′	γ	3.197	34.2	34.1	0.0	0.4003
000 011 011 0	-543.215144	22.62	γ′	β	3.154	24.8	37.2	45.4	0.4003
000 011 011 0	-543.215144	22.62	β′	γ	3.153	37.3	24.7	-45.2	0.4003
000 011 011 0	-543.215144	22.62	β′	β	2.541	57.1	57.0	0.1	0.4003
000 011 011 0	-543.215144	22.62	γ	β	1.351	55.7	55.1	0.5	0.4003
000 011 100 1	-543.207151	43.61	γ	β	1.357	58.9	59.0	-1.8	0.5159
000 011 100 1	-543.207151	43.61	γ	δ′	2.675	46.9	45.1	-2.1	0.5159
000 011 100 1	-543.207151	43.61	γ	α	2.540	28.1	40.3	1.1	0.5159
000 011 100 1	-543.207151	43.61	β	δ′	3.262	13.6	24.2	28.6	0.5159
000 011 100 1	-543.207151	43.61	β	α	1.541	63.3	67.1	2.8	0.5159
000 011 100 1	-543.207151	43.61	δ′	α	3.117	11.7	20.3	16.9	0.5159
000 011 101 0	-543.217729	15.84	γ	β	1.352	56.0	55.1	0.0	0.2993
000 011 101 0	-543.217729	15.84	γ	δ′	2.673	48.3	45.3	3.0	0.2993
000 011 101 0	-543.217729	15.84	γ	β′	3.117	25.4	35.2	39.3	0.2993
000 011 101 0	-543.217729	15.84	β	δ′	3.226	14.1	24.3	-51.0	0.2993
000 011 101 0	-543.217729	15.84	β	β′	2.520	56.3	54.1	-3.1	0.2993
000 011 101 0	-543.217729	15.84	δ′	β′	2.531	41.5	30.7	-0.6	0.2993
000 011 110 0	-543.213770	26.23	γ	β	1.351	55.9	54.9	0.2	0.5898
000 011 110 0	-543.213770	26.23	γ	δ′	2.691	48.9	47.0	-1.0	0.5898
000 011 110 0	-543.213770	26.23	γ	γ′	3.175	35.3	30.7	13.6	0.5898
000 011 110 0	-543.213770	26.23	β	δ′	3.255	13.5	25.0	-59.4	0.5898
000 011 110 0	-543.213770	26.23	β	γ′	3.176	35.6	27.4	-28.9	0.5898
000 011 110 0	-543.213770	26.23	δ′	γ′	1.491	63.7	62.7	-1.7	0.5898
000 100 011 1	-543.207204	43.47	δ′	γ	2.674	45.0	46.6	-1.9	0.5204
000 100 011 1	-543.207204	43.47	δ′	β	3.256	24.2	15.4	31.5	0.5204
000 100 011 1	-543.207204	43.47	δ′	α	3.114	11.8	20.0	17.3	0.5204
000 100 011 1	-543.207204	43.47	γ	β	1.357	59.1	59.2	0.1	0.5204
000 100 011 1	-543.207204	43.47	γ	α	2.541	28.3	40.3	0.3	0.5204
000 100 011 1	-543.207204	43.47	β	α	1.541	63.2	67.1	0.3	0.5204
000 100 101 1	-543.209013	38.72	δ′	δ	1.538	61.0	61.5	0.2	0.3850
000 100 101 1	-543.209013	38.72	δ′	β	3.249	20.2	17.7	14.0	0.3850
000 100 101 1	-543.209013	38.72	δ′	α	3.145	15.2	19.1	0.6	0.3850
000 100 101 1	-543.209013	38.72	δ	β	2.570	45.1	34.9	4.7	0.3850

000 100 101 1	-543.209013	38.72	δ	α	3.126	16.1	12.2	12.2	0.3850
000 100 101 1	-543.209013	38.72	β	α	1.533	61.1	67.1	0.0	0.3850
000 100 110 1	-543.206971	44.08	δ′	δ	1.547	61.0	63.3	2.7	0.8614
000 100 110 1	-543.206971	44.08	δ′	γ	2.641	40.0	42.4	-3.4	0.8614
000 100 110 1	-543.206971	44.08	δ′	α	3.118	16.0	16.4	17.5	0.8614
000 100 110 1	-543.206971	44.08	δ	γ	1.497	65.6	63.0	-6.6	0.8614
000 100 110 1	-543.206971	44.08	δ	α	3.133	12.1	17.6	-20.8	0.8614
000 100 110 1	-543.206971	44.08	γ	α	2.566	34.5	45.9	3.1	0.8614
000 100 111 0	-543.203636	52.84	δ′	δ	1.546	60.6	64.4	-3.6	0.5379
000 100 111 0	-543.203636	52.84	δ′	γ	2.665	40.3	46.5	3.3	0.5379
000 100 111 0	-543.203636	52.84	δ′	β	3.224	19.5	13.5	45.5	0.5379
000 100 111 0	-543.203636	52.84	δ	γ	1.509	65.8	65.6	9.3	0.5379
000 100 111 0	-543.203636	52.84	δ	β	2.545	40.4	26.1	5.9	0.5379
000 100 111 0	-543.203636	52.84	γ	β	1.356	59.6	55.0	-4.1	0.5379
000 101 001 1	-543.211278	32.77	δ	β	2.559	42.4	35.1	3.0	0.2609
000 101 001 1	-543.211278	32.77	δ	β′	3.230	24.1	19.7	-23.3	0.2609
000 101 001 1	-543.211278	32.77	δ	α	3.126	13.1	14.7	-21.4	0.2609
000 101 001 1	-543.211278	32.77	β	β′	2.485	52.6	52.5	0.2	0.2609
000 101 001 1	-543.211278	32.77	β	α	1.537	61.2	68.4	-7.6	0.2609
000 101 001 1	-543.211278	32.77	β′	α	1.538	61.1	68.5	7.8	0.2609
000 101 010 1	-543.214731	23.71	δ	β	2.557	42.4	34.4	0.1	0.4743
000 101 010 1	-543.214731	23.71	δ	γ′	2.642	44.5	44.5	-0.8	0.4743
000 101 010 1	-543.214731	23.71	δ	α	3.103	12.9	12.3	-1.3	0.4743
000 101 010 1	-543.214731	23.71	β	γ′	3.126	32.6	27.4	-22.7	0.4743
000 101 010 1	-543.214731	23.71	β	α	1.535	61.0	67.4	-0.4	0.4743
000 101 010 1	-543.214731	23.71	γ′	α	2.560	30.7	47.4	-5.4	0.4743
000 101 011 0	-543.217733	15.83	δ′	β′	2.531	41.5	30.7	0.9	0.2959
000 101 011 0	-543.217733	15.83	δ′	γ	2.673	45.2	48.3	-3.1	0.2959
000 101 011 0	-543.217733	15.83	δ′	β	3.225	24.2	14.4	51.2	0.2959
000 101 011 0	-543.217733	15.83	β′	γ	3.119	35.0	25.2	-39.5	0.2959
000 101 011 0	-543.217733	15.83	β′	β	2.520	54.0	56.5	2.6	0.2959
000 101 011 0	-543.217733	15.83	γ	β	1.352	56.0	55.1	0.4	0.2959
000 101 100 1	-543.209013	38.72	δ	β	2.570	45.1	34.8	-4.4	0.3837
000 101 100 1	-543.209013	38.72	δ	δ′	1.538	61.5	61.0	-0.1	0.3837
000 101 100 1	-543.209013	38.72	δ	α	3.126	16.1	12.2	-12.6	0.3837
000 101 100 1	-543.209013	38.72	β	δ′	3.249	17.5	20.3	-13.7	0.3837
000 101 100 1	-543.209013	38.72	β	α	1.534	61.1	67.1	-0.3	0.3837
000 101 100 1	-543.209013	38.72	δ′	α	3.145	15.2	19.2	-0.6	0.3837
000 101 101 0	-543.216658	18.65	δ′	β′	2.551	44.4	31.5	-5.3	0.1730
000 101 101 0	-543.216658	18.65	δ′	δ	1.538	61.3	61.2	0.0	0.1730
000 101 101 0	-543.216658	18.65	δ′	β	3.213	20.2	16.3	26.0	0.1730
000 101 101 0	-543.216658	18.65	β′	δ	3.214	16.2	20.2	-25.5	0.1730
000 101 101 0	-543.216658	18.65	β′	β	2.481	53.7	53.9	-0.1	0.1730
000 101 101 0	-543.216658	18.65	δ	β	2.551	44.4	31.5	5.6	0.1730
000 101 110 0	-543.211289	32.74	δ	β	2.551	45.2	31.3	6.0	0.4899
000 101 110 0	-543.211289	32.74	δ	δ′	1.546	61.2	63.1	2.6	0.4899
000 101 110 0	-543.211289	32.74	δ	γ′	2.638	40.1	42.1	-3.3	0.4899
000 101 110 0	-543.211289	32.74	β	δ′	3.242	15.8	19.6	36.8	0.4899
000 101 110 0	-543.211289	32.74	β	γ′	3.107	34.8	31.2	22.6	0.4899
000 101 110 0	-543.211289	32.74	δ′	γ′	1.497	65.7	62.8	-6.3	0.4899
000 110 001 1	-543.211756	31.52	δ′	γ′	1.490	63.4	63.1	-0.4	0.5248
000 110 001 1	-543.211756	31.52	δ′	β	3.271	24.2	16.4	-29.3	0.5248

000 110 001 1	-543.211756	31.52	δ′	α	3.132	8.7	20.3	-13.5	0.5248
000 110 001 1	-543.211756	31.52	γ′	β	3.156	28.9	31.9	-16.4	0.5248
000 110 001 1	-543.211756	31.52	γ′	α	2.578	34.0	48.2	-5.2	0.5248
000 110 001 1	-543.211756	31.52	β	α	1.534	60.7	67.4	-1.7	0.5248
000 110 010 1	-543.214090	25.39	δ	γ	1.492	63.7	63.0	0.4	0.9505
000 110 010 1	-543.214090	25.39	δ	γ′	2.668	46.3	45.3	3.3	0.9505
000 110 010 1	-543.214090	25.39	δ	α	3.109	8.6	17.7	-0.5	0.9505
000 110 010 1	-543.214090	25.39	γ	γ′	3.144	31.5	33.5	-6.7	0.9505
000 110 010 1	-543.214090	25.39	γ	α	2.566	33.4	46.2	-1.0	0.9505
000 110 010 1	-543.214090	25.39	γ′	α	2.542	29.9	45.3	1.4	0.9505
000 110 011 0	-543.213744	26.30	δ′	γ′	1.491	63.7	62.7	-1.1	0.5930
000 110 011 0	-543.213744	26.30	δ′	γ	2.690	46.9	48.8	-1.0	0.5930
000 110 011 0	-543.213744	26.30	δ′	β	3.253	24.9	13.8	-60.0	0.5930
000 110 011 0	-543.213744	26.30	γ′	γ	3.173	31.1	35.3	13.7	0.5930
000 110 011 0	-543.213744	26.30	γ′	β	3.173	27.8	36.0	-29.3	0.5930
000 110 011 0	-543.213744	26.30	γ	β	1.351	55.9	54.8	-0.1	0.5930
000 110 100 1	-543.206983	44.05	δ	γ	1.497	65.6	62.9	-7.0	0.8593
000 110 100 1	-543.206983	44.05	δ	δ′	1.547	63.3	61.0	2.7	0.8593
000 110 100 1	-543.206983	44.05	δ	α	3.133	12.1	17.6	-20.9	0.8593
000 110 100 1	-543.206983	44.05	γ	δ′	2.640	42.6	40.0	-3.8	0.8593
000 110 100 1	-543.206983	44.05	γ	α	2.566	34.5	45.9	3.7	0.8593
000 110 100 1	-543.206983	44.05	δ′	α	3.118	16.0	16.4	17.7	0.8593
000 110 101 0	-543.211245	32.86	δ′	γ′	1.497	65.6	62.8	6.2	0.4884
000 110 101 0	-543.211245	32.86	δ′	δ	1.546	63.1	61.2	-2.8	0.4884
000 110 101 0	-543.211245	32.86	δ′	β	3.243	19.6	15.7	-36.7	0.4884
000 110 101 0	-543.211245	32.86	γ′	δ	2.638	42.0	40.1	3.1	0.4884
000 110 101 0	-543.211245	32.86	γ′	β	3.109	31.1	34.6	-22.6	0.4884
000 110 101 0	-543.211245	32.86	δ	β	2.551	45.3	31.3	-5.6	0.4884
000 110 110 0	-543.205433	48.12	δ′	γ′	1.498	66.3	62.6	-8.4	0.9068
000 110 110 0	-543.205433	48.12	δ′	δ	1.557	63.0	63.0	-0.2	0.9068
000 110 110 0	-543.205433	48.12	δ′	γ	2.655	41.1	43.2	10.3	0.9068
000 110 110 0	-543.205433	48.12	γ′	δ	2.655	43.0	41.0	-10.3	0.9068
000 110 110 0	-543.205433	48.12	γ′	γ	3.086	36.4	36.6	0.0	0.9068
000 110 110 0	-543.205433	48.12	δ	γ	1.498	66.3	62.7	8.8	0.9068
000 111 001 0	-543.212485	29.60	δ	γ	1.503	63.7	65.9	0.3	0.3864
000 111 001 0	-543.212485	29.60	δ	β	2.531	37.5	25.6	-1.3	0.3864
000 111 001 0	-543.212485	29.60	δ	β′	3.224	24.8	15.4	47.1	0.3864
000 111 001 0	-543.212485	29.60	γ	β	1.356	58.6	54.9	-0.7	0.3864
000 111 001 0	-543.212485	29.60	γ	β′	3.148	26.6	35.3	31.1	0.3864
000 111 001 0	-543.212485	29.60	β	β′	2.514	58.4	53.8	-3.2	0.3864
000 111 010 0	-543.211438	32.35	δ	γ	1.504	63.9	65.8	1.0	0.6048
000 111 010 0	-543.211438	32.35	δ	β	2.530	37.6	25.5	0.9	0.6048
000 111 010 0	-543.211438	32.35	δ	γ′	2.666	47.4	44.6	3.7	0.6048
000 111 010 0	-543.211438	32.35	γ	β	1.356	58.6	54.9	-0.5	0.6048
000 111 010 0	-543.211438	32.35	γ	γ′	3.181	32.3	32.9	0.8	0.6048
000 111 010 0	-543.211438	32.35	β	γ′	3.136	37.0	26.2	-38.9	0.6048
000 111 100 0	-543.203646	52.81	δ	γ	1.509	65.8	65.6	-9.2	0.5395
000 111 100 0	-543.203646	52.81	δ	β	2.545	40.3	26.1	-5.6	0.5395
000 111 100 0	-543.203646	52.81	δ	δ′	1.546	64.4	60.4	3.5	0.5395
000 111 100 0	-543.203646	52.81	γ	β	1.356	59.6	55.0	4.2	0.5395
000 111 100 0	-543.203646	52.81	γ	δ′	2.665	46.5	40.2	-3.3	0.5395
000 111 100 0	-543.203646	52.81	β	δ′	3.225	13.4	19.3	-45.1	0.5395

001 001 001 1	-543.207757	42.02	β	β′	2.521	49.2	49.4	0.4	0.2054
001 001 001 1	-543.207757	42.02	β″	β	2.516	49.7	49.7	-0.1	0.2054
001 001 001 1	-543.207757	42.02	β″	α	1.544	60.9	70.4	0.4	0.2054
001 001 001 1	-543.207757	42.02	β″	β	2.521	49.3	49.2	-0.3	0.2054
001 001 001 1	-543.207757	42.02	β′	α	1.544	60.9	70.5	0.1	0.2054
001 001 001 1	-543.207757	42.02	β′	α	1.544	60.9	70.4	-0.5	0.2054
001 001 010 1	-543.213382	27.25	β	β′	2.486	53.1	53.1	0.1	0.1735
001 001 010 1	-543.213382	27.25	β	γ″	3.162	29.2	26.6	23.4	0.1735
001 001 010 1	-543.213382	27.25	β	α	1.538	61.0	68.8	8.5	0.1735
001 001 010 1	-543.213382	27.25	β′	γ″	3.161	29.3	26.7	-23.5	0.1735
001 001 010 1	-543.213382	27.25	β′	α	1.538	61.0	68.6	-8.3	0.1735
001 001 010 1	-543.213382	27.25	γ″	α	2.577	31.3	50.3	-0.2	0.1735
001 001 011 0	-543.220959	7.36	β″	β′	2.510	54.1	54.1	-0.2	0.2382
001 001 011 0	-543.220959	7.36	β″	γ	3.137	34.9	25.0	39.9	0.2382
001 001 011 0	-543.220959	7.36	β″	β	2.531	53.8	56.4	-2.6	0.2382
001 001 011 0	-543.220959	7.36	β′	γ	3.136	34.7	25.0	-40.0	0.2382
001 001 011 0	-543.220959	7.36	β′	β	2.530	53.7	56.5	2.4	0.2382
001 001 011 0	-543.220959	7.36	γ	β	1.352	55.9	55.2	0.0	0.2382
001 001 100 1	-543.211517	32.15	β	β′	2.489	53.0	52.7	-0.2	0.1368
001 001 100 1	-543.211517	32.15	β	δ″	3.267	14.6	22.9	-14.4	0.1368
001 001 100 1	-543.211517	32.15	β	α	1.538	61.1	68.5	-8.7	0.1368
001 001 100 1	-543.211517	32.15	β′	δ″	3.266	14.9	22.9	15.0	0.1368
001 001 100 1	-543.211517	32.15	β′	α	1.538	61.0	68.5	8.3	0.1368
001 001 100 1	-543.211517	32.15	δ″	α	3.150	11.9	22.1	-0.1	0.1368
001 001 101 0	-543.223761	0.00	β″	β′	2.514	53.7	53.5	-0.4	0.2654
001 001 101 0	-543.223761	0.00	β″	δ	3.220	14.7	23.3	-34.4	0.2654
001 001 101 0	-543.223761	0.00	β″	β	2.510	53.0	53.5	-0.5	0.2654
001 001 101 0	-543.223761	0.00	β′	δ	3.219	15.1	23.4	35.0	0.2654
001 001 101 0	-543.223761	0.00	β′	β	2.508	53.2	53.5	0.2	0.2654
001 001 101 0	-543.223761	0.00	δ	B	2.536	41.5	31.0	-0.1	0.2654
001 001 110 0	-543.219802	10.39	β	β′	2.509	54.4	54.2	0.2	0.2058
001 001 110 0	-543.219802	10.39	β	δ″	3.250	14.1	24.0	42.6	0.2058
001 001 110 0	-543.219802	10.39	β	γ″	3.157	33.3	28.1	23.8	0.2058
001 001 110 0	-543.219802	10.39	β′	δ″	3.249	14.3	24.0	-42.9	0.2058
001 001 110 0	-543.219802	10.39	β′	γ″	3.154	33.5	28.4	-23.8	0.2058
001 001 110 0	-543.219802	10.39	δ″	γ″	1.492	63.6	62.8	0.1	0.2058
001 010 010 1	-543.216707	18.52	β	γ′	3.140	32.8	27.7	-23.6	0.5755
001 010 010 1	-543.216707	18.52	β	γ″	3.140	32.9	27.7	23.4	0.5755
001 010 010 1	-543.216707	18.52	β	α	1.535	60.8	67.5	0.0	0.5755
001 010 010 1	-543.216707	18.52	γ′	γ″	3.157	32.2	32.2	0.2	0.5755
001 010 010 1	-543.216707	18.52	γ′	α	2.559	30.5	47.7	-6.7	0.5755
001 010 010 1	-543.216707	18.52	γ′	α	2.559	30.5	47.7	6.6	0.5755
001 010 011 0	-543.220027	9.80	β′	γ″	3.142	34.4	27.1	31.7	0.3118
001 010 011 0	-543.220027	9.80	β′	γ	3.130	35.7	25.7	-39.7	0.3118
001 010 011 0	-543.220027	9.80	β′	β	2.519	54.6	57.5	2.1	0.3118
001 010 011 0	-543.220027	9.80	γ″	γ	3.185	32.2	34.3	7.3	0.3118
001 010 011 0	-543.220027	9.80	γ″	β	3.168	25.9	35.3	-37.3	0.3118
001 010 011 0	-543.220027	9.80	γ	β	1.352	55.8	55.1	0.7	0.3118
001 010 100 1	-543.214856	23.38	β	γ′	3.144	32.5	27.2	-23.0	0.4453
001 010 100 1	-543.214856	23.38	β	δ″	3.255	16.8	23.5	22.7	0.4453
001 010 100 1	-543.214856	23.38	β	α	1.536	60.8	67.4	0.1	0.4453
001 010 100 1	-543.214856	23.38	γ′	δ″	2.658	44.6	44.4	0.2	0.4453

001 010 100 1	-543.214856	23.38	γ′	α	2.559	30.7	47.5	-6.0	0.4453
001 010 100 1	-543.214856	23.38	δ″	α	3.123	12.0	19.4	13.7	0.4453
001 010 101 0	-543.222765	2.61	β′	γ″	3.147	33.7	26.1	-30.3	0.1435
001 010 101 0	-543.222765	2.61	β′	δ	3.217	15.6	23.7	35.6	0.1435
001 010 101 0	-543.222765	2.61	β′	β	2.500	53.8	54.1	0.1	0.1435
001 010 101 0	-543.222765	2.61	γ″	δ	2.655	44.7	44.7	0.0	0.1435
001 010 101 0	-543.222765	2.61	γ″	β	3.125	26.9	34.1	30.5	0.1435
001 010 101 0	-543.222765	2.61	δ	β	2.536	41.6	30.9	-0.5	0.1435
001 010 110 0	-543.218583	13.59	β	γ″	3.142	34.7	26.7	-30.8	0.5476
001 010 110 0	-543.218583	13.59	β	δ′	3.247	14.8	24.2	43.9	0.5476
001 010 110 0	-543.218583	13.59	β	γ′	3.153	34.1	28.4	23.6	0.5476
001 010 110 0	-543.218583	13.59	γ″	δ′	2.675	45.1	46.5	-3.5	0.5476
001 010 110 0	-543.218583	13.59	γ″	γ′	3.158	33.4	31.8	7.1	0.5476
001 010 110 0	-543.218583	13.59	δ′	γ′	1.492	63.7	62.8	0.2	0.5476
001 011 010 0	-543.219986	9.91	β′	γ	3.131	35.4	25.6	39.8	0.3101
001 011 010 0	-543.219986	9.91	β′	β	2.520	54.3	57.2	-2.3	0.3101
001 011 010 0	-543.219986	9.91	β′	γ″	3.139	34.7	27.3	-31.4	0.3101
001 011 010 0	-543.219986	9.91	γ	β	1.352	55.8	55.1	-0.3	0.3101
001 011 010 0	-543.219986	9.91	γ	γ″	3.186	34.3	32.1	-7.1	0.3101
001 011 010 0	-543.219986	9.91	β	γ″	3.166	35.6	25.9	36.7	0.3101
001 011 100 0	-543.217838	15.55	β′	γ	3.137	35.1	25.0	-39.6	0.2536
001 011 100 0	-543.217838	15.55	β′	β	2.528	54.0	56.9	2.4	0.2536
001 011 100 0	-543.217838	15.55	β′	δ″	3.229	14.8	23.0	37.8	0.2536
001 011 100 0	-543.217838	15.55	γ	β	1.352	56.0	55.1	0.4	0.2536
001 011 100 0	-543.217838	15.55	γ	δ″	2.681	48.5	45.2	2.4	0.2536
001 011 100 0	-543.217838	15.55	β	δ″	3.241	13.3	24.0	-51.9	0.2536
001 100 010 1	-543.214790	23.55	β	δ″	3.254	17.1	23.7	-23.3	0.4444
001 100 010 1	-543.214790	23.55	β	γ′	3.147	32.2	27.0	23.0	0.4444
001 100 010 1	-543.214790	23.55	β	α	1.536	60.8	67.4	0.3	0.4444
001 100 010 1	-543.214790	23.55	δ″	γ′	2.657	44.3	44.7	0.2	0.4444
001 100 010 1	-543.214790	23.55	δ″	α	3.123	11.9	19.4	-14.3	0.4444
001 100 010 1	-543.214790	23.55	γ	α	2.560	30.7	47.5	5.7	0.4444
001 100 011 0	-543.217797	15.66	β′	δ″	3.229	14.7	23.0	38.1	0.2536
001 100 011 0	-543.217797	15.66	β′	γ	3.135	35.1	25.1	-39.6	0.2536
001 100 011 0	-543.217797	15.66	β′	β	2.527	54.1	56.9	2.4	0.2536
001 100 011 0	-543.217797	15.66	δ″	γ	2.682	45.3	48.4	2.5	0.2536
001 100 011 0	-543.217797	15.66	δ″	β	3.241	24.1	13.3	-52.2	0.2536
001 100 011 0	-543.217797	15.66	γ	β	1.352	56.0	55.0	0.3	0.2536
001 100 100 1	-543.208991	38.78	β	δ′	3.268	16.9	26.1	13.7	0.3588
001 100 100 1	-543.208991	38.78	β	δ″	3.268	17.1	26.2	-14.0	0.3588
001 100 100 1	-543.208991	38.78	β	α	1.535	61.0	67.2	0.1	0.3588
001 100 100 1	-543.208991	38.78	δ′	δ″	1.541	61.3	61.3	0.1	0.3588
001 100 100 1	-543.208991	38.78	δ′	α	3.145	15.3	19.2	25.5	0.3588
001 100 100 1	-543.208991	38.78	δ″	α	3.145	15.3	19.2	-25.7	0.3588
001 100 101 0	-543.216676	18.60	β	δ″	3.247	14.5	25.9	25.3	0.1146
001 100 101 0	-543.216676	18.60	β	δ	3.231	15.9	26.3	-26.4	0.1146
001 100 101 0	-543.216676	18.60	β	β	2.507	53.4	53.4	0.2	0.1146
001 100 101 0	-543.216676	18.60	δ′	δ	1.541	61.2	61.6	-0.2	0.1146
001 100 101 0	-543.216676	18.60	δ′	β	3.228	19.8	15.4	-25.9	0.1146
001 100 101 0	-543.216676	18.60	δ″	β	2.551	44.4	31.5	-4.3	0.1146
001 100 110 0	-543.211294	32.73	β	δ″	3.247	15.4	26.8	-26.1	0.4697
001 100 110 0	-543.211294	32.73	β	δ′	3.263	14.9	27.4	33.7	0.4697

001 100 110 0	-543.211294	32.73	β	γ′	3.172	33.3	26.2	19.0	0.4697
001 100 110 0	-543.211294	32.73	δ′′	δ′	1.551	61.2	63.4	-2.7	0.4697
001 100 110 0	-543.211294	32.73	δ′′	γ′	2.646	40.2	42.6	4.4	0.4697
001 100 110 0	-543.211294	32.73	δ′	γ′	1.497	65.6	62.8	7.2	0.4697
001 101 010 0	-543.222754	2.64	β′	δ	3.218	15.6	23.7	35.6	0.1343
001 101 010 0	-543.222754	2.64	β′	β	2.499	53.8	54.3	0.3	0.1343
001 101 010 0	-543.222754	2.64	β′	γ′′	3.145	33.8	26.6	-30.6	0.1343
001 101 010 0	-543.222754	2.64	δ	β	2.536	41.7	30.9	-0.9	0.1343
001 101 010 0	-543.222754	2.64	δ	γ′′	2.656	44.7	44.4	0.5	0.1343
001 101 010 0	-543.222754	2.64	β	γ′′	3.129	33.7	26.4	30.2	0.1343
001 101 100 0	-543.216628	18.73	β′	δ	3.231	15.9	26.3	-26.5	0.1159
001 101 100 0	-543.216628	18.73	β′	β	2.508	53.5	53.4	0.2	0.1159
001 101 100 0	-543.216628	18.73	β′	δ′′	3.248	14.5	25.8	25.6	0.1159
001 101 100 0	-543.216628	18.73	δ	β	2.551	44.5	31.5	-4.4	0.1159
001 101 100 0	-543.216628	18.73	δ	δ′′	1.541	61.6	61.3	-0.1	0.1159
001 101 100 0	-543.216628	18.73	β	δ′′	3.229	15.4	19.9	-26.0	0.1159
001 110 010 0	-543.21860	13.55	β	δ′	3.246	15.0	24.2	43.8	0.5507
001 110 010 0	-543.21860	13.55	β	γ′	3.150	34.3	28.7	23.5	0.5507
001 110 010 0	-543.21860	13.55	β	γ′′	3.144	34.4	26.4	-30.7	0.5507
001 110 010 0	-543.21860	13.55	δ′	γ′	1.492	63.8	62.8	-0.1	0.5507
001 110 010 0	-543.21860	13.55	δ′	γ′′	2.674	46.5	45.3	-3.8	0.5507
001 110 010 0	-543.21860	13.55	γ′	γ′′	3.157	31.6	33.6	6.8	0.5507
001 110 100 0	-543.211265	32.81	β	δ′	3.263	14.8	27.5	33.4	0.4679
001 110 100 0	-543.211265	32.81	β	γ′	3.175	33.1	25.7	18.7	0.4679
001 110 100 0	-543.211265	32.81	β	δ′′	3.248	15.6	26.9	-26.2	0.4679
001 110 100 0	-543.211265	32.81	δ′	γ′	1.497	65.6	62.8	7.8	0.4679
001 110 100 0	-543.211265	32.81	δ′	δ′′	1.551	63.3	61.1	-2.8	0.4679
001 110 100 0	-543.211265	32.81	γ′	δ′′	2.644	42.9	40.2	4.9	0.4679
010 010 010 1	-543.219091	12.26	γ′	γ′	3.152	33.1	33.1	-0.1	1.0082
010 010 010 1	-543.219091	12.26	γ′′	γ	3.152	33.0	33.1	-0.1	1.0082
010 010 010 1	-543.219091	12.26	γ′′	α	2.547	29.8	45.7	0.1	1.0082
010 010 010 1	-543.219091	12.26	γ′′	γ	3.152	33.1	33.0	0.0	1.0082
010 010 010 1	-543.219091	12.26	γ′	α	2.546	29.8	45.6	0.1	1.0082
010 010 010 1	-543.219091	12.26	γ′	α	2.546	29.8	45.6	0.0	1.0082
010 010 011 0	-543.218926	12.69	γ′′	γ′	3.167	33.6	33.4	-0.1	0.6330
010 010 011 0	-543.218926	12.69	γ′′	γ	3.182	32.5	34.7	7.0	0.6330
010 010 011 0	-543.218926	12.69	γ′′	β	3.158	26.4	36.7	-36.4	0.6330
010 010 011 0	-543.218926	12.69	γ′	γ	3.180	32.8	35.0	-6.9	0.6330
010 010 011 0	-543.218926	12.69	γ	β	3.159	26.5	36.4	36.9	0.6330
010 010 011 0	-543.218926	12.69	γ	β	1.351	55.8	55.0	-0.3	0.6330
010 010 100 1	-543.217194	17.24	γ	γ′	3.158	32.4	32.5	0.3	0.8848
010 010 100 1	-543.217194	17.24	γ	δ′′	2.658	45.1	44.7	0.0	0.8848
010 010 100 1	-543.217194	17.24	γ	α	2.547	30.0	45.4	-0.6	0.8848
010 010 100 1	-543.217194	17.24	γ′	δ′′	2.659	44.9	44.6	0.1	0.8848
010 010 100 1	-543.217194	17.24	γ′	α	2.547	30.1	45.5	0.2	0.8848
010 010 100 1	-543.217194	17.24	δ′′	α	3.099	11.9	16.7	0.4	0.8848
010 010 101 0	-543.221662	5.51	γ′′	γ′	3.170	32.8	32.6	-0.2	0.4925
010 010 101 0	-543.221662	5.51	γ′′	δ	2.657	44.6	44.8	-0.6	0.4925
010 010 101 0	-543.221662	5.51	γ′′	β	3.123	26.7	34.5	-30.3	0.4925
010 010 101 0	-543.221662	5.51	γ′	δ	2.656	44.7	45.0	0.5	0.4925
010 010 101 0	-543.221662	5.51	γ′	β	3.122	26.9	34.8	30.3	0.4925
010 010 101 0	-543.221662	5.51	δ	β	2.535	41.7	30.8	0.2	0.4925

010 010 110 0	-543.217491	16.46	γ″	γ′	3.178	32.2	32.6	-0.2	0.9150
010 010 110 0	-543.217491	16.46	γ″	δ	2.674	45.5	46.5	-4.2	0.9150
010 010 110 0	-543.217491	16.46	γ″	γ	3.153	34.3	32.3	6.8	0.9150
010 010 110 0	-543.217491	16.46	γ′	δ	2.674	45.4	46.7	3.6	0.9150
010 010 110 0	-543.217491	16.46	γ′	γ	3.158	33.8	31.7	-6.9	0.9150
010 010 110 0	-543.217491	16.46	δ	γ	1.493	63.9	62.8	0.4	0.9150
010 011 100 0	-543.216860	18.12	γ′	γ	3.189	32.0	34.1	7.0	0.5222
010 011 100 0	-543.216860	18.12	γ′	β	3.165	25.8	36.0	-36.8	0.5222
010 011 100 0	-543.216860	18.12	γ′	δ″	2.665	45.1	44.8	-1.3	0.5222
010 011 100 0	-543.216860	18.12	γ	β	1.352	55.9	55.0	0.0	0.5222
010 011 100 0	-543.216860	18.12	γ	δ″	2.680	48.7	45.4	-2.0	0.5222
010 011 100 0	-543.216860	18.12	β	δ″	3.236	14.3	24.2	52.7	0.5222
010 100 011 0	-543.216835	18.18	γ′	δ″	2.665	45.0	44.8	-1.5	0.5229
010 100 011 0	-543.216835	18.18	γ′	γ	3.188	31.9	34.1	7.2	0.5229
010 100 011 0	-543.216835	18.18	γ′	β	3.163	25.9	36.4	-36.0	0.5229
010 100 011 0	-543.216835	18.18	δ″	γ	2.681	45.4	48.7	-2.1	0.5229
010 100 011 0	-543.216835	18.18	δ″	β	3.240	24.2	13.8	52.5	0.5229
010 100 011 0	-543.216835	18.18	γ	β	1.352	55.9	55.0	-0.4	0.5229
010 100 100 1	-543.211495	32.20	γ	δ′	2.662	45.4	45.4	5.8	0.8106
010 100 100 1	-543.211495	32.20	γ	δ″	2.663	45.0	45.6	-6.9	0.8106
010 100 100 1	-543.211495	32.20	γ	α	2.546	30.2	45.2	0.9	0.8106
010 100 100 1	-543.211495	32.20	δ′	δ″	1.544	61.4	61.4	-0.2	0.8106
010 100 100 1	-543.211495	32.20	δ′	α	3.122	15.2	16.5	-11.6	0.8106
010 100 100 1	-543.211495	32.20	δ″	α	3.121	15.2	16.6	12.2	0.8106
010 100 101 0	-543.215660	21.27	γ′	δ″	2.669	45.3	45.7	5.9	0.4270
010 100 101 0	-543.215660	21.27	γ′	δ	2.662	44.9	45.8	-6.8	0.4270
010 100 101 0	-543.215660	21.27	γ′	β	3.130	26.1	33.6	-30.0	0.4270
010 100 101 0	-543.215660	21.27	δ″	δ	1.543	61.1	61.6	0.0	0.4270
010 100 101 0	-543.215660	21.27	δ″	β	3.226	20.0	16.0	26.7	0.4270
010 100 101 0	-543.215660	21.27	δ	β	2.550	44.4	31.4	5.4	0.4270
010 100 110 0	-543.210233	35.52	γ′	δ″	2.671	45.6	46.3	-7.3	0.8431
010 100 110 0	-543.210233	35.52	γ′	δ	2.682	45.6	48.1	3.2	0.8431
010 100 110 0	-543.210233	35.52	γ′	γ	3.182	32.4	28.1	7.3	0.8431
010 100 110 0	-543.210233	35.52	δ″	δ	1.552	61.1	63.4	2.5	0.8431
010 100 110 0	-543.210233	35.52	δ″	γ	2.646	40.2	42.8	-4.7	0.8431
010 100 110 0	-543.210233	35.52	δ	γ	1.497	65.7	62.8	-7.3	0.8431
010 101 100 0	-543.215670	21.24	γ′	δ	2.662	44.9	45.8	-6.9	0.4272
010 101 100 0	-543.215670	21.24	γ′	β	3.132	26.0	33.5	-30.3	0.4272
010 101 100 0	-543.215670	21.24	γ′	δ″	2.669	45.3	45.6	5.8	0.4272
010 101 100 0	-543.215670	21.24	δ	β	2.550	44.5	31.3	5.6	0.4272
010 101 100 0	-543.215670	21.24	δ	δ″	1.543	61.6	61.2	0.0	0.4272
010 101 100 0	-543.215670	21.24	β	δ″	3.225	16.2	20.1	27.0	0.4272
010 110 100 0	-543.210282	35.39	γ′	δ	2.682	45.8	48.2	-3.1	0.8410
010 110 100 0	-543.210282	35.39	γ′	γ	3.180	32.7	28.2	-7.4	0.8410
010 110 100 0	-543.210282	35.39	γ′	δ″	2.672	45.5	46.2	7.7	0.8410
010 110 100 0	-543.210282	35.39	δ	γ	1.497	65.8	62.8	7.4	0.8410
010 110 100 0	-543.210282	35.39	δ	δ″	1.552	63.3	61.1	-2.6	0.8410
010 110 100 0	-543.210282	35.39	γ	δ″	2.645	42.7	40.2	4.6	0.8410
011 100 100 0	-543.210698	34.30	γ	β	1.351	56.1	54.9	0.3	0.4735
011 100 100 0	-543.210698	34.30	γ	δ′	2.686	48.9	46.3	8.3	0.4735
011 100 100 0	-543.210698	34.30	γ	δ″	2.686	48.8	46.3	-8.8	0.4735
011 100 100 0	-543.210698	34.30	β	δ′	3.252	13.8	26.9	-43.0	0.4735

011 100 100 0	-543.210698	34.30	β	δ″	3.251	14.1	26.9	43.2	0.4735
011 100 100 0	-543.210698	34.30	δ′	δ″	1.548	61.4	61.4	0.0	0.4735
100 100 100 1	-543.202482	55.87	δ″	δ′	1.541	60.8	61.0	0.2	0.7129
100 100 100 1	-543.202482	55.87	δ″	δ	1.541	61.0	61.0	0.0	0.7129
100 100 100 1	-543.202482	55.87	δ″	α	3.147	17.8	16.5	-0.5	0.7129
100 100 100 1	-543.202482	55.87	δ′	δ	1.541	60.9	60.9	0.0	0.7129
100 100 100 1	-543.202482	55.87	δ′	α	3.148	17.7	16.4	0.0	0.7129
100 100 100 1	-543.202482	55.87	δ′	α	3.147	17.8	16.4	0.2	0.7129
100 100 101 0	-543.206421	45.52	δ″	δ′	1.543	61.0	61.0	0.0	0.3467
100 100 101 0	-543.206421	45.52	δ″	δ	1.540	60.8	61.2	0.1	0.3467
100 100 101 0	-543.206421	45.52	δ″	β	3.239	22.9	15.8	16.6	0.3467
100 100 101 0	-543.206421	45.52	δ′	δ	1.540	60.7	61.1	0.0	0.3467
100 100 101 0	-543.206421	45.52	δ′	β	3.239	22.9	15.6	-16.0	0.3467
100 100 101 0	-543.206421	45.52	δ	β	2.565	46.9	31.9	0.2	0.3467
100 100 110 0	-543.199442	63.85	δ″	δ′	1.540	60.7	60.7	-0.1	0.7632
100 100 110 0	-543.199442	63.85	δ″	δ	1.547	61.0	63.5	-2.4	0.7632
100 100 110 0	-543.199442	63.85	δ″	γ	2.657	41.2	40.6	-4.9	0.7632
100 100 110 0	-543.199442	63.85	δ′	δ	1.548	60.9	63.4	2.4	0.7632
100 100 110 0	-543.199442	63.85	δ′	γ	2.657	41.1	40.6	4.7	0.7632
100 100 110 0	-543.199442	63.85	δ	γ	1.504	67.5	62.6	-0.1	0.7632

2.5 References

1 W. von E. Doering and W. R. Roth, *Tetrahedron*, 1963, **19**, 715–737.

2 M. He and J. W. Bode, *Org. Biomol. Chem.*, 2013, **11**, 1306–1317.

3 R. S. Cahn, C. Ingold and V. Prelog, *Angew. Chem. Int. Ed. Engl.*, 1966, **5**, 385–415.

4 O. Yahiaoui, L. F. Pašteka, B. Judeel and T. Fallon, *Angew. Chem. Int. Ed.*, 2018, **57**, 2570–2574.

5 B. M. Gimarc and A. R. Brant, *J. Chem. Inf. Comput. Sci*, 1994, **34**, 1167–1173.

6 O. Yahiaoui, L. F. Pašteka, C. J. Blake, C. G. Newton and T. Fallon, *Org. Lett.*, 2019, **21**, 9574–9578.

7 F. Lovering, J. Bikker and C. Humblet, *J. Med. Chem.*, 2009, **52**, 6752–6756.

8 (a) N. C. Firth, N. Brown and J. Blagg, *J. Chem. Inf. Model.*, 2012, **52**, 2516–2525; (b) J. K. G. Sadowski and J. Gasteiger, *J. Chem. Inf. Comput. Sci,* 1994, **34**, 1000–1008.

9 J. A. Grant, M. A. Gallardo and B. T. Pickup, *J. Comput. Chem.*, 1996, **17**, 1653–1666.

10 J. Timmermans, *Nature. 1954,* **174**, 235–235.

11 A. Y. Meyer, *J. Comput. Chem.*, 1986, **7**, 144–152.

12 W. H. B. Sauer and M. K. Schwarz, *J. Chem. Inf. Comput. Sci.*, 2003, **43**, 987–1003.

13 G. Lauri and P. A. Bartlett, *CAVEAT: A program to facilitate the design of organic molecules*, 1994, Vol. 8.

14 O. O. Grygorenko, R. Prytulyak, D. M. Volochnyuk, V. Kudrya, O. V. Khavryuchenko and I. V. Komarov, *Mol. Divers.*, 2012, **16**, 477–487.

15 O. O. Grygorenko, P. Babenko, D. M. Volochnyuk, O. Raievskyi and I. V. Komarov, *RSC. Adv.*, 2016, **6**, 17595–17605.

16 O. O. Grygorenko, D. Demenko, D. M. Volochnyuk Ac and I. V Komarov, *New. J. Chem.*, 2018, **42**, 8355.

17 O. O. Grygorenko, D. M. Volochnyuk, S. V. Ryabukhin and D. B. Judd, *Chem. Eur. J.*, 2020, **26**, 1196–1237.

18 P. K. Mykhailiuk, *Org. Biomol. Chem.*, 2019, **17**, 2839–2849.

19 E. G. Tse, S. D. Houston, C. M. Williams, G. Paul Savage, L. M. Rendina, I. Hallyburton, M. Anderson, R. Sharma, G. S. Walker, R. Scott Obach and M. H. Todd, *J. Med. Chem.*, 2020, **63**, 11585–11601.

20 M. A. M. Subbaiah and N. A. Meanwell, *J. Med. Chem.*, 2021, **64**, 14046–14128.

21 M. P. Wiesenfeldt, J. A. Rossi-Ashton, I. B. Perry, J. Diesel, O. L. Garry, F. Bartels, S. C. Coote, X. Ma, C. S. Yeung, D. J. Bennett and D. W. C. MacMillan, *Nature*, 2023, **618**, 513–518.

22 R. C. Epplin, S. Paul, L. Herter, C. Salome, E. N. Hancock, J. F. Larrow, E. W. Baum, D. R. Dunstan, C. Ginsburg-Moraff, T. C. Fessard and M. K. Brown, *Nat. Commun.,* 2022, **13**, 1–5.

23 A. A. Kirichok, H. Tkachuk, Y. Kozyriev, O. Shablykin, O. Datsenko, D. Granat, T. Yegorova, Y. P. Bas, V. Semirenko, I. Pishel, V. Kubyshkin, D. Lesyk, O. Klymenko-Ulianov and P. K. Mykhailiuk, *Angew. Chem. Int. Ed.*, 2023, **62**, e202311583.

24 J. F. Teichert, D. Mazunin and J. W. Bode, *J. Am. Chem. Soc.*, 2013, **135**, 11314–11321.

25 J. Font, F. López and F. Serratosa, *Tetrahedron Lett.*, 1972, **13**, 2589–2590.

26 C. Hoogzand, J. Nielsen and J. F. M. Oth, *Tetrahedron Lett.*, 1970, **11**, 2287–2292.

27 W. K. Sarma and W. and G. Schröder, *Chem. Ber.*, 1986, **119**, 2339.

28 H. R. and G. S. J. F. M. Oth, E. Machens, *Justus. Liebigs. Ann. Chem.*, 1971, **745**, 112.

29 L. A. Paquette, J. R. Malpass, G. R. Krow and T. J. Barton, *J. Am. Chem. Soc.*, 1969, **91**, 5296–5306.

30 O. Yahiaoui, L. F. Pašteka, B. Judeel and T. Fallon, *Angew. Chem. Int. Ed.*, 2018, **57**, 2570–2574.

31 H. D. Patel, T. H. Tran, C. J. Sumby, L. F. Pašteka and T. Fallon, *J. Am. Chem. Soc.*, 2020, **142**, 3680–3685.

32 O. Yahiaoui, H. D. Patel, K. S. Chinner, L. F. Pasteka and T. Fallon, *Org. Lett.*, 2021, **23** 1157–1162.

33 S. Ferrer and A. M. Echavarren, *Angew. Chem. Int. Ed.*, 2016, **55**, 11178–11182.

34 A. N. Bismillah, B. M. Chapin, B. A. Hussein and P. R. McGonigal, *Chem. Sci.*, 2020, **11**, 324–332.

35 J. F. Teichert, D. Mazunin and J. W. Bode, *J. Am. Chem. Soc.*, 2013, **135**, 11314–11321.

36 M. N. Pomfret, P. B. Sun, Z. Huang, A. C. Freund, T. Miyoshi and M. R. Golder, *Angew. Chem. Int. Ed.*, 2023, **62**, e202301695.

37 A. Ottonello, J. A. Wyllie, O. Yahiaoui, S. Sun, R. A. Koelln, J. A. Homer, R. M. Johnson, E. Murray, P. Williams, J. R. Bolla, C. V. Robinson, T. Fallon, T. P. Soares da Costa and J. E. Moses, *Proc. Natl. Acad. Sci. U. S. A.*, 2023, **120**, e2208737120.

38 A. Sanchez, A. Gurajapu, W. Guo, W.-Y. Kong, C. J. Laconsay, N. S. Settineri, D. J. Tantillo and T. J. Maimone, *J. Am. Chem. Soc.*, 2023, **145**, 13452–13461.

39 E. P. Gillis, K. J. Eastman, M. D. Hill, D. J. Donnelly and N. A. Meanwell, *J. Med. Chem.*, 2015, **58**, 8315–8359.

40 E. Vitaku, D. T. Smith and J. T. Njardarson, *J. Med. Chem.*, 2014, **57**, 10257–10274.

41 G. Wu, T. Zhao, D. Kang, J. Zhang, Y. Song, V. Namasivayam, J. Kongsted, C. Pannecouque, E. De Clercq, V. Poongavanam, X. Liu and P. Zhan, *J. Med. Chem.*, 2019, **62**, 9375–9414.

42 Z. Zhao, Q. Liu, S. Bliven, L. Xie and P. E. Bourne, *J. Med. Chem.*, 2017, **60**, 2879–2889.

43 R. A. Bauer, *Drug. Discov. Today.*, 2015, **20**, 1061–1073.

44 R. P. Murelli, A. X. Zhang, J. Michel, W. L. Jorgensen and D. A. Spiegel, *J. Am. Chem. Soc.*, 2009, **131**, 17090–17092.

45 E. Comer, J. A. Beaudoin, N. Kato, M. E. Fitzgerald, R. W. Heidebrecht, M. duPont Lee IV, D. Masi, M. Mercier, C. Mulrooney, G. Muncipinto, A. Rowley, K. Crespo-Llado, A. E. Serrano, A. K. Lukens, R. C. Wiegand, D. F. Wirth, M. A. Palmer, M. A. Foley, B. Munoz, C. A. Scherer, J. R. Duvall and S. L. Schreiber, *J. Med. Chem.*, 2014, **57**, 8496–8502.

46 P. Klán, T. Šolomek, C. G. Bochet, A. Blanc, R. Givens, M. Rubina, V. Popik, A. Kostikov and J. Wirz, *Chem. Rev.*, 2012, **113**, 119–191.

47 X. Wang, B. Huang, X. Liu and P. Zhan, *Drug. Discov. Today.*, 2016, **21**, 118–132.

48 C. P. Ramil and Q. Lin, *Chem. Commun.*, 2013, **49**, 11007.

49 N. Nosengo, *Nature*, 2016, **534**, 314–316.

50 T. T. Ashburn and K. B. Thor, *Nat. Rev. Drug. Discov.* 2004, **3**, 673–683.

51 J. Boström, D. G. Brown, R. J. Young and G. M. Keserü, *Nat. Rev. Drug. Discov*., 2018, **17**, 709–727.

52 G. W. Bemis and M. A. Murcko, *J. Med. Chem.*, 1996, **39**, 2887–2893.

53 G. W. Bemis and M. A. Murcko, *J. Med. Chem.*, 1999, **42**, 5095–5099.

54 J. Wang and T. Hou, *J. Chem. Inf. Model.*, 2009, **50**, 55–67.

55 R. D. Taylor, M. MacCoss and A. D. G. Lawson, *J. Med. Chem.*, 2016, **60**, 1638–1647.

56 A. D. Morley, A. Pugliese, K. Birchall, J. Bower, P. Brennan, N. Brown, T. Chapman, M. Drysdale, I. H. Gilbert, S. Hoelder, A. Jordan, S. V. Ley, A. Merritt, D. Miller, M. E. Swarbrick and P. G. Wyatt, *Drug. Discov. Today.*, 2013, **18**, 1221–1227.

57 M. Baker, *Nat. Rev. Drug. Discov.*, 2013, **12**, 5–7.

58 C. W. Murray and D. C. Rees, *Nat. Chem.*, 2009, **1**, 187–192

59 N. Fuller, L. Spadola, S. Cowen, J. Patel, H. Schönherr, Q. Cao, A. McKenzie, F. Edfeldt, A. Rabow and R. Goodnow, *Drug. Discov. Today.*, 2016, **21**, 1272–1283.

60 C. W. Murray and D. C. Rees, *Angew. Chem. Int. Ed.*, 2016, **55**, 488–492.

61 P. Kirsch, A. M. Hartman, A. K. H. Hirsch and M. Empting, *Molecules.*, 2019, **24**, 4309

62 C. R. Rankine, *bullviso*, 2024, https://gitlab.com/conor.rankine/bullviso.

63 RDKit: Open-Source Cheminformatics, https://rdkit.org.

64 RDKit, 2023, https://github.com/rdkit/rdkit.

65 S. Riniker and G. A. Landrum, *J. Chem. Inf. Model.*, 2015, **55**, 2562–2574.

66 S. Wang, J. Witek, G. A. Landrum and S. Riniker, *J. Chem. Inf. Model.*, 2020, **60**, 2044–2058.

67 A. K. Rappe, C. J. Casewit, K. S. Colwell, W. A. Goddard III and W. M. Skiff, *J. Am. Chem. Soc.*, 2002, **114**, 10024–10035.

68 M. J. Frisch, G. W. Trucks, H. B. Schlegel, G. E. Scuseria, M. A. Robb, J. R. Cheeseman, G. Scalmani, V. Barone, G. A. Petersson, H. Nakatsuji, X. Li, M. Caricato, A. V. Marenich, J. Bloino, B. G. Janesko, R. Gomperts, B. Mennucci, H. P. Hratchian, J. V. Ortiz, A. F. Izmaylov, J. L. Sonnenberg, D. Williams-Young, F. Ding, F. Lipparini, F. Egidi, J. Goings, B. Peng, A. Petrone, T. Henderson, D. Ranasinghe, V. G. Zakrzewski, J. Gao, N. Rega, G. Zheng, W. Liang, M. Hada, M. Ehara, K. Toyota, R. Fukuda, J. Hasegawa, M. Ishida, T. Nakajima, Y. Honda, O. Kitao, H. Nakai, T. Vreven, K. Throssell, J. A. Jr. Montgomery, J. E. Peralta, F. Ogliaro, M. J. Bearpark, J. J. Heyd, E. N. Brothers, K. N. Kudin, V. N. Staroverov, T. A. Keith, R. Kobayashi, J. Normand, K. Raghavachari, A. P. Rendell, J. C. Burant, S. S. Iyengar, J. Tomasi, M. Cossi, J. M. Millam, M. Klene, C. Adamo, R. Cammi, J. W. Ochterski, R. L. Martin, K. Morokuma, O. Farkas, J. B. Foresman and D. J. Fox, Gaussian Inc., Wallingford CT, 2016.

69 F. Neese and J. Wiley, *Wiley Interdiscip. Rev. Comput. Mol. Sci.*, 2012, **2**, 73–78.

70 F. Neese, *Wiley Interdiscip. Rev. Comput. Mol. Sci.*, 2018, **8**, e1327.

71 F. Neese, F. Wennmohs, U. Becker and C. Riplinger, *J. Chem. Phys.*, 2020, **152**, 224108.

72 A. W. Hung, A. Ramek, Y. Wang, T. Kaya, J. A. Wilson, P. A. Clemons and D. W. Young, *Proc. Natl. Acad. Sci. U. S. A.*, 2011, **108**, 6799–6804.

73 W. R. J. D. Galloway, A. Isidro-Llobet and D. R. Spring, *Nat. Commun*., 2010, **1**, 1–13.

74 W. H. B. Sauer and M. K. Schwarz, *J. Chem. Inf. Comput. Sci.*, 2003, **43**, 987–1003.

75 B. Over, S. Wetzel, C. Grütter, Y. Nakai, S. Renner, D. Rauh and H. Waldmann, *Nat. Chem.*, 2013, **5**, 21–28.

76 S. P. Jones, J. D. Firth, M. C. Wheldon, M. Atobe, R. E. Hubbard, D. C. Blakemore, C. De Fusco, S. C. C. Lucas, S. D. Roughley, L. R. Vidler, M. A. Whatton, A. J. A. Woolford, G. L. Wrigley and P. O'Brien, *RSC. Med. Chem.*, 2022, **13**, 1614–1620.

77 P. Garner, P. B. Cox, U. Rathnayake, N. Holloran and P. Erdman, *ACS Med. Chem. Lett*, 2019, **10**, 811–815.

78 T. D. Downes, S. P. Jones, H. F. Klein, M. C. Wheldon, M. Atobe, P. S. Bond, J. D. Firth, N. S. Chan, L. Waddelove, R. E. Hubbard, D. C. Blakemore, C. De Fusco, S. D. Roughley, L. R. Vidler, M. A. Whatton, A. J. A. Woolford, G. L. Wrigley and P. O'Brien, *Chem. Eur. J.*, 2020, **26**, 8969–8975.

79 C. Adamo and V. Barone, *J. Chem. Phys.*, 1999, **110**, 6158–6170.

80 J. P. Perdew, K. Burke and M. Ernzerhof, *Phys. Rev. Lett.*, 1996, **77**, 3865.

81 S. Grimme, J. Antony, S. Ehrlich and H. Krieg, *J. Chem. Phys.*, 2010, **132**, 154104.

82 F. Weigend and R. Ahlrichs, *Phys. Chem. Chem. Phys.*, 2005, **7**, 3297–3305.

83 M. R. Berthold, N. Cebron, F. Dill, T. R. Gabriel, T. Kötter, T. Meinl, P. Ohl, C. Sieb, K. Thiel, B. Wiswedel, *KNIME: The Konstanz Information Miner*, Springer, 2007.

84 S. D. Roughley, *Curr. Med. Chem.*, 2018, **27**, 6495–6522.

85 R. D. Taylor, M. MacCoss and A. D. G. Lawson, *J. Med. Chem.*, 2014, **57**, 5845–5859.

86 J. Shearer, J. L. Castro, A. D. G. Lawson, M. MacCoss and R. D. Taylor, *J. Med. Chem.*, 2022, **65**, 8699–8712.

87 B. A. Chalmers, H. Xing, S. Houston, C. Clark, S. Ghassabian, A. Kuo, B. Cao, A. Reitsma, C. E. P. Murray, J. E. Stok, G. M. Boyle, C. J. Pierce, S. W. Littler, D. A. Winkler, P. V. Bernhardt, C. Pasay, J. J. De Voss, J. McCarthy, P. G. Parsons, G. H. Walter, M. T. Smith, H. M. Cooper, S. K. Nilsson, J. Tsanaktsidis, G. P. Savage and C. M. Williams, *Angew. Chem. Int. Ed.*, 2016, **55**, 3580–3585.

88 T. A. Reekie, C. M. Williams, L. M. Rendina and M. Kassiou, *J. Med. Chem.*, 2018, **62**, 1078–1095.

89 K. C. Nicolaou, J. Yin, D. Mandal, R. D. Erande, P. Klahn, M. Jin, M. Aujay, J. Sandoval, J. Gavrilyuk and D. Vourloumis, *J. Am. Chem. Soc.*, 2016, **138**, 1698–1708.

90 L. Wanka, K. Iqbal and P. R. Schreiner, *Chem. Rev.*, 2013, **113**, 3516–3604.

91 S. Ferrer and A. M. Echavarren, *Synthesis*, 2019, **51**, 1037–1048.

92 A. N. Bismillah, J. Sturala, B. M. Chapin, D. S. Yufit, P. Hodgkinson and P. R. McGonigal, *Chem. Sci.*, 2018, **9**, 8631–8636.

93 G. Schröder and W. Witt, *Angew. Chem. Int. Ed. Engl.*, 1979, **18**, 311–312.

94 A. R. Lippert, V. L. Keleshian and J. W. Bode, *Org. Biomol. Chem.* 2009, **7**, 1529–2532.

95 A. R. Lippert, A. Naganawa, V. L. Keleshian and J. W. Bode, *J. Am. Chem. Soc.,* 2010, **132**, 15790–15799.

96 A. P. Birvé, H. D. Patel, J. R. Price, W. M. Bloch and T. Fallon, *Angew. Chem. Int. Ed.,* 2022, **61**, e202115468.

97 C. Dohmen, H. Ihmels and T. Paululat, *Eur. J. Org. Chem*., 2022, e202201172.

98 C. Bannwarth, S. Ehlert and S. Grimme, *J. Chem. Theory. Comput.*, 2019, **15**, 1652–1671.

99 C. Bannwarth, E. Caldeweyher, S. Ehlert, A. Hansen, P. Pracht, J. Seibert, S. Spicher and S. Grimme, *Wiley Interdiscip. Rev. Comput. Mol. Sci.*, 2021, **11**, e1493.

100 F. Weigend, *Phys. Chem. Chem. Phys.*, 2006, **8**, 1057–1065.

CHAPTER 3

ADAPTIVE SHAPESHIFTING LIGANDS FOR BIOMOLECULES

Synopsis

Here, we investigate the shapeshifting properties of barbaralanes and bullvalenes, in order to understand their behaviour in biological environments. We first synthesise a series of hydroxy barbaralanes and hydroxy bullvalenes for use biological studies. As a proof of concept investigation, these compounds are then subjected to co-crystallisation experiments with serum albumins in an attempt to obtain a protein-ligand crystal structure. Isosteric compounds, such as adamantanes, are also screened with serum albumins for comparison purposes. Additionally, the attempted synthesis of water soluble bullvalenes is attempted, in order to aid co-crystallisation experiments with serum albumins. Moreover, a carbohydrate appended bullvalene has been designed and synthesised as a potential active site inhibitor for use in the protein, Lysozyme. The co-crystallisation, enzymatic assay and computational modelling of Lysozyme have been carried out with the carbohydrate-appended bullvalene, as a targeted approach to obtain protein-ligand complexation with a shapeshifting molecule. Insights from these experiments suggest a more methodical 'design to function' approach is required, especially in terms of ligand design, modelling and protein selection in the future.

Acknowledgments

The following people are gratefully acknowledged for their contribution to this chapter: Dr. S. Freitag-Pohl contributed to serum albumin crystallisations and solved all serum albumin X-ray crystal structures; Dr. A. N. Bismillah synthesised the series of barbaralanes and performed the VT NMR; W. Maturi synthesised one hydroxy-containing bullvalene and assigned the VT NMR; L. Corbett carried out all studies on Lysozyme with supervision from Dr. C. H. Hill; J. Fair, Dr. M. A. Fascione and Prof. A. M. Brzozowski provided useful discussions. The research was conceived by Prof. E. Pohl and Prof. P. R. McGonigal.

3.1. Introduction

3.1.1 Molecular Recognition in Biomolecules

In 1987, Pedersen, Lehn and Cram received the Nobel Prize for their development and use of molecules (i.e. crown ethers and cryptands) with structure-specific interactions of high selectivity.[1–4] This gave rise to a more profound focus on chemistry relating to molecular recognition, leading to the field known as supramolecular chemistry, otherwise familiar as the chemistry containing intermolecular (noncovalent) bonds.

Amongst numerous avenues, the concept of molecular recognition has revealed the complexity of the recognition of ligands within biomolecules. For example, well known cases include substrates bound to enzymes in biocatalysis,[5] ligand-activated cell signalling[6] and antibody-antigen recognition.[7] In most known cases, one or more low molecular weight compounds, with complementary specificity, binds to a particular region in a higher molecular weight compound, such as a protein.[8] A common challenge, however, when trying to replicate these recognition processes, is designing bioorthogonal synthetic molecules with superior molecular recognition properties. The impact of bioorthogonal chemistry, independently introduced at the start of the 21st century by Sharpless, Meldal and Bertozzi, is undisputed – progressing the understanding of how living systems function through the development and use of click chemistry.[9–20] The ultimate aim in the field of biorthogonal chemistry has been to accumulate a chemical toolbox to study biomolecules in their native environment, without disrupting the normal chemistry of the cell. This goal, however, is complicated by a number of considerations. Most notably, the time-dependent targeting of specific areas of different cells is a key challenge, in addition to achieving adequate water solubility, whilst conserving solvent dependent molecular recognition.[21]

Accordingly, molecular recognition plays a ubiquitous role in numerous biological processes on the molecular level.[21] There are a number of popular models for protein–ligand binding; namely the lock and key model,[22] the induced-fit model[23,24] and the conformational selection mechanism.[25] Over one hundred years ago, Fischer published

an article entitled the 'effect of configuration on the activity of enzymes'. Fischer's pioneering theory proposed two assertions for the specificity of enzymes: 1) biology at the molecular level becomes chemistry and 2) the substances of life fit together like lock and key. The 'lock and key' model, now a central concept in enzyme chemistry, details that a specified action can be activated *via* the insertion of a substrate (the key) into the active site of an enzyme (the lock) (Figure 3.1). The foundation of the lock and key model requires the enzyme and substrate to possess complementary geometry so that the substrate and binding site match exactly. Hence, any molecular interaction requires no significant conformational change in either molecule.

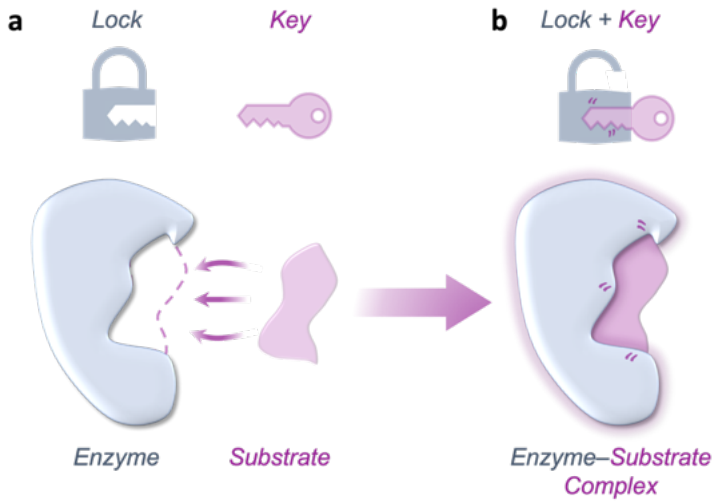

Figure 3.1. Depiction of the lock and key model of enzyme action.[22] The enzyme (grey) is shown with its complementary substrate (magenta) in (**a**) the unbound state and (**b**) the bound state as an enzyme-substrate complex. The lock and key provides a cartoon representation of this model and mechanism of action.

Building upon the lock and key model, Koshland introduced the mutual induced fit model, whereby the ligand first binds to a protein in its unbound conformation, which subsequently induces the protein to transition to the bound state. The mutual induced fit model conceptualises the fact that the enzyme and substrate can undergo conformational changes upon an interaction, in order to induce optimal geometric complementarity. Resultantly, this model is analogous to a handshake, whereby both hands adjust to fit together (Figure 3.2).

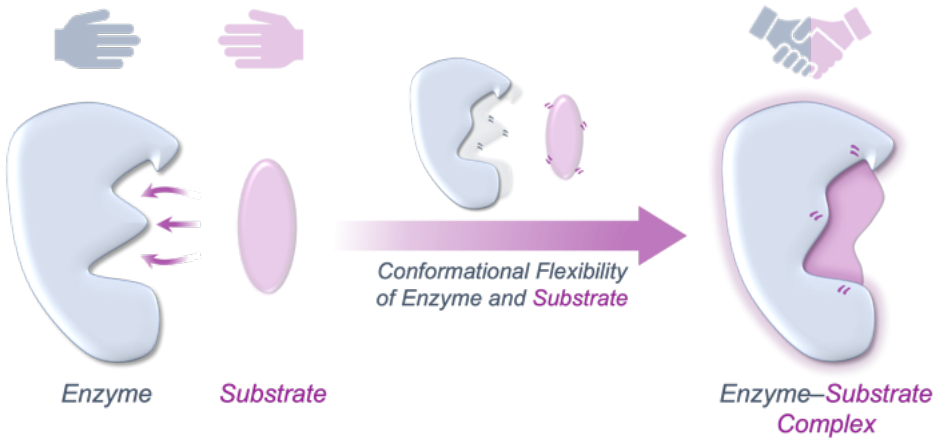

Figure 3.2. Depiction of the mutual induced fit model of enzyme action.[23] The flexible enzyme (grey) is shown with its substrate (magenta). The flexibility of the enzyme and substrate permits conformational changes, allowing for the substrate to bind, to produce an enzyme-substrate complex. The handshake provides a cartoon representation of this mechanism of action.

Furthermore, in 1965, an alternative method for ligand binding was proposed by Monod, Wyman and Changeux, who described the conformational selection model.[25–27] This method describes how a host molecule (such as an enzyme) can adopt several discrete conformations that are in equilibrium with one another in its unbound state. Based upon this conformational equilibrium of the host, the ligand can then bind selectively to the most complementary pre-existing conformer (without itself undergoing any conformational change), to form a host-guest complex (Figure 3.3).

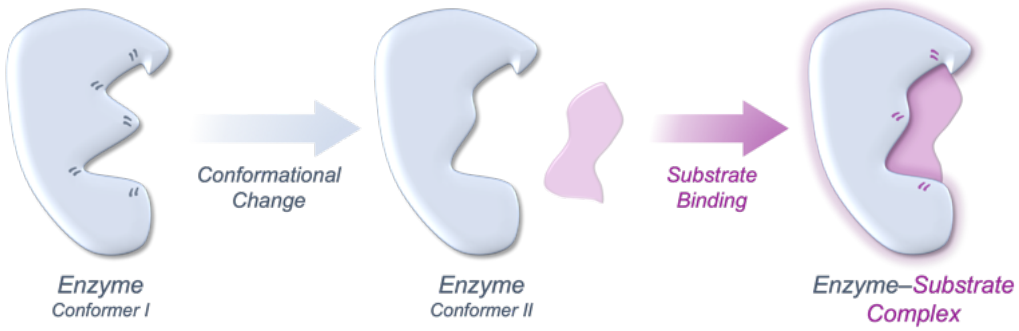

Figure 3.3. Depiction of the conformational selection model.[25,26] The depiction of enzyme conformer I (grey) is shown. A conformational change of enzyme conformer I allows for the change to enzyme conformer II. The flexibility of the enzyme permits conformational changes, allowing for the substrate (magenta) to bind, producing an enzyme-substrate complex.

The premise from the aforementioned models has led to intermolecular dynamic covalent chemistry being used to discover unexplored binding modes. For example, a

dynamic combinatorial chemistry approach has been shown to allow for the reversible chemical exchange of building blocks, to generate a library of compounds encompassing all chemical combinations under thermodynamic control.[28,29] As such, the addition of a molecular host to a dynamic combinatorial library provides the means to select a covalent structure (from a dynamic library) that forms the best-binding constituent for a given host target receptor (Figure 3.4).[30] In principle, this method aims to significantly accelerate the identification of compounds required to bind with host molecules (even provided this method is highly concentration dependent), and has found particular use in drug discovery.[30–33]

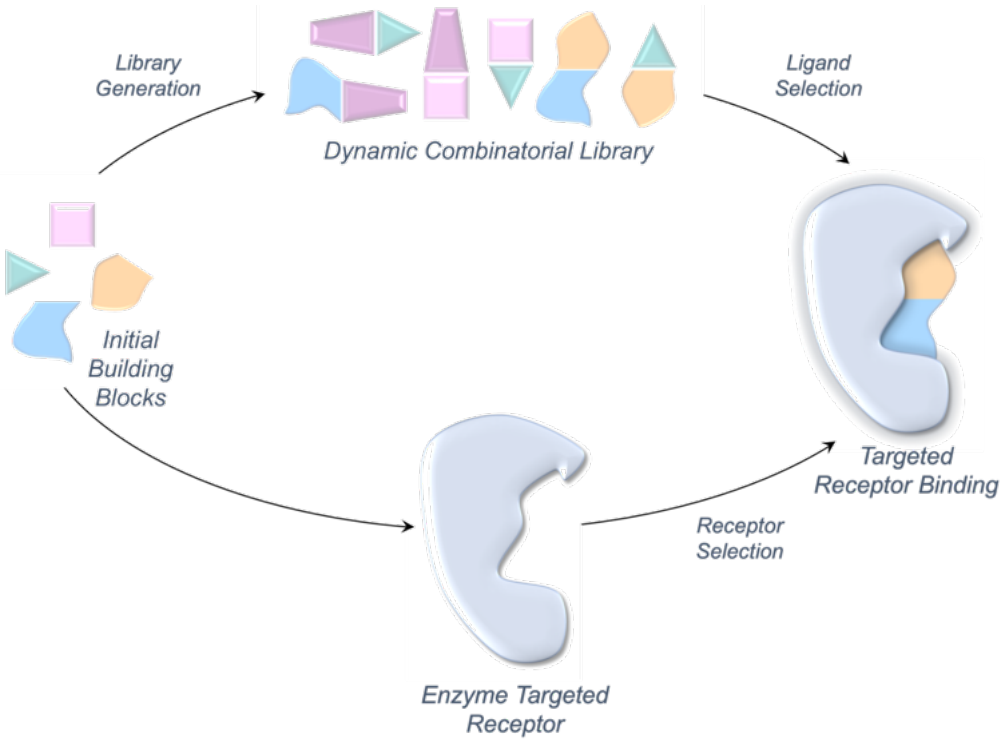

Figure 3.4. Depiction of the conformational selection model. The initial building blocks (coloured shapes) that can form a dynamic combinatorial library *via* covalent chemistry are shown. The addition of the host enzyme (grey) provides the means of ligand selection, to provide targeted receptor binding. Figure adapted from previously reported results.[30]

3.1.2 Principles of Macromolecular Protein Crystallisation

Determining the structure of a macromolecule is fundamental when understanding its structure-function relationship. The crystallisation of such macromolecules, including large biomolecules (such as proteins), is highly dependent on the formation of a supersaturated solution that is not significantly detrimental to the species being crystallised (i.e. denaturation). Achieving crystals that are suitable for structure determination by X-ray crystallography is often referred to as the limiting step.[34] Supersaturation is commonly achieved *via* the addition of salts and polymers, as well as through variation of physical parameters such as pH and temperature. Living systems are almost exclusively dependent on aqueous chemistry to function properly within a narrow pH and temperature range.[35] Consequently, the evolution of such biomacromolecular species has resulted in poor tolerance to significant deviations from native conditions. Therefore, it is paramount that crystals are grown from an aqueous solution (referred to as the mother liquor), which the species can tolerate and is stable. There are several key practical differences between conventional crystallisation of low molecular mass compounds and biomacromolecular structures.[35] As such, Figure 3.5 shows the simplest outline of a protein solubility phase diagram, by which saturation levels are exemplified relative to two parameters that can alter solubility: 1) the protein concentration and 2) the concentration of the precipitating agent. The successful crystallisation of a macromolecule unequivocally requires the creation of supersaturation. Hence, to produce a supersaturated solution, the properties of an undersaturated solution must be modified in order to reduce the solubility of the macromolecule, thus achieving a supersaturated solution. This is typically achieved by alternating the aforementioned parameters to find ideal crystallisation conditions.

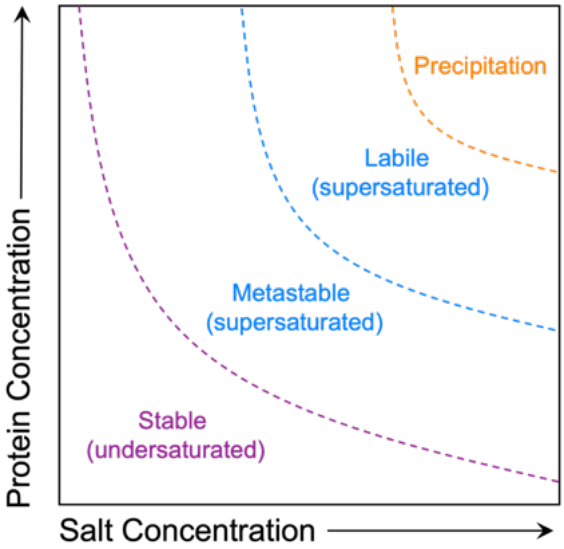

Figure 3.5 Two-dimensional phase diagram idealising the solubility of small globular proteins.[34] The diagram is divided into regions of undersaturation and supersaturation divided by a line (purple dashed line) representing the maximum solubility at a specified precipitant (salt) concentration. The supersaturated region is sub-divided into the metastable and labile regions (blue dashed line). The metastable region signifies when nuclei will develop into crystals with the absence of nucleation. In the labile region, nucleation is expected to also occur. The precipitation region (orange dashed line) denotes very high supersaturation, whereby a successful crystallisation result is most likely.

Furthermore, there are several methods which increase the likelihood of saturation in a crystallisation experiment. The vapour diffusion by the sitting-drop method is the most widely used, owing to its simplicity and ability to test different parameters quickly.[34] The sitting drop method requires the sample and reservoir solution to be mixed together, whereby a drop of the sample and reservoir solution are placed on the seat (Figure 3.6).[34] The aforementioned set-up is then sealed air-tight, allowing equilibration to commence between the reservoir solution and sample-containing drop. As a result of the reservoir solute concentration being in excess, in comparison to the sitting drop, water diffuses from the sample drop to the reservoir through the vapour phase, allowing for natural equilibration of solute concentrations.[34] Subsequently, the size of the sample drop reduces, resulting in an increase in the concentration of the drop components, which results in crystalline material. In theory, this process moves through each boundary of the phase diagram (Figure 3.5) before yielding the desired crystal.

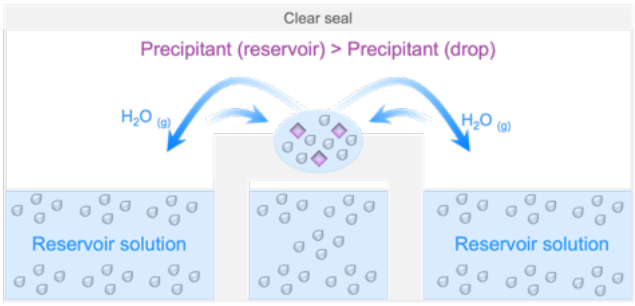

Figure 3.6 Schematic representation of a sitting-drop vapour-diffusion experiment.[35] The precipitant in the drop and crystallisation conditions is represented by the blue circle and the macromolecular sample present in the drop is depicted by the purple diamonds.

3.1.3 Serum Albumins: Structure and Ligand Binding

Serum albumins (SAs) are relatively large biomolecules (66 kDa) and are the most abundant globular plasma protein found in the blood plasma of all vertebrates.[36] For example, the Bovine Serum Albumin (**BSA**) monomer is composed of 583 amino acids, and is composed of three similar helical domains (I, II and III) arranged in a heart-shaped tertiary architecture (Figure 3.7), which is 74% α-helical in nature.[37] Each of these three domains can be further divided into two subdomains (A and B).

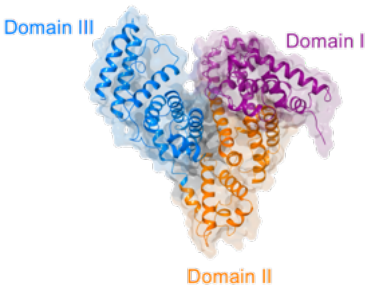

Figure 3.7. Domain assignment of **BSA** molecular structure, where each domain (I/II/III) is represented in magenta, orange and blue, respectively.[37]

Moreover, the structural similarity of **BSA** to Human Serum Albumin (**HSA**) is 75.6%, as portrayed through comparisons of the conservation of the residual molecular surfaces of **BSA** and **HSA** in Figure 3.8.[37]

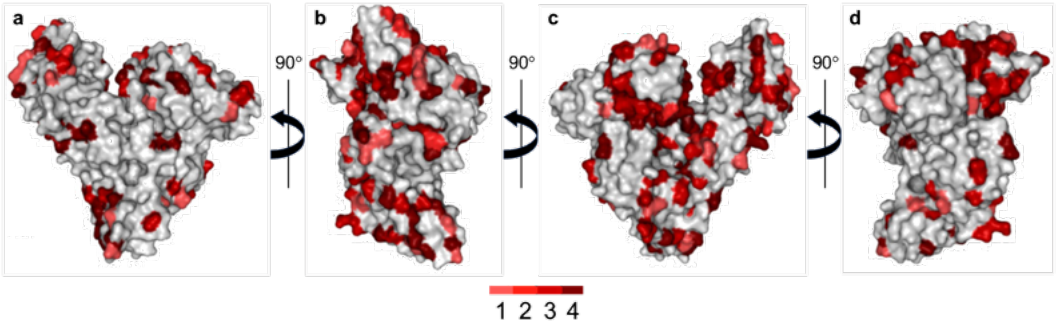

Figure 3.8. **BSA** molecular surface from the (**a**) front view, (**b**) side view, (**c**) back view and (**d**) side view showing residue conservation compared with **HSA**, according to the conservation of that residue in **HSA** of a known sequence in the same or similar order. The scale indicates the number of other SAs in which the marked residue is conserved in **BSA**.[37]

Furthermore, SAs are a natural carrier of hydrophobic molecules in mammalian blood, exhibited by the wide range of compounds studied in SAs including fatty acids, hormones, drug molecules and metal ions (Figure 3.9).[38] Physiologically, it is a major protein responsible for regulating osmotic pressure of the blood and binding the breakdown product of haem, namely bilirubin.[39]

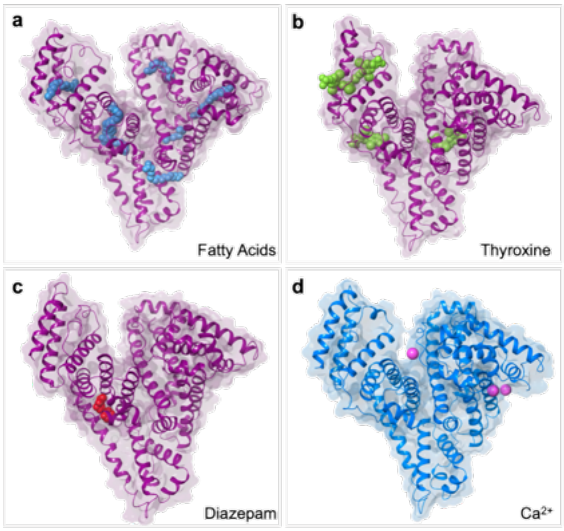

Figure 3.9. Structures of serum albumin (SA) binding in many separate binding sites. The are seven separate binding sites for (**a**) Fatty acids (blue) with **HSA** (PDB: 1e7i)[40] and several binding sites for (**b**) Thyroxine (green) with **HSA** (PDB: 1hk1).[41] Drug compounds are, more often than not, designed with greater specificity thus binding in a single site as seen (**c**) Diazepam (red) with **HSA** (PDB: 2bxf).[42] Metal ion binding is also possible as shown in (**d**) Ca^{2+} (pink) which binds to three locations in **BSA** (PDB: 3V03).[37]

Unlike many other proteins, SAs have robust stability over a wide pH (5-9) and they are structurally stable for up to 10 hours at 60 °C, where this temperature would usually be considered as elevated.[43] This aforementioned structural stability is complemented by SA's excellent solubility in aqueous solution. These properties, along with the preferential uptake in tumour tissue, biodegradability and lack of toxicity make it suitable as a transport vessel in biodistribution and drug delivery.[43] Evidently, the literature precedent for SA-ligand binding makes SAs a suitable choice for co-crystallisation experiments, in order to investigate protein–ligand binding.

3.1.4 Lysozyme: Structure and Mechanism

Lysozyme is an enzyme which catalyses the breakdown of the polysaccharide peptidoglycan, a major component of the gram-positive bacterial cell wall.[44,45] Mechanistically, this bacterial breakdown involves the hydrolysis of the *β*-1,4-glycosidic bond between two amino sugars: *N*-acetylmuramic acid (MurNAc) and *N*-acetylglucosamine (GlcNAc) in the polysaccharide backbone.[46,47] This breakdown results in penetration of the bacterial cell wall and subsequent bacteria lysis.

Owing to the important biological processes of Lysozyme, its structure has been extensively characterised through a combination of kinetic studies, X-ray crystallography and nuclear magnetic resonance spectroscopy. The first Lysozyme structure was elucidated in 1967, and therefore is one of the first protein structures to be solved – notably the first structure of any enzyme.[48,49] The Lysozyme architecture is ellipsoidal in shape, with a large cleft on one side which forms the active site. Its structure consists of 129 amino acids, which form 5 *α*-helices, 3 anti-parallel *β*-sheets – it therefore belongs to the *α*+*β* class of proteins, where *α*-helices and *β*-sheets occur separately along the backbone. Lysozyme contains 11 anionic residues and 19 cationic residues.[50] As such, in aqueous solution at pH 7.4, it is positively charged. Some residues are further stabilised by cross-linking between the thiol group, present in corresponding cysteine (C) residues, to form disulfide bridges in four different locations: C6–C127, C30–C115, C64–C80, C76–C94. These disulfide bridges contribute highly to the stability of the Lysozyme secondary and tertiary structure (Figure

3.10a).[51,52] The Lysozyme protein structure also contains many solvent channels per unit cell, where the active site is exposed to the solvent channels (Figure 3.10b).[53] This makes Lysozyme a suitable choice for crystal soaking experiments, in order to investigate protein–ligand binding.

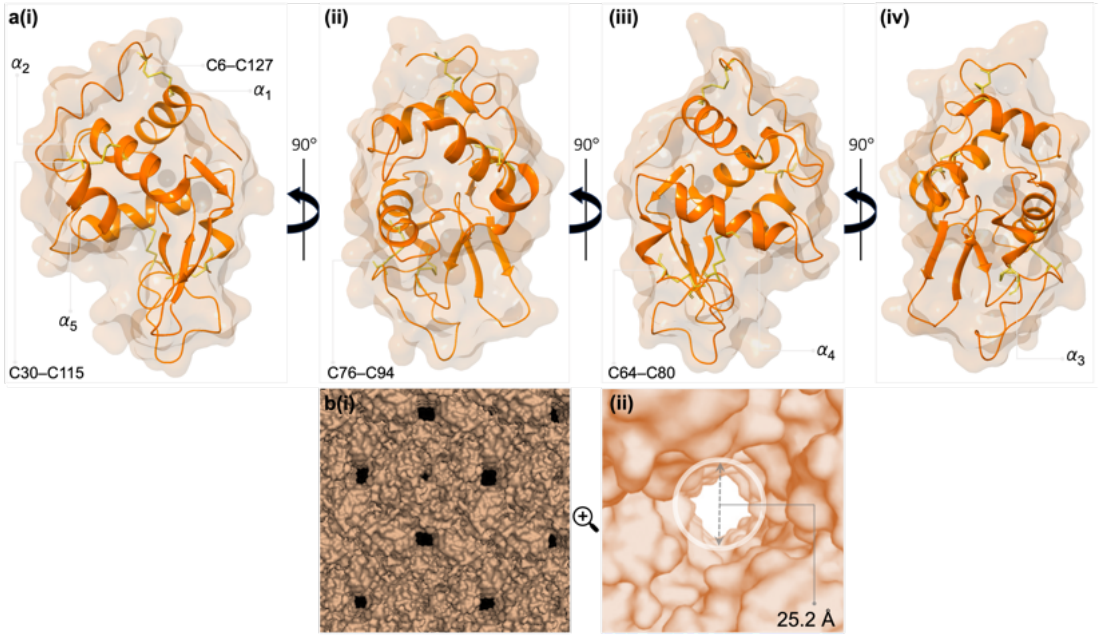

Figure 3.10. (**a**) Ribbon diagram with solid molecular surface (90% transparency) of the hen egg-white Lysozyme (PDB: 1HEW)[54] with resolution 1.75 Å from the (**i**) front view, (**ii**) side view, (**iii**) back view and (**iv**) side view. The five α-helix structures are labelled accordingly; the 8 cysteine residues (C6–C127, C30–C115, C64–C80 and C76–C94) that contribute to disulfide bridges within the tertiary structure are shown in yellow tube representation. (**b**) (**i**) Lysozyme lattice structure along the *z*-crystallographic axis, displaying the large solvent channels within the crystal structure (shown in black) (**ii**) Close-up view of the Lysozyme crystal solvent channel; the diameter of the solvent channel, given in Å, is indicated with a dashed line. All structures were modelled in Schrödinger Maestro.

In 1965, Phillips and co-workers proposed the origins for the active site and the catalytic mechanism of Lysozyme, based on crystallographic data obtained with a hexasaccharide (Scheme 3.1a(i)).[55] The proposed mechanism states that two Lysozyme active site residues, glutamic acid-35 (E35) and aspartic acid-52 (D52), play an essential role in the catalytic activity of the enzyme. In this proposed mechanistic pathway, the E35 residue acts as a proton donor presented *via* its carboxylic acid side chain, where the acidic proton is provided to the glycosidic bond, resulting in the cleavage of the C–O bond in the substrate (**3.1**). This results in the formation of an oxo-carbenium ion

intermediate (**3.2**). Subsequently, the oxo-carbenium ion interacts with the D52 residue, to form a stable glycosyl intermediate. Then, the surrounding bulk water provides a hydroxyl ion which binds to the oxo-carbenium ion to form species **3.3**, whilst the basic E35 residue is protonated.[46,52]

In 1953, however, Koshland proposed an alternative covalent mechanism for Lysozyme catalysis, involving a glycosyl–enzyme intermediate (**3.4**), in which the substrate is covalently bonded to the D52 residue (Scheme 3.1a(ii)).[56] Koshland proposed that the D52 residue acts as a nucleophile, attacking the C_1 carbon of the MurNAc sugar (**3.1**), forming a glycosyl-enzyme intermediate (**3.4**). The E35 residue has the ability to donate an acidic proton to the sugar leaving group, before acting as a Brønsted–Lowry base, by accepting a proton from a surrounding water molecule. This proton exchange results in a free hydroxyl ion, that can perform a nucleophilic attack on the glycosyl-enzyme intermediate, releasing the D52 residue as the leaving group through hydrolysis, thus leaving the enzyme unchanged and forming product **3.3**.

Additionally, in 2001, Vocadlo and co-workers provided conclusive evidence towards a mechanism, which included Koshland's proposed covalent intermediate (**3.4**).[57] ESI mass spectrometry, along with an X-ray co-crystal structure, proved Koshland's theory of the existence of a covalent intermediate between substrate and the nucleophilic D52 residue.

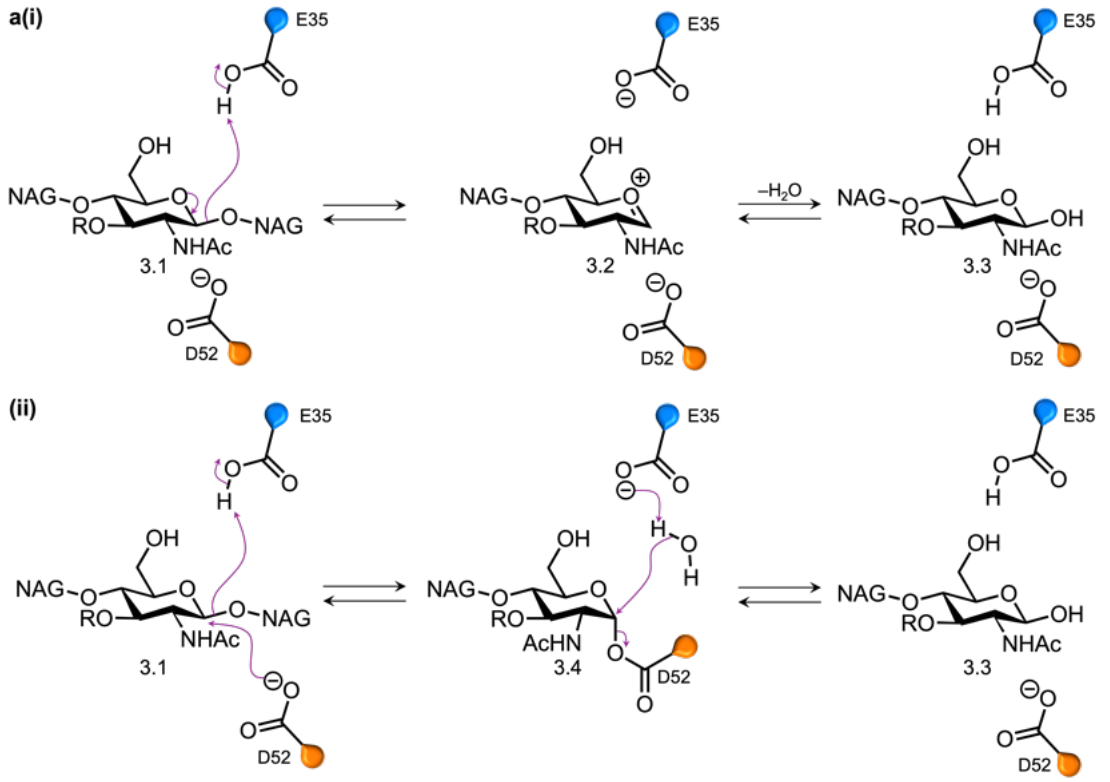

Scheme 3.1. (a)(i) The mechanism of action for Lysozyme, as proposed by Phillips, which proceeds through an oxo-carbenium ion intermediate (3.2) (ii) the mechanism of action for Lysozyme, as proposed by Koshland, which proceeds through a glycosyl-enzyme intermediate (3.4) involving the D52 residue. The coloured pendants represent the key amino acid residues where blue = E35 and orange = D52.

3.1.5 Aims and Objectives

This research aims to initiate the translation of fundamental dynamic chemistry to unique and useful functional molecules and materials. The ultimate goal is to utilise shapeshifting properties combined with bioorthogonal chemistry to develop new methods of exploration in biological chemistry. This study aims to probe how non-covalent interactions between fluxional molecules and protein targets influence the shapeshifting equilibria, and to what extent these properties influence binding affinities. Theoretically, there is the potential for shapeshifting molecules to adopt specific isomeric configurations, leading to high association constants that can be utilised in unexplored complex biochemical targets (Figure 3.11).

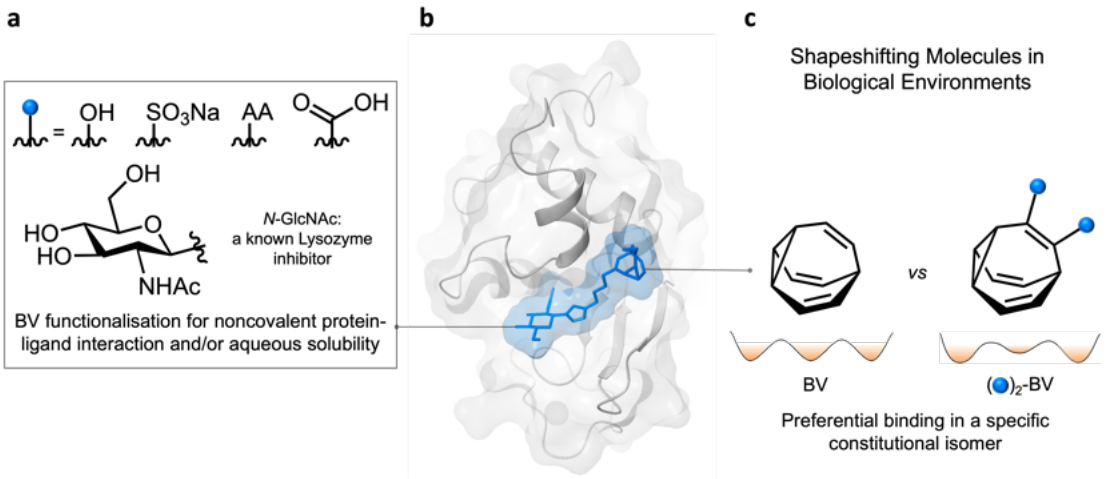

Figure 3.11. (a) The introduction of functionality to aid aqueous solubility and/or increase host-guest specificity, where specific examples are shown. AA denotes amino acid. For example, a possible Lysozyme inhibitor, BV-GlcNAc (blue) is depicted in the typical binding pocket of Lysozyme and is shown in tube representation with solid molecular surface (85% transparency). (b) Example depiction of a functionalised **BV** molecule binding within a protein, where Lysozyme is presented as a representative example; Lysozyme is shown in ribbon representation with solid molecular surface (90% transparency) of Lysozyme (grey, PDB: 1HEW).[54] (c) The comparison of a native degenerate **BV** with a functionalised non-degenerate **BV**. The blue circles represent a functional group. The schematic illustrates the change in degeneracy upon functionalisation of native **BV** to a substituted **BV**, where we would expect preferential binding of **BV** in a specific constitutional isomer of a non-degenerate **BV** population within a protein binding site.

This consideration, where there is the potential for shapeshifting molecules to adapt their molecular shape, could allow for mutually induced binding with a biomacromolecular target, such as a protein. Interestingly, to date, there have been no investigations carried out to specifically probe the potential interactions between fluxional carbon-based species and complex biomolecules crystallographically. The only exception is provided by the biological study of the **BV** vancomycin dimer, which was investigated for its effect on the gram-positive bacteria MRSA. As a result, this work aims to investigate how the shapeshifting equilibria of fluxional carbon cages, such as **BBs** and **BVs** may influence interactions in protein-ligand binding, and thereafter whether their shapeshifting properties have any effect on the affinity of ligand binding.

3.2 Results and Discussion

3.2.1 Synthesis of Fluxional Carbon Cages

As discussed in Chapter 1, substituted **BBs** and **BVs** are relatively unexplored fluxional carbon cages that have been, albeit scarcely, methodically exploited for developing new materials with various applications.[58–65] Herein, the work presented builds upon the published work by McGonigal and co-workers who reported the shape-selective crystallisation[66] and the control of dynamic sp^3-C stereochemistry[67] of substituted **BBs**. This investigation also builds on previous studies by Fallon and co-workers, who investigated the synthesis and analysis of substituted **BV** systems.[64] These reported studies show that substituted **BVs** are accessible *via* a more efficient synthetic method,[64] compared with historical syntheses to access substituted **BVs**. With this information in hand, **BBs** and **BVs** have been synthesised for use in biological studies, particularly protein co-crystallisation experiments. As described in the introduction, achieving water solubility is a key consideration when trying to attain molecular recognition and subsequent co-crystallisation within a biological environment. Thus, owing to its hydrogen bonding capability in aqueous solution, it was proposed that the presence of a hydroxyl moiety throughout the set of compounds studied would allow for dissolution in aqueous medium and co-crystallisation with biological molecules, with possible noncovalent interactions (such as hydrogen bonding) with amino acid side chains within a protein binding site.

3.2.1.1 Synthesis of Barbaralanes

First, **BBL** was synthesised, which was formed through the gold-catalysed cycloisomerisation reaction of 7-ethynylcyclohepta-1,3,5-triene (**3.5**), proceeding through a barbaralyl cation intermediate.[68] The ensuing fluxional intermediate was then oxidised in situ by diphenyl sulphoxide to yield barbaralone (**BBO**). The resultant **BBO** was then treated with lithium aluminium hydride, under inert conditions, to afford barbaralol (**BBL**), which exists as a mixture of $\mathbf{BBL}_S$ and $\mathbf{BBL}_R$ (Scheme 3.2).

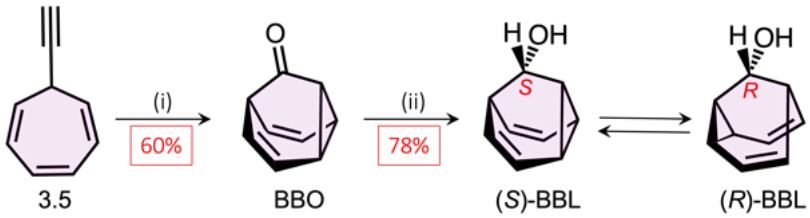

Scheme 3.2. The synthesis of **BBL**. Reagents and conditions: (i) IPrAu(MeCN)BF_4 (5 mol%) / Ph_2SO (2.0 eq.) / CH_2Cl_2 / rt / 16 h / 60%; (ii) $LiAlH_4$ / Et_2O / 0 °C / 3 h / 78%. IPr = 1,3-bis(2,6-diisopropylphenyl)imidazol-2-ylidene. Synthetic steps (i) and (ii) were not performed by the author (see experimental).[†]

The internal mirror plane (along the plane of the carbonyl bridge) present in **BBO** results in the species being an achiral molecule. An additional mirror plane (that is orthogonal to the aforementioned plane) can be foreseen as a result of the internal **BB** dynamics. As a result of this mirror plane, the olefinic and cyclopropane environments emerge as a broad singlet, evidenced by ^{1}H NMR spectroscopy. Yet, upon reduction of the carbonyl group on **BBO** (Figure 3.12a), a stereogenic centre is created at position 9 to produce ***(S)*-BBL** and ***(R)*-BBL**. This transformation results in the formation of two valence enantiomers, where the aforementioned mirror plane no longer exists. Consequently, the absence of a mirror plane in **BBL** brings about the desymmetrisation of the molecule. This occurrence causes the olefinic (Figure 3.12b, signals H_3 and H_7) and the cyclopropane (Figure 3.12b, signals H_2 and H_8) proton signals to separate into two distinct signals, indicating inequivalent environments, where the ***(S)*-BBL** and ***(R)*-BBL** exist in fast exchange on the ^{1}H NMR timescale.

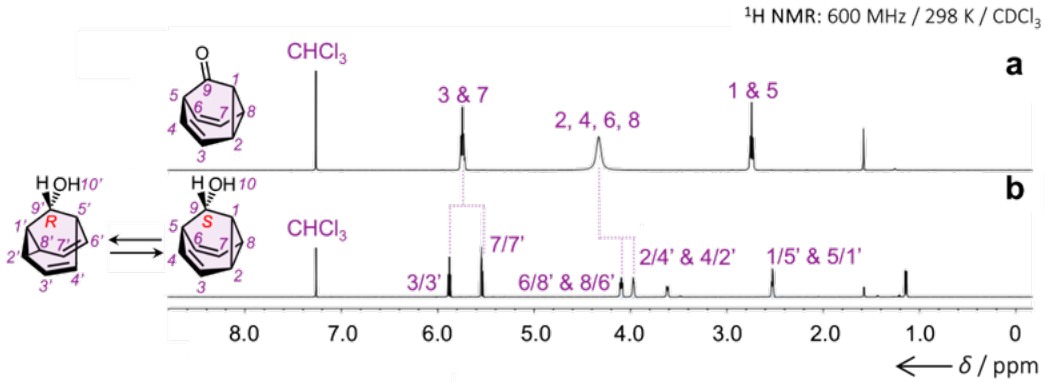

Figure 3.12. Partial ^{1}H NMR spectra of (**a**) **BBO**; and (**b**) ***(R)*-BBL** and ***(S)*-BBL**. The spectra shows the desymmetrisation of the barbaralyl core, with signals splitting as the proton environments become chemically inequivalent. The NMR spectra are re-formatted from previously reported results.[69a]

Synthesis of Mono-Substituted Hydroxy Barbaralanes

Next, non-degenerate fluxional **BBs** containing two groups were synthesised. Similarly, the gold-catalysed cycloisomerisation of the alkynyl CHT precursor (**3.5**) led to the barbaralyl cation intermediate, which was subsequently oxidised by diphenyl sulphoxide to give **BBO**. Then, the addition of aryl magnesium bromides to **BBO** afforded **BBs** ((*S*)-**3.6**/(*R*)-**3.6** and (*S*)-**3.7**/(*R*)-**3.7**), functionalised with one *p*-substituted phenyl moiety and a tertiary alcohol (Scheme 3.3).

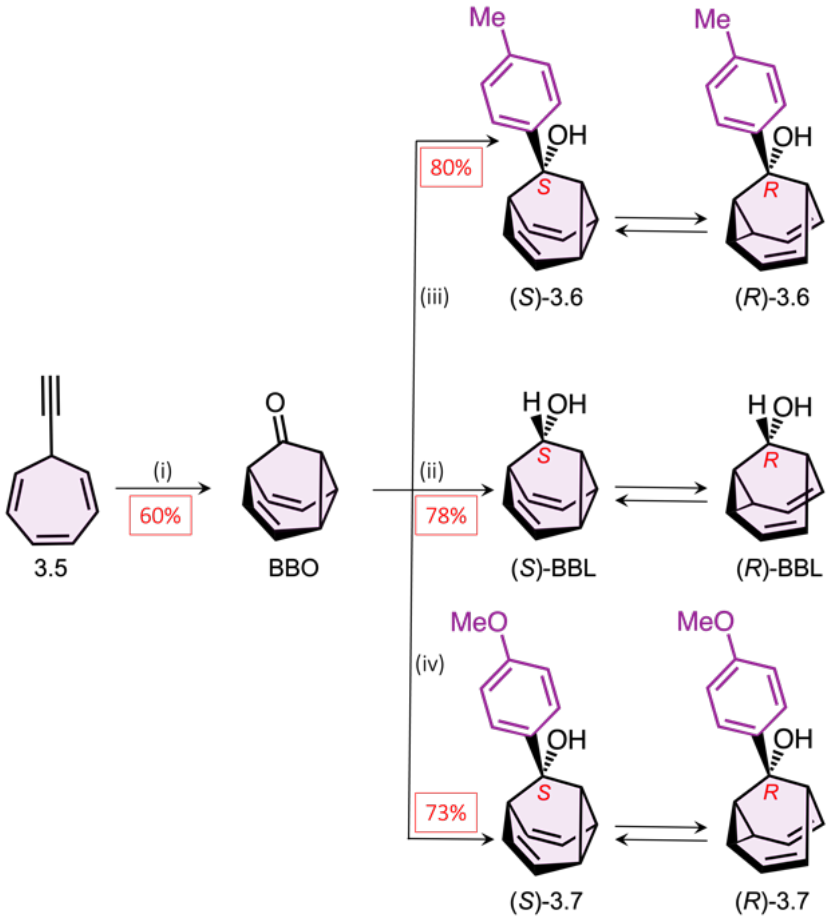

Scheme 3.3. Synthesis of (*S*)-**3.6**/(*R*)-**3.6** and (*S*)-**3.7**/(*R*)-**3.7**; Reagents and conditions: (i) IPrAu(MeCN)BF_4 (5 mol%) / Ph_2SO (2.0 eq.) / CH_2Cl_2 / rt / 16 h / 60%; (ii) $LiAlH_4$ / Et_2O / 0 °C / 3 h / 78%; (iii) magnesium turnings / THF / 4-bromotoluene / reflux to rt then **BBO** / 0 °C → rt / 80%; (iv) magnesium turnings / THF / 1-bromo-4-methoxybenzene / reflux to rt then **BBO** / 0 °C → rt / 73%. IPr = 1,3-bis(2,6- diisopropylphenyl)imidazol-2-ylidene. Synthetic steps (i)–(iv) were not performed by the author (see experimental).[†]

Given that **3.6** and **3.7** consist of a mixture of the *R* and *S* enantiomers in the solution-state, experimental ^{1}H NMR spectroscopy evidences the average in chemical shifts,

that represents two different chemical environments (a divinylcyclopropane and a *cis*-dialkylolefin) on the **BB** scaffold. This provides irrefutable confirmation of the interconversion between the *R* and *S* enantiomers of **3.6** (Figure 3.13).

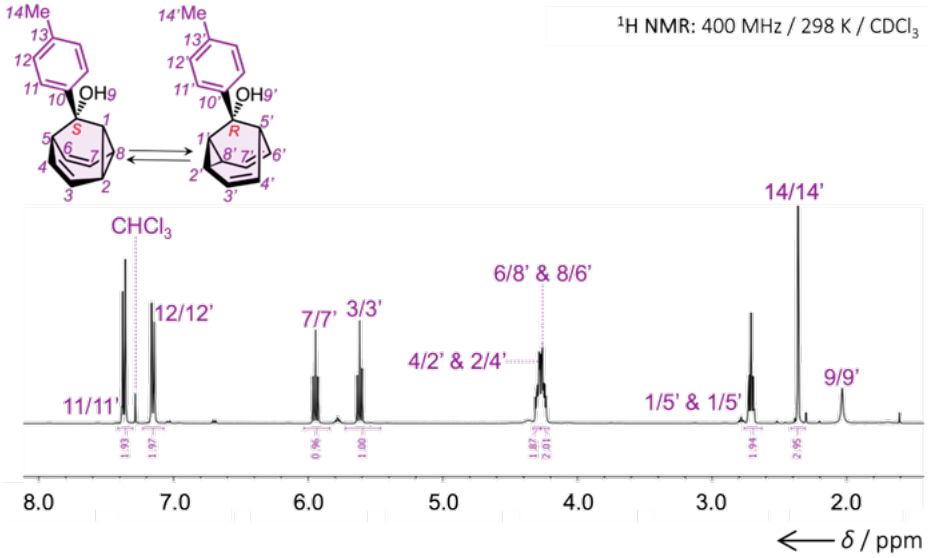

Figure 3.13. Partial ^{1}H NMR spectrum of mono-substituted hydroxy **BB** (**3.6**), highlighting the existence of the interconverting *R* and *S* enantiomers. The NMR spectrum is re-formatted from previously reported results.[69a]

Synthesis of Di-Substituted Hydroxy Barbaralanes

Then, Echavarren's procedure was utilised towards the synthesis of **BBOs** to form di-substituted hydroxy **BBs**, where the aryl ring is positioned at either the 1 or 9 position on the **BB** scaffold. This synthetic methodology, which provides a means to **BBOs** bearing different aryl functionality, allows for a library of di-substituted hydroxy **BBs** to be populated *via* the Grignard transformation of the **BBO** carbonyl moiety to a tertiary alcohol.

The syntheses of di-substituted hydroxy **BBs** started with the formation of an aryl substituted alkynyl CHT (**3.8**$_{a\text{-}f}$). This species (**3.8**) is then subjected to gold-catalysed cycloisomerisation, resulting in the formation of fluxional barbaralyl cation intermediate. The ensuing barbaralyl cation then forgoes oxidation *in situ* by the presence of diphenyl sulphoxide, providing access to a range of mono-substituted **BBOs**$_{a\text{-}f}$. The resulting **BBOs**$_{a\text{-}f}$ were then treated with the respective aryl magnesium

bromide reagent, giving rise to di-substituted hydroxy **BBs** (**3.10**$_{a\text{-}f}$), which present two aryl functionalities (Scheme 3.4). These molecules (**3.10**$_{a\text{-}f}$) exist as a dynamic mixture of two valence isomers and enantiomers, that interconvert at a fast rate making them indistinguishable on the NMR timescale, in solution at room temperature. As such, solution state ^{1}H NMR spectroscopy evidences averaged proton resonances for the interconverting mixture.

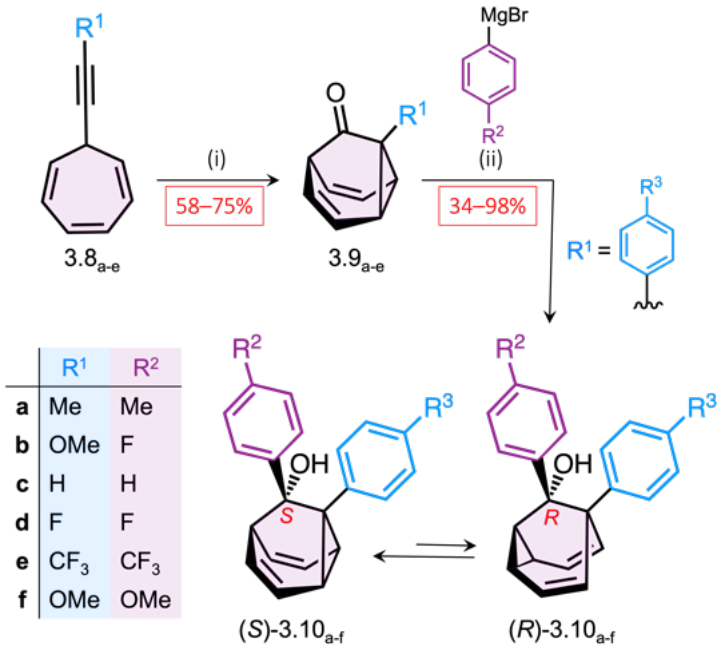

Scheme 3.4. Synthesis of di-substituted hydroxy **BBs** (**3.10**$_{a\text{-}f}$) from alkynyl CHTs (**3.8**$_{a\text{-}e}$) and intermediate **BBOs** (**3.9**$_{a\text{-}e}$). Reagents and conditions: (i) IPrAu(MeCN)BF_4 (5 mol%) / rt / 16 h / 58–75%; (ii) THF / reflux → rt then 0 °C → rt / 34–98%; IPr = 1,3-bis(2,6-diisopropylphenyl)imidazol-2-ylidene. Synthetic steps (i) and (ii) were not performed by the author (see experimental).†

3.2.1.2 Synthesis of Bullvalenes

Hydroxy-Containing Bullvalenes for Protein Co-Crystallisations

With the synthetic procedure in hand (previously reported by Fallon *et al.*[64]), the initial target was the *bis*(hydroxymethylene) **BDT** (**3.12**). Cyclooctatetraene (**COT**) was treated with two equivalents of 2-butyne-1,4-diol (**3.11**) under cobalt-catalysed conditions in anhydrous TFE and stirred at 55 °C for 48 hours. Initial attempts to reproduce this synthesis proved challenging, not producing the desired **BDT** compound at all (Scheme 3.5), whereas the literature reported a yield of 86%.[64] This eventuality

was problematic as the **BDT** acts as a precursor for the desired **BV**, therefore a substantial amount of **BDT** was needed. Thus, troubleshooting of this reaction was required.

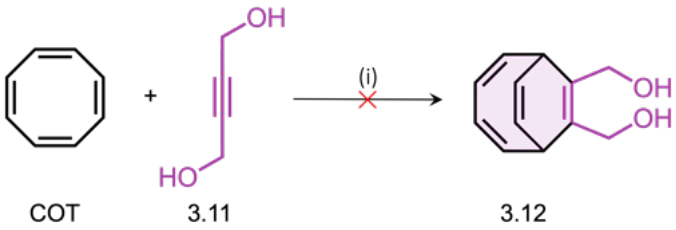

Scheme 3.5. Synthetic route to bis(hydroxymethylene) **BDT** (**3.12**) *via* a cobalt catalysed formal [6+2] cycloaddition of **COT** with 2-butyne-1,4-diol (**3.11**). Conditions (i) $CoBr_2$(dppe) / Zn / ZnI_2 in a 5:15:10 mol % ratio / TFE / 55 °C / 48 h.

In order to troubleshoot the cause of this apparent low conversion to **BDT** (**3.12**), a screen was conducted (Table 3.1). Three key reaction variables were considered in the screen: zinc dust, oxygen sensitivity and the zinc iodide. Preparation and activation of the zinc dust was achieved through treatment with 1 M $HCl_{(aq)}$ for 30 minutes, followed by sequential washing with water, ethanol and diethyl ether. The zinc dust was then dried thoroughly overnight under reduced pressure to remove any residual solvent that may degrade other metal catalysts in the reaction mixture.[70] Similarly, since zinc iodide is a hygroscopic compound and moisture sensitive, it was essential to ensure this component of the catalytic mixture was dry. Consequently, zinc iodide was heated to 280 °C under reduced pressure for 5 min before the reaction proceeded. This precondition was similarly used by Fallon *et al.,* however, only when synthesising moisture-sensitive boronate esters.[71] Finally, in order to probe the effect of oxygen on reaction conversion, three freeze-pump-thaw cycles were performed in some cases in an attempt to degas the solvent in the system. Preliminary investigations were completed with 2-pentyn-1-ol as the alkyne for the formal [6+2] cycloaddition with **COT** (Table 3.1). The initial results were promising and displayed a marked improvement on previous results – especially on the conditions including zinc dust activation and zinc iodide treatment (entries 1 and 5). When attempting to reproduce these reaction conditions with 2-butyne-1,4-diol (**3.11**), the results were not reproducible therefore further investigation was required.

Table 3.1. Reaction condition screen for **BDT** synthesis subjecting the alkyne 2-pentyn-1-ol to the cobalt-catalysed cycloaddition with COT. Performed on a 0.5 mmol scale relative to COT. × = present, / = absent. Percentage conversion calculated by ^{1}H NMR spectroscopy from the ratio of the product and the sum of the total starting material and product.

Reaction Entry	Zn Activation	ZnI_2 Treatment	FPT	Conversion %
1	×	×	×	73
2	×	/	×	47
3	/	×	×	38
4	/	/	×	46
5	×	×	/	83
6	×	/	/	19
7	/	×	/	20
8	/	/	/	29

Further investigations subjected 2-butyne-1,4-diol (**3.11**) to formal [6+2] cycloaddition conditions with **COT** with a series of cobalt catalysts and ligands (Table 3.2) in order to determine whether the cobalt catalyst could promote a cycloaddition reaction to form the **BDT** intermediate (**3.12**). Analysis *via* ^{1}H NMR spectroscopy showed only starting material in all reaction mixtures.

Table 3.2. Cobalt catalyst screen for the attempted synthesis of bis(methylenehydroxy) **BDT** (**3.12**). Starting material = SM.

Reaction Entry[a]	Cobalt Catalyst	Ligand	Result[b]
1	$CoBr_2$(dppe)	–	SM
2	CoI_2(dppe)	–	SM
3	$Co(acac)_2$	dppe	SM
4	$CoBr_2$	XantPhos[c]	SM
5	$CoBr_2$	SPhos[d]	SM
6	$CoBr_2$	XPhos[e]	SM
7	$CoBr_2$	*rac*-BINAP[f]	SM
8	$CoBr_2$	PPh_3	SM
9	$CoBr_2$	$P(OC_6H_5)_3$	SM

[a]Conditions: Cobalt catalyst (5 mol%) / ZnI_2 (10 mol%) / Zn dust (15 mol%) / TFE / 55 °C / 48 h; [b]Analysed by ^{1}H NMR spectroscopy of the reaction mixture; [c]XanthPhos = (9,9-Dimethyl-9H-xanthene-4,5-diyl)bis(diphenylphosphane); [d]SPhos = Dicyclohexyl(2′,6′-dimethoxy[1,1′-biphenyl]-2-yl)phosphane; [e]XPhos = Dicyclohexyl[2′,4′,6′-tris(propan-2-yl)[1,1′-biphenyl]-2-yl]phosphane; [f]BINAP = [1,1-Binaphthalene]-2,2-diyl)bis(diphenylphosphane.

Due to the continuing lack of conversion of the cobalt-catalysed cycloaddition of COT with 2-butyne-1,4-diol, alternative routes were explored to attain a transformation. First, protection of the two hydroxyl groups on 2-butyne-1,4-diol (**3.11**) with *tert*-

butylmethylsilyl to form **3.13** was pursued, in case the free hydroxyl groups were detrimentally interacting with components of the catalytic mixture. 2-Butyne-1,4-diol (**3.11**) was treated with two equivalents of *tert*-butyldimethylsilyl (TBS) chloride to form the TBS protected alkyne (**3.13**) in a 82% yield (Scheme 3.6).

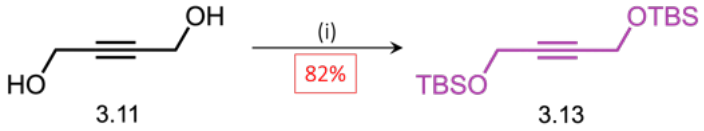

Scheme 3.6. Synthetic route to TBS protected alkyne (**3.13**) Conditions: (i) DMAP then TBDMSCl / CH_2Cl_2 / rt / 18h / 82%. DMAP = *N,N*-4-dimethylaminopyridine; TBDMSCl = chloro-*tert*-butyldimethylsilane.

The TBS protected butyne diol (**3.13**) was then subjected to the cobalt-catalysed conditions with **COT**, in an attempt to form the TBS protected **BDT** intermediate (**3.14**) (Scheme 3.7). Observations by ^{1}H NMR spectroscopy showed this reaction to be unsuccessful due to the absence of **BDT** signals, as well as a large amount of TBS alkyne starting material.

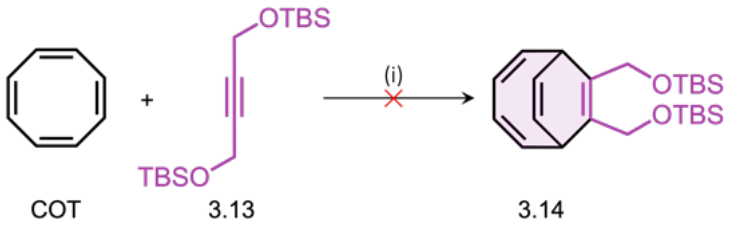

Scheme 3.7. Synthetic route to TBS protected **BDT** (**3.14**) with the respective 1,4-bis-(*tert*-butyl-dimethyl-silanyloxy)-but-2-yne (**3.13**). Conditions: (i) $CoBr_2$(dppe) / Zn / ZnI_2 in a 5:15:10 mol% ratio / TFE / 55 °C / 24 h.

Next, to find an alternative route to synthesise alcohol containing **BDTs**, a strained alkyne was used to introduce phenyl substituents bridged by a carbon-carbon bond connection, which in theory, could be cleaved upon **BDT** formation to reveal the hydroxy groups. The carbon-carbon bond connection of two substituents makes this compound an interesting proposition as **BVs** with this functionality have not been reported. First, 2-butyne-1,4-bistosylate (**3.15**) was readily prepared as a suitable electrophile in preparation of the strained alkyne target in 50% yield (Scheme 3.8).

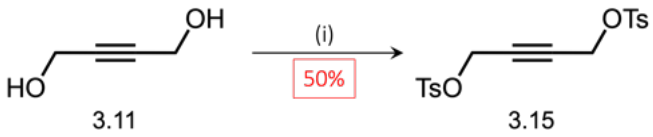

3.11 3.15

Scheme 3.8. Synthetic route to 4-(4-methylphenyl)sulfonyloxybut-2-ynyl 4-methylbenzenesulfonate (**3.15**) through tosylation of 2-butyne-1,4-diol. Conditions and reagents: (i) TsCl then KOH / Et_2O / –15 °C → rt / 2 h / 50%.

Based on previous successful syntheses reported by Harris *et al.*,[72] caesium carbonate was used as an appropriate base for the ensuing cyclisation of (*R*)-1,1'-bi(2-naphthol) (BINOL). Its treatment with the 2-butyne-1,4-bistosylate (**3.15**) allowed access to the more sterically demanding, enantiopure (*R*)-2,2'-binaphthyldioxacyclodecyne (BINOC) (**3.16**), albeit in a poor yield of 12% (Scheme 3.9).

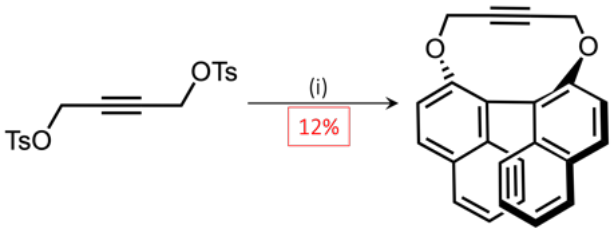

3.15 3.16

Scheme 3.9. Synthetic route to (*R*)-BINOC alkyne (**3.16**) from 4-(4-methylphenyl)sulfonyloxybut-2-ynyl (**3.15**). Conditions and reagents: (i) (*R*)-BINOL / Cs_2CO_3 / MeCN / rt / 32 h / 12%.

The subsequent (*R*)-BINOC alkyne (**3.16**) was then subjected to the cobalt-catalysed cycloaddition conditions with **COT**, in an effort to obtain the corresponding **BDT** (**3.17**) (Scheme 3.10). The desired masses were not detected by mass spectrometry for all reaction conditions detailed in Table 3.3. This indicated that the desired product had not formed, likely due to the poor solubility of the (*R*)-BINOC alkyne (**3.16**) in TFE and DCE, even at the elevated temperatures screened.

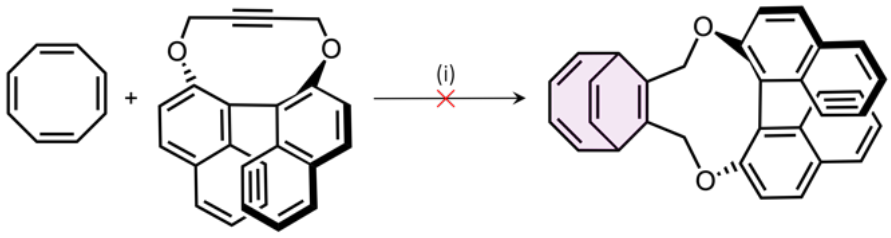

COT 3.16 3.17

Scheme 3.10. Attempted synthetic route to **BDT** (**3.17**) from COT and (*R*)-2,2'-binaphthyldioxacyclodecyne (**3.16**). Conditions: (i) $CoBr_2$(dppe) / Zn / ZnI_2 in a 5:15:10 mol % ratio / solvent / T °C / t. Solvent selection and reaction temperatures are listed in Table 3.3.

Table 3.3. Reaction screen for the attempted synthesis of (*R*)-BINOC **BDT**. No product = NP.

Reaction Entry[a]	Solvent	Temperature / °C	Comment[b]
1	TFE	55	NP
2	TFE	70	NP
3	DCE	40	NP
4	DCE	55	NP

[a]Conditions: Cobalt catalyst (5 mol%) / ZnI_2 (10 mol%) / Zn dust (15 mol%) / 48 h; [b]Analysed by mass spectrometry.

Given the limited success in previous attempts, a further effort was made to resolve the cycloaddition reaction conditions, based on a the literature precedent involving slow alkyne addition within cobalt-catalysed reactions.[73] As such, 2-butyne-1,4-diol (**3.11**) was dissolved in TFE and added to **COT** and the metal-catalyst mixture *via* syringe pump over 12 hours. This resulted in slower addition of the alkyne at a lower concentration into the reaction mixture. Encouragingly, the results demonstrated an improved, cleaner conversion to *bis*(hydroxymethylene) **BDT** (**3.12**) in 50% yield (Scheme 3.11). Progress of the reaction was monitored by ^{1}H NMR spectroscopy. Characteristically, **COT** exhibits eight hydrogen signals at δ 5.78 ppm corresponding to its eight equivalent proton environments, owing to the structure's two C_2 axes perpendicular to the main C_2 axis. Following the cobalt-catalysed formal [6+2] cycloaddition with 2-butyne-1,4-diol (**3.11**), key signals in the ^{1}H NMR spectrum included four hydrogen multiplets spanning δ 5.70–5.75, which correspond to the vicinal vinylic protons H_1 and H_2 (Figure 3.14). Owing to the success of this methodology, this technique was taken forward for all future **BDT** syntheses.

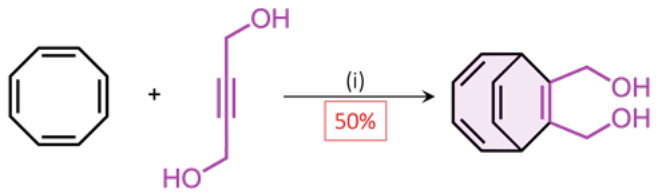

Scheme 3.11. Synthetic route to **BDT** bis(hydroxymethylene) (**3.12**) *via* a cobalt catalysed formal [6+2] cycloaddition of **COT** with 2-butyne-1,4-diol (**3.12**) *via* syringe pump addition over 12 h. Conditions (i) $CoBr_2$(dppe) / Zn / ZnI_2 in a 5:15:10 mol % ratio / TFE / 55 °C / 48 h / 50%.

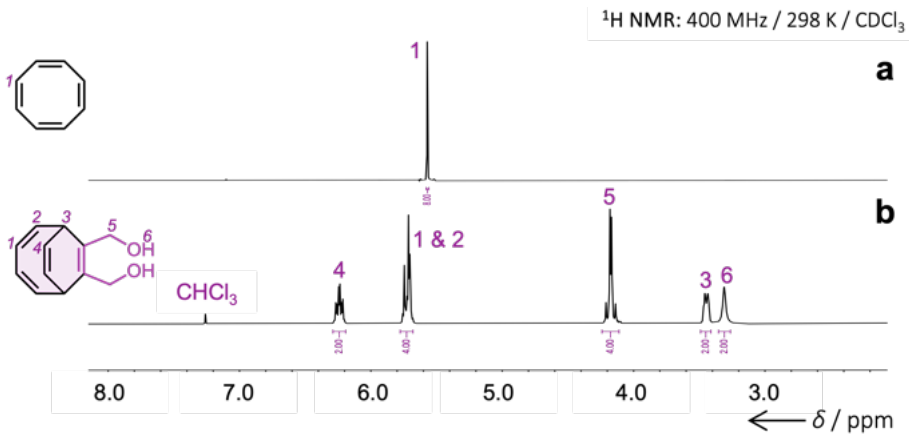

Figure 3.14. Partial ^{1}H NMR spectra for (**a**) **COT** and (**b**) *bis*(hydroxymethylene) **BDT** (**3.12**). The spectra show the changes in symmetry between the two molecules.

Resultantly, this synthetic methodology was applied to 1) pro-2-yn-1-ol; 2) pent-2-yn-1-ol; and 3) hex-3-yn-1-ol to form a series of related hydroxy-containing **BDTs** (**3.18**–**3.20**) (Scheme 3.12) that could be used as an intermediate to hydroxy-containing **BVs**.

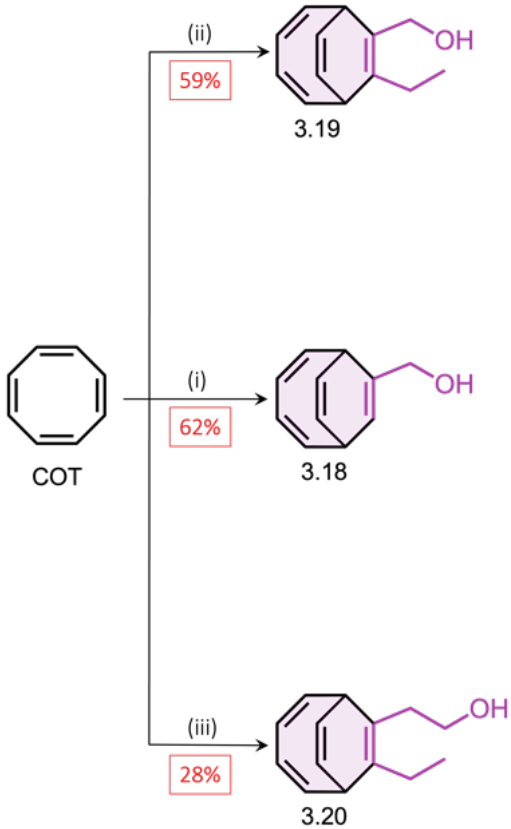

Scheme 3.12. Synthetic route to substituted hydroxy **BDTs** (**3.18**–**3.20**). Conditions: CoI_2(dppe) / Zn / ZnI_2 in a 5:15:10 mol % ratio, where (i) pro-2-yn-1-ol (1.2 eq.) / TFE / 55 °C / 24 h / 62%; (ii) pent-2-yn-1-ol (1.2 eq.) / TFE / 55 °C / 18 h / 59%; (iii) hex-3-yn-1-ol (1.2 eq.) / TFE / 55 °C / 72 h / 28%.

Photochemical Isomerisation to Hydroxy Bullvalenes

Having successfully synthesised a sufficient quantity of hydroxy-containing **BDTs** (**3.12** and **3.18**–**3.20**), these compounds were then subjected to photochemical conditions as previously described by Fallon and co-workers.[64] The irradiation of the **BDTs** (**3.12** and **3.18**–**3.20**) in separate vessels at 365 nm at –5 °C in the presence of a thioxanthene-9-one photosensitiser in THF solvent produced the corresponding **BVs** (**3.21**–**3.24**) in moderate yields (Scheme 3.13).

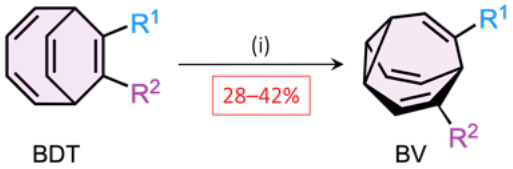

	R^1	R^2
3.21	CH_2OH	CH_2OH
3.22	CH_2OH	–
3.23	CH_2OH	Et
3.24	CH_2CH_2OH	Et

Scheme 3.13. Synthetic route to hydroxy **BVs** (**3.21**–**3.24**) *via* a photochemical di-π-methane rearrangement of **BDTs** (**3.12** and **3.18**–**3.20**). Conditions: (i) Thioxanthen-9-one (5 mol%) / 365 nm / anhydrous THF / –5 °C / 6 h / 28–42%.

As previously described in Chapter 1, the photochemical occurrence of the di-π-methane was first documented by Zimmerman *et al*. in 1967, who accessed SBV from barrelene.[74–76] Subsequent employment of the same methodology by Scott and Jones allowed a photochemical synthetic route to **BV**.[77] With the prerequisite for a di-π-methane rearrangement to contain two π-systems separated by a sp^3 hybridised carbon, the rearrangement is accessible in both **BDT** and **BV** species. Problematically, however, **BV** is capable of undergoing a subsequent di-π-methane rearrangement, which opens up the possibility of further rearrangements to form another tricyclic species, namely lumibullvalene (**LBV**) (Scheme 3.14), which was first isolated by Jones in 1967.[65,78]

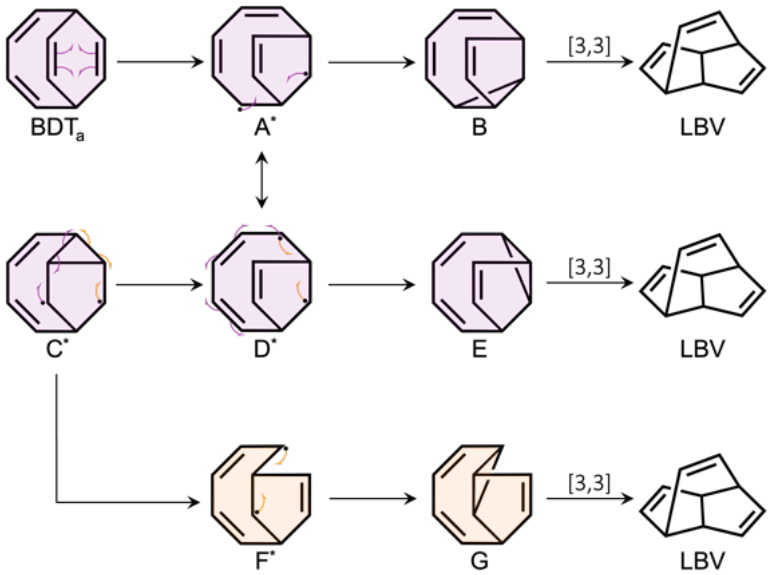

Scheme 3.14. Schematic showing the possible mechanism of the triplet photosensitised formation of the by-product (**LBV**) from **BDT$_a$**, proceeding *via* the radical intermediates (**A**, **C**, **D** and **F**) and intermediates (**B**, **E** and **G**).[65]

The ^{1}H NMR spectroscopic analysis shows the formation of broad signals for **BV**, which are characteristic of fluxional species, due to multiple isomers being present in solution. The **BV** isomers are not only difficult to identify because they form part of a convoluted mixture of compounds but also because **BV** forms a dynamic equilibrium between an array of constitutional isomers. Resultantly, broad **BV** peaks produced in the ^{1}H NMR spectrum cannot be integrated accurately, and are therefore difficult to interpret. For example, however, VT ^{1}H NMR spectroscopy has been carried out on **BV** (**3.22**) showing the sharpening of signals as the temperature decreases (Figure 3.15). In doing so, the integration of signals becomes more distinguishable allowing for a more comprehensible proton assignment, compared with the ^{1}H NMR spectrum at room temperature.

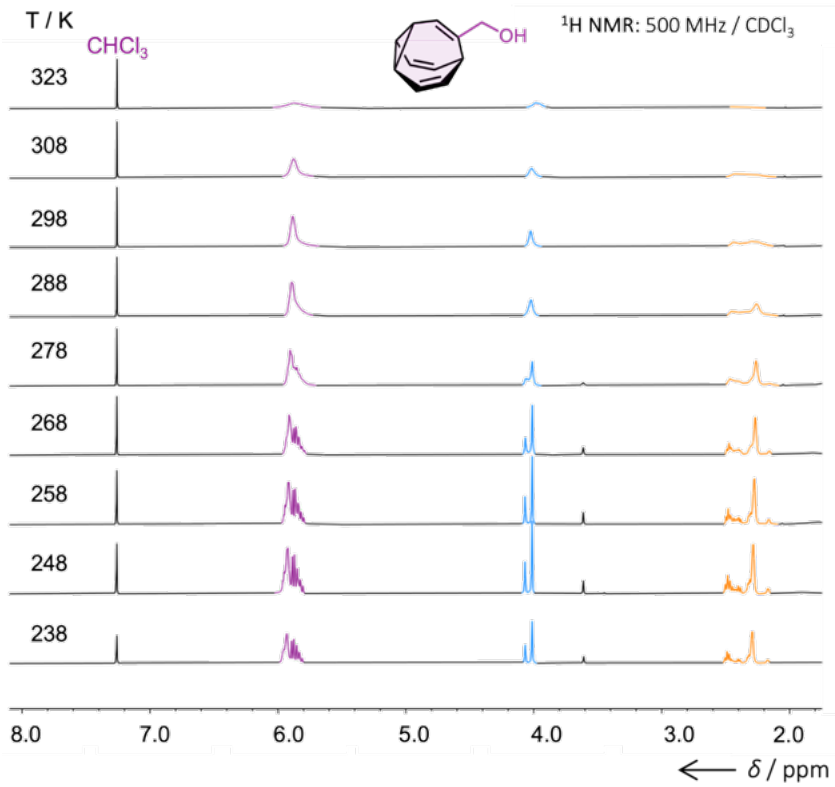

Figure 3.15. Partial VT ^{1}H NMR spectra of **BV** (**3.22**) in the range 323–238 K. The successive decrease in temperature gives rise to more distinct, sharp signals.

3.2.2 Serum Albumin Crystallisation Studies

The initial synthetic investigations allowed for a series of **BBs** and **BVs** (containing hydroxy groups) to be populated. Henceforth, with these compounds in hand, protein co-crystallisation studies were attempted, with the aim of obtaining a protein-ligand complex, as well as isolating a particular constitutional isomer of a given shapeshifting ligand (as described in the introduction).

3.2.2.1 Crystallisation of Bovine Serum Albumin

Crystallisation Screening

Initial crystallisation studies focused on obtaining good quality **BSA** crystals that were suitable for structure determination by X-ray crystallography. It was important to develop a reliable method for growing crystalline **BSA** for further co-crystal studies with ligands. Therefore, preliminary crystallisation trials were conducted using commercially available **BSA**, followed by SEC purification and screening conditions. In the first round of screening, crystalline material was identified in 0.1 M

Triaminomethane(tris)-HCl, pH 7.0, 0.2 M $Ca(OAc)_2$, 20% PEG3350. This screen (**BSA** screen 1, Tables S3.1–S3.4) was manually varied by changing the polyethylene glycol (PEG) percentage and the $Ca(OAc)_2$ concentration of the tris buffer system in 24-well sitting drop trays. Vapour diffusion by the sitting-drop method is the most widely used owing to its simplicity and ability to test different parameters quickly. The sitting drop method requires the sample and reservoir solution to be mixed together, whereby a drop of the sample and reservoir solution are placed on the seat (Figure 3.6). The aforementioned set-up is then sealed airtight allowing equilibration to commence between the reservoir solution and the sample-containing drop. As a result of the reservoir solute concentration being in excess in comparison to the sitting drop, water diffuses from the sample drop to the reservoir through the vapour phase in an effort to naturally equilibrate solute concentrations. Subsequently, the size of the sample drop reduces, increasing the concentration of the drop components resulting in crystallised material.

In addition to apo-**BSA** crystallisation screening, a preliminary co-crystallisation screen was also attempted with the two ligands: 1) **BBL** and 2) *p*-methoxyphenyl **BB** (**3.7**). The crystals produced by the 24-well optimisation trays yielded thin, needle-like crystals (Figure 3.16a) that could not tolerate the stress of mounting, and so further optimisation was required.

Bovine Serum Albumin Crystal Optimisation

Screening was repeated to improve the quality of the **BSA** crystals varying $Ca(OAc)_2$ concentration and glycerol percentage, as it was thought this may provide conditions to slow crystal growth, and therefore aid **BSA** crystallisation (**BSA** screen 2, Tables S3.5–S3.8). Although the crystals produced (Figure 3.16b) were slightly improved on those obtained in optimisation screen 1, they were not deemed good enough to be tested at the DLS for XRD to yield any good enough resolution to solve the **BSA** protein structure. Following screen 2, it was decided in corroboration with crystallographers in the Pohl group (Biophysical Sciences Institute (BSI), Durham University) that an effort to obtain better quality **BSA** crystals should be attempted before further co-crystallisation

attempts. Consequently, a third screen for the optimisation of BSA crystals was attempted, this time varying the pH (7.0–7.5) of the tris buffer system and the PEG 3350 concentration in 24 well sitting drop trays (BSA screen 3, Tables S3.9–S3.10). The crystals produced were more well defined and not as stacked or clustered as previously obtained (Figure 3.16c).

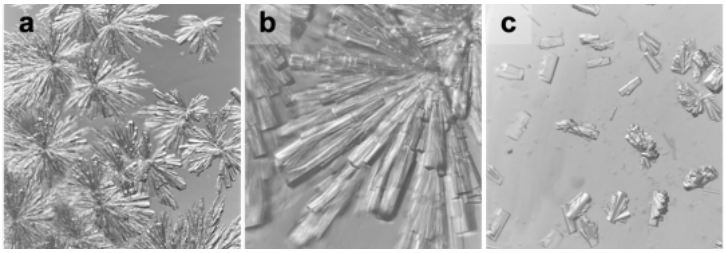

Figure 3.16. BSA crystals grown using the (a) OPT1 crystallisation conditions, sitting drop. (b) OPT2 crystallisation conditions, sitting drop. (c) OPT3 crystallisation conditions, sitting drop. The largest crystals are approximately 100 µm at their largest dimension.

Although these stacks of thin, needle-like crystals were not ideal for XRD analysis, the BSA crystals were harvested and mounted in loops for cryo-cooling[79] in order to successfully transfer for data collection, for the crystal quality to be evaluated at the DLS, beam line I04. The crystals from screen 3 were shown to have diffraction limits of 3.0 Å Bragg spacing. Figure 3.17 shows a typical example of a mounted BSA crystal in the loop (Figure 3.17a) used and the diffraction pattern obtained (Figure 3.17b) The unit cell was then determined from the diffraction pattern and the phase problem was solved by molecular replacement using PHASER,[80] which provided a unit cell that is identical to a previously reported BSA crystal structure (PDB: 4F5S).[81] The solved BSA protein structure is shown as its model (asymmetric unit) which consists of two protein chains (Figure 3.18a), which includes: residues 1–583 in chain A (Figure 3.18b) and residues 1–583 in chain B (Figure 3.18c).

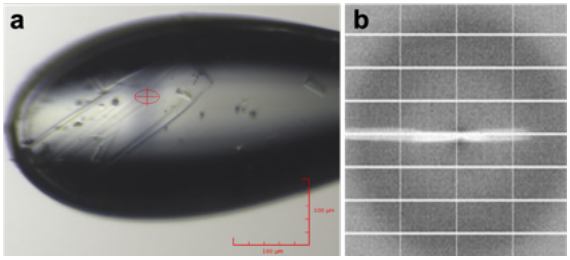

Figure 3.17. (a) BSA crystal mounted in a cryo loop. 100 um scale bars are shown in the bottom right corner (b) Diffraction pattern of BSA crystal, 3.0 Å resolution, giving the ribbon diagram of the BSA protein structure shown in Figure 3.18.

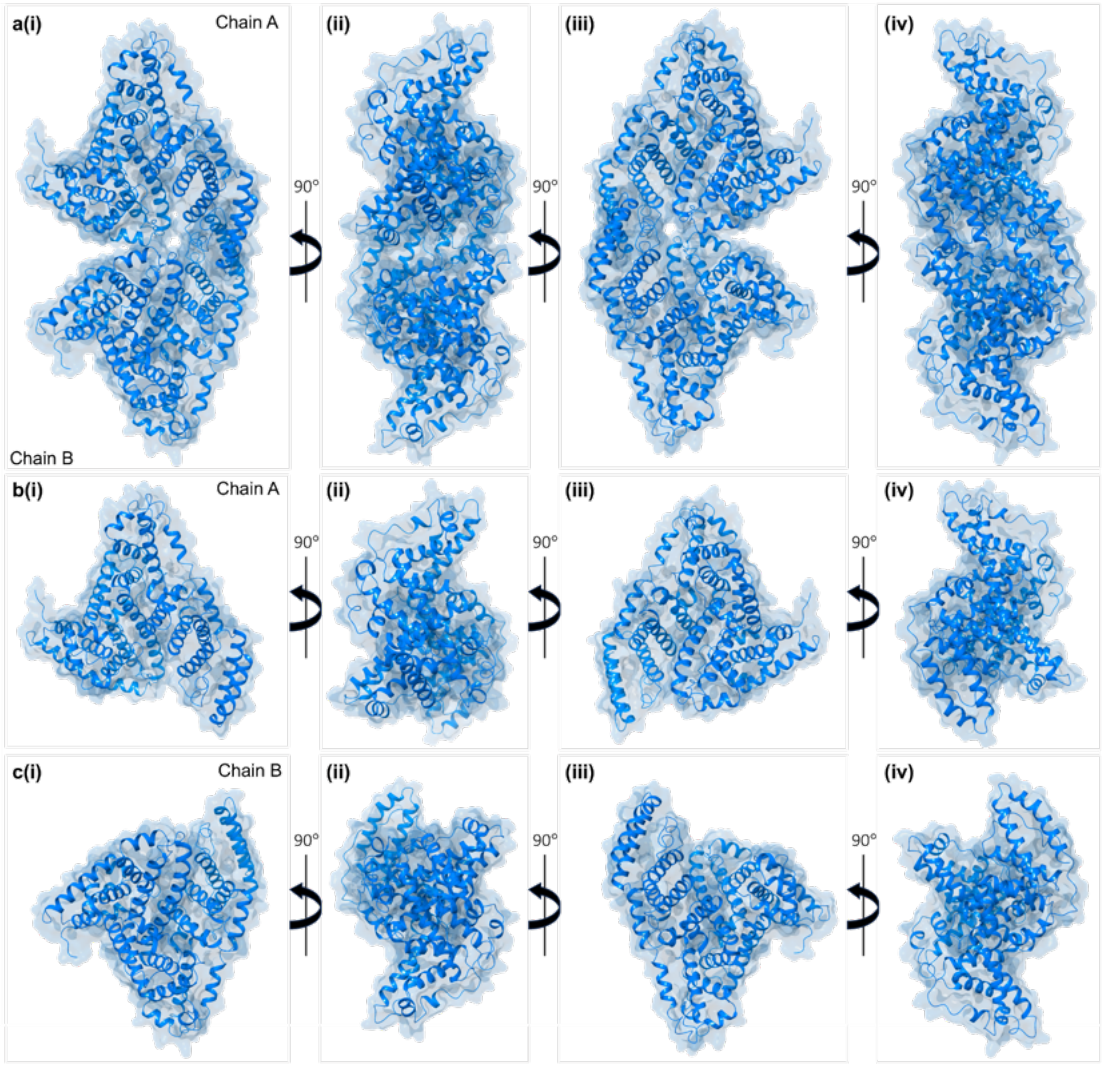

Figure 3.18. (**a**) Ribbon diagram with solid molecular surface (90% transparency) of the **BSA** asymmetric unit with resolution 3.0 Å from the (**i**) front view, (**ii**) side view, (**iii**) back view and (**iv**) side view with unit cell identical to previously reported **BSA** (PDB: 4F5S).[81] (**b**) Ribbon diagram with solid molecular surface (90% transparency) of the **BSA** chain A (residues 1–583) from the (**i**) front view, (**ii**) side view, (**iii**) back view and (**iv**) side view. (**c**) Ribbon diagram with solid molecular surface (90% transparency) of the **BSA** chain B (residues 1–583) from the (**i**) front view, (**ii**) side view, (**iii**) back view and (**iv**) side view.

Irrespective of the promising result to replicate the protein structure of **BSA** with the aforementioned conditions, this proved difficult, inefficient and unreliable. Given these observations, the decision to change approach was taken. An analogous serum albumin, **HSA**, was chosen as a more appropriate choice of protein for screening due to; 1) successful crystals were found to be previously obtained within the Pohl group at Durham BSI; and 2) **HSA** protein also exhibits multiple binding sites to increase the probability of a protein-ligand binding event with small molecule ligands.

3.2.2.2 Crystallisation of Human Serum Albumin

Crystallisation Screening

In the first instance, HSA did not crystallise at all when set up to crystallise alone (HSA screen 1, Tables S3.11–S3.12). In order to improve the quality of crystal growth, thawed HSA was incubated with sodium myristate prior to purification to aid crystallisation – as previously shown by Curry *et al*. in 1998 (PDB entry: 1BJ5).[82] Initially, HSA crystals were observed in sitting drop experiments with set up composition of protein (1 µL), a combination of the reservoir solution (1 µL) and HSA (1 µL) and reservoir solution (2 µL). These initial attempts yielded HSA as hollow rod-like crystals (Figure 3.19a) that were difficult to handle and were deemed unsatisfactory for XRD experiments. In an attempt to obtain better quality crystals, a seeding method[83,84] was investigated (in conjunction with the sitting-drop method), whereby a crystal cluster from initial HSA crystallisation experiments was harvested and diluted to 50 µL with reservoir solution. This solution was vortexed with a seed bead to obtain microcrystals of HSA (see Experimental, screen 3). The aforementioned seed solution was then added to the crystallisation mixture to act as a nucleation site and promote crystal growth (see Experimental, screen 3). It was found that the HSA crystalline additive worked to a good degree, allowing for newly formed HSA crystals of XRD quality to be obtained more reliably on more screening attempts (Figures 3.19b and 3.19c), than previously compared with BSA.

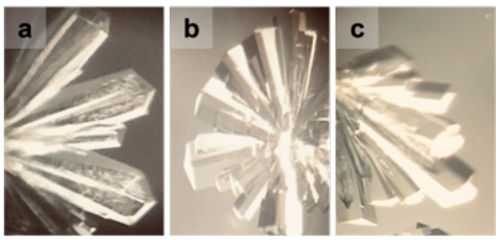

Figure 3.19. (a) HSA–myristate crystal with sodium myristate crystallisation conditions. (b and c) HSA crystal with sodium myristate and seed microcrystal crystallisation conditions.

A data set of myristate bound HSA was collected at DLS, beam line I04, resulting in a HSA structure with resolution 2.1 Å in the triclinic crystallographic space group, P1. The crystal structure was solved and refined in a new crystal form with unit cell dimensions: a = 38.3 Å, b = 87.1 Å, c = 97.5 Å, α = 74.4°, β = 89.8°, γ = 78.6° (see Experimental, Table

S3.22).The model (asymmetric unit) consists of two protein chains (Figure 3.20a), which includes: residues 3–584 in chain A (Figure 3.20b) and residues 2–585 in chain B (Figure 3.20c); three myristate molecules per protein chain; two ethylene glycol polymers (PGE = triethylene glycol in A, PG4 = tetraethylene glycol in B); and 211 water molecules. The final refinement R-value is 0.213 (R_{free} = 0.260). It was apparent there were no obvious interactions at the interface of protein chains A and B, indicating the monomeric nature of the HSA molecule, as opposed to dimeric.

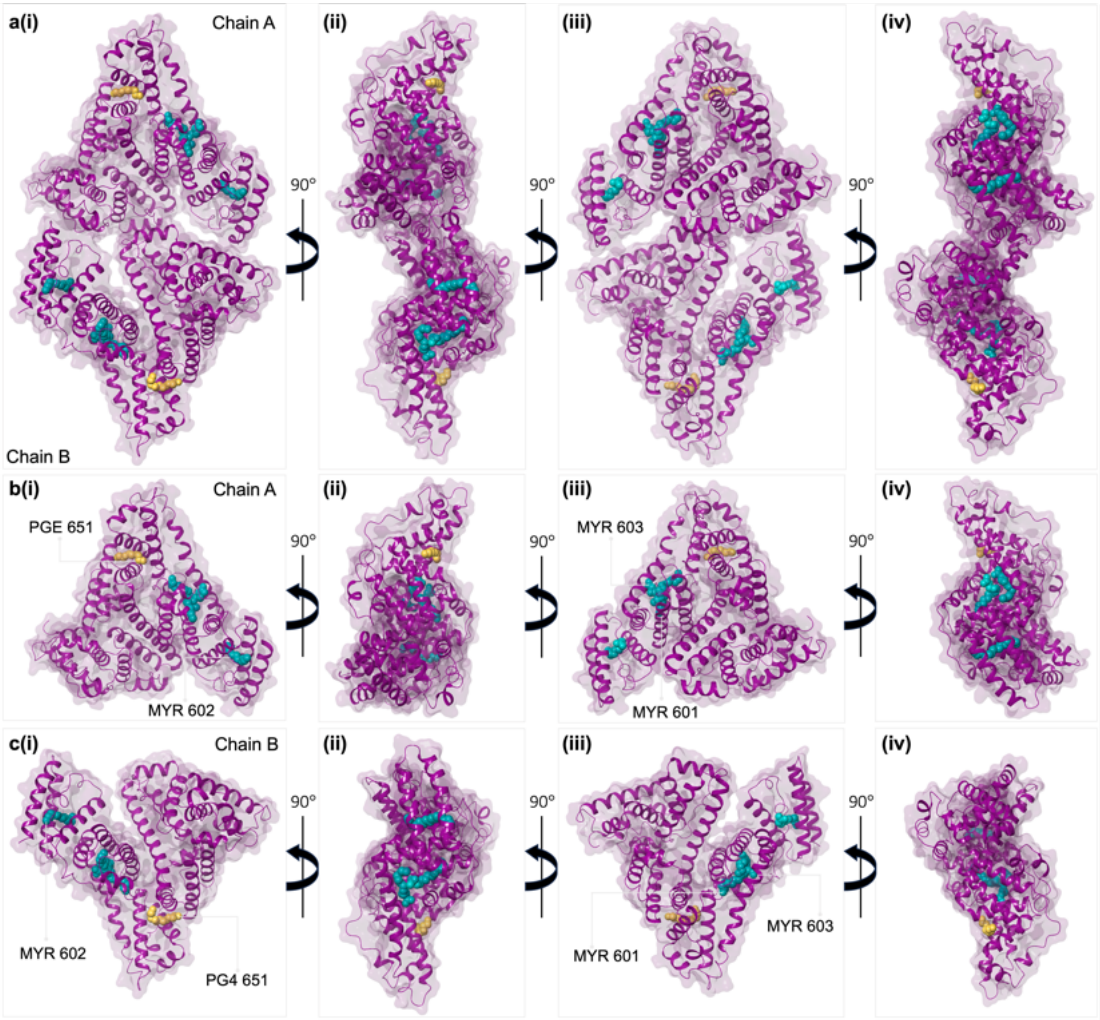

Figure 3.20. (a) Ribbon diagram of the HSA asymmetric unit with resolution 2.1 Å from the (i) front view, (ii) side view, (iii) back view and (iv) side view. The ligands are shown in space-fill representation, where teal = myristate (MYR) and yellow = poly(*n*)glycol (PGE/PG4). (b) Ribbon diagram with solid molecular surface (90% transparency) of the HSA chain A (residues 3–584) from the (i) front view, (ii) side view, (iii) back view and (iv) side view. The ligands are shown in space-fill representation, where teal = MYR601 / MYR 602 / MYR 603 and yellow = PGE 651. (c) Ribbon diagram with solid molecular surface (90% transparency) of the HSA chain B (residues 2–585) from the (i) front view, (ii) side view, (iii) back view and (iv) side view. The

ligands are shown in space-fill representation, where teal = MYR601 / MYR 602 / MYR 603 and yellow = PG4 651.

Henceforth, the ability to more reliably obtain better quality crystals of HSA (compared with BSA) allowed for a more extensive range of ligands to be screened with HSA by co-crystallisation experiments, to investigate protein-ligand binding. Resultantly, an extensive co-crystallisation screen (see Experimental, HSA screens 6 and 7) subjecting a range of BBs and BVs (Figure 3.21) to HSA optimised crystallisation conditions was attempted, utilising the 1) sodium myristate and 2) HSA crystal seeding additives.

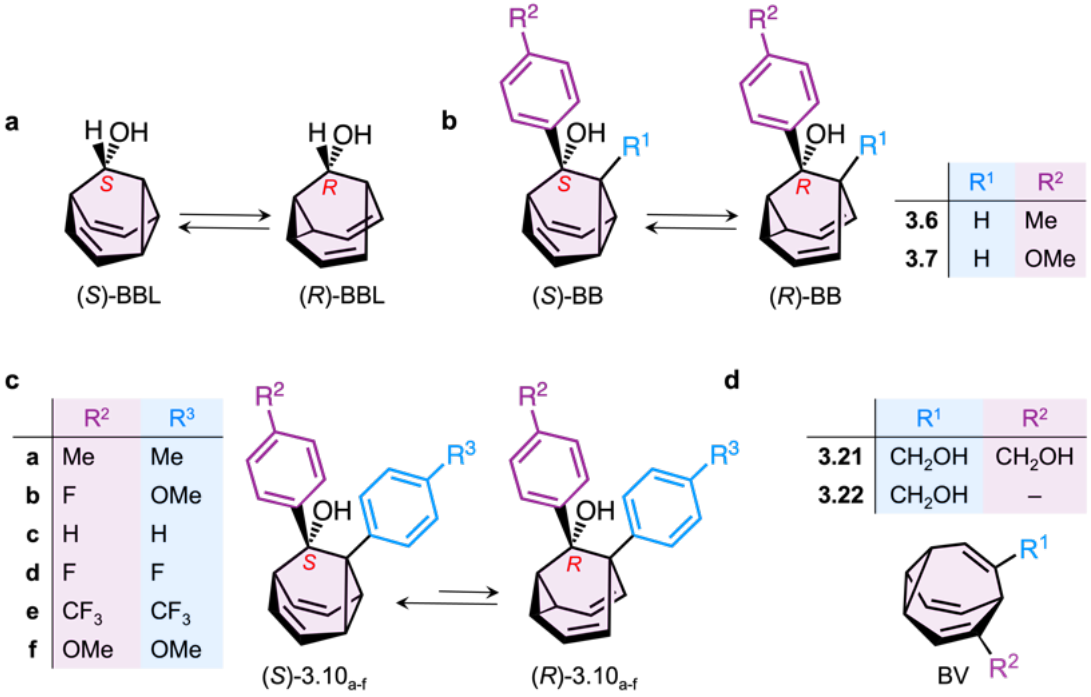

Figure 3.21. Schematic of compounds attempted to be co-crystallised with HSA: (a) BBL, shown as (b) mono-substituted hydroxyl BBs (3.6–3.7), (c) di-substituted hydroxy BBs ($3.10_{a\text{-}f}$), (d) hydroxy BVs (3.21–3.22).

Once HSA–ligand co-crystals had been visually attained (by microscopy, Figure 3.22a), crystals were harvested, mounted in crystallisation loops and frozen in liquid nitrogen in order to successfully transfer to the synchrotron for XRD evaluation at the DLS. A typical example of a co-crystal, mounted in a cryo-loop used for data collection, is shown in Figure 3.22b. The data was then collected at the DLS, beamline I04 – the diffraction image of the aforementioned crystal (Figure 3.22c). From the crystallisation results obtained (see Experimental, HSA screens 6 and 7), crystal data sets with

resolution in the range 2.0 – 5.7 Å were achieved. A total of 20 data sets were obtained with a resolution better than 2.5 Å, which was deemed sufficient to solve the **HSA** protein structure, whilst also being able to distinguish additional electron density of any ligands present within the **HSA** structure.

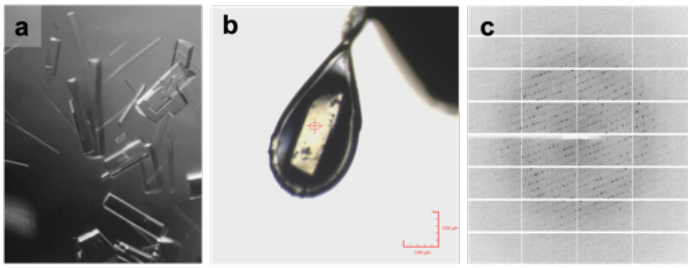

Figure 3.22. (**a**) **HSA-BBL** crystals visualised by microscopy. (**b**) **HSA-BBL** crystal mounted in a cryo-loop for XRD data collection at the I04 beamline, Diamond Light Source (DLS) Beam size (32 µm × 20 µm) and the position is indicated with a red cross and oval. 100 µm scale bars are shown in the bottom right corner. (**c**) The resulting diffraction image collected during crystal screening at a wavelength of 1.8–2.1 Å.

Throughout this crystallographic trial to obtain fluxional carbon cages in SAs, more than 100 crystals have been mounted, whereby more than 30 data sets have been collected. All high-resolution data sets (≤ 3.0 Å) were processed, the structures solved and refined to the point where myristate could be identified within the electron density maps (see Experimental, Protein Crystallography Methods). Initial crystallographic refinement for 9 of the 30 data sets (resolution 1.9–2.7 Å) did not identify any electron density that could be interpreted as a co-crystallised compound. For one data set from a **HSA-BBL** co-crystallisation attempt, the model (asymmetric unit) was solved with resolution 1.9 Å, which consists of two protein chains (Figure 3.23a), which includes: residues 3–583 in chain A (Figure 3.23b) and residues 3–584 in chain B (Figure 3.23c); 4 myristate molecules in chain A and 5 myristate molecules in chain B; two ethylene glycol polymers (PGE = triethylene glycol in A, PG4 = tetraethylene glycol in B); and 214 water molecules (see Experimental, Table S3.22, PDB 9EOS). The final refinement R-value is 0.211 (R_{free} = 0.269). Subsequently, in this one data set (see Experimental, screen 6, entry 1), an F_O-F_C difference electron density map showed three-dimensional density in a mainly hydrophobic cavity (neighbouring residues: S202, F206, A210, F211, W214, V344, L347, L481, V482, MYR901, PEG1402) that could accommodate **BBL** (Figure

3.24a(i)). The molecule was included in the crystallographic refinements with an occupancy of 0.5, indicating that half of the asymmetric units in the crystal have **BBL** in this position.

Additional molecules of myristate, PEG components (from the crystallisation conditions) and water molecules were also identified. The possible electron density indicated that two **BBL** molecules could potentially reside back-to-back in the hydrophobic cavity (Figure 3.24a(ii)). Additionally, the refinement was stable and resulted in reasonable displacement parameters, *B*. This refinement resulted in a $2F_O$-F_C electron density map, where no electron density for **BBL** in this position was found, indicating that the occupancy was far lower than 0.5. Unfortunately, even co-crystallisation experiments at higher **BBL** concentrations (see Experimental, screen 8, entry 1) did not result in crystals and data sets with protein-ligand complexation.

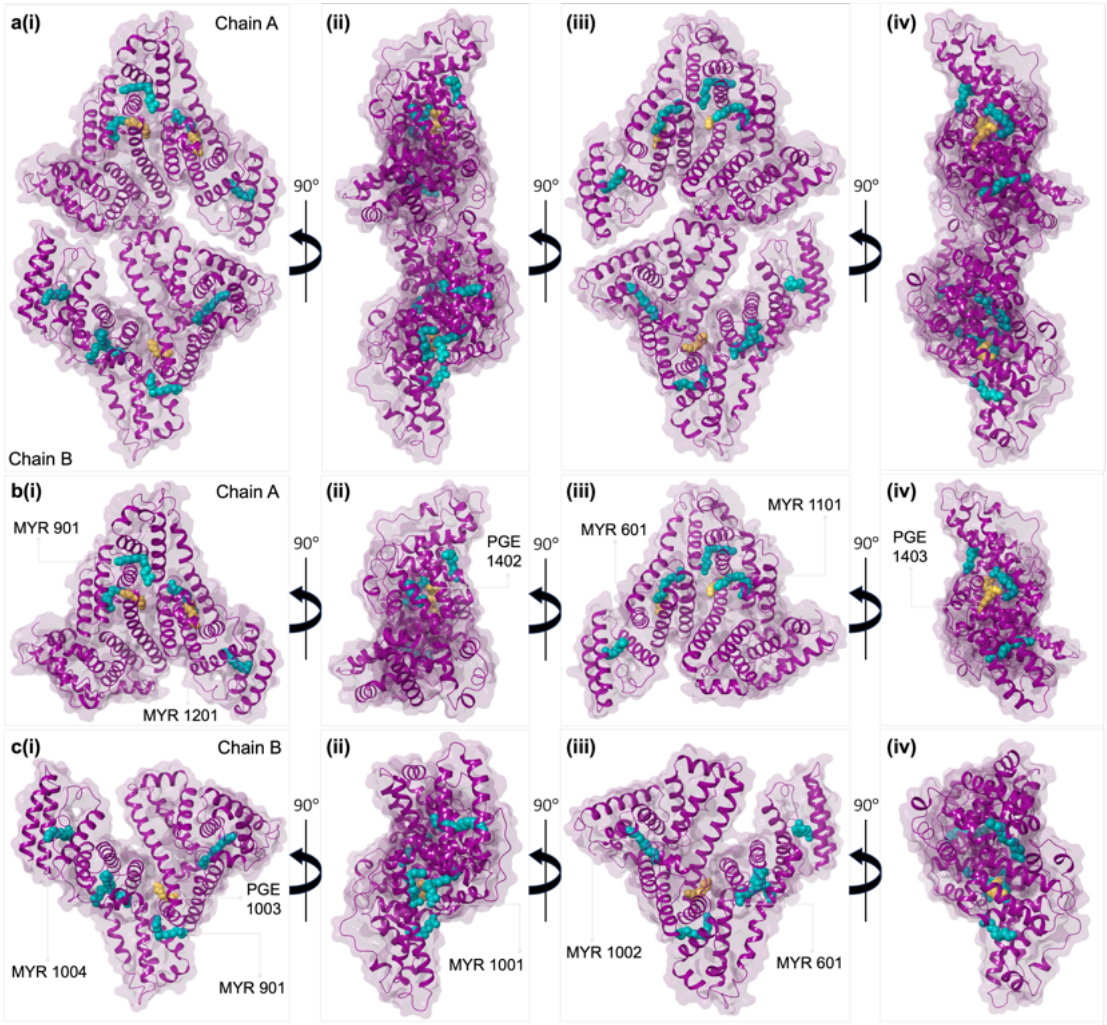

Figure 3.23. (**a**) Ribbon diagram of the **HSA** asymmetric unit with resolution 1.9 Å from the (**i**) front view, (**ii**) side view, (**iii**) back view and (**iv**) side view. The ligands are shown in space-fill representation, where teal = myristate (MYR) and yellow = poly(*n*)glycol (PGE). (**b**) Ribbon diagram with solid molecular surface (90% transparency) of the **HSA** chain A (residues 3–583) from the (**i**) front view, (**ii**) side view, (**iii**) back view and (**iv**) side view. The ligands are shown in space-fill representation, where teal = MYR 601 / MYR 901 / MYR 1101 / MYR 1201 and yellow = PGE 1402 / PGE 1403. (**c**) Ribbon diagram with solid molecular surface (90% transparency) of the **HSA** chain B (residues 3–584) from the (**i**) front view, (**ii**) side view, (**iii**) back view and (**iv**) side view. The ligands are shown in space-fill representation, where teal = MYR 601 / MYR 901 / MYR 1001 / MYR 1002 / MYR 1004 and yellow = PGE 1003.

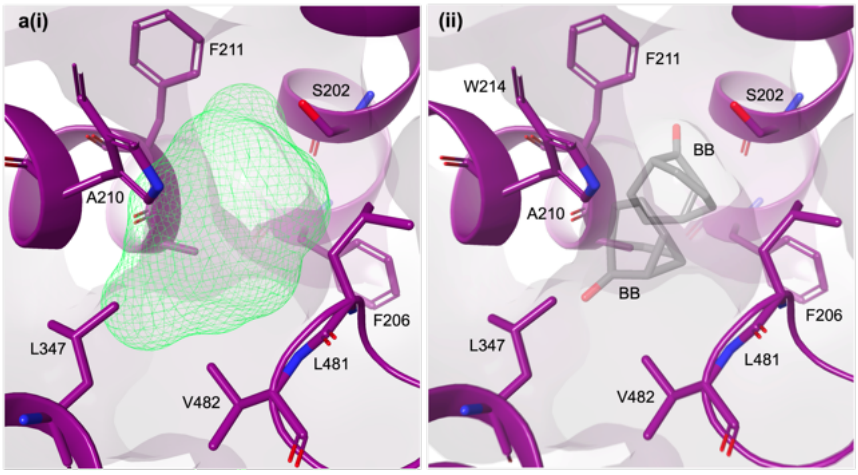

Figure 3.24. (a) Close-up view of the proposed back-to-back **HSA-BB** binding site. Side chains are shown with cylinder representation, O atoms (red), N atoms (blue). **BB** is shown in tube representation with electron density shown in mesh representation (green). The **HSA-BB** binding site, showing **BB** residing in the hydrophobic cavity (neighbouring residues: S202, S206, A210, F211, W214, L347, L481, V482) from the perspective of (**i**) electron density at 100% occupancy and (**ii**) proposed orientation of **BBs** in the hydrophobic cavity.

3.2.2.3 Co-Crystallisation of Human Serum Albumin and Isosteric Compound

Given the unsuccessful co-crystallisations of SAs with shapeshifting ligands, isosteric compounds were sought to test for further co-crystallisations, in order to troubleshoot why co-crystals were not obtained. Adamantane (**Ad**) is isosteric to **BB** and **BV**, therefore commercially available **Ad** compounds were pursued. **Ad** has been of particular interest in organic chemistry due to its rigid yet strain-free ring system and structural symmetry. **Ad** has a rigid tricyclo[3.3.1.1^{3,7}]decane skeleton composed of three fused chair cyclohexane rings (Figure 3.25) and is the smallest homologue of the diamondoid series.[85]

Figure 3.25. Structural representation of tricyclo[3.3.1.1^{3,7}]decane, commonly known as adamantane (**Ad**).

The structure-property relationship of the adamantane moiety has been taken into consideration upon optimising the physiochemical profile of a compound towards protein targets. The most significant physiochemical property that the **Ad** moiety

exhibits is its high lipophilicity. This characteristic – included in the well-established Lipinski's rules[86] – is considered the most important physical property for compounds when studied in regards to water solubility and oral bioavailability. The lipophilic value is described as the logarithm of the partition coefficient (LogP) between two non-miscible solvents, commonly measured in a water-*n*-octanol phase system.[87] The greater the LogP value, the greater the lipophilicity – where in drug discovery, a value of LogP > 5 is generally considered too high.[88] In almost all cases, compounds bearing the **Ad** moiety will be more lipophilic than those lacking it,[89] whilst also exhibiting lower LogP values compared to linear constitutional isomers (Figure 3.26). Noteworthily, compared to the close lateral packing of linear decane in solution, **Ad**-based molecules present interstitial space in solution, increasing the propensity towards solvation. As a result, the **Ad** group presents superior aqueous solubility properties for medicinal chemistry reasons compared with linear undecanoic acid (**3.25**).[89]

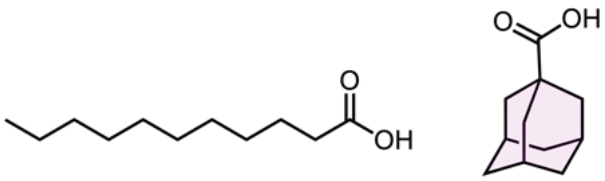

Figure 3.26. LogP values of linear undecanoic acid (**3.25**) and adamantyl-1-carboxylic acid (**3.26**).[89]

In order to verify that isosteric cage-like structures could bind to **HSA**, ad-1-carboxylic acid (**3.26**) was chosen as a suitable non-fluxional ligand to test with **HSA** for binding. The purification of myristate-doped **HSA** and crystallisation was conducted, with the addition of ad-1-carboxylic acid (**3.26**) in sitting-drop crystallisation experiments. A data set of rod-shaped crystals was collected to a resolution of 1.9 Å in the monoclinic crystallographic space group I2. Subsequently, the crystal structure was solved and refined in a new crystal form with unit cell dimensions: a = 174.86 Å, b = 38.13 Å, c = 190.97 Å, α = 90°, β = 106.15°, γ = 90°. The model (asymmetric unit) consisted of 2 protein chains (Figure 3.27a) comprising of: residues 4–584 in chain A (Figure 3.27b); residues 3–584 in chain B (Figure 3.27c); 2 myristate molecules per protein; 5 PEG molecules, 1 molecule of ad-1-carboxylic acid (**3.26**) bound in chain A and B (occupancy

0.75) and an extra disordered molecule in chain B; and 250 water molecules see Experimental, Table S3.22, PDB 9EOD). The final refinement R-value = 0.217 (R_{free} = 0.268). Similarly to the previous **HSA** refinement, it was apparent there were no obvious interactions at the interface of protein chains A and B, indicating the monomeric nature of the **HSA** molecule, as opposed to dimeric. Ad-1-carboxylic acid (**3.26**) was found to be located in a pocket surrounded by two arginine (R117, R186) and tyrosine (Y138, Y161), coordinated by an arginine residue (R117) and a well-defined water molecule (Figures 3.28a(i) and 3.28a(ii)).

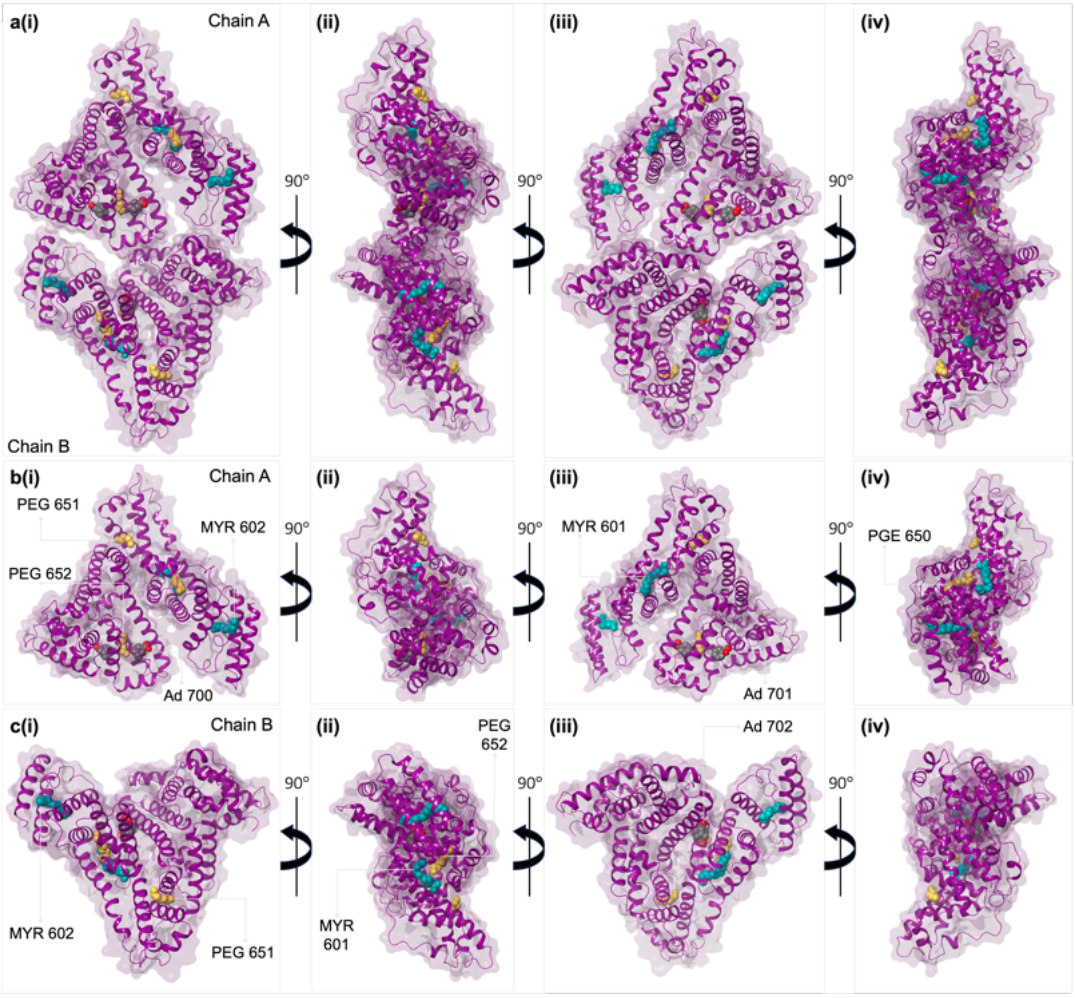

Figure 3.27. (**a**) Ribbon diagram with solid molecular surface (90% transparency) of the **HSA-Ad** asymmetric unit with resolution 1.9 Å from the (**i**) front view, (**ii**) side view, (**iii**) back view and (**iv**) side view. The ligands are shown in space-fill representation, where teal = myristate (MYR) and yellow = poly(*n*)glycol (PGE/PEG). (**b**) Ribbon diagram with solid molecular surface (90% transparency) of the **HSA** chain A (residues 4–584) from the (**i**) front view, (**ii**) side view, (**iii**) back view and (**iv**) side view. The ligands are shown in space-fill representation, where teal

= MYR 601 / MYR 602, yellow = PGE 650 / PEG 651 / PEG 652. (c) Ribbon diagram with solid molecular surface (90% transparency) of the HSA chain B (residues 3–584) from the (i) front view, (ii) side view, (iii) back view and (iv) side view. The ligands are shown in space-fill representation, where teal = MYR 601 / MYR 602 and yellow = PEG 651 / PEG 652. Ad-1-carboxylic acid (3.26) is shown in space-fill representation, where grey = carbon and red = oxygen in all cases.

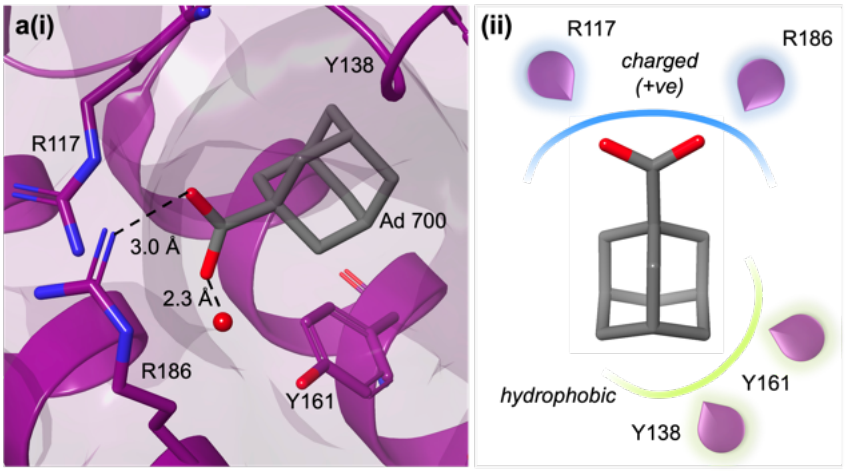

Figure 3.28. (a)(i) Close-up view of the HSA-Ad binding site of the Ad 700 (3.26) ligand in HSA chain A. Distances in Å are indicated with dashed lines; side chains are shown with cylinder representation, O atoms (red), N atoms (blue); ad-1-carboxylic acid is shown in tube representation. The binding site shows Ad 700 (3.26) coordination to the R117 residue and a water molecule; the coordinated water molecule is shown as a red sphere. (ii) HSA-Ad binding site schematic highlighting the R117/R186 residues (positively charged region) and the Y138/R161 residues (hydrophobic region) of the binding pocket.

3.2.3 Synthesis Towards Water Soluble Bullvalenes

As a result of the limited success of obtaining a SA-ligand co-crystal, the synthesis of alternate shapeshifting ligands, which could possibly display greater solubility in an aqueous solution, was attempted. Therefore, the initial target was to synthesise a BV derivative with a tetraethyleneglycol (TEG) monomethyl ether substituent as this was thought to increase aqueous solubility, based on previously reports of the use of polyethylene glycols to aid water solubility in biological applications.[90–94] First, TEG (3.27) was treated with one equivalent of sodium hydride, followed by the subsequent addition of iodomethane in anhydrous THF and was stirred at 60 °C for 24 hours to yield the Me-TEG (3.28) in 75% yield (Scheme 3.15).

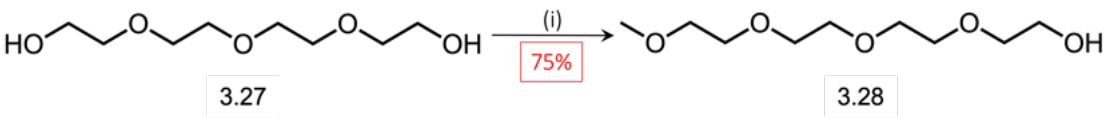

Scheme 3.15. Synthetic route to Me-TEG (**3.28**) from TEG (**3.27**). Reagents and Conditions: (i) NaH, then MeI / THF / 24 h / 60 °C / 75%.

The Me-TEG was then treated with *p*-TsCl, providing the installation of a Ts group, which acts as a good leaving group, onto the terminal hydroxy group of the Me-TEG (**3.28**) to form Me-TEG-OTs (**3.29**) (Scheme 3.16). The installation of the Ts group primed the TEG moiety for nucleophilic substitution on to the hydroxymethylene **BV** (**3.22**).

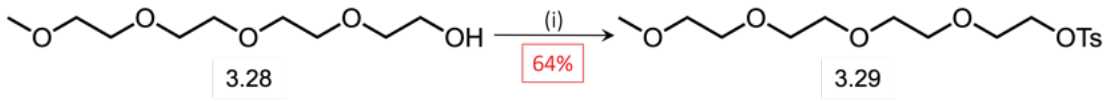

Scheme 3.16. Synthetic route to Me-TEG-OTs (**3.29**) from Me-TEG (**3.28**). Reagents and Conditions: (i) *p*-TsCl, then KOH / Et_2O / 24 h / rt.

Following the synthesis of Me-TEG-OTs (**3.29**), hydroxymethylene **BV** (**3.22**) was treated with 1.2 equivalents of sodium hydride at 0 °C, followed by the addition of compound **3.29** and allowed to warm to room temperature over 24 hours (Scheme 3.17). The desired product mass was not detected by mass spectrometry. Subsequently, the reaction was repeated with a range of conditions as detailed in Table 3.4, varying the solvent and amount of sodium hydride. The repeat reactions showed no formation of the desired product, possibly due to insufficient deprotonation of the **BV** hydroxy group to promote effective substitution.

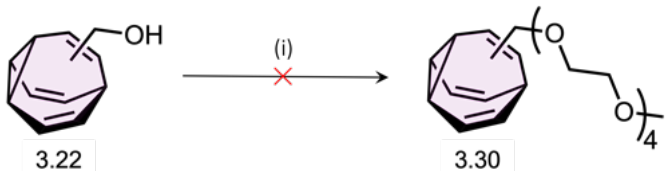

Scheme 3.17. Attempted synthesis of TEG **BV** (**3.30**) from hydroxymethylene **BV** (**3.22**) and Me-TEG-OTs (**3.29**). Reagents and Conditions: (i) NaH, then Me-TEG-OTs (**3.29**) / solvent / 24 h / 0 °C → rt.

Table 3.4. Reaction screen for the attempted synthesis of TEG **BV** (**3.30**). No product = NP.

Reaction Entry[a]	Solvent	NaH / eq.	Result[b]
1	THF	1.2	NP
2	THF	2.0	NP
3	MeOH	1.2	NP
4	MeOH	2.0	NP

[a]Conditions: NaH / Me-TEG-OTs (1.2 eq.) / solvent / 24 h / 0 °C → rt; [b]Analysed by mass spectrometry.

3.2.3.1 Amino Acid Appended Bullvalenes Approach

The installation of an amino acid (AA) moiety onto the **BV** core served as an attractive proposition, owing to the zwitterionic nature of the AA moiety. AAs can undergo an intramolecular acid-base reaction. Since the molecule contains both a basic amine group (H_2N) and an acidic carboxylic acid group (CO_2H), there is the ability for an internal proton transfer from the CO_2H group to the H_2N group. The resulting $^{+}H_3NCH(R)CO_2^{-}$ ion contains both a positive and negative charge, so is termed a zwitterion, meaning AAs can form ionic interactions with the surrounding water in aqueous environments. The extent of AA solubility in water can vary depending on the chemical nature of the variable (R) group.[95] With this idea in mind, the plan was to install an AA *via* the previously reported cobalt(II)-catalysed cycloaddition of **COT** with an alkyne. This methodology was not deemed unreasonable since it appeared that the terminal alkyne would not be sterically restricted within the amino acid once obtained.

Based on previous successful syntheses of AA alkynes,[96] Boc-G (**3.31**) was treated with potassium carbonate in anhydrous DMF, which was then subjected to propargyl bromide to obtain the corresponding propargylic Boc-G (**3.35**) in 75% yield. This procedure was repeated from the commercially available Boc-AA reagents (3.32–3.34) to form the propargylic Boc-A (**3.36**), Boc-L (**3.37**) and Boc-P (**3.38**) respectively, as detailed in Scheme 3.18.

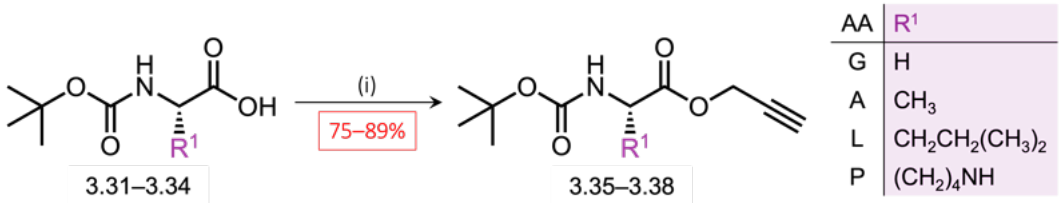

Scheme 3.18. Synthetic route to propargylic Boc-AAs (**3.35**–**3.38**). Conditions and reagents: (i) propargyl bromide then K_2CO_3 / DMF / 24 h / 70 °C. AAs have L stereochemistry, excluding G.

The AA alkynes (**3.35**–**3.38**) were then subjected to cobalt(II)-catalysed cycloaddition reaction conditions in an attempt to form the corresponding AA-appended **BDT**s (**3.39**–**3.42**) (Scheme 3.19). Mass spectrometry, however, showed that the mass of the desired **BDT** was not detected, with only starting material remaining. The reaction was repeated subjecting only propargylic Boc-G (**3.35**) to the same conditions, varying solvent and temperature (Table 3.5). The G AA exhibits the smallest variable group from the four AAs synthesised, decreasing the steric barrier to cobalt coordination with the alkyne. Unfortunately, no **BDT** signals were present in any of these conditions. The outcome of these experiments may be explained by the steric bulk of the Boc group, which may have contributed to insufficient alkyne coordination to the cobalt, therefore preventing the cycloaddition reaction from occurring.

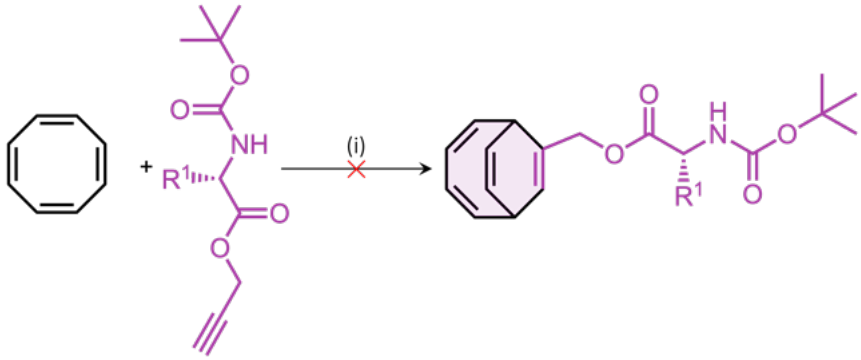

COT | **3.35–3.38** | **3.39–3.42**

Scheme 3.19. Attempted synthetic route to form Boc-AA **BDT**s (**3.39**–**3.42**) from propargylic Boc-AAs (**3.35**–**3.38**) and **COT**. Conditions: (i) $CoBr_2$(dppe) / Zn / ZnI_2 5:15:10 mol% ratio / solvent / 48 h / T °C. R^1 = variable group.

Table 3.5. Reaction screen for the attempted synthesis of amino acid **BDT**. No product = NP.

Reaction Entry[a]	Amino Acid	Solvent	Temperature / °C	Result[b]
1	G	TFE	55	NP
2	A	TFE	55	NP
3	L	TFE	55	NP
4	P	TFE	55	NP
5	G	TFE	70	NP
6	G	DCE	40	NP
7	G	DCE	50	NP

[a]Conditions: Cobalt catalyst (5 mol%) / ZnI_2 (10 mol%) / Zn dust (15 mol%) / 48 h; [b]Analysed by MS.

3.2.3.2 Bullvalene Salt Approach

The synthesis of **BV** salts was also pursued given that these were likely to be soluble in water, and therefore provide suitable solubility for co-crystallisation experiments with protein species in aqueous buffer.

First a sulfonate-appended **BV** was pursued. For the synthesis of the mono sulfonate alkyne, propargyl bromide was added to a methanol/water mixture, followed by the addition of sodium sulfite and stirred at 65 °C for 14 hours, yielding the prop-2-yne-1-sulfonate (**3.43**) species, in an albeit moderate 38% yield (Scheme 3.20).

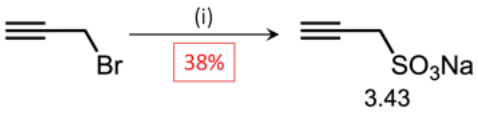

Scheme 3.20. Synthetic route to propargyl sodium sulfite (**3.43**) from propargyl bromide. Reagents and Conditions: (i) Na_2SO_3 / MeOH:H_2O / 18 h / 65 °C / 38%.

Similarly, an ammonium containing **BV** was pursued. Triethylammonium alkyne (**3.44**) was synthesised by the addition of triethylamine to propargyl bromide and stirred at room temperature for 15 minutes, yielding the compound **3.44** in an excellent 93% yield (Scheme 3.21). The salt 2-carboxy-*N,N,N*-trimethylethan-1-ammonium bromide (**3.45**) was also prepared (Scheme 3.22), however, the subsequent installation of a propargylic group was not carried out until cycloaddition reactions with other propargylic salts had been attempted.

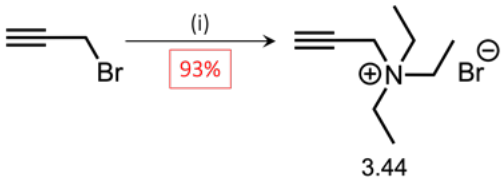

Scheme 3.21. Synthetic route to the triethylammonium alkyne (**3.44**) from propargyl bromide. Reagents and Conditions: (i) Et_3N; CH_2Cl_2 / 15 min / rt / 93%.

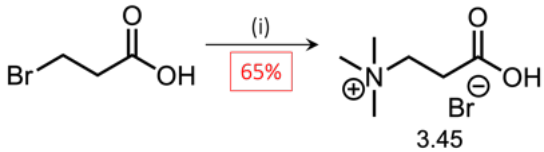

Scheme 3.22. Synthetic route to the 2-carboxy-*N,N,N*-trimethylethan-1-ammonium bromide (**3.45**) from 3-bromopropanoic acid. Reagents and Conditions: (i) Me_3N / EtOH / 3 d / rt / 65%.

The two synthesised propargylic salts (**3.43** and **3.44**) were then subjected to a formal [6+2] cobalt(II)-catalysed cycloaddition with **COT**. The desired product masses of **3.46** and **3.47** were not detected by mass spectrometry (Scheme 3.23). This may explained by solubility issues of the propargylic salts in TFE, the solvent of the cycloaddition. The cycloaddition was not explored with the typical alternative solvent for this cycloaddition reaction, namely DCE.

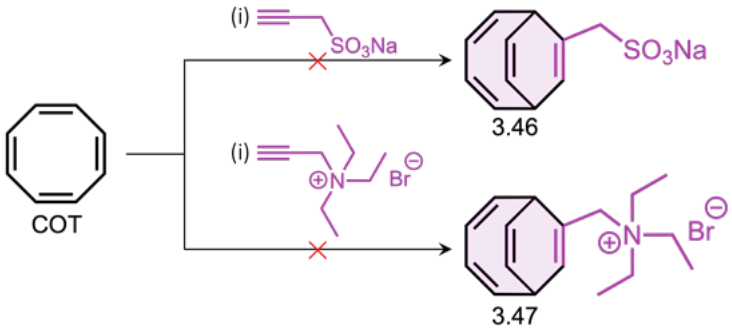

Scheme 3.23. Attempted synthetic route to **BDT** salts (**3.46** and **3.47**) from **COT** and the respective propargylic salt (**3.43** and **3.44**). Conditions: (i) $CoBr_2$(dppe) (5 mol%) / ZnI_2 (10 mol%) / Zn dust (15 mol%) / TFE / 48 h / 55 °C; Analysed by ^{1}H NMR spectroscopy and MS.

3.2.3.3 Carboxylic Acid Bullvalene Approach

Following the co-crystallisation result, obtaining a co-crystal structure of 1-Ad carboxylic acid (**3.26**) with **HSA**, the synthetic strategy was to produce a **BV** containing a carboxylic acid moiety, as this would serve as a good comparison. As such, commercially available carboxylic acid alkynes were subjected to cobalt(II)-catalysed cycloaddition conditions, in an attempt to directly install carboxylic acid groups onto the **BDT** framework, whilst also avoiding tricky post-functionalisation. Thus, the propargylic carboxylic acids: 1) propiolic acid, 2) 4-pentynoic acid and 3) 2-butynoic acid were examined under these conditions, as detailed in Table 3.6. The apparent failure of these cycloaddition reactions to produce **BDTs 3.48**, **3.49** and **3.50** (Scheme 3.24) is not known, however, given that the insights from previous failed reactions of this type point towards steric bulk preventing catalyst coordination. It is possible that the carboxylic acid group presented may not be compatible with the metal-containing reaction mixture required for catalysis of the cycloaddition reaction. This explanation, however, seems unlikely given that two of the three carboxylic acids are propargylic,

thus do not present any steric hindrance to the terminal alkyne. It may also be possible that an alternative coordination mechanism, involving the carboxylic acid moiety can occur, thus preventing the desired coordination for the cycloaddition reaction to proceed.

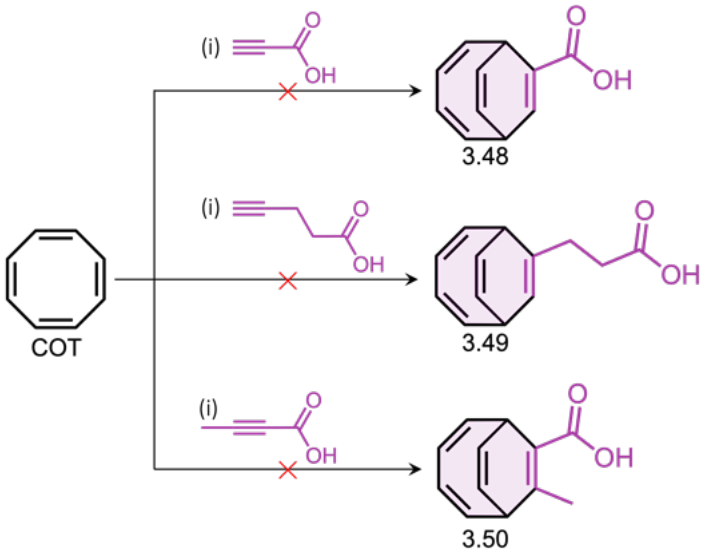

Scheme 3.24. Attempted synthetic route to **BDTs** (**3.48**, **3.49** and **3.50**) from **COT** and the respective alkyne carboxylic acids. Conditions: (i) $CoBr_2$(dppe) (5 mol%) / ZnI_2 (10 mol%) / Zn dust (15 mol%) / solvent / 48 h / T °C.

Table 3.6. Reaction screen for the attempted synthesis of carboxylic acid **BDTs**. Starting material = SM.

Reaction Entry[a]	Alkyne Substrate	Reaction Solvent	Temperature / °C	Scale / mg	Result[b]
1	propiolic acid	TFE	55	100	SM
2	propiolic acid	TFE	55	250	SM
3	propiolic acid	TFE	55	500	SM
4	4-pentynoic acid	TFE	55	100	SM
5	4-pentynoic acid	TFE	55	250	SM
6	4-pentynoic acid	TFE	55	500	SM
7	propiolic acid	DCE	40	250	SM
8	propiolic acid	DCE	50	250	SM
9	4-pentynoic acid	DCE	40	250	SM
10	4-pentynoic acid	DCE	50	250	SM
11	2-butynoic acid	TFE	55	100	SM

[a]Conditions: (i) $CoBr_2$(dppe) (5 mol%) / ZnI_2 (10 mol%) / Zn dust (15 mol%) / solvent / 48 h / T °C; [b]Analysed by ^{1}H NMR spectroscopy and MS.

Given the aforementioned failure with regards to installing terminal carboxylic acid alkynes within the **BDT** structure, an alternate route was attempted to circumnavigate any compatibility issues with carboxylic acid alkynes by using ester-containing alkynes.

This route gave the possibility of base hydrolysis of the ester functionality following the cycloaddition, which would allow access to **BDT** carboxylic acids. Therefore, diethylacetylenedicarboxylate (**3.51**) was selected as a suitable ester alkyne for this investigation. Thus, diethylacetylenedicarboxylate (**3.51**) was subjected to cycloaddition conditions with **COT** in an attempt to form the diester-containing **BDT** (**3.52**) (Scheme 3.25). The reaction was only performed in DCE due to suitable solubility of the diester alkyne starting material. Preliminary tests to dissolve the starting material in TFE resulted in only partial dissolution, so this was not taken forward to full set-up.

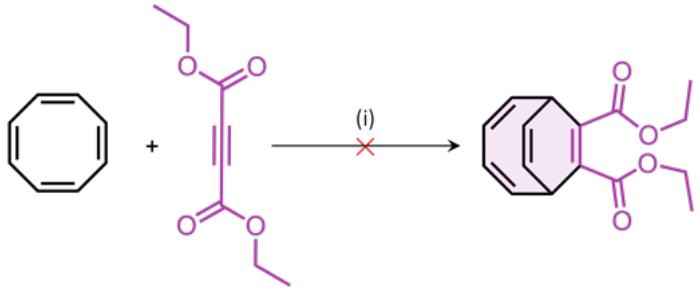

Scheme 3.25. Attempted synthetic route to diester **BDT** (**3.52**) from **COT** and diethylacetylenedicarboxylate (**3.51**). Conditions: (i) $CoBr_2$(dppe) (5 mol%) / ZnI_2 (10 mol%) / Zn dust (15 mol%) / DCE / 48 h / 40 °C.

Given the aforementioned attempts to directly form a **BDT** carboxylic acid derivative by the routes stated, post functionalisation to the hydroxy moiety(s) of a **BDT** was proposed. First, bis(hydroxymethylene) diol (**3.12**) was subjected to Jones oxidation[97] reaction conditions (Scheme 3.26) with the aim of transforming both diol groups to carboxylic acids.

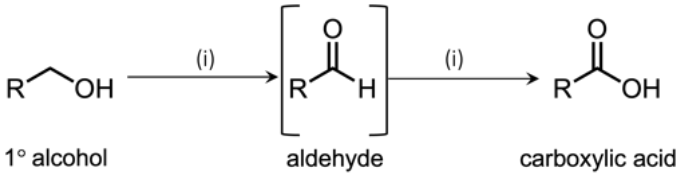

Scheme 3.26. General scheme for the Jones oxidation of primary alcohols, to form aldehydes and carboxylic acids. Conditions: (i) CrO_3 or $Cr_2O_7^{2-}$ acid / H_2O / $(CH_3)_2CO$.

Therefore, the Jones oxidant was prepared by dissolving CrO_3 (2.5 g) in concentrated H_2SO_4 (5 mL), which was then diluted in water (5 mL). This resulted in incomplete dissolution, so was diluted further until observing complete dissolution (15 mL in total).

For the first attempt, Jones oxidant was added dropwise to a vigorously stirred solution of *bis*(hydroxymethylene) **BDT** (**3.12**) dissolved in $(CH_3)_2CO$ at 0 °C. This resulted in a clear colour change from a transparent yellow solution to a translucent light brown solution. Following stirring for a further 1 hour, allowing to warm to room temperature and post work up, MS established the absence of any of the desired **BDT** dicarboxylic acid product (**3.53**) (Scheme 3.27). In a second attempt, a greater quantity of Jones oxidant was added, as such to maintain the orange colour of the reagent in the reaction mixture. Yet again, MS established the absence of any of the desired **BDT** dicarboxylic acid product.

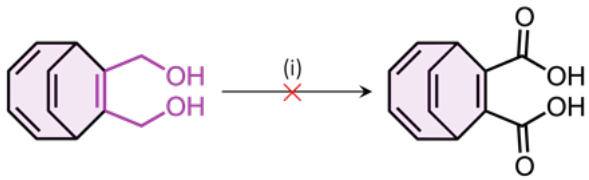

3.12 3.53

Scheme 3.27. Attempted synthetic route to dicarboxylic acid **BDT** (**3.53**) by Jones oxidation of *bis*(hydroxymethylene) diol (**3.12**). Reagents and conditions: (i) CrO_3 (dissolved in H_2SO_4 / H_2O); acetone / 1 h / 0 °C → rt.

The Jones oxidation was also attempted on an analogous hydroxyethylene **BDT** (**3.20**) due to the proposition that the extended ethylene linker between the hydroxy group and **BDT** core may allow for better conversion to the carboxylic acid (Scheme 3.28). Analysis by MS and ^{1}H NMR spectroscopy, however, demonstrated that no **BDT** oxidation product (**3.54**) had formed.

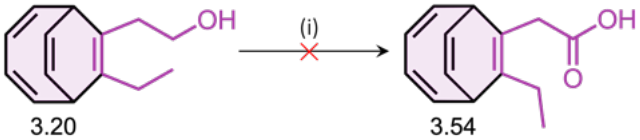

3.20 3.54

Scheme 3.28. Attempted synthetic route to carboxylic acid **BDT** (**3.54**) by Jones oxidation of hydroxyethylene **BDT** (**3.20**). Reagents and conditions: (i) CrO_3 (dissolved in H_2SO_4 / H_2O); acetone / 1 h / 0 °C → rt.

Following the attempted Jones oxidation, an alternate route using pyridinium dichromate (PDC)[98] was attempted. The hydroxyethylene **BDT** (**3.20**) was subjected to oxidation conditions with 2.0 equivalents of PDC and the reaction mixture was stirred in DMF for 72 h at 80 °C (Scheme 3.29). Promisingly, the crude reaction mixture showed the presence of the product *via* MS, whilst ^{1}H NMR spectroscopy also indicated

a transformation had occurred, with the emergence of new peaks in the region δ 9.90–10.35 ppm. These peaks, however, were sharp and not indicative of typically broad (or not distinguishable from the base line) carboxylic acid proton peaks. Also, the emergence of a new ^{13}C signal at δ 188 ppm was another indication that a carboxylic acid group may have formed. A change in retention factor, however, was not observed *via* TLC, nor was the appearance of any other product spot observed. Still, purification by flash column chromatography (hexanes–EtOAc, 0–25%) was attempted, to which successful isolation of the carboxylic **BDT** (**3.54**) was not achieved, and the purification yielded predominantly the starting material and other by-products that could not be identified. This reaction was repeated once more with 3.0 equivalents of PDC in order to achieve complete oxidation of the **BDT** hydroxy group, however, the same outcome was reached as previously described.

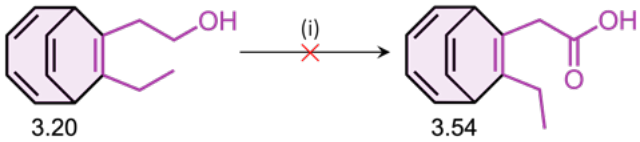

Scheme 3.29. Attempted synthetic route to carboxylic acid **BDT** (**3.54**) by PDC oxidation of hydroxyethylene **BDT** (**3.20**). Reagents and conditions: (i) PDC; anhydrous DMF / 72 h / 80 °C.

Summary of Serum Albumin Studies

In summary, following the synthesis of the aforementioned **BB** and **BV** compounds for use in SA studies, the absence of any conclusive binding with a SA host through X-ray crystallography experiments was identified. Consequently, the decision was taken to identify a new target biomolecule, that would present greater suitability towards obtaining a protein-ligand complex. This direction aims to provide evidence of noncovalent biosupramolecular control of shapeshifting equilibria.

3.2.4 Lysozyme Crystallisation Studies

With the attempted crystallisation of shapeshifting ligands proving unsuccessful within SAs, the decision was made to synthesise targeted **BVs** with warheads that could induce ligand-targeted binding to Lysozyme. Native hen-egg white Lysozyme was selected as an ideal biosupramolecular host as it has been: 1) structure has been extensively characterised and 2) its efficient and reproducible crystallisation.

Since Lysozyme was identified as a suitable protein for crystallisation, a Lysozyme-specific warhead was required for incorporation into a **BV**-containing molecule. Therefore, the Lysozyme-specific substrate inhibitor, GlcNAc, was selected, with the aim of initiating complementary binding to the Lysozyme active site. Based on findings published by Moses and co-workers in 2023,[62] where alkyne appended **BVs** were synthesised to form **BV** vancomycin dimers, similar methodology was used in order to form a GlcNAc containing **BV**. With the fundamental goal to co-crystallise the carbohydrate-appended **BV** within Lysozyme, the design process pointed towards exploiting a hetero-disubstituted **BV** because this would allow for: 1) thirty possible constitutional isomers; and 2) two appended substituents, potentially allowing for the crystal structure of any given **BV** isomer to be more easily distinguished and refined from other possible accessible **BV** isomers, in the solid state by XRD (Scheme 3.30).

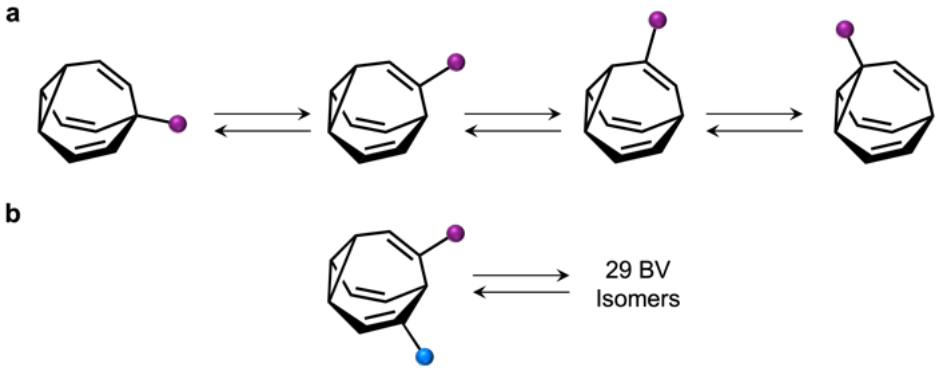

Scheme 3.30. (**a**) mono-substituted **BV** that can access only 4 constitutional isomers; (**b**) hetero-disubstituted **BV** that can access 30 constitutional isomers within the isomer population in solution. The design of a hetero-disubstituted **BV** may allow for the crystal structure of any given **BV** isomer to be more easily distinguished. The magenta and blue circles represent a functional group.

3.2.4.1 Synthesis of a Carbohydrate-Appended Bullvalene

Building upon the synthesis performed from previous investigations, therefore with the hydroxyethylene **BDT** (**3.20**) in hand, alkyne functionality was installed onto the terminal alcohol through the sequential treatment with 1) sodium hydride; and then 2) propargyl bromide. This transformation resulted in the formation of **BDT** alkyne (**3.55**) in a moderate 42% yield (Scheme 3.31). The resulting **BDT** alkyne was then subjected to 365 nm irradiation to achieve photochemical isomerisation, yielding the **BV** alkyne (**3.56**) in 30% yield (Scheme 3.31).

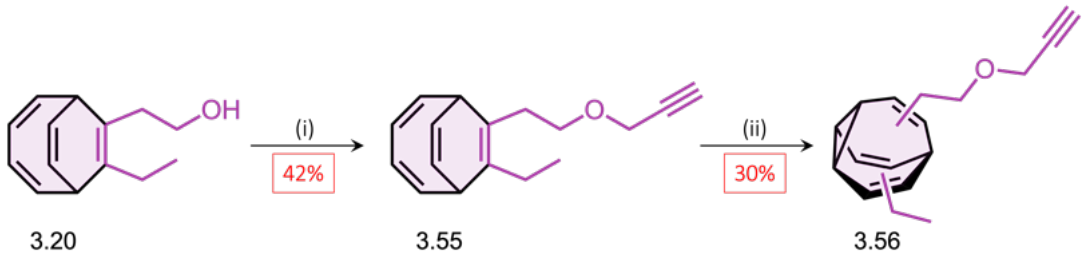

Scheme 3.31. Synthetic route to **BV** alkyne (**3.56**). Conditions (i) NaH (6.0 eq.) then propargyl bromide (7.0 eq.); anhydrous THF / 18 h / 0 °C → rt / 42%; (ii) thioxanthen-9-one (5 mol%) / 365 nm / anhydrous THF / 5 h / –5 °C / 30%.

Installation of *N*-acetyl glucosamine (GlcNAc) was then performed through the copper(I)-catalysed azide-alkyne cycloaddition (CuAAC) reaction, colloquially termed 'click chemistry', as developed by Sharpless and co-workers in 2002,[10] has found use in protein immobilisation[12] and biological probes,[19,20] amongst many other applications. An initial attempt to install the Ac-GlcNAc-azide (**3.57**) to form the **BV**-Ac-GlcNAc (**3.58**) used the Cu(II) salt $CuSO_4$ to generate the active Cu(I) catalyst, whilst sodium ascorbate was used as a reducing agent (Scheme 3.32). The reaction was carried out in a H_2O:^{t}BuOH (1:1) mixture at room temperature, but it was evident that the **BV** alkyne (**3.56**) was somewhat insoluble in this solvent system. Analysis by MS and ^{1}H NMR confirmed this issue as the desired product peaks were not detected by these methods.

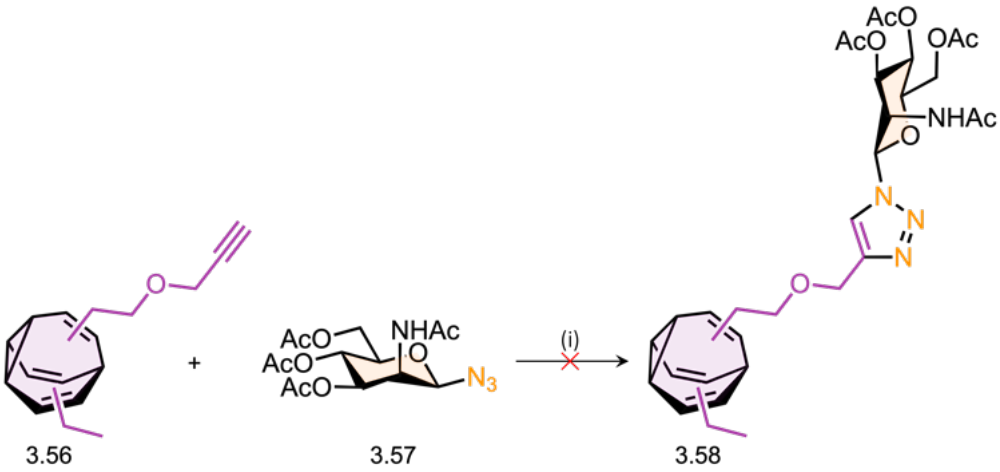

Scheme 3.32. Attempted synthetic route to **BV** Ac-GlcNAc (**3.58**). Conditions (i) $Cu(SO)_4$ (0.5 eq.) / 2-Acetamido-3,4,6-tri-*o*-acetyl-2-deoxy-β-D-glucopyranosyl azide (1.2 eq.) / sodium ascorbate (0.2 eq.) / H_2O:^{t}BuOH (1:1 *v*/*v*) / rt.

In light of this solubility issue, the **BV** alkyne (**3.56**) was dissolved in MeOH, followed by the addition of commercially available Ac-GlcNAc azide (**3.57**). Then, the addition of tetrakis(acetonitrile)copper(I) hexafluorophosphate, which provided the source of an active Cu(I) catalyst, allowed for the formation of the **BV** Ac-GlcNAc adduct (**3.58**) through the CuAAC. The Ac-protected **BV**-GlcNAc intermediate (**3.58**) was then subjected to base mediated deacetylation through treatment with sodium methoxide, affording **BV**-GlcNAc analogue (**3.59**) in 39% yield (Scheme 3.33a). The corresponding **BDT** Ac-GlcNAc product (**3.60**) was also synthesised from **BDT** alkyne (**3.55**) in situ, subsequently yielding **BDT** GlcNAc (**3.61**) in 29% yield (Scheme 3.33b), as a static control compound that does not display fluxional properties for comparison purposes.

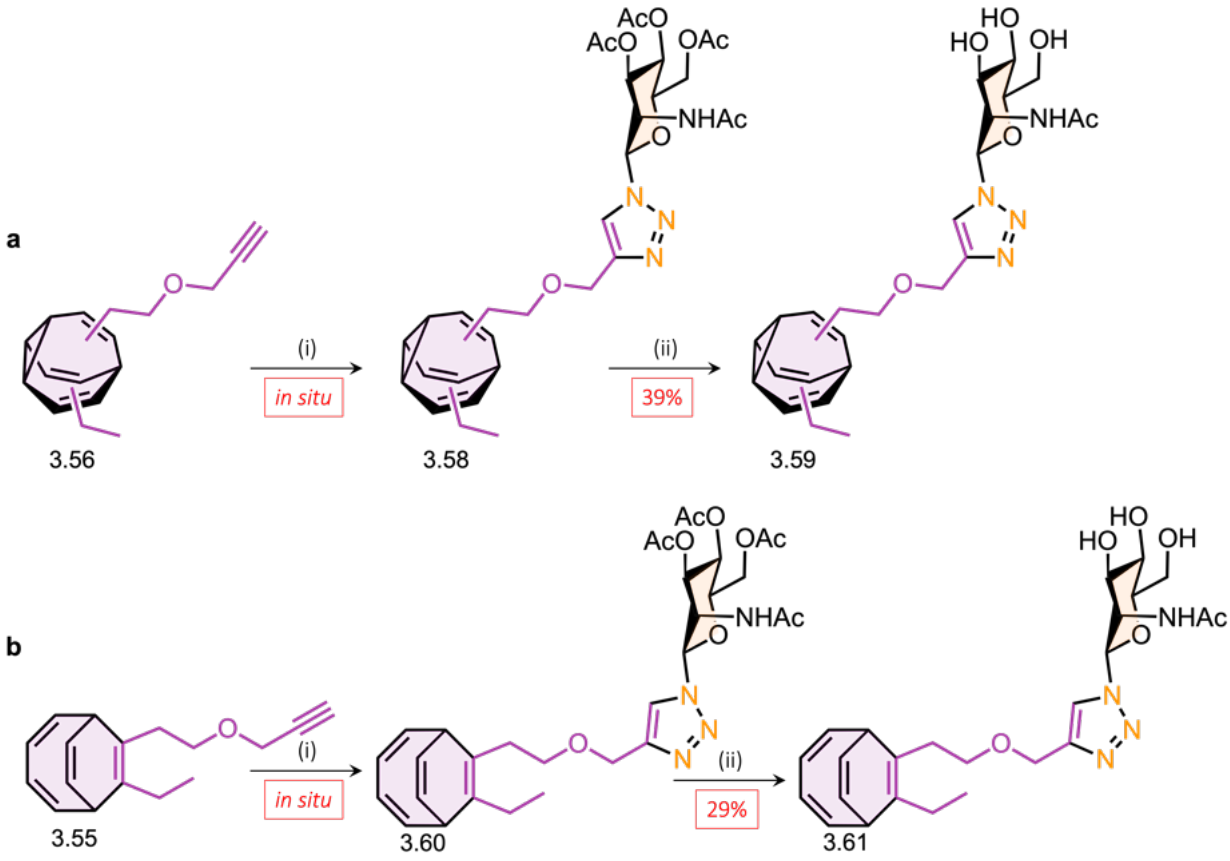

Scheme 3.33. Synthetic route to (**a**) **BV** GlcNAc (**3.59**) and (**b**) **BDT** GlcNAc (**3.61**); Conditions (i) $CuPF_6(MeCN)_4$ (0.5 eq.) / 2-Acetamido-3,4,6-tri-*o*-acetyl-2-deoxy-β-D-glucopyranosyl azide (1.2 eq.) / MeOH / rt; (ii) NaOMe / 24 h / rt; then Amberlite® IR120 hydrogen resin / rt / 29–39%.

3.2.4.2 Lysozyme Enzymatic Assay Studies

In order to determine: 1) confirmation of binding and 2) determination of Michaelis–Menten kinetic parameters (K_m, V_{max} and K_{cat}) of the **BV**–GlcNAc ligand (**3.58**) to Lysozyme, the development of a fast and reproducible enzymatic activity assay, building upon the protocol published by Shugar and co-workers,[99] was investigated. The ML substrate appears as a yellow water-insoluble pigment. In the presence of Lysozyme, however, the ML pigment is cleaved to its constituent saccharides, resulting in a colour change from yellow to transparent (Scheme 3.34). This means the absorbance at 450 nm can be measured over time throughout the ML cleavage by Lysozyme. Therefore, to decipher and validate an assay range, control experiments were carried out to validate the linearity of the rate of lysis of the *Micrococcus lysodeikticus* (ML) substrate, as suggested by Shugar in 1952,[99] measuring the rate *vs*

absorption relationship at 450 nm (Figure 3.29a), in addition to investigating the necessary absorbance range (Figure 3.29b).

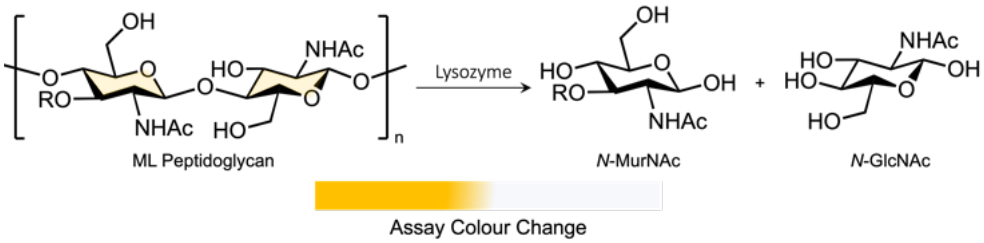

Scheme 3.34. Schematic of the enzymatic assay showing the ML peptidoglycan cleavage by Lysozyme to *N*-MurNAc and *N*-GlcNAc, with its corresponding colour change from yellow to transparent.

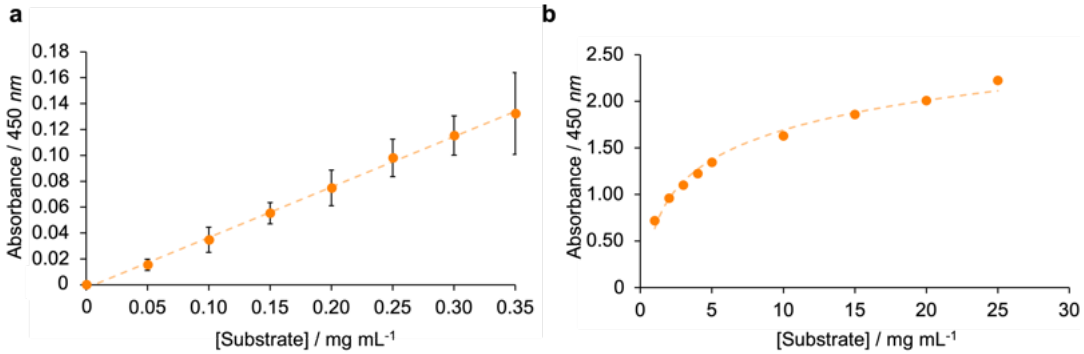

Figure 3.29. Investigations to validate the enzymatic assay experimentation: (a) plot of [ML] *vs* absorption; the mean values of three independent data measurements are plotted, with ± standard deviation error bars; (b) plot of [ML] *vs* absorption, demonstrating the spectrophotometer absorption range for use in enzymatic assays.

Following these control experiments, the concentration of Lysozyme was incrementally (by 0.02 mg mL^{-1}, ranging 0.02–0.14 mg mL^{-1}) tested based on previously reported results in order to obtain an optimal enzyme concentration for use in the design of the enzymatic assay experiments (Figure 3.30a(i)). For comparison purposes, the substrate concentration was constant (0.5 mg mL^{-1}) throughout. This investigation demonstrated the cleavage of all the available substrates by [Lysozyme] = 0.14 mg mL^{-1}, indicated by the plateau within 300 seconds (Figure 3.30a(i)). Following this enzyme concentration test, the ML substrate was then varied incrementally (by 0.05 mg mL^{-1}, ranging 0.05–0.50 mg mL^{-1}), with a constant [Lysozyme] = 0.14 mg mL^{-1} (Figure 3.30a(ii)). This Lysozyme concentration was, however, found to reach the lysed ML state very quickly, meaning that an accurate rate of reaction could not be calculated (Figure 3.30a(iii)). As a result, the ML substrate was altered to range 0–1.0 mg mL^{-1},

whilst the enzymatic concentration was decreased (0.02 mg mL^{-1}) in order to achieve a quantifiable rate of ML substrate lysis (Figure 3.30a(iv)). Resultantly, accuracy of the reaction rate was improved (Figure 3.30a(v)). The differentiation of the 1) [enzyme] and 2) [ML] allowed for greater linearity between the rate and substrate concentration relationship, thus, the [ML] = 0.95 mg mL^{-1} was selected for use in the enzymatic assay, allowing a greater range of rate of reaction data. Then, to ensure the optimal conditions which exhibited good reproducibility in triplet data sets, parameters including the: 1) pipetting method and 2) timescale were modified in order to minimise human error and protein aggregation, respectively. As shown by Figure 3.30a(vi), these modifications had a good effect on the reproducibility of the rate of reaction, which further confirming the assay conditions were suitable for use with potential Lysozyme inhibitors.

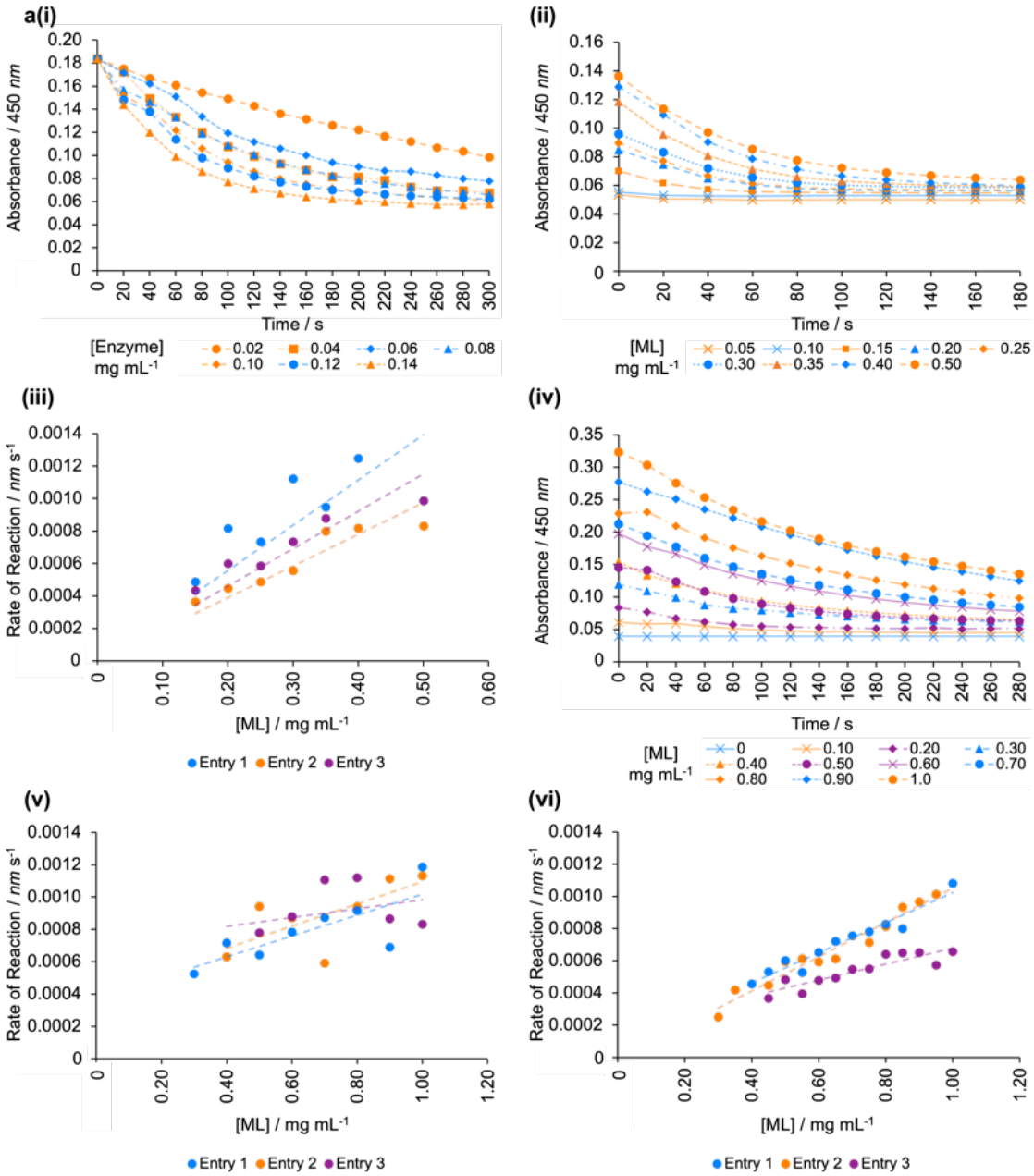

Figure 3.30. (a) (i) plot to investigate the optimal [Lysozyme] for the enzymatic assay; a constant [ML] = 0.5 mg mL^{-1} was used, with [Lysozyme] = 0.02–0.14 mg mL^{-1}. (ii) plot to investigate the optimal [ML]; a constant [Lysozyme] = 0.14 mg mL^{-1} was used, with [ML] = 0.05–0.50 mg mL^{-1}. (iii) plot for the rate of reaction *vs* [ML] for the initial 60 seconds of the reaction, where the mean rate was taken from triplet results. (iv) plot to investigate the optimal [ML]; a constant [Lysozyme] = 0.02 mg mL^{-1} was used, with [ML] = 0–1.0 mg mL^{-1} at 0.10 mg mL^{-1} intervals; (v) plot for the rate of reaction *vs* [ML], where the mean rate was taken from triplet results. A multi-pipette was used to dispense Lysozyme immediately prior to the first recording. (vi) Plot for the rate of reaction *vs* [ML] for the optimisation of reaction conditions, where the mean rate was taken from triplet results. A multi-pipette was used to dispense Lysozyme immediately prior to the first recording and the buffer absorption value was subtracted from all values to allow for more accurate results.

3.2.4.3 Crystallisation of Lysozyme

Crystal Soaking

The first crystallisation studies focused on obtaining good quality Lysozyme crystals that were suitable for XRD. In the first round of screening, crystalline material 16 Lysozyme crystals were identified (Figure 3.31a(i)). This screen (Lysozyme screen 1, Table S3.24) was manually varied by changing the sodium acetate concentration (10–100 mM) of the buffer system in 96-well sitting drop vapour diffusion plates, following a previously successful protocol for Lysozyme crystal growth.[100] Resultantly, the 16 crystals were soaked with **BV**-GlcNAc (**3.59**) cryo-solution (16 mM) for 60 seconds and frozen in liquid nitrogen to prevent ice formation when cryocooling. The XRD analysis provided unsuccessful results, where no **BV**-GlcNAc (**3.59**) ligand electron density was found to be present within the Lysozyme structure.

Co-Crystallisation

Following the unsuccessful results from the crystal soaking method, it was decided the alternative approach of co-crystallisation may provide the desired outcome. There is the possibility that the binding of the **BV**-GlcNAc (**3.59**) could occur in another location of the Lysozyme, other than the active site. If this was the case, the crystal soaking method would not allow allosteric binding at an alternative site, likely due to the restricted access *via* the solvent channels present in the Lysozyme structure. Another consideration this method would resolve is if the **BV**-GlcNAc (**3.59**) ligand was too sterically hindered to pass through the crystal solvent channels. Therefore, Lysozyme (2.8 mM/ 100 uL) was combined with **BV**-GlcNAc (**3.59**) (14 mM) at a five-fold ligand excess and left for 15 min to allow for binding. The **BV**-GlcNAc (**3.59**) ligand was presented at a five-fold excess in order to ensure high occupancy of the crystalline Lysozyme structure. Following crystal growth by sitting drop-vapour diffusion (Figures 3.31a(ii) and 3.31a(iii)), the crystal was then soaked with **BV**-GlcNAc (**3.59**) (16 mM) in order to ensure complete co-crystallisation (see Experimental).

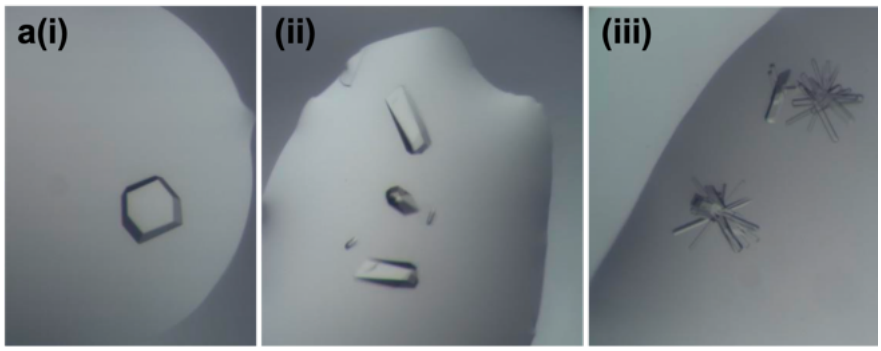

Figure 3.31. (a)(i) Lysozyme crystals visualised by microscopy from the soak experiments. (ii and iii) Lysozyme crystals visualised by microscopy from the co-crystallisation experiments.

Lysozyme Structure Analysis

The crystals obtained from both the **BV**-GlcNAc (**3.59**) soaking crystallisation and the co-crystallisation experiments were both solved and refined to a resolution of 1.35 Å and 1.25 Å, respectively. Each result was then further validated to a previously reported Lysozyme structure (PDB: 1HEW),[54] through the construction of an RMSD plot (Figure 3.32), allowing for the average distances between corresponding residues to be compared based on crystallographic data. This comparison showed little differences between the structures, particularly for active site residues, indicating that the solved crystallographic Lysozymes structures were accurate.

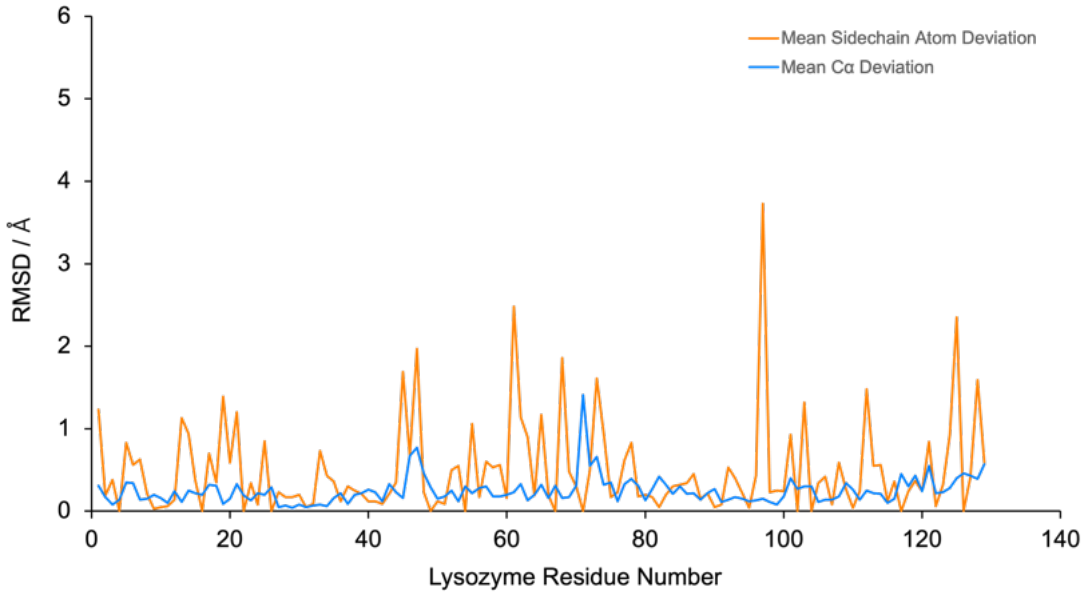

Figure 3.32. RMSD plot comparing each Lysozyme sidechain positional deviation (orange line) and alpha carbon deviation (blue line) between the crystallography data and reported Lysozyme structure (PDB: 1HEW).[54]

Following the Lysozyme structure validation, the previously reported Lysozyme structure (PDB: 1HEW) was modelled with the experimental electron density present, in order to: 1) correct any mis-orientated residual side chains; and to 2) screen for any additional electron density, which could indicate the presence of the **BV**-GlcNAc (**3.59**) ligand. The comparison of both the crystal soak (see Experimental) and co-crystallisation (see Experimental) experiments with the Lysozyme (PDB: 1HEW)[54] electron density showed no obvious indication for the presence of **BV**-GlcNAc (**3.59**) ligand.(Figure 3.33). Interestingly, for 7 of 32 results, an additional area of electron density, which was located in the vicinity of the Lysozyme active site cleft, was identified. The further refinement of the aforementioned electron density allowed for this unknown ligand to be identified as 4-(2-Hydroxyethyl)piperazine-1-ethane sulfonic acid (HEPES), a zwitterionic *N*-substituted amino sulfonic acid buffer, which was found in some buffer environments used in crystallisation conditions. The presence of the HEPES ligand was confirmed through the addition of the HEPES SMILES string, showing overlap with the previously unidentified electron density (Figure 3.34).

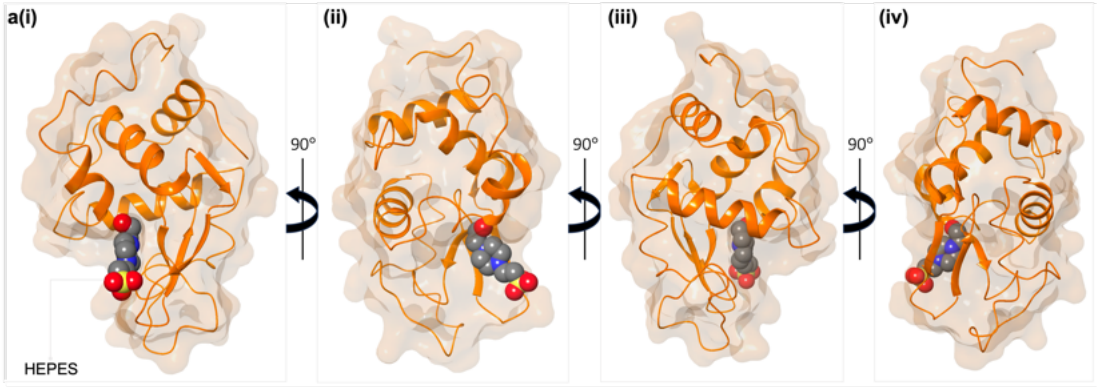

Figure 3.33. (**a**) Ribbon diagram with solid molecular surface (90% transparency) of the solved Lysozyme structure with resolution 1.25 Å from the (**i**) front view, (**ii**) side view, (**iii**) back view and (**iv**) side view. The HEPES ligand is shown in space-fill representation, where grey = carbon, red = oxygen, blue = nitrogen and yellow = sulfur.

On further inspection, the HEPES ligand was found to be located in a binding pocket surrounded by the two Lysozyme active site residues (E35 and D52), with possible coordination by the residing glutamate residue (E35) (Figure 3.34). The binding configuration and possible coordination (with distances) are shown in Figure 31.

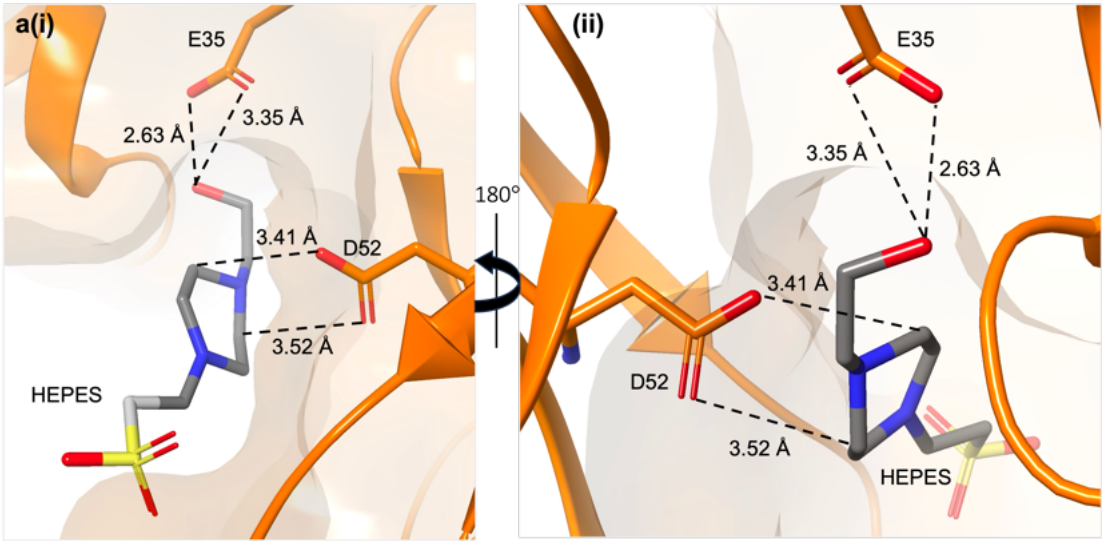

Figure 3.34. (a) Close-up view of the Lysozyme binding site of the HEPES ligand: distances in Å are indicated with dashed lines; side chains are shown with cylinder representation, where O atoms (red), N atoms (blue), S atoms (yellow); HEPES is shown in tube representation. The Lysozyme binding site is shown, with the active site residues (E35 and D52) and HEPES in the binding pocket from the (i) side view and (ii) a rotated view by 180°.

The result obtained from the aforementioned crystallographic analysis was then compared to previously reported data, where tri-*N*-acetylchitotriose was found to partially occupy hen egg-white Lysozyme (PDB: 1HEW).[54] This evaluation, which was considered through crystallographic superimposition (Figure 3.35), provided a comparison of binding modes of the HEPES ligand with tri-*N*-acetylchitotriose, comparing the noncovalent interactions between the active site residues and the ligand present. Specifically, the crystallographic superimposition showed the distance between the: 1) HEPES (2.63 Å) and tri-*N*-acetylchitotriose (7.77 Å) with the E35 residue and 2) HEPES (3.51 Å) and tri-*N*-acetylchitotriose (5.62 Å) with the D52 residue (Figure 3.36). For comparison purposes, however, comparing non covalent interaction distances are possibly unreliable due to the difference in ligand spatiality, where quantitative binding parameters are required to certify the possible higher binding affinity of the HEPES ligand.

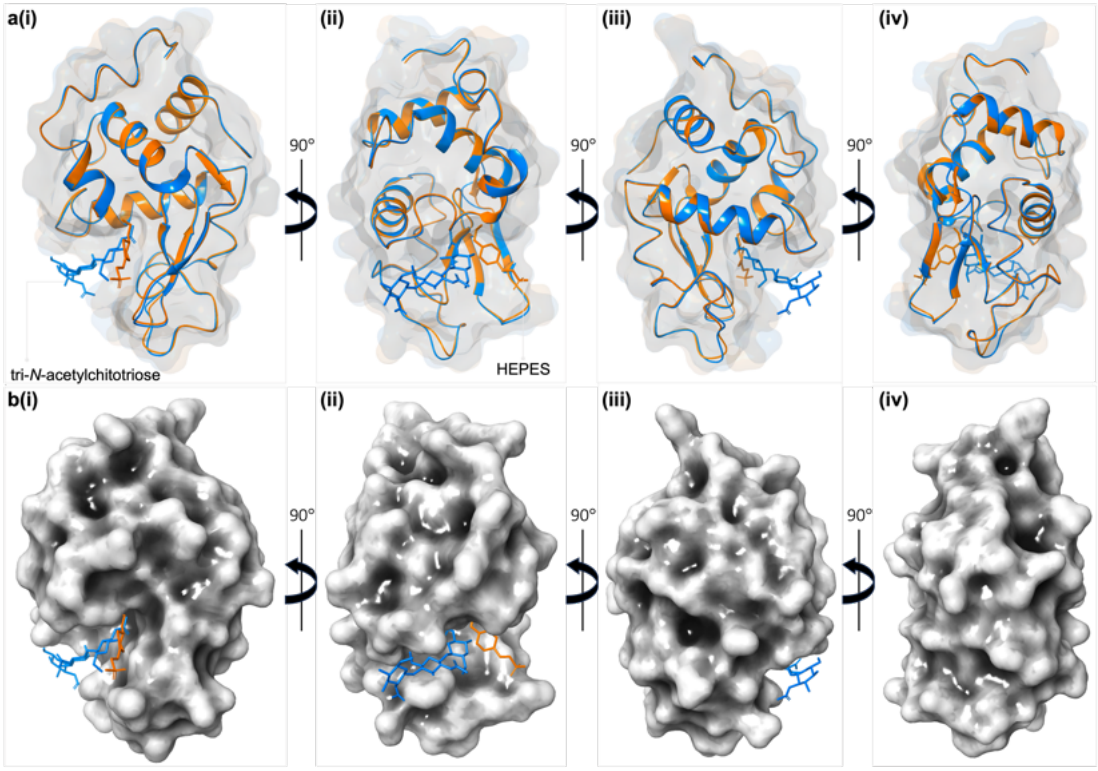

Figure 3.35. (a) Ribbon diagram with solid molecular surface (95% transparency) of the solved Lysozyme structure (orange) with resolution 1.25 Å, superimposed with Lysozyme (blue, PDB: 1HEW)[54] with resolution 1.75 Å from the (i) front view, (ii) side view, (iii) back view and (iv) side view. The HEPES (orange) and tri-*N*-acetylchitotriose (blue) ligands are shown in tube representation (b) Solid molecular surface (0% transparency) of the solved Lysozyme structure with resolution 1.25 Å, superimposed with Lysozyme (PDB: 1HEW)[54] with resolution 1.75 Å, showing the relative position of ligand binding of HEPES (orange) and tri-*N*-acetylchitotriose (blue) in the active site from the (i) front view, (ii) side view, (iii) back view and (iv) side view.

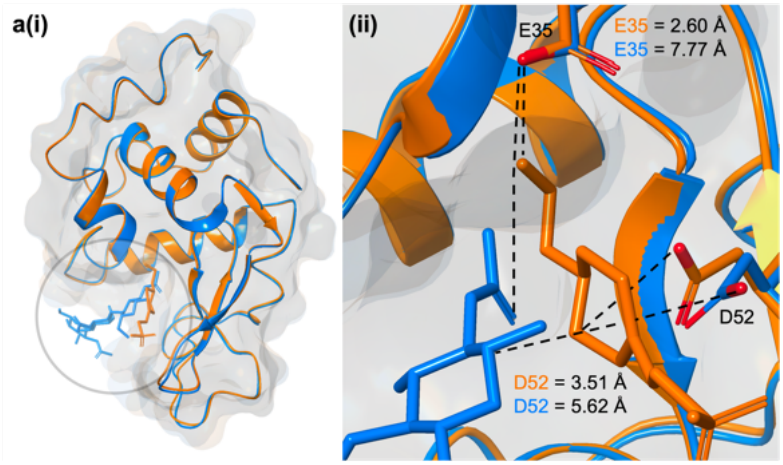

Figure 3.36. (a) (i) Ribbon diagram with solid molecular surface (95% transparency) of the solved Lysozyme structure (orange) with resolution 1.25 Å, superimposed with Lysozyme (blue, PDB: 1HEW)[54] with resolution 1.75 Å from the front view. The active site is highlighted with the HEPES (orange) and tri-*N*-acetylchitotriose (blue) ligands shown in tube representation. (ii)

Close-up view of the superimposed Lysozyme binding site: distances in Å are indicated with dashed lines; the HEPES (orange) and tri-*N*-acetylchitotriose (blue) is shown in tube representation. The active site residues (E35 and D52) are shown in tube representation, where the solved Lysozyme (orange), PDB: 1HEW[54] Lysozyme (blue) and O atoms (red) for side chains only.

Furthermore, the solved Lysozyme crystal structure with a HEPES ligand (1.25 Å resolution) was also superimposed with a previously published structure (PDB: 3RZ4)[101] of a Lysozyme–HEPES complex (1.80 Å resolution) from Peretoltchine *et al.* in 2011 to compare binding modes (Figure 3.37). Although the comparison in RMSD of residual sidechains between the obtained crystal structure and Lysozyme 3RZ4 showed a variety of deviations (Figure 3.38), the crystallographic superimposition provided evidence that the critical E35 and D52 residues, present in the active site, were both highly conserved. Here, the superimposition of both protein structures showed that the E35 and D52 residues resided at similar distances to the HEPES ligand, considering experimental uncertainties respectively (Figure 3.39). The comparative evidence cannot confirm that the HEPES ligand binds more strongly to Lysozyme than the tri-*N*-acetylchitotriose (or vice versa), however, it is noteworthy that the HEPES ligand is not likely to be a competing ligand with **BV**-GlcNAc (**3.59**), which is evidenced through the non-existent binding of **BV**-GlcNAc (**3.59**) to Lysozyme in the absence of a HEPES-containing crystallisation buffer, in either the active site or an allosteric site.

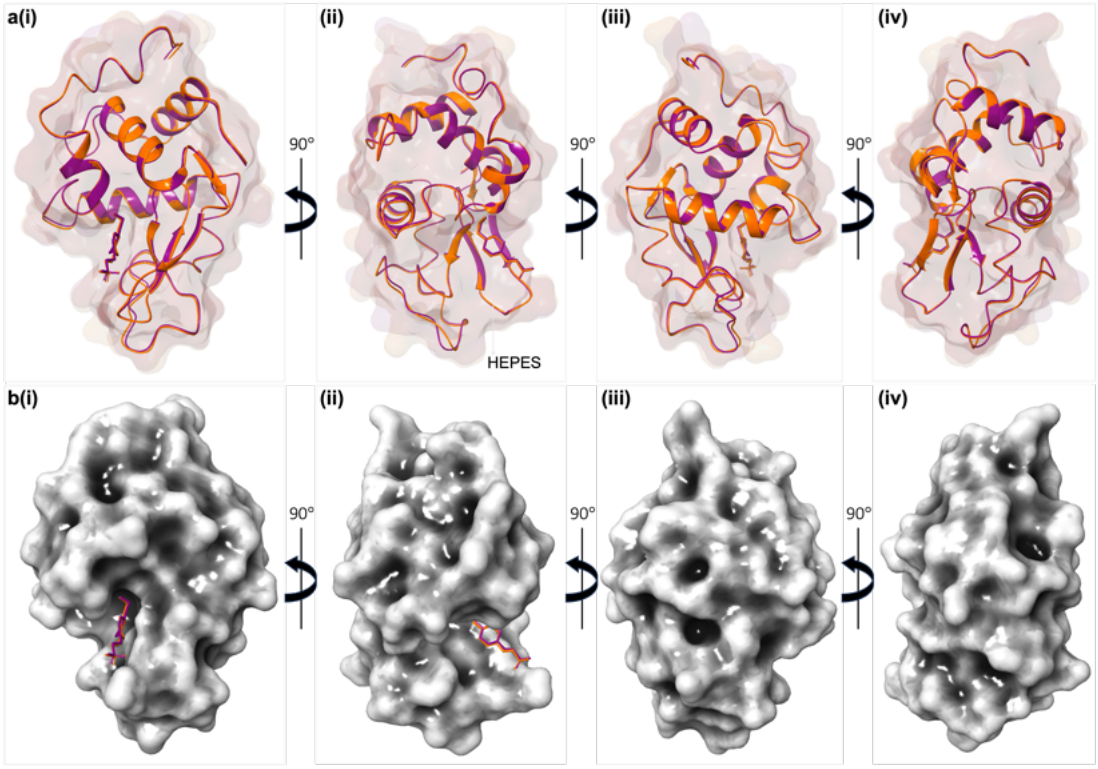

Figure 3.37. (a) Ribbon diagram with solid molecular surface (95% transparency) of the solved Lysozyme structure (orange) with resolution 1.25 Å, superimposed with Lysozyme (magenta, PDB: 3RZ4)[101] with resolution 1.80 Å from the (i) front view, (ii) side view, (iii) back view and (iv) side view. The HEPES (orange and magenta) correspond to their respective Lysozyme host and are shown in tube representation. (b) Solid molecular surface (0% transparency) of the solved Lysozyme structure with resolution 1.25 Å, superimposed with Lysozyme (PDB: 3RZ4)[101] with resolution 1.80 Å, showing the relative position of ligand binding of HEPES (orange and magenta) ligands in the active site from the (i) front view, (ii) side view, (iii) back view and (iv) side view.

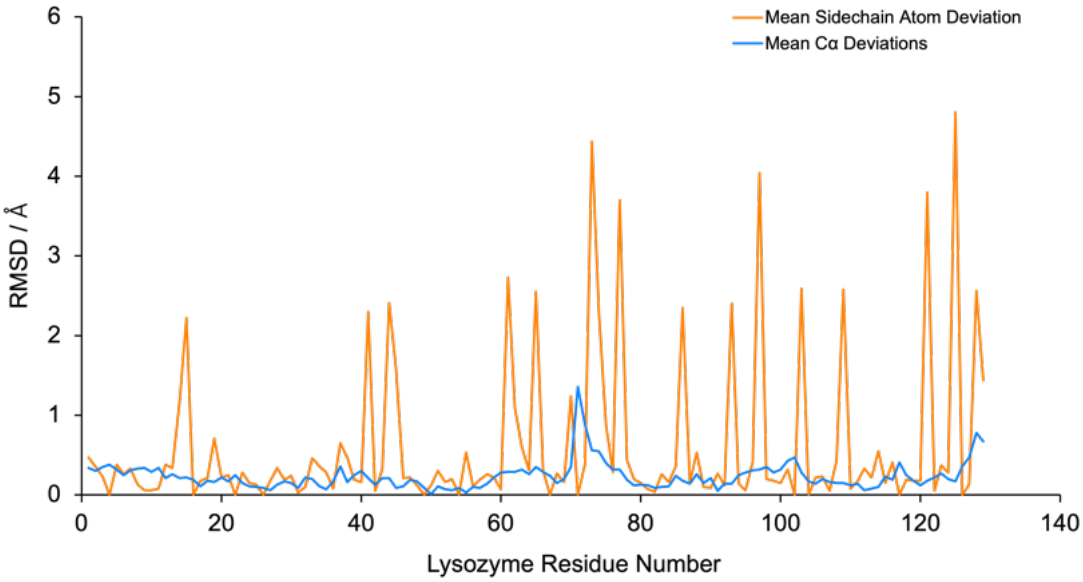

Figure 3.38. RMSD plot comparing each Lysozyme sidechain positional deviation (orange line) and alpha carbon deviation (blue line) between the crystallography data and reported Lysozyme structure (PDB: 3RZ4).[101]

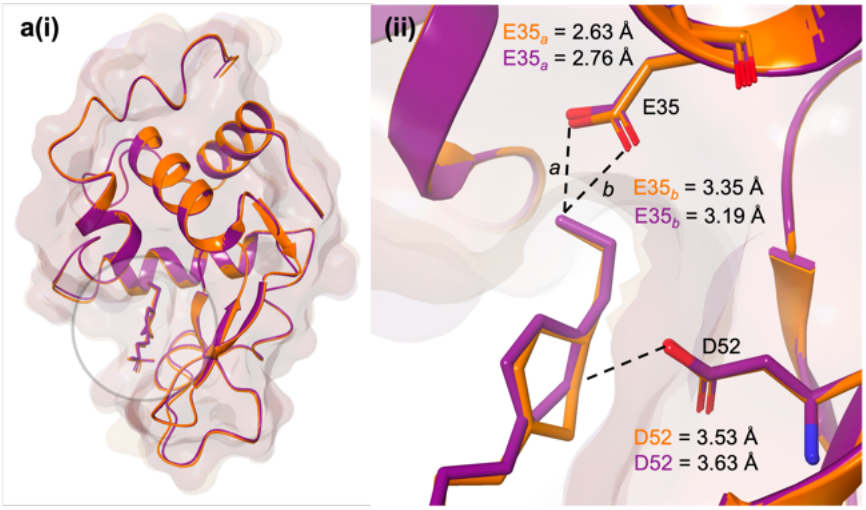

Figure 3.39. (a) (i) Ribbon diagram with solid molecular surface (95% transparency) of the solved Lysozyme structure (orange) with resolution 1.25 Å, superimposed with Lysozyme (magenta, PDB: 3RZ4)[101] with resolution 1.80 Å from the front view. The active site is highlighted with the HEPES (orange and magenta) ligands shown in tube representation. (ii) Close-up view of the superimposed Lysozyme binding site: distances in Å are indicated with dashed lines; the HEPES ligands (orange and magenta) are shown in tube representation. The active site residues (E35 and D52) are shown in tube representation, where the solved Lysozyme (orange), PDB: 3RZ4[101] Lysozyme (magenta), O atoms (red) and N atoms (blue) for side chains only.

3.2.4.4 Lysozyme Binding Studies

In order to assess the potential binding of the **BV**-GlcNAc (**3.59**) ligand as a Lysozyme inhibitor, the **BV**-GlcNAc (**3.59**) was compared to native GlcNAc, allowing for a direct comparison as to how the **BV** moiety affects binding. The GlcNAc ligand was subjected to Lysozyme through an enzymatic assay, showing inhibitory properties through the differences in rate at [GlcNAc] = 20 mM, 50 mM and 100 mM, respectively (Figure 3.40a(i)). This Lysozyme inhibition is further demonstrated through the rate vs [GlcNAc] plot, as shown in Figure 3.40a(ii). Comparatively, the **BV**-GlcNAc (**3.59**) ligand was shown to have no significant change in the Lysozyme rate of reaction, where [**BV**-GlcNAc] ≤ 50 mM (Figures 3.40a(iii) and 3.40a(iv)).

This result indicated the lack of any Lysozyme inhibition, meaning that it is likely the **BV**-GlcNAc (**3.59**) ligand does not bind to the Lysozyme active site. Additionally, due to the fact that native GlcNAc binds to Lysozyme at [GlcNAc] = 20 mM, this implied that the appended **BV** moiety prevented the GlcNAc from complexation with the Lysozyme active site. To further support this theory, literature precedent shows that GlcNAc has been found to bind to Lysozyme with K_d = 23 mM. The combination of experimental results and literature data suggests that the **BV** moiety prevents **BV**-GlcNAc (**3.59**) from binding to Lysozyme. Unfortunately, due to the small quantity of available ligand, Michaelis–Menten experiments could not be carried out to validate these findings by obtaining binding parameters.

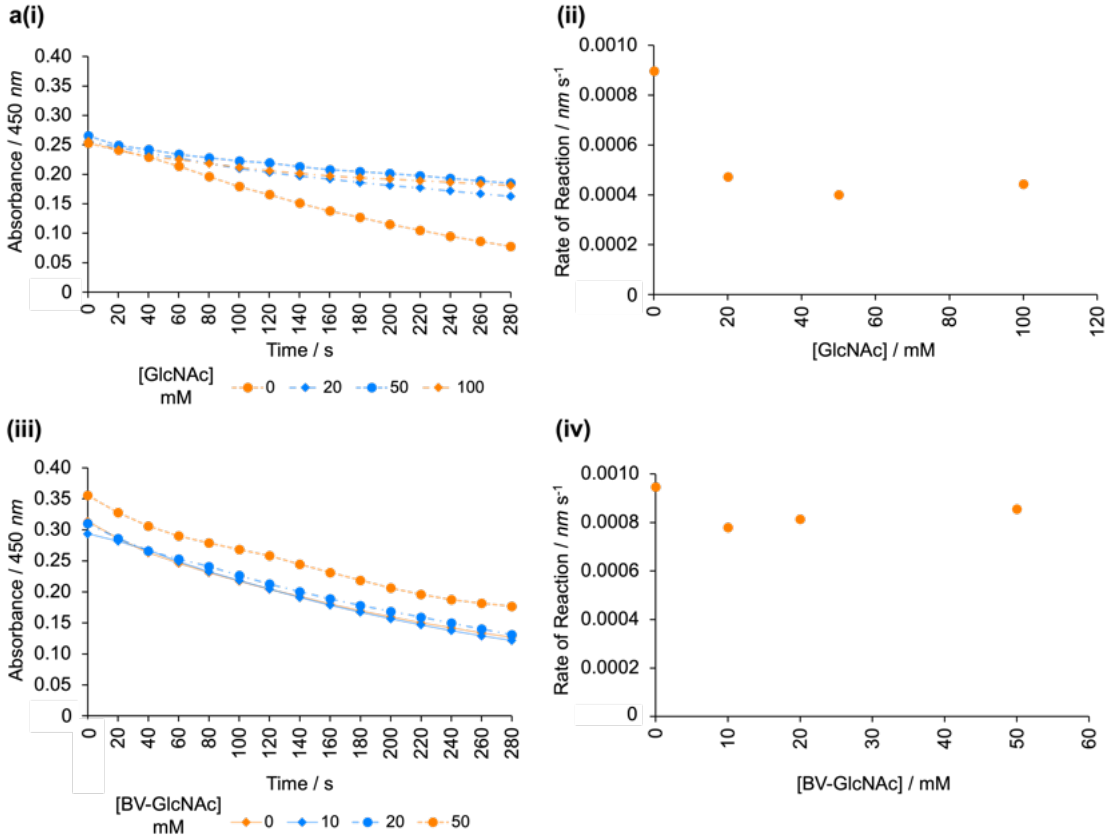

Figure 3.40. (a) (i) plot to investigate the effect of GlcNAc inhibition of Lysozyme, showing the [GlcNAc] vs absorbance plot for Lysozyme lysis of the ML substrate. (ii) Plot for the rate of reaction *vs* [GlcNAc], to investigate the Lysozyme rate of reaction in the absence and present of GlcNAc, with [GlcNAc] = 0–100 mM. (iii) Plot to investigate the effect of **BV**-GlcNAc (**3.59**) inhibition of Lysozyme, showing the [**BV**-GlcNAc] vs absorbance plot for Lysozyme lysis of the ML substrate. (iv) Plot for the rate of reaction *vs* [**BV**-GlcNAc], to investigate the Lysozyme rate of reaction in the absence and present of **BV**-GlcNAc (**3.59**), with [**BV**-GlcNAc] = 0–50 mM.

3.2.4.5 Computational Analysis of *N*-Acetylglucosamine Bullvalene Binding

Following binding studies and co-crystallisation attempts of Lysozyme with **BV**-GlcNAc (**3.59**), computational analysis was used to investigate the possible binding modes of **BV**-GlcNAc (**3.59**) to Lysozyme. The possibility that **BV**-GlcNAc (**3.59**) could bind to an allosteric site in Lysozyme was considered, however, computational studies focussed on the active site, assuming that **BV**-GlcNAc (**3.59**) would bind similarly to GlcNAc. Therefore, the GlcNAc appended to **BV** was superimposed on the analogous GlcNAc site found in the crystal structure of Lysozyme (PDB: 1HEW)[54] (Figure 3.41a), allowing for a direct comparison in binding modes.

Furthermore, the electrostatic potential molecular surface was calculated through Adaptive Poisson-Boltzmann Solver (APBS) electrostatics and mapped onto Lysozyme (PDB: 1HEW)[54] in PyMol. The electrostatic potential molecular surface indicated that the active site cleft, where the **BV**-GlcNAc (**3.59**) would likely reside, exhibits predominantly negative electrostatics (Figure 3.41b), therefore this region would probably suit the carbon-rich **BV**-GlcNAc (**3.59**) framework. Additionally, the hydrophobic molecular surface, based on the Kyte-Doolittle hydrophobic model,[102] was mapped on the Lysozyme surface (Figure 3.41c) indicating that in this specific ligand orientation, the **BV** moiety and corresponding linker resides in a hydrophilic region. Since the carbon-rich **BV** framework is hydrophobic in nature, this insight may provide inconclusive evidence as to why the **BV**-GlcNAc (**3.59**) moiety has not been shown to bind to Lysozyme. This insight, however, does not take into consideration the range of **BV** isomers that are accessible to this molecule. Thus, more detailed simulations would be required to assess this outcome in more detail.

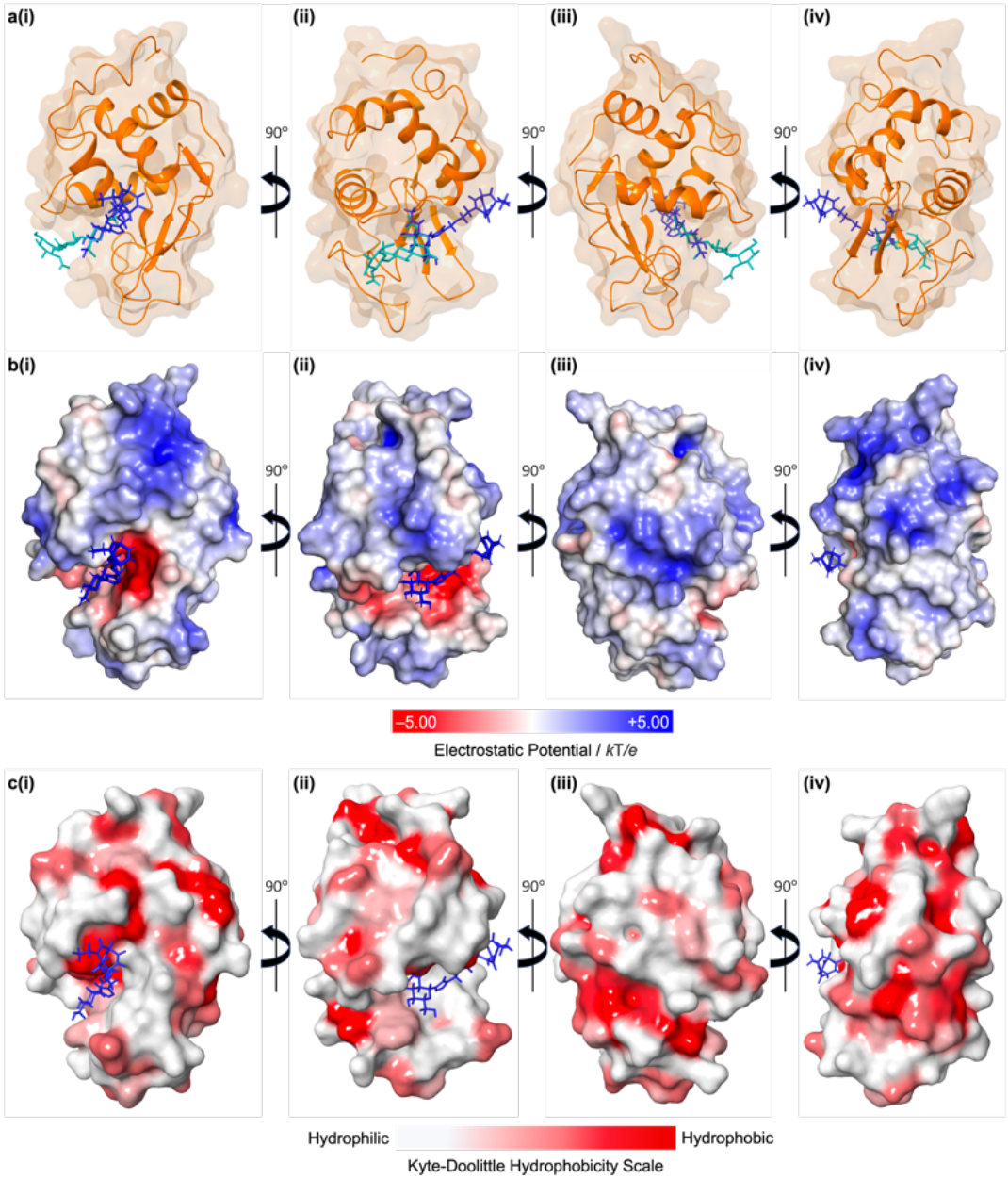

Figure 3.41. (**a**) Ribbon diagram with solid molecular surface (90% transparency) of Lysozyme (orange, PDB: 1HEW)[54] with resolution 1.75 Å from the (**i**) front view, (**ii**) side view, (**iii**) back view and (**iv**) side view. The tri-*N*-acetylchitotriose (teal) ligand crystal structure is shown; the **BV**-GlcNAc (**3.59**) (royal blue) ligand has been modelled in the active site based upon the position of the terminal residue of tri-*N*-acetylchitotriose and is shown in tube representation. (**b**) Electrostatic potential molecular surface of Lysozyme (PDB: 1HEW),[54] visualised by colouration according to its sign and value, where red (negative), white (neutral) and blue (positive); the possible relative position of **BV**-GlcNAc (**3.59**) ligand (royal blue) in a negatively charged cleft is shown from the (**i**) front view, (**ii**) side view, (**iii**) back view and (**iv**) side view. (**c**) Hydrophobicity molecular surface of Lysozyme (PDB: 1HEW), visualised by colouration according to the residue hydrophobicity in the Kyte-Doolittle scale,[102] where white (hydrophilic), and red (hydrophobic). The possible relative position of **BV**-GlcNAc (**3.59**) ligand

(royal blue) in a hydrophobic area is shown from the (**i**) front view, (**ii**) side view, (**iii**) back view and (**iv**) side view.

3.2.4.6 Identifying Alternative Target Proteins and Potential Ligand Modifications

Given the unsuccessful attempts to obtain a co-crystal structure of a Lysozyme-**BV** complex, a screen or co-crystallisation conditions could be trialled, however, the pursuit of alternative approaches may be required. The predominant modifications to consider throughout future investigations are: 1) choice of protein biosupramolecular host and 2) ligand modifications. In light of these considerations, a short search was conducted to identify possible proteins that may exhibit more suitable binding properties. Interestingly, Concanavalin A (ConA), a lectin well known for its carbohydrate-binding properties,[103–109] was identified as a potential choice for further **BV**-GlcNAc studies. The literature precedent shows that ConA binds GlcNAc at a K_d = 0.93 mM and its crystal structure has been solved to a resolution of 2.7 A.

To assess ConA as a potential candidate for further co-crystallisation studies, ConA (PDB: 1TEI)[103] was modelled computationally, whilst the GlcNAc moiety of **BV**-GlcNAc was superimposed on the GlcNAc within the crystallised ligand structure for comparison purposes (Figure 3.42a). Since ConA (PDB: 1TEI)[103] is comprised of four protein chains, where each chain is occupied by one polysaccharide ligand, only one chain was subjected to superimposition of the **BV**-GlcNAc ligand to avoid replicate results. This superimposition of GlcNAc residues established that the **BV** moiety was able to position itself in a hydrophobic region of chemical space within the ConA binding site (Figure 3.42b). In addition, in this same position, it was apparent that the GlcNAc residue was able to reside in a favourable hydrophilic position. These insights, along with the fact that the ConA binding site was entirely sterically accessible to the whole **BV**-GlcNAc molecule, provides promise that ConA could be used for co-crystallisation studies with a **BV**-sugar compound.

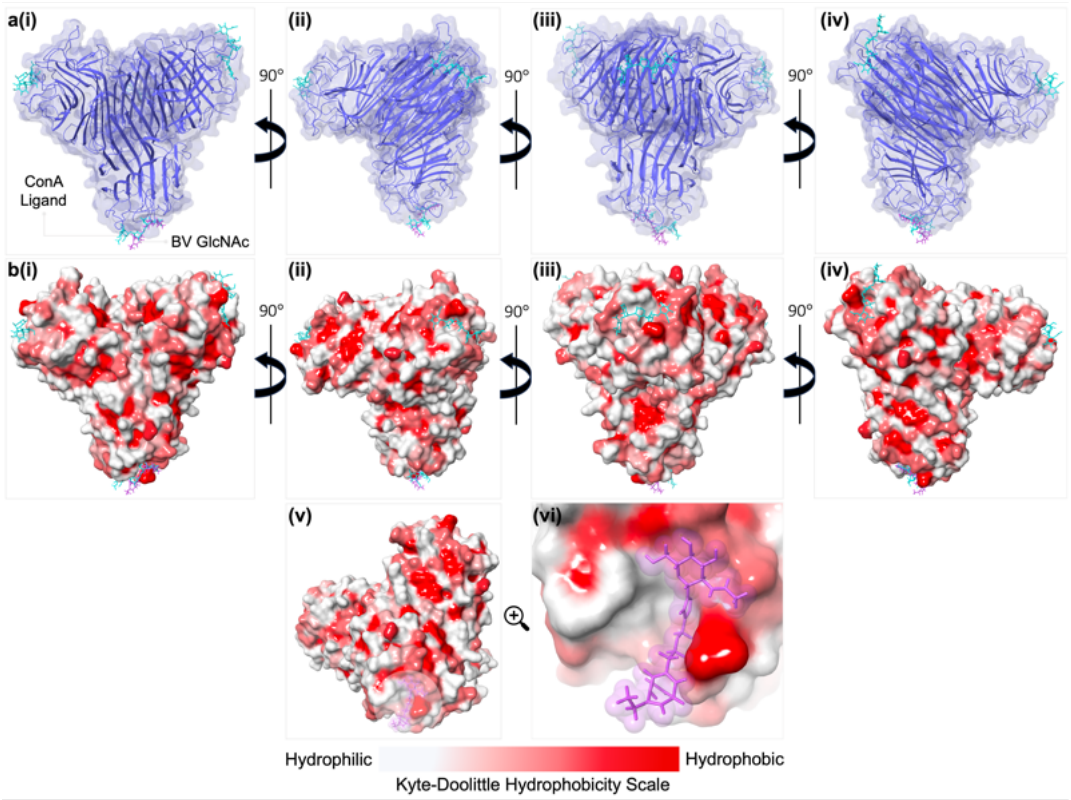

Figure 3.42. (**a**) Ribbon diagram with solid molecular surface (90% transparency) of ConA (violet, PDB: 1TEI)[103] with resolution 2.70 Å from the (**i**) front view, (**ii**) side view, (**iii**) back view and (**iv**) side view. The polysaccharide ligands (cyan) crystal structure are shown; the **BV**-GlcNAc (lilac) ligand has been modelled in the active site based upon the position of the GlcNAc in the polysaccharide ligand and is shown in tube representation. (**b**) Hydrophobicity molecular surface of ConA (PDB: 1TEI),[103] visualised by colouration according to the residue hydrophobicity in the Kyte-Doolittle scale, where white (hydrophilic), and red (hydrophobic) is shown from the (**i**) front view, (**ii**) side view, (**iii**) back view and (**iv**) side view. The polysaccharide ligands (cyan) crystal structures are shown; the **BV**-GlcNAc (lilac) ligand has been modelled in one binding position, based upon the position of the GlcNAc in the polysaccharide ligand in one protein chain and is shown in tube representation. (**v**) The **BV**-GlcNAc highlighted in a polysaccharide binding site of ConA. (**vi**) Close-up view of the hydrophobicity surface of the superimposed ConA binding site; the possible relative position of **BV**-GlcNAc ligand (lilac) is shown in tube representation and space fill representation (75% transparency), where the **BV** and GlcNAc moieties are sterically accessible and occupy hydrophobic and hydrophilic regions, respectively.

In terms of ligand design, it is proposed that the addition of a longer polysaccharide moiety would be a sensible option for ligand modification, in order to lower the K_d of ligand binding to Lysozyme, which would likely result in a higher binding affinity to the Lysozyme target site. Since the desired *N*,*N*-diacetyl chitobiose azide (**3.63**) is not

commercially available, a plausible route to synthesise these materials to subsequently perform click chemistry has been devised. The unprotected *N*-acetyl chitin sugar, *N*,*N*-diacetyl chitobiose (**3.62**) is commercially available. Next, subjecting these to reaction conditions established by Shoda *et. al.*[110] allows for the conversion to the *β*-azide sugar (**3.63**) in one-step (Scheme 3.35), which has previously been reported in a good yield of 77%.

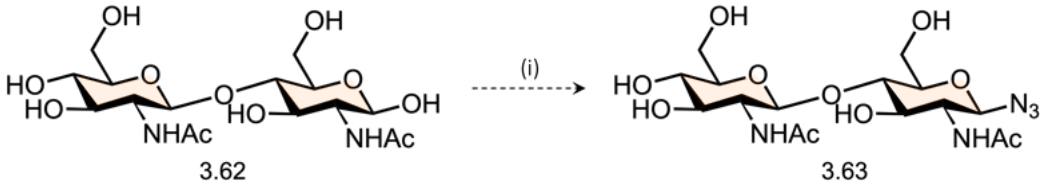

3.62 3.63

Scheme 3.35. Proposed synthetic route to *β*-azide *N*,*N*-diacetyl chitobiose (**3.63**). Reagents and conditions: (i) 2-chloro-1,3-dimethylimidazolinium chloride (3.0 eq.) / NaN_3 (2.5 M) / 2,6-Lutidine (6.0 eq.) / 48 h / 0 °C.

The *β*-azide *N*,*N*-diacetyl chitobiose (**3.63**) can then be used in subsequent click reactions with analogous **BV** alkynes (such as compound **3.56**), implementing established chemistry, to create novel carbohydrate-appended **BVs** with increased affinity for binding to Lysozyme (Scheme 3.36).

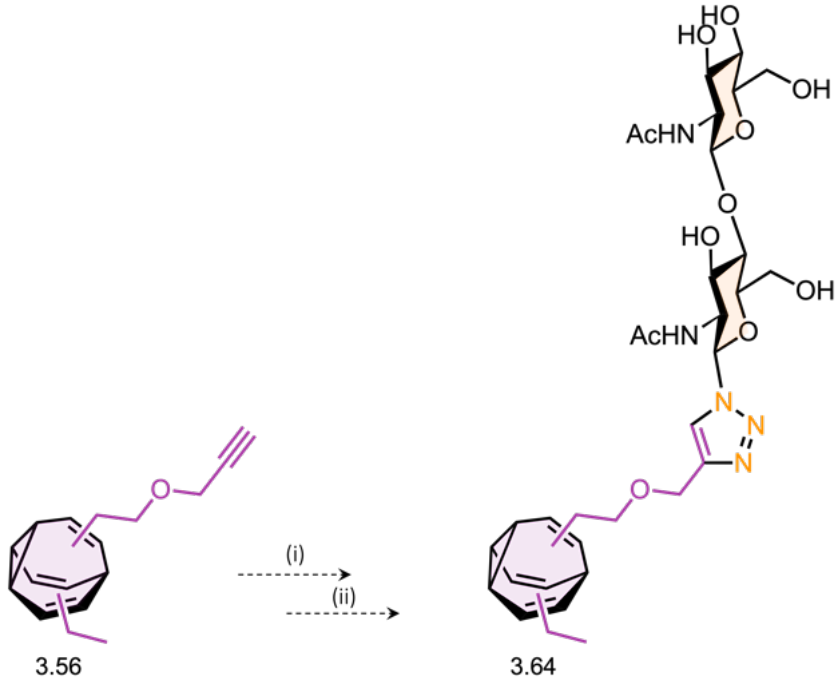

3.56 3.64

Scheme 3.36. Proposed synthetic route to *N*,*N*-diacetyl chitobiose **BV** (**3.64**). Reagents and conditions: (i) $CuPF_6(MeCN)_4$ (0.5 eq.) / *β*-azide *N*,*N*-diacetyl chitobiose (1.2 eq.) / MeOH / rt; (ii) NaOMe / 24 h / rt; then Amberlite® IR120 hydrogen resin / rt.

3.3 Conclusions and Future Work

Throughout this project, a series of hydroxy-containing **BBs** have been successfully synthesised and characterised. Moreover, cobalt(II)-catalysed cycloaddition conditions were successfully optimised and these protocols were then applied to obtain a range of hydroxy **BVs**, with differing linker lengths and substitutions for use in co-crystallisation experiments with SAs. The co-crystallisation of hydroxy **BBs** and **BVs** in both **BSA** and **HSA** proved challenging, showing issues with solubility in aqueous buffers, which were required for protein crystallisation. For comparison purposes, the co-crystal structure of **HSA** with ad-1-carboxylic acid (**3.26**) was obtained, demonstrating that the co-crystal of a compound that shows isosteric properties of **BB** and **BV** can be obtained. The two novel **HSA** crystal structures acquired from these investigations have been published on the PDB (PDB: 9EOS and 9EOD). Subsequent investigations to install and/or post-functionalise to obtain water-soluble functionality on the **BDT** and **BV** frameworks, including the installation of the TEG group, AAs, ionic salts, esters and the carboxylic acid moiety, has been attempted unsuccessfully for reasons that are unknown. The protein, Lysozyme, was targeted as a more specific binding target for co-crystallisation. Therefore, the GlcNAc-appended **BV** (**3.59**) was synthesised, and was subjected to an enzymatic assay and co-crystallisation experiments with Lysozyme. The results from these investigations have shown that the **BV**-GlcNAc (**3.59**) is unable to bind to the Lysozyme active site. In addition, the computational models carried out in this study point towards unfavourable electrostatic interactions of the Lysozyme binding site preventing protein-ligand interactions with **BV**-GlcNAc (**3.59**). There is also a possibility that the compound present in the crystallisation buffer (i.e. HEPES) can act as a competitive inhibitor in the crystallisation studies, thus preventing **BV**-GlcNAc (**3.59**) from occupying the Lysozyme binding site.

On-going work is aimed at developing water soluble **BVs**, by the means of using chemistries that are well-established and are shown to work on **BDT** and **BV** species. For example, the installation of the propargylic moiety to **BDT** and **BVs** has been shown

previously and within some of our previous investigations, thus this is a sensible option to ensure good conversion *via* click chemistry with functionalised azides. Therefore, current work is aimed at producing a *bis*(TEG)-**BV** (**3.69**) from the *bis*(alkyne)-**BV** (**3.68**) (Scheme 3.37), which is likely to display more hydrophilic properties, relative to the **BBs** and **BVs** previously synthesised.

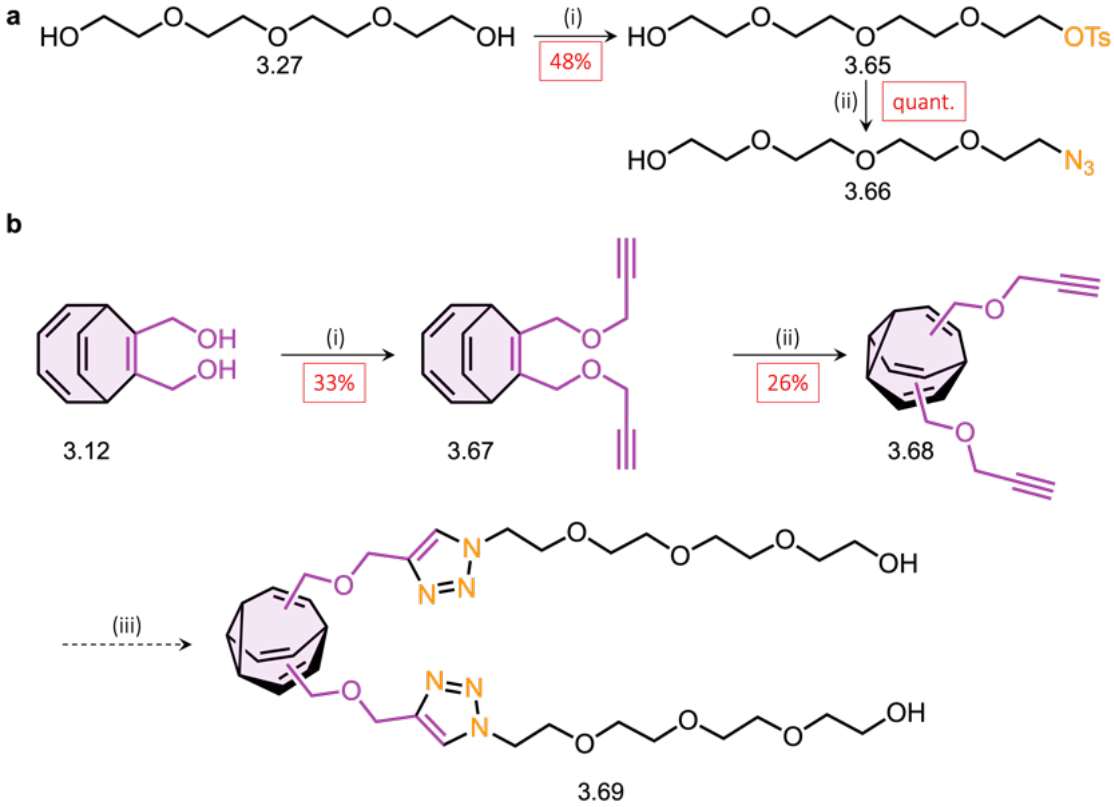

Scheme 3.37. Current synthetic route to *bis(*TEG*)*-**BV** (**3.69**). Reagents and conditions: (**a**) (i) NaOH / TsCl / H_2O:THF / 0 °C → rt / 24 h / 48%; (ii) NaN_3 / MeCN / 80 °C / 18 h. (**b**) (i) NaH (6.0 eq.) then propargyl bromide (7.0 eq.); anhydrous THF / 18 h / 0 °C → rt / 33%; (ii) thioxanthen-9-one (5 mol%) / 365 nm / anhydrous THF / 5 h / –5 °C / 26%; (iii) $CuPF_6(MeCN)_4$ (0.5 eq.) / TEG-N_3 (2.4 eq.) / MeOH / rt.

Future work should include the consideration of developing more targeted **BBs** and **BVs** with specific warheads to target proteins. Performing preliminary docking simulations (using AutoDock Vina software)[111] would allow for a more accurate assessment of ligand complexation with the selected protein. In addition, ligands should be tested against a wider range of common, easily crystallised proteins, in order to carry out titration analyses to determine binding confirmation before any co-crystallisation experiments are carried out on specific protein-ligand selections. Once

confirmation of binding has been achieved through titration analyses, this investigation would benefit from robot-assisted crystallisation screening, in order to test a wider range of conditions for potential protein-ligand co-crystallisation. Lastly, an alternative strategy should also be considered, whereby reported protein-ligand co-crystals are identified *via* the PDB, as a way to understand protein suitability and plausible ligand modifications for this study. In particular, comparison of protein co-crystals with carbon-rich molecules, such as hetero- and carbocyclic systems whose exit vectors were described in Chapter 2.

3.4 Experimental

Synthesis

Synthesis of Barbaralanes†

7-Ethynylcyclohepta-1,3,5-triene (3.5)

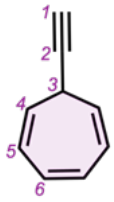

Anhydrous LiCl (0.524 g, 12.40 mmol, 2.2 eq.) was placed in an oven-dried round-bottomed flask fitted with a septum under an N_2 atmosphere. Anhydrous THF was added (38 mL) and the resulting solution was cooled to –78 °C before adding a solution of ethynyl magnesium bromide (22.5 mL, 12.2 mmol, 0.5 M in THF, 2.2 eq.) and stirring for 10 min at this temperature. Tropylium tetrafluoroborate (1.00 g, 5.62 mmol, 1.0 eq.) was added to the reaction mixture and the reaction mixture was stirred for 16 h, where the temperature was raised to rt, following removal of the ice bath. The reaction was quenched with a saturated aqueous solution of NH_4Cl (20 mL), then extracted with Et_2O (3 × 30 mL). The combined organic extracts were then dried over $MgSO_4$, filtered and the solvent removed under reduced pressure (rotary evaporator bath at 16 °C, ≥ 100 mbar). The crude residue was purified by column chromatography (Teledyne Isco CombiFlash Rf+ system, 24 g SiO_2, *n*-pentane) to give the title compound as a colourless oil (539 mg, 4.60 mmol, 83%). **^{1}H NMR** (600 MHz, 298 K, $CDCl_3$) δ 6.66 (dd, *J* = 3.7, 2.7 Hz, 2H, H_6), 6.33 – 6.07 (m, 2H, H_5), 5.40 – 5.16 (m, 2H, H_4), 2.73 – 2.43 (m, 1H, H_3), 2.17 (d, *J* = 2.6 Hz, 1H, H_1). **^{13}C NMR** (151 MHz, 298 K, $CDCl_3$) δ 131.2 (C_6), 125.1 (C_5), 123.0 (C_4), 85.8

(C_2), 68.5 (C_1), 31.5 (C_3). **HRMS-ASAP** *m/z* = 117.0701 $[M+H]^+$ (calculated for C_9H_9 = 117.0704).

Spectroscopic data are consistent with those previously published.[112]

Tricyclo[3.3.1.$0^{2,8}$]nona-3,6-dien-9-one | Barbaralone (BBO)

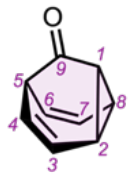

7-Ethynylcyclohepta-1,3,5-triene (**3.5**, 1.00 g, 8.68 mmol, 1.0 eq.) and diphenyl sulfoxide (3.51 g, 17.0 mmol, 2.0 eq.) were charged in a flask and dissolved in anhydrous CH_2Cl_2 (15 mL) at 25 °C, with no particular precautions taken to exclude air. (Acetonitrile)[1,3-bis(2,6-diisopropylphenyl)-imidazol-2-ylidene]gold(I) tetrafluoroborate (309 mg, 0.43 mmol, 5 mol%) was added in one portion at the same temperature and the reaction mixture was stirred for 16 h. The reaction was quenched with Et_3N (10 drops) and the solvent was removed under reduced pressure. The crude residue was purified by column chromatography (Teledyne Isco CombiFlash Rf+ system, 24 g SiO_2, hexanes–EtOAc, 0–100% gradient elution) to give the title compound as a light yellow solid (685 mg, 5.18 mmol, 60%). **M.P.** 55 – 57 °C (lit.[112] 50 – 51 °C). **^{1}H NMR** (700 MHz, 298 K, $CDCl_3$) δ 5.97 – 5.51 (m, 2H, H_1 and H_5), 4.32 (br s, 4H, H_2 and H_4 and H_6 and H_8), 2.90 – 2.55 (m, 2H, H_3 and H_7). **^{13}C NMR** (176 MHz, 298 K, $CDCl_3$) δ 211.0 (C_9), 121.7 (C_3 and C_7 or C_2, C_4, C_6 and C_8), 121.5 (C_3 and C_7 or C_2, C_4, C_6 and C_8), 38.3 (C_1 and C_5). **HRMS-ASAP** *m/z* = 133.0648 $[M+H]^+$ (calculated for C_9H_9O = 133.0653).

Spectroscopic data are consistent with those previously published.[112]

(±)-Tricyclo[3.3.1.$0^{2,8}$]nona-3,6-dien-9-ol | Barbaralol (BBL)

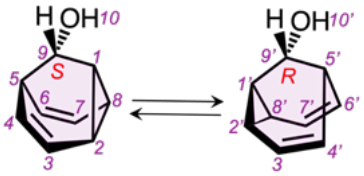

$LiAlH_4$ (120 mg, 3.16 mmol, 2.1 eq.) in anhydrous Et_2O (5 mL) was placed and suspended in an oven-dried round-bottomed flask fitted with a septum under a N_2 atmosphere. The solution was cooled to 0 °C and then a solution of tricyclo[3.3.1.$0^{2,8}$]nona-3,6-dien-9-one (**BBO**, 200 mg, 1.51 mmol, 1.0 eq.) in anhydrous Et_2O (5 mL) was added dropwise. The reaction mixture was stirred at this temperature for 3 h. The reaction was quenched with saturated potassium sodium tartrate solution (25 mL) and allowed to warm to rt before being extracted with Et_2O

(3 × 30 mL). The combined organic extracts were dried over $MgSO_4$ and the solvent was removed under reduced pressure (rotary evaporator bath at 16 °C, ≥ 100 mbar). The crude residue was purified by column chromatography (Teledyne Isco CombiFlash Rf+ system, 24 g SiO_2, *n*-pentane–Et_2O, 0–100% gradient elution) to give the title compound as a white solid (159 mg, 1.18 mmol, 78%). **M.P.** 82 – 84 °C (lit.[112] 86 – 88 °C). **^{1}H NMR** (400 MHz, 298 K, $CDCl_3$) δ 5.88 (t, *J* = 7.9 Hz, 1H, H_3), 5.54 (t, *J* = 7.6 Hz, 1H, H_7), 4.16 – 4.04 (m, 2H, H_6 and H_8), 4.02 – 3.92 (m, 2H, H_2 and H_4), 3.61 (d, *J* = 3.3 Hz, 1H, H_9), 2.59 – 2.47 (m, 2H, H_5 and H_1), 1.14 (s, 1H, H_{10}). **^{13}C NMR** (151 MHz, 298 K, $CDCl_3$) δ 123.3 (C_3), 120.9 (C_7), 76.5 (C_6 and C_8), 72.3 (C_2 and C_4), 62.5 (C_9), 31.8 (C_5 and C_1). **HRMS-ASAP** *m/z* = 117.0699 [*M*–OH]$^+$ (calculated for C_9H_9 = 117.0704). Spectroscopic data are consistent with those previously published.[112]

Synthesis of Mono-substituted Hydroxy Barbaralanes†

(±)-6-(4-Tolyl)bicyclo[3.2.2]nona-3,8-dien-6-ol (3.6)

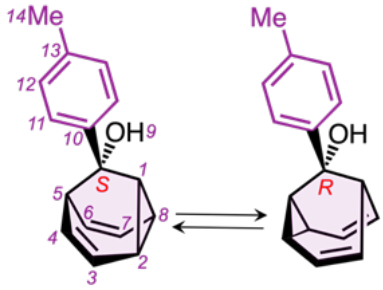

Magnesium turnings (100 mg, 4.54 mmol, 1.0 eq.) and I_2 (57 mg, 0.23 mmol, 5 mol%) were placed in an oven-dried two-necked round-bottomed flask fitted with a condenser and a septum under a N_2 atmosphere. The flask was gently heated with a heat gun until the I_2 started to sublime. The flask was cooled down to rt. A quarter of a solution of 4-bromotoluene (760 mg, 4.50 mmol, 1.0 eq.) in anhydrous THF (10 mL) was added to the reaction mixture, which was heated until it reached reflux. Upon gentle reflux, the remaining solution of 4-bromotoluene in anhydrous THF was added dropwise over 30 min. The reaction mixture was heated at reflux for 30 min before cooling to rt. Tricyclo[3.3.1.0^{2,8}]nona-3,6-dien-9-one (**BBO**, 111 mg, 0.84 mmol, 0.2 eq.) was transferred to an oven-dried round-bottomed flask, and the flask was purged with N_2. Anhydrous THF (10 mL) was added and the solution was cooled to 0 °C. The Grignard solution (prepared above) was added dropwise over 30 min to the tricyclo[3.3.1.0^{2,8}]nona-3,6-dien-9-one (**BBO**) solution. The reaction mixture was stirred for 16 h, and the temperature was raised from 0 °C to rt, following

removal of the ice bath. The reaction was quenched with a saturated aqueous solution of NH_4Cl (10 mL), then extracted with EtOAc (3 × 20 mL). The combined organic extracts were dried over $MgSO_4$, filtered and the solvent removed under reduced pressure. The crude residue was purified by column chromatography (Teledyne Isco CombiFlash Rf+ system, 24 g SiO_2, hexanes–CH_2Cl_2, 0–100% gradient elution including 0.5% Et_3N in the elution) to yield the title compound as a cream-coloured solid (136 mg, 0.61 mmol, 80%). **M.P.** 59 – 61°C. **^{1}H NMR** (700 MHz, 298 K, $CDCl_3$) δ 7.33 (d, *J* = 8.2 Hz, 2H, H_{11}), 7.12 (d, *J* = 7.9 Hz, 2H, H_{12}), 5.91 (t, *J* = 7.7 Hz, 1H, H_7), 5.58 (t, *J* = 7.6 Hz, 1H, H_3), 4.28 – 4.24 (m, 2H, H_8 and H_6), 4.24 – 4.21 (m, 2H, H_4 and H_2), 2.83 – 2.57 (m, 2H, H_5 and H_1), 2.33 (d, *J* = 0.7 Hz, 3H, H_{14}), 1.98 (s, 1H, H_9). **^{13}C NMR** (176 MHz, 298 K, $CDCl_3$) δ 140.4 (C_{10}), 136.8 (C_{13}), 128.6 (C_{12}), 126.4 (C_{11}), 123.2 (C_7), 120.9 (C_3), 77.8 (C_4 and C_2), 75.5 (C_8 and C_6), 68.6 (C_9), 38.2 (C_5 and C_1), 21.2 (C_{14}). **HRMS-ASAP** *m/z* = 207.1154 $[M–OH]^+$ (calculated for $C_{16}H_{15}$ = 207.1174).

(±)-6-(4-Ansiyl)bicyclo[3.2.2]nona-3,8-dien-6-ol (3.7)

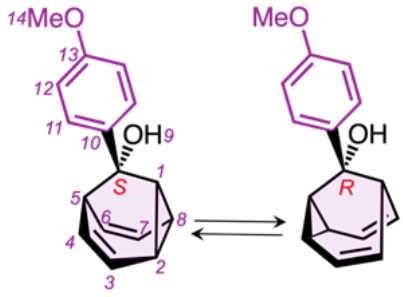

Magnesium turnings (240 mg, 10.0 mmol, 1.0 eq.) and I_2 (124 mg, 0.49 mmol, 5 mol%) were placed in an oven-dried two-necked round-bottomed flask fitted with a condenser and a septum under a N_2 atmosphere. The flask was gently heated with a heat gun until the I_2 started to sublime. The flask was cooled down to rt. A quarter of a solution of 4-bromoanisole (1.68 g, 9.80 mmol, 1.0 eq.) in anhydrous THF (10 mL) was added to the reaction mixture, which was heated until it reached reflux. Upon gentle reflux, the remaining solution of 4-bromoanisole in anhydrous THF was added dropwise over 30 min. The reaction mixture was heated at reflux for 30 min before cooling to rt. Tricyclo[3.3.1.0^{2,8}]nona-3,6-dien-9-one (**BBO**, 125 mg, 0.95 mmol, 0.1 eq.) was transferred to an oven-dried round-bottomed flask, and the flask was purged with N_2. Anhydrous THF (10 mL) was added and the solution was cooled to 0 °C. The Grignard solution (prepared above) was added dropwise over 30 min to the barbaralone. The reaction mixture was stirred for 16 h, and the temperature was raised from 0 °C to rt, following removal of the ice bath. The reaction was

quenched with a saturated aqueous solution of NH_4Cl (10 mL), then extracted with EtOAc (3 × 20 mL). The combined organic extracts were dried over $MgSO_4$, filtered and the solvent removed under reduced pressure. The crude residue was purified by column chromatography (Teledyne Isco CombiFlash Rf+ system, 24 g SiO_2, hexanes–CH_2Cl_2, 0–100% gradient elution including 0.5% Et_3N in the elution) to yield the title compound as a yellow oil (176 mg, 0.73 mmol, 73%). **^{1}H NMR** (700 MHz, 298 K, $CDCl_3$) δ 7.36 (d, *J* = 8.9 Hz, 2H, H_{12}), 6.84 (d, *J* = 8.9 Hz, 2H, H_{11}), 5.91 (t, *J* = 7.7 Hz, 1H, H_7), 5.58 (t, *J* = 7.6 Hz, 1H, H_3), 4.28 – 4.24 (m, 2H, H_8 and H_6), 4.24 – 4.20 (m, 2H, H_4 and H_2), 3.79 (s, 3H, H_{14}), 2.78 – 2.51 (m, 2H, H_5 and H_1), 1.98 (s, 1H, H_9). **^{13}C NMR** (176 MHz, 298 K, $CDCl_3$) δ 158.7 (C_{10}), 135.6 (C_{13}), 127.6 (C_{12}), 123.2 (C_7), 120.9 (C_3), 113.2 (C_{11}), 77.8 (C_4 and C_2), 75.5 (C_8 and C_6), 68.4 (C_9), 55.3 (C_{14}), 38.2 (C_5 and C_1). **HRMS-ASAP** *m/z* = 223.1123 [*M*–OH]$^+$ (calculated for $C_{16}H_{15}O$ = 223.1123).

† Compounds synthesised by A. N. Bismillah.

Synthesis of Di-Substituted Hydroxy Barbaralanes†

7-[2-(4-Tolyl)ethynyl]cyclohepta-1,3,5-triene (3.8$_a$)

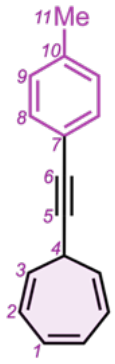

4-Ethynyltoluene (580 mg, 5.0 mmol, 1.0 eq.) was placed into an oven-dried round-bottomed flask fitted with a septum under a N_2 atmosphere. Anhydrous THF (15 mL) was added and the resulting solution was cooled to –78 °C before adding *n*-BuLi (2.0 mL, 5.12 mmol, 2.5 M in hexanes, 1.0 eq.) and stirring for 40 min at this temperature. Tropylium tetrafluoroborate (910 mg, 5.0 mmol, 1.0 eq.) was added, and the mixture was allowed to reach rt and stirred for 16 h. The reaction was quenched with a saturated aqueous solution of NH_4Cl (30 mL), then extracted with EtOAc (3 × 20 mL). The combined organic extracts were dried over $MgSO_4$, filtered and the solvent removed under reduced pressure. The crude residue was purified by column chromatography (Teledyne Isco CombiFlash Rf+ system, 24 g SiO_2, hexanes–EtOAc, 0–100% gradient elution) to yield the title compound as a yellow oil (838 mg, 4.06 mmol, 81%). **^{1}H NMR** (600 MHz, 298 K, $CDCl_3$) δ 7.37 (d, *J* = 8.1 Hz, 2H, H_8), 7.12 (d, *J* = 7.8 Hz, 2H, H_9), 6.77–6.59 (m, 2H, H_1), 6.30 – 6.14 (m, 2H, H_2), 5.44 (dd, *J* = 9.0, 5.5 Hz, 2H, H_3), 2.71 (tt, *J* =

5.1, 1.1 Hz, 1H, H_4), 2.36 (s, 3H, H_{11}). **^{13}C NMR** (151 MHz, 298 K, $CDCl_3$) δ 137.9 (C_{10}), 131.5 (C_8), 130.9 (C_1), 128.9 (C_9), 124.6 (C_2), 123.3 (C_3), 120.3 (C_7), 90.2 (C_5), 80.6 (C_6), 32.2 (C_4), 21.4 (C_{11}). **HRMS-ASAP** *m/z* = 207.1165 $[M+H]^+$ (calculated for $C_{16}H_{15}$ = 207.1174).

Spectroscopic data are consistent with those published previously.[68]

7-[2-(4-Anisyl)ethynyl]cyclohepta-1,3,5-triene (3.8$_b$)

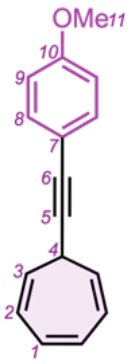

4-Ethynylanisole (330 mg, 2.5 mmol, 1.0 eq.) was placed into an oven-dried round-bottomed flask fitted with a septum under a N_2 atmosphere. Anhydrous THF (15 mL) was added and the resulting solution was cooled to –78 °C before adding *n*-BuLi (1.0 mL, 2.6 mmol, 2.5 M in hexanes, 1.0 eq.) and stirring for 40 min at this temperature. Tropylium tetrafluoroborate (455 mg, 2.5 mmol, 1.0 eq.) was added, and the mixture was allowed to reach rt and stirred for 16 h. The reaction was quenched with a saturated aqueous solution of NH_4Cl (30 mL), then extracted with EtOAc (3 × 20 mL). The combined organic extracts were dried over $MgSO_4$, filtered and the solvent removed under reduced pressure. The crude residue was purified by column chromatography (Teledyne Isco CombiFlash Rf+ system, 24 g SiO_2, hexanes–EtOAc, 0–100% gradient elution) to yield the title compound as a pale yellow solid (470 mg, 2.11 mmol, 85%). **M.P.** 70 – 72 °C. **^{1}H NMR** (400 MHz, 298 K, $CDCl_3$) δ 7.40 (d, *J* = 8.7 Hz, 2H, H_8), 6.84 (d, *J* = 8.7 Hz, 2H, H_9), 6.78 – 6.53 (m, 2H, H_1), 6.28 – 6.09 (m, 2H, H_2), 5.51 – 5.31 (m, 2H, H_3), 3.81 (s, 3H, H_{11}), 2.69 (tt, *J* = 5.6, 1.5 Hz, 1H, H_4). **^{13}C NMR** (151 MHz, 298 K, $CDCl_3$) δ 159.5 (C_{10}), 133.2 (C_8), 131.2 (C_1), 124.8 (C_2), 123.6 (C_3), 115.7 (C_7), 114.0 (C_9), 89.7 (C_5), 80.5 (C_6), 55.4 (C_{11}), 32.4 (C_4). **HR-ASAP-MS** *m/z* = 223.1123 $[M+H]^+$ (calculated for $C_{16}H_{15}O^+$ = 223.1117).

Spectroscopic data are consistent with those published previously.[68,112]

7-[2-Phenylethynyl]cyclohepta-1,3,5-triene (3.8_c)

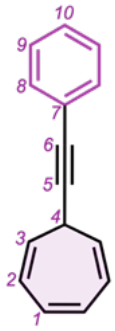

Phenylacetylene (255 mg, 2.5 mmol, 1.0 eq.) was placed into an oven-dried round-bottomed flask fitted with a septum under a N_2 atmosphere. Anhydrous THF (15 mL) was added and the resulting solution was cooled to –78 °C before adding *n*-BuLi (1.0 mL, 2.6 mmol, 2.5 M in hexanes, 1.0 eq.) and stirring for 40 min at this temperature. Tropylium tetrafluoroborate (455 mg, 2.5 mmol, 1.0 eq.) was added, and the mixture was allowed to reach rt and stirred for 16 h. The reaction was quenched with a saturated aqueous solution of NH_4Cl (30 mL), then extracted with EtOAc (3 × 20 mL). The combined organic extracts were dried over $MgSO_4$, filtered and the solvent removed under reduced pressure. The crude residue was purified by column chromatography (Teledyne Isco CombiFlash Rf+ system, 24 g SiO_2, hexanes–EtOAc, 0–100% gradient elution) to yield the title compound as a yellow oil (281 mg, 1.46 mmol, 58%). **^{1}H NMR** (700 MHz, 298 K, $CDCl_3$) δ 7.50 – 7.47 (m, 2H, H_8), 7.34 – 7.321 (m, 3H, H_9 and H_{10}), 6.73 – 6.68 (m, 2H, H_1), 6.26 – 6.21 (m, 2H, H_2), 5.45 (dd, *J* = 8.7, 5.5 Hz, 2H, H_3), 2.73 (tt, *J* = 5.6, 1.5 Hz, 1H, H_4). **^{13}C NMR** (176 MHz, 298 K, $CDCl_3$) 131.9 (C_8), 131.2 (C_1), 128.4 (C_9), 128.0 (C_{10}), 124.9 (C_2), 123.6 (C_7), 123.3 (C_3), 91.2 (C_5), 80.7 (C_6), 32.4 (C_4). **HR-ASAP-MS** *m/z* = 191.0857 $[M–H]^+$ (calculated for $C_{15}H_{11}^+$ = 191.0855).
Spectroscopic data are consistent with those published previously.[68,112]

7-[2-(4-Fluorophenyl)ethynyl]cyclohepta-1,3,5-triene (3.8_d)

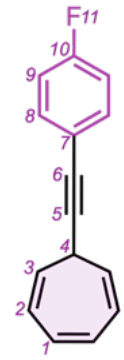

1-Ethynyl-4-fluorobenzene (600 mg, 5.0 mmol, 1.0 eq.) was placed into an oven-dried round-bottomed flask fitted with a septum under a N_2 atmosphere. Anhydrous THF (15 mL) was added and the resulting solution was cooled to –78 °C before adding *n*-BuLi (2.0 mL, 5.1 mmol, 2.5 M in hexanes, 1.0 eq.) and stirring for 40 min at this temperature. Tropylium tetrafluoroborate (910 mg, 5.0 mmol, 1.0 eq.) was added, and the mixture was allowed to reach rt and stirred for 16 h. The reaction was quenched with a saturated aqueous solution of NH_4Cl (30 mL), then extracted with EtOAc (3 × 20 mL). The combined organic extracts were dried over $MgSO_4$, filtered and the solvent removed under reduced pressure. The crude residue was purified by column

chromatography (Teledyne Isco CombiFlash Rf+ system, 24 g SiO_2, hexanes–EtOAc, 0–100% gradient elution) to yield the title compound as a yellow oil (852 mg, 3.88 mmol, 81%). **^{1}H NMR** (400 MHz, 298 K, $CDCl_3$) δ 7.53 – 7.34 (m, 2H, H_8), 7.08 – 6.93 (m, 2H, H_9), 6.77 – 6.63 (m, 2H, H_1), 6.29 – 6.18 (m, 2H, H_2), 5.42 (dd, *J* = 9.1, 5.5 Hz, 2H, H_3), 2.71 (t, *J* = 5.5, 1.5 Hz, 1H, H_4). **^{13}C NMR** (151 MHz, 298 K, $CDCl_3$) δ 162.4 (d, J_{CF} = 248.8 Hz, C_{10}), 133.7 (d, J_{CF} = 8.3 Hz, C_8), 132.0 (C_1), 125.0 (C_2), 123.0 (C_3), 120.0 (C_7), 115.6 (d, J_{CF} = 22.0 Hz, C_9), 90.8 (C_5), 79.7 (C_6), 32.3 (C_4). **^{19}F NMR** (376 MHz, 298 K, $CDCl_3$) δ –114.9 (m, F_{11}). **HR-ASAP-MS** *m/z* = 209.0768 $[M–H]^+$ (calculated for $C_{15}H_{10}F^+$ = 209.0761).

Spectroscopic data are consistent with those published previously.[68,112]

7-{2-[4-(Trifluoromethyl)phenyl]ethynyl}cyclohepta-1,3,5-triene (3.8$_e$)

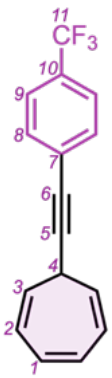

4-Ethynyl-α-α-α-trifluorotoluene (425 mg, 2.5 mmol, 1.0 eq.) was placed into an oven-dried round-bottomed flask fitted with a septum under a N_2 atmosphere. Anhydrous THF (15 mL) was added and the resulting solution was cooled to –78 °C before adding *n*-BuLi (1.0 mL, 2.56 mmol, 2.5 M in hexanes, 1.0 eq.) and stirring for 40 min at this temperature. Tropylium tetrafluoroborate (455 mg, 2.5 mmol, 1.0 eq.) was added, and the mixture was allowed to reach rt and stirred for 16 h. The reaction was quenched with a saturated aqueous solution of NH_4Cl (30 mL), then extracted with EtOAc (3 × 20 mL). The combined organic extracts were dried over $MgSO_4$, filtered and the solvent removed under reduced pressure. The crude residue was purified by column chromatography (Teledyne Isco CombiFlash Rf+ system, 24 g SiO_2, hexanes–EtOAc, 0–100% gradient elution) to yield the title compound as a yellow solid (483 mg, 1.86 mmol, 74%). **M.P.** 67 – 68 °C (lit.[68] 65 – 67 °C). **^{1}H NMR** (700 MHz, 298 K, $CDCl_3$) δ 7.57 (d, *J* = 2.6 Hz, 2H, H_9), 7.56 (d, *J* = 8.8 Hz, 2H, H_8), 6.70 (dddd, *J* = 3.5, 2.7, 0.8, 0.8 Hz, 2H, H_1), 6.26 – 6.21 (m, 2H, H_2), 5.47 – 5.37 (m, 2H, H_3), 2.75 (tt, *J* = 5.6, 1.5 Hz, 1H, H_4). **^{13}C NMR** (176 MHz, 298 K, $CDCl_3$) δ 132.1 (C_8), 131.2 (C_1), 129.8 (q, J_{CF} = 32.6 Hz, C_{11}), 127.5 (d, J_{CF} = 1.5 Hz, C_7), 125.3 (q, J_{CF} = 3.8 Hz, C_9), 125.2 (C_2), 123.3 (C_{10}), 122.6 (C_3), 93.9 (C_5), 79.6 (C_6), 32.3 (C_4). **^{19}F NMR** (376 MHz, 298 K, $CDCl_3$) δ –62.9 (s, F_{11}). **HRMS-ASAP** *m/z* = 260.0824 $[M]^+$ (calculated for $C_{16}H_{11}F_3$ = 260.0813).

Spectroscopic data are consistent with those published previously.[68]

(±)-1-(4-Tolyl)tricyclo[3.3.1.0^{2,8}]nona-3,6-dien-9-one (3.9$_a$)

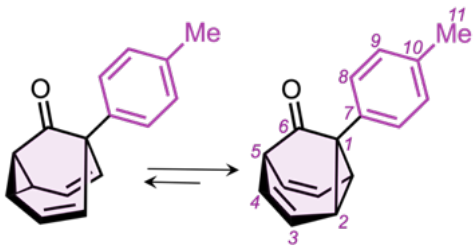

7-[2-(4-Tolyl)ethynyl]cyclohepta-1,3,5-triene (**3.8$_a$**, 830 mg, 4.02 mmol, 1.0 eq.) and diphenyl sulfoxide (1.62 g, 8.04 mmol, 2.0 eq.) were charged in a flask and dissolved in anhydrous CH_2Cl_2 (15 mL) at rt, with no particular precautions to exclude air. (Acetonitrile)[1,3-bis(2,6-diisopropylphenyl)imidazol-2-ylidene]gold(I) tetrafluoroborate (143 mg, 0.20 mmol, 5 mol%) was added in one portion at the same temperature and the reaction mixture was stirred for 16 h. The reaction was quenched with Et_3N (8 drops) and the solvent was removed under reduced pressure. The crude residue was purified by column chromatography (Teledyne Isco CombiFlash Rf+ system, 24 g SiO_2, hexanes–EtOAc, 0–100% gradient elution) to yield the title compound as a cream solid (554 mg, 2.49 mmol, 62%). **M.P.** 121 – 123 °C (lit.[68] 123 – 125 °C). **^{1}H NMR** (700 MHz, 298 K, $CDCl_3$) δ 7.19–7.16 (m, 2H, H_8), 7.13 (d, *J* = 8.1 Hz, 2H, H_9), 5.93 – 5.89 (m, 2H, H_4), 5.88 – 5.84 (m, 2H, H_3), 3.23 (tt, *J* = 6.5, 0.9 Hz, 1H, H_5), 3.11 – 3.02 (m, 2H, H_2), 2.34 (s, 3H, H_{11}). **^{13}C NMR** (176 MHz, 298 K, $CDCl_3$) δ 208.5 (C_6), 137.8 (C_{10}), 134.1 (C_7), 129.8 (C_9), 129.6 (C_8), 125.0 (C_4), 121.7 (C_3), 49.3 (C_5), 42.5 (C_2), 31.3 (C_1), 21.5 (C_{11}). **HRMS-ASAP** *m/z* = 223.1112 $[M+H]^+$ (calculated for $C_{16}H_{15}O$ = 223.1123).

Spectroscopic data are consistent with those published previously.[68]

(±)-1-(4-Anisyl)tricyclo[3.3.1.0^{2,8}]nona-3,6-dien-9-one (3.9$_b$)

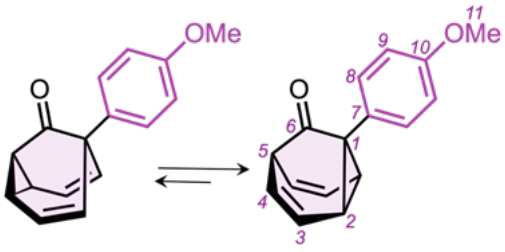

7-[2-(4-Anisyl)ethynyl]cyclohepta-1,3,5-triene (**3.8$_b$**, 1.0 g, 4.5 mmol, 1.0 eq.) and diphenyl sulfoxide (1.8 g, 9.0 mmol, 2.0 eq.) were charged in a flask and dissolved in anhydrous CH_2Cl_2 (15 mL) at rt, with no particular precautions to exclude air. (Acetonitrile)[1,3-bis(2,6-diisopropylphenyl)imidazol-2-ylidene]gold(I) tetrafluoroborate (160 mg, 0.2 mmol, 5

mol%) was added in one portion at the same temperature and the reaction mixture was stirred for 16 h. The reaction was quenched with Et_3N (10 drops) and the solvent was removed under reduced pressure. The crude residue was purified by column chromatography (Teledyne Isco CombiFlash Rf+ system, 24 g SiO_2, hexanes–EtOAc, 0–100% gradient elution) to yield the title compound as a cream solid (0.81 g, 3.39 mmol, 75%). **M.P.** 78 – 80 °C (lit.[112] 79 – 81 °C). **^{1}H NMR** (600 MHz, 298 K, $CDCl_3$) δ 7.16 (d, *J* = 8.8 Hz, 2H, H_8), 6.90 (d, *J* = 8.7 Hz, 2H, H_9), 5.93 – 5.89 (m, 2H, H_4), 5.88 – 5.84 (m, 2H, H_3), 3.80 (s, 3H, H_{11}), 3.34 – 3.17 (m, 2H, H_5), 3.10 – 2.98 (m, 2H, H_2). **^{13}C NMR** (151 MHz, 298 K, $CDCl_3$) δ 208.5 (C_6), 159.2 (C_{10}), 130.8 (C_8), 128.9 (C_7), 125.0 (C_4), 121.5 (C_3), 114.2 (C_9), 55.4 (C_{11}), 49.1 (C_5), 42.2 (C_2), 39.1 (C_1). **HR-ASAP-MS** *m/z* = 239.1075 $[M+H]^+$ (calculated for $C_{16}H_{15}O_2^+$ = 239.1067).

Spectroscopic data are consistent with those published previously.[112]

(±)-1-Phenyltricyclo[3.3.1.0.^{2,8}]nona-3,6-dien-9-one (3.9$_c$)

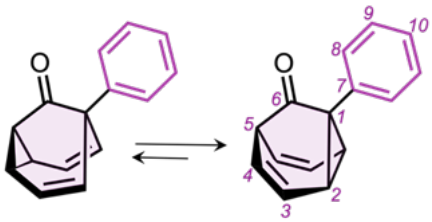

7-[2-Phenylethynyl)cyclohepta-1,3,5-triene (**3.8$_c$**, 475 mg, 2.47 mmol, 1.0 eq.) and diphenyl sulfoxide (1.0 g, 4.94 mmol, 2.0 eq.) were charged in a flask and dissolved in anhydrous CH_2Cl_2 (15 mL) at rt, with no particular precautions to exclude air. (Acetonitrile)[1,3-bis(2,6-diisopropylphenyl)imidazol-2-ylidene]gold(I) tetrafluoroborate (88 mg, 0.1 mmol, 5 mol%) was added in one portion at the same temperature and the reaction mixture was stirred for 16 h. The reaction was quenched with Et_3N (5 drops) and the solvent was removed under reduced pressure. The crude residue was purified by column chromatography (Teledyne Isco CombiFlash Rf+ system, 24 g SiO_2, 0–100% hexanes–EtOAc, gradient elution) to yield the title compound as a cream solid (297 mg, 1.43 mmol, 58%). **M.P.** 104 – 105 °C (lit.[112] 104 – 105 °C). **^{1}H NMR** (700 MHz, 298 K, $CDCl_3$) δ 7.35 (dd, *J* = 8.2, 6.9 Hz, 2H, H_9), 7.31 – 7.27 (m, 1H, H_{10}), 7.24 (dd, *J* = 8.1, 1.4 Hz, 2H, H_8), 5.94 – 5.90 (m, 2H, H_4), 5.89 – 5.83 (m, 2H, H_3), 3.30 – 3.17 (m, 1H, H_5), 3.15 – 2.96 (m, 2H, H_2). **^{13}C NMR** (176 MHz, 298 K, $CDCl_3$) δ 208.2 (C_6), 136.9 (C_7), 129.7

(C_8), 128.7 (C_9), 127.9 (C_{10}), 125.0 (C_4), 121.5 (C_3), 49.2 (C_5), 42.0 (C_2), 39.7 (C_1). **HR-ASAP-MS** *m/z* = 209.0952 $[M+H]^+$ (calculated for $C_{15}H_{13}O^+$ = 209.0961). Spectroscopic data are consistent with those published previously.[112]

(±)-1-(4-Fluorophenyl)tricyclo[3.3.1.$0^{2,8}$]nona-3,6-dien-9-one (3.9_d)

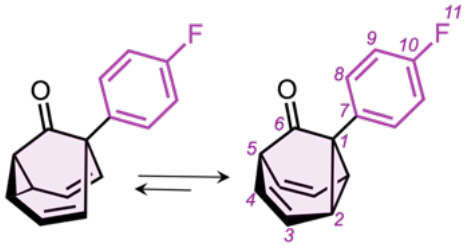

7-[2-(4-Fluorophenyl)ethynyl]cyclohep-ta-1,3,5-triene (**3.8**$_d$, 374 mg, 1.8 mmol, 1.0 eq.) and diphenyl sulfoxide (720 mg, 3.6 mmol, 2.0 eq.) were charged in a flask and dissolved in anhydrous CH_2Cl_2 (15 mL) at rt, with no particular precautions to exclude air. (Acetonitrile)[1,3-bis(2,6-diisopropylphenyl)-imidazol-2-ylidene]gold(I) tetrafluoroborate (63.5 mg, 0.1 mmol, 5 mol%) was added in one portion at the same temperature and the reaction mixture was stirred for 16 h. The reaction was quenched with Et_3N (4 drops) and the solvent was removed under reduced pressure. The crude residue was purified by column chromatography (Teledyne Isco CombiFlash Rf+ system, 24 g SiO_2, 0–100% hexanes–EtOAc, gradient elution) to yield the title compound as a pale yellow crystalline solid (262 mg, 1.24 mmol, 65%). **M.P.** 111 – 113 °C (lit.[112] 112 – 115 °C). **^{1}H NMR** (600 MHz, 298 K, $CDCl_3$) δ 7.24 – 7.19 (m, 2H, H_8), 7.04 (dd, *J* = 8.7, J_{HF} = 8.7 Hz, 2H, H_9), 5.96 – 5.88 (m, 2H, H_4), 5.88 – 5.84 (m, 2H, H_3), 3.23 (tt, *J* = 6.3, 1.2 Hz, 1H, H_5), 3.10 – 3.05 (m, 2H, H_2). **^{13}C NMR** (151 MHz, 298 K, $CDCl_3$) δ 207.8 (C_6), 162.2 (d, J_{CF} = 246.3 Hz, C_{10}), 132.7 – 132.4 (m, C_7), 132.1 (d, J_{CF} = 8.2 Hz, C_8), 124.4 (C_4), 121.2 (C_3), 115.4 (d, J_{CF} = 21.5 Hz, C_9), 48.7 (C_5), 42.4 (C_2), 39.0 (C_1). **^{19}F NMR** (376 MHz, 298 K, $CDCl_3$) δ –117.7 (tt, J_{FH} = 8.7, 5.3 Hz, F_{11}). **HR-ASAP-MS** *m/z* = 227.0876 $[M+H]^+$ (calculated for $C_{15}H_{12}OF^+$ = 227.0867). Spectroscopic data are consistent with those published previously.[112]

(±)-1-[4-(Trifluoromethyl)phenyl]tricyclo[3.3.1.0^{2,8}]nona-3,6-dien-9-one (3.9$_e$)

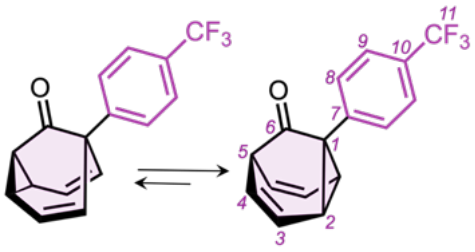

7-{2-[4-(Trifluoromethyl)phenyl]ethynyl}-cyclohepta-1,3,5-triene (**3.8$_e$**, 542 mg, 1.74 mmol, 1.0 eq.) and diphenyl sulfoxide (704 mg, 3.48 mmol, 2.0 eq.) were charged in a flask and dissolved in anhydrous CH_2Cl_2 (15 mL) at rt, with no particular precautions to exclude air. (Acetonitrile)[1,3-bis(2,6-diisopropyl-phenyl)imidazol-2-ylidene]gold(I) tetrafluoroborate (61 mg, 0.09 mmol, 5 mol%) was added in one portion at the same temperature and the reaction mixture was stirred for 16 h. The reaction was quenched with Et_3N (6 drops) and the solvent was removed under reduced pressure. The crude residue was purified by column chromatography (Teledyne Isco CombiFlash Rf+ system, 24 g SiO_2, hexanes–EtOAc, 0–100% gradient elution) to yield the title compound as a yellow solid (279 mg, 1.01 mmol, 58%). **M.P.** 138 – 140 °C (lit.[68] 137 – 140 °C). **^{1}H NMR** (700 MHz, 298 K, $CDCl_3$) δ 7.62 (d, *J* = 8.1 Hz, 2H, H_9), 7.37 (d, *J* = 8.0 Hz, 2H, H_8), 5.94–5.90 (m, 2H, H_4), 5.89–5.86 (m, 2H, H_3), 3.26 (t, *J* = 6.4 Hz, 1H, H_5), 3.15–3.11 (m, 2H, H_2). **^{13}C NMR** (176 MHz, 298 K, $CDCl_3$) δ 207.5 (C_6), 141.0–140.9 (m, C_7), 130.1 (C_8), 129.9 (q, J_{CF} = 32.4 Hz, C_{10}), 125.5 (q, J_{CF} = 3.8 Hz, C_9), 124.4 (C_4), 124.2 (q, J_{CF} = 272.1 Hz, C_{11}), 121.2 (C_3), 48.8 (C_5), 42.6 (C_2), 39.5 (C_1). **^{19}F NMR** (376 MHz, 298 K, $CDCl_3$) δ –62.6 (s, F_{11}). **HRMS-ASAP** *m/z* = 277.0833 $[M+H]^+$ (calculated for $C_{16}H_{12}OF_3$ = 277.0840).

Spectroscopic data are consistent with those published previously.[68]

(±)-1,9-Bis(4-tolyl)tricyclo[3.3.1.02,8]nona-3,6-dien-9-ol (3.10$_a$)

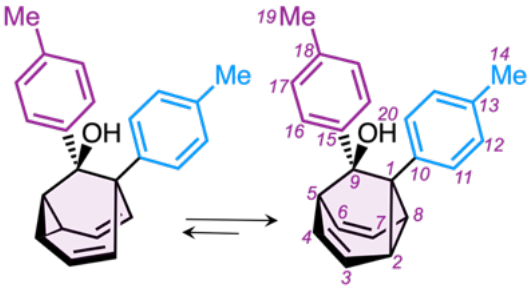

Magnesium turnings (350 mg, 14.40 mmol, 1.0 eq.) and I_2 (183 mg, 0.72 mmol, 5 mol%) were placed in an oven-dried two-necked round-bottomed flask fitted with a condenser and a septum under a N_2 atmosphere. The flask was gently heated with a heat gun until the I_2 started to sublime. The flask was cooled down to rt. A

quarter of a solution of 4-bromotoluene (2.47 g, 14.44 mmol, 1.0 eq.) in anhydrous THF (10 mL) was added to the reaction mixture, which was heated until it reached reflux. Upon gentle reflux, the remaining solution of 1-bromo-4-fluorobenzene in anhydrous THF was added dropwise over 30 min. The reaction mixture was heated at reflux for 30 min before cooling to rt. 1-(4-Tolyl)tricyclo[3.3.1.$0^{2,8}$]nona-3,6-dien-9-one (**3.9**$_a$, 540 mg, 2.43 mmol, 0.17 eq.) was transferred to an oven-dried round-bottomed flask, and the flask was purged with N_2. Anhydrous THF (10 mL) was added and the solution was cooled to 0 °C. The Grignard solution (prepared above) was added dropwise over 30 min to the barbaralone (**BBO**). The reaction mixture was stirred for 16 h, and the temperature was raised from 0 °C to rt, following removal of the ice bath. The reaction was quenched with a saturated aqueous solution of NH_4Cl (10 mL), then extracted with EtOAc (3 × 20 mL). The combined organic extracts were dried over $MgSO_4$, filtered and the solvent removed under reduced pressure. The crude residue was purified by column chromatography (Teledyne Isco CombiFlash Rf+ system, 24 g SiO_2, hexanes–CH_2Cl_2, 0–100% gradient elution including 0.5% Et_3N in the elution) to yield the title compound as a white powder (623 mg, 1.98 mmol, 81%). **M.P.** 101 – 103 °C. **^{1}H NMR** (700 MHz, 298 K, $CDCl_3$) δ 7.21 (d, *J* = 6.6 Hz, 2H, H_{16}), 7.20 (d, *J* = 6.6 Hz, 2H, H_{11}), 6.97 (d, *J* = 7.8 Hz, 2H, H_{12}), 6.95 (d, *J* = 8.0 Hz, 2H, H_{19}), 6.04 (ddd, *J* = 8.8, 6.8, 0.8 Hz, 1H, H_7), 5.83 (ddd, *J* = 8.8, 6.7, 0.6 Hz, 1H, H_3), 5.68 (dddd, *J* = 8.9, 6.6, 1.1, 1.1 Hz, 1H, H_4), 5.55 (dddd, *J* = 8.6, 6.9, 1.6, 0.9 Hz, 1H, H_6), 3.42 (ddd, *J* = 6.9, 6.9, 1.5 Hz, 1H, H_8), 2.98 (ddd, *J* = 6.9, 6.9, 1.5 Hz, 1H, H_2), 2.81 (t, *J* = 6.8 Hz, 1H, H_5), 2.24 (s, 3H, H_{19} or H_{14}), 2.24 (s, 3H, H_{19} or H_{14}), 2.16 (s, 1H, H_{20}). **^{13}C NMR** (176 MHz, 298 K, $CDCl_3$) δ 139.9 (C_{15}), 137.5 (C_{10}), 136.2 (C_{18} or C_{13}), 136.0 (C_{18} or C_{13}), 130.2 (C_{11}), 128.5 (C_{12}), 128.0 (C_{17}), 127.3 (C_{16}), 124.0 (C_7), 121.9 (C_3), 115.4 (C_6), 114.3 (C_4), 70.0 (C_5), 47.5 (C_8), 46.2 (C_1), 46.1 (C_2), 43.6 (C_9), 21.1 (C_{19} or C_{14}), 21.1 (C_{19} or C_{14}). **HRMS-ASAP** m/z = 313.1592 $[M–H]^+$ (calculated for $C_{23}H_{21}O$ = 313.1593).

(±)-9-(4-Fluorophenyl)-1-(4-anisyl)tricyclo[3.3.1.$0^{2,8}$]nona-3,6-dien-9-ol (3.10$_b$)

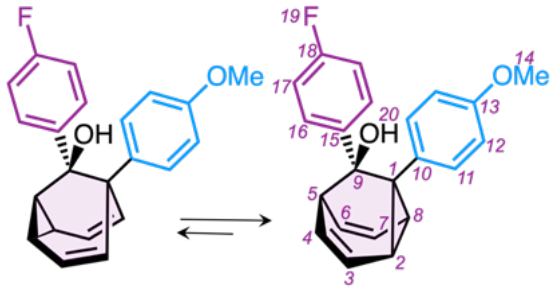

Magnesium turnings (57 mg, 2.4 mmol, 1.0 eq.) and I_2 (30 mg, 0.12 mmol, 5 mol%) were placed in an oven-dried two-necked round-bottomed flask fitted with a condenser and a septum under a N_2 atmosphere. The flask was gently heated with a heat gun until the I_2 started to sublime. The flask was cooled down to rt. A quarter of a solution of 1-bromo-4-fluorobenzene (410 mg, 2.4 mmol, 1.0 eq.) in anhydrous THF (10 mL) was added to the reaction mixture, which was heated until it reached reflux. Upon gentle reflux, the remaining solution of 1-bromo-4-fluorobenzene in anhydrous THF was added dropwise over 30 min. The reaction mixture was heated at reflux for 30 min before cooling to rt. 1-(4-Anisyl)tricyclo[3.3.1.$0^{2,8}$]nona-3,6-dien-9-one (**3.9$_b$**, 94 mg, 0.40 mmol, 0.17 eq.) was transferred to an oven-dried round-bottomed flask, and the flask was purged with N_2. Anhydrous THF (10 mL) was added and the solution was cooled to 0 °C. The Grignard solution (prepared above) was added dropwise over 30 min to the barbaralone (**BBO**). The reaction mixture was stirred for 16 h, and the temperature was raised from 0 °C to rt, following removal of the ice bath. The reaction was quenched with a saturated aqueous solution of NH_4Cl (10 mL), then extracted with EtOAc (3 × 20 mL). The combined organic extracts were dried over $MgSO_4$, filtered and the solvent removed under reduced pressure. The crude residue was purified by column chromatography (Teledyne Isco CombiFlash Rf+ system, 24 g SiO_2, hexanes–CH_2Cl_2, 0–100% gradient elution including 0.5% Et_3N in the elution) to yield the title compound as a light yellow solid (73 mg, 0.23 mmol, 59%). **M.P.** 122 – 124 °C. **^{1}H NMR** (700 MHz, 298 K, $CDCl_3$) δ 7.25 – 7.23 (m, 2H, H_{16}), 7.19 – 7.09 (m, 2H, H_{11}), 6.81 (d, *J* = 8.8 Hz, 2H, H_{17}), 6.70 (d, *J* = 8.8 Hz, 2H, H_{12}), 6.05 (ddd, *J* = 8.6, 6.9, 0.8 Hz, 1H, H_3), 5.83 (ddd, *J* = 8.8, 6.9, 0.6 Hz, 1H, H_7), 5.51 (ddd, *J* = 8.2, 6.7, 1.4 Hz, 1H, H_4), 5.45 (ddd, *J* = 8.4, 6.8, 1.4 Hz, 1H, H_6), 3.73 (s, 3H, H_{14}), 3.53 (dd, *J* = 6.7, 1.5 Hz, 1H, H_8), 3.19 (dd, *J* = 6.7, 1.4 Hz, 1H, H_2), 2.79 (ddd, *J* = 6.7, 1.4 Hz, 1H, H_5), 2.19 (s, 1H, H_{20}). **^{13}C NMR** (176 MHz, 298 K, $CDCl_3$) δ 161.6

(d, J_{CF} = 244.6 Hz, C_{18}), 158.4 (C_{13}), 138.5 (d, J_{CF} = 3.2 Hz, C_{15}), 132.2 (C_{10}), 131.4 (C_{11}), 129.1 (d, J_{CF} = 7.8 Hz, C_{16}), 124.1 (C_3), 121.9 (C_7), 113.9 (d, J_{CF} = 21.0 Hz, C_{17}), 113.2 (C_{12}), 110.4 (C_6), 109.0 (C_4), 69.7 (C_9), 55.3 (C_{14}), 52.4 (C_8), 51.1 (C_2), 44.9 (C_5), 44.5 (C_1). **^{19}F NMR** (376 MHz, 298 K, $CDCl_3$) δ –120.2 – 120.4 (m, F_{19}). **HR-ASAP-MS** *m/z* = 317.1330 [*M*–OH]$^+$ (calculated for $C_{22}H_{18}OF^+$ = 317.1336).

(±)-1,9-Diphenyltricyclo[3.3.1.0.2,8]nona-3,6-dien-9-ol (3.10$_c$)

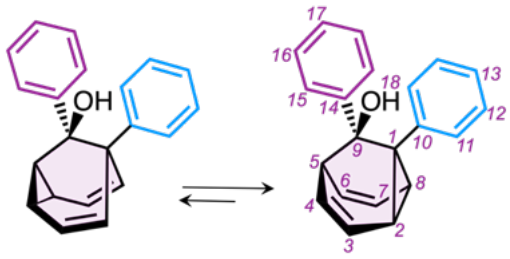

Magnesium turnings (70 mg, 2.78 mmol, 1.0 eq.) and I_2 (33 mg, 0.13 mmol, 5 mol%) were placed in an oven-dried two-necked round-bottomed flask fitted with a condenser and a septum under a N_2 atmosphere. The flask was gently heated with a heat gun until the I_2 started to sublime. The flask was cooled down to rt. A quarter of a solution of bromobenzene (430 mg, 2.60 mmol, 1.0 eq.) in anhydrous THF (10 mL) was added to the reaction mixture, which was heated until it reached reflux. Upon gentle reflux, the remaining solution of 1-bromo-4-fluorobenzene in anhydrous THF was added dropwise over 30 min. The reaction mixture was heated at reflux for 30 min before cooling to rt. 1-Phenyltricyclo[3.3.1.0.^{2,8}]nona-3,6-dien-9-one (**3.9$_c$**, 96 mg, 0.46 mmol, 0.17 eq.) was transferred to an oven-dried round-bottomed flask, and the flask was purged with N_2. Anhydrous THF (10 mL) was added and the solution was cooled to 0 °C. The Grignard solution (prepared above) was added dropwise over 30 min to the barbaralone (**BBO**). The reaction mixture was stirred for 16 h, and the temperature was raised from 0 °C to rt, following removal of the ice bath. The reaction was quenched with a saturated aqueous solution of NH_4Cl (10 mL), then extracted with EtOAc (3 × 20 mL). The combined organic extracts were dried over $MgSO_4$, filtered and the solvent removed under reduced pressure. The crude residue was purified by column chromatography (Teledyne Isco CombiFlash Rf+ system, 24 g SiO_2, hexanes–CH_2Cl_2, 0–100% gradient elution including 0.5% Et_3N in the elution) to yield the title compound as a white solid (45 mg, 0.16 mmol, 34%). **M.P.** 88 – 90 °C. **^{1}H NMR** (700 MHz, 298 K, $CDCl_3$) δ 7.32 –

7.29 (m, 2H, H_{15}), 7.28 – 7.26 (m, 2H, H_{11}), 7.18 – 7.13 (m, 3H, H_{12} and H_{13}), 7.13 – 7.08 (m, 3H, H_{16} and H_{17}), 6.07 (ddd, J = 8.7, 6.9, 0.8 Hz, 1H, H_3), 5.88 – 5.82 (m, 1H, H_7), 5.62 – 5.56 (m, 1H, H_4), 5.51 – 5.47 (m, 1H, H_6), 3.59 – 3.52 (m, 1H, H_8), 3.24 – 3.13 (m, 1H, H_2), 2.85 (t, J = 6.8 Hz, 1H, H_5), 2.22 (s, 1H, H_{18}). **^{13}C NMR** (176 MHz, 298 K, $CDCl_3$) δ 142.7 (C_{14}), 140.5 (C_{10}), 130.3 (C_{11}), 127.7 (C_{12}), 127.4 (C_{15}), 127.2 (C_{16}), 126.6 (C_{17}), 126.6 (C_{13}), 124.0 (C_3), 121.8 (C_7), 112.1 (C_6), 110.8 (C_4), 70.0 (C_1), 50.9 (C_8), 49.5 (C_2), 45.4 (C_5), 44.6 (C_9). **HRMS-ASAP** *m/z* = 269.1324 $[M+H]^+$ (calculated for $C_{21}H_{17}$ = 269.1330).

(±)-1,9-Bis(4-fluorophenyl)tricyclo-[3.3.1.0^{2,8}]nona-3,6-dien-9-ol (3.10_d)

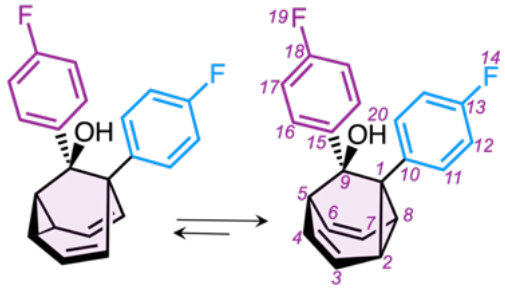

Magnesium turnings (118 mg, 4.9 mmol, 1.0 eq.) and I_2 (62 mg, 0.2 mmol, 5 mol%) were placed in an oven-dried two-necked round-bottomed flask fitted with a condenser and a septum under a N_2 atmosphere. The flask was gently heated with a heat gun until the I_2 started to sublime. The flask was cooled down to rt. A quarter of a solution of 1-bromo-4-fluorobenzene (0.5 mL, 823 mg, 4.7 mmol, 1.0 eq.) in anhydrous THF (10 mL) was added to the reaction mixture, which was heated until it reached reflux. Upon gentle reflux, the remaining solution of 1-bromo-4-fluorobenzene in anhydrous THF was added dropwise over 30 min. The reaction mixture was heated at reflux for 30 min before cooling to rt. 1-(4-Fluorophenyl)tricyclo[3.3.1.0^{2,8}]nona-3,6-dien-9-one (**3.9_d**, 162 mg, 0.70 mmol, 0.1 eq.) was transferred to an oven-dried round-bottomed flask, and the flask was purged with N_2. Anhydrous THF (10 mL) was added and the solution was cooled to 0 °C. The Grignard solution (prepared above) was added dropwise over 30 min to the barbaralone (**BBO**). The reaction mixture was stirred for 16 h, and the temperature was raised from 0 °C to rt, following removal of the ice bath. The reaction was quenched with a saturated aqueous solution of NH_4Cl (10 mL), then extracted with EtOAc (3 × 20 mL). The combined organic extracts were dried over $MgSO_4$, filtered and the solvent removed under reduced pressure. The crude residue was purified by column chromatography (Teledyne Isco CombiFlash Rf+ system, 24 g SiO_2,

hexanes–CH_2Cl_2, 0–100% gradient elution) to yield the title compound as an off-white powder (215 mg, 0.67 mmol, 93%). **M.P.** 116 – 118 °C. **^{1}H NMR** (700 MHz, 298 K, $CDCl_3$) δ 7.28 (ddd, *J* = 8.6, 5.4, 2.7 Hz, 2H, H_{16}), 7.23 (ddd, *J* = 8.5, 5.4, 2.6 Hz, 2H, H_{11}), 6.90 – 6.84 (m, 4H, H_{12} and H_{17}), 6.07 (ddd, *J* = 8.7, 7.0, 0.8 Hz, 1H, H_3), 5.87 (dd, *J* = 8.6, 7.0 Hz, 1H, H_7), 5.46 (dddd, *J* = 8.2, 7.0, 1.3, 1.5 Hz, 1H, H_4), 5.43 (dddd, *J* = 8.5, 6.9, 1.5, 1.5 Hz, 1H, H_6), 3.63 (ddd, *J* = 6.7, 6.7, 1.5 Hz, 1H, H_8), 3.31 (ddd, *J* = 7.1, 7.1, 1.4 Hz, 1H, H_2), 2.84 (t, *J* = 6.8 Hz, 1H, H_5), 2.28 (s, 1H, H_{20}). **^{13}C NMR** (176 MHz, 298 K, $CDCl_3$) δ 161.7 (d, J_{CF} = 245.5 Hz, C_{13}), 160.6 (d, J_{CF} = 245.0 Hz, C_{18}), 138.2 (d, J_{CF} = 3.1 Hz, C_{15}), 136.0 (d, J_{CF} = 3.2 Hz, C_{10}), 131.8 (d, J_{CF} = 7.9 Hz, C_{11}), 128.9 (d, J_{CF} = 7.8 Hz, C_{16}), 123.9 (C_3), 121.7 (C_7), 114.4 (d, J_{CF} = 21.1 Hz, C_{12}), 113.9 (d, J_{CF} = 20.9 Hz, C_{17}), 108.3 (C_6), 106.7 (C_4), 69.5 (C_9), 54.3 (C_8), 53.1 (C_2), 44.7 (C_1), 44.3 (C_5). **^{19}F NMR** (376 MHz, $CDCl_3$) δ –119.3 (tt, J_{FH} = 8.6, 5.5 Hz, F_{14} or F_{19}), –120.0 (tt, J_{FH} = 8.6, 5.5 Hz, F_{14} or F_{19}). **HR-ASAP-MS** *m/z* = 322.1176 $[M]^+$ (calculated for $C_{21}H_{16}OF_2^+$ = 322.1168).

(±)-1,9-bis(4-Trifluoromethyl)tricyclo-[3.3.1.0^{2,8}]nona-3,6-dien-9-ol (3.10$_e$)

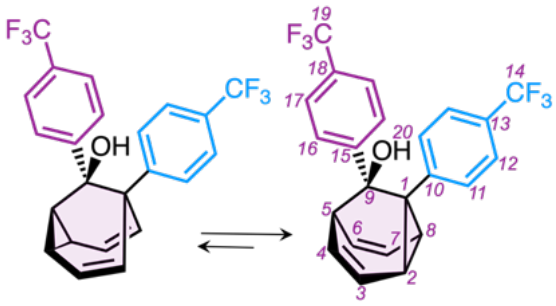

Magnesium turnings (115 mg, 6.36 mmol, 1.0 eq.) and I_2 (81 mg, 0.32 mmol, 5 mol%) were placed in an oven-dried two-necked round- bottomed flask fitted with a condenser and a septum under a N_2 atmosphere. The flask was gently heated with a heat gun until the I_2 started to sublime. The flask was cooled down to rt. A quarter of a solution of 4- bromobenzotrifluoride (1.36 g, 6.06 mmol, 1.0 eq.) in anhydrous THF (10 mL) was added to the reaction mixture, which was heated until it reached reflux. Upon gentle reflux, the remaining solution of 1-bromo-4-fluorobenzene in anhydrous THF was added dropwise over 30 min. The reaction mixture was heated at reflux for 30 min before cooling to rt. 1-[4-(Trifluoromethyl)phenyl]tricyclo[3.3.1.0^{2,8}]nona-3,6-dien-9-one (**3.9$_e$**, 162 mg, 0.72 mmol, 0.1 eq.) was transferred to an oven-dried round-bottomed flask, and the flask was purged with N_2. Anhydrous THF (10 mL) was added and the solution was cooled to

0 °C. The Grignard solution (prepared above) was added dropwise over 30 min to the barbaralone (**BBO**). The reaction mixture was stirred for 16 h, and the temperature was raised from 0 °C to rt, following removal of the ice bath. The reaction was quenched with a saturated aqueous solution of NH_4Cl (10 mL), then extracted with EtOAc (3 × 20 mL). The combined organic extracts were dried over $MgSO_4$, filtered and the solvent removed under reduced pressure. The crude residue was purified by column chromatography (Teledyne Isco CombiFlash Rf+ system, 24 g SiO_2, hexanes–CH_2Cl_2, 0–100% gradient elution including 0.5% Et_3N in the elution) to yield the title compound as a sticky yellow gel (416 mg, 0.99 mmol, 98%). **^{1}H NMR** (600 MHz, 298 K, $CDCl_3$) δ 7.53 (d, *J* = 8.5 Hz, 2H, H_{16}), 7.49–7.45 (m, 6H, H_{11}, H_{12} and H_{17}), 6.13 (dd, *J* = 8.7, 6.9 Hz, 1H, H_3), 5.93 (dd, *J* = 8.6, 7.0 Hz, 1H, H_7), 5.64 (dddd, *J* = 8.3, 6.7, 1.3, 1.3 Hz, 1H, H_4), 5.53 (dddd, *J* = 8.7, 6.9, 1.4, 1.4 Hz, 1H, H_6), 3.66 (ddd, *J* = 6.9, 6.8, 1.5 Hz, 1H, H_8), 3.23 (ddd, *J* = 6.8, 6.8, 1.4 Hz, 1H, H_2), 2.89 (t, *J* = 6.8 Hz, 1H, H_5), 2.45 (s, 1H, H_{20}). **^{13}C NMR** (151 MHz, 298 K, $CDCl_3$) δ 146.5 (C_{15}), 144.4 (s, C_{10}), 130.2 (C_{11}), 128.9 (q, J_{CF} = 32.2 Hz, C_{13}), 128.8 (q, J_{CF} = 32.3 Hz, C_{18}), 127.6 (C_{16}), 124.6 (q, J_{CF} = 3.6 Hz, C_{12}), 124.4 (q, J_{CF} = 271.9 Hz, C_{19}), 124.3 (q, J_{CF} = 272.0, C_{14}), 124.3 (q, J_{CF} = 3.8 Hz, C_{17}),124.3 (C_3), 121.9 (C_7), 112.1 (C_6), 110.6 (C_4), 70.0 (C_1), 50.5 (C_8), 49.4 (C_2), 45.4 (C_5), 44.2 (C_9). **^{19}F NMR** (376 MHz, 298 K, $CDCl_3$) δ –62.4 (s, F_{14} or F_{19}), –62.5 (s, F_{14} or F_{19}). **HRMS-ASAP** *m/z* = 422.1125 $[M]^+$ (calculated for $C_{23}H_{16}OF_2$ = 422.1105).

(±)-1,9-bis(4-Tolyl)tricyclo-[3.3.1.0^{2,8}]nona-3,6-dien-9-ol (3.10$_f$)

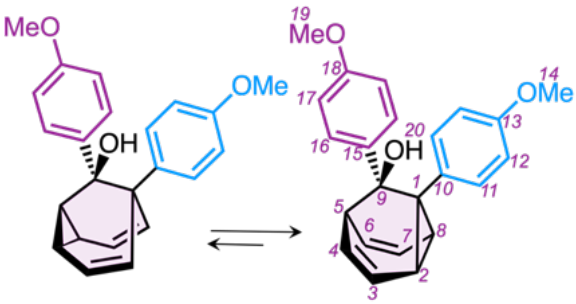

Magnesium turnings (115 mg, 4.78 mmol, 1.0 eq.) and I_2 (59 mg, 0.2 mmol, 5 mol%) were placed in an oven-dried two-necked round-bottomed flask fitted with a condenser and a septum under a N_2 atmosphere. The flask was gently heated with a heat gun until the I_2 started to sublime. The flask was cooled down to rt. A quarter of a solution of 4-bromoanisole (980 mg, 4.60 mmol, 1.0 eq.) in anhydrous THF (10 mL) was added to the reaction mixture, which was heated until it

reached reflux. Upon gentle reflux, the remaining solution of 4-bromoanisole in anhydrous THF was added dropwise over 30 min. The reaction mixture was heated at reflux for 30 min before cooling to rt. In an oven-dried round-bottomed flask, under an atmosphere of N_2, was added Bu_4NI (36.0 mg, 0.1 mmol), anhydrous diglyme (0.21 mL, 201 mg, 1.5 mmol), and the Grignard solution (prepared above). Anhydrous THF (15 mL) was added and the solution was cooled to 0 °C for 30 min with stirring. 1-(4-Anisyl)tricyclo[3.3.1.$0^{2,8}$]nona-3,6-dien-9-one (**3.9**$_b$, 225 mg, 0.90 mmol, 0.2 eq.) was added dropwise over 30 min at the same temperature. The reaction mixture was stirred for 16 h, where the temperature was raised from 0 °C to rt, following removal of the ice bath. The reaction was quenched with a saturated aqueous solution of NH_4Cl (10 mL), then extracted with EtOAc (3 × 20 mL). The combined organic extracts were dried over $MgSO_4$, filtered and the solvent removed under reduced pressure. The crude residue was purified by column chromatography (Teledyne Isco CombiFlash Rf+ system, 24 g Al_2O_3, hexanes–CH_2Cl_2, 0–100% gradient elution) to yield the title compound as a white solid (158 mg, 0.46 mmol, 43%). **M.P.** 128 – 130 °C. **^{1}H NMR** (700 MHz, 298 K, $CDCl_3$) δ 7.20 (d, *J* = 9.0 Hz, 2H, H_{16}), 7.18 (d, *J* = 9.5 Hz, 2H, H_{11}), 6.70 (d, *J* = 8.7 Hz, 2H, H_{12}), 6.68 (d, *J* = 8.9 Hz, 2H, H_{17}), 6.07 – 6.00 (m, 1H, H_3), 5.84 – 5.79 (m, 1H, H_7), 5.59 – 5.53 (m, 1H, H_4), 5.50 – 5.46 (m, 1H, H_6), 3.73 (s, 6H, H_{19} and H_{14}), 3.50 – 3.45 (m, 1H, H_8), 3.17 – 3.10 (m, 1H, H_2), 2.80 (t, *J* = 6.8 Hz, 1H, H_5), 2.14 (s, 1H, H_{20}). **^{13}C NMR** (176 MHz, 298 K, $CDCl_3$) δ 158.3 (C_{13}), 158.2 (C_{18}), 135.0 (C_{15}), 132.6 (C_{10}), 131.4 (C_{11}), 128.5 (C_{16}), 123.9 (C_3), 121.8 (C_7), 113.1 (C_{12}), 112.6 (C_{17}), 111.9 (C_6), 110.6 (C_4), 69.7 (C_9), 55.3 (C_{14} or C_{19}), 55.2 (C_{14} or C_{19}), 51.0 (C_8), 49.6 (C_2), 45.2 (C_5), 44.1 (C_1). **HR-ASAP-MS** *m/z* = 346.1568 $[M]^+$ (calculated for $C_{23}H_{22}O_3^+$ = 346.1564).

† Compounds synthesised by A. N. Bismillah.

Synthesis of Hydroxy Bullvalenes

Dibromocobalt(II)-diphenylphosphanylethyl(diphenyl)phosphane | $CoBr_2$(dppe)

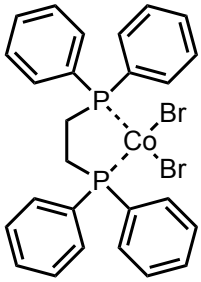

An oven-dried Schlenk flask was cooled under N_2. The flask was then charged with $CoBr_2$ (1.0 g, 4.8 mmol, 1.0 eq.) and dppe (1.9 g, 4.9 mmol, 1.0 eq.). To this mixture THF (40 mL) was added and the reaction mixture stirred at rt for 18 h. The precipitate formed was filtered and washed with Et_2O (30 mL). The solid was then dried under high *vacuo* for 24 h to afford a green solid (2.74 g, 4.45 mmol, 91%), which was used without further purification or characterisation.[113]

1,4-bis-(*tert*-Butyl-dimethyl-silanyloxy)-but-2-yne (3.13)

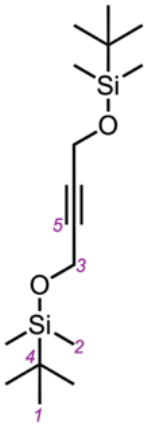

2-Butyne-1,4-diol (1.00 g, 11.6 mmol, 1.0 eq.), imidazole (1.90 g, 27.9 mmol, 2.4 eq.) and *N,N*-4-dimethylaminopyridine (142 mg, 1.16 mmol, 10 mol%) were placed in a oven-dried 100 mL round-bottomed flask. CH_2Cl_2 (60 mL) was added and the solution was stirred at rt. Chloro-*tert*-butyldimethylsilane (4.20 g, 27.9 mmol, 2.4 eq.) was then added and the solution was stirred at rt for 18 h. The solution was the poured over 10% aqueous K_2CO_3 (40 mL) and the organic layer extracted. The resulting aqueous layer was extracted further with Et_2O (3 × 15 mL). The combined organic layers were dried over $MgSO_4$, filtered and the filtrate was concentrated *in vacuo* to give the crude product which was purified by column chromatography (Teledyne Isco CombiFlash Rf+ system, 24 g SiO_2; hexanes–EtOAc, 0–10% gradient elution) to yield the title compound as a colourless oil (2.25 g, 7.16 mmol, 82%). **^{1}H NMR** (400 MHz, 298 K, $CDCl_3$) δ 4.33 (s, 4H, H_3), 0.90 (s, 18H, H_1), 0.11 (s, 12H, H_2). **^{13}C NMR** (101 MHz, 298 K, $CDCl_3$) δ 83.5 (C_5), 51.9 (C_3), 25.8 (C_1), 18.4 (C_4), 5.0 (C_2). **HR-ESI-MS**: *m/z* = 315.2198 $[M + H]^+$ (calculated for $[M + H]^+$ = 315.2185).

Spectroscopic data are consistent with those published previously.[114]

4-(4-Methylphenyl)sulfonyloxybut-2-ynyl 4-methylbenzenesulfonate (3.15)

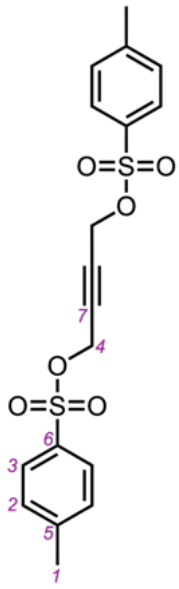

A round-bottomed flask was oven-dried and cooled under N_2. *p*-Toluenesulfonyl chloride (5.53 g, 29.0 mmol, 2.5 eq.) was added and dissolved in Et_2O (70 mL). 2-Butyne-1,4,-diol (1.00 g, 11.6 mmol, 1.0 eq.) was then added to the solution. The reaction mixture was then put in a NaCl/ice (1:1) bath at –15 °C. Potassium hydroxide (4.68 g, 83.5 mmol, 7.2 eq.) was added at regular intervals over five mins. Once added, the reaction mixture was allowed to warm to 0 °C in an ice/water bath while stirring for 2 h. After 2 h, cold H_2O (40 mL) was added to the reaction mixture and stirred until all the contents were dissolved. The solution was then allowed to warm to rt. The organic layer was decanted and the aqueous layer was extracted with CH_2Cl_2 (3 × 40 mL). The combined organic fractions were dried over $MgSO_4$, filtered and the solvent removed under reduced pressure. The crude residue was purified by column chromatography (Teledyne Isco CombiFlash Rf+, 40 g SiO_2; hexanes–CH_2Cl_2, 0–80% gradient elution) to afford the title compound as a white solid (2.28 g, 5.78 mmol, 50%). **^{1}H NMR** (400 MHz, 298 K, $CDCl_3$) δ 7.76 (d, 4H, H_2), 7.35 (d, 4H, H_3), 4.58 (s, 4H, H_4), 2.46 (s, 6H, H_1). **^{13}C NMR** (101 MHz, 298 K, $CDCl_3$) δ 145.6 (C_6), 132.9 (C_5), 130.0 (C_2), 128.2 (C_3), 81.1 (C_7), 57.2 (C_4), 21.8 (C_1). **HR-ESI-MS**: *m/z* = 365.0641 $[M + H]^+$ (calculated for $[M + H]^+$ = 365.0637).

Spectroscopic data are consistent with those published previously.[115]

(*R*)-2,2'-Binaphthyldioxacyclodecyne (3.16)

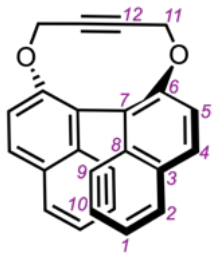

(*R*)-BINOL (1.45 g, 5.07 mmol, 1.0 eq.) and but-2-yne-1,4-diyl bis(4-methylbenzenesulfonate) (2.00 g, 5.07 mmol, 1.0 eq.) were added to a 40 mL oven-dried Erlenmeyer flask and put under a N_2 atmosphere. The contents were dissolved in MeCN (23 mL). Cs_2CO_3 (3.63 g, 11.15 mmol, 2.2 eq.) was added to a 250 mL oven-dried round-bottomed flask under an N_2 atmosphere and MeCN (77 mL) was then added. The contents of the Erlenmeyer flask were then taken up into a syringe and added into

the round-bottomed flask using a syringe pump over 8 h (~ 2.8 mL/hr). After 24 h, the reaction mixture was filtered through a sintered funnel by vacuum filtration and washed with EtOAc (50 mL). The solvent was evaporated *in vacuo*, redissolved in CH_2Cl_2 and then filtered. The solvent was then removed *in vacuo* to give the crude product, which was purified by column chromatography (Teledyne Isco CombiFlash Rf+, 40 g SiO_2; hexanes–EtOAc, 0–20% gradient elution) to yield the title compound as a pale brown solid (0.282 g, 0.834 mmol, 12%). **^{1}H NMR** (400 MHz, 298 K, $CDCl_3$) δ 8.04 – 8.01 (d, 2H, *J* = 8.8 Hz, H_1), 7.93 – 7.91 (d, *J* = 8.2 Hz, 2H, H_{10}), 7.45 – 7.41 (m, 4H, H_2 and H_9), 7.36 – 7.31 (m, 4H, H_4 and H_5), 4.59 – 4.44 (m, 4H, H_{11}). **^{13}C NMR** (101 MHz, 298 K, $CDCl_3$) δ 152.6 (C_6), 133.7 (C_7), 131.9 (C_8), 130.4 (C_5), 128.2 (C_4), 128.0 (C_3), 126.7 (C_9), 126.3 (C_{10}), 125.4 (C_2), 121.3 (C_1) 88.2 (C_{12}), 62.5 (C_{11}). **HR-ASAP-MS**: *m/z* = 337.1212 $[M + H]^+$ (calculated for $[M + H]^+$ = 337.1229).

Spectroscopic data are consistent with those previously published.[72]

((2*Z*,4*Z*)-Bicyclo[4.2.2]deca-2,4,7,9-tetraene-7,8-diyl)dimethanol| *bis*(Hydroxymethylene) BDT (3.12)

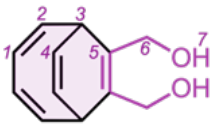

ZnI_2 (1.22 g, 3.84 mmol, 24 mol%), $CoBr_2$(dppe) (1.18 g, 1.92 mmol, 12 mol%) and activated Zn dust (0.377 g, 5.76 mmol, 36 mol%) was added to an oven-dried round-bottomed flask which was then flushed with N_2 and evacuated under high vacuum three times. Anhydrous TFE (10 mL) was added and the reaction mixture was stirred for 15 min at 55 °C. Cyclooctatetraene (1.67 g, 16.0 mmol, 1.0 eq.) was then added, followed by 2-butyne-1,4-diol (1.98 g, 23.0 mmol, 1.4 eq.) dissolved in TFE (6 mL) over 12 h *via* syringe pump, whilst stirring at 55 °C. The reaction mixture was then allowed to stir for an additional 36 h at 55 °C, before being filtered through a short pad of SiO_2 (10 g), eluting with EtOAc (250 mL). The solvent was removed *in vacuo* and the crude residue purified using column chromatography (Teledyne Isco CombiFlash Rf+ system, 40 g SiO_2, hexanes–EtOAc, 0–100% gradient elution) to yield the title compound as a white solid (1.77 g, 9.31 mmol, 58%). **^{1}H NMR** (400 MHz, 298 K, $CDCl_3$); δ 6.34–6.20 (m, 2H, H_2), 5.80–5.66 (m, 4H, H_1 and H_4), 4.36–4.16 (m, 4H, H_6), 3.48–3.41 (ddd, *J* = 8.8, 4.0, 2.5 Hz, 2H, H_3), 1.38 (s, 2H, OH_7); **^{13}C NMR** (101 MHz, 298 K, $CDCl_3$) δ 141.8 (C_2), 132.9 (C_5),

125.0 (C_1), 121.2 (C_4), 61.0 (C_6), 38.2 (C_3). **HR-ESI-MS**: *m/z* = 213.0898 $[M + Na]^+$ (calculated for $[M + Na]^+$ = 213.0900).

Spectroscopic data are consistent with those published previously.[64,116]

((2*Z*,4*Z*)-Bicyclo[4.2.2]deca-2,4,7,9-tetraen-7-yl)methanol | Hydroxymethylene BDT (3.18)

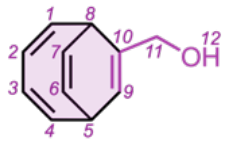

ZnI_2 (221 mg, 0.69 mmol, 20 mol%), $CoBr_2$(dppe) (214 mg, 0.35 mmol, 10 mol%) and activated Zn dust (68 mg, 1.04 mmol, 30 mol%) was added to an oven-dried round-bottomed flask which was then flushed with N_2 and evacuated under high vacuum three times. Anhydrous TFE (3 mL) was added to the vial and the reaction mixture was stirred for 15 min at rt. Cyclooctatetraene (361 mg, 3.50 mmol, 1.0 eq.) was then added, followed by 2-Prop-2-yn-1-ol (291 mg, 5.20 mmol, 1.5 eq.) dissolved in TFE (4 mL) over 12 h *via* syringe pump, whilst stirring at 55 °C. The reaction mixture was then allowed to stir for an additional 48 h at 55 °C, before being filtered through a short pad of SiO_2 (5 g), eluting with CH_2Cl_2 (100 mL). The solvent was removed *in vacuo* and the crude residue purified using column chromatography (Teledyne Isco CombiFlash Rf+ system, 12 g SiO_2, hexanes–EtOAc, 0–100% gradient elution) to yield the title compound as a pale-yellow oil (347 mg, 2.17 mmol, 62%). **^{1}H NMR** (400 MHz, 298 K, $CDCl_3$); δ 6.29–6.18 (m, 2H, H_1 and H_4), 5.82–5.74 (m, 2H, H_2 and H_3), 5.74–5.68 (m, 1H, H_7), 5.68–5.60 (m, 2H, H_6 and H_9), 4.20–4.06 (m, 2H, H_{11}), 3.44 (dd, *J* = 8.8, 5.8 Hz, 1H, H_8), 3.24–3.17 (m, 1H, H_5), 1.38 (s, 1H, OH_{12}); **^{13}C NMR** (101 MHz, 298 K, $CDCl_3$,); δ 141.9 (C_4), 141.4 (C_1), 136.1 (C_{10}), 124.7 (C_2), 124.4 (C_3), 121.1 (C_6), 121.0 (C_7), 118.8 (C_9), 64.7 (C_{11}), 36.4 (C_8), 34.7 (C_5); **HR-ESI-MS**: *m/z* = 161.0978 $[M + H]^+$ (calculated for $[M + H]^+$ = 161.0966).

Spectroscopic data were consistent with those published previously.[64,116]

((2*Z*,4*Z*)-8-Ethylbicyclo[4.2.2]deca-2,4,7,9-tetraen-7-yl)methanol | Ethyl hydroxymethylene BDT (3.19)

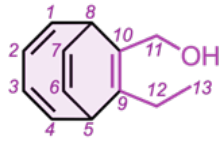

ZnI_2 (111 mg, 0.35 mmol, 20 mol%), $CoBr_2$(dppe) (107 mg, 0.18 mmol, 10 mol%) and activated Zn dust (34 mg, 0.52 mmol, 30 mol%) was added to an oven-dried round-bottomed flask which was then flushed with N_2 and evacuated under high vacuum three times. Anhydrous TFE (1.5

mL) was added to the vial and the reaction mixture was stirred for 15 min at rt. Cyclooctatetraene (181 mg, 1.75 mmol, 1.0 eq.) was then added, followed by 2-pentyn-1-ol (177 mg, 2.10 mmol, 1.2 eq.) dissolved in TFE (4 mL) over 12 h *via* syringe pump, whilst stirring at 55 °C. The reaction mixture was then allowed to stir for an additional 48 h at 55 °C, before being filtered through a short pad of SiO_2 (5 g), eluting with Et_2O (100 mL). The solvent was removed *in vacuo* and the crude residue purified using column chromatography (Teledyne Isco CombiFlash Rf+ system, 12 g SiO_2, hexanes–EtOAc, 0–50% gradient elution) to yield the title compound as a colourless oil (194 mg, 1.03 mmol, 59%). **^{1}H NMR** (400 MHz, 298 K, $CDCl_3$); δ 6.32–6.16 (m, 2H, H_1 and H_4), 5.74–5.62 (m, 4H, $H_{2,3,6,7}$), 4.27 (d, *J* = 11.9 Hz, 1H, H_{11}), 4.10 (d, *J* = 11.9 Hz, 1H, H_{11}), 3.48–3.40 (m, 1H, H_8), 3.24–3.18 (m, 1H, H_5), 2.28–2.12 (m, 2H, H_{12}), 1.00 (t, *J* = 7.6 Hz, 3H, H_{13}). **^{13}C NMR** (101 MHz, 298 K, $CDCl_{3,}$); δ 142.7 (C_1), 141.8 (C_4), 135.9 (C_9), 129.5 (C_{10}), 124.6 ($C_{2\text{ or }3}$), 124.5 ($C_{2\text{ or }3}$), 121.5 ($C_{6\text{ or }7}$), 121.3 ($C_{6\text{ or }7}$), 61.2 (C_{11}), 39.6 (C_5), 37.8 (C_8), 24.4 (C_{12}), 15.1 (C_{13}). **HR-ESI-MS**: *m/z* = 171.1172 $[M - OH]^+$ (calculated for $[M - OH]^+$ = 171.1174).

2-((2*Z*,4*Z*)-8-Ethylbicyclo[4.2.2]deca-2,4,7,9-tetraen-7-yl)ethan-1-ol | Ethyl hydroxyethylene BDT (3.20)

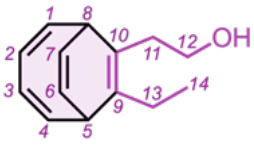

ZnI_2 (4.88 g, 15.4 mmol, 20 mol%), $CoBr_2$(dppe) (4.74 g, 7.68 mmol, 10 mol%) and activated Zn dust (2.51 g, 38.4 mmol, 50 mol%) was added to an oven-dried round-bottomed flask which was then flushed with N_2 and evacuated under high vacuum 3 times. Anhydrous TFE (25 mL) was added to the vessel and the reaction mixture was stirred for 15 min at 55 °C. Cyclooctatetraene (8.7 mL, 77 mmol, 1.0 eq.) was then added followed by the dropwise addition of 3-hexyn-1-ol (8.1 g, 10 mL, 92 mmol, 1.2 eq.) dissolved in TFE (15 mL) over 10 min whilst stirring at 55 °C. The reaction mixture was then allowed to stir for an additional 72 h at 55 °C, before being filtered through a short pad of SiO_2 (15 g), eluting with EtOAc (100 mL) and MeOH (100 mL). The solvent was removed *in vacuo* and the crude residue purified using column chromatography (Teledyne Isco CombiFlash Rf+ system, 48 g SiO_2, hexanes–EtOAc, 0–25% gradient elution) to yield the title compound as a pale-yellow oil (4.41 g, 21.8 mmol, 28%). **^{1}H NMR** (400 MHz, 298

K, $CDCl_3$); δ 6.29–6.22 (m, 2H, $H_{1,4}$), 5.72–5.67 (m, 4H, $H_{2,3,6,7}$), 3.693.57 (m, 2H, $H_{5,8}$), 3.25–3.21 (m, 1H, H_{12}), 3.13–3.09 (m, 1H, H_{12}), 2.64–2.57 (m, 4H, $H_{11,13}$), 0.99 (t, *J* = 7.5 Hz, 3H, H_{14}); **^{13}C NMR** (101 MHz, 298 K, $CDCl_3$,); δ 143.0 (C_4), 142.1 (C_1), 136.6 (C_{10}), 125.3 (C_9) 124.3 (C_2), 124.1 (C_3), 121.3 (C_6), 121.1 (C_7), 62.0 (C_{12}), 40.0 (C_8), 39.6 (C_5), 35.0 (C_{11}), 24.5 (C_{13}), 14.7 (C_{14}); **HR-ESI-MS:** *m/z* = 225.1252 $[M + Na]^+$ (calculated for $[M + Na]^+$ = 225.1250.

Tricyclo[3.3.2.0^{2,8}]deca-3,6,9-trien-4-yl dimethanol | Bis(hydroxymethylene) BV (3.21)

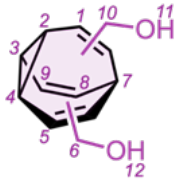

Bis(Hydroxymethylene) BDT (**3.12**, 200 mg, 1.05 mmol, 1.0 eq.) and thioxanthene-9-one (11 mg, 0.005 mmol, 5 mol%) were dissolved in anhydrous THF (4 mL) in an oven-dried microwave vial. The mixture was stirred for 6 h, undergoing a fully enclosed irradiation with 360 nm UV light at –5 °C. Following irradiation, the solvent was removed *in vacuo* and the crude residue purified by column chromatography (Teledyne Isco CombiFlash Rf+ system, 24 g SiO_2, hexanes–EtOAc, 0–100% gradient elution) to give the title compound as a pale yellow oil (56 mg, 0.29 mmol, 28%). **^{1}H NMR** (400 MHz, 298 K, $CDCl_3$) δ 5.89 (s, 5H, H_1, H_2, H_5, H_8 and H_9), 4.06–3.91 (m, 3H, H_3, H_4 and H_7), 2.20 (bs, 2H, H_{11} and H_{12}), 2.02 (s, 4H, H_6 and H_{10}). **HR-ESI-MS:** *m/z* = 189.0924 $[M + H]^+$ (calculated for $[M + H]^+$ = 189.0916). Spectroscopic data are consistent with those previously published.[64]

Tricyclo[3.3.2.0^{2,8}]deca-3,6,9-trien-1-yl methanol | Hydroxymethylene BV (3.22)

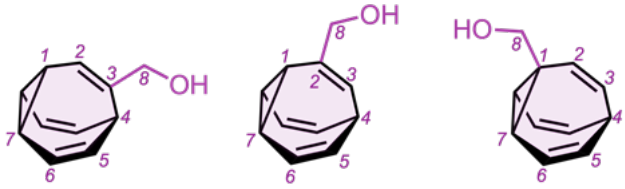

β-3.22 *γ*-3.22 *δ*-3.22

Isomer Ratio
β:*γ*:*δ* | 59:24:17

Hydroxymethylene BDT (**3.18**, 145 mg, 0.90 mmol, 1.0 eq.) and thioxanthene-9-one (2 mg, 0.005 mmol, 5 mol%) were dissolved in anhydrous THF (3 mL) in an oven-dried microwave vial. The mixture was stirred for 6 h, undergoing a fully enclosed irradiation with 360 nm UV light at –5 °C. Following irradiation, the solvent was removed *in vacuo*

and the crude residue purified by column chromatography (Teledyne Isco CombiFlash Rf+ system, 12 g SiO_2, hexanes–EtOAc, 0–100% gradient elution) to give the title compound as a pale yellow oil (40 mg, 0.25 mmol, 28%). **^{1}H NMR** (500 MHz, 223 K, CD_3CD_2OD) δ 5.86–5.67 (m, 5.17H, H_2, H_3, H_5 and H_6), 3.93 (s, 0.48H, *γ*-H_8), 3.88 (s, 1.18H, *β*-H_8), 3.48 (s, 0.34H, *δ*-H_8), 2.38–2.06 (m, 3.83H, H_1,H_4 and H_7). **^{13}C NMR** (125 MHz, 223 K, CD_3CD_2OD) δ 141.2 (*β*-C_3), 138.8 (*γ*-C_2), 129.7 (*δ*-$C_{3/5/6}$), 129.0 (*δ*-C_2), 128.3 (*δ*-$C_{3/5/6}$), 128.0 (*β*-$C_{5/6}$ / *γ*-$C_{5/6}$), 127.9 (*β*-$C_{5/6}$ / *γ*-$C_{5/6}$), 127.7 (*β*-$C_{5/6}$ / *γ*-$C_{5/6}$), 127.4 (*δ*-$C_{3/5/6}$), 122.0 (*γ*-C_3), 121.8 (*β*-C_2), 71.0 (*δ*-C_8), 68.9 (*γ*-C_8), 67.6 (*β*-C_8), 33.3 (*β*-C_4), 32.1 (*δ*-C_4), 31.8 (*δ*-C_1), 31.2 (*γ*-C_4), 26.0 (*δ*-C_7), 21.8 (*γ*-C_1), 21.3 (*β*-C_1), 20.8 (*γ*-C_7), 19.8 (*β*-C_7). **HR-ESI-MS**: *m/z* = 161.0914 $[M + H]^+$ (calculated for $[M + H]^+$ = 161.0908). Spectroscopic data are consistent with those previously reported.[64, 69b]

Ethyltricyclo[3.3.2.0^{2,8}]deca-3,6,9-trien-4-yl)methanol | Ethyl hydroxymethylene BV (3.23)

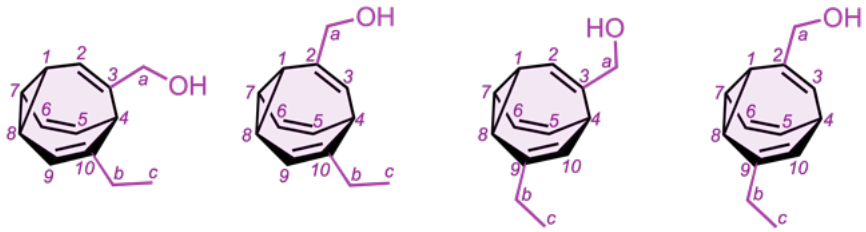

Isomer Ratio
β,β : γ,β : β,γ : γ,γ | 50:22:20:8

Ethyl hydroxymethylene BDT (**3.19**, 224 mg, 1.20 mmol, 1.0 eq.) and thioxanthene-9-one (2 mg, 0.006 mmol, 5 mol%) were dissolved in anhydrous THF (3 mL) in an oven-dried microwave vial. The mixture was stirred for 6 h, undergoing a fully enclosed irradiation with 360 nm UV light at –5 °C. Following irradiation, the solvent was removed *in vacuo* and the crude residue purified by column chromatography (Teledyne Isco CombiFlash Rf+ system, 24 g SiO_2, hexanes–EtOAc, 0–50% gradient elution) to give the title compound as a pale yellow oil (76 mg, 0.41 mmol, 34%). **^{1}H NMR** (500 MHz, 223 K, $CDCl_3$) δ 6.16–5.74 (m, 3.00H, *β,β*-$H_{2,5,6}$ / *γ,β*-$H_{3,5,6}$ / *β,γ*-$H_{2,5,6}$ / *γ,γ*-$H_{3,5,6}$), 5.74–5.63 (m, 0.72H, *β,β*-H_9, *γ,β*-H_9), 5.62–5.49 (m, 0.28H, *β,γ*-H_{10}, *γ,γ*-H_{10}), 4.08–3.94 (m, 2.00H, H_a), 2.58–1.95 (m, 6.00H, $H_{1,4,7,b}$), 1.04–0.88 (m, 3.00H, H_c). **^{13}C NMR** (125 MHz, 223 K, $CDCl_3$) δ 144.5, 143.7 (*β,β*-C_{10}), 143.7, 140.7, 140.6, 140.5, 140.1 (*β,β*-C_3), 137.6,

129.0, 128.2, 128.0, 127.9, 127.6, 127.4 (*β,β*-C_6), 127.3, 127.2, 127.0, 127.0 (*β,β*-C_5), 126.7, 126.2, 126.2, 122.8, 122.4 (*β,β*-C_2), 122.1, 121.7, 118.0 (*β,β*-C_9), 117.9 (*β,γ*-C_9), 117.6, 117.2, 69.5 (C_a), 68.6 (*β,β*-C_a), 68.3 (C_a), 36.60 (*β,β*-C_4), 34.8, 34.3, 33.3, 32.6, 32.6 (*β,β*-C_b), 31.3, 29.9, 24.2, 23.3 (*β,γ*-C_1), 22.9, 22.8, 20.1, 20.0 (*β,β*-C_1), 19.7, 19.6, 19.0, 19.0, 18.7, 13.2 (C_c), 13.1 (C_c), 12.9 (*β,β*- C_c), 12.2 (C_c). **HR-ESI-MS**: *m/z* =171.1178 $[M–OH]^+$ (calculated for $[MOH]^+$ = 171.1174).

Spectroscopic data are consistent with those previously reported.[69b]

Ethyltricyclo[3.3.2.$0^{2,8}$]deca-3,6,9-trien-4-yl)ethan-1-ol | Ethyl hydroxyethylene BV (3.24)

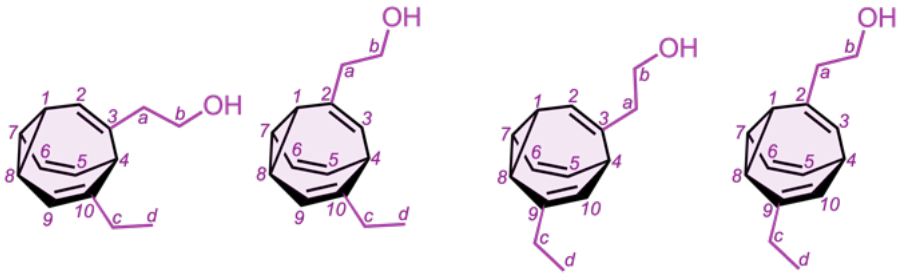

Isomer Ratio
β,β : γ,β : β,γ : γ,γ | 50:23:20:7

Ethyl hydroxyethylene BDT (**3.20**, 250 mg, 1.24 mmol, 1.0 eq.) and thioxanthene-9-one (2 mg, 0.006 mmol, 5 mol%) were dissolved in anhydrous THF (4 mL) in an oven-dried microwave vial. The mixture was stirred for 6 h, undergoing a fully enclosed irradiation with 360 nm UV light at –5 °C. Following irradiation, the solvent was removed *in vacuo* and the crude residue purified by column chromatography (Teledyne Isco CombiFlash Rf+ system, 24 g SiO_2, hexanes–EtOAc, 0–30% gradient elution) to give the title compound as a pale yellow oil (105 mg, 0.52 mmol, 42%). **^{1}H NMR** (500 MHz, 223 K, $CDCl_3$) δ 5.95–5.79 (m, 2.00H), 5.79–5.72 (m, 1.00H), 5.69 (d, *J* = 6.7 Hz, 0.50H, *β,β*-H_9), 5.64 (d, *J* = 8.1 Hz, 0.20H, *β,γ*-H_{10}), 5.58 (d, *J* = 16.0 Hz, 0.07H, *γ,γ*- H_{10}), 5.53 (d, *J* = 9.0 Hz, 0.23H, *γ,β*-H_9), 3.71–3.55 (m, 2.00H, H_b), 2.52–1.94 (m, 8.00H, $H_{1,4,7,8,a,c}$), 1.04–0.91 (m, 3.00H, H_d). **^{13}C NMR** (126 MHz, 223 K, $CDCl_3$) δ 144.2 (*γ,β*-C_{10}), 142.9 (*β,β*-C_{10}), 141.0 (*β,γ*-C_9), 140.2 (*γ,γ*-C_9), 137.3 (*γ,β*-C_2), 136.5 (*β,β*- C_3), 134.1 (*β,γ*-C_3), 133.7 (*γ,γ*-C_2), 128.2, 127.8, 127.5 (*β,β*-C), 127.3, 127.1, 126.7 (*β,β*-C), 126.6, 126.6, 126.2, 125.0, 124.5, 124.3 (*β,β*-C), 123.9, 118.6 (*β,β*-C_9), 118.5 (*γ,γ*-C_{10}), 117.7 (*β,γ*-C_{10}), 117.4 (*γ,β*-

C_9), 60.1 (*γ,γ*-C_b), 60.1 (*γ,β*-C_b), 60.0 (*β,γ*-C_b), 59.9 (*β,β*-C_b), 44.1 (*β,γ*-C_a), 44.0 (*γ,γ*-C_a), 43.2 (*β,β*-C_a), 43.0 (*γ,β*-C_a), 38.9, 34.7, 34.3, 33.9, 33.6, 33.5, 33.5, 32.8 (*β,β*-C), 32.7, 29.6, 27.9, 23.2, 22.9, 22.2, 20.3, 20.1, 20.1, 19.9, 19.9, 19.6, 19.2, 13.5 (*β,γ*-C_d), 13.1 (*β,β*-C_d), 12.6 (*γ,γ*-C_d), 12.5 (*γ,β*-C_d). **HR-ESI-MS**: *m/z* =225.1252 $[M + Na]^+$ (calculated $[M + Na]^+ = 225.1250$).

Spectroscopic data are consistent with those previously reported.[69b]

2,5,8,11-Tetraoxatridecan-13-ol | Me-TEG (3.28)

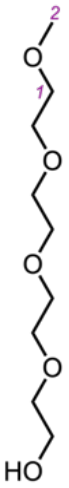

To a round bottomed flask, TEG (4.00 g, 20.6 mmol, 1.0 eq.) and anhydrous THF (75 mL) was added. The reaction mixture was stirred for 5 min at 0 °C. Then, NaH (0.86 g, 35.8 mmol, 1.7 eq.) was added over 5 min. Iodomethane (2.98 g, 1.31 mL, 21.0 mmol, 1.0 eq.) was then added dropwise over 15 min at 0 °C. The mixture was then refluxed for 24 h. The reaction mixture was concentrated *in vacuo* and extracted with CH_2Cl_2 (3 × 25 mL). The combined organic fractions were dried over $MgSO_4$ and filtered then concentrated *in vacuo* to give the crude product, which was purified by column chromatography (Teledyne Isco Combiflash Rf+ system, 12 g SiO_2, CH_2Cl_2–MeOH 0–5% gradient elution) to give the title compound as a pale yellow liquid (3.22 g, 15.5 mmol, 75%). **^{1}H NMR** (400 MHz, 298 K, $CDCl_3$) δ 2.94 (m, 16H, H_1), 3.36 (s, 3H, H_2).

Spectroscopic data are consistent with those previously reported.[117]

2,5,8,11-Tetraoxatridecan-13-yl 4-methylbenzenesulfonate | Me-TEG-OTs (3.29)

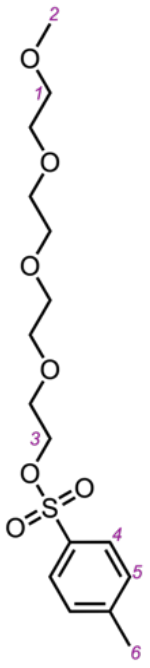

A round-bottomed flask was oven-dried and cooled under N_2. *p*-Toluenesulfonyl chloride (476 mg, 2.50 mmol, 1.0 eq.) was added and dissolved in Et_2O (15 mL). Me-TEG (**3.28**, 0.50 g, 2.39 mmol, 1.0 eq.) was then added to the solution. The reaction mixture was then put in a NaCl/ice (1:1) bath at –15 °C. Potassium hydroxide (412 mg, 7.35 mmol, 3.0 eq.) was added at regular intervals over 5 min. Once added, the reaction mixture was allowed to warm to 0 °C in an ice/water bath while stirring for 2 h. After 2 h, cold H_2O (10 mL) was added to the reaction mixture and stirred until all the contents were dissolved. The solution was then allowed to warm to rt. The organic layer was decanted and the aqueous layer was extracted with CH_2Cl_2 (3 × 10 mL). The combined organic fractions were dried over $MgSO_4$,filtered and solvent removed under reduced pressure. The crude residue was purified by column chromatography (Teledyne Isco Combiflash Rf+ system, 24 g SiO_2, CH_2Cl_2–MeOH 0—10% gradient elution) to give the title compound as a colourless liquid (554 mg, 1.53 mmol, 64%).**^{1}H NMR** (400 MHz, 298 K, $CDCl_3$) δ 7.79 (d, 2H, H_4), 7.33 (d, 2H, H_5), 4.18–4.12 (m, 2H, H_3), 3.71 – 3.60 (m, 14H, H_2), 3.40 –3.33 (m, 3H, H_1), 2.44 (s, 3H, H_6).

Spectroscopic data are consistent with those previously reported.[118]

Prop-2-yn-1-yl (*tert*-butoxycarbonyl)glycinate | Propargyl Boc-G (3.35)

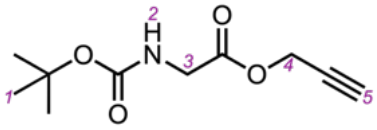

Boc-G-OH (500 mg, 2.90 mmol, 1.0 eq.) and K_2CO_3 (442 mg, 3.20 mmol, 1.1 eq.) were dissolved in anhydrous DMF (6 mL). Propargyl bromide (476 mg, 3.20 mmol, 80% wt in toluene, 1.1 eq.) was added to the solution dropwise and the solution was stirred at rt for 24 h under a N_2 atmosphere. The resulting mixture was decanted into ice-cold water (50 mL) and the resultant white precipitate was collected by filtration and washed with cold water (3 × 20 mL). The product was dried *in vacuo* to give the title compound as a white solid (464 mg, 2.17 mmol, 75%). **^{1}H NMR** (400 MHz, 298 K, $CDCl_3$) δ 4.99 (s, 1H, H_2), 4.75 (d, *J* = 2.5 Hz, 2H, H_4), 3.97 (d, *J* = 5.7 Hz, 2H,

H_3), 2.50 (t, *J* = 2.5 Hz, 1H, H_5), 1.45 (s, 9H, H_1). **HR-ESI-MS:** *m/z* =236.0909 $[M + Na]^+$ (calculated for $[M + Na]^+$ = 236.0909).

Spectroscopic data are consistent with those previously reported.[119]

Prop-2-yn-1-yl (*tert*-butoxycarbonyl)-*L*-alaninate | (*L*)-Propargyl Boc-A (3.36)

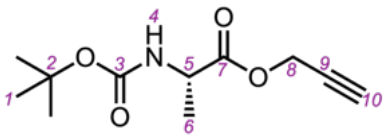

Boc-(*L*)-A-OH (500 mg, 2.64 mmol, 1.0 eq.) and K_2CO_3 (428 mg, 3.19 mmol, 1.2 eq.) were dissolved in anhydrous DMF (6 mL). Propargyl bromide (461 mg, 3.19 mmol, 80% wt in toluene, 1.2 eq.) was added to the solution dropwise and the solution was stirred at rt for 24 h under a N_2 atmosphere. The resulting mixture was concentrated *in vacuo* to give the crude product, which was purified by column chromatography (Teledyne Isco Combiflash Rf+ system, 24 g SiO_2, hexanes–EtOAc, 20% isocratic elution) to give the title compound as a colourless liquid (501 mg, 2.21 mmol, 84%). **^{1}H NMR** (400 MHz, 298 K, $CDCl_3$) δ 5.02 (s, 1H, H_4), 4.71 (dd, *J* = 15.7, 2.2 Hz, 1H, H_{8a}), 4.66 (dd, *J* = 15.9, 2.3 Hz, 1H, H_{8b}), 4.46 – 4.24 (m, 1H, H_5), 2.48 (t, *J* = 2.5 Hz, 1H, H_{10}), 1.43 (s, 9H, H_1) 1.40 (d, *J* = 7.2 Hz, 3H, H_6). **^{13}C NMR** (101 MHz, 298 K, $CDCl_3$) δ 172.8 (C_7), 155.2 (C_3), 80.1 (C_2), 77.3 (C_9), 75.4 (C_{10}), 52.8 (C_8), 49.3 (C_5), 28.4 (C_1), 18.6 (C_6). **HR-ESI-MS:** *m/z* = 228.1251 $[M + H]^+$ (calculated for $[M + H]^+$ = 228.1249).

Spectroscopic data are consistent with those previously reported.[120]

Prop-2-yn-1-yl (*tert*-butoxycarbonyl)-*L*-leucinate | (*L*)-Propargyl Boc-L (3.37)

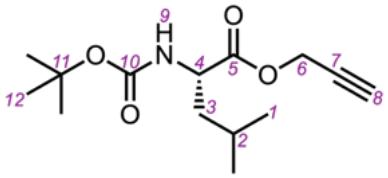

Boc-(*L*)-L-OH (500 mg, 2.16 mmol, 1.0 eq.) and K_2CO_3 (357 mg, 2.59 mmol, 1.2 eq.) were dissolved in anhydrous DMF (6 mL). Propargyl bromide (385 mg, 2.59 mmol, 80% wt in toluene, 1.2 eq.) was added to the solution dropwise and the solution was stirred at rt for 24 h under a N_2 atmosphere. The resulting mixture was concentrated *in vacuo* to give the crude product, which was purified by column chromatography (Teledyne Isco Combiflash Rf+, 24 g SiO_2; hexanes—EtOAc, 20% isocratic elution) to give the title compound as a colourless liquid (436 mg, 1.62 mmol, 75%). **^{1}H NMR** (400 MHz, 298 K, $CDCl_3$) δ 4.89 (d, *J* = 8.9 Hz, 1H, H_9), 4.75 (dd, *J* = 15.6, 1.5 Hz, 1H, H_{6a}), 4.65 (dd, *J* = 15.7, 1.6 Hz, 1H, H_{6b}), 4.42 –

4.24 (m, 1H, H_4), 2.47 (t, *J* = 2.4 Hz, 1H, H_8), 1.74 — 1.47 (m, 3H, H_2 and H_3), 1.42 (s, 9H, H_{12}) 0.93 (d, *J* = 6.6 Hz, 6H, H_1). **^{13}C NMR** (101 MHz, 298 K, $CDCl_3$) δ 172.9 (C_5), 155.5 (C_6), 80.1 (C_{11}), 77.3 (C_7), 75.3 (C_8), 52.6 (C_6), 52.1 (C_4), 41.6 (C_3), 28.4 (C_{12}), 24.9 (C_2) 21.9 (C_1). **HR-ESI-MS:** *m/z* = 270.1717 $[M + H]^+$ (calculated for $[M + H]^+$ = 270.1719). Spectroscopic data are consistent with those previously reported.[121]

1-(*tert*-Butyl) 2-(prop-2-yn-1-yl)-*L*-pyrrolidine-1,2-dicarboxylate | (*L*)-Propargyl Boc-P (3.38)

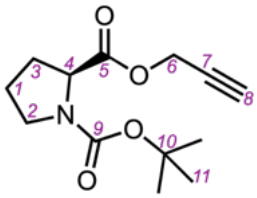

Boc-(*L*)-P-OH (500 mg, 2.32 mmol, 1.0 eq.) and K_2CO_3 (384 mg, 2.78 mmol, 1.2 eq.) were dissolved in anhydrous DMF (6 mL). Propargyl bromide (413 mg, 2.78 mmol, 80% wt in toluene, 1.2 eq.) was added to the solution dropwise and the solution was stirred at rt for 24 h under a N_2 atmosphere. The resulting mixture was concentrated *in vacuo* to give the crude product, which was purified by column chromatography (Teledyne Isco Combiflash Rf+ system, 24 g SiO_2, hexanes—EtOAc, 20% isocratic elution) to give the title compound as a colourless liquid (523 mg, 2.07 mmol, 89%). **^{1}H NMR** (400 MHz, 298 K, $CDCl_3$) δ 4.77 (dd, *J* = 15.7, 2.1 Hz, 1H, H_{6a}), 4.63 (dd, *J* = 15.6, 1.9 Hz, 1H, H_{6b}), 4.39 — 4.19 (m, 1H, H_4), 3.60 – 3.30 (m, 2H, H_2), 2.45 (m, 1H, H_8), 2.30 — 2.11 (m, 1H, H_1 and H_3), 2.04 — 1.77 (m, 3H, H_1 and H_3) 1.42 (m, 9H, H_{11}). **^{13}C NMR** (for both rotamers) (101 MHz, 298 K, $CDCl_3$) δ 172.5 (C_5), 172.3 (C_5) 154.5 (C_9), 153.8 (C_9), 80.2 (C_{10}), 80.0 (C_{10}), 77.6 (C_7), 77.5 (C_7), 75.3 (C_8), 75.1 (C_8), 59.0 (C_4), 58.8 (C_4), 52.5 (C_6), 52.4 (C_6), 46.7 (C_2), 46.4(C_2), 30.9 (C_3), 29.9 (C_3), 28.5 (C_{11}), 28.4 (C_{11}), 24.4 (C_1), 23.7 (C_1). **HR-ESI-MS:** *m/z* = 254.1406 $[M + H]^+$ (calculated for $[M + H]^+$ = 254.1406). Spectroscopic data are consistent with those previously reported.[96]

Prop-2-yne-1-sulfonate (3.43)

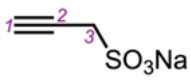

Propargyl bromide (3.17 g, 26.6 mmol, 80% wt in toluene, 1.0 eq.) and Na_2SO_3 (4.39 g, 34.8 mmol, 1.3 eq.) were added to a round bottomed flask and dissolved in MeOH (7 mL) and H_2O (7 mL) and the mixture was stirred at 65 °C for 18 h. After cooling, MeOH (120 mL) was added and the mixture was filtered. The filtrate was concentrated to an approximate volume of 5 mL. $(CH_3)_2CO$ (100 mL) was added and the precipitate was filtered, washed with $(CH_3)_2CO$ (3 x 10 mL)

and dried *in vacuo* to yield the desired product as white solid (1.16 g, 8.16 mmol, 38%). **^{1}H NMR** (400 MHz, 298 K, $(CD_3)_2SO$) δ 3.28 – 3.27 (d, *J* = 2.7 Hz, 2H, H_3), 2.91 (t, *J* = 2.7 Hz, 1H, H_1). **^{13}C NMR** (101 MHz, 298 K, $(CD_3)_2SO$) δ 79.0 (C_2), 73.2 (C_1), 42.1 (C_3). **HR-ESI-MS:** *m/z* = 164.9606 $[M + 2Na]^+$ (calculated for $[M + 2Na]^+$ = 164.9607).

N,N,N-Triethyl-propargyl ammonium bromide (3.44)

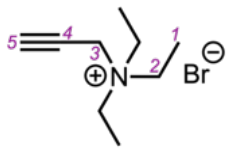

Propargyl bromide (1.07 g, 7.20 mmol, 80% wt in toluene, 1.0 eq.) was stirred in CH_2Cl_2 (4 mL). Et_3N (1.46 g, 14.5 mmol, 2.0 eq.) was added and the solution was stirred at rt for 15 min. A white precipitate formed which was then filtered and dried *in vacuo* to yield the title compound as a white powder (1.46 g, 10.5 mmol, 93%). **^{1}H NMR** (400 MHz, 298 K, $CDCl_3$) δ 4.65 (d, *J* = 2.6 Hz, 2H, H_3), 3.66 (q, *J* = 7.3 Hz, 6H, H_2), 2.81 (t, *J* = 2.6 Hz, 1H, H_5), 1.47 (t, *J* = 7.3 Hz, 9H, H_1). **^{13}C NMR** (101 MHz, 298 K, $CDCl_3$) δ 81.0 (C_4), 71.6 (C_5), 54.4 (C_2), 31.4 (C_2) 8.6 (C_1). **HR-ESI-MS:** *m/z* = 140.1451 $[M - ^{79}Br]^+$ (calculated for $[M - ^{79}Br]^+$ = 140.1439).

Spectroscopic data are consistent with those previously reported.[122]

2-Carboxy-*N,N,N*-trimethylethan-1-ammonium bromide (3.45)

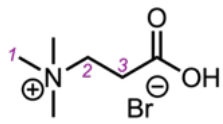

3-Bromopropanoic acid (2.04 g, 13.3 mmol) dissolved in ethanol (10 mL) was added into a $N(Me)_3$ solution (329 mL, 120 mmol, 13% in MeCN) and the reaction mixture was stirred at rt for 72 h. Excess $N(Me)_3$ was removed *via* distillation and the remaining residue filtered, washed with MeCN (3 × 20 mL) and dried in vacuo to yield the title compound as a white solid (1.84 g, 8.70 mmol, 65%). **^{1}H NMR** (400 MHz, 298 K, D_2O) δ 3.62 (t, *J* = 8.0 Hz, 2H, H_2), 3.12 (s, 9H, H_1), 2.82 (t, *J* = 7.0 Hz, 2H, H_3). **^{13}C NMR** (101 MHz, 298 K, D_2O) δ 62.5 (C_2), 54.5 (C_1), 29.6 (C_3). **HR-ASAP-MS:** *m/z* = 265.2528 $[2M - ^{79}Br + H]^+$ (calculated $[2M - ^{79}Br + H]^+$ = 265.2529).

Spectroscopic data are consistent with those previously reported.[123]

7-Ethyl-8-(2-(prop-2-yn-1-yloxy)ethyl)bicyclo[4.2.2]deca-2,4,7,9-tetraene | BDT Alkyne (3.55)

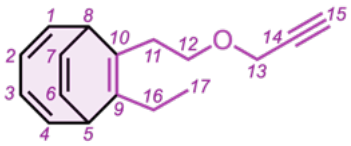

8-Ethylbicyclo[4.2.2]deca-2,4,7,9-tetraen-7-yl)ethan-1-ol (**3.20**, 500 mg, 2.48 mmol, 1.0 eq.) was added to an oven-dried 50 mL rbf which was then dissolved in anhydrous THF (15 mL). The reaction mixture was then cooled to 0 °C with a constant flow of N_2. Sodium hydride (600 mg, 14.9 mmol, 60% wt in mineral oil, 6.0 eq.) was then added slowly over 5 min. After 15 min of vigorous stirring, propargyl bromide (2.30 g, 15.8 mmol, 60% wt in toluene, 6.4 eq.) was added and the reaction was allowed to warm to rt and stirred for 18 h. After this time, the reaction was quenched with MeOH (5 mL). CH_2Cl_2 (10 mL) was then added and the organic fraction was washed with brine (3 × 20 mL) and the organic fractions combined, dried with $MgSO_4$ and filtered. The solvent was removed *in vacuo* and the crude residue purified using column chromatography (Teledyne Isco CombiFlash Rf+ system, 12 g SiO_2, hexanes–EtOAc, 0–10% gradient elution) to yield the title compound as a yellow oil (252 mg, 1.05 mmol, 42%). **^{1}H NMR** (400 MHz, 298 K, $CDCl_3$); δ 6.27–6.16 (m, 2H, $H_{1,4}$), 5.71–5.64 (m, 4H, H_2, H_3, H_6 and H_7), 4.13 (d, J = 2.4 Hz, 2H, H_{13}), 3.533.43 (m, 2H, $H_{5,8}$), 3.23–3.11 (m, 2H, H_{12}), 2.51 (m, 1H, H_{11}), 2.42 (t, J = 2.4 Hz, 1H, H_{15}), 2.37 (m, 1H, H_{11}), 2.17–2.01 (m, 2H, H_{16}), 0.99 (t, J = 7.5 Hz, 3H, H_{17}); **^{13}C NMR** (101 MHz, 298 K, $CDCl_3$); δ 142.4 (C_4), 141.9 (C_1), 134.4 (C_{10}), 124.4 (C_2), 124.3 (C_3), 121.4 (C_6), 121.3 (C_7), 118.8 (C_9), 79.9 (C_{14}), 74.3 (C_{15}), 70.0 (C_{12}), 58.1 (C_{13}), 40.2 (C_8), 39.4 (C_5), 31.9 (C_{11}), 24.4 (C_{16}), 14.8 (C_{17}); **HR-ESI-MS**: m/z = 263.1407 $[M + Na]^+$ (calculated for $[M + Na]^+$ = 263.1406).

Ethyl-3-(2-(prop-2-yn-1-yloxy)ethyl)tricyclo[3.3.2.0]deca-3,6,9-triene | BV Alkyne (3.56)

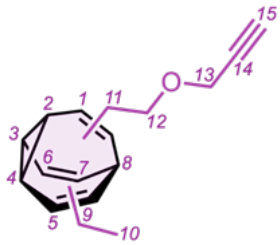

7-Ethyl-8-(2-(prop-2-yn-1-yloxy)ethyl)bicyclo[4.2.2]deca-2,4,7,9-tetraene (**3.55**, 152 mg, 0.633 mmol, 1.0 eq.) and thioxanthene-9-one (12 mg, 0.031 mmol, 5 mol%) were dissolved in anhydrous THF (3 mL) in an oven-dried microwave vial. The mixture was stirred for 6 h, undergoing a fully enclosed irradiation with 365 nm UV light at –5 °C. After this time,

the solvent was then removed *in vacuo* and the crude residue purified by column chromatography (Teledyne Isco CombiFlash Rf+ system, 12 g SiO_2, hexanes–EtOAc, 0–15% gradient elution) to give the title compound as a pale yellow oil (45 mg, 0.19 mmol, 30%). **^{1}H NMR** (400 MHz, 298 K, $CDCl_3$,) δ 5.90–5.55 (m, 5H, H_1, H_2, H_5, H_6 and H_7), 4.14 (m, 2H, H_{13}), 3.58 (t, 2H, *J* = 7.1 Hz, H_{12}), 2.42 (t, *J* = 2.4 Hz, 1H, H_{15}), 2.38–1.95 (m, 7H, H_3, H_4, H_8, H_9 and H_{11}), 1.01 (t, *J* = 7.4 Hz, 3H, H_{10}); **^{13}C NMR:** VT required; **HR-ESI-MS:** *m/z* = 263.1407 $[M + Na]^+$ (calculated for $[M + Na]^+$ = 263.1406).

6-Ethyltricyclo[3.3.2.0^{2,8}]deca-3,6,9-trien-3-yl)ethoxy)methyl)-1*H*-1,2,3-triazol-1-yl)-4,5-dihydroxy-6-(hydroxymethyl)tetrahydro-2*H*-pyran-3-yl)acetamide | BV GlcNAc (3.59)

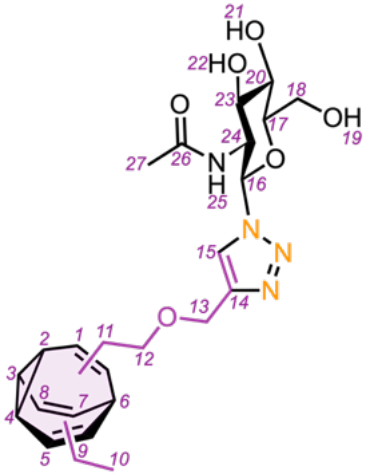

6-Ethyl-3-(2-(prop-2-yn-1-yloxy)ethyl)tricyclo[3.3.2.0]deca-3,6,9-triene (**3.56**, 23 mg, 0.095 mmol, 1.0 eq.) and 2-acetamido-3,4,6-tri-*o*-acetyl-2-deoxy-β-D-glucopyranosyl azide (42 mg, 0.11 mmol, 1.2 eq.) were dissolved in MeOH (2 mL) in an over-dried microwave vial. Tetrakis(acetonitrile)copper(I) hexafluorophosphate (18 mg, 0.048 mmol, 0.5 eq.) was then added and the reaction mixture was stirred under air for 24 h at rt. After this time, the solvent was removed *in vacuo* and the crude residue was examined by ^{1}H NMR spectroscopy in CD_3OD. After confirmation of the product, the crude residue was redissolved in MeOH (4 mL) and NaOMe (0.3 mL) was added dropwise until the solution reached pH 10. The solution was then stirred at rt for 24 h. Following this period, the solution was neutralised with Amberlite® IR120 hydrogen resin (~ 2 mg) until the solution reached pH 7. The reaction mixture was then filtered, washed with MeOH (5 mL), the solvent removed *in vacuo* and the crude residue purified by column chromatography (reversed-phase 6 mL supelco™ superclean LC-18, H_2O–MeCN, 0–100%, 10% incremental elution) which was then lypholised to give the title compound as a white powder (18 mg, 0.037 mmol, 39%).**^{1}H NMR** (400 MHz, 298 K, CD_3OD) δ 8.11 (s, 1H, H_{15}), 5.79 (d, *J* = 9.8 Hz, 1H, H_{25}), 5.66 (m, 5H, H_1, H_2, H_5, H_7 and H_8), 4.56 (m, 2H, H_{13}), 4.25–

4.17 (m, 1H, H_{16}), 3.91 (m, 2H, H_{18}), 3.80–3.65 (m, 2H, H_{12}), 3.63–3.47 (m, 7H, H_{17}, H_{19}, H_{20}, H_{21}, H_{22}, H_{23} and H_{24}), 2.36–1.94 (m, 7H, H_3, H_4, H_6, H_9 and H_{11}), 1.77 (s, 3H, H_{27}), 0.98 (t, *J* = 7.3 Hz, 3H, H_{10}); **^{13}C NMR:** VT required; **HR-ESI-MS:** *m/z* = 509.2388 [*M* + Na]$^+$ (calculated for [*M* + Na]$^+$ = 509.2371).

8-Ethylbicyclo[4.2.2]deca-2,4,7,9-tetraen-7-yl)ethoxy)methyl)-1*H*-1,2,3-triazol-1-yl)-4,5-dihydroxy-6-(hydroxymethyl)tetrahydro-2*H*-pyran-3-yl)acetamide | BDT GlcNAc (3.61)

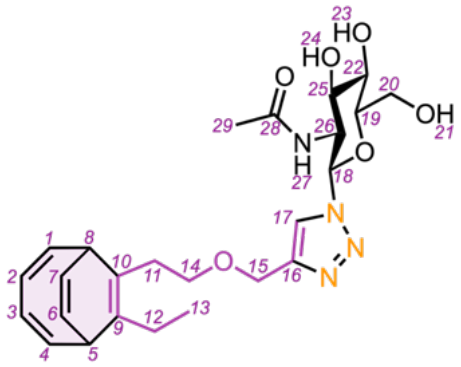

(2*Z*,4*Z*)-7-Ethyl-8-(2-(prop-2-yn-1-yloxy)ethyl)bicyclo[4.2.2]deca-2,4,7,9-tetraene (**3.55**, 25 mg, 0.10 mmol, 1.0 eq.) and 2-acetamido-3,4,6-tri-*o*-acetyl-2-deoxy-β-D-glucopyranosyl azide (46 mg, 0.12 mmol, 1.2 eq.) were dissolved in MeOH (1 mL) in an over-dried microwave vial. Tetrakis(acetonitrile)copper(I) hexafluorophosphate (19 mg, 0.052 mmol, 0.5 eq.) was then added and the reaction mixture was stirred under air for 24 h at rt. After this time, the solvent was removed *in vacuo* and the crude residue was examined by ^{1}H NMR spectroscopy in CD_3OD. After confirmation of the product, the crude residue was redissolved in MeOH (4 mL) and NaOMe (0.3 mL) was added dropwise until the solution reached pH 10. The solution was then stirred at rt for 24 h. Following this period, the solution was neutralised with Amberlite® IR120 hydrogen resin (~ 4 mg) until the solution reached pH 7. The reaction mixture was then filtered, washed with MeOH (5 mL), the solvent removed *in vacuo* and the crude residue purified by column chromatography (reversed-phase 6 mL supelco™ superclean LC-18, H_2O–MeCN, 0–100%, 10% incremental elution) which was then lyophilised to give the title compound as a white powder (15 mg, 0.031 mmol, 29%). **^{1}H NMR** (600 MHz, 298 K, CD_3OD); δ 8.13 (s, 1H, H_{17}), 6.26–6.16 (m, 2H, $H_{1,4}$), 5.81 (d, *J* = 9.9 Hz, 1H, H_{27}), 5.67–5.58 (m, 4H, H_2, H_3, H_6 and H_7), 4.59 (m, 2H, H_{15}), 4.23 (t, *J* = 10.0 Hz, 1H, H_{18}), 3.92–3.87 (m, 2H, H_{20}), 3.80–3.56 (m, 7H, H_{19}, H_{21}, H_{22}, H_{23}, H_{24}, H_{25} and H_{26}), 3.54–3.40 (m, 2H, H_{14}), 3.20–3.08 (m, 2H, H_5 and H_8), 2.52–2.42 (m, 1H, H_{11}), 2.36–2.29 (m, 1H, H_{11}), 2.24–2.16 (m, 1H,

H_{12}), 2.12–2.02 (m, 1H, H_{12}), 1.79 (s, 3H, H_{29}), 0.97 (t, *J* = 7.5 Hz, 3H, H_{13}); **^{13}C NMR** (151 MHz, 298 K, CD_3OD); δ 173.4 (C_{28}), 141.7 (C_4), 141.4 (C_1), 136.4 (C_{10}), 133.9 (C_{16}), 125.5 (C_9), 124.1 (C_2), 124.0 (C_3), 122.3 (C_{17}), 121.3 (C_6), 121.1 (C_7), 88.2 (C_{18}), 81.3 (C_{22}), 75.7 (C_{25}), 71.4 (C_{19}), 70.0 (C_{14}), 63.3 (C_{15}), 62.4 (C_{20}), 56.8 (C_{26}), 40.0 (C_5 or C_8), 39.4 (C_5 or C_8), 31.3 (C_{11}), 23.9 (C_{12}), 21.2 (C_{29}), 13.7 (C_{13}); **HR-ESI-MS:** *m/z* = 509.2379 [*M* + Na]$^+$ (calculated for [*M* + Na]$^+$ = 509.2371).

2-(2-(2-(2-Hydroxyethoxy)ethoxy)ethoxy)ethyl *p*-tosylate | TEG-OTs (3.65)

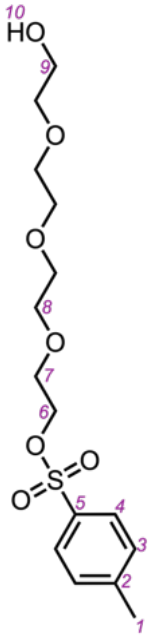

NaOH (345 g, 8.63 mmol, 0.2 eq.) dissolved in water (5 mL) was added to a solution of TEG (11.0 g, 56.6 mmol, 1.0 eq.) dissolved in THF (15 mL) at 0 °C. *p*-Toluenesulfonylchloride (1.04 g, 5.46 mmol, 0.1 eq.) dissolved in THF (10 mL) was then added and the solution was allowed to warm to rt whilst stirring over 24 h. The reaction mixture was then poured into ice-cold water (50 mL). The organic layer was separated and the aqueous layer was extracted with CH_2Cl_2 (3 × 50 mL). The organic fractions were then combined and washed with water (2 × 50 mL). The organic fraction was then dried with $MgSO_4$ and evaporated *in vacuo* to yield the desired product as a yellow oil (9.46 g, 27.2 mmol, 48%). **^{1}H NMR** (400 MHz, 298 K, $CDCl_3$) δ 7.77 (d, *J* = 8.5, 2H, H_4), 7.32 (d, *J* = 8.5, 2H, H_3), 4.13 (t, *J* = 4.9, 2H, H_6), 3.68–3.53 (m, 14H, H_7, H_8 and H_9), 2.43 (s, 3H, H_1), 2.302.10 (bs, 1H, H_{10}); **^{13}C NMR** (400 MHz, 298 K, $CDCl_3$) δ 144.7 (C_5), 132.9 (C_2), 130.2 (C_3), 128.3 (C_4), 72.6 (C_8), 70.8 (C_8), 70.7 (C_8), 70.6 (C_8), 70.5 (C_8), 69.2 (C_7), 68.7 (C_6), 61.6 (C_9), 21.5 (C_1). **HR-ESI-MS:** *m/z* = 371.1134 [*M* + Na]$^+$ (calculated for [*M* + Na]$^+$ = 371.1135).

Spectroscopic data are consistent with those previously reported.[124]

11-Azido-3,6,9-trioxaundecan-1-ol (3.66)

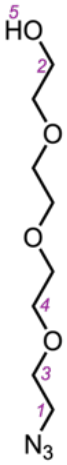

OH-TEG-OTs (**3.65**, 500 mg, 1.44 mmol, 1.0 eq.) was dissolved in MeCN (10 mL) and sodium azide (140 mg, 2.16 mmol, 1.5 eq.) was added to the reaction mixture which was then allowed to stir for 18 h at 50 °C. After this time, the solvent was removed *in vacuo* and the crude residue was dissolved in CH_2Cl_2 (20 mL), washed with water (3 × 15mL), then dried with $MgSO_4$ and evaporated *in vacuo* to yield the desired product without further purification as a yellow oil (316 mg, 1.44 mmol, 100%). **^{1}H NMR** (400 MHz, 298 K, $CDCl_3$) δ 4.18–4.13 (m, 2H, H_2), 3.72–3.56 (m, 12H, H_3 and H_4), 3.43–3.34 (t, *J* = 5.0 Hz, 2H, H_1), 2.24 (bs, 1H, H_5); **^{13}C NMR** (400 MHz, 298 K, $CDCl_3$) δ 72.6 (C_4), 70.8 (C_4), 70.7 (C_4), 70.6 (C_4), 70.5 (C_4), 70.1 (C_3), 61.8 (C_2), 50.8 (C_1). **HR-ESI-MS:** *m/z* = 242.1101 $[M + Na]^+$ (calculated for $[M + Na]^+$ = 242.1111).

Spectroscopic data are consistent with those previously reported.[124]

(2*Z*,4*Z*)-7,8-bis((Prop-2-yn-1-yloxy)methyl)bicyclo[4.2.2]deca-2,4,7,9-tetraene | Bis(Alkyne) BDT (3.67)

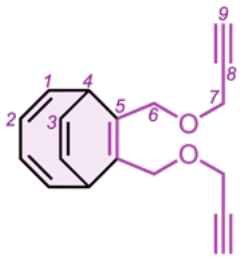

bis(Hydroxymethylene) BDT (**3.12**, 600 mg, 3.15 mmol, 1.0 eq.) was added to an oven-dried 100 mL round-bottomed flask which was then dissolved in anhydrous THF (20 mL). The reaction mixture was then cooled to 0 °C with a constant flow of N_2. Sodium hydride (756 mg, 18.9 mmol, 60% wt in mineral oil, 6.0 eq.) was then added slowly over 10 min. After 15 min of vigorous stirring, propargyl bromide (3.30 g, 22.1 mmol, 60% wt in toluene, 7.0 eq.) was added and the reaction was allowed to warm to rt and stirred for 18 h. After this time, the reaction was quenched with MeOH (10 mL). CH_2Cl_2 (10 mL) was then added and the organic fraction was washed with brine (3 × 20 mL) and the organic fractions combined, dried with $MgSO_4$ and filtered. The solvent was removed *in vacuo* and the crude residue purified using column chromatography (Teledyne Isco CombiFlash Rf+ system, 24 g SiO_2, hexanes–EtOAc, 0–15% gradient elution) to yield the title compound as a yellow oil (274 mg, 1.03 mmol, 33%). **^{1}H NMR** (400 MHz, 298 K, $CDCl_3$); δ 6.26–6.17 (td, *J* = 8.8, 3.4 Hz, 2H, H_1), 5.78–5.65 (m, 4H, H_2 and H_3), 4.32–4.26 (m, 2H, H_7), 4.174.12 (m, 2H,

H_7), 4.04 (m, 4H, H_6), 3.47–3.38 (m, 2H, H_4), 2.43 (t, *J* = 2.4 Hz, 2H, H_9); **^{13}C NMR** (101 MHz, 298 K, $CDCl_3$); δ 141.7 (C_1), 131.8 (C_5), 124.7 (C_2), 121.1 (C_3), 80.1 (C_8), 74.5 (C_9), 65.9 (C_6), 56.6 (C_7), 37.7 (C_4); **HR-ESI-MS:** *m/z* = 289.1199 $[M + Na]^+$ (calculated for $[M + Na]^+$ = 289.1199).

Spectroscopic data are consistent with those previously reported.[62]

bis((Prop-2-yn-1-yloxy)methyl)tricyclo[3.3.2.0^{2,8}]deca-3,6,9-triene | Bis(alkyne) BV (3.68)

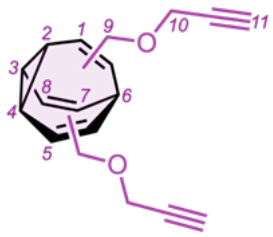

7,8-bis((Prop-2-yn-1-yloxy)methyl)bicyclo[4.2.2]deca-2,4,7,9-tetraene (**3.67**, 184 mg, 0.615 mmol, 1.0 eq.) and thioxanthene-9-one (12 mg, 0.031 mmol, 5 mol%) were dissolved in anhydrous THF (4 mL) in an oven-dried microwave vial. The mixture was stirred for 6 h, undergoing a fully enclosed irradiation with 365 nm UV light at –5 °C. After this time, the solvent was then removed *in vacuo* and the crude residue purified by column chromatography (Teledyne Isco CombiFlash Rf+ system, 12 g SiO_2, hexanes–EtOAc, 0–10% gradient elution) to give the title compound as a pale yellow oil (40 mg, 0.15 mmol, 26%). **^{1}H NMR** (400 MHz, 298 K, $CDCl_3$) δ 5.87 (s, 5H, H_1, H_2, H_5, H_7 and H_8), 4.14 (m, 4H, H_{10}), 4.02–3.82 (m, 3H, H_3, H_4 and H_6), 2.75–2.05 (m, 4H, H_9), 2.40 (t, *J* = 2.4 Hz, 2H, H_{11}); **HR-ESI-MS:** *m/z* = 289.1197 $[M + Na]^+$ (calculated for $[M + Na]^+$ = 289.1199).

Spectroscopic data are consistent with those previously reported.[62]

Protein Crystallisation Materials and Methods

Crystallographic data were processed with Xia2 software.[125] Data reduction was processed with aimless[126] in the CCP4 package.[127] The structure solution was processed with Molecular Replacement methods using Phaser[80] and as a search model 6WUW[128] for SAs. Refinement was performed with Refmac[129] and Coot.[130] The crystal structures of HSA with myristate and HSA with Ad-1-carboxylic acid (**3.26**) have been deposited within the Protein Data Bank (PDB) with the accession codes 9EOS and 9EOD, respectively.

BSA Crystallisation Methods

BSA was purchased from Sigma–Aldrich. Prior to crystallisation, the proteins were dissolved in 0.1 M Triaminomethane(tris)-HCl, pH 7.0, 0.2 M $Ca(OAc)_2$, 20% PEG3350 buffer and were passed through a column attached to the ÅKTA FPLC gel filtration system (GE Healthcare). After gel filtration, fractions containing monomeric proteins were pooled and concentrated to the stated concentrations. BSA crystals were grown using a sitting-drop and hanging-drop setup. The crystallisation drops were composed of the stated mixture of the protein solution and the reservoir solution from the wells.

Amino acid sequence of the BSA used

```
DTHKSEIAHRFKDLGEEHFKGLVLIAFSQYLQQCPFDEHVKLVNELTEFAKTCVADESHAGC
EKSLHTLFGDELCKVASLRETYGDMADCCEKQEPERNECFLSHKDDSPDLPKLKPDPNTLCD
EFKADEKKFWGKYLYEIARRHPYFYAPELLYYANKYNGVFQECCQAEDKGACLLPKIETMRE
KVLTSSARQRLRCASIQKFGERALKAWSVARLSQKFPKAEFVEVTKLVTDLTKVHKECCHGD
LLECADDRADLAKYICDNQDTISSKLKECCDKPLLEKSHCIAEVEKDAIPENLPPLTADFAE
DKDVCKNYQEAKDAFLGSFLYEYSRRHPEYAVSVLLRLAKEYEATLEECCAKDDPHACYSTV
FDKLKHLVDEPQNLIKQNCDQFEKLGEYGFQNALIVRYTRKVPQVSTPTLVEVSRSLGKVGT
RCCTKPESERMPCTEDYLSLILNRLCVLHEKTPVSEKVTKCCTESLVNRRPCFSALTPDETY
VPKAFDEKLFTFHADICTLPDTEKQIKKQTALVELLKHKPKATEEQLKTVMENFVAFVDKCC
AADDKEACFAVEGPKLVVSTQTALA
```

BSA Screen 1

Crystallisation tray composition. Buffer: 0.1 M Triaminomethane(tris)-HCl, pH 7.0, 0.2 M $Ca(OAc)_2$, 20% PEG3350.

		$Ca(OAc)_2$ / M					
		0.05	0.10	0.15	0.20	0.25	0.30
PEG3350 %	10	A1	A2	A3	A4	A5	A6
	15	B1	B2	B3	B4	B5	B6
	20	C1	C2	C3	C4	C5	C6
	25	D1	D2	D3	D4	D5	D6

Buffer solution made up of 1 M Tris-HCl pH 7.0 (24 mL), 1 M $Ca(OAc)_2$ (42 mL), 50 % PEG3350 (84 mL).
In a given crystallisation plate with well positions, **A1**–**D6**.

A1	A2	A3	A4	A5	A6
B1	B2	B3	B4	B5	B6
C1	C2	C3	C4	C5	C6
D1	D2	D3	D4	D5	D6

Table S3.1. Composition of 10 mL reservoir solutions for **BSA** screen 1. Crystallisation tray developed at room temperature.

Position	Tris HCl pH 7.0 / mL	$Ca(OAc)_2$ / mL	PEG3350 / mL	H_2O / mL
A1	1.0	0.5	2.0	6.5
A2	1.0	1.0	2.0	6.0
A3	1.0	1.5	2.0	5.5
A4	1.0	2.0	2.0	5.0
A5	1.0	2.5	2.0	4.5
A6	1.0	3.0	2.0	4.0
B1	1.0	0.5	3.0	5.5
B2	1.0	1.0	3.0	5.0
B3	1.0	1.5	3.0	4.5
B4	1.0	2.0	3.0	4.0
B5	1.0	2.5	3.0	3.5
B6	1.0	3.0	3.0	3.0
C1	1.0	0.5	4.0	4.5
C2	1.0	1.0	4.0	4.0
C3	1.0	1.5	4.0	3.5
C4	1.0	2.0	4.0	3.0
C5	1.0	2.5	4.0	2.5
C6	1.0	3.0	4.0	2.0
D1	1.0	0.5	5.0	3.5
D2	1.0	1.0	5.0	3.0
D3	1.0	1.5	5.0	2.5
D4	1.0	2.0	5.0	2.0
D5	1.0	2.5	5.0	1.5
D6	1.0	3.0	5.0	1.0

Table S3.2. Crystallisation conditions for **BSA** screen 1.

Entry	BSA / µL	BSA / mg mL^{-1}	Reservoir / µL	Temperature / °C	Substrate / µL
1	1.0	10.8	1.0	25	–

Table S3.3. Co-crystallisation conditions for **BSA** screen 1 with **BBL**.

Entry	BSA / µL	BSA / mg mL^{-1}	Reservoir / µL	Temperature / °C	Substrate / µL
1	1.0	10.8	1.0	25	1.0

Table S3.4. Co-crystallisation conditions for **BSA** screen 1 with **3.7**.

Entry	BSA / µL	BSA / mg mL^{-1}	Reservoir / µL	Temperature / °C	Substrate / µL
1	1.0	10.8	1.0	25	1.0

BSA Screen 2

Crystallisation tray composition. Buffer: 0.1 M Triaminomethane(tris)-HCl, pH 7.0, 0.2 M $Ca(OAc)_2$, 2% Glycerol.

		Glycerol / %					
		0	1	2	3	4	5
$Ca(OAc)_2$ / M	0.05	A1	A2	A3	A4	A5	A6
	0.10	B1	B2	B3	B4	B5	B6
	0.15	C1	C2	C3	C4	C5	C6
	0.20	D1	D2	D3	D4	D5	D6

In a given crystallisation plate with wells A1–D6.

A1	A2	A3	A4	A5	A6
B1	B2	B3	B4	B5	B6
C1	C2	C3	C4	C5	C6
D1	D2	D3	D4	D5	D6

Table S3.5. Composition of 10 mL reservoir solutions for **BSA** screen 2. Crystallisation tray developed at room temperature.

Position	Tris HCl pH 7.5 / mL	$Ca(OAc)_2$ / mL	PEG3350 / mL	Glycerol / µL	H_2O / mL
A1	1.0	0.5	4.0	0	4.5
A2	1.0	0.5	4.0	200	4.3
A3	1.0	0.5	4.0	400	4.1
A4	1.0	0.5	4.0	600	3.9
A5	1.0	0.5	4.0	800	3.7
A6	1.0	0.5	4.0	1000	3.5
B1	1.0	1.0	4.0	0	4.0
B2	1.0	1.0	4.0	200	3.8
B3	1.0	1.0	4.0	400	3.6
B4	1.0	1.0	4.0	600	3.4
B5	1.0	1.0	4.0	800	3.2
B6	1.0	1.5	4.0	1000	3.0
C1	1.0	1.5	4.0	0	3.5
C2	1.0	1.5	4.0	200	3.3
C3	1.0	1.5	4.0	400	3.1
C4	1.0	1.5	4.0	600	2.9
C5	1.0	1.5	4.0	800	2.7
C6	1.0	1.5	4.0	1000	2.5
D1	1.0	2.0	4.0	0	3.0
D2	1.0	2.0	4.0	200	2.8
D3	1.0	2.0	4.0	400	2.6
D4	1.0	2.0	4.0	600	2.4
D5	1.0	2.0	4.0	800	2.2
D6	1.0	2.0	4.0	1000	2.0

Table S3.6. Crystallisation conditions for **BSA** screen 2.

Entry	BSA / µL	BSA / mg mL^{-1}	Reservoir / µL	Temperature / ˚C	Substrate / µL
1	1.0	10.0	1.0	25	–
2	1.0	10.0	1.0	4	–
3	1.0	8.3	1.0	25	–
4	1.0	8.3	1.0	4	–
5	2.0	10.0	1.0	25	–
6	2.0	8.3	1.0	25	–

Table S3.7. Co-crystallisation conditions for **BSA** screen 2 with **BBL** (1 mg) dissolved in buffer stock solution (1 mL).

Entry	BSA / µL	BSA / mg mL^{-1}	Reservoir / µL	Temperature / °C	Substrate / µL
1	1.0	10.0	1.0	25	1.0
2	1.0	8.3	1.0	25	1.0
3	1.0	10.0	1.0	4	1.0
4	1.0	8.3	1.0	4	1.0
5	1.0	10.0	1.0	25	2.0
6	1.0	8.3	1.0	25	2.0

Table S3.8. Co-crystallisation conditions for **BSA** screen 2 with **3.7** (1 mg) dissolved in buffer stock solution (2 mL) and DMSO (0.2 mL).

Entry	BSA / µL	BSA / mg mL^{-1}	Reservoir / µL	Temperature / ˚C	Substrate / µL
1	1.0	10.0	1.0	25	–
2	1.0	8.3	1.0	25	–
3	1.0	10.0	1.0	4	–
4	1.0	8.3	1.0	4	–

BSA Screen 3

Crystallisation tray composition. Buffer: 0.1 M Triaminomethane(tris)-HCl, pH 6.5, 0.2 M $Ca(OAc)_2$, 20% PEG3350.

			$Ca(OAc)_2$ / M					
			0.05	0.10	0.15	0.20	0.25	0.30
PEG3350 %	18	Tris-HCl pH 7.0						
	20					×		
	22							
	18	Tris-HCl pH 7.5						
	20							
	22							

N.B. Buffer solution made up of 1 M Tris-HCl pH 7.0 (12 mL), 1 M Tris-HCl pH 7.5 (12 mL), 1 M $Ca(Oac)_2$ (42 mL), 50 % PEG3350 (48 mL).

Table S3.9. Composition of 10 mL buffer solutions for **BSA** screen 3 (sitting drop method). Crystallisation tray developed at room temperature.

Position	Tris pH 7.0 / mL	Tris pH 7.5 / mL	$Ca(OAc)_2$ / mL	PEG3350 / mL	H_2O / mL
A1	1.0	–	1.0	1.8	6.2
A2	1.0	–	1.0	2.0	6.0
A3	1.0	–	1.0	2.2	5.8
A4	–	1.0	1.0	1.8	6.2
A5	–	1.0	1.0	2.0	6.0
A6	–	1.0	1.0	2.2	5.8
B1	1.0	–	1.5	1.8	5.2
B2	1.0	–	1.5	2.0	5.0
B3	1.0	–	1.5	2.2	4.8
B4	–	1.0	1.5	1.8	5.2
B5	–	1.0	1.5	2.0	5.0
B6	–	1.0	1.5	2.2	4.8
C1	1.0	–	2.0	1.8	5.2
C2	1.0	–	2.0	2.0	5.0
C3	1.0	–	2.0	2.2	4.8
C4	–	1.0	2.0	1.8	5.2
C5	–	1.0	2.0	2.0	5.0

C6	–	1.0	2.0	2.2	4.8
D1	1.0	–	2.5	1.8	4.7
D2	1.0	–	2.5	2.0	4.5
D3	1.0	–	2.5	2.2	4.3
D4	–	1.0	2.5	1.8	4.7
D5	–	1.0	2.5	2.0	4.5
D6	–	1.0	2.5	2.2	4.3

Table S3.10. Composition of 10 mL buffer solutions for BSA screen 3 (hanging drop method). Crystallisation tray developed at room temperature.

Position	Tris pH 7.0 / mL	Tris pH 7.5 / mL	$Ca(OAc)_2$ / mL	PEG3350 / mL	H_2O / mL
A1	1.0	–	1.0	1.8	6.2
A2	1.0	–	1.0	2.0	6.0
A3	1.0	–	1.0	2.2	5.8
A4	–	1.0	1.0	1.8	6.2
A5	–	1.0	1.0	2.0	6.0
A6	–	1.0	1.0	2.2	5.8
B1	1.0	–	1.5	1.8	5.2
B2	1.0	–	1.5	2.0	5.0
B3	1.0	–	1.5	2.2	4.8
B4	–	1.0	1.5	1.8	5.2
B5	–	1.0	1.5	2.0	5.0
B6	–	1.0	1.5	2.2	4.8
C1	1.0	–	2.0	1.8	5.2
C2	1.0	–	2.0	2.0	5.0
C3	1.0	–	2.0	2.2	4.8
C4	–	1.0	2.0	1.8	5.2
C5	–	1.0	2.0	2.0	5.0
C6	–	1.0	2.0	2.2	4.8
D1	1.0	–	2.5	1.8	4.7
D2	1.0	–	2.5	2.0	4.5
D3	1.0	–	2.5	2.2	4.3
D4	–	1.0	2.5	1.8	4.7
D5	–	1.0	2.5	2.0	4.5
D6	–	1.0	2.5	2.2	4.3

HSA Crystallisation Methods

HSA was purchased from Sigma–Aldrich and stored in 100 µL aliquots at –80 °C. Prior to crystallisation, the proteins were dissolved in 50 mM potassium phosphate, pH 7.5, 150 mM NaCl buffer[131] and were passed through a column attached to the ÅKTA FPLC gel filtration system (GE Healthcare). After gel filtration, the peak fractions were collected and concentrated to the stated concentrations (~100 mg/mL). HSA crystals were grown using a sitting-drop vapour diffusion method. The crystallisation drops were composed of the stated mixture of the protein-ligand solution, the reservoir solution from the wells and seed stock solutions. Preparation of Phosphate Buffer: Phosphate buffer for size-exclusion chromatography (SEC): 50 mM potassium phosphate, pH 7.5, 150 mM NaCl for 1 L. Adamantane-1-carboxylic acid was purchased from Sigma-Aldrich.

Amino acid sequence of the HSA used

KWVTFISLLFLFSSAYSRGVFRRDAHKSEVAHRFKDLGEENFKALVLIAFAQYLQQCPFEDH
VKLVNEVTEAKTCVADESAENCDKSLHTLFGDKLCTVATLRETYGEMADCCAKQEPERNECF
LQHKDDNPNLPRLVRPEVDVMCTAFHDNEETFLKKYLYEIARRHPYFYAPELLFFAKRYKAA
FTECCQAADKAACLLPKLDELRDEGKASSAKQRLKCASLQKFGERAFKAWAVARLSQRFPKA
EFAEVSKLVTDLTKVHTECCHGDLLECADDRADLAKYICENQDSISSKLKECCEKPLLEKSH
CIAEVENDEMPADLPSLAADFVESKDVCKNYAEAKDVFLGMFLYEYARRHPDYSVVLLLRLA
KTYETTLEKCCAAADPHECYAKVFDEFKPLVEEPQNLIKQNCELFEQLGEYKFQNALLVRYT
KKVPQVSTPTLVEVSRNLGKVGSKCCKHPEAKRMPCAEDYLSVVLNQLCVLHEKTPVSDRVT
KCCTESLVNRRPCFSALEVDETYVPKEFNAETFTFHADICTLSEKERQIKKQTALVELVKHK
PKATKEQLKAVMDDFAAFVEKCCKADDKETCFAEEGKKLVAASQAALGLL

HSA Screen 1

Crystallisation tray composition. Buffer: 50 mM potassium phosphate, pH 7.5, 31 – 34% PEG3350.

		PEG3350 / %					
		30	31	32	33	34	35
Potassium phosphate / pH	6.5	A1	A2	A3	A4	A5	A6
	7.0	B1	B2	B3	B4	B5	B6
	7.5	C1	C2	C3	C4	C5	C6
	8.0	D1	D2	D3	D4	D5	D6

In a given crystallisation plate with wells A1–D6.

A1	A2	A3	A4	A5	A6
B1	B2	B3	B4	B5	B6
C1	C2	C3	C4	C5	C6
D1	D2	D3	D4	D5	D6

Table S3.11. Composition of 10 mL buffer solutions for **HSA** screen 1 (sitting drop method). Crystallisation tray developed at room temperature.

Position	K_2PO_4 buffer / mL	50 % PEG3350 / mL	H_2O / mL
A1	0.5	6.0	3.5
A2	0.5	6.2	3.3
A3	0.5	6.4	3.1
A4	0.5	6.6	2.9
A5	0.5	6.8	2.7
A6	0.5	7.0	2.5
B1	0.5	6.0	3.5
B2	0.5	6.2	3.3
B3	0.5	6.4	3.1
B4	0.5	6.6	2.9
B5	0.5	6.8	2.7
B6	0.5	7.0	2.5
C1	0.5	6.0	3.5
C2	0.5	6.2	3.3
C3	0.5	6.4	3.1
C4	0.5	6.6	2.9
C5	0.5	6.8	2.7
C6	0.5	7.0	2.5
D1	0.5	6.0	3.5
D2	0.5	6.2	3.3
D3	0.5	6.4	3.1
D4	0.5	6.6	2.9
D5	0.5	6.8	2.7

D6	0.5	7.0	2.5

Table S3.12 . Crystallisation conditions for HSA screen 1.

Entry	HSA / µL	HSA / mg mL^{-1}	Reservoir / µL	Temperature / °C	Substrate / µL
1	1.0	100	1.0	25	–

HSA Screen 2

HSA (200 µL) was thawed and sodium myristate solution (433 µL) added (6.3 mg sodium myristate and 1 mL phosphate buffer with 0.5 mL EtOH). The solution was incubated at rt for 1 h and was afterwards subjected to purification on a Superdex 200 SEC column. The peak fractions were collected and concentrated to ~ 100 mg mL^{-1} for crystallisation.

Crystallisation tray composition. Buffer: 50 mM potassium phosphate, pH 7.5, 31–34% PEG3350.

		PEG3350 / %					
		30	31	32	33	34	35
Potassium phosphate / pH	6.5	A1	A2	A3	A4	A5	A6
	7.0	B1	B2	B3	B4	B5	B6
	7.5	C1	C2	C3	C4	C5	C6
	8.0	D1	D2	D3	D4	D5	D6

In a given crystallisation plate with wells A1–D6.

A1	A2	A3	A4	A5	A6
B1	B2	B3	B4	B5	B6
C1	C2	C3	C4	C5	C6
D1	D2	D3	D4	D5	D6

Table S3.13. Composition of 10 mL buffer solutions for HSA screen 1 (sitting drop method). Crystallisation tray developed at room temperature.

Position	K_2PO_4 buffer / mL	50 % PEG3350 / mL	H_2O / mL
A1	0.5	6.0	3.5
A2	0.5	6.2	3.3
A3	0.5	6.4	3.1
A4	0.5	6.6	2.9
A5	0.5	6.8	2.7
A6	0.5	7.0	2.5
B1	0.5	6.0	3.5
B2	0.5	6.2	3.3
B3	0.5	6.4	3.1
B4	0.5	6.6	2.9
B5	0.5	6.8	2.7
B6	0.5	7.0	2.5
C1	0.5	6.0	3.5
C2	0.5	6.2	3.3
C3	0.5	6.4	3.1
C4	0.5	6.6	2.9
C5	0.5	6.8	2.7
C6	0.5	7.0	2.5
D1	0.5	6.0	3.5

D2	0.5	6.2	3.3
D3	0.5	6.4	3.1
D4	0.5	6.6	2.9
D5	0.5	6.8	2.7
D6	0.5	7.0	2.5

Table S3.14. Crystallisation conditions for **HSA-myristate** screen 2 with HSA (100 mg mL^{-1}).

Entry	HSA / µL	Reservoir / µL
1	1.0	1.0
2	1.0	2.0

HSA Screen 3

HSA (200 µL) was thawed and sodium myristate solution (433 µL) added (6.3 mg sodium myristate and 1 mL phosphate buffer with 0.5 mL EtOH). The solution was incubated at rt for 1 h and was afterwards subjected to purification on a Superdex 200 SEC column. The peak fraction were collected and concentrated to ~ 100 mg mL^{-1} for crystallisation. Then, a crystal cluster from initial crystallisation experiments (HSA (1 µL) and well D6 reservoir (2 µL)) was harvested into an Eppendorf vial and diluted with reservoir solution (50 µL). This solution was vortexed with a seed bead for 3 min to obtain microcrystals. This solution was called seed stock 1 (ss1). For seed stock solution 2–6 (ss2–ss6), dilutions were prepared by taking the higher concentrated seed stock solution (5 µL) and adding OPT1 stock solution D6 (45 µL), so that a dilution series was created with 10× less protein/seed concentration from seed stock 1–6. Vortexing seed stocks is essential before any withdrawing of the solution for crystallisation to ensure dispersity of the HSA microcrystals.

Crystallisation tray composition. Buffer: 50 mM potassium phosphate, pH 7.5, 30–35% PEG3350.

		PEG3350 / %					
		30	31	32	33	34	35
Potassium phosphate / pH	6.5	A1	A2	A3	A4	A5	A6
	7.0	B1	B2	B3	B4	B5	B6
	7.5	C1	C2	C3	C4	C5	C6
	8.0	D1	D2	D3	D4	D5	D6

In a given crystallisation plate with wells A1–D6.

A1	A2	A3	A4	A5	A6
B1	B2	B3	B4	B5	B6
C1	C2	C3	C4	C5	C6
D1	D2	D3	D4	D5	D6

Table S3.15. Composition of 10 mL buffer solutions for HSA screen 1 (sitting drop method). Crystallisation tray developed at room temperature.

Position	K_2PO_4 buffer / mL	50 % PEG3350 / mL	H_2O / mL
A1	0.5	6.0	3.5
A2	0.5	6.2	3.3
A3	0.5	6.4	3.1
A4	0.5	6.6	2.9
A5	0.5	6.8	2.7
A6	0.5	7.0	2.5
B1	0.5	6.0	3.5
B2	0.5	6.2	3.3
B3	0.5	6.4	3.1
B4	0.5	6.6	2.9
B5	0.5	6.8	2.7
B6	0.5	7.0	2.5
C1	0.5	6.0	3.5
C2	0.5	6.2	3.3
C3	0.5	6.4	3.1
C4	0.5	6.6	2.9
C5	0.5	6.8	2.7
C6	0.5	7.0	2.5
D1	0.5	6.0	3.5
D2	0.5	6.2	3.3
D3	0.5	6.4	3.1
D4	0.5	6.6	2.9
D5	0.5	6.8	2.7
D6	0.5	7.0	2.5

Table S3.16. Crystallisation conditions for HSA-myristate seed stock screen with HSA (100 mg mL^{-1}).

Entry	HSA / µL	Reservoir / µL	Seed stock / µL
1	1.0	4.0	1.0 (ss1)
2	1.0	2.0	1.0 (ss2)
3	1.0	2.0	1.0 (ss3)
4	1.0	2.0	1.0 (ss4)
5	1.0	2.0	1.0 (ss5)
6	1.0	2.0	1.0 (ss6)

HSA Screen 4

Crystallisation tray composition. Buffer: 50 mM potassium phosphate, pH 7.5, 30–35% PEG3350.

		PEG3350 / %					
		30	31	32	33	34	35
Potassium phosphate / pH	6.5	A1	A2	A3	A4	A5	A6
	7.0	B1	B2	B3	B4	B5	B6
	7.5	C1	C2	C3	C4	C5	C6
	8.0	D1	D2	D3	D4	D5	D6

Table S3.17. Crystallisation conditions for HSA-myristate seed stock screen with HSA (102 mg mL^{-1}) and BBL (25× excess).

Entry	HSA / µL	Reservoir / µL	Seed stock / µL
1	1.0	4.0	1.0 (ss1)

Entry 1: In a given crystallisation plate with wells A1–D6 (shaded = mounted).
Observations: Many hollow crystals.

A1	A2	A3	A4	A5	A6
B1	B2	B3	B4	B5	B6
C1	C2	C3	C4	C5	C6
D1	D2	D3	D4	D5	D6

HSA Screen 5

Crystallisation tray composition. Buffer: 50 mM potassium phosphate, pH 7.5, 30–35% PEG3350.

		PEG3350 / %					
		30	31	32	33	34	35
Potassium phosphate / pH	6.5	A1	A2	A3	A4	A5	A6
	7.0	B1	B2	B3	B4	B5	B6
	7.5	C1	C2	C3	C4	C5	C6
	8.0	D1	D2	D3	D4	D5	D6

Table S3.18. Crystallisation conditions for **HSA-myristate seed stock** screen with **HSA** (102 mg mL^{-1}) and **BBL** (25× excess).

Entry	HSA / µL	Reservoir / µL	Seed stock / µL
1	2.0	1.0	–
2	2.0	4.0	–
3	2.0	2.0	–
4	2.0	2.0	1.0 (ss1)

Entry 1. In a given crystallisation plate with wells A1–D6 (shaded = mounted).
Observations: No crystals / heterogeneous.

A1	A2	A3	A4	A5	A6
B1	B2	B3	B4	B5	B6
C1	C2	C3	C4	C5	C6
D1	D2	D3	D4	D5	D6

Entry 2. In a given crystallisation plate with wells A1–D6 (shaded = mounted).
Observations: Many hollow crystals.

A1	A2	A3	A4	A5	A6
B1	B2	B3	B4	B5	B6
C1	C2	C3	C4	C5	C6
D1	D2	D3	D4	D5	D6

Entry 3. In a given crystallisation plate with wells A1–D6 (shaded = mounted).
Observations: No crystals.

A1	A2	A3	A4	A5	A6
B1	B2	B3	B4	B5	B6
C1	C2	C3	C4	C5	C6
D1	D2	D3	D4	D5	D6

Entry 4. In a given crystallisation plate with wells A1–D6 (shaded = mounted).
Observations: Many small crystals.

A1	A2	A3	A4	A5	A6
B1	B2	B3	B4	B5	B6
C1	C2	C3	C4	C5	C6
D1	D2	D3	D4	D5	D6

HSA Screen 6

Crystallisation tray composition. Buffer: 50 mM potassium phosphate, pH 7.5, 30 – 35% PEG3350.

		PEG3350 / %					
		30	31	32	33	34	35
Potassium phosphate / pH	6.5	A1	A2	A3	A4	A5	A6
	7.0	B1	B2	B3	B4	B5	B6
	7.5	C1	C2	C3	C4	C5	C6
	8.0	D1	D2	D3	D4	D5	D6

In a given crystallisation plate with wells A1–D6, where in all cases seed stock (1 µL) / reservoir (2 µL) / protein–ligand mixture (1 µL) / reservoir in reservoir (500 µL) was added.

	1	2	3	4	5	6
A	ss1 + reservoir	ss1 + reservoir	ss1 + reservoir	ss1 + reservoir	ss1 + reservoir	ss1 + reservoir
B	ss2 + reservoir	ss2 + reservoir	ss2 + reservoir	ss2 + reservoir	ss2 + reservoir	ss2 + reservoir
C	ss3 + reservoir	ss3 + reservoir	ss3 + reservoir	ss3 + reservoir	ss3 + reservoir	ss3 + reservoir
D	reservoir	reservoir	reservoir	reservoir	reservoir	reservoir

The following exceptions apply:

- Entry 3: DMSO (2 µL) added to aid dissolution of ligand.
- Entry 4: EtOH (2 µL) + DMSO (2 µL) added to aid dissolution of ligand.
- Entry 5: DMSO (2 µL) added to aid dissolution of ligand.

Table S3.19. Co-crystallisation conditions for **HSA** (102 mg mL^{-1}) screen 6 with shapeshifting ligands. Conditions: 25x excess of the ligand and the crystallisation tray was incubated at 25 °C.

Entry	Ligand
1	BBL
2	BB 3.6
3	BB 3.10_d
4	BB 3.10_b
5	BB 3.10_a
6	BB 3.10_c
7	BB 3.10_f
8	BB 3.10_e
9	BV 3.22
10	BV 3.21

Entry 1: In a given crystallisation plate with wells A1–D6 (shaded = mounted).
Observations: Row A: many small crystals. Row B: good size crystals. Row C and D: many hollow crystals.

A1	A2	A3	A4	A5	A6
B1	B2	B3	B4	B5	B6
C1	C2	C3	C4	C5	C6
D1	D2	D3	D4	D5	D6

Entry 2: In a given crystallisation plate with wells A1–D6 (shaded = mounted).

A1	A2	A3	A4	A5	A6
B1	B2	B3	B4	B5	B6
C1	C2	C3	C4	C5	C6
D1	D2	D3	D4	D5	D6

Entry 3: In a given crystallisation plate with wells A1–D6 (shaded = mounted).
Observations: only precipitate and fragments.

A1	A2	A3	A4	A5	A6
B1	B2	B3	B4	B5	B6
C1	C2	C3	C4	C5	C6
D1	D2	D3	D4	D5	D6

Entry 4: In a given crystallisation plate with wells A1–D6 (shaded = mounted).

A1	A2	A3	A4	A5	A6
B1	B2	B3	B4	B5	B6
C1	C2	C3	C4	C5	C6
D1	D2	D3	D4	D5	D6

Entry 5: In a given crystallisation plate with wells A1–D6 (shaded = mounted).
Observations: needle-like crystals.

A1	A2	A3	A4	A5	A6
B1	B2	B3	B4	B5	B6
C1	C2	C3	C4	C5	C6
D1	D2	D3	D4	D5	D6

Entry 6: In a given crystallisation plate with wells A1–D6 (shaded = mounted).
Observations: mostly hollow crystals.

A1	A2	A3	A4	A5	A6
B1	B2	B3	B4	B5	B6
C1	C2	C3	C4	C5	C6
D1	D2	D3	D4	D5	D6

Entry 7: In a given crystallisation plate with wells A1–D6 (shaded = mounted).

A1	A2	A3	A4	A5	A6
B1	B2	B3	B4	B5	B6
C1	C2	C3	C4	C5	C6
D1	D2	D3	D4	D5	D6

Entry 8: In a given crystallisation plate with wells A1–D6.
Observations: crystals too small or hollow.

A1	A2	A3	A4	A5	A6
B1	B2	B3	B4	B5	B6
C1	C2	C3	C4	C5	C6
D1	D2	D3	D4	D5	D6

Entry 9: In a given crystallisation plate with wells A1–D6.
Observations: needle-like crystals.

A1	A2	A3	A4	A5	A6
B1	B2	B3	B4	B5	B6
C1	C2	C3	C4	C5	C6
D1	D2	D3	D4	D5	D6

Entry 10: In a given crystallisation plate with wells A1–D6.
Observations: crystals too small or hollow.

A1	A2	A3	A4	A5	A6
B1	B2	B3	B4	B5	B6
C1	C2	C3	C4	C5	C6
D1	D2	D3	D4	D5	D6

HSA Screen 7

Crystallisation tray composition. Buffer: 50 mM potassium phosphate, pH 7.5, 30–35% PEG3350.

		PEG3350 / %					
		30	31	32	33	34	35
Potassium phosphate / pH	6.5	A1	A2	A3	A4	A5	A6
	7.0	B1	B2	B3	B4	B5	B6
	7.5	C1	C2	C3	C4	C5	C6
	8.0	D1	D2	D3	D4	D5	D6

In a given crystallisation plate with wells A1–D6, where in all cases seed stock (1 µL) / reservoir (2 µL) / protein–ligand mixture (1 µL) / reservoir in reservoir (500 µL).

	1	2	3	4	5	6
A	ss1 + reservoir	ss1 + reservoir	ss1 + reservoir	ss1 + reservoir	ss1 + reservoir	ss1 + reservoir
B	ss2 + reservoir	ss2 + reservoir	ss2 + reservoir	ss2 + reservoir	ss2 + reservoir	ss2 + reservoir
C	ss3 + reservoir	ss3 + reservoir	ss3 + reservoir	ss3 + reservoir	ss3 + reservoir	ss3 + reservoir
D	reservoir	reservoir	reservoir	reservoir	reservoir	reservoir

The following exceptions apply:

- Entry 1: ss2 used only.
- Entry 2: ss3 used only.
- Entry 3: no seed solution used.
- Entry 6: no seed solution used and water (2 µL) and hexane (8 µL) added to aid dissolution.
- Entry 10: ss3 used only.
- Entry 11 ss3 used only.

Table S3.20. Co-crystallisation conditions for **HSA** (96.6 mg mL^{-1}) screen 7 with shapeshifting ligands. Conditions: 25x excess of the ligand and the crystallisation tray was incubated at 25 °C.

Entry	Ligand
1	BBL
2	BBL
3	BB 3.10_a
4	BB 3.10_d
5	BB 3.10_b
6	BB 3.10_a
7	BB 3.10_c
8	BB 3.10_f
9	BB 3.10_e
10	BV 3.21
11	BV 3.23

Entry 1: In a given crystallisation plate with wells A1–D6 (shaded = mounted).

A1	A2	A3	A4	A5	A6
B1	B2	B3	B4	B5	B6
C1	C2	C3	C4	C5	C6
D1	D2	D3	D4	D5	D6

Entry 2: In a given crystallisation plate with wells A1–D6.

A1	A2	A3	A4	A5	A6
B1	B2	B3	B4	B5	B6
C1	C2	C3	C4	C5	C6
D1	D2	D3	D4	D5	D6

Entry 3: In a given crystallisation plate with wells A1–D6.

A1	A2	A3	A4	A5	A6
B1	B2	B3	B4	B5	B6
C1	C2	C3	C4	C5	C6
D1	D2	D3	D4	D5	D6

Entry 4: In a given crystallisation plate with wells A1–D6.

A1	A2	A3	A4	A5	A6
B1	B2	B3	B4	B5	B6
C1	C2	C3	C4	C5	C6
D1	D2	D3	D4	D5	D6

Entry 5: In a given crystallisation plate with wells A1–D6 (shaded = mounted).

A1	A2	A3	A4	A5	A6
B1	B2	B3	B4	B5	B6
C1	C2	C3	C4	C5	C6
D1	D2	D3	D4	D5	D6

Entry 6: In a given crystallisation plate with wells A1–D6 (shaded = mounted).

A1	A2	A3	A4	A5	A6
B1	B2	B3	B4	B5	B6
C1	C2	C3	C4	C5	C6
D1	D2	D3	D4	D5	D6

Entry 7: In a given crystallisation plate with wells A1–D6 (shaded = mounted).

A1	A2	A3	A4	A5	A6
B1	B2	B3	B4	B5	B6
C1	C2	C3	C4	C5	C6
D1	D2	D3	D4	D5	D6

Entry 7: In a given crystallisation plate with wells A1–D6 (shaded = mounted).

A1	A2	A3	A4	A5	A6
B1	B2	B3	B4	B5	B6
C1	C2	C3	C4	C5	C6
D1	D2	D3	D4	D5	D6

Entry 8: In a given crystallisation plate with wells A1–D6.

A1	A2	A3	A4	A5	A6
B1	B2	B3	B4	B5	B6
C1	C2	C3	C4	C5	C6
D1	D2	D3	D4	D5	D6

Entry 9: In a given crystallisation plate with wells A1–D6.

A1	A2	A3	A4	A5	A6
B1	B2	B3	B4	B5	B6
C1	C2	C3	C4	C5	C6
D1	D2	D3	D4	D5	D6

Entry 10: In a given crystallisation plate with wells A1–D6 (shaded = mounted).

A1	A2	A3	A4	A5	A6
B1	B2	B3	B4	B5	B6
C1	C2	C3	C4	C5	C6
D1	D2	D3	D4	D5	D6

Entry 11: In a given crystallisation plate with wells A1–D6 (shaded = mounted).

A1	A2	A3	A4	A5	A6
B1	B2	B3	B4	B5	B6
C1	C2	C3	C4	C5	C6
D1	D2	D3	D4	D5	D6

HSA Screen 8

Crystallisation tray composition. Buffer: 50 mM potassium phosphate, pH 7.5, 30–35% PEG3350.

		PEG3350 / %					
		30	31	32	33	34	35
Potassium phosphate / pH	6.5	A1	A2	A3	A4	A5	A6
	7.0	B1	B2	B3	B4	B5	B6
	7.5	C1	C2	C3	C4	C5	C6
	8.0	D1	D2	D3	D4	D5	D6

In a given crystallisation plate with wells A1–D6, where in all cases seed stock (1 µL) / reservoir (2 µL) / protein–ligand mixture (1 µL) / reservoir in reservoir (500 µL).

Table S3.21. Co-crystallisation conditions for HSA (100 mg mL^{-1}) screen 8 with ligands. Conditions: 100x excess of the ligand and the crystallisation tray was incubated at 25 °C.

Entry	Ligand
1	BBL
2	1-Ad carboxylic acid (**3.26**)
3	1-Ad carboxylic acid (**3.26**)

Entry 1: In a given crystallisation plate with wells A1–D6 (shaded = mounted).

A1	A2	A3	A4	A5	A6
B1	B2	B3	B4	B5	B6
C1	C2	C3	C4	C5	C6
D1	D2	D3	D4	D5	D6

Entry 2: In a given crystallisation plate with wells A1–D6 (shaded = mounted).

A1	A2	A3	A4	A5	A6
B1	B2	B3	B4	B5	B6
C1	C2	C3	C4	C5	C6
D1	D2	D3	D4	D5	D6

Entry 3: In a given crystallisation plate with wells A1–D6 (shaded = mounted).

A1	A2	A3	A4	A5	A6
B1	B2	B3	B4	B5	B6
C1	C2	C3	C4	C5	C6
D1	D2	D3	D4	D5	D6

Table S3.22. SA Crystallographic Data. The data processing software calculated the crystallographic unit cell to be identical to that of BSA crystals (PDB: 4F5S) so was not refined further.† All crystallographic data was processed by Stefanie Freitag-Pohl.

	HSA-Myristate (PDB: 9EOS)	HSA-Ad (PDB: 9EOD)	BSA (≡ PDB: 4F5S)[81†]
Beamline	I04, DLS	I04, DLS	I04, DLS
Space group	P1	I2	C2
Unit-cell parameters			
a (Å)	38.32	174.86	215.08
b (Å)	87.11	38.13	44.40
c (Å)	97.47	190.97	145.27
α (˚)	74.44	90.00	90.00
β (˚)	89.78	106.15	111.88
γ (˚)	78.57	90.00	90.00
Wavelength (Å)	0.9763	0.9537	0.9795
Resolution (Å)	2.10	1.90	3.00
No. of unique reflections	67849	96690	–
R_{merge}	0.059	0.110	–
$R_{p.i.m.}$	0.036	0.063	–
$\langle I/\sigma(I)\rangle$	9.6	5.96	7.7
$CC_{1/2}$	0.997	0.994	–
Completeness (%)	97.7	99.8	99.9
Multiplicity	3.6	6.5	–
Refinement			
R_{work}/R_{free}	0.211/0.269	0.217/0.268	–
No. of atoms	17921	18075	–
Ligands	9 Myristate, 2 PEG	4 Myristate, 5 PEG, 2 Ad COOH	–
No. of waters	214	250	–
R.m.s.d. bonds (Å)	0.0079	0.0081	–
R.m.s.d. angles (°)	1.408	1.511	–
Ramachandran plot			
Favoured (%)	98.28	97.84	–
Allowed (%)	1.72	2.16	–

Lysozyme Crystallisation Methods

Hen egg white Lysozyme was purchased from Sigma–Aldrich and its purity assessed by dissolution in 10 mM HEPES pH 7.4, 150 mM NaCl buffer and subsequent SDS-PAGE gel electrophoresis. The presence of one band (14 kD) confirmed the presence and purity of Lysozyme.[132] The proteins were then dissolved in 50mM potassium phosphate, pH 6.2 buffer and were passed through a column attached to the ÅKTA FPLC gel filtration system (GE Healthcare). After gel filtration, the peak fractions were collected and concentrated to the stated concentrations (~ 6.0 mg/mL) before being frozen under liquid nitrogen and stored at –80 °C. All protein concentrations were determined by a NanoDrop 1000 spectrophotometer.

Amino acid sequence of the Hen Egg White Lysozyme used

KVFGRCELAAAMKRHGLDNYRGYSLGNWVCAAKFESNFNTQATNRNTDGSTDYGILQINSRW
WCNDGRTPGSRNLCNIPCSALLSSDITASVNCAKKIVSDGNGMNAWVAWRNRCKGTDVQAWI
RGCRL

Table S3.23. Lysozyme Crystallographic Data.

	Soak	Co-Crystallisation
Data Completeness (%)	100	99.6
Resolution (Å)	1.35	1.25
R_{work}	0.261	0.263
R_{Free}	0.264	0.268

Soaking Crystallisations[§]

Lysozyme was reconstituted in 10mM NaOAc pH 4.5, 150 mM NaCl, centrifuged and concentrated to a working concentration of 2.2 mM. Crystallisation experiments were then set up in 96-well sitting drop vapour diffusion plates with the reservoir solution containing a range of 10–100 mM Sodium Acetate, 650–1000 mM NaCl and deionised H_2O (Table S3.24) at different intervals to develop a previously reported protocol on Lysozyme crystal growth.[100] Lysozyme (150 nL) and reservoir buffer (150 nL) were pipetted *via* a Mosquito Machine onto the two prepared interval plates and two additional commercial plates (HR XTAL and PDB), before being stored for two weeks (21 °C, 20% humidity). After this time, 16 Lysozyme crystals were soaked for 60 s with BV-GlcNAc (**3.59**) cryo-solution (16 mM), fished and frozen in liquid nitrogen in order to keep the crystal compact and prevent protein degradation.

Table S3.24. Soaking crystallisations of Lysozyme, Sodium Acetate, pH 4.5, NaCl with GlcNAc-BV (**3.59**), input concentrations in each cell, units in mM.

Sodium Acetate, pH 4.5	Lysozyme, Sodium Acetate, pH 4.5, NaCl									
NaCl	1	2	3	4	5	6	7	8	9	10
A	10 000	20 000	30 000	40 000	50 000	60 000	70 000	80 000	90 000	100 000
	650	650	650	650	650	650	650	650	650	650
B	10 000	20 000	30 000	40 000	50 000	60 000	70 000	80 000	90 000	100 000
	700	700	700	700	700	700	700	700	700	700
C	10 000	20 000	30 000	40 000	50 000	60 000	70 000	80 000	90 000	100 000
	750	750	750	750	750	750	750	750	750	750
D	10 000	20 000	30 000	40 000	50 000	60 000	70 000	80 000	90 000	100 000
	800	800	800	800	800	800	800	800	800	800
E	10 000	20 000	30 000	40 000	50 000	60 000	70 000	80 000	90 000	100 000
	850	850	850	850	850	850	850	850	850	850
F	10 000	20 000	30 000	40 000	50 000	60 000	70 000	80 000	90 000	100 000
	900	900	900	900	900	900	900	900	900	900
G	10 000	20 000	30 000	40 000	50 000	60 000	70 000	80 000	90 000	100 000
	950	950	950	950	950	950	950	950	950	950
H	10 000	20 000	30 000	40 000	50 000	60 000	70 000	80 000	90 000	100 000
	1000	1000	1000	1000	1000	1000	1000	1000	1000	1000

Co-Crystallisations§

Lysozyme was dissolved 10mM NaOAc pH 4.5, 150 mM NaCl and filtered to a working concentration of 2.8 mM. BV-GlcNAc (**3.59**) was dissolved in deionised H_2O (14 mM) and was combined with lysozyme (100 µL) at a five-fold ligand excess and incubated for 15 min to allow for binding. BV-GlcNAc was selected to be at five-fold excess to ensure high occupancy in crystals of the complex. The crystals were grown *via* a Mosquito machine, pipetting the complex (20 µL) onto four pre-prepared commercial plates (JENA XP, PDB, XP SCREEN) in order to screen multiple crystallisation conditions, before being stored for two weeks (21 °C, 20% humidity). The co-crystalised complex was then further soaked with BV-GlcNAc dissolved in deionised H_2O (16 mM).

Enzymatic Assay Inhibition Experiments§

An enzymatic assay protocol was designed building upon the previously reported protocol from Shugar *et. al.*[99] A 96-well-microplate contained the ML substrate, Lysozyme and activity buffer/inhibitor (8:1:1 ration), where the lysozyme was added immediately before an initial reading. Following the addition of Lysozyme, the absorption was recorded in 30 s intervals (5 s of shaking), with path length = 1 cm, recorded by a Tecan Microplate Reader. The assay was designed to be compatible on a small scale (100 µL) due to the small quantity of the BV-GlcNAc (**3.59**) available. Once optimal concentrations were determined for Lysozyme and ML, the assay procedure was altered by changing parameters: 1) Temperature, 2) shaking rate, 3) time of first measurement and 4) pipetting method. The assay was changed until reproducible data sets were obtained. Following this optimisation, the activity buffer was replaced with a solution of the inhibitors (GlcNAc or BV-GlcNAc) and the [GlcNAc] and [BV-GlcNAc] were varied. The rate of reaction was measured through absorption of the solution over time.

Protein Computational Modelling

All PDB structures and solved XRD data were superimposed in the molecular visualisation software, PyMol,[133] in order to compare structural differences of protein-ligand complexes. The electrostatic potential molecular surfaces were calculated using the APBS electrostatics function in PyMol, which were then mapped and visualised by colouration in PyMol.[133] All hydrophobicity molecular surfaces were visualised by colouration according to the residue hydrophobicity in the Kyte-Doolittle scale[102] (an available function in Schrödinger Maestro). All protein structures were modelled in Schrödinger Maestro.[134]

§ Experiments and analysis performed by L. Corbett.

3.5 References

1 C. J. Pedersen, *J. Am. Chem. Soc.*, 1967, **89**, 2495–2496.

2 B. Dietrich, J. M. Lehn and J. P. Sauvage, *Tetrahedron Lett.*, 1969, **10**, 2885–2888.

3 D. J. Cram, *J. Incl. Phenom.*, 1988, **6**, 397–413.

4 B. Dietrich, J. M. Lehn and J. P. Sauvage, *Tetrahedron Lett.*, 1969, **10**, 2889–2892.

5 A. Labourel, K. E. H Frandsen, F. Zhang, N. Brouilly, S. Grisel, M. Haon, L. Ciano, D. Ropartz, M. Fanuel, F. Martin, D. Navarro, M.-N. Rosso, T. Tandrup, B. Bissaro, K. S. Johansen, A. Zerva, P. H. Walton, B. Henrissat, L. Lo Leggio and J.-G. Berrin, *Nat. Chem. Biol.,* 2020, **16**, 345–350.

6 C. H. Heldin, B. Lu, R. Evans and J. S. Gutkind, *Cold Spring Harb Perspect Biol*., 2016, **8**, a005900.

7 I. Sela-Culang, V. Kunik and Y. Ofran, *Front Immunol*., 2013, **4**, 1–13.

8 J. -M Lehn, *Angew. Chem. Int. Ed. Engl.*, 1988, **27**, 89–112.

9 H. C. Kolb, M. G. Finn and K. B. Sharpless, *Angew. Chem. Int. Ed.,*2001, **40**, 2004–2021.

10 V. V. Rostovtsev, L. G. Green, V. V. Fokin and K. B. Sharpless, *Angew. Chem. Int. Ed.,* 2002, **41**, 2596–2599.

11 C. J. Smedley, G. Li, A. S. Barrow, T. L. Gialelis, M. C. Giel, A. Ottonello, Y. Cheng, S. Kitamura, D. W. Wolan, K. B. Sharpless and J. E. Moses, *Angew. Chem. Int. Ed.*, 2020, **59**, 12460–12469.

12 M. Steinhagen, K. Holland-Nell, M. Meldal and A. G. Beck-Sickinger, *Chem. Bio. Chem.*, 2011, **12**, 2426–2430.

13 K. Holland-Nell and M. Meldal, *Angew. Chem. Int. Ed.,* 2011, **50**, 5204–5206.

14 E. M. Sletten and C. R. Bertozzi, *Angew. Chem. Int. Ed.,* 2009, **48**, 6974–6998.

15 J. Kim and C. R. Bertozzi, *Angew. Chem. Int. Ed.,* 2015, **54**, 15777–15781.

16 P. Agarwal, B. J. Beahm, P. Shieh and C. R. Bertozzi, *Angew. Chem. Int. Ed.,* 2015, **54**, 11504–11510.

17 K. E. Beatty, J. D. Fisk, B. P. Smart, Y. Y. Lu, J. Szychowski, M. J. Hangauer, J. M. Baskin, C. R. Bertozzi and D. A. Tirrell, *Chem. Bio. Chem.*, 2010, **11**, 2092–2095.

18 M. J. Hangauer and C. R. Bertozzi, *Angew. Chem. Int. Ed.,* 2008, **47**, 2394–2397.

19 A. M. Embaby, S. Schoffelen, C. Kofoed, M. Meldal and F. Diness, *Angew. Chem. Int. Ed.,* 2018, **57**, 8022–8026.

20 S. Vutti, S. Schoffelen, J. Bolinsson, N. Buch-Månson, N. Bovet, J. Nygård, K. L. Martinez and M. Meldal, *Chem. Eur. J.*, 2016, **22**, 496–500.

21 T. J. Mooibroek, S. Scheiner and H. Valkenier, *ChemPhysChem.*, 2021, **22**, 433–434.

22 E. Fischer, *Chem. Ber.*, 1894, **27**, 2985–2993.

23 D. E. Koshland, *Proc. Natl. Acad. Sci. U.S.A.*, 1958, **44**, 98–104.

24 J. A. Thoma and D. E. Koshland, *J. Am. Chem. Soc.*, 1960, **82**, 3329–3333.

25 J. Monod, J. Wyman and J. P. Changeux, *J. Mol. Biol.*, 1965, **12**, 88–118.

26 M. M. Rubin and J. P. Changeux, *J. Mol. Biol.*, 1966, **21**, 265–274.

27 J. P. Changeux and S. Edelstein, *F1000 Biol. Rep.*, 2011, **3**, 1–15

28 P. T. Corbett, J. Leclaire, L. Vial, K. R. West, J. L. Wietor, J. K. M. Sanders and S. Otto, *Chem. Rev.*, 2006, **106**, 3652–3711.

29 R. A. R. Hunt and S. Otto, *Chem. Comm.*, 2010, **47**, 847–858.

30 O. Ramström and J. M. Lehn, *Nat. Rev. Drug. Discov.,* 2002, **1**, 26–36.

31 G. Nasr, E. Petit, C. T. Supuran, J. Y. Winum and M. Barboiu, *Bioorg. Med. Chem. Lett.*, 2009, **19**, 6014–6017.

32 G. Nasr, E. Petit, D. Vullo, J. Y. Winum, C. T. Supuran and M. Barboiu, *J. Med. Chem.*, 2009, **52**, 4853–4859.

33 A. Canal-Martín and R. Pérez-Fernández, *ACS Omega*, 2020, **5**, 26307–26315.

34 F. Gorrec, *Biochem (Lond).*, 2021, **43**, 36–43.

35 A. McPherson and J. A. Gavira, *Acta. Cryst.*, 2014, **F70**, 2–20.

36 T. Peters, *All About Albumin: Biochemistry, Genetics and Medical Applications*, Academic Press Limited, San Diego, CA, 1996.

37 K. A. Majorek, P. J. Porebski, A. Dayal, M. D. Zimmerman, K. Jablonska, A. J. Stewart, M. Chruszcz and W. Minor, *Mol. Immunol.*, 2012, **52**, 174–182.

38 M. J. Hawkins, P. Soon-Shiong and N. Desai, *Adv. Drug. Deliv. Rev.*, 2008, **60**, 876–885.

39 T. Peters, *Adv. Protein. Chem.*, 1985, **37**, 161–245.

40 A. A. Bhattacharya, T. Grüne and S. Curry, *J. Mol. Biol.*, 2000, **303**, 721–732.

41 I. Petitpas, C. E. Petersen, C. E. Ha, A. A. Bhattacharya, P. A. Zunszain, J. Ghuman, N. V. Bhagavan and S. Curry, *Proc. Natl. Acad. Sci. U. S. A.*, 2003, **100**, 6440–6445.

42 J. Ghuman, P. A. Zunszain, I. Petitpas, A. A. Bhattacharya, M. Otagiri and S. Curry, *J. Mol. Biol.*, 2005, **353**, 38–52.

43 F. Kratz, *J. Control. Release.,* 2008, **132**, 171–183.

44 A. Fleming, *Proc. R. Soc. Lond. B. Biol. Sci.,* 1922, **93**, 306–317.

45 D. M. Chipman, J. J. Pollock and N. Sharon, *J. Biol. Chem.*, 1968, **243**, 487–496.

46 P. Ferraboschi, S. Ciceri and P. Grisenti, *Antibiotics.,* 2021, **10**, 1534

47 S. A. Ragland and A. K. Criss, *PLOS Path*., 2017, **13**, e1006512.

48 C. C. Blake, L. N. Johnson, G. A. Mair, A. C. North, D. C. Phillips and V. R. Sarma, *Proc. R. Soc. Lond. B. Biol. Sci.*, 1967, **167**, 378–388.

49 I. D. Campbell, C. M. Dobson and R. J. P. Williams, *Proc. R. Soc. Lond. B. Biol. Sci.*, 1975, **189**, 503–509.

50 M. Jafari and F. Mehrnejad, *PLOS One*, 2016, **11**, e0165213.

51 P. J. Artymiuk and C. C. F. Blake, *J. Mol. Biol.*, 1981, **152**, 737–762.

52 N. Khorshidian, E. Khanniri, M. R. Koushki, S. Sohrabvandi and M. Yousefi, *Front. Nutr.*, 2022, **9**, 1–12.

53 M. C. Salinas-Garcia, M. Plaza-Garrido, D. Alba-Elena and A. Camara-Artigas, *Acta Cryst.,* 2019, **F75**, 687–696.

54 J. C. Cheetham, P. J. Artymiuk and D. C. Phillips, *J. Mol. Biol.*, 1992, **224**, 613–628.

55 C. C. F. Blake, D. F. Koenig, G. A. Mair, A. C. T. North, D. C. Phillips and V. R. Sarma, *Nature*, 1965, **206**, 757–761.

56 D. E. Koshland, *Biol. Rev.*, 1953, **28**, 416–436.

57 D. J. Vocadlo, G. J. Davies, R. Laine and S. G. Withers, *Nature.,* 2001, **412**, 835–838.

58 A. N. Bismillah, B. M. Chapin, B. A. Hussein and P. R. McGonigal, *Chem. Sci.,* 2020, **11**, 324–332.

59 A. R. Lippert, V. L. Keleshian and J. W. Bode, *Org. Biomol. Chem.,* 2009, **7**, 1529–1532.

60 K. K. Larson, M. He, J. F. Teichert, A. Naganawa and J. W. Bode, *Chem. Sci.*, 2012, **3**, 1825–1828.

61 J. F. Teichert, D. Mazunin and J. W. Bode, *J. Am. Chem. Soc.*, 2013, **135**, 11314–11321.

62 A. Ottonello, J. A. Wyllie, O. Yahiaoui, S. Sun, R. A. Koelln, J. A. Homer, R. M. Johnson, E. Murray, P. Williams, J. R. Bolla, C. V. Robinson, T. Fallon, T. P. Soares da Costa and J. E. Moses, *Proc. Natl. Acad. Sci. U. S. A.*, 2023, **120**, e2208737120.

63 M. N. Pomfret, P. B. Sun, Z. Huang, A. C. Freund, T. Miyoshi and M. R. Golder, *Angew. Chem. Int. Ed.*, 2023, **62**, e202301695.

64 O. Yahiaoui, L. F. Pašteka, B. Judeel and T. Fallon, *Angew. Chem. Int. Ed.*, 2018, **57**, 2570–2574.

65 C. Dohmen, H. Ihmels and T. Paululat, *Eur. J. Org. Chem.*, 2022, **45**, e202201172.

66 A. N. Bismillah, J. Sturala, B. M. Chapin, D. S. Yufit, P. Hodgkinson and P. R. McGonigal, *Chem. Sci.*, 2018, **9**, 8631–8636.

67 A. N. Bismillah, T. G. Johnson, B. A. Hussein, A. T. Turley, P. K. Saha, H. C. Wong, J. A. Aguilar, D. S. Yufit and P. R. McGonigal, *Nat. Chem.*, 2023, **15**, 615–624.

68 P. R. McGonigal, C. De León, Y. Wang, A. Homs, C. R. Solorio-Alvarado and A. M. Echavarren, *Angew. Chem. Int. Ed.*,, 2012, **51**, 13093–13096.

69 (a) A. N. Bismillah, PhD Thesis, Durham University, 2019; (b) W. Maturi, PhD Thesis, Durham University, 2024.

70 C. R. Smith, *Synlett*, 2009, **9**, 1522–1523.

71 H. D. Patel, T. H. Tran, C. J. Sumby, L. F. Pašteka and T. Fallon, *J. Am. Chem. Soc.*, 2020, **142**, 3680–3685.

72 T. Harris, G. dos P. Gomes, S. Ayad, R. J. Clark, V. V. Lobodin, M. Tuscan, K. Hanson and I. V. Alabugin, *Chem*, 2017, **3**, 629–640.

73 A. Anand, P. Singh, V. Kumar and G. Bhargava, *RSC. Adv.*, 2019, **9**, 25554–25568.

74 H. E. Zimmerman and D. Armesto, *Chem. Rev.*, 1996, **96**, 3065–3112.

75 H. E. Zimmerman and G. L. Grunewald, *J. Am. Chem. Soc.*, 1966, **88**, 183–184.

76 H. E. Zimmerman, R. W. Binkley, R. S. Givens and M. A. Sherwin, *J. Am. Chem. Soc.*, 1967, **89**, 3932–3933.

77 M. Jones and L. T. Scott, *J. Am. Chem. Soc.*, 1967, **89**, 150–151.

78 M. Jones, *J. Am. Chem. Soc.*, 1967, **89**, 4236–4238.

79 T.-Y. Teng, *J. Appl. Cryst.*, 1990, **23**, 387–391.

80 A. J. McCoy, R. W. Grosse-Kunstleve, P. D. Adams, M. D. Winn, L. C. Storoni and R. J. Read, *J. Appl. Cryst.*, 2007, **40**, 658–674.

81 A. Bujacz, *Acta Cryst.*, 2012, **D68**, 1278–1289.

82 S. Curry, H. Mandelkow, P. Brick and N. Franks, *Nat. Struc. Biol.,* 1998*,* **5**, 827–835.

83 T. Bergfors, *J. Struct. Biol.*, 2003, **142**, 66–76.

84 E. A. Stura and I. A. Wilson, *J. Cryst. Growth.*, 1991, **110**, 270–282.

85 R. C. Fort and P. von R. Schleyer, *Chem. Rev.*, 2002, **64**, 277–300.

86 C. A. Lipinski, F. Lombardo, B. W. Dominy and P. J. Feeney, *Adv. Drug. Deliv. Rev.*, 1997, **23**, 3–25.

87 T. Constantinescu, C. N. Lungu and I. Lung, *Molecules*, 2019, **24**, 1–11.

88 P. D. Leeson and B. Springthorpe, *Nat. Rev. Drug. Discov.*, 2007, **6**, 881–890.

89 A. A. El-Emam, K. A. Alrashood, M. A. Al-Omar and A. M. S. Al-Tamimi, *Molecules*, 2012, **17**, 3475–3483.

90 R. B. Greenwald, *J. Control. Release*, 2001, **74**, 159–171.

91 R. B. Greenwald and H. Zhao, *Prodrugs*, 2007, 283–338.

92 C. Elvira, A. Gallardo, J. San Roman and A. Cifuentes, *Molecules,* 2005, **10**, 114–125.

93 G. Yakub, N. E. Manolova, I. B. Rashkov, N. Markova, R. Toshkova, A. Georgieva, R. Mincheva, A. Toncheva, J. M. Raquez and P. Dubois, *ACS Omega*, 2022, **7**, 36403–36414.

94 H. Ohkawa, Y. Teramura, S. Takeoka and E. Tsuchida, *Bioconjugate Chem*, 2000, **11**, 815–821.

95 A. Burrows, J. Holman, A. Parsons, G. Pilling and G. Price, *Chemistry3,* Oxford University Press, 2013.

96 S. P. Bew and G. D. Hiatt-Gipson, *J. Org. Chem.*, 2010, **75**, 3897–3899.

97 K. Bowden, M. Heilbron, E. R. H. Jones and B. C. L. Weedon, *J. Chem. Soc.,* 1946, **0**, 39–45.

98 E. J. Corey and G. Schmidt, *Tetrahedron Lett.*, 1979, **20**, 399–402.

99 D. Shugar, *Biochim. Biophys. Acta.*, 1952, **8**, 302–309.

100 M. Aherne, J. A. Lyons and M. Caffrey, *J. Appl. Cryst.*, 2012, **45**, 1330–1333.

101 K. Peretoltchine, S. Bryson and E. F. Pai, PDB 3RZ4, DOI: 10.2210/pdb3RZ4/pdb.

102 J. Kyte and R. F. Doolittle, *J. Mol. Biol.*, 1982, **157**, 105–132.

103 D. N. Moothoo and J. H. Naismith, *Glycobiol.*, 1998, **8**, 173–181.

104 G. N. Reeke, J. W. Becker and G. M. Edelman, *J. Biol. Chem.*, 1975, **250**, 1525–1547.

105 K. D. Hardman and C. F. Ainsworth, *Biochemistry*, 1976, **15**, 1120–1128.

106 J. R. Helliwell and M. Helliwell, *Chem. Commun.*, 1996, **14**, 1595–1602.

107 Z. Derewenda, J. Yariv, J. R. Helliwell, A. J. Kalb, E. J. Dodson, M. Z. Papiz, T. Wan and J. Campbell, *EMBO J.*, 1989, **8**, 2189–2193.

108 I. J. Goldstein *et. al.*, *Properties, Functions and Applications in Biology and Medicine*, 1986, 35–214.

109 J. H. Naismith, C. Emmerich, J. Habash, S. J. Harrop, J. R. Helliwell, W. N. Hunter, J. Raftery, A. J. Kalb and J. Yariv, *Acta Cryst.*, 1994, **D50**, 847–858.

110 T. Tanaka, H. Nagai, M. Noguchi, A. Kobayashi and S. I. Shoda, *Chem. Commun.*, 2009, **23**, 3378–3379.

111 O. Trott and A. J. Olson, *J. Comput. Chem.*, 2009, **31**, 455–461.

112 S. Ferrer and A. M. Echavarren, *Angew. Chem. Int. Ed.*, 2016, **55**, 11178–11182.

113 K. Nogi, T. Fujihara, J. Terao and Y. Tsuji, *Chem.l Commun.*, 2014, **50**, 13052–13055.

114 A. Tenaglia and S. Marc, *J. Org. Chem.*, 2008, **73**, 1397–1402.

115 J. P. Lutz, O. Davydovich, M. D. Hannigan, J. S. Moore, P. M. Zimmerman and A. J. McNeil, *J. Am. Chem. Soc.*, 2019, **141**, 14544–14548.

116 M. Achard, M. Mosrin, A. Tenaglia and G. Buono, *J. Org. Chem.*, 2006, **71**, 2907–2910.

117 H. Zhang, X. Li, Q. Shi, Y. Li, G. Xia, L. Chen, Z. Yang and Z. X. Jiang, *Angew. Chem. Int. Ed.*, 2015, **54**, 3763–3767.

118 C. Gehin, J. Montenegro, E. K. Bang, A. Cajaraville, S. Takayama, H. Hirose, S. Futaki, S. Matile and H. Riezman, *J. Am. Chem. Soc.*, 2013, **135**, 9295–9298.

119 K. Tsubokura, K. K. H. Vong, A. R. Pradipta, A. Ogura, S. Urano, T. Tahara, S. Nozaki, H. Onoe, Y. Nakao, R. Sibgatullina, A. Kurbangalieva, Y. Watanabe and K. Tanaka, *Angew. Chem. Int. Ed.*, 2017, **56**, 3579–3584.

120 G. Gao, F. Sanda and T. Masuda, *Macromolecules*, 2003, **36**, 3932–3937.

121 P. Thomopoulou, J. Sachs, N. Teusch, A. Mariappan, J. Gopalakrishnan and H. G. Schmalz, *ACS Med. Chem. Lett.*, 2016, **7**, 188–191.

122 P. Zare, A. Stojanovic, F. Herbst, J. Akbarzadeh, H. Peterlik and W. H. Binder, *Macromolecules*, 2012, **45**, 2074–2084.

123 Y. L. Sun, Y. Zhou, Q. L. Li and Y. W. Yang, *Chem. Commun.*, 2013, **49**, 9033–9035.

124 K. Brunner, J. Harder, T. Halbach, J. Willibald, F. Spada, F. Gnerlich, K. Sparrer, A. Beil, L. Möckl, C. Bräuchle, K. K. Conzelmann and T. Carell, *Angew. Chem. Int. Ed.*, 2015, **54**, 1946–1949.

125 G. Winter, C. M. C. Lobley and S. M. Prince, *Acta Cryst.,* 2013, **D69**, 1260–1273.

126 P. R. Evans and G. N. Murshudov, *Acta Cryst.,* 2013, **D69**, 1204–1214.

127 M. D. Winn, C. C. Ballard, K. D. Cowtan, E. J. Dodson, P. Emsley, P. R. Evans, R. M. Keegan, E. B. Krissinel, A. G. W. Leslie, A. McCoy, S. J. McNicholas, G. N. Murshudov, N. S. Pannu, E. A. Potterton, H. R. Powell, R. J. Read, A. Vagin and K. S. Wilson, *Acta Cryst.,* 2011, **D67**, 235–242.

128 M. P. Czub, A. M. Boulton, E. J. Rastelli, N. R. Tasker, T. S. Maskrey, I. K. Blanco, K. E. McQueeney, J. H. Bushweller, W. Minor, P. Wipf, E. R. Sharlow and J. S. Lazo, *Mol. Pharmacol.*, 2020, **98**, 648–657.

129 G. N. Murshudov, P. Skubák, A. A. Lebedev, N. S. Pannu, R. A. Steiner, R. A. Nicholls, M. D. Winn, F. Long and A. A. Vagin, *Acta Cryst.,* 2011, **D67**, 355–367.

130 P. Emsley, B. Lohkamp, W. G. Scott and K. Cowtan, *Acta Cryst.,* 2010, **D66**, 486–501.

131 K. L. Hein, U. Kragh-Hansen, J. P. Morth, M. D. Jeppesen, D. Otzen, J. V. Møller and P. Nissen, *J. Struct. Biol.*, 2010, **171**, 353–360.

132 A. S. Parmar and M. Muschol, *Biophys. J.*, 2009, **97**, 590–598.

133 PyMOL, The PyMOL Molecular Graphics System, Version 3.0 Schrödinger, LLC.

134 Maestro, Schrödinger, LLC, New York, NY, 2024.

CHAPTER 4

TOWARDS VIOLOGEN-INSPIRED SHAPESHIFTING LIGANDS

Synopsis

In this Chapter, we principally investigate synthetic routes to viologen appended bullvalenes, with the aim of understanding the fluxional properties which they exhibit. To start, we synthesised CB[8] for use in host-guest studies. Then, the design of viologen appended bullvalenes was considered, with the aim of limiting the conformational degrees of freedom *via* linker length. The synthetic routes proposed towards obtaining the target compounds included: 1) cycloaddition of functionalised alkynes; 2) BDT and BV hydroxy group modification; 3) Steglich esterification; 4) extended alkyl linker approach and 5) Zincke coupling. The results of the aforementioned investigations provides further knowledge towards the current understanding of BDT and BV functionalisation within the field.

Acknowledgments

The following people are gratefully acknowledged for their contribution to this chapter: L. Nichols synthesised the *bis*(Ms) alkyne; W. Maturi provided useful discussions and obtained the *bis*(Bpin) BDT and *bis*(BPin) bullvalene NMR and mass spectrometry data; Dr. Y. Sun and Dr. C. Hogg provided useful discussions. The research was conceived by Prof. P. R. McGonigal.

4.1 Introduction

4.1.1 Viologens

The trivial name, viologen, refers to the homologous series of *N,N*′-substituted 4,4′-bipyridinium salts, where the generic structure for this set of compounds is shown in Figure 4.1. Owing to their well-established reversible redox properties, viologens have shown versatility within a wide range of potential applications, such as use within materials for organic electronics,[1–4] energy storage,[5–8] gas storage[9,10] and in biochemical applications,[11–13] for example.

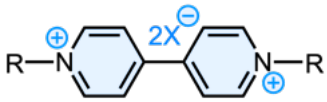

Viologen

Figure 4.1. General structure of a viologen. R represents a variable group; X represents a counter ion.

Furthermore, the relative ease to synthetically modify viologens has made them an attractive proposition for incorporation into functional materials, primarily through the ability to readily tune their physicochemical properties.[14] In addition, the noncovalent interactions of viologen derivatives with supramolecular macrocycles,[15–18] where complexation can be mediated through redox control, make these dynamic systems of particular interest in supramolecular chemistry.

4.1.2 Spectro-Electrochemical Properties of Viologens

Viologens are well known for their desirable electronic properties and ability to self-dimerise, where these processes are routinely characterised by UV–Vis spectroscopy and cyclic voltammetry (CV). The dimethyl viologen dication (M_2V^{2+}) can undergo a one electron reduction to form its radical cation ($M_2V^{+\bullet}$), followed by the subsequent electron reduction to form the neutral viologen species (M_2V^0) (Scheme 4.1).[19]

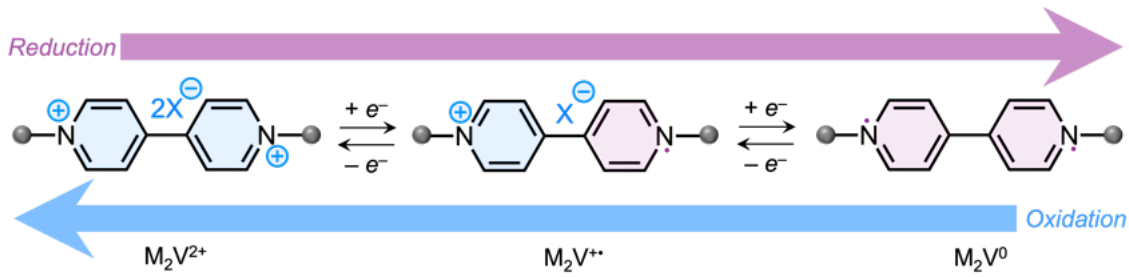

Scheme 4.1. The reversible redox states of the dimethyl viologen dication (M_2V^{2+}) to the radical cation ($M_2V^{+\bullet}$) and then the neutral species (M_2V^0). X = negative counter ion; The grey circle = Me. The arrows represent electrochemical oxidation and reduction processes.[19]

As demonstrated by the cyclic voltammogram (Figure 4.2), the M_2V^{2+} species displays two well-defined, electrochemically reversible one-electron charge transfer processes, which are attributed to consecutive reductions which are reached within a very accessible potential.[20] The first of these redox processes at –0.70 V corresponds to the reversible reduction of M_2V^{2+} to the radical cation species ($M_2V^{+\bullet}$), which is then followed by the subsequent one-electron reduction of $M_2V^{+\bullet}$ to the neutral species, M_2V^0 at –1.01 V.[17]

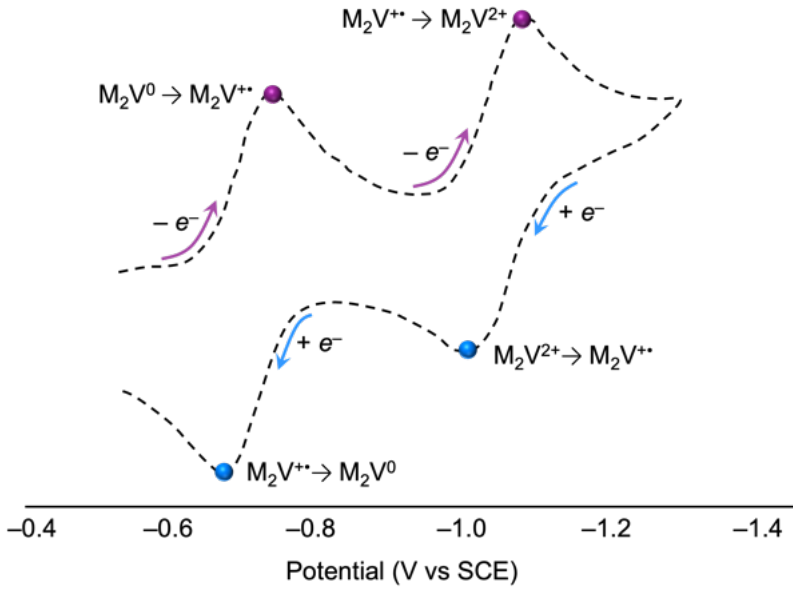

Figure 4.2. Cyclic voltammogram (0.1 V s^{-1}) of **M_2V dichloride** (0.5 mM) in 0.1 M phosphate buffer (pH 7.0), 298 K. SCE = saturated calomel electrode. The key electrochemical processes are labelled. Figure reproduced from previously reported results.[17]

The CV trace profile of viologen derivatives can be highly dependent on their solubility in the electrolyte, their constituent counterion and the type of substitution.[21] Viologens that are typically soluble in organic solvents include those with the counterion PF_6^-, BF_4^-, NO_3^- and ClO_4^-, however, when the counterion is F^-, Cl^-, Br^- I^-, PO_4^- or SO_4^{2-}, these viologen species are insoluble in many organic solvents.[21] When viologen salts are subjected to electrochemical reduction in water, the solution becomes coloured due to the presence of viologen radicals.[20]

In the case of M_2V, the colour of the solution can vary from blue to purple depending on the ratio of the monomer and dimer species in solution, where in aqueous solution, the $M_2V^{+\bullet}$ species exhibits blue colouration with an absorption peak at 600 nm.[22] Increasing the concentration of $M_2V^{+\bullet}$ in aqueous solution, results in the gradual change in colour from blue to violet, as a result of the π-dimerisation and subsequent formation of a M_2V^{2+} dimer. The formation of the M_2V^{2+} dimer results in a blue-shifted absorption in the 400–600 nm region (Figure 4.3), which is attributed to interactions between the dipole moments of the two $M_2V^{+\bullet}$ molecules.[22] Additionally, the presence of a new signal (~850 nm) appears for the M_2V^{2+} dimer, that is not present in the UV-Vis spectrum for that of the $M_2V^{+\bullet}$ monomer. This band, in the near IR region, corresponds to the electronic transition from the occupied bonding molecular orbital to the anti-bonding SOMO present in the diamagnetic M_2V^{2+} dimer.[23,24] Furthermore, the equilibrium in this system can be controlled by temperature, where the equilibrium shifts from the M_2V^{2+} dimer towards the $M_2V^{+\bullet}$ monomeric species with increased temperature, resulting in a colour change from violet to blue, and vice versa.[22]

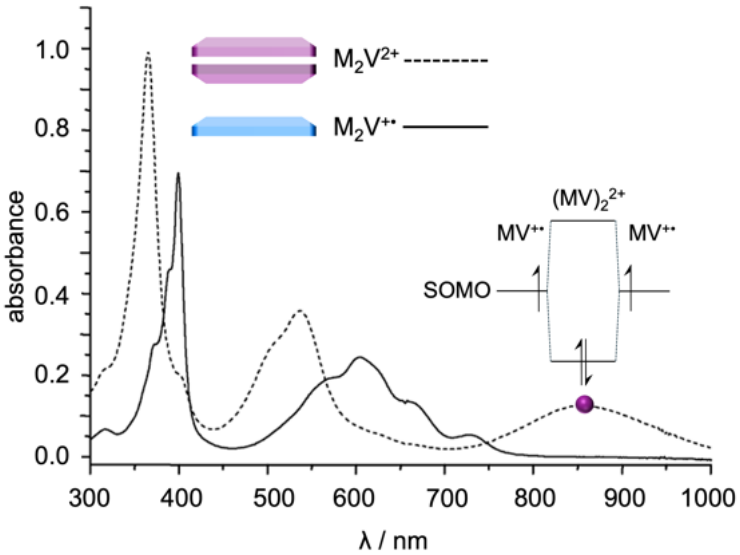

Figure 4.3. UV-Vis spectra of the $M_2V^{+\bullet}$ monomer (solid black line) and M_2V^{2+} dimer (dashed black line) for the alkylated-$V(PF_6)_2$ after exhaustive one-electron reduction in DMF. Figure adapted from previously reported results.[25]

4.1.3 Synthetic Routes to Viologens

The synthetic methods to access a diverse range of viologen derivatives can be categorised into two general routes: 1) coupling reactions to obtain viologen species and their derivatives and 2) structural modification of the viologen through *N*-substitution. Coupling reactions provides a powerful means towards the formation of new C–C bonds between two chemical units. The following coupling reactions have been heavily utilised for the formation of viologens:

1) Winters Coupling: where a 1-substituted pyridinium salt (**4.1**) is coupled in the presence of cyanide ions to form viologen (**4.2**).[26,27]
2) Suzuki Coupling: where two aryl moieties (**4.3**) are coupled *via* C–C cross coupling conditions to form aryl-bridged viologens (**4.4**).[28–30]

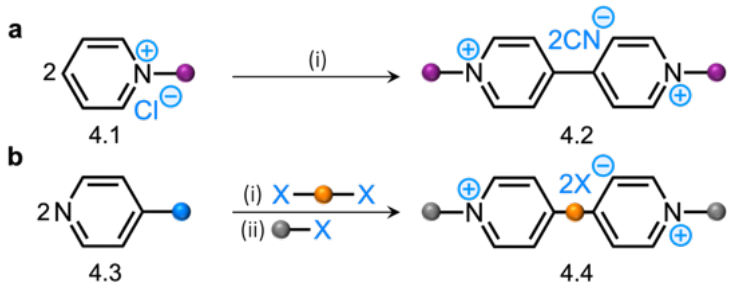

Scheme 4.2. (**a**) Reaction scheme for a generic Winters Coupling for viologen (**4.2**) formation. Reagents and conditions: (i) Cyanide (2 eq.) in 50% *v*/*v* Me_2CO:H_2O under anaerobic conditions. The magenta circle represents a variable group (e.g. Ph, CH_2Ph). (**b**) Reaction scheme for a generic Suzuki Coupling for viologen (**4.4**) formation. Reagents and conditions: (i) alkyl halide / base / $Pd(PPh_3)_4$ / solvent; (ii) alkylation. The blue circle represents a boronic ester, the orange circle represents an aryl group and the grey circle represents an alkyl group (where X = Cl, Br, I).

Furthermore, the structural modification of viologens generally takes place through the *N*-substitution of 4,4′-bipyridine, owing to basicity of the nitrogen atoms present in the molecule. The following reactions have been shown to provide structural modification to viologens:

1) Menshutkin Reaction: substituted viologens (**4.6**) are accessed *via* an *N*-alkylation reaction between halogenated alkanes and bipyridine (**4.5**) following an S_N2 process. This method to directly prepare and isolate a range of alkyl *N*-substituted viologen (di)cations with the respective halide as the counterion, which is generally high yielding.[31–34]
2) Mitsunobu Reaction: where *N*-alkyl pyridinium salts (**4.8**) are accessed through the pyridinium moiety (**4.7**) acting as an acidic nucleophile.[35]
3) Zincke Reaction: demonstrates the formation *N*-aryl pyridinium species (**4.10**) from bipyridine (**4.5**) and *N,N*′-2,4-dinitrobenzene viologen (**4.9**), where this reaction is widely used for the synthesis of symmetric and asymmetric viologens.[36–41]

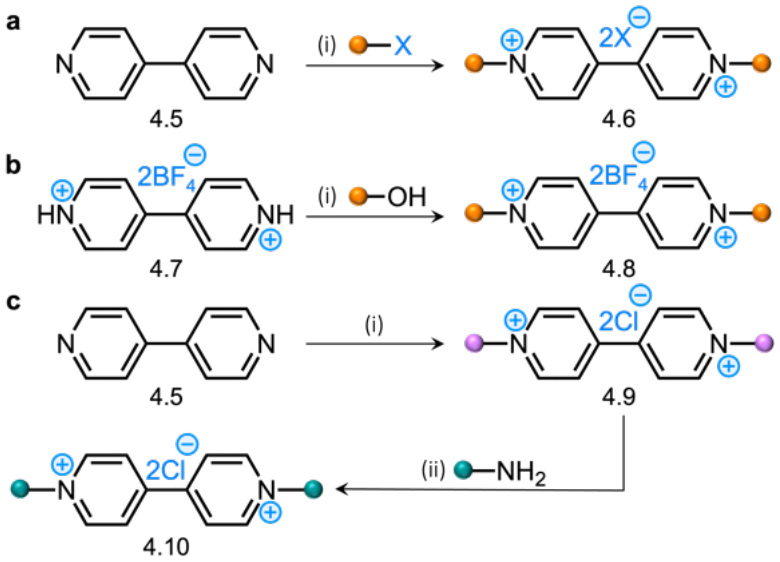

Scheme 4.3. General reaction schemes for viologen modification where: (**a**) Reaction scheme for a generic Menshutkin reaction for viologen (**4.6**) modification. Reagents and conditions: (i) alkyl halide / solvent / heat. The orange circle represents a variable alkyl group and X represents a halide. (**b**) Reaction scheme for a generic Mitsunobu reaction for viologen (**4.8**) formation. Reagents and conditions: (i) PPh_3 / DEAD / solvent. The orange circle represents variable functionality of the alcohol moiety. **c**) Reaction scheme for a generic Zincke reaction for viologen (**4.10**) functionalisation. Reagents and conditions: (i) 2,4-dinitrochlorobenzene; (ii) primary amine / heat. The pink circle represents 2,4-dinitrobenzene and the green circle represents variable functionality on a primary amine.

4.1.4 Host-Guest Chemistry of Cucurbit[*n*]urils

Macrocyclic compounds have been used in a variety of research fields and applications, owing to their inherent ability to recognise and encapsulate guest molecules within their cavity. The macrocycle cucurbituril (**CB**) (which has been studied extensively, amongst others), was first reported by Behrend in 1905[42], who synthesised **CB[6]**. The naming of CB followed the realisation by Mock in the 1980s,[43] who isolated the XRD structure of **CB[6]**, which was shown to resemble a pumpkin (*Cucurbitaceae* in Latin).[44] Synthetically, **CBs** have been accessed *via* the acid-catalysed condensation of glycoluril (**4.11**) with formaldehyde (**4.12**), allowing for the formation of a mixture of **CB[*n*]** derivatives (Figure 4.4a).[45–47] These **CB[*n*]** derivatives differentiate *via* the glycoluril units (*n* = 5, 6, 7, 8, 10), which are connected by methylene bridges (Figure 4.4b). The separation of each derivative from one another relies upon their respective solubility in water, water and methanol mixtures, and hydrochloric acid solutions.[45–47]

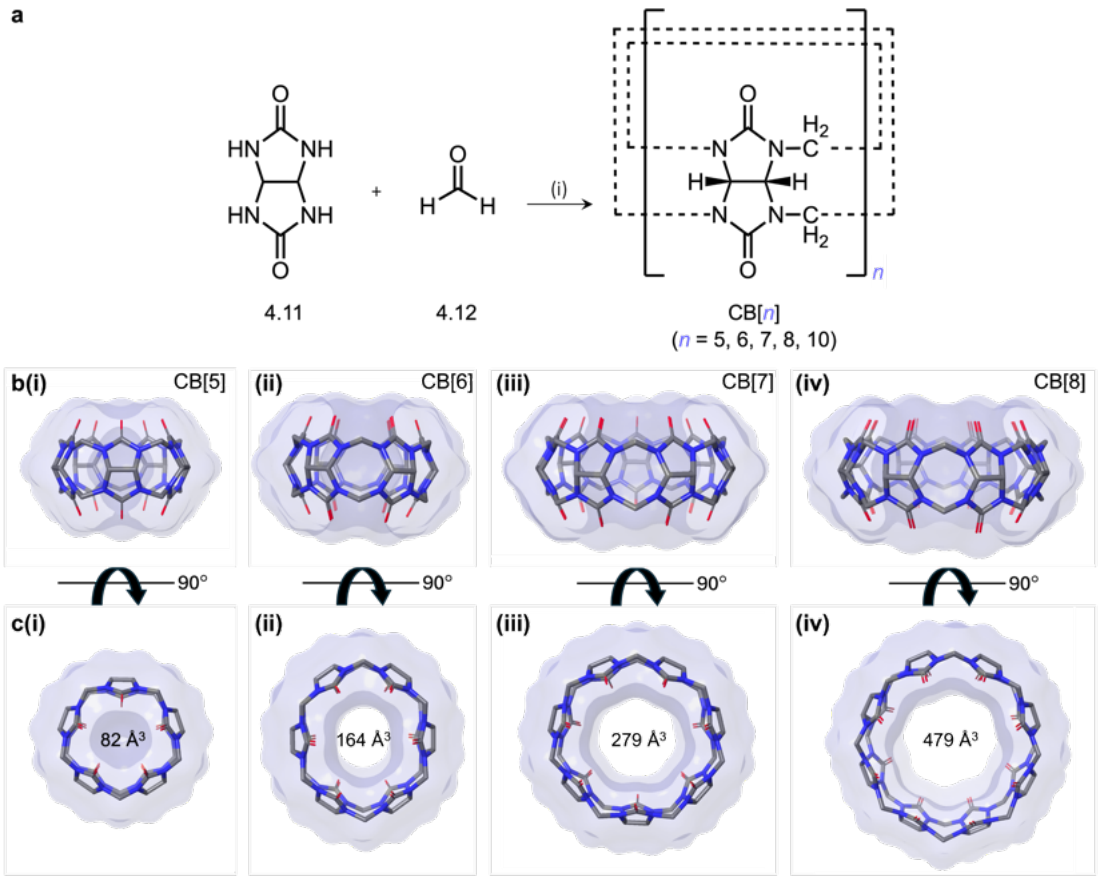

Figure 4.4. (**a**) Synthetic route to **CB[*n*]** homologues between glycoluril (**4.11**) and formaldehyde (**4.12**). Reagents and conditions: HCl / 100 °C / 18 h. (**b(i–iv)**) CB[*n*] (*n* = 5, 6, 7, 8) x-ray diffraction crystal structures from the side view and from the (**c(i–iv)**) top view following rotation by 90°. The cavity volume is shown for each CB species. The CB species are shown in tube representation with solid molecular surface (80% transparency), where O atoms (red) and N atoms (blue). Figure adapted from previously reported results.[46,48]

Owing to their varying cavity size, **CB[*n*]** homologues have been shown to accommodate and interact with a range of different molecules.[48] The smallest macrocycles in this range of **CB[*n*]** homologues, **CB[5]** and **CB[6]**, have been shown to be capable of accommodating only one guest within their cavity.[48] The **CB[5]** species, for example, has been demonstrated to form complexes with a range of cations through its carbonyl portals, including alkali metal,[49] ammonium[49] and transition metal cations.[50] Moreover, **CB[5]'s** small cavity size allows for the encapsulation of gaseous molecules,[51] in both the aqueous and solid state, which provides a niche in comparison to larger **CB** species. Once more, the **CB[6]** homologue, which is the most abundant **CB[*n*]** species, has a larger cavity than **CB[5]**, which allows for organic compounds, such as aliphatic ammonium cations, to be encapsulated.[43,52,53] For the larger **CB[*n*]**

homologues, which include **CB[7]** and **CB[8]**, larger and bulkier guest molecules are able to form inclusion complexes with **CB**, that otherwise out-size the cavity of **CB[5]** and **CB[6]**. In the form of an example, **CB[8]** has been shown to encapsulate ferrocene derivatives, as well as adamantanes, owing to its large cavity size.[48] **CB[8]** has also been shown to be capable of encapsulating two guests simultaneously, making them an attractive proposition for applications in chemical sensors,[54] drug delivery methods[55,56] and complex biochemical applications.[57]

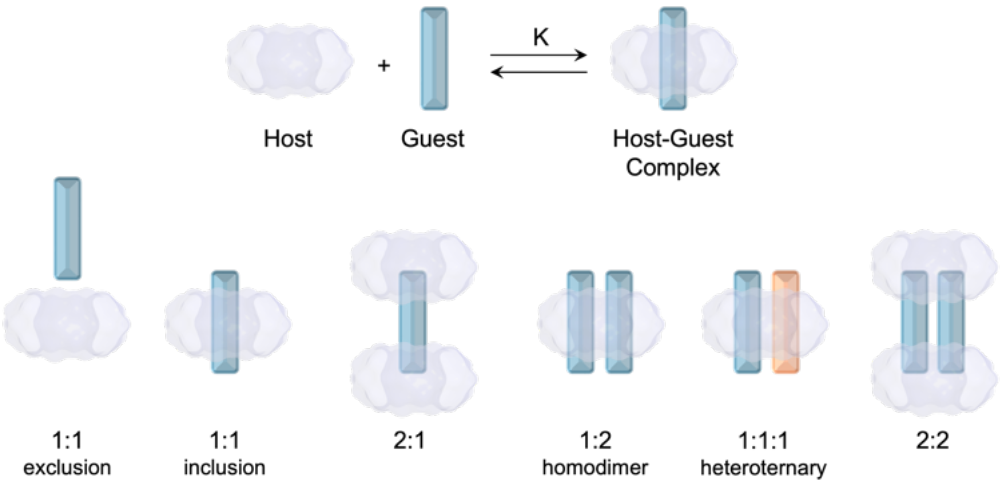

Figure 4.5. Depiction of the **CB[*n*]** inclusion and exclusion complexes between host (**CB**) and guests (blue and orange rectangles). The **CB** species is shown with solid molecular surface (90% transparency). Figure adapted from previously reported results.[48]

More specifically, and in particular relation to this research, **CB** hosts have also been shown to form stable inclusion complexes with viologen species as dication guests in the solution state. By way of example, in 2002, Kaifer and co-workers reported findings showing the formation of such complexes, where a **CB[7]** host was paired with a *bis*(3-hydroxypropyl) viologen (**4.13**) guest (Scheme 4.4).[58] Formation of the complex was evidenced by ^{1}H NMR spectroscopic analysis with the aromatic protons of viologen **4.13** showing an upfield shift of 1.5 ppm in the presence of **CB[7]**. This system was also found to display fast electrochemically reversible one electron reduction on encapsulation.[58]

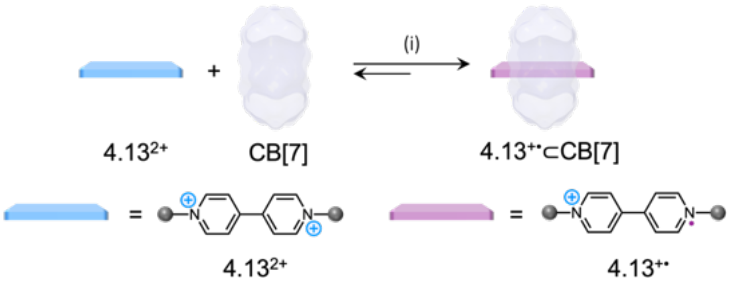

Scheme 4.4. Depiction for the formation of inclusion complex **4.13**$^{\bullet+}$**⊂CB[7]** between viologen dication **4.13**$^{2+}$. Reagents and conditions: (i) 0.2 M NaCl / H_2O. The grey circles = C_3H_6O; the blue and magenta rectangles represent the dication and radical cation species, respectively. The **CB[7]** species is shown with solid molecular surface (90% transparency).[58]

In regards to our considerations, and most importantly, viologen radical cation dimers have been found to be the most investigated guest neutral host molecule complexation. Pivotally, also in 2002, Kim *et al*. showed that a **CB-M$_2$V** host-guest complex can be controlled by the redox chemistry of the **M$_2$V** guest.[18] This principle was demonstrated by the formation of a 1:1 inclusion complex of **M$_2$V**$^{2+}$ in **CB[8]** that was shown to be reversible, converting to the 2:1 inclusion complex of the **M$_2$V**$^{\bullet+}$ species when reduced (Scheme 4.5).[18]

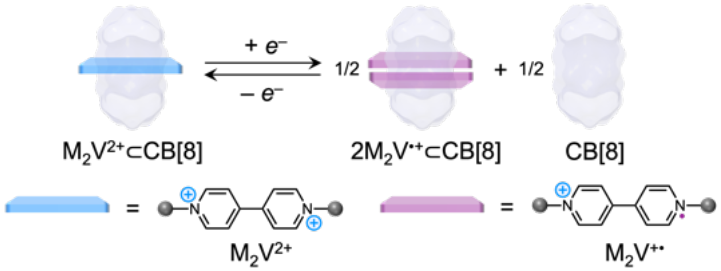

Scheme 4.5. Depiction of the 1:1 Inclusion complex (**M$_2$V**$^{2+}$**⊂CB[8]**) and reduction leading to the 2:1 inclusion complex (**2M$_2$V**$^{\bullet+}$**⊂CB[8]**) and **CB[8]**. The grey circles = Me; the blue and magenta rectangles represent the dication and radical cation species, respectively. The **CB[8]** species is shown with solid molecular surface (90% transparency).[18]

4.1.5 Aims and Objectives

This research initially aimed to focus on the synthesis and property characterisation of a viologen functionalised **BV**. The synthetic routes to yield such a viologen-appended **BV**, however, proved challenging resulting in far greater efforts in synthetic investigations than first anticipated. Resultantly, this body of work aims to cover a range of synthetic strategies towards viologen-inspired **BV** compounds. Combining the

shapeshifting properties of **BV** with viologen functionality may allow for the investigation of unexplored aspects of this versatile moiety. This, in turn, may lead to emergent optoelectronic properties that do not currently exist in previous viologen studies. In continuation from the previous work on viologens, an attempt to understand how constitutionally dynamic guests interact in a supramolecular host was initiated. The design of a di-substituted viologen **BV** was targeted with the original aim of assessing how the fluxional dynamics influences the: 1) dimerisation of the viologens in the radical-cation state following electrochemical reduction; 2) complexation of the **BV** species within a macrocycle and 3) the optical and electrochemical properties of viologens incorporated onto a shapeshifting scaffold.

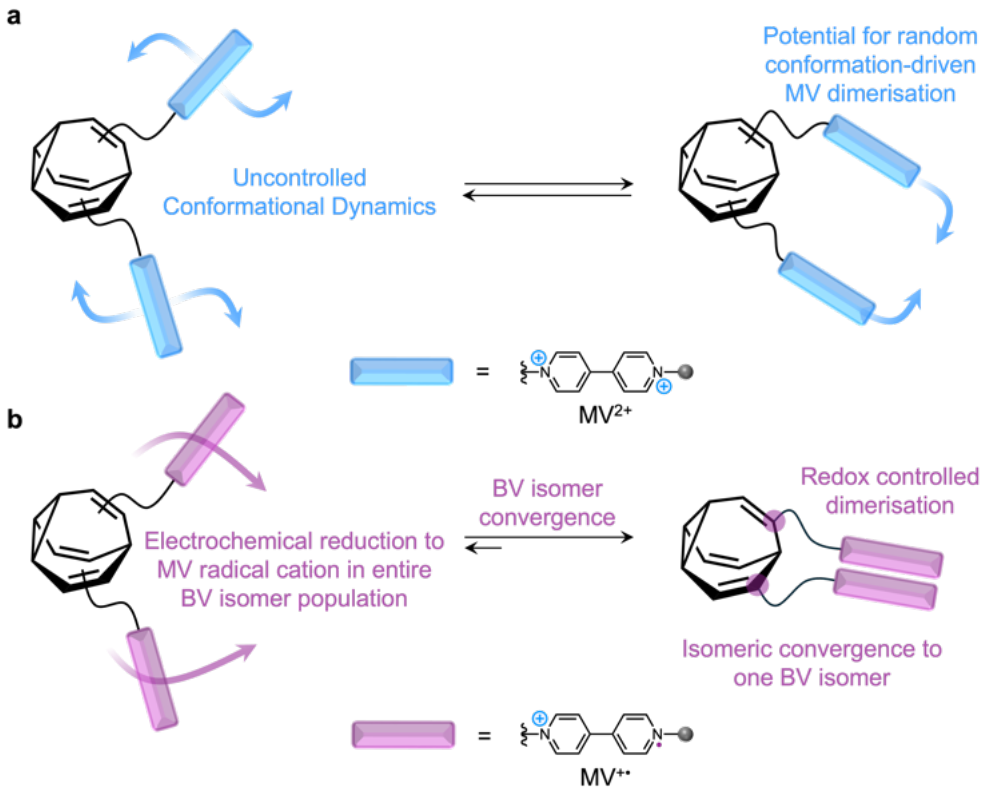

Scheme 4.6. (**a**) bis(MV) **BV** dication likely shows an equal distribution between species, where there is the potential for uncontrolled conformational dynamics and the random conformation-driven dimerisation of the attached MV moiety. (**b**) bis(MV) **BV** cation radical has the potential to be accessed *via* electrochemical potential within the **BV** isomer population, displaying preference for redox controlled viologen dimerisation with convergence to one **BV** isomer. The grey circles = Me; the blue and magenta rectangles represent the dication and radical cation species, respectively. The magenta circles in (**b**) highlight the potential **BV** isomer that could be accessed within the isomer population.

4.2 Results and Discussion

4.2.1 Synthesis of Cucurbit[8]uril

The well-defined cavities of macrocycles are ideally suited to probing the responses of shapeshifting equilibria to noncovalent interactions. The pending macrocycle-ligand investigations were proposed to be well suited to binding specific **BV** isomers, thereby perturbing the inherent shapeshifting equilibria. The macrocycle, **CB[7]**, has been shown to associate strongly with derivatives of the known **BV** isostere, adamantane (Ad). In comparison, **CB[8]** is large enough to encapsulate at least two substituents and/or the appended **BV** within its cavity.

Therefore, for the synthesis of **CB[8]**, glycoluril (**4.11**) was first synthesised following a literature procedure reported by Sabatini and co-workers in 2016.[59] The synthesis proceeded by the sulfuric acid-catalysed condensation of glyoxal (**4.14**) with an excess of urea (Scheme 4.7). The simple subsequent filtration afforded glycoluril (**4.11**) in a very good yield of 82%.

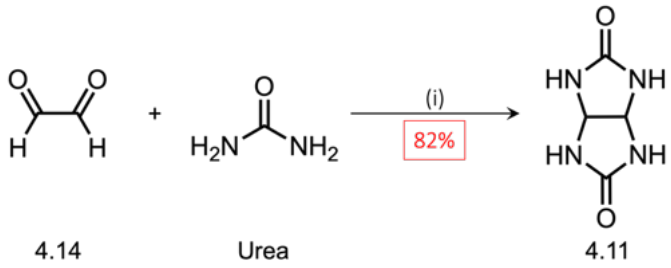

Scheme 4.7. Synthetic route to glycoluril (**4.11**). Conditions and reagents: (i) glyoxal (1.0 eq.) / urea (2.5 eq.) / H_2SO_4 (cat.) / H_2O / 90 °C / 12 h / 82%.

Then, using glycoluril (**4.11**) as a precursor, **CB[8]** was then synthesised following a previously reported transformation by Bardelang, Ratcliffe and co-workers.[46] Formaldehyde (**4.12**) was slowly added to glycoluril (**4.11**) to form a mixture of **CB[*n*]** (*n* = 5, 6, 7, 8) species *via* a condensation reaction (Scheme 4.8). As previously shown, the purification of **CB[8]** relied upon the crystallisation and solubility of the **CB** species in 37% $HCl_{(aq)}$. Thus, to isolate solely the **CB[8]** species, formic acid and water were added to the mixture to form a white suspension which was isolated by filtration to

yield **CB[8]** in 10% yield (Scheme 4.8). Confirmation for the isolation of **CB[8]** was shown by ^{1}H NMR spectroscopy.

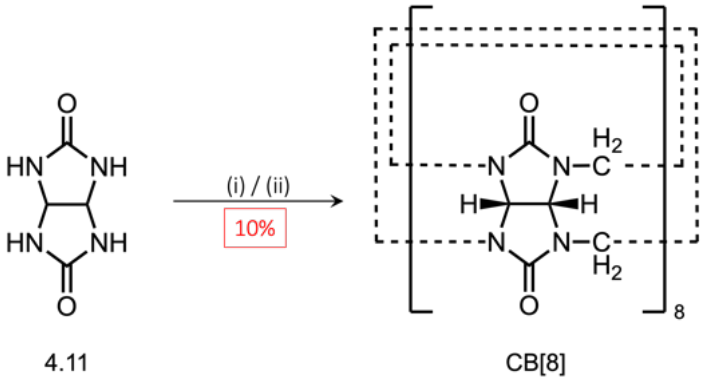

4.11 CB[8]

Scheme 4.8. Synthetic route to **CB[8]**. Conditions and reagents: (i) $HCl_{(aq)}$ / 90 °C / 12 h; (ii) HCOOH / H_2O / 75 °C / 1 h / 10%.

4.2.2 Design of Viologen-Inspired Bullvalenes

The end-goal of this project aimed towards understanding how the fluxional dynamics of a viologen-inspired **BV** influences its spectro-electrochemical properties. As such, the primary consideration focussed on limiting the conformational degrees of freedom of the appended viologen moiety, by affixing the viologen in close proximity to the central **BV** framework, through covalent bonding.

First, building upon the previously reported results from Buono and co-workers who reported the synthesis of a ethylene tosylate (Ts) **BV** derivative,[60] the original synthetic strategy was to directly install a methylene bridged Ts within the **BV** framework *via* the same [6+2] cycloaddition with **COT**. It was envisaged that the tosylate group, which is a well-known leaving group, would allow for nucleophilic attack from the amine moiety embedded in a MV species. Additionally, the modification to install a methylene bridge between the **BV** and Ts functionality, was chosen to limit the amount of conformational freedom of the subsequently appended MV group (Figure 4.6a). It was also proposed, based on the previous reports from Buono and co-workers,[60] that the incorporation of an ethylene linker could be considered, based on these results. In comparison to the methylene linker, however, this would introduce a greater number of degrees of

freedom (Figure 4.6b); therefore, the methylene-linked MV species would be attempted first.

Throughout the design process, a number of synthetic routes were devised as potential candidates for MV appended **BVs**, based on the current limited scope and understanding of **BDT** and **BV** functionalisation. In regards to the project goals, however, the potential conformational flexibility introduced through these targets was deemed unsuitable in some cases, especially since extended linker lengths may allow for the dimerisation of viologen species, irrespective of the **BV** shapeshifting equilibria. For example, the simplest plausible click chemistry approach was deemed unsuitable. This is due to the fact the only possible way to install the necessary functionality would require: 1) a flexible C_4 (shortest) linker bridging the alkyne and the **BV** and 2) a C_2 linker to enable azide functionality on the MV to avoid elimination. In this case, the resulting linker between the **BV** and MV moiety would provide a large amount of conformational dynamics (Figure 4.6c), which intrinsically provide an uncontrollable variable when attempting to analyse MV dimerisation and **BV** equilibria, in both the solid and solution state. In addition, an approach to more stringently control the conformational dynamics of the MV moiety was considered, by introducing a rigid phenyl linker (Figure 4.6d). This approach, which would utilise the previously reported **BV** boronate ester as described by Fallon and co-workers,[61] would allow for the installation of phenyl functionality through Suzuki–Miyaura cross coupling. In particular, it was considered that this may allow for use of a *p*-aniline derivative to append primary amine functionality to the **BV**. As such, the presence of an appended primary amine would allow for a proposed Zincke reaction to be pursued, thereby installing a MV moiety through the use of a 2,4-dinitrochlorobenzene derivative, which has been previously described in many literature precedents.

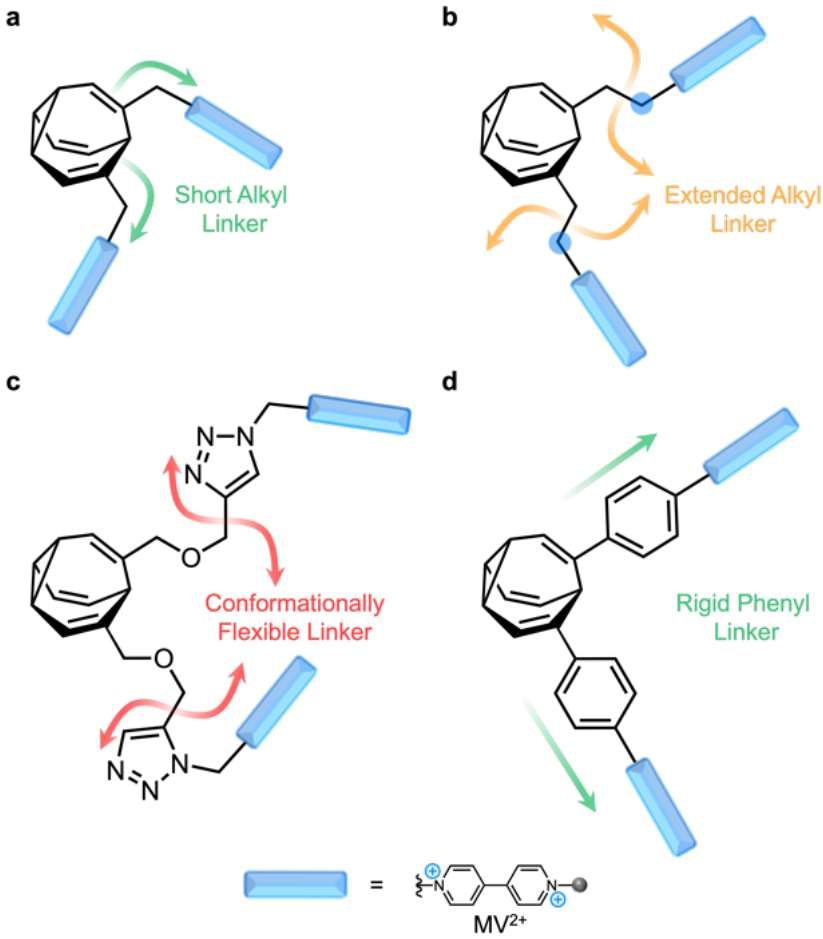

Figure 4.6. Depiction of designed MV **BVs** with a: (**a**) short alkyl linker, (**b**) extended alkyl linker, (**c**) conformationally flexible linker, and (**d**) a rigid phenyl linker. The grey circles = Me; the blue and magenta rectangles represent the dication and radical cation species, respectively. The blue circles in (**b**) highlight the additional carbon atom in the extended alkyne linker, relative to the species in (**a**). The green, orange and red arrows represent the good, adequate and poor rigidity of the proposed linker, respectively.

4.2.3 Cycloaddition Approach with Functionalised Alkynes

First, 1-methyl-4-(4′-pyridyl) pyridinium iodide (**MVI**) was synthesised in a good yield of 73%, through the treatment of 4,4′-bipyridine (**4.5**) with methyl iodide in dichloromethane (Scheme 4.9). This was initially synthesised for the installation on subsequently synthesised **BDT** intermediates and **BVs**.

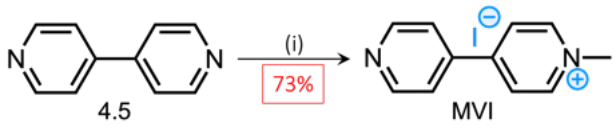

Scheme 4.9. Synthesis of 1-methyl-4(4′-pyridyl) pyridinium iodide (**MVI**) *via* the treatment of 4,4′-bipyridine (**4.5**) with methyl iodide. Conditions and reagents: MeI (1.3 eq.) / CH_2Cl_2 / 22 h / rt / 73%.

To mediate installing **MVI** within a **BDT** intermediate, the process to install a satisfactory leaving group on the **BDT** was pursued, with the intention of performing nucleophilic substitution chemistry with 1-methyl-4-(4′-pyridyl) pyridinium iodide (**MVI**), where **MVI** would act as the nucleophilic species.

Initial attempts focussed on trying to directly install a Ts group *via* a [6+2] cycloaddition with **COT** and a di-functionalised Ts alkyne. First, by this route, but-2-yne-1,4-diyl bis(4-methylbenzenesulfonate) (**4.15**) was synthesised through the sequential addition of *p*-toluenesulfonyl chloride to 2-butyne-1,4-diol (**4.16**), which was stirred at room temperature for 12 hours, affording the desired di-Ts alkyne (**4.15**) an excellent yield of 99% (Scheme 4.10).

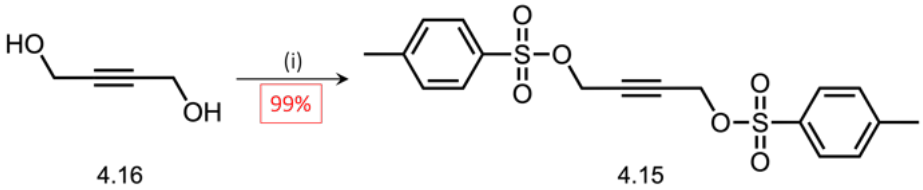

Scheme 4.10. Synthetic route to but-2-yne-1,4-diyl bis(4-Ts) (**4.15**) from but-2-yne 1,4-diol (**4.16**). Conditions: (i) *p*-TsCl / NaOH / 24 h / 0 °C → rt / 99%.

The but-2-yne-1,4-diyl bis(4-Ts) (**4.15**) was then subjected to viable [6+2] cycloaddition conditions with **COT** (Scheme 4.11). Unfortunately, ^{1}H NMR spectroscopy showed the lack of any desired bis(4-Ts) **BDT** (**4.17**) product, with only the alkyne starting material and **COT** present in the post-reaction mixture. The exact reasons for the failure of this transformation is unclear. Based on the previous results reported by Buono and co-workers in 2005 (who successfully obtained an ethylene-linked Ts **BDT**),[60] however, it is possible that the alkyne functionality was detrimentally sterically hindered, thus preventing a significant degree of cobalt coordination in the mechanistic pathway.

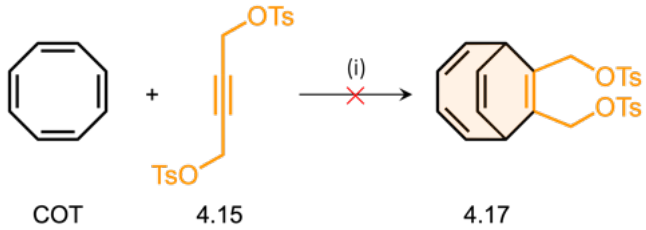

Scheme 4.11. Attempted synthetic route to **BDT** bis(methylene Ts) (**4.17**) from **COT** and but-2-yne-1,4-diyl bis(Ts) (**4.15**). Ts = 4-methylbenzenesulfonate; Conditions: (i) $CoBr_2$(dppe) / Zn / ZnI_2 in a 5:15:10 mol% ratio; TFE / 55 °C / 24 h.

Based on the unsuccessful observation from the cycloaddition with the bis(Ts) alkyne (**4.15**), and with the apparent adverse influence of steric hindrance in mind, the corresponding, less sterically hindered, but-2-yne-1,4-diyl bis(Ms) (**4.18**) was synthesised and then subjected to [6+2] cycloaddition reaction conditions with **COT** (Scheme 4.12). It was postulated that the smaller, terminal Ms moiety could potentially allow for cobalt coordination, thus allowing the cycloaddition to proceed. Disappointingly, however, ^{1}H NMR spectroscopy showed only starting material following this attempt, indicating that the desired bis(Ms) **BDT** product (**4.19**) had not formed.

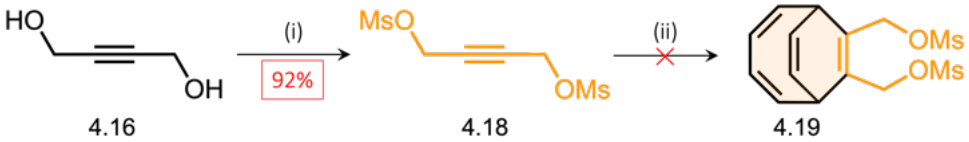

Scheme 4.12. Synthetic route to but-2-yne-1,4-diyl bis(Ms) (**4.18**); and attempted synthetic route to **BDT** bis(methylene Ms) (**4.19**). Ms = methylsulfonate. Conditions and reagents: (i) Et_3N / MsCl / CH_2Cl_2 / 0 °C → rt / 24 h / 92%; (ii) $CoBr_2$(dppe) / Zn / ZnI_2 in a 5:15:10 mol% ratio; TFE / 55 °C / 24 h.

Following the unsuccessful reactions with Ts and Ms alkyne substrates (**4.15** and **4.18**), a range of reaction conditions guided by the seminal reports of **BDT** species by Buono and co-workers in 2005 were attempted, as detailed in Table 4.1.[60] The report described the importance of solvent choice for cycloaddition reactions with **COT**, specifically highlighting the compatibility of DCE with alkynes bearing wide-ranging functionalities, with most success materialising at 40 °C. Additionally, TFE was underlined as a successful solvent choice for its use in alkynol cycloadditions. Therefore, with insight from this work, the Ts and Ms alkynes (**4.15** and **4.18**) were subjected to a range of reaction conditions, varying solvent and temperature, as highlighted in Table 1. Yet, the changes in reaction parameters yielded no apparent difference in the formation of any desired **BDT** products (**4.17** and **4.19**).

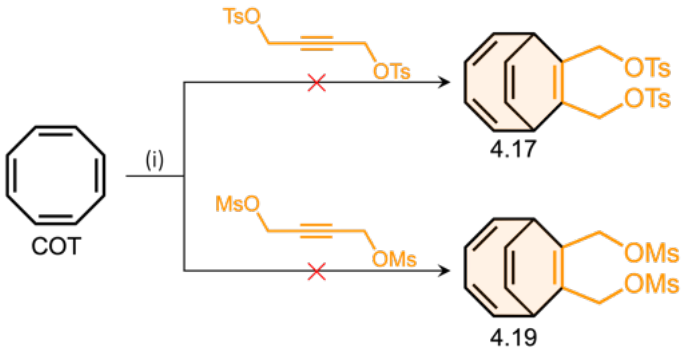

Scheme 4.13. Attempted synthetic route to **BDT** bis(Ts) (**4.17**) and **BDT** bis(Ms) (**4.19**) species. Ts = 4-methylbenzenesulfonate, Ms = methylsulfonate. Conditions: (i) $CoBr_2$(dppe) / Zn / ZnI_2 in a 5:15:10 mol% ratio; solvent / T °C / 24 h. The specific range of reaction conditions are detailed in Table 4.1.

Table 4.1. Attempted reaction conditions for the [6+2] cycloaddition of **COT** with alkynes **4.15** and **4.18** to form the corresponding **BDTs** (**4.17** and **4.19**). Conditions: (i) $CoBr_2$(dppe) / Zn / ZnI_2 5:15:10 mol% ratio. [a]Reaction monitored by mass spectrometry. NP = no product.

Alkyne R Group	Solvent	Temperature / °C	Comment[a]
OTs	TFE	55	NP
OTs	DCE	40	NP
OTs	DCE	55	NP
OMs	TFE	40	NP
OMs	DCE	55	NP
OMs	DCE	55	NP

4.2.4 Hydroxy Post Modification Approach

Based on the aforementioned findings, the [6+2] cycloaddition methodology was not proceeding as planned, for the Ts and Ms alkyne substrates. Consequently, the next synthetic plan was to attempt direct functionalisation of a good leaving group in place of the **BDT** hydroxy groups. In the first instance, bis(hydroxymethylene) **BDT** (**4.20**) was synthesised following a [6+2] cycloaddition between **COT** and 2-butyne-1,4-diol (**4.16**) (Scheme 4.14).

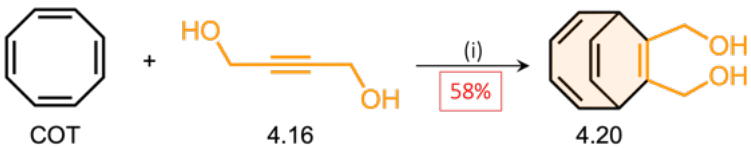

Scheme 4.14. Synthetic route to **BDT** bis(hydroxymethylene) (**4.20**) *via* a cobalt catalysed [6+2] cycloaddition of **COT** and 2-butyne-1,4-diol (**4.16**). Conditions: (i) $CoBr_2$(dppe) / Zn / ZnI_2 in a 5:15:10 mol % ratio / TFE / 55 °C / 48 h / 58%.

Then, **BDT** bis(hydroxymethylene) (**4.20**) was then treated with two equivalents of *p*-toluenesulfonyl chloride with base (Scheme 4.15), converting the alcohol groups to Ts groups *via* an S_N2 substitution. The crude ^1H NMR spectroscopy exhibited a wide range of broad signals indicating the formation of wide range of alternative products that could not be separated by flash column chromatography, nor identified by ^1H NMR spectroscopy or mass spectrometry. Additionally, mass spectrometry also indicated the absence of any of the desired **BDT** bis(Ts) (**4.17**) product. Furthermore, a range of base and solvent conditions was also screened, ensuring a range of bases was used and solvents chosen to ensure suitable solubility of the reaction mixture (Table 4.2). These attempts, however, showed no combination to yield the desired **BDT** bis(Ts) (**4.17**) product.

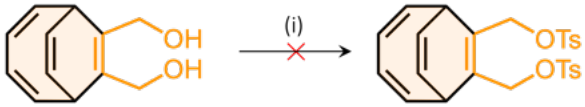

4.20 4.17

Scheme 4.15. Attempted synthetic route to **BDT** bis(Ts) (**4.17**) from **BDT** bis(hydroxymethylene) (**4.20**). Conditions and reagents: (i) *p*-TsCl / base / solvent / 24 h / 0 °C → rt. The specific range of reaction conditions are detailed in Table 4.2.

Table 4.2. Attempted reaction conditions for the installation of the Ts group with **BDT** bis(hydroxymethylene) (**4.20**) to form the corresponding **BDT** bis(Ts) (**4.17**). Conditions and reagents: (i) base / solvent / rt / 24 h. [a]Reaction monitored by ^1H NMR and mass spectrometry. NP = no product.

Base	Solvent	Comment[a]
pyridine	CH_2Cl_2	NP
pyridine	pyridine	NP
NaOH	CH_2Cl_2	NP
NaOH	THF	NP
NaOH	$(CH_3)_2CO$	NP
Et_3N	CH_2Cl_2	NP
Et_3N	THF	NP
Et_3N	$(CH_3)_2CO$	NP

Following the aforementioned unsuccessful attempts, but still with **BDT** bis(hydroxymethylene) (**4.20**) in hand, an alternative post-functional modification was attempted on the **BDT** to install a bromide or a chloride moiety in place of the hydroxy groups, to act as effective leaving groups. First, **BDT** bis(hydroxymethylene) (**4.20**) was

subjected to phosphorus tribromide, a common brominating reagent to convert alcohols into alkyl bromides (Scheme 4.16).[62,63] Both ^{1}H NMR spectroscopy and mass spectrometry showed complete decomposition of the starting material and no observable di-bromide **BDT** (**4.21**) product was detected. In light of this, the chlorination of the **BDT** hydroxy groups was attempted, employing thionyl chloride as a chlorinating reagent (Scheme 4.16).[64] Similarly, no desired di-chloride **BDT** (**4.22**) product was found to have been formed.

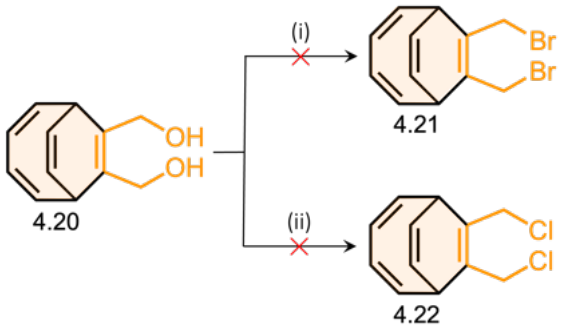

Scheme 4.16. Attempted synthetic route to **BDT** bis(methylenebromide) (**4.21**) and **BDT** bis(methylenechloride) (**4.22**). Conditions and reagents: (i) PBr_3 / CH_2Cl_2 / 0 °C → rt / 24 h; (ii) $SOCl_2$ / CH_2Cl_2 / rt / 24 h.

The installation of any effective leaving group onto hydroxy-containing **BDT** proved elusive. Shortly after attempting this work, the aforementioned observations were corroborated by Worrell and co-workers who published a patent describing their attempts to leaving group-containing **BDTs** in their synthetic methodology towards shapeshifting cyclic peptides.[65] Analogously, in order to establish that the difficulty installing common leaving groups was indeed due to the proximity of the hydroxyl group to the **BDT** framework, parallel reaction conditions were attempted on bis(hydroxymethylene) **BV** (**4.23**) as well. First, bis(hydroxymethylene) **BV** (**4.23**) was synthesised *via* the photochemical rearrangement of **BDT** bis(hydroxymethylene) (**4.20**), proceeding at 365 nm at –5 °C in the presence of a thioxanthene-9-one photosensitiser in THF, to yield the corresponding **BV** (**4.23**) in a moderate yield of 28% (Scheme 4.17). Separately, the treatment of bis(hydroxymethylene) **BV** (**4.23**) with either phosphorous tribromide or thionyl chloride, in an attempt to provide the brominated **BV** (**4.24**) or chlorinated **BV** (4.25) product, both proved unsuccessful (Scheme 4.17).

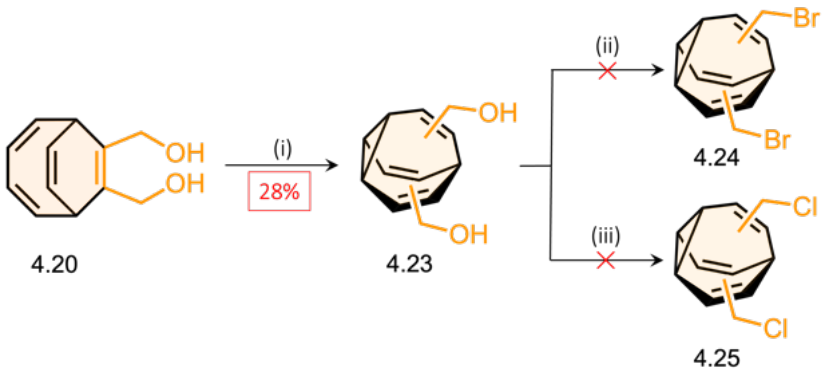

Scheme 4.17. Synthetic route to bis(hydroxymethylene) **BV** (**4.23**) *via* a photochemical di-π-methane rearrangement of **BDT** bis(hydroxymethylene) (**4.20**); the attempted synthesis of di-bromide **BV** (**4.24**) and di-chloride **BV** (**4.25**). Conditions and reagents: (i) Thioxanthen-9-one (5 mol%) / 365 *nm* / anhydrous THF / 6 h / –5 °C / 28%; (ii) PBr_3 / CH_2Cl_2 / 0 °C → rt / 24 h; (iii) $SOCl_2$ / CH_2Cl_2 / rt / 24 h.

As mentioned in Chapter 1 and Chapter 3, the irradiation of **BDT** species can result in the formation of radical species that are capable of undergoing subsequent di-π-methane rearrangements, resulting in the formation of Lumibullvalene (**LBV**), which is another tricyclic species. During the process of purification of bis(hydroxymethylene) **BV** (**4.23**), a static by-product (signified by sharp, well-defined signals with distinct multiplicity patterns in the ^{1}H NMR spectrum) was also separately isolated (Figure 4.7). The initial assessment of this by-product by ^{1}H NMR spectroscopy proved difficult and uncertain, and could not be attributed to any particular compound. The previous discussions by Ihmels and co-workers, however, provided indications that the by-product formed was a mixture of bis(hydroxymethylene) **LBV** isomers (**4.26**). Owing to the signal overlap using conventional 2D-NMR experiments, Ihmels and co-workers had previously revealed the possibility for the formation of three static **LBV** products within the by-product mixture.[66] The use of 1D-selective TOCSY pulse sequences (which separates the spin systems in **LBV** isomers) provided the means to elucidate the three possible **LBV** products; therefore, this previously reported study provided confirmation towards the formation and presence of the **LBV** isomers within the rearrangement reaction mixture (as shown by ^{1}H NMR, Figure 4.7).[66] On this occasion, however, the bis(hydroxymethylene) **LBV** (**4.26**) species were not fully characterised as they were not required for the purposes of this study.

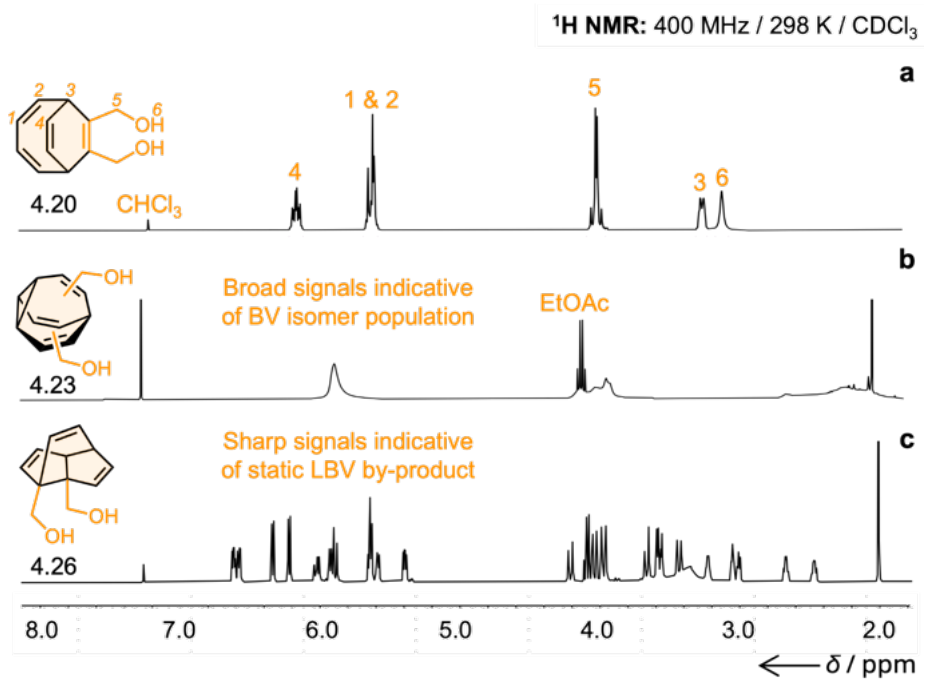

Figure 4.7. Partial ^{1}H NMR spectrum showing (a) **BDT** bis(hydroxymethylene) (**4.20**); demonstrating the sharp signals of the starting material, (b) **BV** bis(hydroxymethylene) (**4.23**); showing broad signals which are indicative of the **BV** isomer population and (c) **LBV** bis(hydroxymethylene) (**4.26**); showing the sharp signals which are indicative of the static **LBV** by-product. Only one of three **LBV** isomers is shown for clarity.

4.2.5 Steglich Esterification Approach

As an alternative approach, the Steglich esterification has been well documented, comprising the conversion of an acid and alcohol to an ester under neutral and mild conditions.[67–69] First developed in 1978 by Steglich,[70] this particular esterification reaction utilises the coupling agent, *N,N'*-dicyclohexylcarbodiimide (**DCC**) and a catalytic amount of DMAP. In this case, the reaction mechanism first proceeds through the reaction between the carbodiimide and the carboxylic acid moiety, resulting in an *O*-acyl urea species as the reaction intermediate. Then, the intermediate can allow for acyl transfer to DMAP, which then subsequently reacts with an alcohol-containing species to yield the corresponding ester.

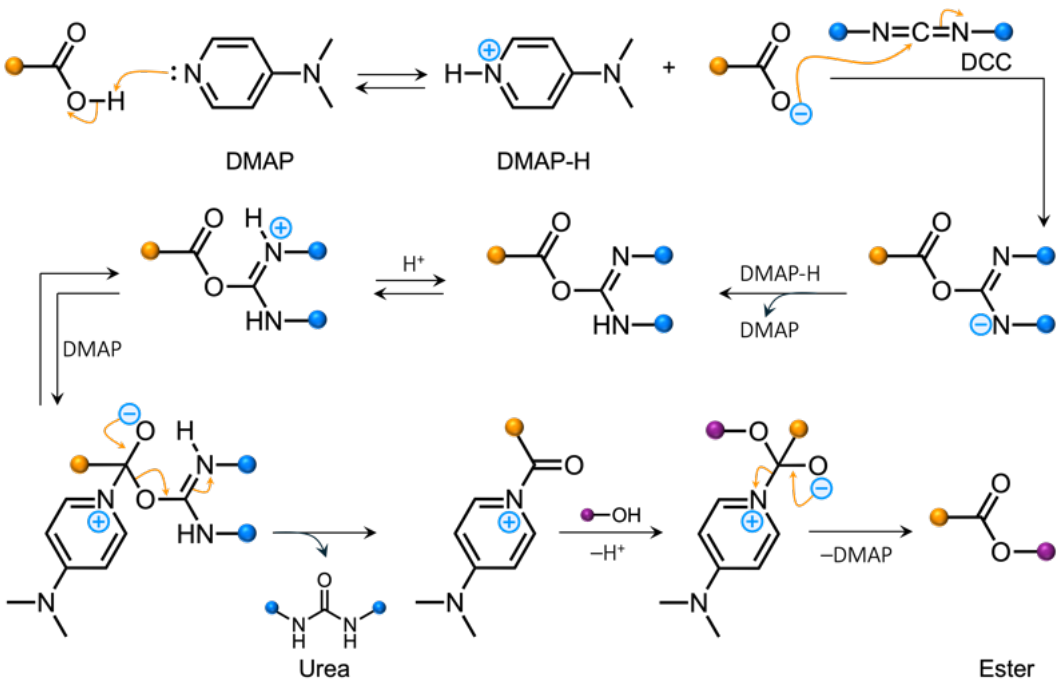

Scheme 4.18. Steglich esterification reaction mechanism with DCC to form the respective ester. The orange circle = variable group of the carboxylic acid moiety; the blue circles = cyclohexane; and the magenta circle = the variable group of the alcohol moiety.

In order to introduce the carboxylic acid functionality required for DCC coupling, the previously synthesised MVI was dissolved in acetonitrile and treated with an excess of bromoacetic acid (4.27), resulting in an instant colour change from yellow to orange on addition of bromoacetic acid.[71] Following the reflux at 90 °C for 24 hours, the product (4.28) was isolated in a yield of 73%.

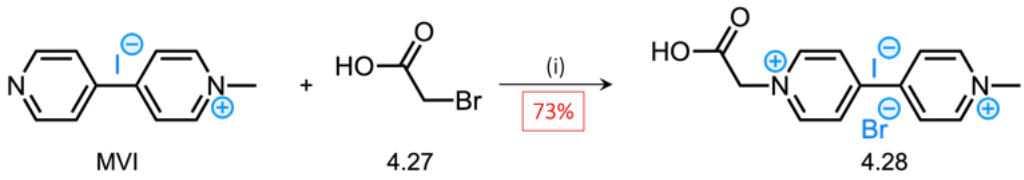

Scheme 4.19. Synthesis of MV carboxylic acid (4.28) *via* the treatment of MVI with bromoacetic acid (4.27). Conditions and reagents: (i) bromoacetic acid (5.0 eq.) / MeCN / 90 °C / 24 h / 73%.

The previously synthesised MV carboxylic acid (4.28) and DMAP were dissolved in acetonitrile and the BDT bis(hydroxymethylene) (4.20) was then added, as to avoid testing on a more precious BV compound. Immediately, upon dissolution of the MV carboxylic acid (4.28) species, the reaction mixture produced a colour change from

transparent colourless solution to an opaque brown solution, possibly indicating the immediate decarboxylation of the MV carboxylic acid (**4.28**). Nevertheless, the DCC coupling reagent was then added and the reaction mixture stirred for 16 hours at room temperature. After this time, mass spectrometry unfortunately indicated the absence of any desired **BDT** product (**4.29**).

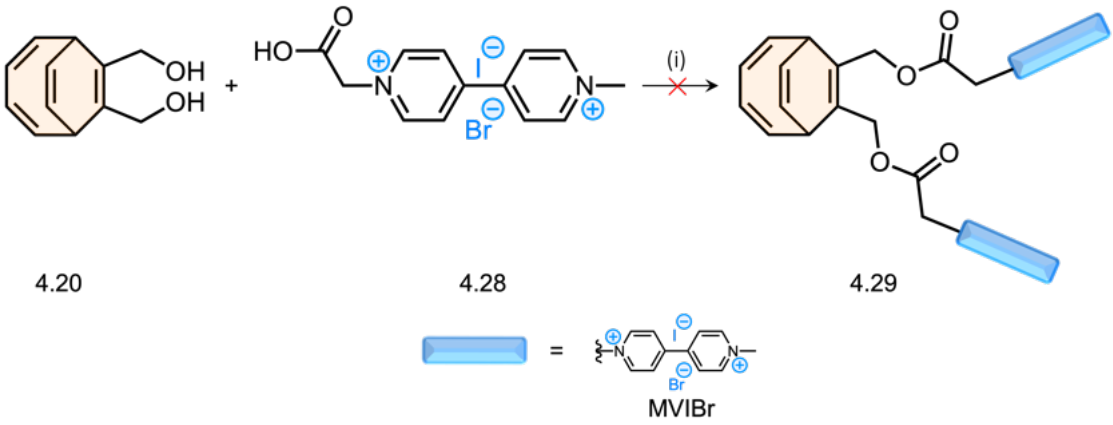

Scheme 4.20. Attempted synthesis of **BDT** bis(MV) (**4.29**) with **MVIBr** functionality *via* the treatment of **BDT** bis(hydroxymethylene) (**4.20**) with MV carboxylic acid (**4.28**) under Steglich esterification conditions. Conditions and reagents: (i) DCC (2.2 eq.) / DMAP (5 mol%) / MeCN / rt / 16 h. The blue rectangles represent the dicationic MV species.

Although the addition of an extra carbon atom within the carboxylic acid-MV linker was a synthetically plausible option In order to circumnavigate the susceptibility to decarboxylation, this was not pursued due to the likely increase in conformational flexibility which would be detrimental to further structure-activity relationship studies.

4.2.6 Extended Alkyl Linker Approach

Based on the previously reported results from Buono and co-workers in 2005,[60] who synthesised an **BDT** ethylene Ts species (**4.31**), a synthetic route was devised to replicate this and install an ethylene functionalised alkyl chain (connecting the alkyne and alcohol moieties).

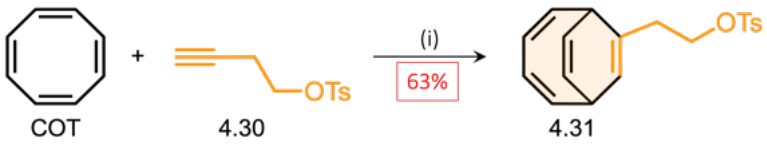

Scheme 4.21. Synthetic route to **BDT** ethylene Ts (**4.31**), as reported by Buono and co-workers. Conditions: (i) $CoBr_2(dppe)$ / Zn / ZnI_2 in a 5:15:10 mol% ratio / TFE / 40 °C / 20 h / 63%.

It was thought that the longer ethylene chain (compared with a methylene chain) may prevent any unwanted conjugation of the installed leaving group to the alkene in close proximity within the **BDT** intermediate species. It is possible that this conjugation, present in **BDTs** bearing methylene alkylation, makes any leaving group more prone to unwanted elimination, resulting in decomposition of the **BDT** framework.

Building upon this insight, the ethan-1-ol **BDT** (**4.32**) was synthesised subjecting **COT** and but-3-yn-1-ol (**4.33**) to cobalt(II)-catalysed cycloaddition conditions affording the ethan-1-ol **BDT** (**4.32**) a good yield of 49% (Scheme 4.22). Following previous attempts of installing a leaving group on the **BDT** bis(hydroxymethylene) (**4.20**), the ethan-1-ol **BDT** (**4.32**) was treated with *p*-toluenesulfonyl chloride, employing sodium hydroxide as a base (given that this methodology had proved successful in previous tosylation reactions) to form the **BDT** ethylene Ts species (**4.31**) (Scheme 4.22). The initial crude synthesis of this transformation proved successful by ^{1}H NMR spectroscopy (Figure 4.8) and mass spectrometry. The **BDT** Ts (**4.31**) product, however, proved unstable evidenced by decomposition on silica, forming a blue decomposition during flash column chromatography. Resultantly, the reaction was repeated and the decision to purify on alumina was taken, affording the **BDT** ethylene Ts (**4.31**) an 84% yield.

Scheme 4.22. Synthetic route to ethan-1-ol **BDT** (**4.32**) and **BDT** ethylene Ts (**4.31**). Conditions and reagents: i) $CoBr_2$(dppe) / Zn / ZnI_2 in a 5:15:10 mol% ratio / TFE / 55 °C / 48 h / 49%; (ii) *p*-TsCl / NaOH / CH_2Cl_2 / 0 °C → rt / 18 h / 84%.

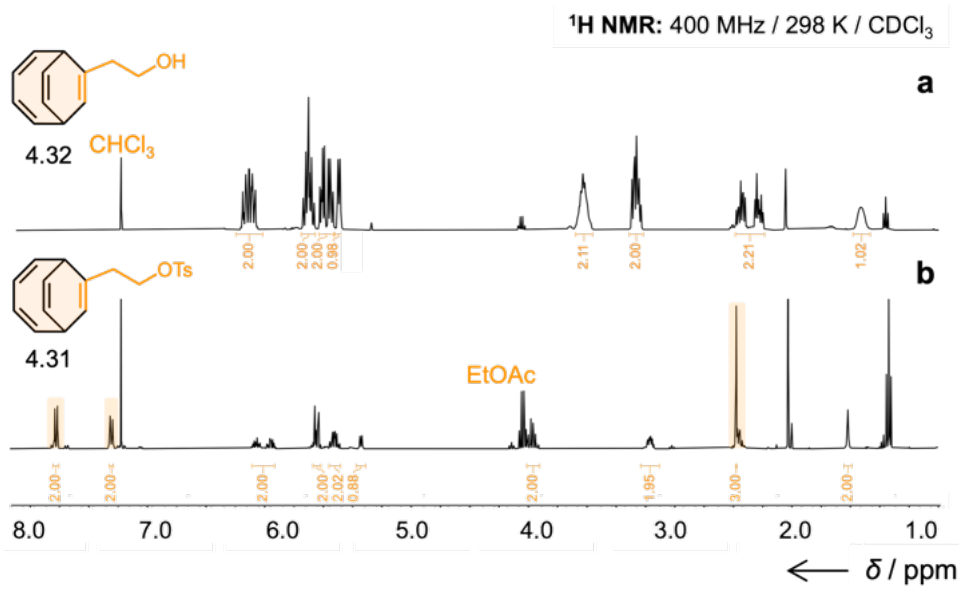

Figure 4.8. Partial ^{1}H NMR spectrum showing the synthetic transformation from (**a**) ethan-1-ol **BDT** (**4.32**) and (**b**) **BDT** ethylene Ts (**4.31**).The key Ts peaks in the newly formed species are highlighted in orange.

Provided with the evidential ability to yield mono-Ts **BDT** (**4.31**) species through an extended alkyl linkage, the next focus was to apply this new found knowledge to yield **BDT** and **BV** species with extended bis-hydroxy functionality. Therefore, we aimed to synthesise a corresponding alkynolic species, which could be used in a subsequent [6+2] cycloaddition with **COT**. If successful, this would present a **BDT** species bearing two ethanolic side chains, which could be similarly tosylated, and be carried forward for S_N2 chemistry with **MV**. Henceforth, the initial synthetic plan involved synthesising the appropriate precursors for the formation of hex-3-yne-1,6-diol (**4.34**), since this was commercially scarce.

In the initial outlook, the Seyferth-Gilbert homologation[72,73] appeared as a suitable synthetic route to the desired hex-3-yne-1,6-diol (**4.34**), given that we were equipped with a suitable starting material in diethyl-3-oxopentanedioate (**4.35**). The homologation comprises a base-promoted reaction of dimethyl (diazomethyl)phosphonate (**4.36**) with the given aldehyde (or in this case a ketone) to yield the corresponding alkyne (Scheme 4.23a). Thus, diethyl-3-oxopentanedioate (**4.35**) was subjected to Seyferth-Gilbert homologation conditions in an attempt to access diethyl hex-3-ynedioate (**4.37**). It was thought the diethyl hex-3-ynedioate

(**4.37**) intermediate could then be simply reduced to access hex-3-yne-1,6-diol (**4.34**) (Scheme 4.23b). This reaction was deemed to be unsuccessful by mass spectrometry. Following this attempt, in hindsight and based on the pK_a, deprotonation of compound **4.35** is more viable rather than undergoing the Seyferth-Gilbert homologation mechanism. This means that compound **4.35** would most likely exist in its enolate form, meaning it would not react in the desired manner to form compound **4.37.**

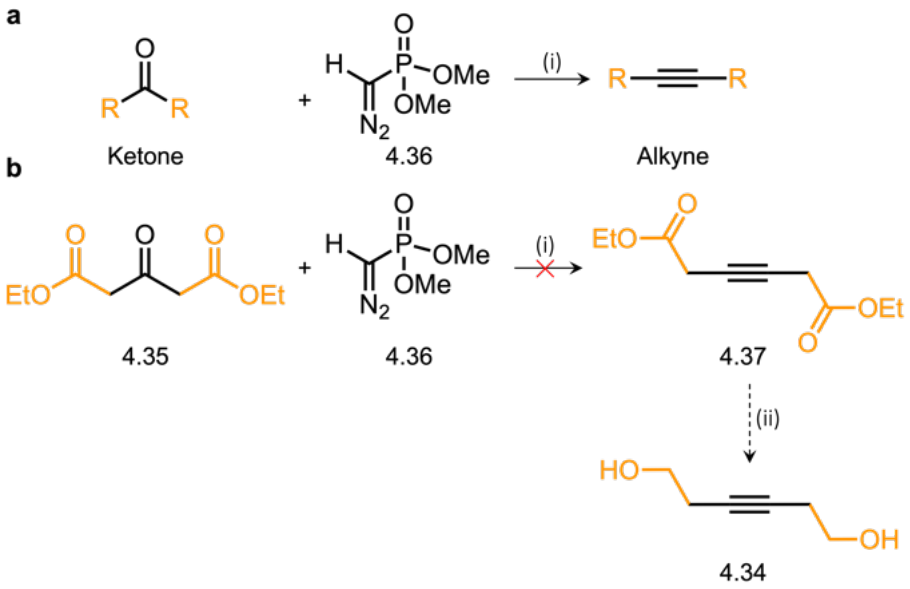

Scheme 4.23. (**a**) Synthetic route to disubstituted alkynes *via* the Seyferth-Gilbert homologation; (R = variable group e.g. CH_2OH) from a ketone and dimethyl (diazomethyl)phosphonate (**4.36**); Conditions: (i) base / –78 °C / THF; (**b**) Attempted synthesis of diethyl hex-3-ynedioate (**4.37**) by Seyferth-Gilbert homologation from diethyl 3-oxopentanedioate (**4.35**). Conditions: (i) K_2CO_3 / –78 °C / THF / 6 h; (ii) suitable reducing agent.

Given the limited success from the attempted homologation, an alternative route was followed. Based on the results published by Micalizio *et al*. in 2016,[74] 3-butyn-1-ol (**4.33**) was treated with dihydro-2*H*-pyran and *p*-toluenesulfonic acid monohydrate, allowing for the protection of the alcohol moiety to form 2-(but-3-yn-1-yloxy)tetrahydro-2*H*-pyran (**4.38**) in an excellent yield of 92% (Scheme 4.24).

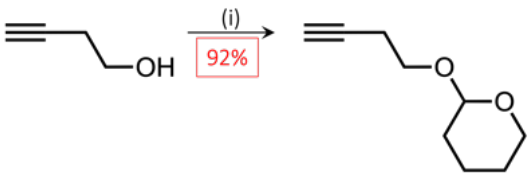

4.33 4.38

Scheme 4.24. Synthetic route to 2-(but-3-yn-1-yloxy)tetrahydro-2*H*-pyran (**4.38**).Conditions and reagents: i) 3,4-dihydro-2H-pyran / *p*-toluenesulfonic acid monohydrate / 0 °C → rt / 24 h / 92%.

In combination with the synthesis of 2-(but-3-yn-1-yloxy)tetrahydro-2*H*-pyran (**4.38**), 2-bromoethanol (**4.39**) was protected as a tetrahydropyranyl ether through the treatment of dihydro-2*H*-pyran and *p*-toluenesulfonic acid monohydrate to give 2-(2-bromoethoxyl)tetrahydro-*2H*-pyran (**4.40**) in a very good yield of 84% (Scheme 4.25).[74]

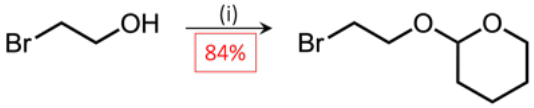

4.39 4.40

Scheme 4.25. Synthetic route to 2-(2-bromoethoxyl)tetrahydro-*2H*-pyran (**4.40**). Conditions: i) 3,4-dihydro-2H-pyran / *p*-toluenesulfonic acid monohydrate / 0 °C → rt / 24 h / 84%.

Following the successful syntheses of the aforementioned precursors (**4.38** and **4.40**), the attempted synthesis of the THP protected hex-3-yne-1,6-diol (**4.41**) was then carried out. The treatment of the 2-(but-3-yn-1-yloxy)tetrahydro-2*H*-pyran (**4.38**) with *n*-BuLi, followed by the sequential addition of the 2-(2-bromoethoxyl)tetrahydro-*2H*-pyran (**4.40**), was attempted to access the alkyne (**4.41**) (Scheme 4.26, conditions (a)).[74] The reaction attempt proved unsuccessful, yielding a large quantity of unreacted starting material along with the unsuccessful isolation of any desired di-THP alkyne (**4.41**). To try and improve on the aforementioned poor yielding reaction, an alternative attempt was pursued, incorporating a catalytic amount of copper iodide (10 mol%) within the reaction mixture. It was postulated that the acetylide formed initially for the S_N2 reaction would be more effective as a soft cuprate nucleophile. This species, therefore, would be less likely to act as a base, causing elimination of any other protons on the starting material (Scheme 4.26, conditions (b)). Even with this consideration, ^{1}H NMR analysis showed only trace conversion of the di-THP alkyne (**4.41**) which was not

purified further, therefore an alternative route to hex-3-yne-1,6-diol (**4.34**) was attempted.

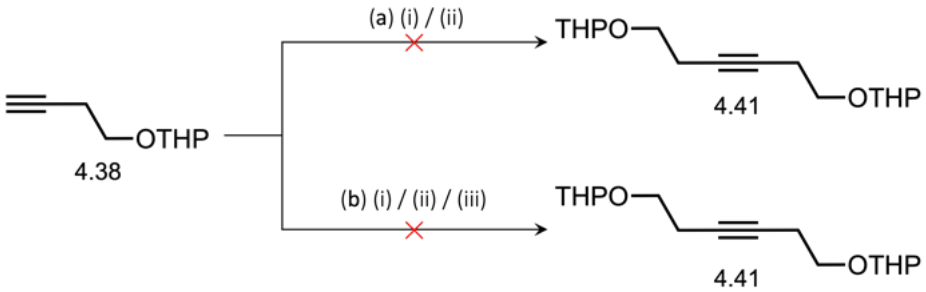

Scheme 4.26. Attempted synthetic route to 1,6-bis((tetrahydro-2H-pyran-2-yl)oxy)hex-3-yne (**4.41**) Conditions and reagents: (**a**) (i) *n*-BuLi / THF / –78 °C → rt; (ii) 2-(2-bromoethoxy)tetrahydro-2H-pyran (**4.40**) / NaI / rt → 60 °C / 5 d. (**b**) (i) *n*-BuLi / THF / –78 °C → rt; (ii) CuI (10 mol%); (iii) 2-(2-bromoethoxy)tetrahydro-2H-pyran (**4.40**) / NaI / rt → 60 °C / 2 d.

Then, another route to hex-3-yne-1,6-diol was tried based on reports from Zhixiang *et al.*.[75] First, (but-3-yn-1-yloxy) TBDMS (**4.42**) was synthesised through the treatment of but-3-yn-1-ol (**4.33**) with *tert*-butylchlorodimethylsilane in a good yield of 77% (Scheme 4.27). The subsequent TBDMS-protected alkynolic species was subjected to *n*-BuLi, allowing for deprotonation of the terminal alkyne, which was then treated in situ with ethylene oxide to form the corresponding alkyne (**4.43**) in an albeit poor yield of 9% (Scheme 4.27, conditions (a)). As detailed by Hirao and co-workers in 1983,[76] boron trifluoride diethyl etherate acts as a Lewis acid, activating the lithium acetylide (the electrophile), resulting in enhanced epoxide opening. Conveniently, *n*-BuLi does not react with the BF_3•OEt_2 complex immediately at –78 °C, allowing for the BF_3•OEt_2 promoted reaction of R-Li with epoxides, where this synthetic methodology has been demonstrated in a number of examples. Therefore, the reaction was repeated with the addition of boron trifluoride diethyl etherate (BF_3•OEt_2), providing a marginally higher yield of 15% for alkyne **4.43** (Scheme 4.27, conditions (b)).

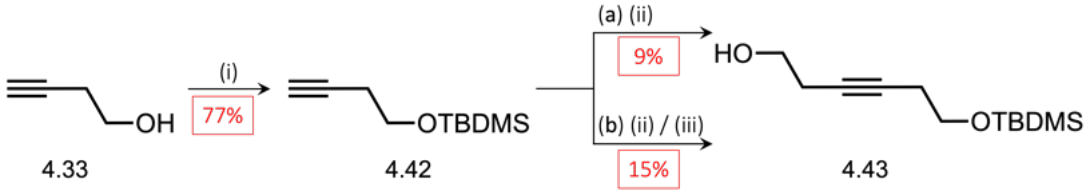

Scheme 4.27. Synthetic route to (but-3-yn-1-yloxy)(*tert*-butyl) (**4.42**) and 6-((*tert*-butyldimethylsilyl)oxy)hex-3-yn-1-ol (**4.43**). Conditions and reagents: (i) imidazole / TBDMSCl /

THF / rt / 24 h / 77%; (**a**) (ii) *n*-BuLi (2.5 M in hexanes) / THF / –78 °C → rt / 30 min / N_2 atmosphere; then ethylene oxide in THF (2.5–3.3 M) / 9%; (**b**) (ii) *n*-BuLi (2.5 M in hexanes) / THF / –78 °C → rt / 30 min / N_2 atmosphere; then ethylene oxide in THF (2.5–3.3 M), (iii) BF_3•OEt_2 / –78 °C → rt / 18 h / N_2 atmosphere / 15%. TBDMS = *tert*-butyldimethylsily.

The next step, in the original synthetic strategy, was to deprotect the TBDMS alkynolic species (**4.43**), employing base deprotection in methanol. Given the poor yielding reaction to form compound **4.43**, however, the ensuing deprotection would not afford a sufficient quantity of the diol alkyne (**4.34**) for a viable cycloaddition, as originally planned. Resultantly, the TBDMS alkynol (**4.43**) was taken forward for cobalt(I)-catalysed cycloaddition with **COT** in an attempt to form the corresponding **BDT** (**4.44**) (Scheme 4.28). Despite the fact the presence of the desired product was confirmed by mass spectrometry, crude ^{1}H NMR analysis provided no indication of any product peaks, indicating the steric hinderance of the TBDMS group may have prevented a significant degree of cobalt-alkyne coordination in the cycloaddition pathway.

Scheme 4.28. Attempted synthetic route to ethan-1-ol ethylene TBDMS **BDT** (**4.44**). Conditions: (i) $CoBr_2$(dppe) / Zn / ZnI_2 in a 10:40:20 mol% ratio / TFE / 55 °C / 48 h.

In light of the unsuccessful cycloaddition between the TBDMS alkyne (**4.43**) and **COT**, hex-3-yne-1,6-diol (**4.34**) was synthesised by the same route as **4.44**, instead of 3-butyn-1-ol (**4.33**) without prior protection, yielding hex-3-yne-1,6-diol (**4.34**) in 16% yield. Owing to its relative lack of steric hindrance, the synthesised alkyne was then subjected to a range of cycloaddition conditions (Table 4.3), in an attempt to yield a **BDT** bis(hydroxyethylene) (**4.45**) species. Analysis of the crude reaction mixture by ^{1}H NMR and mass spectrometry showed no evidence of **BDT** product formation for the conditions investigated.

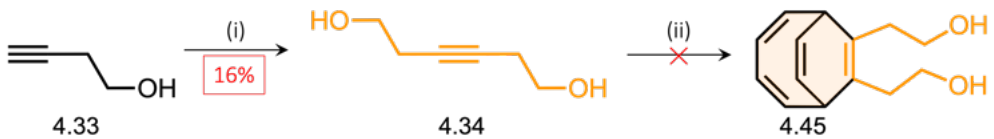

Scheme 4.29. Synthesis of hex-3-yne-1,6-diol (**4.34**) and the attempted synthetic route to **BDT** bis (hydroxyethylene) (**4.45**). Conditions: (i) *n*-BuLi / ethylene oxide / boron trifluoride diethyl

etherate / anhydrous THF / –78 °C → rt / 18 h / 16%; (ii) $CoBr_2$(dppe) / Zn / ZnI_2 in a 10:40:20 in a mol% ratio / solvent / T °C / t h. The specific range of reaction conditions is detailed in Table 4.3.

Table 4.3. Attempted reaction conditions for the [6+2] cycloaddition of **COT** with hex-3-yne-1,6-diol (**4.34**) to form the corresponding **BDT** (**4.45**). Conditions: (i) $CoBr_2$(dppe) / Zn / ZnI_2 5:15:10 mol% ratio. [a]Reaction monitored by mass spectrometry and ^{1}H NMR. NP = no product.

Solvent	Temperature / °C	Reaction Time / h	Comment[a]
TFE	55	24	NP
TFE	55	48	NP
TFE	65	24	NP
TFE	75	24	NP
DCE	40	24	NP
DCE	40	48	NP

4.2.7 Zincke Coupling Approach

As mentioned in the introduction, the Zincke reaction allows for the formation of *N*-aryl pyridinium salt, exploiting the reaction between a primary amine and *N*'-2,4-dinitrochlorobenzene derivatives.[36,38–41] First, the *N*'-2,4-dinitrobenzene pyridinium salt (**4.46**) is synthesised and typically isolated by filtration and recrystallisation. The reaction mechanistic pathway proceeds *via* the initial heating of the primary amine with the *N*-2,4-dinitrobenzene pyridinium salt, leading to the ring opening of the pyridinium moiety (**4.47**). The subsequent aliquot of the amine moiety then leads to the displacement of 2,4-dinitroaniline, leading to the formation of a König salt (**4.48**).[77] The ensuing König salt can react *via* either a intramolecular sigmatropic rearrangement or a nucleophilic addition reaction, to give the cyclised intermediate. Finally, the cyclic intermediate can then undergo proton transfer from a pyridinium ion, resulting in the elimination of an amine and the formation of the desired pyridinium product (**4.49**).[78] Intuitively, this mechanistic pathway is commonly referred to as ANRORC mechanism, where nucleophilic addition (A_N), ring opening (RO) and ring closing (RC) occurs consecutively.

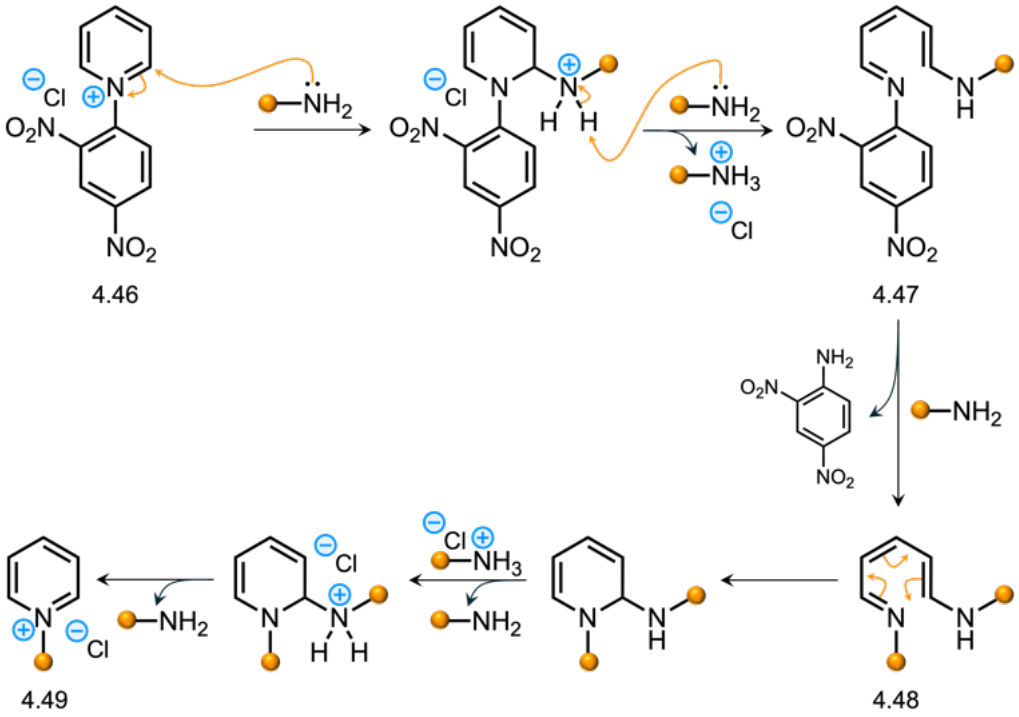

Scheme 4.30. Zincke reaction mechanism to form the respective pyridinium salt (**4.49**). The orange circle = variable group of the amine moiety.

As an alternative approach to the previous synthetic strategies, a *N'*-2,4-dinitrobenzene pyridinium (**4.51**) moiety was synthesised, allowing for a Zincke reaction approach to be taken. First, 4,4'-bipyridine (**4.5**) was treated with 1-chloro-2,4-dinitrobenzene (**4.50**) in ethanol at 80 °C for 18 hours to yield the *N'*-2,4-dinitrobenzene viologen derivative (**4.51**) in a 47% yield (Scheme 4.31). This species was then dissolved in acetonitrile and treated with methyl iodide to obtain the methylated product (**4.52**), however, this was not isolated as a pure product for characterisation at this stage (Scheme 4.31).

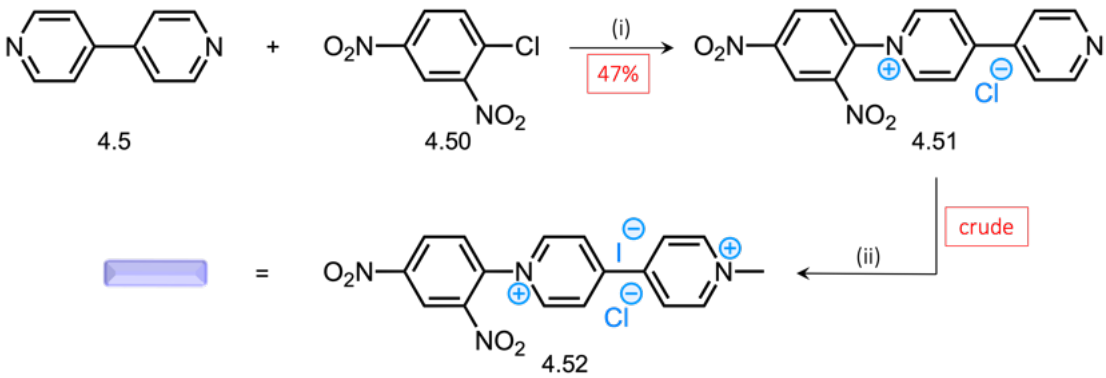

Scheme 4.31. Synthesis of 2,4-dinitrophenyl MV (**4.52**). Conditions and reagents: (i) 1-chloro-2,4-dinitrobenzene / EtOH / 80 °C / 18 h / 47%; (ii) MeI / MeCN / rt / 18 h.

Next, building upon the work from Fallon and co-workers,[61] the synthesis of a di-substituted boronate ester containing **BV** was carried out. Initially, trichloroethylene (**4.53**) was treated with *n*-BuLi at –78 °C in anhydrous THF. After warming to room temperature over 2 hours, the reaction mixture was transferred to a solution of 2-methoxy-4,4,5,5-tetramethyl-1,3,2-dioxaborolane (**4.54**) in anhydrous THF and was allowed to react over 4 hours, which, after work up, allowed for the formation of the bis(Bpin) acetylene (**4.55**) in 11% yield (Scheme 4.32). The bis-Bpin acetylene (**4.55**) was then subjected to [6+2] cycloaddition conditions with **COT** (Scheme 4.32), which resulted in the formation of the bis(Bpin) **BDT** (**4.56**) in 37% yield. The ensuing photo-sensitised rearrangement of the bis(BPin) **BDT** (**4.56**) then afforded the bis(BPin) **BV** (**4.57**) a yield of 36% (Scheme 4.32). Following the successful synthesis of the bis(BPin) **BV** (**4.57**), the synthetic strategy was to treat the bis(BPin) species with 4-bromoaniline, allowing for the Suzuki coupling to access a bis(aniline) **BV** (**4.58**) derivative.

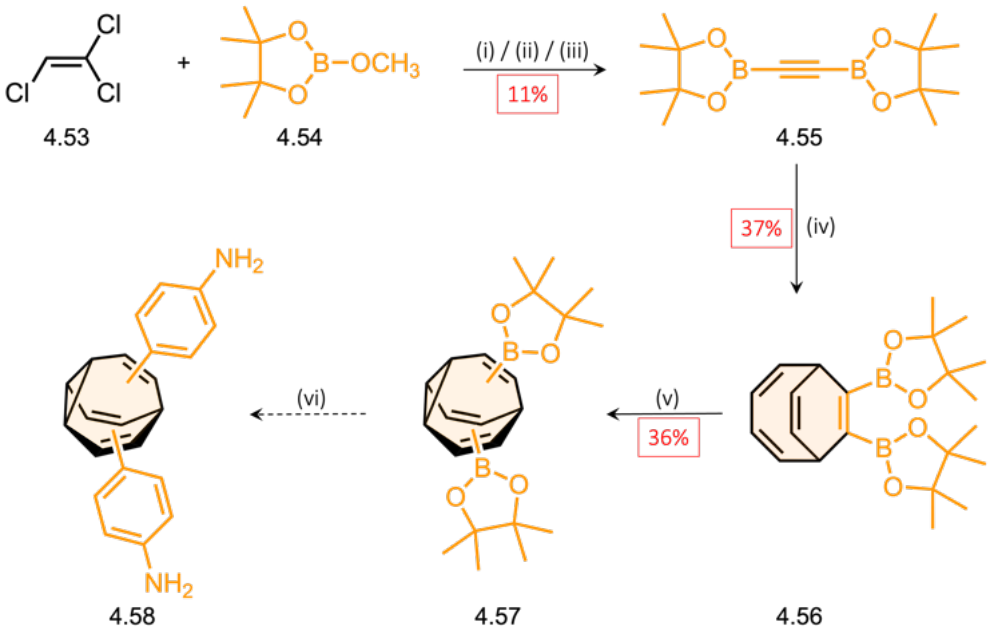

Scheme 4.32. Synthesis of the bis(BPin) acetylene (**4.55**), bis(BPin) **BDT** (**4.56**), bis(Bpin) (**BV**) (**4.57**) and the proposed route to bis(aniline) **BV** (**4.58**). Conditions and reagents: (i) *n*-BuLi / anhydrous THF / N_2 atmosphere / –78 °C → rt / 2 h; (ii) 2-methoxy-4,4,5,5-tetramethyl-1,3,2-dioxaborolane / anhydrous THF / –78 °C → rt / 4 h; (iii) HCl in dioxane / –78 °C → rt / 30 min / 11%; (iv) $CoBr_2$(dppe) / Zn / ZnI_2 in a 10:30:20 mol% ratio; DCE / 55 °C / 24 h / 37%; (v) Thioxanthen-9-one (5 mol%) / 365 nm / anhydrous THF / –5 °C / 6 h / 36%; (vi) 4-bromoaniline / $Pd(Ph_3)_4$) / THF / NaOH (10% aqueous) / 60 °C / 18 h. Synthetic steps (iv) and (v) were not performed by the author (see experimental).†

It was then envisioned that the bis(aniline) **BV** (**4.58**) could be used as an amine source to append the MV moiety *via* the Zincke reaction with the 2,4-dinitrobenzene MV (**4.52**) derivative, as detailed in Scheme 4.33.

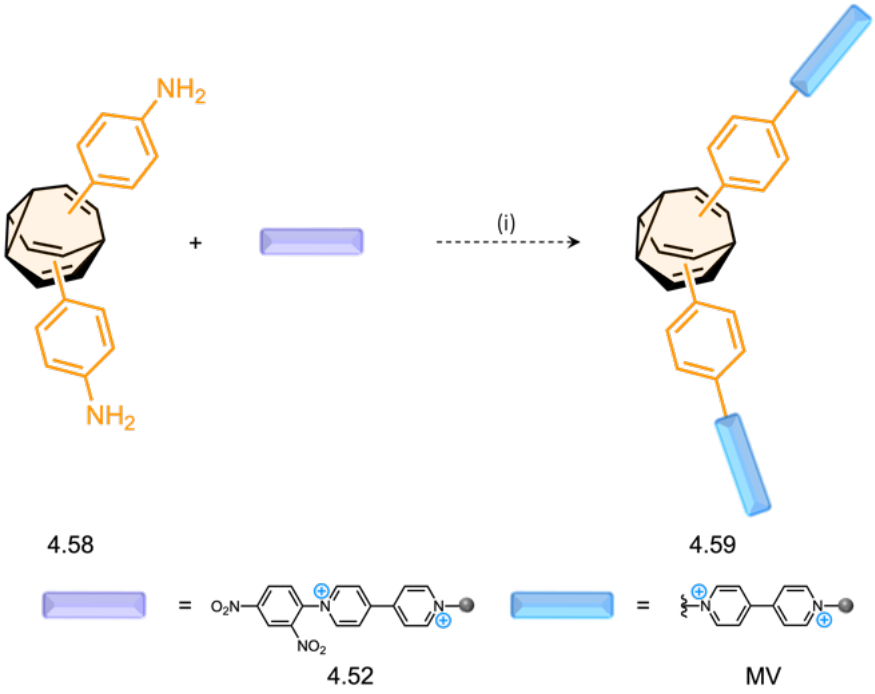

Scheme 4.33. Proposed synthetic route to bis(MV) **BV** (**4.59**) by the Zincke reaction. Conditions: (i) EtOH:water (1:1) / reflux / t h. The grey circles = Me; the violet and blue rectangles represent the 2,4-dinitrobenzene MV dication and MV dication species, respectively.

4.3 Conclusions and Future Work

In summary of this work, a range of synthetic strategies have been attempted to access a bis(MV) **BV** derivative, that is suitable for structure-activity relationship studies. The synthetic investigations towards this aim have involved a range of approaches which include: 1) cycloaddition of functionalised alkynes; 2) **BDT** and **BV** hydroxy group modification; 3) Steglich esterification; 4) extended alkyl linker approach and 5) Zincke coupling. The synthetic approaches 1–4, although unsuccessful for the purposes of these studies, has allowed us to gather a greater understanding of the synthetic adaptability of both **BDT** and **BV** species in general, that until now, has yet to be explored. The Zincke coupling approach, which was proposed towards the end of these

studies, provided more promising results, especially given that these proposals (detailed in Section 4.7) are based on notable literature precedent.

Upon the successful synthesis of a bis(MV) **BV** derivative, a crystal structure of the compound should be obtained by XRD in order to confirm the isomer form in the solid state, as well as analysing the isomer distribution in the solution state by NMR spectroscopy. Given that macrocycles are ideal hosts to probe the effect of shapeshifting equilibria on noncovalent bonding interactions, attempts to obtain a co-crystal with CB[8] should be attempted. Furthermore, full optoelectronic characterisation of the **BV** species will be vital, in order to understand its fundamental structure-activity relationship. This could be studied by UV-Vis spectroscopy, cyclic voltammetry and spectroelectrochemistry, to probe these effects of the unbound species and inclusion complex. Additionally, DFT calculations should be performed in order to provide a qualitative visualisation of the electronic excitations and transition densities. The aforementioned analysis would provide a visual representation of the donor/acceptor states within the bis(MV) **BV** species, in both the oxidised and reduced states, and prior to and after dimerisation. This would allow for a clearer understanding of the through-space interactions between MV moieties in a fluxional **BV** species.

4.4 Experimental

Glycoluril (4.11)

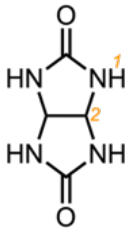

Glyoxal (40 g, 0.690 mol 1.0 eq.) and urea (103.4 g, 1.724 mol, 2.5 eq.) were dissolved in H_2O (200 mL) at rt in a round-bottomed flask. The reaction mixture was heated to 90 °C and stirred for 5 min. Concentrated H_2SO_4 (8 mL) was then added dropwise over 5 min resulting in the formation of a white solid 10 min after addition. The reaction mixture was stirred at 90 °C for a further 12 h followed by cooling to rt and adding 50% $NaOH_{(aq)}$ (100 mL) until the pH was adjusted to pH 14. The reaction mixture was cooled to 0 °C, and the suspension was filtered, dried and washed with H_2O (2 × 500 mL). The solid was dried under vacuum for 16 h affording the title compound as an off-white solid (80.5 g, 0.566 mol, 82%). **^{1}H NMR** (400 MHz, 298 K, $((CD_3)_2SO)$ δ 7.16 (s, 4H, H_1), 5.25 (s, 2H, H_2).

Spectroscopic data consistent with those previously reported.[59]

Cucurbit[8]uril (CB[8])

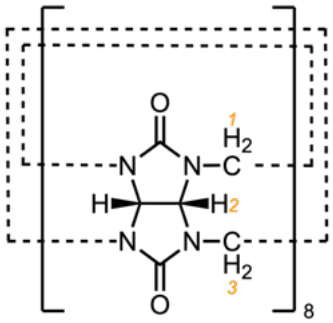

Glycoluril (**4.11**, 50 g, 0.352 mol, 1.0 eq.) was dissolved in 37% $HCl_{(aq)}$ (81 mL) at rt in a round-bottomed flask. Paraformaldehyde (21.1 g, 0.703 mol, 2.0 eq.) was slowly added and the solution stirred until the solution set as a gel. The gel was then heated to 100 °C allowing for dissolution of the gel followed by refluxing for 20 h at 100 °C. The solution was allowed to cool to rt, allowing for the formation of crystals over 72 h. The solution was then separated from the CB[6] crystals and evaporated by distillation yielding a brown solid. Then, 45% Formic acid (44 mL) was added to the brown solid with vigorous stirring which formed a white suspension. An additional 45% formic acid (35 mL) was added to dissolve the remaining brown solid. The mixture was stirred for 1 h at 75 °C to aid dissolution. The white suspension was then collected by vacuum filtration to afford the title compound as a white powder (5.20 g, 3.91 mmol,

10%). **^{1}H NMR** (400 MHz, 298 K, D_2O) δ 5.75 (d, *J* = 15.1 Hz, 2H, H_1), 5.47 (s, 2H, H_2), 4.16 (d, *J* = 14.9 Hz, 2H, H_3).

Spectroscopic data consistent with those previously reported.[46]

1-Methyl-4-(4'-pyridyl) pyridinium iodide (MVI)

MeI (3.88 g, 27.3 mmol, 1.2 eq.) was added to a CH_2Cl_2 (20 mL) solution containing 4,4'-bipyridine (3.50 g, 22.4 mmol, 1.0 eq.). The reaction mixture was refluxed at 40 °C for 22 h, forming a yellow precipitate. The yellow precipitate was isolated by filtration and washed with CH_2Cl_2 (3 × 25 mL) and dried *in vacuo* yielding the title compound as a yellow solid (4.78 g, 16 mmol, 73%). **^{1}H NMR** (400 MHz, 298 K, D_2O) δ 8.89 (d, *J* = 6.7 Hz, 2H, H_6), 8.72 (m, 2H, H_5), 8.37 (d, *J* = 7.1 Hz, 2H, H_2), 7.92 – 7.83 (m, 2H, H_1), 4.42 (s, 3H, H_7). **^{13}C NMR** (101 MHz, 298 K, D_2O) δ 153.5 (C_4), 149.9 (C_1), 145.6 (C_6), 142.6 (C_3), 125.7 (C_5), 122.5 (C_2), 47.8 (C_7). **HR-ASAP-MS:** *m/z* = 157.0747 $[M + H]^+$ (calculated for $[M + H]^+$ = 157.0739).

Spectroscopic data consistent with those previously reported.[79]

But-2-yne-1,4-diyl bis(4-methylbenzenesulfonate) (4.15)

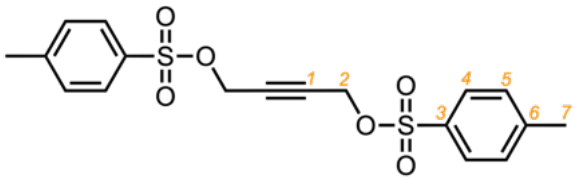

But-2-yne-1,4-diol (3.00 g, 0.035 mol, 1.0 eq.) and *p*-toluenesulfonyl chloride (26.6 g, 0.14 mol, 4.0 eq.) were added to a round bottomed flask and dissolved in Et_2O (40 mL). The reaction mixture was then put in a NaCl/ice (1:1) bath at 0 °C. Sodium hydroxide (11.2 g, 0.28 mol, 8.0 eq.) was added at regular intervals over ten min. Once added, the reaction mixture was allowed to warm to rt in an ice/water bath while stirring for 24 h. After 24 h, the reaction precipitant was dissolved in CH_2Cl_2 (100 mL) and washed with H_2O (3 × 50 mL). The organic layer was dried with $MgSO_4$, filtered and the solvent was then removed *in vacuo* to give the product as an off-white solid (13.6 g, 0.034 mol, 99%). **^{1}H NMR** (400 MHz, 298 K, $CDCl_3$) δ 7.78 – 7.76 (d, *J* = 8.5 Hz, 4H, H_4), 7.36 – 7.35 (d, 4H, H_5), 4.58 (s, 4H, H_2), 2.46 (s, 6H, H_7). **^{13}C NMR** (101 MHz,

298 K, $CDCl_3$) δ 145.6 (C_3), 133.0 (C_6), 130.1 (C_5), 128.3 (C_4), 81.1 (C_1), 57.2 (C_2), 21.8 (C_7). **HR-ASAP-MS:** *m/z* = 395.0631 $[M + H]^+$ (calculated for $[M + H]^+$ = 395.0635).

Spectroscopic data consistent with those previously reported.[80]

But-2-yne-1,4-diyl dimethanesulfonate (4.18)

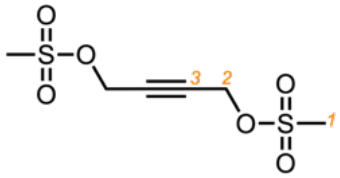

2-Butyne-1,4,-diol (0.856 g, 9.94 mmol) and methanesulfonyl chloride (1.8 mL, 22.9 mmol, 2.3 eq.) were added to a round bottomed flask and dissolved in CH_2Cl_2 (25 mL). The reaction mixture was then put in a NaCl/ice (1:1) bath at 0 °C. Et_3N (3.4 mL, 24.9 mmol, 2.5 eq.) was then added and the reaction mixture was allowed to warm to rt in an ice/water bath while stirring for 18 h. After 18 h, the reaction precipitant was dissolved in CH_2Cl_2 (100 mL) and washed with H_2O (3 × 50 mL). The organic layer was dried with $MgSO_4$, filtered and the solvent was then removed *in vacuo* to give the product as an off-white powder (2.22, 9.17 mmol, 92%). **^{1}H NMR** (400 MHz, 298 K, DMSO-d_6) δ 5.04 (s, 4H, H_2) 3.22 (s, 6H,H_1). **^{13}C NMR** (400 MHz, 298 K, DMSO-d_6) δ 81.7 (C_2) 57.5 (C_3) 37.4 (C_1). Spectroscopic data are consistent with those previously reported.

Spectroscopic data consistent with those previously reported.[81]

((2*Z*,4*Z*)-Bicyclo[4.2.2]deca-2,4,7,9-tetraene-7,8-diyl)dimethanol| *bis*(hydroxymethylene) BDT (4.20)

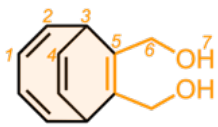

ZnI_2 (1.22 g, 3.84 mmol, 24 mol%), $CoBr_2$(dppe) (1.18 g, 1.92 mmol, 12 mol%) and activated Zn dust (0.377 g, 5.76 mmol, 36 mol%) were added to an oven-dried round-bottomed flask which was then flushed with N_2 and evacuated under high vacuum three times. Anhydrous TFE (10 mL) was added and the reaction mixture was stirred for 15 min at 55 °C. Cyclooctatetraene (1.67 g, 16.0 mmol, 1.0 eq.) was then added, followed by 2-butyne-1,4-diol (1.98 g, 23.0 mmol, 1.4 eq.) dissolved in TFE (6 mL) over 12 h *via* syringe pump, whilst stirring at 55 °C. The reaction mixture was then allowed to stir for an additional 36 h at 55 °C, before being filtered through a short pad of SiO_2 (10 g), eluting with EtOAc (250 mL). The solvent was removed *in vacuo* and the crude residue purified using

column chromatography (Teledyne Isco CombiFlash Rf+ system, 40 g SiO_2, hexanes–EtOAc, 0–100% gradient elution) to yield the title compound as a white solid (1.77 g, 9.31 mmol, 58%). **^{1}H NMR** (400 MHz, 298 K, $CDCl_3$); δ 6.34–6.20 (m, 2H, H_2), 5.80–5.66 (m, 4H, H_1 and H_4), 4.36–4.16 (m, 4H, H_6), 3.48–3.41 (ddd, *J* = 8.8, 4.0, 2.5 Hz, 2H, H_3), 1.38 (s, 2H, OH_7); **^{13}C NMR** (101 MHz, 298 K, $CDCl_3$) δ 141.8 (C_2), 132.9 (C_5), 125.0 (C_1), 121.2 (C_4), 61.0 (C_6), 38.2 (C_3). **HR-ESI-MS**: *m/z* = 213.0898 $[M + Na]^+$ (calculated for $[M + Na]^+$ = 213.0900).

Spectroscopic data consistent with those previously reported.[82]

Tricyclo[3.3.2.0^{2,8}]deca-3,6,9-trien-4-yl dimethanol | bis(hydroxymethylene) BV (4.23)

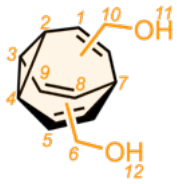

bis(Hydroxymethylene) BDT (**4.20**, 200 mg, 1.05 mmol, 1.0 eq.) and thioxanthene-9-one (11 mg, 0.005 mmol, 5 mol%) were dissolved in anhydrous THF (4 mL) in an oven-dried microwave vial. The mixture was stirred for 6 h, undergoing a fully enclosed irradiation with 360 *nm* UV light at –5 °C. Following irradiation, the solvent was removed *in vacuo* and the crude residue was purified by column chromatography (Teledyne Isco CombiFlash Rf+ system, 24 g SiO_2, hexanes–EtOAc, 0–100% gradient elution) to give the title compound as a pale yellow oil (56 mg, 0.29 mmol, 28%). **^{1}H NMR** (400 MHz, 298 K, $CDCl_3$) δ 5.89 (s, 5H, H_1, H_2, H_5, H_8 and H_9), 4.06–3.91 (m, 3H, H_3, H_4 and H_7), 2.20 (bs, 2H, H_{11} and H_{12}), 2.02 (s, 4H, H_6 and H_{10}). **HR-ESI-MS:** *m/z* = 189.0924 $[M + H]^+$ (calculated for $[M + H]^+$ = 189.0916).

Spectroscopic data are consistent with those previously published.[82]

1-(Carboxymethyl)-1'-methyl-4,4'-bipyridinium bromide iodide | Carboxylic Acid MV (4.28)

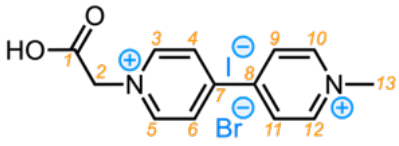

Methyl viologen (**MVI**, 1.00 g, 3.36 mmol, 1.0 eq.) was added to an oven-dried round bottomed flask and dissolved in MeCN (25 mL). Bromoacetic acid (2.33 g, 16.8 mmol, 5.0 eq.) was then added and the mixture was stirred for 24h, under reflux at 90 °C. After this time, the reaction mixture was allowed to cool to rt, and was

filtered and washed with cold MeCN (25 mL). The solid residue was then allowed to dry under vacuo to give the title compound as a yellow solid powder (1.06 g, 2.44 mmol, 73%). **^{1}H NMR** (400 MHz, 298 K, D_2O) δ 9.06 (m, 4H, H_3, H_5, H_{10} and H_{12}), 8.60–8.56 (d, *J* = 7.2 Hz, 2H, H_4, and H_6), 8.56–8.52 (d, *J* = 7.0 Hz, 2H, H_9 and H_{11}), 5.50 (s, 2H, H_2), 4.50 (s, 3H, H_{13}). **^{13}C NMR** (101 MHz, 298 K, D_2O) δ 169.4 (C_1), 150.8 (C_7), 149.8 (C_8), 146.8(C_3 and C_5), 146.7(C_{10} and C_{12}), 126.8 (C_4 and C_6), 126.7 (C_9 and C_{11}), 62.3 (C_2), 48.4 (C_{13}). **HR-ESI-MS:** *m/z* = 229.0970 $[M - H]^+$ (calculated for $[M - H]^+$ = 229.0972).

2-((2*Z*,4*Z*)-Bicyclo[4.2.2]deca-2,4,7,9-tetraen-7-yl)ethyl 4-methylbenzenesulfonate | BDT (ethylene Ts) (4.31)

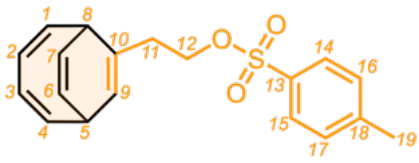

BDT (hydroxyethylene) (**4.32**, 180 mg, 1.03 mmol, 1.0 eq.) was added to an oven-dried round bottomed flask and dissolved in CH_2Cl_2 (2.5 mL). *p*-Toluenesulfonyl chloride (411 mg, 2.15 mmol, 2.1 eq.) was then added to the solution and stirred for 10 min at 0 °C. Sodium hydroxide (86 mg, 2.15 mmol, 2.1 eq.) was added at regular intervals over 5 min. Once added, the reaction mixture was allowed to warm to rt while stirring for 18 h. After 24 h, the reaction precipitant was dissolved in CH_2Cl_2 (10 mL) and washed with H_2O (3 × 10 mL). The organic layer was dried with $MgSO_4$, filtered and the solvent was then removed *in vacuo* to give the crude residue, which was purified by column chromatography (Teledyne Isco CombiFlash Rf+ system, 24 g Al_2O_3, hexanes–EtOAc, 0–20% gradient elution) to give the title compound as a yellow oil (284 mg, 0.866 mmol, 84%). **^{1}H NMR** (400 MHz, 298 K, $CDCl_3$) δ 7.78–7.76 (d, *J* = 8.4, 2H, H_{14} and H_{15}), 7.36–7.32 (d, *J* = 7.8, 2H, H_{16} and H_{17}), 6.25 – 6.05 (m, 2H, H_2 and H_3), 5.76–5.70 (m, 2H, H_1 and H_4), 5.63–5.54 (m, 2H, H_6 and H_7), 5.38 (m, 1H, H_9), 4.09—3.99 (m, 2H, H_{12}), 3.19–3.10 (m, 2H, H_5 and H_8), 2.45 (s, 3H, H_{19}), 1.58 (s, 2H, H_{11}). **^{13}C NMR** (101 MHz, 298 K, $CDCl_3$) δ 144.8 (C_{13}), 141.6 (C_2), 140.8 (C_3), 133.3 (C_{18}), 130.1 (C_{10}), 130.0 (C_{16} and C_{17}), 128.1 (C_{14} and C_{15}), 125.1 (C_6 or C_7), 124.3 (C_6 or C_7), 121.0 (C_1 or C_4), 120.7 (C_1 or C_4), 120.2 (C_9), 69.5 (C_{12}), 39.0 (C_5), 35.1 (C_8), 34.4 (C_{11}), 21.8 (C_{19}). **HR-ESI-MS:** *m/z* = 351.1031 $[M + Na]^+$ (calculated for $[M + Na]^+$ = 351.1025).

Spectroscopic data consistent with those previously reported.[60]

Bicyclo[4.2.2]deca-2,4,7,9-tetraen-7-yl)ethan-1-ol | BDT (hydroxyethylene) (4.32)

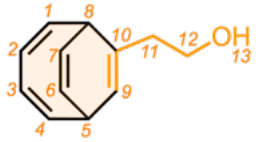

$CoBr_2$(dppe) (296 mg, 0.48 mmol, 10 mol%) and activated Zn dust (94 mg, 1.44 mmol, 30 mol%) were added to an oven-dried 25 mL round bottomed flask. ZnI_2 (306 mg, 0.96 mmol, 20 mol%) was then added. The tube was sealed and flushed with N_2 and evacuated under high vacuum three times and backfilled with N_2, three times. Then, anhydrous TFE (4 mL) was added and the reaction mixture was stirred for 15 min at 55 °C. Cyclooctatetraene (500 mg, 4.80 mmol, 1.0 eq.) was added to the solution followed by but-3-yn-1-ol (403 mg, 5.76 mmol, 1.2 eq.) dissolved in TFE (4 mL) *via* syringe pump over 12 h (0.33 mL/h). The reaction was stirred for 48 h at 55 °C. The suspension was filtered through a short pad of SiO_2 (5 g), washed with EtOAc (150 mL) and concentrated *in vacuo* to give the crude product, which was purified by column chromatography (Teledyne Isco Combiflash Rf+, 12 g SiO_2; hexanes—EtOAc, 0—20% gradient elution) to give the title compound as a pale yellow oil (414 mg, 2.37 mmol, 49%). **^{1}H NMR** (600 MHz, 298 K, $CDCl_3$) δ 6.30 – 6.20 (m, 2H, $H_{2,3}$), 5.82 – 5.74 (m, 2H, $H_{1,4}$), 5.69 – 5.66 (m, 1H, H_7), 5.62 – 5.60 (m, 1H, H_6), 5.54 (m, 1H, H_9). 3.67 — 3.58 (m, 2H, H_{12}), 3.25 — 3.18 (m, 2H, $H_{5,8}$), 2.39 — 2.22 (m, 2H, H_{11}), 1.63 (bs, 1H, H_{13}). **^{13}C NMR** (150 MHz, 298 K, $CDCl_3$) δ 142.4 (C_2), 141.5 (C_3), 132.1 (C_{10}), 124.7 (C_1), 124.0 (C_4), 121.1 (C_7), 121.0 (C_9), 120.8 (C_6), 61.4 (C_{12}), 39.1 (C_5), 39.0 (C_{11}), 35.2 (C_8). **HR-ESI-MS:** *m/z* = 175.1117. $[M + H]^+$ (calculated for $[M + H]^+$ = 175.1119).

Spectroscopic data consistent with those previously reported.[60]

Hex-3-yne-1,6-diol (4.34)

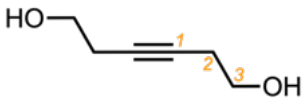

3-Butyn-1-ol (2.50 g, 35.7 mmol, 1.0 eq.) was added to a oven-dried round bottomed flask and dissolved in anhydrous THF (25 mL) under a N_2 atmosphere. The reaction mixture was then cooled to –78 °C and *n*-BuLi (15.7 mL, 39.3 mmol, 2.5 M in hexanes, 1.1 eq.) was then added dropwise over 30 min and stirred at –78 °C for 10 min. Ethylene oxide (17.1 mL, 42.8 mmol, 2.5–3.3 M in THF, 1.2 eq.) was then added dropwise over 10 min, followed by

the dropwise addition of boron trifluoride diethyl etherate (5.30 mL, 42.8 mmol, 1.2 eq.) at –78 °C over 10 min. The reaction mixture was then allowed to warm to rt whilst stirring over 18 h under a N_2 atmosphere. After this period, the reaction was quenched with saturated NH_4Cl (5 mL) and the organic phase extracted with Et_2O (10 mL). The organic phase was then washed with water (2 × 5 mL) and brine (5 mL). The combined organic extracts were dried over $MgSO_4$, filtered and concentrated *in vacuo*, to give the crude product, which was purified by column chromatography (Teledyne Isco Combiflash NextGen 300+, 80 g SiO_2; CH_2Cl_2—MeOH, 0—10% gradient elution) to give the title compound as a yellow oil (656 mg, 5.75 mmol, 16%). **^{1}H NMR** (400 MHz, 298 K, $CDCl_3$) δ 3.37 (m, 4H, H_3), 2.46 (m, 4H, H_2). **^{13}C NMR** (101 MHz, 298 K, $CDCl_3$) δ 78.1 (C_1), 61.8 (C_3), 26.5 (C_2). **HR-ESI-MS:** *m/z* = 117.0909 $[M + H]^+$ (calculated for $[M + H]^+$ = 117.0910).

2-(But-3-yn-1-yloxy)tetrahydro-2*H*-pyran (4.38)

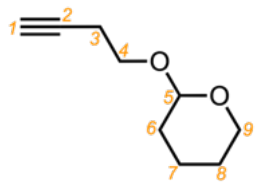

3-Butyn-1-ol (9.26 g, 132 mmol, 1.0 eq.) was added *via* a dropping funnel to a stirred solution of 3,4-dihydro-2*H*-pyran (22.2 g 264 mmol, 2.0 eq.) and *p*-toluenesulfonic acid monohydrate (253 mg, 1.33 mmol, 1 mol%) at 0 °C over 15 min. The resulting solution was allowed to warm to rt and stirred for 48 h. After this period, the reaction was quenched with brine (50 mL) and the aqueous phase was extracted with EtOAc (3 × 50 mL). The combined organic extracts were dried over $MgSO_4$, filtered and concentrated *in vacuo*. The crude isolate was purified by distillation under vacuum to yield the title compound as a colourless liquid (18.7 g, 121 mmol, 92%). **^{1}H NMR** (400 MHz, 298 K, $CDCl_3$) δ 4.64 (t, *J* = 3.6 Hz, 1H, H_5), 3.91 – 3.80 (m, 2H, H_9), 3.60 – 3.48 (m, 2H, H_4), 2.49 (td, *J* = 7.0, 2.7 Hz, 2H, H_3), 1.97 (t, *J* = 2.7 Hz, 1H, H_1), 1.89 – 1.66 (m, 3H, $H_{5,6}$), 1.62 –1.54 (m, 4H, $H_{7,8}$).**^{13}C NMR** (101 MHz, 298 K, $CDCl_3$) δ 98.9 (C_5), 81.6 (C_2), 69.3 (C_1), 65.6 (C_9), 62.4 (C_4), 30.7 (C_6), 25.5 (C_8), 20.1 (C_7), 19.5 (C_3). **HR-ESI-MS:** *m/z* = 177.0890 $[M + Na]^+$ (calculated for $[M + Na]^+$ = 177.0880).

Spectroscopic data consistent with those previously reported.[74]

2-(2-Bromoethoxy)tetrahydro-2*H*-pyran (4.40)

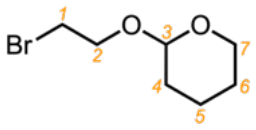

2-Bromoethanol (17.6 g, 141 mmol, 1.0 eq.) was added *via* a dropping funnel to a stirred solution of 3,4-dihydro-2*H*-pyran (25.8 mL, 283 mmol, 2.0 eq.) and *p*-toluenesulfonic acid monohydrate (264 mg, 1.39 mmol, 1 mol%) at 0 °C over 15 min . The resulting solution was allowed to warm to rt and stirred for 48 h. After this period, the reaction was quenched with a saturated aqueous solution of $NaHCO_3$ (50 mL) extracted with EtOAc (3 × 50 mL). The combined organic extracts were dried over $MgSO_4$, filtered and the solvent was removed *in vacuo* to afford the crude isolate which was purified by distillation (90 °C / 1-2 mbar) to yield the title compound as a colourless oil (24.7 g, 119 mmol, 84%). **^{1}H NMR** (400 MHz, 298 K, $CDCl_3$) δ 4.64 (t, *J* = 3.6 Hz, 1H, H_3), 4.02 3.92 (m, 1H, H_2), 3.91 – 3.81 (m, 1H, H_2), 3.80 – 3.68 (m, 1H, H_1), 3.53 – 3.42 (m, 3H, $H_{1,7}$), 1.88 –1.64 (m, 2H, H_4), 1.64 – 1.44 (m, 4H, $H_{5,6}$).**^{13}C NMR** (101 MHz, 298 K, $CDCl_3$) δ 99.0 (C_3), 67.6 (C_2), 62.3 (C_7), 30.9 (C_1), 30.5 (C_4), 25.4 (C_6), 19.3 (C_5). **HR-ESI-MS**: *m/z* = 209.1171 [*M* + H]$^+$ (calculated for [*M* + H]$^+$ = 209.0177).

Spectroscopic data consistent with those previously reported.[74]

(But-3-yn-1-yloxy)(*tert*-butyl)dimethylsilane (4.42)

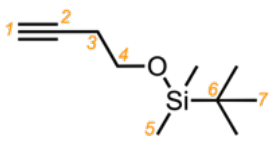

3-Butyn-1-ol (5.0 g, 71.4 mmol, 1.0 eq.) and imidazole (10.3 g, 142.8 mmol, 2.0 eq.) were dissolved in anhydrous THF (100 mL) and stirred at rt for 5 min. *tert*-Butyl-dimethyl-silyl chloride (12.9 g, 85.7 mmol, 1.2 eq.) was then added and the reaction mixture was stirred at rt for 24 h. After this time, the reaction mixture was filtered through a pad of SiO_2 (10 g), eluted with CH_2Cl_2 (3 × 25 mL) and the solvent removed *in vacuo* to afford the crude isolate which was purified by column chromatography (Teledyne Isco Combiflash NextGen 300+, 80 g SiO_2 GOLD; hexanes—EtOAc, 0—10% gradient elution) to give the title compound as a colourless liquid (10.1 g, 54.9 mmol, 77%).**^{1}H NMR** (400 MHz, 298 K, $CDCl_3$) δ 3.74 (t, *J* = 7.2 Hz, 2H, H_4), 2.40 (td, *J* = 7.1, 2.7 Hz, 2H, H_3), 1.96 (t, *J* = 2.7 Hz, 1H, H_1), 0.90 (s, 9H, H_7), 0.07 (s, 6H, H_5). **HR-ESI-MS**: *m/z* = 185.1356 [*M* + H]$^+$ (calculated for [*M* + H]$^+$ = 185.1283).

Spectroscopic data are consistent with those previously reported.[83]

6-((*tert*-Butyldimethylsilyl)oxy)hex-3-yn-1-ol (4.43)

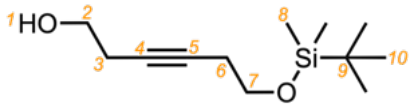

But-3-yn-1-yloxy(*tert*-butyl)dimethylsilane (**4.42**, 1.00 g, 5.42 mmol, 1.0 eq.) was dissolved in anhydrous THF (5 mL) and was cooled to –78 °C. *n*-BuLi (2.6 mL, 6.50 mmol, 2.5 M in hexanes, 1.2 eq.) was then added dropwise over 10 min and stirred at –78 °C for 15 min. Ethylene oxide (0.5 mL, 9.80 mmol, 2.5 M in THF, 1.8 eq.) was then added *via* syringe over 5 min, followed by boron trifluoride diethyl etherate (0.8 mL, 6.50 mmol, 1.2 eq.) added dropwise over 5 min at –78 °C. The reaction mixture was then allowed to warm to rt and stirred for 18 h. The reaction mixture was then quenched with saturated ammonium chloride (5 mL) and extracted with Et_2O (10 mL). The organic phase was decanted and washed with H_2O (2 × 5 mL) and brine (5 mL) and the organic phase was decanted. The combined organic extracts were dried over $MgSO_4$, filtered and the solvent was removed *in vacuo* to afford the crude isolate which was purified by column chromatography (Teledyne Isco Combiflash NextGen 300+, 12 g SiO_2; hexanes–EtOAc, 0–10% gradient elution) to give the title compound as a colourless oil (184 mg, 0.806 mmol, 15%). **^{1}H NMR** (400 MHz, 298 K, $CDCl_3$) δ 3.73 – 3.62 (m, 4H, $H_{2,7}$), 2.46 – 2.33 (m, 4H, $H_{3,6}$), 1.94 (bs, 1H, H_1), 0.89 (d, *J* = 0.6 Hz, 9H, H_{10}), 0.06 (d, *J* = 0.6 Hz, 6H, H_8). **^{13}C NMR** (100 MHz, 298 K, $CDCl_3$) δ 79.7 (C_4), 77.8 (C_5), 62.3 (C_7), 61.4 (C_2), 26.0 (C_{10}), 23.3 ($C_{3,6}$), 18.5 (C_9), –5.2 (C_8). **HR-ESI-MS:** *m/z* = 251.1435 $[M + H]^+$ (calculated for $[M + H]^+$ = 251.1438).

Spectroscopic data are consistent with those previously reported. [75]

1-(2,4-Dinitrophenyl)-4,4′-bipyridinium chloride (4.51)

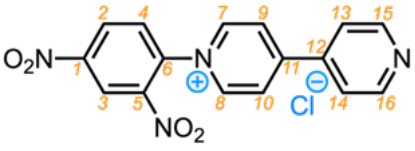

4,4′-Bipyridine (1.52 g, 9.73 mmol, 1.0 eq.) and 1-chloro-2,4-dinitrobenzene (1.97 g, 9.73 mmol, 1.0 eq.) were dissolved in EtOH (50 mL) and the reaction mixture was stirred at 80 °C for 18 h. The reaction mixture was then allowed to cool to rt over 20 min whilst stirring. After cooling to rt, Et_2O (100 mL) was added to the reaction mixture allowing a precipitate to form. The precipitate was then filtered

through a sintered glass funnel and washed with cold EtOAc (3 × 20 mL), dissolved in MeOH (20 mL) and the solvents removed in vacuo to afford the title compound as a dark brown sticky solid (694 mg, 1.94 mmol, 47%). **^{1}H NMR** (400 MHz, 298 K, D_2O) δ 9.39 (d, *J* = 2.5 Hz, 1H, H_4), 9.25 (d, *J* = 6.0 Hz, 2H, $H_{7,8}$), 8.93 (dd, *J* = 2.5 Hz, 8.7 Hz, 1H, H_2), 8.84 (d, *J* = 6.3 Hz, 2H, $H_{15,16}$), 8.70 (d, *J* = 6.9 Hz, 2H, $H_{9,10}$), 8.28 (d, *J* = 8.7 Hz, 1H, H_3), 8.05 (d, *J* = 6.3 Hz, 2H, $H_{13,14}$); **^{13}C NMR** (101 MHz, 298 K, $CDCl_3$) δ 157.0 (C_{11}), 150.2 ($C_{15,16}$), 149.7 (C_1), 145.8 ($C_{7,8}$), 143.0 (C_5), 142.0 (C_{12}), 138.5 (C_6), 131.2 (C_3), 130.7 (C_2), 126.2 ($C_{9,10}$),, 122.7 ($C_{13,14}$), 122.2 (C_4). **HR-ESI-MS:** *m/z* = 323.0775 $[M]^+$ (calculated for $[M]^+$ = 323.0775).

Spectroscopic data consistent with those previously reported.[36]

1,2-Bis(4,4,5,5-tetramethyl-1,3,2-dioxaborolan-2-yl)ethyne | bis(Bpin) acetylene (4.55)

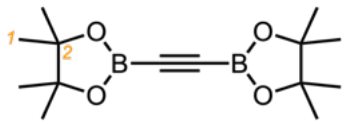

Bis-Bpin acetylene was prepared with a modification to the reported procedure by Fallon.[61] A solution of *n*-BuLi in hexanes (2.5 M, 30 mL, 75 mmol, 3.0 eq.) was slowly added to a stirred solution of anhydrous THF (80 mL) at –78 °C under an atmosphere of N_2. Trichloroethylene (2.25 mL, 25.0 mmol, 1.0 eq.) in anhydrous THF (25 mL) was then added dropwise over 15 min. The cooling bath was then removed and the reaction mixture was allowed to warm to rt whilst stirring for 2 h. The reaction mixture was then cooled to –78 °C and transferred slowly *via* cannular through a 5 mm diameter Teflon tube into a stirred solution of 2-methoxy-4,4,5,5-tetramethyl-1,3,2-dioxaborolane (8.2 mL, 50 mmol, 2.0 eq.) in anhydrous THF (40 mL) over 15 min. After stirring for 2 h at –78 °C and then for 2 h at rt, the mixture was cooled back down to –78 °C and hydrogen chloride solution (4.0 M in dioxane, 20 mL) was added dropwise over 10 min. The cooling bath was removed and the reaction mixture was allowed to warm to rt over 30 min. The reaction was then filtered through a sintered glass funnel and the solvents removed in vacuo. The solid residue was then dissolved in Et_2O (25 mL) and filtered through a pad of celite (5 g) which was washed with hexanes (3 × 50 mL). The filtrate was then evaporated to dryness and washed with cold hexanes (5 ×

20 mL), which was then decanted. The remaining solid was then dried *in vacuo* to afford the title compound as a white solid (748 mg, 2.69 mmol, 11%). **^{1}H NMR** (400 MHz, 298 K, $CDCl_3$) δ 1.25 (s, 24H, H_1); **^{13}C NMR** (101 MHz, 298 K, $CDCl_3$) δ 84.8 (C_2), 24.7 (C_1).

Spectroscopic data consistent with those previously reported.[61]

(2Z,4Z)-7,8-bis(4,4,5,5-Tetramethyl-1,3,2-dioxaborolan-2-yl)bicyclo[4.2.2]deca-2,4,7,9-tetraene | bis(Bpin) BDT (4.56)†

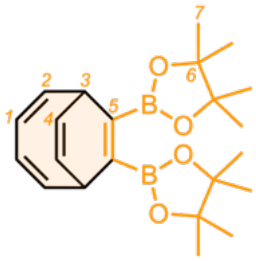

$CoBr_2$(dppe) (296 mg, 0.48 mmol, 10 mol%) and activated Zn dust (94 mg, 1.44 mmol, 30 mol%) were added to an oven-dried 25 mL round bottomed flask. ZnI_2 (306 mg, 0.96 mmol, 20 mol%) was then added. The tube was sealed and flushed with N_2 and evacuated under high vacuum three times. Then, anhydrous 1,2-DCE (4 mL) was added and the reaction mixture was stirred for 15 min at rt. Cyclooctatetraene (500 mg, 4.80 mmol, 1.0 eq.) was added to the solution followed by the dropwise addition of 1,2-bis(4,4,5,5-tetramethyl-1,3,2-dioxaborolan-2-yl)ethyne (**4.55**, 1.60 g, 5.76 mmol, 1.2 eq.) dissolved in 1,2-DCE (6 mL) over 15 min. The reaction was stirred for 48 h at rt. After this time, the suspension was filtered through a short pad of SiO_2 (5 g), washed with Et_2O (150 mL) and concentrated *in vacuo* to give the crude product, which was purified by column chromatography (Teledyne Isco Combiflash Rf+, 24 g SiO_2; hexanes—EtOAc, 0—100% gradient elution) to give the title compound as a white solid (665 mg, 1.74 mmol, 37%). **^{1}H NMR** (400 MHz, 298 K, $CDCl_3$) δ 6.19–6.10 (m, 2H, H_2), 5.77–5.68 (m, 4H, H_3 and H_4), 3.42–3.36 (m, 2H, H_1), 1.28 (s, 24H, H_7). **^{13}C NMR** (101 MHz, 298 K, $CDCl_3$) δ 140.7 (C_2), 124.9 (C_1), 122.0 (C_4), 83.7 (C_6), 37.4 (C_3), 25.0 (C_7), **HR-ESI-MS**: *m/z* = 381.2638 $[M + H]^+$ (calculated for $[M + H]^+$ = 381.2638).

Spectroscopic data consistent with those previously reported.[61]
† Compound synthesised by W. Maturi.

bis(4,4,5,5-Tetramethyl-1,3,2-dioxaborolan-2-yl) bullvalene | bis(Bpin) BV (4.57)†

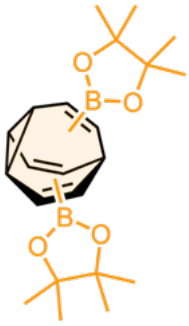

Bis(BPin) BDT (**4.56**, 200 mg, 0.523 mmol, 1.0 eq.) and thioxanthene-9-one (6 mg, 0.026 mmol, 5 mol%) were dissolved in anhydrous THF (4 mL) in an oven-dried microwave vial. The mixture was stirred for 6 h, undergoing a fully enclosed irradiation with 360 *nm* UV light at –5 °C. Following irradiation, the solvent was removed *in vacuo* and the crude residue was purified by column chromatography (Teledyne Isco CombiFlash Rf+ system, 24 g SiO_2, hexanes–EtOAc, 0–50% gradient elution) to give the title compound as a white solid (74 mg, 0.19 mmol, 36%). **^{1}H NMR** (400 MHz, 298 K, $CDCl_3$) δ 7.05–6.05 (bm, 2.8H), 4.69–4.22 (bm, 1.2H), 3.68–2.37 (bm, 4H), 1.23 (s, 24H). **HR-ESI-MS:** *m/z* = 381.2628 $[M + H]^+$ (calculated for $[M + H]^+$ = 381.2638).

Spectroscopic data consistent with those previously reported.[61]
† Compound synthesised by W. Maturi.

4.5 References

1 S. Durben and T. Baumgartner, *Angew. Chem. Int. Ed.*, 2011, **50**, 7948–7952.

2 E. Hwang, S. Seo, S. Bak, H. Lee, M. Min and H. Lee, *Adv. Mat.*, 2014, **26**, 5129–5136.

3 A. Beneduci, S. Cospito, M. La Deda, L. Veltri and G. Chidichimo, *Nat. Commun.* 2014, **5**, 1–8.

4 K. Wadhwa, S. Nuryyeva, A. C. Fahrenbach, M. Elhabiri, C. Platas-Iglesias and A. Trabolsi, *J. Mater. Chem. C,* 2013, **1**, 2302–2307.

5 T. Janoschka, N. Martin, U. Martin, C. Friebe, S. Morgenstern, H. Hiller, M. D. Hager and U. S. Schubert, *Nature,* 2015, **527**, 78–81.

6 J. Luo, B. Hu, C. Debruler and T. L. Liu, *Angew. Chem. Int. Ed.*, 2018, **57**, 231–235.

7 B. Hu, C. Debruler, Z. Rhodes and T. L. Liu, *J. Am. Chem. Soc.*, 2017, **139**, 1207–1214.

8 T. Janoschka, N. Martin, M. D. Hager and U. S. Schubert, *Angew. Chem. Int. Ed.*, 2016, **55**, 14427–14430.

9 O. Buyukcakir, S. H. Je, D. S. Choi, S. N. Talapaneni, Y. Seo, Y. Jung, K. Polychronopoulou and A. Coskun, *Chem. Commun.*, 2016, **52**, 934–937.

10 Y. Sun, T. Masuda and K. Uosaki, *Chem. Lett.*, 2012, **41**, 328–330.

11 Z. Shi, K. G. Neoh and E. T. Kang, *Biomaterials*, 2005, **26**, 501–508.

12 S. Asaftei, D. Huskens and D. Schols, *J. Med. Chem.*, 2012, **55**, 10405–10413.

13 S. Asaftei and E. De Clercq, *J. Med. Chem.*, 2010, **53**, 3480–3488.

14 J. Ding, C. Zheng, L. Wang, C. Lu, B. Zhang, Y. Chen, M. Li, G. Zhai and X. Zhuang, *J. Mater. Chem. A*, 2019, **7**, 23337–23360.

15 T. B. Gasa, J. M. Spruell, W. R. Dichtel, T. J. Sørensen, D. Philp, J. F. Stoddart and P. Kuzmič, *Chem. Eur. J.,* 2009, **15**, 106–116.

16 N. Hickey, B. Medagli, A. Pedrini, R. Pinalli, E. Dalcanale and S. Geremia, *Cryst. Growth. Des.*, 2021, **21**, 3650–3655.

17 H. J. Kim, W. S. Jeon, Y. H. Ko and K. Kim, *Proc. Natl. Acad. Sci. U. S. A.*, 2002, **99**, 5007–5011.

18 W. S. Jeon, H. J. Kim, C. Lee and K. Kim, *Chem. Commun.*, 2002, **11**, 1828–1829.

19 T. M. Bockman and J. K. Kochi, *J. Org. Chem*, 1990, **55**, 4127–4135.

20 C. L. Bird and A. T. Kuhn, *Chem. Soc. Rev.*, 1981, **10**, 49–82.

21 P. M. Monk, *The Viologens Physiochemical Properties, Synthesis and Application of the Salts of 4,4'-Bipyridine*, John Wiley & Sons, 1998.

22 E. M. Kosower and J. L. Cotter, *J. Am. Chem. Soc.*, 1964, **86**, 5524–5527.

23 J. B. Torrance, B. A. Scott, B. Welber, F. B. Kaufman and P. E. Seiden, *Phys. Rev. B.,* 1979, **19**, 730.

24 J. M. Lü, S. V. Rosokha and J. K. Kochi, *J. Am. Chem. Soc.*, 2003, **125**, 12161–12171.

25 R. Kannappan, C. Bucher, E. Saint-Aman, J. C. Moutet, A. Milet, M. Oltean, E. Métay, S. Pellet-Rostaing, M. Lemaire and C. Chaix, *New J. Chem.*, 2010, **34**, 1373–1386.

26 L. J. Winters, N. G. Smith and M. I. Cohen, *J. Chem. Soc. D Chem. Commun.*, 1970, **11**, 642–643.

27 R. H. Reuss and L. J. Winters, *J. Org. Chem.*, 1973, **38**, 3993–3995.

28 N. Miyaura and A. Suzuki, *Chem. Rev.*, 1995, **95**, 2457–2483.

29 M. Olesínska, G. Wu, D. Antón, I. Szabó, E. Rosta and O. A. Scherman, *Chem. Sci.,* 2019, **10**, 8806–8811.

30 K. Wei Shah, S.-X. Wang, D. Xiang Yun Soo and J. Xu, *Polymers*, 2019, **11**, 1839.

31 N. Menschutkin, *Z. Phys. Chem.,* 1890, **5U**, 589–600.

32 G. Das, T. Skorjanc, T. Prakasam, S. Nuryyeva, J.-C. Olsen and A. Trabolsi, *RSC Adv.,* 2017, **7**, 3594–3598.

33 Y. Zhang, K. Zhang, L. Wu, K. Liu, R. Huang, Z. Long, M. Tong and G. Chen, *RSC Adv.,* 2020, **10**, 3606–3614.

34 T. Škorjanc, D. Shetty, M. A. Olson and A. Trabolsi, *ACS Appl. Mater. Interfaces*, 2019, **11**, 6705–6716.

35 S. Petit, R. Azzouz, C. Fruit, L. Bischoff and F. Marsais, *Tetrahedron Lett.*, 2008, **49**, 3663–3665.

36 P. Cortón, P. Novo, V. López-Sobrado, M. D. García, C. Peinador and E. Pazos, *Synthesis,* 2020, **52**, 537–543.

37 O. Domarco, I. Neira, T. Rama, A. Blanco-Goámez, M. D. Garciáa, C. Peinador and J. M. Quintela, *Org. Biomol. Chem.*, 2017, **15**, 3594–3602.

38 T. Zincke and W. Walter, *Justus Liebigs Ann. Chem.*, 1904, **334**, 367–385.

39 T. Zincke, G. Heuser and W. Möller, *Justus Liebigs Ann. Chem.*, 1904, **333**, 296–345.

40 T. Zincke and G. Weißpfenning, *Justus Liebigs Ann. Chem.*, 1913, **396**, 103–131.

41 G. Das, T. Skorjanc, S. K. Sharma, F. Gándara, M. Lusi, D. S. Shankar Rao, S. Vimala, S. Krishna Prasad, J. Raya, D. S. Han, R. Jagannathan, J. C. Olsen and A. Trabolsi, *J. Am. Chem. Soc.*, 2017, **139**, 9558–9565.

42 R. Behrend, E. Meyer and F. Rusche, *Justus Liebigs Ann. Chem.*, 1905, **339**, 1–37.

43 W. L. Mock and N. Y. Shih, *J. Org. Chem.*, 1983, **48**, 3618–3619.

44 W. A. Freeman, W. L. Mock and N. Y. Shih, *J. Am. Chem. Soc.*, 1981, **103**, 7367–7368.

45 J. Kim, I. S. Jung, S. Y. Kim, E. Lee, J. K. Kang, S. Sakamoto, K. Yamaguchi and K. Kim, *J. Am. Chem. Soc.*, 2000, **122**, 540–541.

46 D. Bardelang, K. A. Udachin, D. M. Leek, J. C. Margeson, G. Chan, C. I. Ratcliffe and J. A. Ripmeester, *Cryst. Growth. Des.*, 2011, **11**, 5598–5614.

47 A. Day, A. P. Arnold, R. J. Blanch and B. Snushall, *J. Org. Chem.*, 2001, **66**, 8094–8100.

48 S. J. Barrow, S. Kasera, M. J. Rowland, J. Del Barrio and O. A. Scherman, *Chem. Rev.*, 2015, **115**, 12320–12406.

49 H. J. Buschmann, E. Cleve, K. Jansen, A. Wego and E. Schollmeyer, *J. Incl. Phenom.*, 2001, **40**, 117–120.

50 H. J. Buschmann, E. Cleve, K. Jansen and E. Schollmeyer, *Anal. Chim. Acta.*, 2001, **437**, 157–163.

51 K. A. Kellersberger, J. D. Anderson, S. M. Ward, K. E. Krakowiak and D. V. Dearden, *J. Am. Chem. Soc.*, 2001, **123**, 11316–11317.

52 L. Liu, N. Zhao and O. A. Scherman, *Chem. Commun.*, 2008, 1070–1072.

53 N. Zhao, L. Liu, F. Biedermann and O. A. Scherman, *Chem. Asian. J.*, 2010, **5**, 530–537.

54 S. Sinn and F. Biedermann, *Isr. J. Chem.*, 2018, **58**, 357–412.

55 S. Walker, R. Oun, F. J. McInnes and N. J. Wheate, *Isr. J. Chem.*, 2011, **51**, 616–624.

56 G. Hettiarachchi, D. Nguyen, J. Wu, D. Lucas, D. Ma, L. Isaacs and V. Briken, *PLOS One*, 2010, **5**, e10514.

57 D. Das, K. I. Assaf and W. M. Nau, *Front. Chem.*, 2019, **7**, 619.

58 W. Ong, M. Gómez-Kaifer and A. E. Kaifer, *Org. Lett.*, 2002, **4**, 1791–1794.

59 L. A. Wingard, E. C. Johnson and J. J. Sabatini, *Tetrahedron Lett.*, 2016, **57**, 1681–1682.

60 M. Achard, M. Mosrin, A. Tenaglia and G. Buono, *J. Org. Chem.*, 2006, **71**, 2907–2910.

61 H. D. Patel, T. H. Tran, C. J. Sumby, L. F. Pašteka and T. Fallon, *J. Am. Chem. Soc.*, 2020, 142, 3680–3685.

62 R. O. Hutchins, D. Masilamani and C. A. Maryanoff, *J. Org. Chem.*, 1976, **41**, 1071–1073.

63 D. Yang, Y. Zhu, N. Yang, Q. Jiang and R. Liu, *Adv. Synth. Catal.*, 2016, **358**, 1731–1735.

64 M. B. Smith and J. March, *March's Advanced Organic Chemistry Reactions, Mechanisms, and Structure*, 6th Edition., John Wiley and Sons, 2007.

65 *US Pat.,* WO2022159430, 2022.

66 C. Dohmen, H. Ihmels and T. Paululat, *Eur. J. Org. Chem.*, 2022, e20221172.

67 R. O. McCourt and E. M. Scanlan, *Org. Lett.*, 2019, **21**, 3460–3464.

68 S. Munawar, A. F. Zahoor, S. M. Hussain, S. Ahmad, A. Mansha, B. Parveen, K. G. Ali and A. Irfan, *Heliyon*, 2024, **10**, e23416.

69 A. Jordan, K. D. Whymark, J. Sydenham and H. F. Sneddon, *Green Chem.,* 2021, **23**, 6405–6413.

70 B. Neises and W. Steglich, *Angew. Chem. Int. Ed. Engl.*, 1978, **17**, 522–524.

71 S. Ikeyama and Y. Amao, *ChemCatChem*, 2017, **9**, 833–838.

72 D. Seyferth, R. S. Marmor and P. Hilbert, *J. Org. Chem.*, 1971, **36**, 1379–1386.

73 J. C. Gilbert and U. Weerasooriya, *J. Org. Chem.*, 1982, **47**, 1837–1845.

74 N. F. Orourke and G. C. Micalizio, *Org. Lett.*, 2016, **18**, 1250–1253.

75 N. Zhou, Q. Shi and Z. Xie, *Chin. J. Org. Chem.*, 2014, **34**, 1104–1109.

76 M. Yamaguchi, Y. Nobayashi and I. Hirao, *Tetrahedron*, 1984, **40**, 4261–4266.

77 W. König, *J. Prakt. Chem.*, 1904, **69**, 105–137.

78 S. Kunugi, T. Okubo and N. Ise, *J. Am. Chem. Soc.*, 1976, **98**, 2282–2287.

79 Z. Chu, Y. Han, P. Král and R. Klajn, *Angew. Chem. Int. Ed.*, 2018, **57**, 7023–7027.

80 J. P. Lutz, O. Davydovich, M. D. Hannigan, J. S. Moore, P. M. Zimmerman and A. J. McNeil, *J. Am. Chem. Soc.*, 2019, **141**, 14544–14548.

81 B. Alcaide, P. Almendros and R. Rodríguez-Acebes, *J. Org. Chem.*, 2002, **67**, 1925–1928.

82 O. Yahiaoui, L. F. Pašteka, B. Judeel and T. Fallon, *Angew. Chem. Int. Ed.*, 2018, **57**, 2570–2574.

83 J. Yi, X. Lu, Y. Y. Sun, B. Xiao and L. Liu, *Angew. Chem. Int. Ed.*, 2013, **52**, 12409–12413.

PUBLISHED PAPERS

Chemical Science

ROYAL SOCIETY OF CHEMISTRY

EDGE ARTICLE

View Article Online
View Journal

Check for updates

Cite this: DOI: 10.1039/d4sc03700f

All publication charges for this article have been paid for by the Royal Society of Chemistry

Received 6th June 2024
Accepted 23rd August 2024

DOI: 10.1039/d4sc03700f

rsc.li/chemical-science

A guide to bullvalene stereodynamics†

Robert A. Ives, ‡[ab] William Maturi,‡[ab] Matthew T. Gill, [a] Conor Rankine *[a] and Paul R. McGonigal *[ab]

Here, we analyze the stereodynamic properties of bullvalenes using principal moments of inertia and exit vector plots to draw comparisons with commonly used ring systems in medicinal chemistry. To aid analyses, we first classify (i) the four elementary rearrangement steps available to substituted bullvalenes, which (ii) can be described by applying positional descriptors (α, β, γ, and δ) to the substituents. We also (iii) derive an intuitive equation to calculate the number of isomers for a given bullvalene system. Using DFT-modelled structures for di-, tri-, and tetrasubstituted bullvalenes, generated using a newly developed computational tool (*bullviso*), we show that their 3D shapes and the exit vectors available from the bullvalene scaffold make them comparable to other bioisosteres currently used to replace planar aromatic ring systems in drug discovery. Unlike conventional ring systems, the shapeshifting valence isomerism of bullvalenes gives rise to numerous shapes and substituent relationships attainable as a concentration-independent dynamic covalent library from a single compound. We visualize this property by applying population weightings to the principal moments of inertia and exit vector analyses to reflect the relative thermodynamic stabilities of the available isomers.

Introduction

The $C_{10}H_{10}$ cage bullvalene (BV, Fig. 1a) fluctuates between 1 209 600 degenerate isomers through rapid and reversible strain-promoted Cope rearrangements.[1] There are now several useful synthetic methods available to prepare substituted derivatives of BV,[1c,2] which fluctuate between nondegenerate constitutional isomers (Fig. 1) with distinct shapes. This 'shapeshifting' property of substituted BVs and other fluxional molecules has presented opportunities for their inclusion as dynamic structural units in functional molecules[3] and materials, such as chemical sensors,[2d,4] fluorophores,[5] metal complexes,[6] components of electromechanical systems,[7] rigid-rod polymers,[8] and antibiotics.[9]

In general, building blocks with rigid three-dimensional (3D) structures are key components of materials, such as metal–organic frameworks[10] and other porous networks.[11] In the context of medicinal chemistry research—particularly for fragment-based drug discovery[12] (FBDD) libraries—it has been acknowledged that drug candidates based on flat or rod-like molecules offer limited shape diversity.[13] Consequently, there is a desire for a greater number of diverse 3D fragments to be included within these libraries to cover more chemical space and, ultimately, to provide better candidates for drug development.[14] One way that this objective can be achieved is by including fragments that possess diverse aliphatic ring systems, particularly as the core ring system is considered the key factor in shape diversity.[13]

The BV ring system has the seemingly contradictory characteristics of, on one hand, being highly dynamic through its reversible Cope rearrangements, while on the other hand, being a rigidly 3D structure. Its tricyclic hydrocarbon skeleton is a shape-persistent structure with substituents projecting outwards at well-defined angles. Therefore, designing effective materials based on BV derivatives requires understanding of their stereodynamics, *i.e.*, their overall 3D shapes, the relative orientations that are accessible to appended substituents, and the relative energies of the isomers at equilibrium.

Here, we quantify the 3D shape diversity accessible from BVs and demonstrate that their fluxional behavior enables them to reversibly access diverse areas of chemical space. We provide a concise guide to the rearrangement processes of substituted BVs and apply computational modelling to categorize and quantify their stereodynamics. To do so, we perform population-weighted principal moment of inertia (PMI)[15] and exit vector (EV)[16] analyses. Much of the analysis can be automated using a new computational tool we have developed, *bullviso*, that generates all the isomers of a given substituted BV, and the input files needed to compute relative energy levels of each isomer. To demonstrate its utility, we apply *bullviso* to examine di-, tri- and tetramethyl BVs. The analysis illustrates that shapeshifting networks of BV derivatives dynamically

[a]Department of Chemistry, University of York, Heslington, York, YO10 5DD, UK. E-mail: paul.mcgonigal@york.ac.uk

[b]Department of Chemistry, Durham University, Lower Mountjoy, Stockton Road, Durham, DH1 3LE, UK

† Electronic supplementary information (ESI) available. See DOI: https://doi.org/10.1039/d4sc03700f

‡ These authors contributed equally.

View Article Online
Chemical Science Edge Article

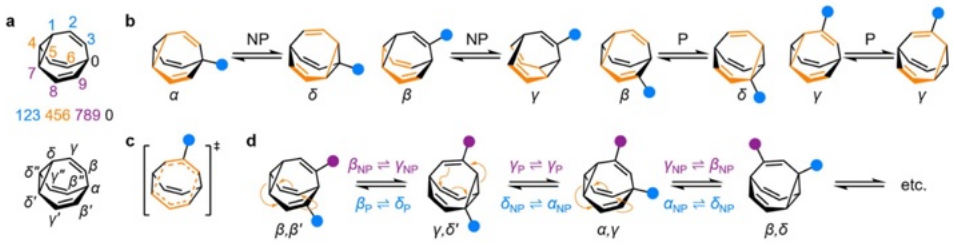

Fig. 1 (a) The BV isomer barcode labelling system, top, and relative positional labels, bottom. (b) The possible exchange processes following one Cope rearrangement step, enumerated for each BV position. Full isomerization requires sequential steps that include (P = participating) and exclude (NP = non-participating) the substituent in the rearranging 1,5-hexadiene motif (shown in orange).[1b] (c) Illustration of the higher symmetry in the transition state for $\gamma_P \rightleftharpoons \gamma_P$ Cope rearrangement relative to the ground state. (d) The partial isomer network of a hetero-disubstituted BV showing the positional exchange arising from three sequential Cope rearrangement steps.

sample many different areas of chemical space from a single starting compound. They do so by positioning their substituents at a range of angles, extending beyond those typically found in *cis*-disubstituted rings, while maintaining a higher degree of sphericity than most common ring systems found in biologically active molecules.

Results and discussion

Given the large number of possible BV isomers, a method for naming them is essential for any discussion involving their interconversion. Bode and coworkers developed an elegant barcode labelling system that can be parsed by computer algorithms to construct a full network map for interconversion of all the non-degenerate isomers of a substituted BV – a task that is otherwise impractical to do by hand. Each digit of the barcode represents one of the carbon atoms in the BV structure (Fig. 1a) and each type of substituent is given a numeral, enabling each isomer to be described with a unique numeric code (see examples in Fig. 2).[17] Importantly, this system enables isomer information to be coded unambiguously. But while this naming system is ideally suited to comprehensively describing the positions of all substituents in any given isomer, its high level of detail is not always needed. Indeed, perhaps because the length of the barcodes and their unfamiliar appearance compared to typical nomenclature for organic structures, there has been a tendency in the literature to name bullvalene isomers with individual labels (such as numbers or letters, *e.g.*, isomer A, isomer B, *etc.*) that lack structural information. Therefore, we suggest that Greek letter locants be used as relative positional labels for succinctly discussing distinct positions in the BV structure and their relationships to one another through Cope rearrangement steps. The threefold rotational symmetry of the parent BV scaffold reduces its number of chemically inequivalent positions to four, which are labelled as α–δ (Fig. 1a) starting from α as the apical position, *i.e.*, the unique sp^3-C, to δ as the cyclopropyl position. The olefin positions, which are typically the energetically favored sites for any non-hydrogen substituents,[2] are labelled as β and γ. Prime and double prime labels can be used distinguish the same locants on different 'arms' of the BV.§[18] We find that this labelling system is a useful shorthand that is complementary to the more detailed barcode system. Where appropriate, both systems are used below.

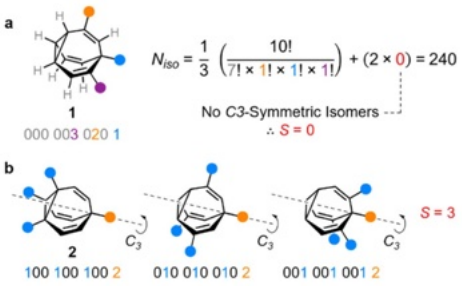

Fig. 2 Structural formulae and isomer barcodes of (a) one of the 240 unique isomers of BV **1**, showing the calculation of N_{iso}, and (b) the three C_3-symmetric isomers of BV **2** that are accounted for by a correction factor of $S = 3$.

Elementary types of positional exchange

Each Cope rearrangement occurs on one of the three 1,5-hexadiene 'faces', involving two arms of the BV. The positions of the BV that are part of the 1,5-hexadiene motif undergoing a given Cope rearrangement can be referred to as participating sites (P), while the other four positions are non-participating sites (NP). Whether a substituent is located on a P or a NP site determines its resulting position following isomerization (Fig. 1b). The α position is never part of the 1,5-hexadiene motif, so it is always considered to be a NP site. On the other hand, for each of the other sites (β, γ, and δ), there exist two potential positional outcomes following a single rearrangement step.

Applying the α–δ and P/NP labels, it becomes clear that there are just four elementary types of positional exchange that occur during any Cope rearrangement step, which are illustrated in Fig. 1b using a monosubstituted BV as a model. Firstly, the sole possible outcome for the α position is migration to a newly formed δ position on the NP arm. A substituent at a β position will migrate to a γ position when on a NP arm, whereas P rearrangement exchanges the β position with a δ site. Finally,

a γ substituent remains at a γ position on a P arm following the Cope rearrangement on account of symmetry in the transition state (Fig. 1c). As the Cope rearrangement is reversible, the reciprocal of each of these exchange processes must also occur. Overall, therefore, the elementary types of positional exchange that govern the outcome of any BV rearrangement are (i) $\alpha_{NP} \rightleftharpoons \delta_{NP}$, (ii) $\beta_{NP} \rightleftharpoons \gamma_{NP}$, (iii) $\beta_P \rightleftharpoons \delta_P$, and (iv) $\gamma_P \rightleftharpoons \gamma_P$. These elementary types of positional exchange apply equally to every BV substituent in every isomer, regardless of the total number of substituents or their relative positions. For example, the functional groups of a heterodisubstituted BV migrate relative to one another during sequential Cope rearrangement steps, allowing them to switch from being on separate arms to occupying the same arm and back again (Fig. 1d).

Calculating the number of unique bullvalene permutations

Deriving the total number of unique nondegenerate isomers for a given substitution pattern is one of the most important considerations for the construction of BV interconversion networks. Bode reported a MATLAB code to calculate the number of unique BV isomers.[17] However, taking account of the symmetry present in BVs, it is possible to perform a simple 'back-of-the-envelope' calculation to determine the number of isomers for a given BV system using eqn (1):

$$N_{iso} = \frac{1}{3}\left(\frac{10!}{\prod_{a=1}^{A} N_a!} + 2S\right) \quad (1)$$

where N_{iso} is the number of unique nondegenerate isomers (enantiomers are considered to be distinct from one another), N_a is the number of occurrences of a given type of substituent, $\prod_{a=1}^{A} N_a!$ the product of multiplying together the factorial of this term for each unique type of substituent (including hydrogen substituents), and S is a correction factor that accounts for the C_3 symmetry of BV and has a value of 0, 1, 3, or 6. In the same manner as the isomer barcode system, eqn (1) treats each substituent as a number within a group of ten numbers.

Combinatorics is used to derive the total number of ways in which these substituents can be ordered. The 1/3 multiplier adjusts for the fact that the parent BV has C_3 symmetry, offsetting triple counting in the $10!/\prod_{a=1}^{A} N_a!$ term that arises for structures related by rotation. A further correction factor, $2S$, readjusts for the BV isomers that have three identically substituted arms and so are represented just once each in the $10!/\prod_{a=1}^{A} N_a!$ term. S is the number of ways that the substituents can be arranged around the BV core to retain its C_3 symmetry, or in other words, where all three arms of the BV possess identical substitution patterns.

Taking heterotrisubstituted BV **1** as a worked example (Fig. 2a), there are seven hydrogen substituents and three distinct non-hydrogen substituents (colored circles). Therefore, the product operation in the denominator of the equation is 7! × 1! × 1! × 1!. The substituents on **1** cannot be arranged in any pattern that gives C_3 symmetry, hence $S = 0$ and applying eqn (1) gives $N_{iso} = 240$.

Taking structure **2** (Fig. 2b) as a second worked example, there are six hydrogens, a substituent type that occurs three times (blue circles), and another substituent type that occurs just once (orange circle), so the product operation is 6! × 3! × 1!. However, three of the substituents of **2** are the same and thus there are three different ways in which they can be arranged such that the BV possesses C_3 symmetry, which are shown in Fig. 2b. These C_3-symmetric isomers arise when the unique substituent is at the α position and the three identical substituents occupy the same position on each of the three BV arms, *i.e.*, either all β, all γ, or all δ. Therefore, $S = 3$ for **2** and applying eqn (1) gives $N_{iso} = 282$.

There are 42 possible variations of substituted BVs having different numbers and identities of substituents. Based on all of these possible substituent patterns, a comprehensive reference table is provided in the ESI (Table S1)† where this method and eqn (1) have been applied to generate N_{iso} and S, as well as the numbers of achiral and chiral isomers.

Generating bullvalene isomers using *bullviso*

We have developed a Python3 code, *bullviso*,[19] which interfaces with RDKit[20] to generate the Cartesian coordinates of substituted BVs. It is publicly available under the GNU Public License (GPLv3) on GitLab. The *bullviso* code generates exhaustively all possible isomer barcodes for a substituted BV and filters out the non-unique isomer barcodes according to the protocol outlined by Bode.¶[17] It also outputs the connectivity between isomers, which can be used to generate interconversion network diagrams.[21] Cartesian coordinates sampling the constitutional isomers of the substituted BV are generated by grafting given substituents (supplied as SMILES strings) onto a BV to produce a unique structure corresponding to each isomer barcode. The *bullviso* code generates up to N configurational and conformational isomers according to the experimental-torsion distance geometry with 'basic knowledge' embedding approach (ETKDGv3)[22] implemented in RDKit. These configurational and conformational isomers are then (pre-)optimized using the Universal Force Field[23] and the M lowest-energy isomers are outputted. Cartesian coordinates can be written in *xyz* file format or, alternatively, as pre-prepared inputs for computational chemistry packages, *e.g.*, Gaussian[24] or Orca,[25] to enable subsequent optimization and analysis at higher levels of theory.

Principal moments of inertia analysis

The PMI analysis developed by Schwartz[15] has been used as a straightforward and quantitative method to assess the shape diversity of potential pharmaceutical building blocks.[12,13] Typical PMI plots are constructed (i) for the lowest energy conformer of any given compound to compare either the inherent shapes of an array of molecules[26] or (ii) for a range of conformers to gain insight into conformational diversity of a limited number of molecules.[14] We selected di-, tri-, and tetrasubstituted BVs (Fig. 3a) as targets to examine shape diversity present in dynamic BV networks arising from rapid constitutional isomerism. To enable us to focus our analysis on the dynamic shape that is inherent to the functionalized BV scaffold itself rather than any potential conformational processes in the

View Article Online
Chemical Science Edge Article

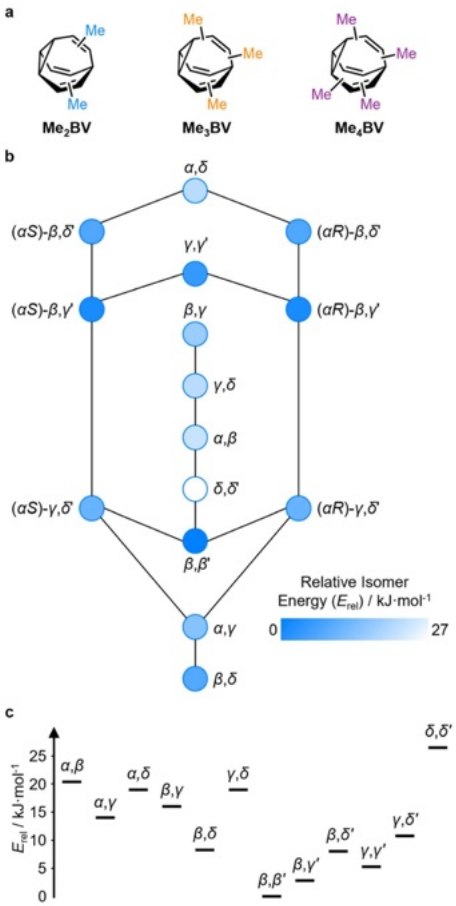

Fig. 3 (a) Structural formulae of methyl-substituted BVs. (b) The population-weighted isomer interconversion network calculated for Me_2BV (PBE0-D3/def2-SV(P)). The diagram has a mirror plane with achiral isomers down the middle and enantiomeric pairs of chiral structures on either side. Chiral structures are labelled with an *R*/*S* descriptor according to the stereogenic α position. (c) A graph of the relative energies of Me_2BV isomers. Pairs of enantiomers are isoenergetic, so are represented just once.

attached substituents, we chose to investigate the methyl-substituted derivatives, *i.e.*, dimethyl- (**Me_2BV**), trimethyl- (**Me_3BV**), and tetramethylbullvalene (**Me_4BV**).

We first generated all possible isomers of the methyl-substituted BVs using *bullviso*, then optimized their geometries by performing density functional theory (DFT) calculations. The PBE0 (ref. 27) functional with Grimme's D3 dispersion correction[28] and the def2-SV(P)[29] basis set were deemed suitable for modelling the energetics of BV systems. Using this level of theory, we constructed isomer interconversion networks and predicted relative isomer populations for **Me_2BV** (Fig. 3), **Me_3BV** (Fig. S1†), and **Me_4BV** (Fig. S2†), which have 15, 42, and 72 unique isomers, respectively.[21] For each of these isomers, we calculated the three principal moments of inertia (I_1, I_2, and I_3 in ascending order) using a KNIME[30] Vernalis[31] chemoinformatic protocol, then used these values to calculate normal PMI ratios, NPR1 (I_1/I_3) and NPR2 (I_2/I_3). The resulting PMI plots (Fig. 4a–g) follow the standard layout (Fig. 4) where the vertices are defined by NPR values associated with rod-like shape [NPR1 = 0, NPR2 = 1], disc-like shape [NPR1 = 0.5, NPR2 = 0.5], and spherical shape [NPR1 = 1, NPR2 = 1]. The diagrams are also labelled with representative structures for each vertex, *i.e.*, butadiyne (rod-like), benzene (disc-like), and adamantane (sphere-like). To guide the eye, parallel lines on the PMI plot correspond to increments of 0.1 in ∑NPR values (∑NPR = NPR1 + NPR2) between the limits of 1.0 and 2.0. The points that lie furthest from the rod–disc axis, *i.e.*, toward the top right of the diagram, are associated with greater sphericity.

The PMI plot of **Me_2BV** (Fig. 4a) shows the structural diversity in the population of constitutional isomers, which fall in the range $1.44 \leq \sum NPR \leq 1.57$. For ease of reference, isomers in Fig. 4a are labelled using the α–δ locants, however, the full isomer barcodes are also given in the ESI (Tables S2–S4).† Darker colored points indicate overlap of enantiomers on the diagram as they give identical PMI coordinates, *e.g.*, for (±)-β,γ'-**Me_2BV**.

As the unique isomers of a substituted BV are non-degenerate, they are present in varying concentrations at equilibrium. To visualize how this property influences which molecular shapes are most prevalent, we made PMI plots with the data points scaled by the Boltzmann distribution at 298 K. A population-weighted PMI plot (Fig. 4d) shows that the shape-shifting network of **Me_2BV** consists predominantly (~93%) of the four lowest-energy isomers, which include two achiral isomers, β,β'-**Me_2BV** and γ,γ'-**Me_2BV**, and the enantiomeric pair of (±)-β,γ'-**Me_2BV**. The β,δ-**Me_2BV**, (±)-β,δ'-**Me_2BV**, and (±)-γ,δ'-**Me_2BV** isomers are also present in ~0.5–2% each (Table S2†), leaving ~0.3% of the remaining six isomers combined.

The introduction of more substituents to the BV scaffold (*i.e.*, in **Me_3BV** and **Me_4BV**) increases structural variety and overall sphericity (Fig. 4b and c). Several structures extend beyond $\Sigma NPR > 1.6$, reaching maxima of 1.89 and 1.90 for **Me_3BV** and **Me_4BV**, respectively. In both cases, the PMI distributions are markedly broader than that of **Me_2BV**, spanning $1.3 \leq \Sigma NPR \leq 1.9$, which reflects the change in shape that can occur when several substituents are located close to one another around the BV scaffold (giving rod-like shape) or are spread around the BV evenly to maintain sphericity. Like **Me_2BV**, a subset of the **Me_3BV** and **Me_4BV** constitutional isomers are most prevalent in the network at equilibrium. The 14 most stable isomers of **Me_3BV** are within ~15 kJ mol^{-1} of one another, so they are each present in amounts ranging from 0.1% to 60% (Table S3†). Similarly, there are 12 isomers of **Me_4BV** present in proportions of 0.1% to 52%.‖[32] The energetically preferred isomers are those with most of their substituents at β and γ positions, and in which substituents do not neighbor one another directly.

View Article Online
Edge Article Chemical Science

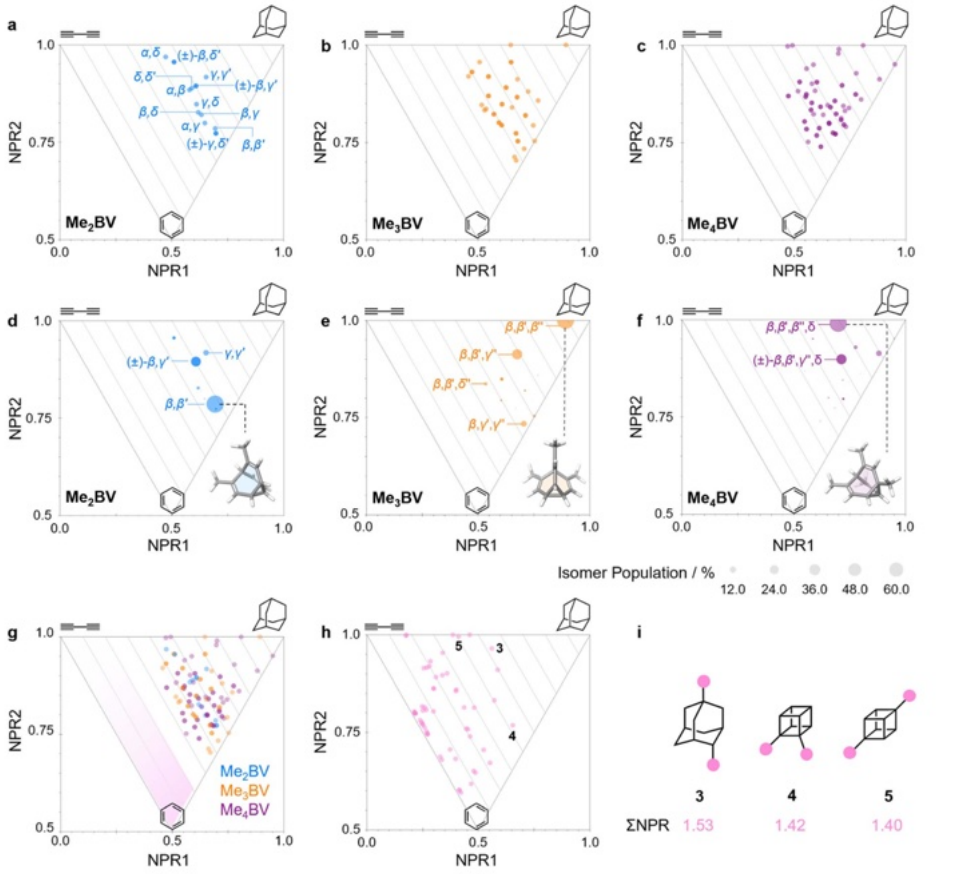

Fig. 4 (a–c) PMI plots for the shapeshifting networks of (a) **Me$_2$BV**, (b) **Me$_3$BV**, and (c) **Me$_4$BV**. Substituent positional labels are given for **Me$_2$BV**. For clarity, these labels are not shown on the plots for **Me$_3$BV** and **Me$_4$BV**. See Tables S6 and S7† for labelled data. (d–e) Population-weighted PMI plots for the shapeshifting networks of (d) **Me$_2$BV**, (e) **Me$_3$BV**, and (f) **Me$_4$BV** where the data points are scaled by calculated Boltzmann distributions at 298 K (PBE0-D3/def2-SV(P)). The modelled structure of the lowest-energy isomer for each BV is shown inset. (g) An overlay of the PMI plots of **Me$_2$BV** (blue), **Me$_3$BV** (orange), and **Me$_4$BV** (purple) showing that none of the isomers have ΣNPR values close to the rod–disc axis. (h) A PMI plot for common ring systems. See Table S8† for compound identities. (i) Structural formulae and ΣNPR values for 1,4-dimethyladamantane (**3**), 1,2-dimethylcubane (**4**), and 1,4-dimethylcubane (**5**).

Therefore, the population-weighted PMI plots (Fig. 4e and f) show that the most spherical isomers are present in higher populations.

To contextualize the PMI data of the functionalized BVs, it is useful to compare the **Me$_2$BV** isomers (Fig. 4a) to a small representative library of rings prominent in pharmaceuticals (Fig. S3†).[33] PMI analysis of the dimethyl derivatives of these pharmaceutical building blocks (Fig. 4h) shows the relative lack of 3D diversity in most currently used ring systems.[32] The majority of compounds are close to the rod–disc axis (ΣNPR ≤ 1.3) with the notable exception of a few structures such as substituted adamantanes and cubanes **3–5** (Fig. 4i), which are increasingly popular as more spherical replacements for flat ring systems.[34] The PMI ratios of the **Me$_2$BV** isomers ($1.44 \leq \sum\text{NPR} \leq 1.57$) and **3–5** ($1.40 \leq \sum\text{NPR} \leq 1.53$) are nearly identical, suggesting that BVs could be similarly useful as 3D scaffolds in medicinal chemistry. BVs have the additional, unique property of spontaneously sampling different structures through their Cope rearrangements and are now readily accessible by short synthetic routes.[1c,2]

Exit vector analysis

EV plots are used to analyze the relationship between two substituents attached to a central scaffold.[16] They are useful in

View Article Online
Chemical Science Edge Article

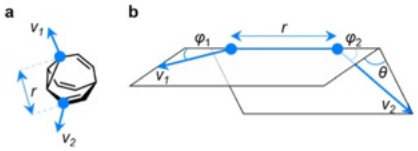

Fig. 5 (a) The vectors v_1 and v_2 for two substituent attachment points on a BV (shown for (αS)-γ,δ′-**Me$_2$BV**) which are defined by (b) the geometric parameters r, φ_1, φ_2, and θ.

FBDD and bioisostere studies to show the geometries that are available when elaborating a structure outward starting from different ring systems. The relative orientations (Fig. 5a) of bonds emanating from the scaffold are defined as the exit vectors, v_1 and v_2. They are described (Fig. 5b) by four geometric parameters; the distance between the functionalized carbon atoms of the scaffold (r), the dihedral angle of the vectors (θ), and the plane angles of each vector (φ_1 and φ_2).[16] Like PMI plots, the EV plot for a single molecule possesses only one data point if a compound is conformationally rigid, whereas multiple points are plotted to show the effects of conformational flexibility or to compare multiple molecules with different covalent structures on a single diagram.

We constructed EV plots (Fig. 6) for the C–Me bonds of the methyl-substituted BVs to quantify the stereodynamics of the BV scaffold, *i.e.*, the relative orientations and spacings of its substituents. Typically, EV plots span θ values of 0° to 180°,

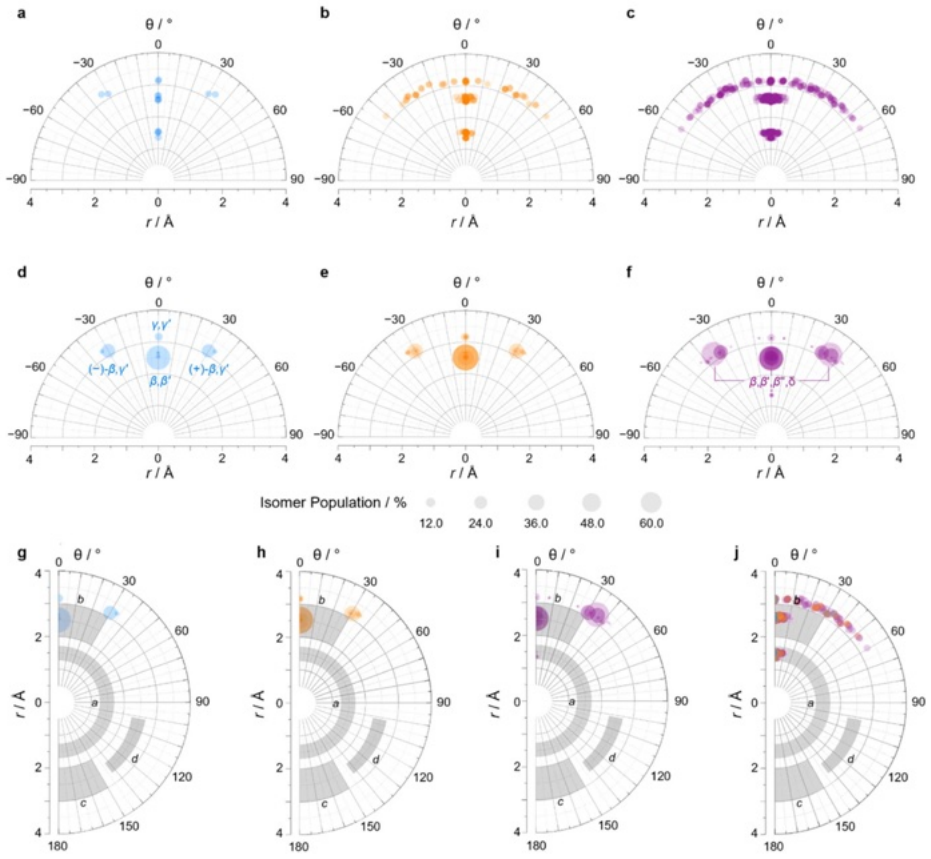

Fig. 6 (a–c) Distance–dihedral angle EV plots and (d–i) Boltzmann population-weighted distance–dihedral angle EV plots (298 K, PBE0-D3/def2-SV(P)) for the isomers of (a, d and g) **Me$_2$BV**, (b, e and h) **Me$_3$BV**, and (c, f and i) **Me$_4$BV**. (j) Overlaid distance *versus* dihedral angle EV plot of all three methyl-substituted BVs. (g–j) Plots include characteristic areas of EV plots in grey that correspond to those found in disubstituted cycloalkanes,[16] a = *cis*-1,2-disubstituted cyclopropanes, b = *cis*-1,3-disubstituted aliphatic rings and *cis*-1,4-disubstituted cyclohexanes, c = *trans*-1,4-disubstituted cyclohexanes, d = *trans*-1,3-disubstituted cyclopentanes and cyclohexanes.

where all dihedral angles are defined as being positive. For BV isomer networks, however, it is also beneficial to extend the EV plots to include negative values of θ, allowing pairs of enantiomers that are present in the dynamic equilibrium to be shown on the same diagram (*e.g.*, (±)-β,γ′-**Me$_2$BV**, Fig. 6d), as well as revealing enantiotopic relationships between substituents at equivalent positions on different arms (*e.g.*, the β′ and β″ positions of β,β′,β″,δ-**Me$_4$BV**, Fig. 6f). As the cage-like structure of BV imposes dihedral angles between −60° and +60°, plotting θ from −90° to +90° (Fig. 6a–f) gives an informative representation of the data.

An EV plot of the **Me$_2$BV** isomers reveals C–Me dihedral angles clustered in two regions of either $\theta \sim 0°$ or $\theta \sim \pm 30°$. The points in the former region span distances of $r \sim 1.3$–3.1 Å (Fig. 6a). The majority of coplanar EVs ($\theta \sim 0°$) arise from isomers that are either functionalized (i) at two different positions on the same arm of the BV or (ii) at the same type of position on BV on different arms, *e.g.*, β,β′-**Me$_2$BV**, accounting for nine of the 15 possible substitution patterns. The four points at $\theta \sim \pm 30°$ correspond to two of the three enantiomer pairs of the isomers with differently substituted arms ((±)-β,γ′-**Me$_2$BV** and (±)-β,δ′-**Me$_2$BV**). The final enantiomer pair, (±)-γ,δ′-**Me$_2$BV**, has coplanar EVs of $\theta = \pm 0.5°$. Boltzmann population-weighted EV analysis of **Me$_2$BV** (Fig. 6d) reveals that the most populated isomers β,β′-**Me$_2$BV** ($r = 2.5$ Å, $\theta = 0°$, $p = 53\%$) and (±)-β,γ′-**Me$_2$BV** ($r = 3.1$ Å, $\theta = 30°$, $p = 17\%$ for each enantiomer) exhibit substantial changes in the dihedral angles between the C–Me EVs.

Standard EV plots of **Me$_2$BV**, **Me$_3$BV**, and **Me$_4$BV** spanning θ values of 0° to 180° (Fig. 6g–j) are also shown to aid comparison to the four regions, a–d, determined by Grygorenko *et al.* that are characteristic of EVs found in common disubstituted cycloalkanes.[16] Note that these four regions were determined by plotting the EVs found for ∼2900 cycloalkanes in the Cambridge Structural Database, so they represent the span of angles that are obtained using a variety of functional groups. The majority of data points for the BV isomers fall within the a or b region. EVs in region *a* are characteristic of *cis*-1,2-disubstituted cyclopropyl compounds while region b is associated with *cis*-1,3-disubstituted and *cis*-1,4-disubstituted aliphatic rings.[16] The presence of EVs in these regions for BV is expected, therefore, as the structure of BV contains these motifs.

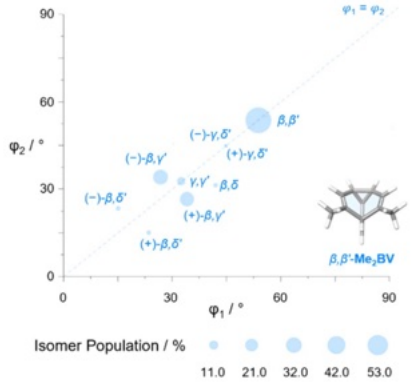

Fig. 7 The plane angles subtended by C–Me EVs in the nine lowest energy isomers of **Me$_2$BV**. Data points are scaled according to the Boltzmann population at 298 K (PBE0-D3/def2-SV(P)).

The diversity of EVs arising from the shapeshifting isomerization becomes even more apparent when considering the plane angles subtended by the C–Me EVs, φ_1 and φ_2 (Fig. 5), of the **Me$_2$BV** isomers. There is a spread of possible plane angles spanning from 15° to 60° found in the most energetically accessible isomers (Fig. 7), extending to 67° for higher-energy isomers (Fig. S4†). Therefore, sequential Cope rearrangements between isomers significantly alter the relative orientations of substituents in space, granting BV its unique stereodynamic properties.

As the cage-like geometry of the BV scaffold is well defined and insensitive to the addition of more substituents, **Me$_3$BV** and **Me$_4$BV** would be expected to exhibit similar EVs between pairs of their C–Me bonds as those found for **Me$_2$BV**. This generalization applies when considering the plane angles (Fig. S7–S14†) and distances between substituents. It is also the case for the dihedral angles, but only when considering the most energetically favorable isomers (Fig. 6e and f).

A wider spread of dihedral angles (Fig. 6b and c) that extends beyond region b to angles between −60° and +60° is apparent when the complete isomer networks of **Me$_3$BV** and **Me$_4$BV** are taken into account (Fig. 6j), including isomers that lie at higher energy. Significant deviations from the 0° and ±30° dihedral angles arise to minimize unfavorable steric interactions when substituents are close to one another in space. For the di-, tri-, and tetrasubstituted BVs investigated here, the isomers that bear methyl groups at neighboring positions are relatively high in energy, so are not very prevalent. The most significant (albeit still low) populations of such isomers are present for **Me$_4$BV** because of the increased likelihood of substituents being close to one another in the tetrasubstituted system, such as the ∼0.1% of β,β′,γ,δ′-**Me$_4$BV**, which has $\theta = 51°$ between its β and δ′ methyl groups. But more highly substituted BVs, or those bearing bulkier substituents, will likely have larger isomer populations with varied dihedral angles.

Of course, shape differentiation between the orientations of functional groups attached to BV diminishes if conformationally flexible linking groups are used, so elaborating BVs with short rigid groups[2c,8b,35] or fused rings[36] may be advantageous. Each of the molecular shapes described by the PMI (Fig. 4a–c) and EV plots (Fig. 6a–c and S4–S14†) correspond to accessible states for the methyl-substituted BVs, demonstrating that a single BV derivative can cover a significant region of chemical space on its own. Heterosubstituted systems with varied functional groups possess still greater structural diversity. Although realizing the full extent of this shape diversity in some BVs may require higher-energy isomers to be invoked, it is important to note that, in the contexts of drug discovery and materials chemistry, noncovalent bonding interactions with biomolecular targets, confinement effects, or forces imposed by the surrounding medium may compensate for the moderately low

View Article Online
Chemical Science Edge Article

energy differences between isomers to amplify certain BV structures within the shapeshifting network.[2d,4,6,37] Therefore, isomers that have otherwise low populations should not be dismissed, as they may become more significant components of the network in the right environment.

Conclusions

In summary, the appealing complexity of dynamic BV networks is built upon four types of positional exchange between different sites around the BV scaffold. Isomers in these networks tend to position functional groups with dihedral angles of either 0° or 30° and at a range of plane angles between 15° and 60°, originating from vertices of the BV that are spaced apart by 1.3–3.1 Å. The BV scaffold itself has quasi-spherical overall structure. Functionalized derivatives generally retain this characteristic, particularly because the most energetically favored isomers that emerge are typically those that space substituents out from one another around the scaffold. PMI analysis shows that they have a similar degree of sphericity as adamantane and cubane building blocks, while they orient functional groups at vectors that are characteristic of *cis*-disubstituted cycloalkanes. Greater shape diversity emerges with the inclusion of more substituents, not just because it gives rise to greater numbers of unique isomers, but also because interactions between neighboring groups reduces the predisposition toward them being coplanar with one another, giving more varied EVs. Currently, the most accessible syntheses of BVs[1c,2a–c] produce structures with two or three functional groups attached, implying it remains advantageous to develop new synthetic approaches that give efficient access to higher-order multifunctional BVs. The analysis described here, which is accelerated using *bullviso*, can be exploited to prescreen computationally the diversity and accessibility of molecular shapes in complex BV libraries.

Data availability

Coordinates of optimized geometries, PMIs and EVs are available in the ESI.† The Python code for *bullviso* is publicly available under the GNU Public License (GPLv3) on GitLab.[19]

Author contributions

Conceptualization: RAI, WM, PRM. Methodology: RAI, WM, CR. Software: CR. Writing: RAI, WM, MTG, CR, PRM. Funding acquisition: PRM.

Conflicts of interest

There are no conflicts to declare.

Acknowledgements

We thank James Firth and Prof Peter O'Brien for useful discussions. R. A. I. and P. R. M. acknowledge a Leverhulme Trust Research Project Grant (RPG-2020-218). W. M., M. G. and P. R. M (EP/T518001/1, EP/V047817/2, EP/V040049/2) thank the EPSRC for funding. We acknowledge the University of York High Performance Computing service, Viking.

Notes and references

§ The use of Greek letter locants to label relative positions and prime symbols to label identical rings in multiple ring systems follows IUPAC conventions.[18]

¶ A Fortran code to generate input geometries of BV isomers is mentioned in ref. 2a but it has not been made publicly available.

‖ A consequence of there being more possible isomers in the networks of highly substituted BVs is that, statistically, any individual isomer is expected to be present in lower concentrations. However, certain BV systems, *e.g.*, hexasubstituted BVs, are biased toward a relatively small number of isomers, which act as energetic sinks that also slow the rate of exchange.[22]

1 (*a*) W. von Eggers Doering and W. R. Roth, *Tetrahedron*, 1963, **19**, 715–737; (*b*) G. Schröder, J. F. M. Oth and R. Merényi, *Angew Chem. Int. Ed. Engl.*, 1965, **4**, 752–761; (*c*) S. Ferrer and A. M. Echavarren, *Synthesis*, 2019, **51**, 1037–1048; (*d*) A. N. Bismillah, B. M. Chapin, B. A. Hussein and P. R. McGonigal, *Chem. Sci.*, 2020, **11**, 324–332; (*e*) P. K. Saha, T. Tran Ngoc, P. R. McGonigal and J. F. Teichert, *Nat. Synth.*, 2024, **3**, 684–697.

2 (*a*) O. Yahiaoui, L. F. Pašteka, B. Judeel and T. Fallon, *Angew. Chem., Int. Ed.*, 2018, **57**, 2570–2574; (*b*) O. Yahiaoui, L. F. Pašteka, C. J. Blake, C. G. Newton and T. Fallon, *Org. Lett.*, 2019, **21**, 9574–9578; (*c*) H. D. Patel, T.-H. Tran, C. J. Sumby, L. F. Pašteka and T. Fallon, *J. Am. Chem. Soc.*, 2020, **142**, 3680–3685; (*d*) J. F. Teichert, D. Mazunin and J. W. Bode, *J. Am. Chem. Soc.*, 2013, **135**, 11314–11321.

3 A. Sanchez, A. Gurajapu, W. Guo, W.-Y. Kong, C. J. Laconsay, N. S. Settineri, D. J. Tantillo and T. J. Maimone, *J. Am. Chem. Soc.*, 2023, **145**, 13452–13461.

4 (*a*) A. R. Lippert, V. L. Keleshian and J. W. Bode, *Org. Biomol. Chem.*, 2009, **7**, 1529–1532; (*b*) A. R. Lippert, A. Naganawa, V. L. Keleshian and J. W. Bode, *J. Am. Chem. Soc.*, 2010, **132**, 15790–15799.

5 C. Dohmen, H. Ihmels and T. Paululat, *Eur. J. Org Chem.*, 2022, **2022**, e202201172.

6 (*a*) A. P. Birvé, H. D. Patel, J. R. Price, W. M. Bloch and T. Fallon, *Angew. Chem., Int. Ed.*, 2022, **61**, e202115468; (*b*) C. Dohmen, T. Paululat and H. Ihmels, *Chem.–Eur. J.*, 2024, **30**, e202304311.

7 J. R. Reimers, T. Li, A. P. Birvé, L. Yang, A. C. Aragonès, T. Fallon, D. S. Kosov and N. Darwish, *Nat. Commun.*, 2023, **14**, 6089.

8 (*a*) D. J. Tantillo and R. Hoffmann, *Acc. Chem. Res.*, 2006, **39**, 477–486; (*b*) M. N. Pomfret, P. B. Sun, Z. Huang, A. C. Freund, T. Miyoshi and M. R. Golder, *Angew. Chem., Int. Ed.*, 2023, **62**, e202301695; (*c*) P. B. Sun, M. N. Pomfret, M. J. Elardo, A. Suresh, Á. Rentería-Gómez, R. F. Lalisse, S. Keating, C. Chen, S. L. Hilburg, P. Chakma, Y. Wu, R. C. Bell, S. J. Rowan, O. Gutierrez and M. R. Golder, *J. Am. Chem. Soc.*, 2024, **146**, 19229–19238.

9 A. Ottonello, J. A. Wyllie, O. Yahiaoui, S. Sun, R. A. Koelln, J. A. Homer, R. M. Johnson, E. Murray, P. Williams, J. R. Bolla, C. V. Robinson, T. Fallon, T. P. Soares da Costa

and J. E. Moses, *Proc. Natl. Acad. Sci. U.S.A.*, 2023, **120**, e2208737120.
10 (*a*) A. E. Baumann, D. A. Burns, B. Liu and V. S. Thoi, *Commun. Chem.*, 2019, **2**, 86; (*b*) Z. Ji, H. Wang, S. Canossa, S. Wuttke and O. M. Yaghi, *Adv. Funct. Mater.*, 2020, **30**, 2000238.
11 (*a*) R.-B. Lin and B. Chen, *Chem*, 2022, **8**, 2114–2135; (*b*) K. Geng, T. He, R. Liu, S. Dalapati, K. T. Tan, Z. Li, S. Tao, Y. Gong, Q. Jiang and D. Jiang, *Chem. Rev.*, 2020, **120**, 8814–8933.
12 (*a*) D. A. Erlanson, S. W. Fesik, R. E. Hubbard, W. Jahnke and H. Jhoti, *Nat. Rev. Drug Discovery*, 2016, **15**, 605–619; (*b*) B. Over, S. Wetzel, C. Grütter, Y. Nakai, S. Renner, D. Rauh and H. Waldmann, *Nat. Chem.*, 2013, **5**, 21–28.
13 (*a*) A. W. Hung, A. Ramek, Y. Wang, T. Kaya, J. A. Wilson, P. A. Clemons and D. W. Young, *Proc. Natl. Acad. Sci. U.S.A.*, 2011, **108**, 6799–6804; (*b*) W. R. J. D. Galloway, A. Isidro-Llobet and D. R. Spring, *Nat. Commun.*, 2010, **1**, 80; (*c*) A. D. Morley, A. Pugliese, K. Birchall, J. Bower, P. Brennan, N. Brown, T. Chapman, M. Drysdale, I. H. Gilbert, S. Hoelder, A. Jordan, S. V. Ley, A. Merritt, D. Miller, M. E. Swarbrick and P. G. Wyatt, *Drug Discov. Today*, 2013, **18**, 1221–1227.
14 T. D. Downes, S. P. Jones, H. F. Klein, M. C. Wheldon, M. Atobe, P. S. Bond, J. D. Firth, N. S. Chan, L. Waddelove, R. E. Hubbard, D. C. Blakemore, C. De Fusco, S. D. Roughley, L. R. Vidler, M. A. Whatton, A. J. A. Woolford, G. L. Wrigley and P. O'Brien, *Chem.–Eur. J.*, 2020, **26**, 8969–8975.
15 W. H. B. Sauer and M. K. Schwarz, *J. Chem. Inf. Comput. Sci.*, 2003, **43**, 987–1003.
16 (*a*) O. O. Grygorenko, D. Demenko, D. M. Volochnyuk and I. V Komarov, *New J. Chem.*, 2018, **42**, 8355–8365; (*b*) O. O. Grygorenko, P. Babenko, D. M. Volochnyuk, O. Raievskyi and I. V. Komarov, *RSC Adv.*, 2016, **6**, 17595–17605.
17 M. He and J. W. Bode, *Org. Biomol. Chem.*, 2013, **11**, 1306–1317.
18 H. A. Favre and W. H. Powell, Nomenclature of Organic Chemistry: IUPAC Recommendations and Preferred Names 2013, *IUPAC Blue book*, RSC Publishing, 2014.
19 bullviso, 2024, **https://gitlab.com/conorrankine/bullviso**.
20 (*a*) RDKit: Open-Source Cheminformatics, **https://rdkit.org**; (*b*) RDKit, 2023, **https://github.com/rdkit/rdkit**.
21 B. M. Gimarc and A. R. Brant, *J. Chem. Inf. Comput. Sci.*, 1994, **34**, 1167–1173.
22 (*a*) S. Riniker and G. A. Landrum, *J. Chem. Inf. Model.*, 2015, **55**, 2562–2574; (*b*) S. Wang, J. Witek, G. A. Landrum and S. Riniker, *J. Chem. Inf. Model.*, 2020, **60**, 2044–2058.
23 A. K. Rappe, C. J. Casewit, K. S. Colwell, W. A. Goddard and W. M. Skiff, *J. Am. Chem. Soc.*, 1992, **114**, 10024–10035.
24 M. J. Frisch, G. W. Trucks, H. B. Schlegel, G. E. Scuseria, M. A. Robb, J. R. Cheeseman, G. Scalmani, V. Barone, G. A. Petersson, H. Nakatsuji, X. Li, M. Caricato, A. V. Marenich, J. Bloino, B. G. Janesko, R. Gomperts, B. Mennucci, H. P. Hratchian, J. V. Ortiz, A. F. Izmaylov, J. L. Sonnenberg, D. Williams-Young, F. Ding, F. Lipparini, F. Egidi, J. Goings, B. Peng, A. Petrone, T. Henderson, D. Ranasinghe, V. G. Zakrzewski, J. Gao, N. Rega, G. Zheng, W. Liang, M. Hada, M. Ehara, K. Toyota, R. Fukuda, J. Hasegawa, M. Ishida, T. Nakajima, Y. Honda, O. Kitao, H. Nakai, T. Vreven, K. Throssell, J. A. Montgomery Jr, J. E. Peralta, F. Ogliaro, M. J. Bearpark, J. J. Heyd, E. N. Brothers, K. N. Kudin, V. N. Staroverov, T. A. Keith, R. Kobayashi, J. Normand, K. Raghavachari, A. P. Rendell, J. C. Burant, S. S. Iyengar, J. Tomasi, M. Cossi, J. M. Millam, M. Klene, C. Adamo, R. Cammi, J. W. Ochterski, R. L. Martin, K. Morokuma, O. Farkas, J. B. Foresman and D. J. Fox, *Gaussian*, Gaussian, Inc., Wallingford CT, 2016.
25 (*a*) F. Neese, *Wiley Interdiscip. Rev. Comput. Mol. Sci.*, 2012, **2**, 73–78; (*b*) F. Neese, *Wiley Interdiscip. Rev. Comput. Mol. Sci.*, 2018, **8**, e1327; (*c*) F. Neese, F. Wennmohs, U. Becker and C. Riplinger, *J. Chem. Phys.*, 2020, **152**, 224108.
26 (*a*) S. P. Jones, J. D. Firth, M. C. Wheldon, M. Atobe, R. E. Hubbard, D. C. Blakemore, C. De Fusco, S. C. C. Lucas, S. D. Roughley, L. R. Vidler, M. A. Whatton, A. J. A. Woolford, G. L. Wrigley and P. O'Brien, *RSC Med. Chem.*, 2022, **13**, 1614–1620; (*b*) P. Garner, P. B. Cox, U. Rathnayake, N. Holloran and P. Erdman, *ACS Med. Chem. Lett.*, 2019, **10**, 811–815.
27 (*a*) C. Adamo and V. Barone, *J. Chem. Phys.*, 1999, **110**, 6158–6170; (*b*) J. P. Perdew, K. Burke and M. Ernzerhof, *Phys. Rev. Lett.*, 1997, **78**, 1396; (*c*) J. P. Perdew, K. Burke and M. Ernzerhof, *Phys. Rev. Lett.*, 1996, **77**, 3865–3868.
28 S. Grimme, J. Antony, S. Ehrlich and H. Krieg, *J. Chem. Phys.*, 2010, **132**, 154104.
29 F. Weigend and R. Ahlrichs, *Phys. Chem. Chem. Phys.*, 2005, **7**, 3297.
30 M. R. Berthold, N. Cebron, F. Dill, T. R. Gabriel, T. Kötter, T. Meinl, P. Ohl, C. Sieb, K. Thiel and B. Wiswedel, *KNIME: The Konstanz Information Miner*, Springer, 2007.
31 S. D. Roughley, *Curr. Med. Chem.*, 2018, **27**, 6495–6522.
32 K. Rebsamen, H. Röttele and G. Schröder, *Chem. Ber.*, 1993, **126**, 1429–1433.
33 (*a*) R. D. Taylor, M. MacCoss and A. D. G. Lawson, *J. Med. Chem.*, 2014, **57**, 5845–5859; (*b*) J. Shearer, J. L. Castro, A. D. G. Lawson, M. MacCoss and R. D. Taylor, *J. Med. Chem.*, 2022, **65**, 8699–8712.
34 (*a*) B. A. Chalmers, H. Xing, S. Houston, C. Clark, S. Ghassabian, A. Kuo, B. Cao, A. Reitsma, C. E. P. Murray, J. E. Stok, G. M. Boyle, C. J. Pierce, S. W. Littler, D. A. Winkler, P. V. Bernhardt, C. Pasay, J. J. De Voss, J. McCarthy, P. G. Parsons, G. H. Walter, M. T. Smith, H. M. Cooper, S. K. Nilsson, J. Tsanaktsidis, G. P. Savage and C. M. Williams, *Angew. Chem., Int. Ed.*, 2016, **55**, 3580–3585; (*b*) L. Wanka, K. Iqbal and P. R. Schreiner, *Chem. Rev.*, 2013, **113**, 3516–3604; (*c*) T. A. Reekie, C. M. Williams, L. M. Rendina and M. Kassiou, *J. Med. Chem.*, 2018, **62**, 1078–1095; (*d*) K. C. Nicolaou, J. Yin, D. Mandal, R. D. Erande, P. Klahn, M. Jin, M. Aujay, J. Sandoval, J. Gavrilyuk and D. Vourloumis, *J. Am. Chem. Soc.*, 2016, **138**, 1698–1708; (*e*) E. G. Tse, S. D. Houston, C. M. Williams, G. Paul Savage, L. M. Rendina,

I. Hallyburton, M. Anderson, R. Sharma, G. S. Walker, R. Scott Obach and M. H. Todd, *J. Med. Chem.*, 2020, **63**, 11585–11601; (*f*) P. K. Mykhailiuk, *Org. Biomol. Chem.*, 2019, **17**, 2839–2849; (*g*) M. A. M. Subbaiah and N. A. Meanwell, *J. Med. Chem.*, 2021, **64**, 14046–14128; (*h*) E. T. Warda, M. B. El-Ashmawy, E.-S. E. Habib, M. S. M. Abdelbaky, S. Garcia-Granda, S. Thamptharon and A. A. El-Emam, *Sci. Rep.*, 2022, **12**, 21058.

35 A. N. Bismillah, J. Sturala, B. M. Chapin, D. S. Yufit, P. Hodgkinson and P. R. McGonigal, *Chem. Sci.*, 2018, **9**, 8631–8636.

36 G. Schröder and W. Witt, *Angew Chem. Int. Ed. Engl.*, 1979, **18**, 311–312.

37 (*a*) A. N. Bismillah, T. G. Johnson, B. A. Hussein, A. T. Turley, P. K. Saha, H. C. Wong, J. A. Aguilar, D. S. Yufit and P. R. McGonigal, *Nat. Chem.*, 2023, **15**, 615–624; (*b*) B. A. Hussein, W. Maturi, M. K. Rylands, A. N. Bismillah, Y. Wen, J. A. Aguilar, R. Ayub, C. D. Rankine and P. R. McGonigal, *Chem. Sci.*, 2024, DOI: **10.1039/D4SC03699A**.